Universidade de Brasília
Instituto de Geociências
Programa de Pós-graduação em Geologia

Caracterização geoquímica e isotópica do magmatismo andino entre os 36° e 42°S em Neuquén, Argentina: implicações na evolução crustal do Arco Andino

Geochemical and isotopic characterization of Andean magmatism between 36° and 42°S in Neuquén, Argentina: implications for the crustal evolution of the Andean Arc

OMAR SEBASTIAN ASSIS

Tese de Doutorado Nº 210

Orientador: Profa. Dra. Natalia Hauser
Co-orientador: Profa. Dra. Claudia Beatriz Zaffarana

Brasília, 9/dezembro/2024

Universidade de Brasília
Instituto de Geociências
Programa de Pós-graduação em Geologia

Caracterização geoquímica e isotópica do magmatismo andino entre os 36° e 42°S em Neuquén, Argentina: implicações na evolução crustal do Arco Andino

OMAR SEBASTIAN ASSIS

Tese apresentada ao Programa de Pós-Graduação em Geologia – Instituto de Geociências – IG da Universidade de Brasília – UnB como requisito parcial obrigatório para a obtenção do título de Doutor em Geologia.

Área de concentração: Geologia Regional

Orientador: Profa. Dra. Natalia Hauser

Comissão Examinadora:

Prof. Dr. Valmir Souza (IG/UnB);
Prof. Dr. Miguel Basei (USP);
Prof. Dr. Andrés Folguera (IDEAN/UBA);
Prof. Dr. Federico Alberto Cuadros (IG/UnB);
Profa. Dra. Catarina Toledo (Suplente IG/UnB).

Ficha catalográfica elaborada automaticamente,
com os dados fornecidos pelo(a) autor(a)

A848c

Assis, Omar Sebastian
Caracterização geoquímica e isotópica do magmatismo andino entre os 36° e 42°S em Neuquén, Argentina: implicações na evolução crustal do Arco Andino / Omar Sebastian Assis; orientador Natalia Hauser; co-orientador Claudia Beatriz Zaffarana. -- Brasília, 2024.
266 p.

Tese(Doutorado em Geologia) -- Universidade de Brasília, 2024.

1. Orogenia Andina. 2. Cretáceo-Paleogeno. 3. granitóide. 4. Geocronologia. 5. Isótopos Sr-Nd-Hf. I. Hauser, Natalia, orient. II. Zaffarana, Claudia Beatriz, co-orient. III. Título.

AGRADECIMENTOS

Em primeiro lugar, às minhas orientadoras de doutorado, Natalia e Claudia, porque sem a sua inestimável ajuda, orientação e conselhos nada disto seria possível, obrigado por me apoiarem sempre e por me contagiarem com a sua paixão pela geologia. Agradeço sinceramente todo esse tempo compartilhado, o conhecimento, as saídas de campo, o trabalho em laboratório, aprendi muitas coisas que me tornaram um cientista e uma pessoa melhor.

O presente trabalho foi realizado com apoio da Coordenação de Aperfeiçoamento de Pessoal de Nível Superior-Brasil (CAPES) – Código de Financiamento 001.

Ao Uwe, que sempre foi prestativo e disposto a nos ajudar no que precisássemos, e a todos os funcionários da LEGGA e do Instituto de Geociências que nos deram espaço para crescer durante todos esses anos.

Às pessoas que conheci nestes anos, com quem convivi e partilhei o trabalho, a casa e o café que por vezes é tão necessário, pessoas que me ajudaram quando cheguei a um país estranho que nunca tinha visitado e que me fizeram sentir em casa. Principalmente Naza, Yuri, Gabi, Raissa, Andy, Marcel, Carol, Arnold, Juliana, Camila, Julia, Igor, André, Ángel, Valentina, Daniela, Arianne, Yeimmy, Gabriella, Enzo, Gerardo, Caro, Elisa, Wilson, Tiago, Luisa, María, Meyre, Aderson, Adriana, Steffanie, Valéria, Georgina, Sofy e Débora.

Aos meus amigos de longa data, que me acompanham desde Argentina e nunca me deixam esquecer, Bruno, Andrea, Cristian, Danilo, Fede, Laura, Sofy, Sil, Steff, Enzo e Martín.

E principalmente à minha família e aos meus irmãos, de quem sinto falta todos os dias que estou ausente, que sempre foram meu apoio e espero revê-los em breve.

RESUMO

O oeste da Província de Neuquén entre os 36-39°S e 70-71°W, Argentina, faz parte hoje dos Andes Centrais Austrais. Neste setor, o ciclo Andino (Jurássico-recente) encontra-se muito bem representado, entanto que o ciclo Gondwánico (Permiano-Triássico) encontra-se pontualmente representado em determinados setores, como no anticlinal da Cordillera del Viento, uma estrutura compressiva terciaria.

A ruptura do continente Gondwana durante o Triássico deu origem à formação de batólitos e um grande magmatismo efusivo, o Grupo Choiyoi. Posteriormente, mudanças na horizontalização da placa oceânica produziram vários pulsos de compressão e extensão que resultam no surgimento dos Andes no início do Jurássico e na migração do arco magmático para o leste coo produto das mudanças no ângulo de subducção da placa oceânica.

O presente trabalho tem como objetivo o entendimento da evolução crustal relacionado com o ciclo Andino. Técnicas de mapeamento, AMS, geoquímica, geoquímica isotópica (Sr-Nd), geocronologia (U-Pb/Hf em zircão) e AFT, dos corpos ígneos associados principalmente com o Ciclo Andino contribuirão no entendimento de processos associados diretamente com: câmbios no ângulo de subducção da placa oceânica, erosão por subducção, subducção de sedimentos, contaminação com crosta inferior e até inferir as características do manto, por exemplo se ele foi previamente metasomatizado. Todos esses processos em conjunto ajudaram no traçado dos processos de evolução crustal dos Andes no oeste de Neuquén, Argentina.

Em função do significado tectônico, a área de estudo e em consequência os objetivos específicos, foram divididos em três partes, de norte para o sul: I) parte norte, Cordillera del Viento, onde existe um registro quase que continuo entre ciclo Gondwánico e Andino, II) parte central Faixa de Naunauco que representa o magmatismo mais oriental ligado com a horizontalização da placa oceânica num evento compressivo Cretáceo-Paleogeno e III) parte sul, na área de Villa Pehuenia e nos lagos Ñorquinco e Pulmarí, que representa o magmatismo no mesmo eixo do arco no final do Cretáceo. A Cordillera del Viento, uma estrutura anticlinal é um dos poucos lugares onde está representado o embasamento, as rochas do ciclo Gondwânico, um evento extensivo intermediário e finalmente as

rochas do ciclo Andino. Nesta área encontram-se os tonalitos Varvarco e Butalón de idade Cretáceo-Paleógena, representantes do ciclo Andino. Na área de Naunauco, que representa a parte oriental do arco, foram encontradas rochas intrusivas nos sedimentos da Bacia Neuquina, que fazem parte do Cinturão de dobras e cavalgamentos de Agrio. O limite sul deste magmatismo está representado na área de Villa Pehuenia e nos lagos Ñorquinco e Pulmarí, pelo Granodiorito Paso de Icalma, Granito Moquehue e o desenvolvimento do Complexo Ígneo-Metamórfico Aluminé (CIMA).

Os resultados obtidos foram apresentados em função de dois artigos. O Artigo 1, representa os resultados obtidos na Cordillera del Viento, especificamente nos corpos do ciclo Andino, tonalitos de Varvarco e Butalón. Observações de campo e análises petrográficas indicam que a hibridização foi o principal processo de diversificação magmática que controlou a geração e evolução dos plútons com características cálcio-alcalinas do tipo I. Dados combinados de traços de fissão em apatita e microssonda eletrônica indicam profundidades de locação raças (12 km) e condições de resfriamento rápido (330°C/My). A análise da anisotropia de susceptibilidade magnética indica que as fábricas são puramente magmáticas, sem a presença de deformações sobrepostas, ou seja, devidas apenas à câmara magmática. Os dados obtidos no Artigo 2, de caracter mais regional, mostrou que em geral, o Jurássico na região foi caracterizado por rochas ígneas e vulcânicas ácidas, com uma tendência alc-alcalina de alto-K e principalmente características de rochas de intraplaca. Os valores de (ƐNd)i e (ƐHf)i apresentam um aumento isotópico em direção ao Cretácico-Paleogeno, com um aumento acentuado em 67 Ma. Essas rochas Cretácico-Paleogenas são principalmente rochas plutônicas e vulcânicas intermediárias, cálcio-alcalinas e com assinatura típica de arco vulcânico, e apresentam valores mais positivos de isótopos ($Ɛ_{Nd}$)i e ($Ɛ_{Hf}$)i.

Palavras-chave: Orogenia Andina; Cretáceo-Paleogeno; granitóide; Geocronologia; Isótopos Sr-Nd-Hf.

ABSTRACT

The west part of the Neuquén Province, between 36-39°S and 70-71°W, Argentina, today is part of the Southern Central Andes. In this sector, the Andean cycle (Jurassic to recent) is well represented, while the Gondwanic cycle (Permian-Triassic) is occasionally represented in certain sectors, such as in the Cordillera del Viento anticline, a tertiary compressive structure.

The rupture of the Gondwana continent during the Triassic gave rise to the formation of batholiths and a large effusive magmatism, the Choiyoi Group. Later, changes in the horizontalization of the oceanic plate produced several pulses of compression and extension that result in the emergence of the Andes in the early Jurassic and the migration of the magmatic arc to the east as a product of changes in the subduction angle of the oceanic plate.

The aim of the present work is to understand the crustal evolution related to the Andean cycle. Mapping techniques, AMS, geochemistry, isotopic geochemistry (Sr-Nd), geochronology (U-Pb/Hf in zircon) and AFT, of igneous bodies mainly associated with the Andean Cycle will contribute to the understanding of associated processes directly with: changes in the subduction angle of the oceanic plate, erosion by subduction, sediment subduction, contamination with lower crust and even inferring the mantle characteristics, for example if it was previously metasomatized. All these processes together helped in tracing the crustal evolution processes of the Andes at the western portion of Neuquén Province, Argentina.

On the basis of the tectonic significance, the study area, and the specific objectives, were divided into three parts from north to south: I) northern part, Cordillera del Viento, where there is an almost continuous record between the Gondwánic and Andean cycles, II) central part were the Naunauco Belt represents the easternmost magmatism connected with the horizontalization of the oceanic plate in a Cretaceous-Paleogene compressive event and III) southern part, in the area of Villa Pehuenia and in the Ñorquinco and Pulmarí lakes, which represents the magmatism on the same axis of the arc in the late Cretaceous. The Cordillera del Viento, an anticline structure, is one of the few places where the basement, the rocks of the Gondwanic cycle, an extensive intermediate event and finally the rocks of the Andean cycle are represented. In

this area are the Huingancó Granite belonging to the Gondwanic cycle and the Cretaceous-Paleogenous tonalites Varvarco and Butalón, representatives of the Andean cycle. In the area of Naunauco, which represents the eastern part of the arc, intrusive rocks were found in the sediments of the Neuquina Basin, which are part of the Agrio fold and thrust belt. The southern limit of this magmatism is represented in Villa Pehuenia and in the lakes Ñorquinco and Pulmarí, by the Granodiorite Paso de Icalma, Granite Moquehue and the development of the Aluminé Igneous-Metamorphic Complex (CIMA).

The results obtained were divided into three articles. Article 1 represents the results obtained in the Cordillera del Viento, specifically in the bodies of the Andean cycle, Varvarco and Butalón tonalites. Field observations and petrographic analysis indicate that hybridization was the main diversification magmatic process that controlled the generation and evolution of these plutons with calc-alkaline I-type characteristics. Combined fission track data on apatite and microprobe analyses indicate race location depths (12 km) and rapid cooling conditions (330°C/My). The analysis of magnetic susceptibility anisotropy indicates that the fabrics are purely magmatic, without the presence of superimposed deformations, that is, controlled only by process in the magmatic chamber. The data obtained in Article 2, of a more regional nature, showed that in general, the Jurassic in the region was characterized by acidic igneous and volcanic rocks, with a high-K alkali trend and mainly intraplate rock characteristics. The values of (ƐNd)i and (ƐHf)i show an isotopic increase towards the Cretaceous-Paleogene, with a sharp increase at 67 Ma. These Cretaceous-Paleogene rocks are mainly intermediate plutonic and volcanic rocks, calc-alkaline and with a typical volcanic arc signature, and present more positive values of isotopes ($Ɛ_{Nd}$)i and ($Ɛ_{Hf}$)i.

Keywords: Andean Orogeny; Cretaceous-Paleogene; granitoids; Geochronology; Sr-Nd-Hf isotopes.

SUMÁRIO

1 INTRODUÇÃO 2

1.1 Objetivos 4
1.1.1 Objetivos Gerais 4
1.1.2 Objetivos Específicos 5

1.2 Área de Estudo 7

1.3 Ciclos orogênicos Gondwánico e Andino na Provincia de Neuquén 10

1.4 Estudo dos Flare-up e Steady-state 13

1.5 Geologia Regional 15
1.5.1 Cordillera del Viento (Varvarco, Butalón Norte e Huingancó) 15
1.5.2 Naunauco 16
1.5.3 Zona de los lagos Aluminé-Moquehue y Ñorquinco-Pulmarí 17

2 MATERIAIS E MÉTODOS 21

2.1 Pesquisa Bibliográfica 21

2.2 Etapa de Campo 21

2.3 Análises de ASM 22

2.4 Análises Petrográficas 22

2.5 Análises Geoquímicas de elementos maiores, menores e traços 23

2.6 Análises por Microssonda Eletrônica 24

2.7 Análises Isotópicas: Sm-Nd em rocha total 24

2.8 Análises Isotópicas: Sr-Sr em rocha total 27

2.9 Análises Isotópicas: U-Pb em zircão 28

2.10 Análise de traços de fissão em apatita 34

3 ARTIGO 1: "EMPLACEMENT CONDITIONS AND EXHUMATION OF THE VARVARCO TONALITE AND ASSOCIATED PLUTONS FROM THE CORDILLERA DEL VIENTO, SOUTHERN CENTRAL ANDES" 38

3.1 Introduction 40

3.2 Geological and structural framework 43

3.3 Analytical methods 46
3.3.1 Anisotropy of magnetic susceptibility (AMS) 49

3.3.2 Apatite fission track dating (AFT) 50
3.3.3 Electron microprobe analysis 51

3.4 Results ... 51
3.4.1 ASTER data, field observations and petrography 51
3.4.2 Plagioclase, amphibole and biotite compositions for the Varvarco Tonalite 61
3.4.3 Anisotropy of magnetic susceptibility (AMS) 67
3.4.4 Mean susceptibility and minerals responsible for the AMS ellipsoids 70
3.4.5 Apatite fission tracks (AFT) results 73

3.5 Discussion ... 74
3.5.1 Magma hybridisation processes in the I-type Varvarco and Butalón intrusive bodies 74
3.5.2 Parental melt conditions of the Varvarco Tonalite 78
3.5.3 Cooling history and exhumation of the Late Cretaceous and Paleogene plutons 84
3.5.4 Magnetic fabrics of magmatic origin in the Late Cretaceous and Paleogene plutons 87

3.6 Conclusions ... 89

3.7 Acknowledgements ... 90

3.8 Competing Interest ... 90

3.9 Supplementary Material ... 90

3.10 References ... 91

4 ARTIGO 2: JURASSIC AND PALEOGENE ANDEAN MAGMATIC EVOLUTION OF THE SOUTHERN CENTRAL ANDES (36º-42ºS) THROUGH U-Pb/Hf, Sr-Nd AND GEOCHEMICAL DATA ... 105

4.1 Introduction ... 108

4.2 Regional geology of Andes between 36-42ºS ... 112
4.2.1 Basement of Andean Arc between 36-42°S 113
4.2.2 The Andean cycle 114

4.3 Analytical methods ... 118
4.3.1 Geochemical analyses 118
4.3.2 Bulk rock Sr-Nd isotopes 119
4.3.3 Zircon U-Pb dating 120
4.3.4 Lu-Hf isotopes on zircon 121
4.3.5 REE in zircon 122

4.4 Field and petrographic descriptions ... 123
4.4.1 Early Andean Cycle: extensional/transtensional stage 123
4.4.2 Andean Cycle: Late Cretaceous-Paleogene compressive/transpressive stage 126

4.5 Whole rock major- and trace-element geochemistry ... 128

4.5.1 Early Andean Cycle during the extensional/transtensional stage 128
4.5.2 Andean Cycle during the compressive/transpressive stage 132

4.6 U–Pb ages and Hf isotopes on zircon ... 136
4.6.1 The Host Granite: GR4 microgranite 136
4.6.2 Moquehue Granite (NPB): MOQUE granite 143
4.6.3 Icalma Granodiorite (NPB): ICAL4 granodiorite 147
4.6.4 Varvarco tonalite: VAR6 148
4.6.5 Varvarco dioritic dike: D2 149
4.6.6 Butalón tonalite: BU4 150

4.7 Sr-Nd isotopes ... 150
4.7.1 Early Andean Cycle during the extensional/transtensional stage 153
4.7.2 Andean Cycle during the compressive/transpressive stage 153

4.8 Trace elements in zircon geochemical data ... 155
4.8.1 The Host Granite: GR4 microgranite 155
4.8.2 Moquehue Granodiorite (NPB): MOQUE granodiorite 155
4.8.3 Icalma Granodiorite (NPB): ICAL4 granodiorite 156
4.8.4 Varvarco tonalite: VAR6 156
4.8.5 Varvarco dioritic dike: D2 157
4.8.6 Butalón tonalite: BU4 158

4.9 Discussion ... 158
4.9.1 Isotopic magmatic characterization of the Early Andean and Andean Cycles 159
4.9.2 Magmatic fertility and crustal thickness 168
4.9.3 Crustal evolution of the Andes between 38-43°S 169
4.9.4 Paleotectonic configuration 172

4.10 Conclusions ... 176

4.11 Acknowledgments ... 177

4.12 References ... 177

MATERIAL COMPLEMENTAR PARA O ARTIGO 2 ... 193

5 CONCLUSÕES PARCIAIS ... 195

5.1 Artigo 1 ... 195

5.2 Artigo 2 ... 195

6 CONCLUSÕES FINAIS E RECOMENDAÇÕES ... 198

REFERENCIAS ... 200

ARTIGOS PUBLICADOS EM COLABORAÇÃO ... 207

CAPÍTULO 1
INTRODUÇÃO

1 INTRODUÇÃO

A história geológica do Paleozóico e Mesozóico da zona cordilherana do norte da Patagônia (Cingolani et al. 1991; Hervé et al. 2018; Giacosa et al. 2014; Pankhurst et al. 2006 e García Sansegundo et al. 2009) pode ser dividida em pelo menos quatro eventos tectono-metamórficos e magmáticos: I) o ciclo orgênico Famatiniano (Ordoviciano-Devoniano), II) o ciclo orogênico Gondwánico (Carbonífero-Permiano), III) o ciclo extensional Triássico-Jurássico tardio e IV) o ciclo orogênico Andino, um evento tectônico e magmático mais jovem (Jurássico Médio até o presente).

A Orogenia Gondwánica foi desenvolvida entre 350-280 Ma e caracterizou-se por um magmatismo voluminoso e pela formação de batólitos e campos ignimbríticos (Llambías et al., 2007; Sato et al., 2008 entre outros). A orogenia Andina se desenvolveu a partir de 180 Ma, como consequência da migração para leste do arco magmático com a subsequente formação de batólitos, devido a uma diminuição na velocidade de subducção da fossa oceânica (*negative trench rollback velocity*). Esse evento controlou a extensão generalizada que dominou na evolução tectônica dos Andes neste período (Parada et al., 2001; Pankurst et al., 1999, entre outros).

Cada uma dessas orogenias resultou em numerosos corpos de granito e extensos campos de rocha vulcânica que permitem interpretar a magnitude desses eventos. Exemplos disso são a província ígnea de Choiyoi (Llambías e Sato 2011), que representa o pico do magmatismo para o ciclo Gondwânico e que foi desenvolvida em uma extensão de mais de 500.000 km^2, e o desenvolvimento durante o Cretáceo-Paleógeno do *Cinturón Andesítico Paleógeno Naunauco* (Llambías e Aragón 2011), composto de vários pequenos plutons alinhados N-S, produto da migração do arco durante o ciclo Andino para leste.

A presente tese de doutorado tem por objetivo estudar a evolução do ciclo magmático Andino entre os 36° e 39° S, no oeste da Argentina, Neuquén. A área encontra-se hoje inserida no contexto da Zona Vulcânica Sul dentro dos *Andes Centrales Australes* (Ramos 2008). Três áreas foram selecionadas devido ao contexto tectônico na evolução do Arco Andino. As mesmas são descritas de norte a sul.

Na parte norte da área de estudo, aproximadamente aos 36.5°S e 71°W encontra-se a *Cordillera del Viento*, uma estrutura da tectônica terciária compressiva, na qual são expostas rochas do ciclo Gondwánico (evento II), rochas relacionadas com a fase extensional Triássica-jurássica (evento III) e rochas intrusivas relacionadas ao ciclo Andino (evento IV). A área foi escolhida devido a: 1) relação espaço-temporal destes três eventos, permitirá entender os processos de evolução crustal entre os ~270 e ~70 Ma e 2) as rochas do ciclo Andino estão relacionadas com o *Cinturón Andesítico Paleógeno Naunauco* (também analisada na parte central e mais oriental da área de estudo).

Na parte central, entre os 37.5°S e 70°W, encontra-se rochas plutônicas e vulcânicas da área de Naunauco, na parte sul da *Cordillera del Viento.* Essas rochas representam *o* magmatismo mais oriental Cretáceo Tardío-Paleogeno reconhecido na área. O mesmo estaria relacionado com a etapa de tectônica compressiva devido ao processo de horizontalização da placa oceânica durante a construção dos Andes. O estudo das rochas que afloram na área de Naunauco, junto com aquelas que afloram na parte norte, ambas como parte do *Cinturón Andesítico Paleógeno Naunauco*, permitirá entender quais foram os processos magmáticos envolvidos na geração de rochas intrusivas e vulcânicas durante esta etapa na parte mais oriental do arco.

Na parte sul, na área de Villa Pehuenia, entre os 38.5°S e 71°W, encontra-se o magmatismo mais ocidental da área de estudo desta tese. Assim o estudo desta área trará informações valiosas sobre os mecanismos envolvidos na geração de rochas no próprio eixo do arco magmático. Essa região não teria experimentado horizontalização da placa oceânica durante a fase compressiva Cretáceo tardía - Paleogena.

Finalmente a comparação entre as três áreas hoje inseridas na Zona Vulcânica Sul dos *Andes Centrales Australes* brindará a possibilidade de entender a evolução crustal (temporal e espacial) do arco Andino desde o início do Jurássico até a primeira fase compressiva do Cretáceo Tardío -Paleogeno. Um dos pontos centrais desta tese é relacionar os dados obtidos nas três áreas com os episódios magmáticos de *flare-up* e steady-state reconhecidos normalmente durante a evolução de um arco. Os eventos de *flare-up* (Ducea et al. 2015), correspondem a episódios de curta duração (10-20 Ma), mas produtores de um grande volume de magmas e corpos plutônicos mais

evoluídos. Um exemplo muito estudado e o batólito da Serra Nevada (Ducea et al. 2015). Esses eventos de *flare-up* são separados por eventos normais de magmatismo denominados de steady-state. A evolução de um arco magmático e dos eventos de *flare-up* e steady-state associados, foram modelados nos últimos anos (Chapman et al., 2019, Martinez Ardilla et al., 2019, Paterson and Ducea 2015) através de geoquímica, geoquímica isotópica (Sr, Nd e Pb), isótopos estáveis ($\delta_{18}O$) e geocronologia (normalmente U-Pb e Lu-Hf em zircão). Nesta tese parte destas ferramentas serão utilizadas no entendimento da evolução crustal do Arco Andino.

1.1 Objetivos

1.1.1 Objetivos Gerais

O objetivo principal desta pesquisa de doutorado é realizar um estudo do magmatismo e evolução crustal durante o ciclo orogênico Andino (Jurássico até o presente) da porção sul dos Andes Centrais, na área de Neuquén. Este estudo envolve as condições de intrusão, fontes dos magmas, geocronologia (U-Pb/Hf em zircão) e características geoquímicas e isotópicas (Sr-Nd) de vários plútons e rochas vulcânicas associadas ao ciclo em pelo menos 3 contextos geológicos diferentes: I e II) relacionados a fase compressiva do Arco Andino em duas posições diferentes no arco e III) relacionado a subducção normal no mesmo eixo do arco.

Em função dos dados geoquímicos e isotópicos obtidos e comparando as três áreas processos como câmbios no ângulo de subducção da placa oceânica, processos de erosão por subducção, presença de um manto previamente metasomatizado, possibilidade de subducção de sedimentos, contaminação com crosta inferior ou mesmo geometria da placa continental serão abordados.

Serão empregadas técnicas como: anisotropia de susceptibilidade magnética (ASM), geoquímica de elementos maiores e traços em rocha total, microssonda eletrônica, geoquímica isotópica (Sr-Nd) em rocha total e geocronologia U-Pb em zircão e traços de fissão em apatita. A informação adquirida possibilitara o entendimento da evolução do arco entre os 36 e 39ºS em termos de composição e principais processos de diversificação magmática

envolvidos; permitindo, além disso, a comparação dessas características com o ciclo Gondwánico, também desenvolvido nessas latitudes.

1.1.2 Objetivos Específicos

Os objetivos específicos serão apresentados em dois contribuições científicas da seguinte forma:

Artigo 1: *Caracterização do Ciclo Andino nas áreas de Varvarco e Butalón Norte. O trabalho foi submetido ao Geological Magazine em março de 2022.*

Objetivo principal: entendimento dos mecanismos de colocação e exumação dos corpos ígneos satélites de *Varvarco e Butalón* a ~130-150 km devido a expansão para final do Cretáceo-Paleogeno, do arco magmático.

- Mapeamento e obtenção de amostras do Ciclo Andino nas áreas do Tonalito Varvarco, Aplito Radales e Tonalito Butalón bem como suas rochas hospedeiras, enclaves máficos microgranulares e diques associados.
- Caracterização da colocação dos corpos através de anisotropia de susceptibilidade magnética no Tonalito Varvarco, rocha de caixa e fácies associadas.
- Petrografia dos plutóns estudados e das rochas metamórficas do embasamento, para classificá-las e avaliar processos de diversificação magmática como misturas (presença de enclaves) ou assimilação (xenólitos).
- Obtenção de idades de exumação, através da análise de traços de fissão em apatita do Tonalito Varvarco e Aplito Radales.
- Obtenção de parâmetros de temperatura e pressão através da Análise de microssonda eletrônica em anfibólio e biotita do Tonalita Varvarco.
- Integração da informação obtida para determinar a história de exumação na área.

Artigo 2:

Objetivo principal: *Comparação entre os periodos Jurássico e Cretáceo-Paleógeno do ciclo orogênico Andino nas áreas de Varvarco, Butalón Norte, Naunauco e Villa Pehuenia. Este trabalho encontra-se em etapa de elaboração.*

- Mapeamento e obtenção de amostras do Ciclo andino (Grupo Naunauco, Formação La Premia, Granodiorito Lago Moquehue y Granodiorito Paso Icalma).
- Petrografia e descrição das amostras e texturas.
- Geoquímica de elementos maiores e traços das amostras. Os resultados serão comparados com aqueles obtidos no Artigo 1, para determinar suas principais assinaturas geoquímicas e fazer uma comparação regional com trabalhos de outros autores.
- Análise isotópica Sr-Nd em rocha total das amostras coletadas, somadas às amostras do Artigo 1, para caracterizar as fontes e fazer uma comparação regional com outros autores.
- Obtenção das idades de cristalização U-Pb em zircão das amostras, somadas às amostras do Artigo 1, para inseri-los em um contexto geológico correto.
- Compilar um banco de dados U-Pb em zircão de corpos plutônicos na área, para determinar os momentos em que poderiam ter desenvolvido estágios de *flare-ups* ou *steady-state* porção sul dos Andes.

1.2 Área de Estudo

A área de estudo encontra-se inserida entre os 36-39°S e 70-71°W (Figura 1). Inclui vários plútons e rochas vulcânicas dentro da província de Neuquén, Argentina, correspondendo a diferentes províncias geológicas e características morfoestruturais.

Parte norte da área de estudo:

Corresponde as rochas que afloram na *Cordillera del Viento*. A mesma localiza-se no norte da *Precordillera Neuquina*. A *Cordillera del Viento*, é uma característica morfoestrutural de sentido N-S que corresponde a um anticlinal erodido, no qual estão expostos o embasamento e as rochas da bacia Neuquina. É delimitado a oeste pela fossa Loncopué, depressão tectônica de idade quaternária; a leste pelo Cinturão de dobras e cabalgamentos de Chos Malal e a sul pelo lineamento Cortaderas, uma estrutura linear e corticais antiga reativada durante a orogenia andina.

O Tonalito Varvarco, o Aplito Radales e as rochas hospedeiras intrusivas de idade jurássica, encontram-se ao norte da *Cordillera del Viento* perto da cidade de Varvarco, 17 km a noroeste da cidade de Las Ovejas. Tem acesso pelas rotas nacionais Nº22 e Nº40 no sentido norte e seguindo as rotas provinciais nº43. Aproximadamente 20 km ao sul da cidade de Varvarco, pela Rota Provincial Nº39, perto do povoado de Butalón Norte, aflora o Tonalito Butalón. Seguindo pela mesma rota e 30 km ao sul, chega-se na cidade de Huingancó, onde aflora o granito gondwánico que recebe o mesmo nome.

Parte central da área de estudo:

Representa a parte mais oriental do magmatismo andino e encontra-se inserida no domínio do Cinturão de dobras do Agrio. A 90 km a sudeste da cidade de Huingancó, e saindo da Precordillera Neuquina Norte se acessa o domínio do Cinturão de dobras do Agrio, onde encontra-se a cidade de Naunauco. Aqui, foram coletadas amostras de rochas vulcânicas do Grupo Naunauco e da Formação La Premia correspondentes a Ciclo Andino.

Parte sul da área de estudo:

Encontra-se mais para oeste, quase no limite com Chile, e encontra-se inserida no domínio da Cordillera Patagónica. A 230 km ao sudoeste da cidade de Naunauco pelas rotas Nº144, 242 e 23, e entrando no domínio da Cordillera Patagónica encontra-se a cidade de Villa Pehuenia. Em frente estão os lagos glaciais Moquehue, onde aflora o Granodiorito Moquehue; e Lago Aluminé, onde foi coletado o Granodiorito Puesto Icalma.

Em direção ao sul de Villa Pehuenia, aproximadamente 56 km ao longo da rota Nº23 e 11 está o Lago Pulmarí e, 15 km ao oeste do último seguindo a rota Nº11, está o Lago Ñorquinco. Ambos os locais serão visitados no próximo trabalho de campo para o desenvolvimento dos objetivos de um terceiro artigo não apresentado nesta tese.

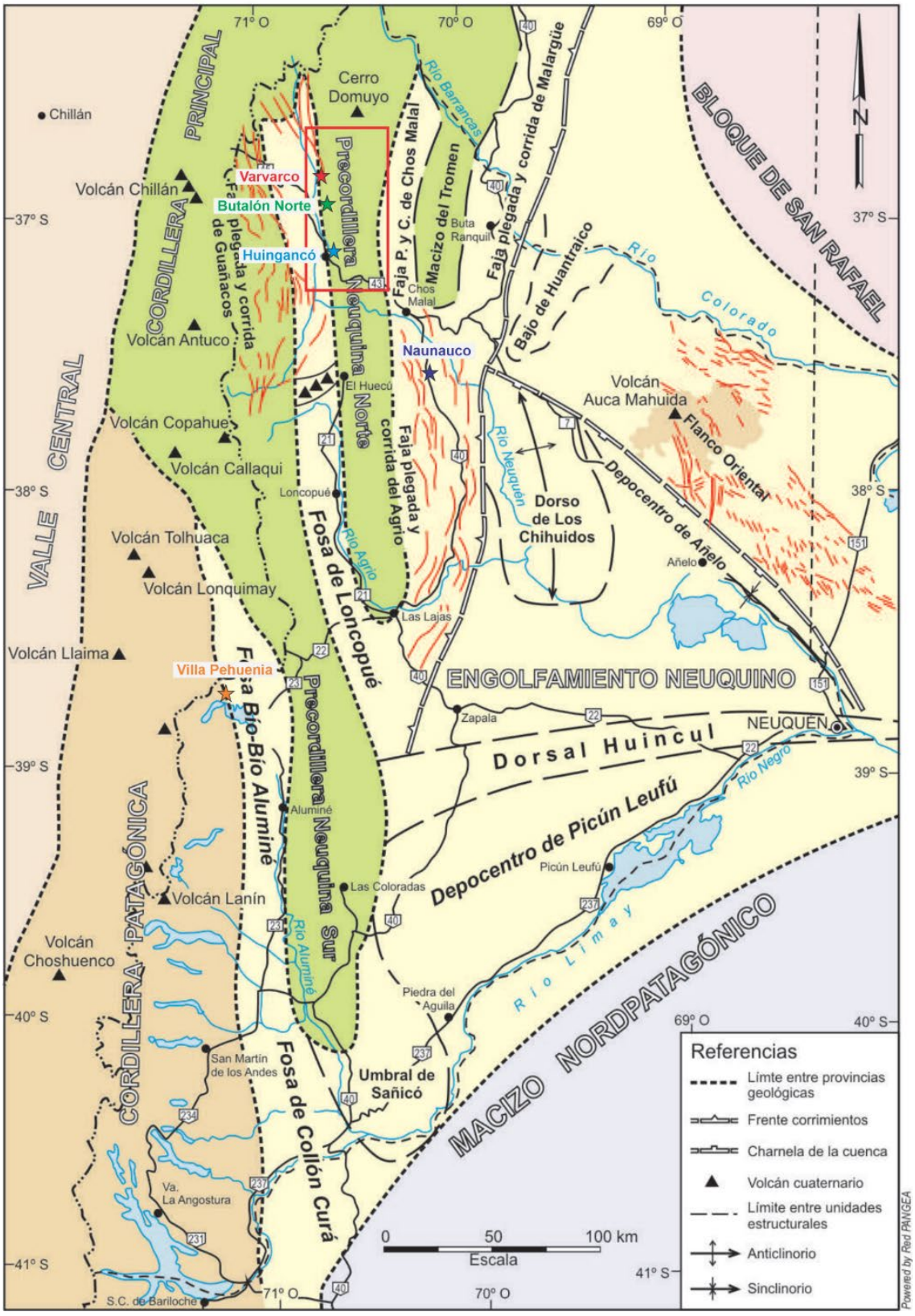


Figura 1: Províncias geológicas do norte da Patagonia: *Cordillera Principal*, *Cordillera Patagónica* e Engolfamiento Neuquino. As estrelas indicam as áreas de estudo: Varvarco (67 Ma), Butalon Norte (67 Ma), Huinganco (283 Ma) e Naunauco (70 Ma). A caixa vermelha indica a localização da *Cordillera del Viento*. Tomado e modificado de Ramos et al. (2011).

1.3 Ciclos orogênicos Gondwánico e Andino na Provincia de Neuquén

A orogenia Gondwánica é caracterizada por um magmatismo volumoso, desenvolvido desde o Carbonífero até o Triássico Inferior. Por esse motivo, as unidades estratigráficas para essa idade correspondem principalmente a rochas ígneas (Llambías et al. 2007). Esse estágio abrange dois processos tectônicos, que correspondem ao final da conformação do continente de Gondwana e ao início de sua subsequente ruptura. Estas são I) a fase orogênica de San Rafael, durante inícios do Permiano, e II) um estágio de rifte que produz fraturas profundas no Triássico Médio. A transição entre esses dois eventos é conhecida como discordância Huárpica (Azcuy e Caminos, 1987). Durante o colapso orogênico após a fase orogênica de San Rafael, o magmatismo se desenvolveu em câmaras magmáticas superficiais, com formação de batólitos. O estágio de rifte, foi caracterizado por emprazamento de rochas menos evoluídas com uma origem mais semelhante ao do manto (Llambías et al. 2007). A fase diastrófica Huárpica deixou uma superfície de erosão, o que facilitou a locação de plútons do Permiano (Llambías e Sato 2011), e posteriormente os cretáceos, como o Tonalito Varvarco.

O pico mais alto de atividade magmática neste ciclo é representado pela província magmática Choiyoi do Permiano ao Triássico Inferior (Kay 1989; Llambías e Sato 2011), que se estendeu por mais de 500.000 km^2 (Fig. 3). Os afloramentos na província de Neuquén são muito escassos ao norte, limitando-se à *Cordillera del Viento*, reaparecendo na parte sudoeste aproximadamente a partir de Villa Pehuenia.

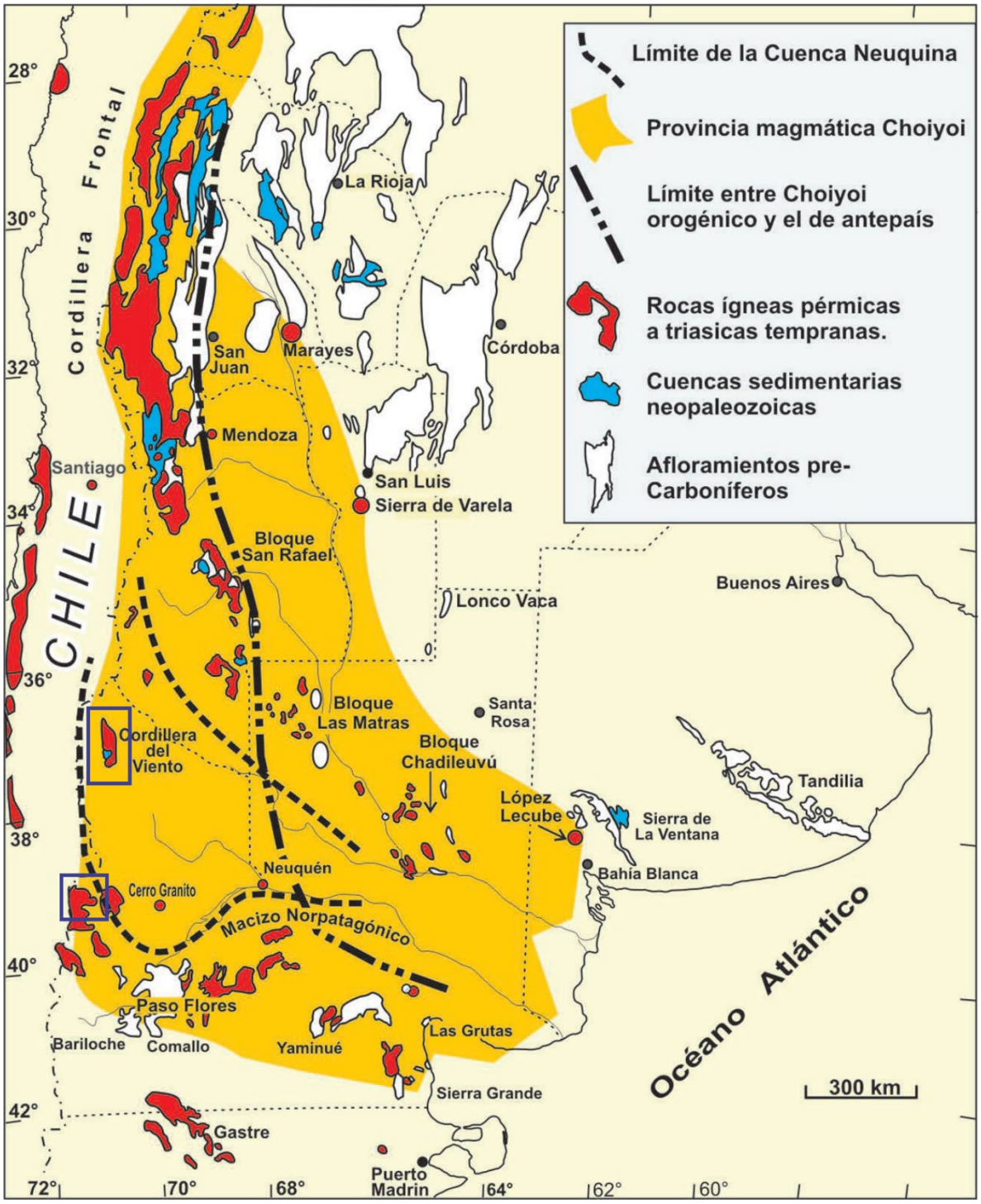


Figura 2: Extensão dos afloramentos província magmática de Choiyoi (Permiano Inferior ao Triássico Inferior), cuja extensão máxima foi destacada em amarelo. As caixas azuis indicam as áreas de estudo deste trabalho. Tomado de Llambías e Sato (2011).

A orogenia andina teve uma ampla extensão no território argentino, afetando muitas das unidades depositadas durante o Ciclo Gondwanico, entre outras. Foi caracterizada por vários pulsos de compressão, seguidos de

extensão, variando de 180 Ma até hoje (Ramos 2009). A horizontalização da loça subdividida durante o Mesozóico e o Cenozóico é de grande importância para a elevação da cadeia andina, além de causar interrupção e migração do magmatismo para o leste (Ramos et al. 2011). Essa migração do arco produziu novos corpos ígneos agrupados no chamado *Cinturón Andesítico Paleógeno Naunauco* (Llambías e Aragón 2011). Essa configuração da loça oceânica não era única e vários segmentos podem ser reconhecidos nos Andes (Ramos 2009).

Do ponto de vista estrutural, na área de estudo existem duas estruturas pré-andinas com um curso oblíquo ao atual trem dos Andes: o lineamento Cortaderas de direção NW-SE (Ramos e Kay 2006) e a Dorsal de Huincul de direção EW (Turic et al. 1987). Ambas as estruturas são interpretadas como características corticais antigas que foram reativadas durante a orogenia andina (Cristallini e Allmendinger 2000; Mosquera and Ramos, 2006; Gregori et al., 2008, 2013; González et al., 2021).

A *Cordillera del Viento* está localizada ao norte do lineamento Cortaderas, mas estruturas paleozóicas NW-SE paralelas a este lineamento também foram reconhecidas naquela região, o que estaria associado à inversão tectônica positiva do *rift* Gondwânico (Giacosa et al. 2014; Sagripanti et al. 2014). Por outro lado, as estruturas do tipo N-S seriam de origem andina e não estariam relacionadas à reativação de falhas anteriores (Sagripanti et al. 2014). A *Cordilheira do Viento* corresponde ao setor norte estudado nesta tese de doutorado.

O setor central de nosso estudo está localizado quase no traço superficial do Lineamiento Cortaderas, enquanto a área sul de nosso estudo está localizada no Dorsal de Huincul. É provável que no surgimento dos magmas e na locação dos plútons tenha havido uma influência conjunta da reativação da fábrica NO do embasamento e da formação das falhas N-S andinas.

1.4 Estudo dos Flare-up e Steady-state

Nos últimos anos a caracterização do magmatismo nos arcos continentais tem adquirido importância. Foi observado que o magmatismo não era continuo, assim períodos de magmatismo normal chamados de *steady-state* estavam separados por períodos curtos de magmatismo intenso chamados *flare-ups* (Ducea, 2001; DeCelles et al., 2009). Esses períodos de alto fluxo magmático cobrem curtos períodos de tempo (de entre 10-20 Ma, Burns et al., 2015), após os quais o magmatismo retorna ao estado normal conhecido como *steady-state*.

O *steady-state* é caracterizado principalmente por um fluxo magmático de longo prazo "normal", no qual o fluxo do manto forma magmas andesíticos e cones compostos (Figura 3-A). A crosta superior é rígida, com uma transição médio crustal frágil-dúctil, e pequenos corpos granodioríticos e tonalíticos se desenvolvem nele. Eles produzem erupções explosivas do VEI ≤ 7 e pequenas caldeiras (de Silva 2008, Burns et al. 2015).

O *flare-up*, por outro lado, possui uma grande energia proveniente do manto (Figura 3-B). A crosta sofre maturação térmica e mecânica, sofrendo adelgaçamento e com uma transição frágil-dúctil na crosta superior. Isso favorece o desenvolvimento de grandes plutóns granodioríticos e graníticos que se acumulam na crosta média e superior (área MASH), alimentando erupções do VEI 8 ou até maior.

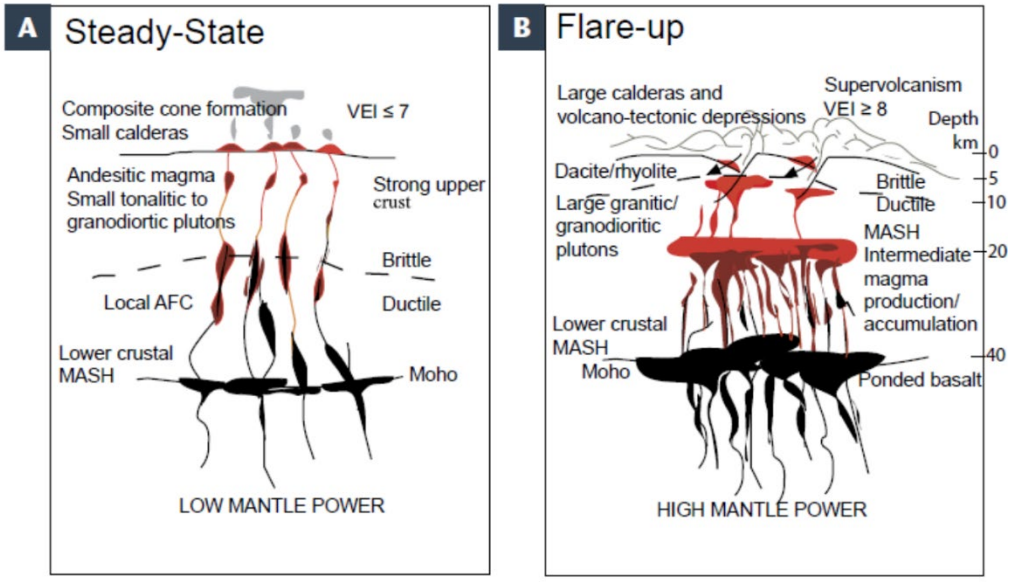


Figura 3: Comparação entre os dois estágios do magmatismo: A) *Steady-state*, B) *Flare-up* (de Silva et al. 2015).

Muitos autores tentaram interpretar os produtos vulcânicos e, assim, chegaram ao processo de desencadeamento, através do uso de isótopos radiogênicos (Sr, Nd e Pb), estáveis ($\delta_{18}O$) e geocronologia (U-Pb em zircão), ainda com algumas inconsistências. O magmatismo do *Steady-state* se caracteriza por vulcanismo predominantemente máfico a andesítico que tem razões $^{87}Sr/^{86}Sr$ menos radiogênicas < 0,708, enquanto durante os *Flare-ups* o magmatismo é predominantemente dacítico e tem razões $^{87}Sr/^{86}Sr$ > 0.708, mais raiogênicas (ou crustais). Essas diferenças podem refletir graus variáveis de assimilação crustal em resposta à mudança dos fluxos térmicos (Silva et al. 2006). Burns et al. (2015) estudaram a transição entre *Flare-up* e *Steady-state* nos Andes Centrais, no Complexo vulcânico Purico-Chascon, no norte do Chile (Fig. 6). Eles viram que a transição entre *Steady-state e Flare-up* e novamente para *Steady-state durante o Neôgeno estava registardo* fisica e quimicamente nos materiais produzidos e eruptados durante a evolução do arco.

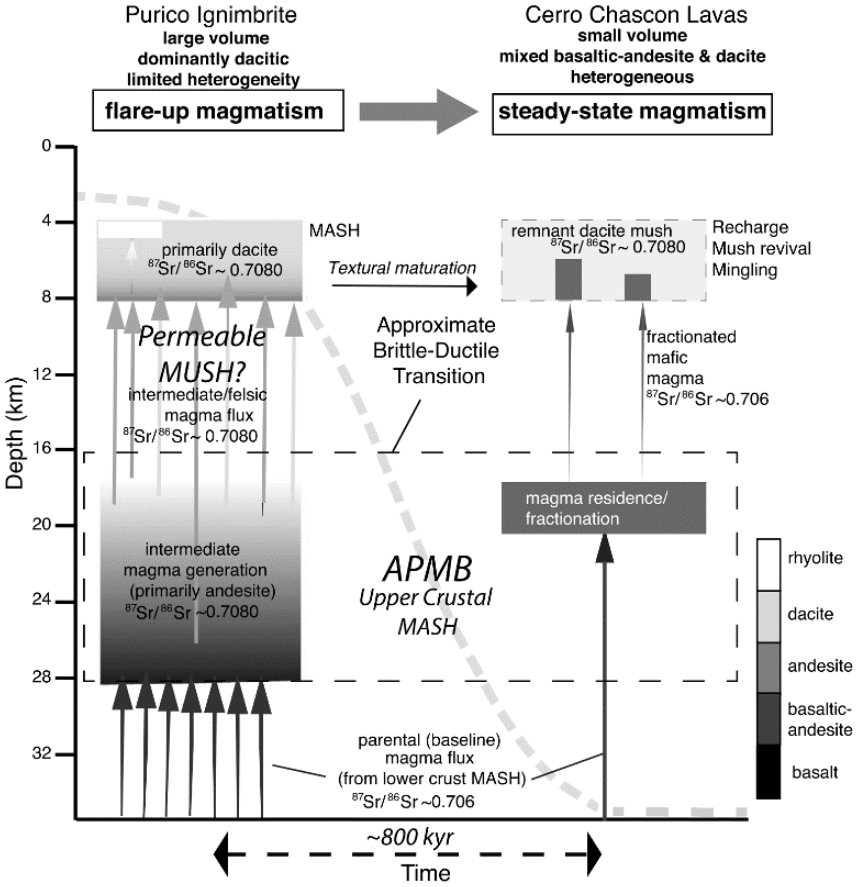


Figura 6: Seção transversal esquemática transgressiva no tempo da dinâmica dos processos envolvidos na geração de magma no Complexo Vulcânico Purico– Chascon (PCVC) entre o Flare-up e Steady-state. Tomada de Burns et al. (2015).

A transição de um estado para outro reflete uma diminuição do gradiente geotérmico para seu estado normal (de Silva 2008, Burns et al., 2015). Eles são responsáveis por produzir aproximadamente 78% da composição de um arco (Ducea 2001), porque produzem 3 a 4 vezes mais magmatismo do que no *steady-state* (Burns et al., 2015). Durante esses momentos, há uma extensa assimilação da crosta e cristalização fracionada. Ambos os estágios magmáticos de arco se traduzem em mudanças na arquitetura da crosta, composição geoquímica e isotópica, além da geoquímica do magma.

As diferenças entre essas hipóteses estão no fato de que o magmatismo pode ser produzido pelo espessamento crustal em áreas de contração, subsequente no aquecimento, fusão e criação de grandes resíduos eclogíticos, ou se a origem do alto fluxo magmático vem diretamente do manto em áreas extensionais. Embora as duas hipóteses sejam baseadas em dados, ainda são necessários mais estudos para se chegar a um consenso sobre a verdadeira origem desses eventos.

1.5 Geologia Regional

1.5.1 Cordillera del Viento (Varvarco, Butalón Norte e Huingancó)

O embasamento na área estudada é representado pela Formação Guaracó Norte (Fm) (Groeber, 1929; Zappettini et al. 1987), composta por metamorfitos, filitos, ardósias e xistos de quartzo. Aparece no centro da anticlina da Cordillera del Viento, no lago Varvarco Campos e na margem direita do Rio Neuquén, perto da cidade de Varvarco. Também nos riachos Chacay e Guaracó Norte. Esta unidade compõe a rocha-caixa da Tonalita Varvarco. Zappettini et al. (2012) analisaram dados geoquímicos da unidade resultando em sedimentos policíclicos de quartzo de proveniência continental madura. Também obteve dados U/Pb/Hf principalmente de zircões ordovicianos (449 ± 5 Ma a 458 ± 5 Ma) com ε_{Hf} entre -4,04 a -0,34 e devonianos (369 ± 5 Ma a 406 ± 4 Ma) com um ε_{Hf} entre -2,84 a -0,70. As idades do modelo para esta unidade variam entre 1.655 Ma e 1.384 Ma, possibilitando determinar que a fonte contém material crustal reciclado da idade do Paleoproterozóico Médio - Mesoproterozóico Médio (Zappettini et al. 2012). Giacosa et al. (2014) pesquisaram dados estruturais sobre essa formação, obtendo folheações de tendências N-S.

O Granito Huingancó (Digregorio 1972) tem uma superfície de 24 km^2. Está integrado por plutóns de granodiorito e monzogranito aos que se associam domos subvulcânicos riolíticos (Llambías et al., 2007). Intrude as rochas vulcânicas do Grupo Andacollo (Digregorio 1972; Llambías et al., 2007) com idades entre 326±3 Ma (Hervé et al., 2013) e de 328±2 Ma (Suárez et al., 2008). Aflora no núcleo de uma estrutura anticlinal que por erosão expõe rochas paleozoicas e consiste de duas fácies distintas: fácies de granodiorito datado em 283 ± 1 Ma (U-Pb SHRIMP, em zircão), e fácies monzogranito, datada em 259±9 Ma (U-Pb SHRIMP em zircão, Sato et al., 2008). Contém abundantes inclusões microgranulares máficas e encontra-se interceptado por diques máficos. Hervé et al. (2013) obteve dados U-Pb (283 ± 2 Ma) e Lu-Hf (Epsilon Hf entre 0 a -2) sobre a fácies de granodiorito. Os resultados de Hf indicaram que os magmas associados seriam mais juvenis que dos outros granitos gondwânicos. Não obstante não existe um estudo detalhado de geoquímica, isótopos Sr-Nd e Hf das duas fácies e dos enclaves microgranulares máficos.

O Tonalito Varvarcó (Franchini et al., 2003) com uma idade cretáceo-paleogeno (Franchini et al., 2003; Kay et al., 2006), é um exemplo das intrusões tardias associadas com o ciclo Andino. Este aflora a apenas 35 km ao norte da área do Granito Huingancó na Cordillera del Viento. Essas intrusões tardias foram atribuídas a um enraisamento da placa oceânica subductada (Spagnuolo et al., 2012). Na área de Butalón, a geoquímica do Granodiorito Varvarco foi estudada por Casé et al. (2008), que apontam que estas são rochas subvulcânicas, principalmente calcialcalinas, meta a peraluminosas, com baixo a médio teor de potássio. Foi datado em 64.7± 3.2 Ma na área de Butalón (^{40}Ar/^{39}Ar em biotita, Franchini et al., 2003) e 69.09 ± 0,13 Ma na área de Varvarco (^{40}Ar/^{39}Ar em biotite, Kay et al., 2006). La Tonalita Butalón, localizada ao sul do granodiorito de Varvarco, possui apenas esses dados geoquímicos, sem estudos detalhados.

1.5.2 Naunauco

A área de estudo está localizada no setor leste do Cinturão de dobras e cavalgamentos do Agrio. Este cinturão, que atualmente está inativo, teria começado a se formar no Cretáceo e teria uma reativação posterior durante o Mioceno (Zapata et al. 2002; Zapata e Folguera, 2006; Zamora Valcarce et al.

2006b). Nele, foram reconhecidos dois setores, um interno onde a estrutura seria consequência da inversão das falhas normais pré-jurássicas (Ramos, 1998), e um setor externo, onde o embasamento participou da deformação, reativando parcialmente as estruturas de pele delgada anteriores (Zapata et al., 1999; Zapata e Folguera, 2005; Zamora Valcarce et al., 2006b).

A estratigrafia da área apresenta algumas das sequências aflorantes da Bacia Neuquina, do Jurássico superior ao Cretáceo superior. Começando com o Grupo Mendoza (Stipanicic et al. 1968) composto por conglomerados, pelitos, calcários e arenitos; a Fm. Rayoso (Legarreta 1985), com conglomerados, arenitos e argilitos, até o Grupo Neuquén (Stipanicic et al. 1965) de arenitos e conglomerados. As rochas vulcânicas e subvulcânicas da área afloram na parte interna do Cinturão de dobras e cavalgamentos do Agrio, principalmente no campo Vulcânico Collipilli e no lacólito Cerro Naunauco.

O Grupo Naunauco (Zamora Valcarce 2007) consiste em duas Formações: Colipilli (Llambías e Rapela 1989), que agrupa os corpos intrusivos e as fácies extrusivas subordinadas, e Cayanta (Rapela e Llambías 1985), composta por rochas extrusivas e corpos subvulcânicos alojados em eles. O Fm. Collipilli apresenta numerosas intrusões de *sills* e lacólitos localizados nos sedimentos da Bacia Neuquina. A fácies extrusiva, denominada Fm. Cayanta, na área de Colipilli, também é intrudida nesses sedimentos e seus melhores afloramentos são encontrados em amplos sinclinais. Zamora Valcarce et al. (2007) dataram as rochas do Grupo Naunauco usando Ar/Ar, obtendo idades de 56.64 ± 0.44 Ma para Collipilli, e 65.5 ± 0.46 e 72.83 ± 0.83 Ma em *sills* e bombas vulcânicas do grupo.

1.5.3 Zona de los lagos Aluminé-Moquehue y Ñorquinco-Pulmarí

Na área dos lagos Aluminé-Moquehue e Ñorquinco-Pulmarí, afloramentos ígneos pré-andinos e andinos intrusivos estão localizados em rochas metamórficas paleozóicas. As rochas mais antigas da região são os gnaisses, migmatitos e os xistos biotíticos e quartzosos que correspondem à Formação Colohuincul, à qual é atribuída uma idade paleozóica (Dalla Salda et al. 1991). Franzese (1995) chamou de Complexo Piedra Santa os xistos de baixo grau do *Cordón de la Piedra Santa*, localizado ao sul-sudeste da área de estudo, e atribuiu-lhes uma idade Devoniana a Carbonífera.

Gregori et al. (2011) descreveram rochas do ciclo orogênico Famatiniano, anterior ao Gondwânico, na área do Lago Ñorquinco, denomina as intrusivas como Granito Lago Ñorquinco para o qual obtiveram uma idade de resfriamento em hornblenda de 398 ± 4 Ma em granodioritos hornblendíferos.

Posteriormente, os andesitos do Grupo Choiyoi (Stipanicic 1965) metamorfoseados e com presença de alteração hidrotermal, interpretada como causada pelas intrusões do Granito Moquehue (Zanettini et al. 2010) e do Granodiorito Paso Icalma (Cucchi e Leanza 2006), com quem estão em contato.

O Granito Moquehue é composto por granitos e tonalitos com indícios de processos metamórficos e alteração hidrotermal, também produzidos pela intrusão do Granodiorito Paso de Icalma. Cingolani et al. (1991) obtiveram idades Rb/Sr para o Granito Moquehue de 209 ± 13 Ma. Ao oeste do Lago Moquehue estendem-se os basaltos e brechas vulcânicas da Fm. Icalma (Emparan et al. 1992; Emparan e Suárez 1992), uma extensão do complexo vulcano-sedimentar Icalma, no Chile. Os contatos entre o embasamento e os granitos são inferidos, devido à cobertura vegetal e depósitos glaciais. Intrudindo esta Formação, estão os tonalitos, dioritos e monzogranitos do Tonalito Santa María (Zanettini et al 2010), datado por K/Ar em 148 ± 8 e 140 ± 5 Ma (Emparan et al. 1992; Emparan e Suárez 1992).

O Granodiorito Paso de Icalma aflora entre o limite internacional e as cabeceiras do rio Aluminé e é composto por granodioritos e tonalitos subordinados e, ocasionalmente, granitos. Em alguns setores, é atravessado por diques dioríticos e apresenta enclaves metamórficos. É intrusivo respeito ao Granito Moquehue e ao Tonalito Santa María. Possui uma idade Rb/Sr de 70 ± 19 Ma (Cingolani et al. 1991) e várias idades K/Ar de 86 ± 4 e 67 ± 4 Ma (Emparan e Suárez 1992; Emparan et al. 1992; Suárez e Emparan 1997), 110 ± 4 e 87 ± 7 Ma (Latorre et al. 2001) e 70 ± 10 Ma (Cucchi e Leanza 2006). Gregori et al. (2011) describe edades de enfriamiento 40Ar-39Ar en anfíbol de 70.8 ± 1.5, 72.2 y 70.6 ± 1 en la zona comprendida entre los lagos Moquehue y Aluminé (orilla norte del lago Aluminé).

Rochas ígneas na área dos lagos Aluminé-Moquehue e Ñorquinco-Pulmarí também foram nomeadas por Urraza et al. (2011a) como Complexo Ígneo-Metamórfico Aluminé (CIMA). Neste trabalho, os autores determinaram que são quartzo dioritos, tonalitos-granodioritos, granodioritos e granitos de

magmas cálcicos a levemente calcoalcalinos de composição metaluminosa associados a margens ativas (tipo I, Cordilheranos). Urraza et al. (2011b) determinaram as idades de ^{40}Ar-^{39}Ar em plagioclásio, hornblenda e biotita de granodioritos e tonalitos da área do Lago Pulmarí que deram 69.9 ± 9 Ma, 67.5 ± 0.9 Ma, 69 ± 1.2 Ma e 73.6 ± 3.6 Ma, correspondendo ao Cretáceo Superior.

CAPÍTULO 2
MATERIAIS E MÉTODOS

2 MATERIAIS E MÉTODOS

2.1 Pesquisa Bibliográfica

A pesquisa inicial antes das etapas de campo consistiu em um estudo bibliográfico detalhado da geologia regional e local, bem como no uso de imagens de satélite ASTER. Para a base geológica, foram utilizadas cartas geológicas na escala 1:250.000, mapas provinciais e dados SIG do *Servicio Geológico Minero Argentino* (SEGEMAR: https://www.argentina.gob.ar/produccion/segemar).

As imagens de acesso livre ASTER (*Advanced Spaceborne Thermal Emission and Reflection*) foram obtidas através do visualizador EarthExplorer (https://earthexplorer.usgs.gov) do *United States Geological Survey* (USGS); e o visualizador Earthdata (https://search.earthdata.nasa.gov/search) da NASA. Foram processadas usando o software ENVI 5.0 (https://www.l3harrisgeospatial.com/Software-Technology/ENVI).

Esta base bibliográfica compilada foi usada para a criação de mapas base, usando o software ArcGIS 10.6 (https://www.esri.com/en-us/arcgis/about-arcgis/overview) e Qgis 3.20 Odense (https://qgis.org/en/site/).

2.2 Etapa de Campo

Para a coleta das amostras, foram realizados três trabalhos de campo. O primeiro foi na área de Varvarco desde o dia 22 a 30 de março de 2017. O segundo na área de Huingancó desde o dia 20 a 24 de fevereiro de 2018. Ambos consistiram na descrição e reconhecimento dos afloramentos e coleta de amostras para estudos petrológicos, isotópicos e geocronológicos, bem como amostras orientadas para estudos de anisotropia de susceptibilidade magnética (ASM).

Os estudos de ASM foram realizados em 17 locais, dos quais 14 compreendem o Tonalito Varvarco, sua fácies associada e sua rocha de caixa (Formação Guaracó Norte), e 3 locais pertencem ao Tonalito Butalón. Em cada um dos locais, foram retirados no mínimo 5 cilindros orientados, usando uma perfuradora portátil, e foram retirados orientados com um orientador magnético.

Todo o trabalho realizado foi registrado por meio de anotações e fotografias. Um total de 95 cilindros orientados foram coletados.

Ou último trabalho de campo foi na área de Naunauco desde o dia 20 a 25 de fevereiro de 2020. O mesmo procedimento anterior foi realizado, mas desta vez nenhuma amostra orientada para ASM foi coletada.

2.3 Análises de ASM

A preparação da coleção de cilindros foi realizada no *Instituto de Investigación en Paleobiología y Geología de la Universidad Nacional de Río Negro* (IIPG-UNRN), General Roca, Río Negro, Argentina. Os cilindros foram fatiados em um comprimento de 2,2 cm. A medição de ASM foi realizada no *Instituto de Geociencias Básicas, Aplicadas y Ambientales de Buenos Aires (IGEBA)* usando um medidor de susceptibilidade Kappabridge MFK-1B sob uma frequência de 200 Hz. O equipamento aplica um campo magnético de baixa frequência que produz uma magnetização induzida, e o vetor de campo aplicado (H) e o vetor de magnetização induzida (Mi) são paralelos. Elipsóides de susceptibilidade magnética foram calculados para um mínimo de cinco espécimes por local usando técnicas de média de matriz (Jelínek, 1978) usando o programa Anisoft 4.2 (Chadima e Jelinek, 2009). Em cada caso, a representação dos elipsóides de susceptibilidade magnética corresponde às projeções equiareais no hemisfério inferior. Os estudos de magnetismo das rochas foram realizados no *Ludwig-Maximilians*, Departamento de Ciências da Terra e Ambientais da Universidade de Munique, na Alemanha, com uma equipe chamada “sushi-bar”.

2.4 Análises Petrográficas

Das amostras coletadas na etapa de campo, 21 seções delgadas foram feitas na Sala de Laminação do *Instituto de Investigación en Paleobiología y Geología de la Universidad Nacional de Río Negro* (IIPG-UNRN), General Roca, Río Negro, Argentina. Posteriormente foram descritas macroscopicamente usando uma lupa binocular, e microscopicamente usando um microscópio óptico binocular da marca Olympus, modelo BX50, da sala de microscopia do *Instituto de Investigación en Paleobiología y Geología de la Universidad Nacional de Río*

Negro (IIPG-UNRN), tendo como objetivos a caracterização petrográfica (texturas, analises de deformação, alteração) e classificação modal de amostras.

Outras 6 seções delgadas foram feitas no Geolab - Solucões em Geologia, e aguardam análise no Laboratório de Microscopia da UnB.

2.5 Análises Geoquímicas de elementos maiores, menores e traços

No total, 17 amostras foram obtidas para análises geoquímicas (elementos maiores, menores e traços). As amostras GV, HU4 e VAR3 foram analisadas no *Servicio General de Geocronología y Geoquímica Isotópica SGIker, Universidad del País Vasco UPV/EHU*, Bilbao, Espanha. As amostras D2, GR1, GR2, GR4, VAR1, VAR2, VAR4A e VAR5 foram analisadas em *AcmeLabs, Bureau Veritas Mineral Laboratories, Commodities Canada Ltd*. As amostras restantes Moque, ICAL4, NAU4, NAU3-B, LP1 e CY1 foram analisadas no Laboratório SGS Geosol, Vespasiano, MG, Brasil (www.sgsgeosol.com.br), cujo pacote comercial recebe o nome de ICP95A/IMS95A. Para a caracterização geoquímica foram selecionadas as amostras de rocha com o menor grau de intemperismo e livres de contaminação.

No *Servicio General de Geocronología y Geoquímica Isotópica SGIker*, os reagentes foram concentrados HF e HNO_3 Merck Pro-Analysi posteriormente destilados no laboratório por destilação de superfície usando Savillex PFA e destiladores de quartzo Acidest. Água desionizada foi obtida usando um dispositivo Millipore Elix e polida para obter uma resistividade ≥ 18 M Ohm cm com um sistema Barnstead EasyPure. Soluções In e Bi, utilizadas como padrão interno, e soluções multielementais para o ajuste inicial e calibração do espectrômetro foram preparadas a partir de soluções padrão multi-elemento Merck 1000 ppm para ICP, estabilizadas em HNO_3 2 a 6%. O padrão interno foi adicionado por meio de um kit de adição online automático para evitar erros aleatórios. A pesagem com precisão de 0,1 mg foi realizada com balança eletrônica GRAM SV 205-A. A calcinação foi realizada em duas etapas, uma a cada a ~ 500 e 1050 ° C em mufla para remover H_2O e compostos de C e S. A fusão alcalina das amostras é realizada usando um sistema automático Claisse Fluxy 30 sobre gás butano em Cadinhos de Pt-Au (95-5) com metaborato de lítio ($LiBO_2$) como fundente e LiBr como agente não umectante. O fundido é automaticamente derramado em um copo de poliestireno contendo 100 ml de

HNO_3 e ~0,05 ml de HF colocado em um agitador magnético. A solução é diluída gravimetricamente para um fator adequado para a análise. As concentrações de elementos traço foram determinadas usando um Thermo XSeries 2 ICP-MS equipado com célula de colisão, uma interface específica para sólidos totais dissolvidos elevados (cones Xt), tocha blindada e um sistema de diluição de gás. Um nebulizador concêntrico e uma câmara de expansão de quartzo foram empregados. Mais detalhes sobre o método instrumental são fornecidos em García de Madinabeitia et al. (2008). A incerteza dos resultados corresponde a um nível de confiança de 95%.

No Laboratório SGS Geosol, os elementos maiores e Ba, V, Zn, Sr e Zr foram analisados por ICP-OES, enquanto os demais elementos foram analisados por ICP-MS. Com base nas informações recebidas, estima-se que as precisões para os elementos maiores (na faixa de concentração aplicável às nossas amostras) são da ordem de 10% para todos os elementos maiores analisados. Para análise de elementos traço, especialmente os elementos de terras raras, os materiais de referência certificados GRE-03 e GRE-05 foram usados, e a precisão com nível de confiança de 95% é cotada nos seguintes níveis (em% do valor analítico): Ce ± 2, Dy ± 4, Eu ± 2, Ga ± 4, Gd ± 3.6, Ho ± 0.3, La ± 36, Lu ± 0.1, Nb ± 44, Nd ± 33, Pr ± 9, Sm ± 5, Ta ± 9, Hf ± 7, Tb ± 0.5, Tm ± 0.1, Y ± 6, Yb ± 0.25, Zr ± 47, Sc ± 0.5, Ti ± 0.1 , Th ± 2.4, U ± 1, W ± 0.5.

O tratamento dos dados de litogeoquímica foram realizados com o auxílio dos softwares GCDkit 3.6 e Excel.

2.6 Análises por Microssonda Eletrônica

Uma análise por microssonda eletrônica dos elementos majoritários foi realizada na *Universidad de Oviedo*, Espanha, utilizando um equipamento Cameca SX-100 com voltagem de 15 KV, corrente de 15 nA e tempo de aquisição de 10 s por elemento, no modo WSD.

2.7 Análises Isotópicas: Sm-Nd em rocha total

Um total de 8 amostras foram analisadas para Sm-Nd em rocha total. As amostras HU4 e VAR3 foram feitas por meio de ID-MC-ICP-MS no *Servicio General de Geocronología y Geoquímica Isotópica SGIker, Universidad del País*

Vasco UPV/EHU, Bilbao, Espanha. As amostras GR4, ICAL4, Moque e VAR6 via ID-TIMS MAT 262 Triton e D2 e BU4 mediante MC-ICP-MS instalado no Laboratório de Estudos Geodinâmicos, Geocronológicos e Ambientais, Instituto de Geociências, Universidade de Brasília (UnB).

No *Servicio General de Geocronología y Geoquímica Isotópica SGIker*, o preparo das amostras foi realizado em gabinetes PP com fluxo laminar vertical e extração total Classe A (ISO-5), localizados em sala limpa 150-7. Uma alíquota de 0,05-0,12 g foi retirada de cada amostra, à qual uma quantidade proporcional de um traçador isotópico misto ^{149}Sm-^{150}Nd foi adicionado. As misturas de amostra-traçador foram dissolvidas em HF-HNO-$HClO_4$, seguindo protocolos adaptados de Pin et al. (1994) e Pin e Santos Zalduegui (1997). Nd e Sm foram separados por meio de resina TRU-resin e resina Ln-resin, seguindo os protocolos detalhados em Pin e Santos Zalduegui (1997) e utilizando ácido ascórbico para redução de Fe (Pin e Gannoun, 2017).

As frações individuais de Nd e Sm foram dissolvidas em 2 mL de HNO_3 a 3% e diluídas para atingir concentrações finais de cerca de 200 ng/g de Nd e 30 ng/g de Sm, respectivamente. As amostras foram introduzidas como aerossóis úmidos em um espectrômetro Thermo Neptune MC-ICP-MS usando um micronebulizador ESI PFA com aspiração nominal de 100 L min^{-1} e uma câmara de expansão dupla ciclônica de passagem dupla Scott.

A medição espectrométrica de Nd foi realizada em 3 blocos de 25 ciclos de medição cada, com um tempo de integração de 8 s por ciclo. As linhas de base eletrônicas dos amplificadores foram subtraídas no início de cada bloco. O fracionamento de massa instrumental e a contribuição do traçador isotópico foram corrigidos usando algoritmos específicos, e considerando uma lei exponencial de fracionamento instrumental. A precisão da medição ^{143}Nd/^{144}Nd é refletida como duas vezes o erro padrão (2SE).

A medição espectrométrica de Sm foi realizada em 1 bloco de 40 ciclos com um tempo de integração de 4 s por ciclo. As linhas de base eletrônicas dos amplificadores foram subtraídas no início do bloco. O fracionamento de massa instrumental foi corrigido de acordo com Hofmann (1971). A confiabilidade e reprodutibilidade do método espectrométrico foram verificadas por medidas esporádicas do material de referência JNdi-1, intercaladas entre as medidas das amostras de teste, e nas mesmas condições. A média da razão ^{143}Nd/^{144}Nd para

2 medições durante a sessão analítica é 0,512098 ± 0,000004 (2 SD). A precisão no cálculo por diluição isotópica da razão $^{147}Sm/^{144}Nd$ é normalmente inferior a 0,2%.

Os procedimentos de separação e método analítico aplicados no Laboratório de Estudos Geodinâmicos, Geocronológicos e Ambientais, foram relatados por Gioia e Pimentel (2000). As amostras foram lavadas e as partes desgastadas foram removidas, então foram trituradas e pulverizadas em um pó de tamanho muito fino. Aproximadamente 50 mg de pó de rocha foram misturados com solução rápida $^{149}Sm/^{150}Nd$ e dissolvidos em cápsulas Savillex. Todas as amostras de rocha inteira utilizadas para extração de Sm-Nd foram submetidas a técnicas convencionais de troca catiônica baseadas em colunas de Teflon® contendo resina LN-Spec (HDEHP - ácido (HDEHP - Di-(2-ethylhexyl) fosfórico suportado por politetrafluoroetileno em pó). Quatro amostras (GR4, ICAL4, MOQUE e VAR6) foram analisadas usando um espectrômetro de massa de ionização térmica Thermo Scientific TRITON ™ Plus (TIMS) operando no modo multicoletor estático. Duas amostras (BU4 e D2) foram analisadas em solução em um instrumento Thermo-Fisher Neptune HR-MC-ICP-MS no mesmo laboratório. As amostras foram introduzidas no espectrômetro em nebulizador com fluxo de 100uL/min. Para Sm, as massas sintonizadas foram ^{146}Nd, ^{147}Sm, ^{148}Sm, ^{149}Sm, ^{150}Sm, ^{152}Sm e ^{154}Sm. Cinco blocos de 10 ciclos cada com um tempo de integração de 4,194 segundos foram considerados para cada análise. O fator de normalização utilizado foi o $^{147}Sm/^{152}Sm$ (valor verdadeiro de 0,556083). Para Nd, as massas sintonizadas foram ^{142}Nd, ^{143}Nd, ^{144}Nd, ^{145}Nd, ^{146}Nd, ^{147}Sm, ^{148}Nd e ^{150}Nd. Sete blocos de 10 ciclos cada com um tempo de integração de 4,194 segundos foram considerados para cada análise. As proporções $^{143}Nd/^{144}Nd$ foram normalizadas para $^{146}Nd/^{144}Nd$ = 0,7219; a constante de decomposição era 6,54 × 10-12. O $^{143}Nd/^{144}Nd$ médio obtido para o padrão USGS BHVO-2 foi 0,512970 ± 0,000002 (2SD) durante o curso deste estudo, o que é consistente com os valores publicados mais recentemente (por exemplo, 0,512986 ± 0,000009, Weis et al., 2005). Os brancos do laboratório foram de ~0,25 ng para Nd e ~0,04 ng para Sm. As incertezas nas relações Sm/Nd e $^{143}Nd/^{144}Nd$ foram melhores que ± 0,5% (2 σ) e ± 0,005% (2 σ), respectivamente, com base em análises repetidas dos padrões internacionais de rocha BHVO-2 e BCR-1.

Os valores de TDM foram calculados com base no modelo de DePaolo (1981). As razões de amostra $^{143}Nd/^{144}Nd$ medidas são expressas em notação Epsilon Neodymium (ε_{Nd}) como o desvio fracionário em parte por 10^4 (unidades) do valor $^{143}Nd/^{144}Nd$ do Reservatório Uniforme Condrítico (CHUR). Os brancos de neodínio eram <100 pg. Os dados para o padrão BHVO-2 são relatados na Tabela 1.

Amostra	Sm (ppm)	Nd (ppm)	$^{147}Sm/^{144}Nd$	$^{143}Nd/^{144}Nd$	± 2SE	eNd (0)	TDM (Ga)
BHVO-2	6.342	25.711	0.1491	0.512970	0.000002	6.47	0.22

Tabela 1: Dados Sm-Nd para o padrão BHVO-2.

2.8 Análises Isotópicas: Sr-Sr em rocha total

Um total de 8 amostras foram analisadas para Sm-Nd em rocha total. As amostras HU4 e VAR3 foram feitas por meio de ID-MC-ICP-MS no *Servicio General de Geocronología y Geoquímica Isotópica SGIker, Universidad del País Vasco UPV/EHU*, Bilbao, Espanha. As amostras GR4, ICAL4, Moque e VAR6 via ID-TIMS MAT 262 Triton e D2 e BU4 mediante MC-ICP-MS instalado no Laboratório de Estudos Geodinâmicos, Geocronológicos e Ambientais, Instituto de Geociências, Universidade de Brasília (UnB).

No *Servicio General de Geocronología y Geoquímica Isotópica SGIker*, o preparo das amostras foi realizado em gabinetes PP com fluxo laminar vertical e extração total Classe A (ISO-5), localizados em sala limpa 150-7. O estrôncio foi purificado por cromatografia de extração em resina Sr-resin, de acordo com o método descrito por Pin et al. (1994). A amostra de estrôncio foi dissolvida em 2 mL de HNO_3 a 3% e diluída para uma concentração final de 200 ng/g Sr. Esta diluição foi introduzida como um aerossol úmido em um espectrômetro Thermo Neptune MC-ICP-MS usando um micronebulizador PFA de ESI com uma sucção nominal de 100 L min^{-1} e uma câmara de expansão dupla ciclônica-Scott de passagem dupla. A medição espectrométrica foi realizada em 4 blocos de 13 ciclos de medição cada, com um tempo de integração de 8 s por ciclo. As linhas de base eletrônicas dos amplificadores foram subtraídas no início de cada ciclo. O fracionamento de massa instrumental e a interferência de Kr foram corrigidos seguindo o protocolo de Balcaen et al. (2005). A precisão das medidas é representada como duas vezes o erro padrão (2SE), em valor absoluto.

A confiabilidade e reprodutibilidade da medição espectrométrica foram verificadas por medições esporádicas do material de referência NBS987 intercaladas entre as medições das amostras de teste, e nas mesmas condições. O valor médio para este material de referência durante a sessão analítica foi 0.7102800 ± 000012 (2 SD, 2 medições).

No Laboratório de Estudos Geodinâmicos, Geocronológicos e Ambientais, após a digestão, uma alíquota da solução de amostra foi carregada diretamente na coluna Teflon® contendo aproximadamente 83 mg de resina Eichrom® Sr-Spec (50-100 µm) para separar a fração Sr da matriz. A concentração de Rb não foi determinada durante este trabalho. A composição isotópica de Sr das amostras selecionadas foi determinada usando um espectrômetro de massa de ionização térmica (TIMS) Thermo Scientific TRITON™, operando no modo multidinâmico. O $^{87}Sr/^{86}Sr$ médio obtido para o padrão NBS-987 foi 0.71031 ± 0.00002 e 0.71030 ± 0.00002 (2SD) durante o curso deste estudo. Este valor concorda bem, dentro do erro analítico, com o valor mais tipicamente recomendado de 0,71025 (Thirlwall, 1991; Faure, 2001; Machado, 2013).

2.9 Análises Isotópicas: U-Pb em zircão

As amostras VAR6, GR4, D2, ICAL4, Moque e BU4 foram analisadas no Laboratório de Estudos Geodinâmicos, Geocronológicos e Ambientais, Instituto de Geociências, Universidade de Brasília (UnB). Inicialmente, cerca de 3 kg de cada amostra de rocha bruta foi triturada em britador de mandíbula, moída em moinho de discos no Laboratório de Estudos Geodinâmicos, Geocronológicos e Ambientais, e peneirada em diferentes frações: 1000 a 300 µm, 300 a 63 µm e < 63 µm. Após ser peneirada, a fração de 300 a 63 µm foi submetida a um processo de separação mecânica dos minerais leves e pesados, por densidade em água, com o auxílio da bateia. A separação magnética manual é aplicada a este pré-concentrado com um ímã de neodímio. O concentrado de minerais pesados foi depositado no separador magnético Frantz, onde acontece a dissociação da fração menos magnética. Do material resultante, foi separado manualmente, com o auxílio de lupa óptica binocular, 50 cristais de zircão, que foram colocados em um suporte de resina epoxy (mount), que foi polido até aproximadamente metade da espessura. O *mount* foi conduzido ao Microscópio Eletrônico de Varredura (MEV) SEM FEI QUANTA 450, no Laboratório de

Estudos Geodinâmicos, Geocronológicos e Ambientais, para a geração de Imagens de Backscattered Electrons (BSE), a fim de caracterizar a provável presença de núcleos herdados e determinar os pontos a serem analisados.

Finalmente os cristais de zircão foram analisados usando um espectrômetro de massa de plasma acoplado indutivamente multicoletor de alta resolução Thermo-Fischer, Neptune, MC-ICP-MS acoplado a um sistema de ablação a laser ESI/New Wave Research, UP-213, Nd:YAG no Laboratório de Estudos Geodinâmicos, Geocronológicos e Ambientais. As análises de U-Pb nos cristais de zircão foram realizadas pelo método de *Bracketing* de amostra padrão com relações $^{207}Pb/^{206}Pb$ e $^{206}Pb/^{238}U$ normalizadas para o material de referência GJ1 (Jackson et al. 2004, Horstwood et al. 2016), para quantificar o fracionamento de ICP-MS. As massas sintonizadas foram ^{238}U no coletor Faraday e as massas ^{202}Hg, ^{204}Pb, ^{206}Pb and ^{207}Pb no coletor MIC. O tempo de integração foi de 1 segundo e o tempo de ablação foi de 40 segundos. O tamanho do spot realizado foi de 25 µm, e o laser foi ajustado para operar em 10 Hz e 3.0-3.5 J/cm^2. O zircão 91500 (Wiedenbeck et al., 1995) também foi analisado como um padrão secundário durante as sessões analíticas. A idade de concordia do padrão 91500 para as amostras Moque, D2 e BU4 foi 1059 ± 6 (2s, MSWDc+e = 1.7, n = 29) e para as amostras GR4, ICAL4 e VA6 foi 1061 ± 5 (2s, MSWDc+e = 1.1, n = 23). Os dados dos padrões GJ1 e 91500 podem ser vistos na Tabela 1. As idades são cotadas em 2s absoluto, a propagação é por adição quadrática. O excesso de variação e a incerteza da idade do material de referência são propagados quando for apropriado. Os dados brutos foram processados off-line e reduzidos com o software Iolite v.4.0 (Paton et al., 2011) e VizualAge (Petrus e Kamber, 2012) usando modelagem exponencial mais linear para correção de LIEF. Nenhuma correção do Pb comum foi feita.

Diagramas Concordia (elipses de erro 2σ), gráficos de densidade de probabilidade e idades médias ponderadas foram calculados usando o software Isoplot 4.15 (Ludwig, 2012). Para representar graficamente as idades de concordia, foram utilizados os diagramas de Tera-Wasserburg, selecionando os grãos com concordância entre 98 e 102%.

Tabela 1: Dados da análise de U-Pb realizada por meio de LA-ICP-MS em zircão do padrão GJ1 e 91500.

							Ratios							Ages						% conc[3]
	f206c	^{206}Pb (cps)	U[1] (ppm)	Th/U	^{206}Pb/^{204}Pb	1s (%)	^{207}Pb/^{206}Pb	1s (%)	^{207}Pb/^{235}U	1s (%)	^{206}Pb/^{238}U	1s (%)	Rho	^{207}Pb/^{206}Pb	2s (abs)	^{206}Pb/^{238}U	2s (abs)	^{207}Pb/^{235}U	2s (abs)	
Moque-D2-BU4 - GJ1																				
Z_GJ1	0.04	251025	298	0.03		94	0.06032	0.41	0.8276	1.7	0.09851	1.6	0.23	614	18	606	18	612	16	98.6
Z_GJ1	0.04	233881	278	0.03	40228	61	0.06042	0.36	0.8120	1.7	0.09642	1.6	0.15	618	15	593	18	604	15	96.1
Z_GJ1	0.08	227738	282	0.03	654	2370	0.06049	0.43	0.8234	1.7	0.09821	1.6	0.26	620	19	604	18	610	15	97.4
Z_GJ1	0.06	231596	289	0.04	2352	698	0.06052	0.36	0.8082	1.7	0.09631	1.6	0.48	621	15	593	18	601	15	95.5
Z_GJ1	0.07	233110	292	0.03	33046	104	0.06021	0.39	0.8222	1.7	0.09853	1.6	0.25	610	17	606	18	609	15	99.3
Z_GJ1	0.00	231918	295	0.04	178	9869	0.06041	0.31	0.8055	1.7	0.09616	1.6	0.51	617	13	592	18	600	15	95.9
Z_GJ1	0.03	222211	291	0.03	40815	139	0.06072	0.42	0.8356	1.7	0.09905	1.6	0.65	628	18	609	18	617	16	96.9
Z_GJ1	0.01	202647	269	0.03	25819	124	0.06017	0.44	0.8113	1.7	0.09701	1.6	0.28	608	19	597	18	603	15	98.1
Z_GJ1	0.05	219310	299	0.03	29919	341	0.06051	0.66	0.8218	1.7	0.09825	1.6	0.27	620	28	604	18	609	16	97.4
Z_GJ1	0.07	205956	283	0.03	141	6281	0.06038	0.46	0.8065	1.7	0.09660	1.6	0.58	616	20	594	18	600	16	96.5
Z_GJ1	0.27	223360	289	0.03	9462	25	0.06038	0.26	0.8138	1.2	0.09767	1.0	0.86	616	11	601	11	605	11	97.5
Z_GJ1	0.01	216553	284	0.03	6970	411	0.06043	0.46	0.8178	1.3	0.09805	0.9	0.80	618	20	603	11	607	12	97.6
Z_GJ1	0.06	201058	286	0.02	21513	55	0.06031	0.43	0.8185	1.2	0.09826	1.0	0.76	613	18	604	11	607	11	98.5
Z_GJ1	0.03	197216	284	0.03	45792	103	0.06057	0.35	0.8126	1.2	0.09714	1.1	0.85	623	15	598	12	604	11	96.0
Z_GJ1	0.00	205807	291	0.02		94	0.06047	0.33	0.8182	1.3	0.09820	1.0	0.89	619	14	604	12	607	12	97.5
Z_GJ1	0.14	191620	269	0.03	7134	214	0.06038	0.38	0.8103	1.2	0.09745	0.9	0.67	616	16	599	11	603	11	97.3
Z_GJ1	0.06	238021	308	0.03	27576	151	0.06047	0.34	0.8225	1.2	0.09914	1.0	0.77	619	15	609	12	609	11	98.4
Z_GJ1	0.16	228818	295	0.04	4126	246	0.06003	0.43	0.7990	1.3	0.09702	1.0	0.86	604	19	597	11	596	12	98.9
Z_GJ1	0.10	218433	271	0.03	16404	41	0.06043	0.24	0.8123	1.3	0.09761	1.1	0.97	618	10	600	12	604	12	97.1
Z_GJ1	0.13	240884	295	0.03	10482	178	0.06044	0.29	0.8151	1.1	0.09792	0.9	0.51	618	13	602	10	605	10	97.4
Z_GJ1	0.10	238336	285	0.03	171419	92	0.06056	0.49	0.8296	2.0	0.09913	1.7	0.82	623	21	609	19	613	19	97.9
Z_GJ1	0.00	230345	284	0.03	37047	83	0.06032	0.30	0.8062	1.9	0.09672	1.6	0.91	614	13	595	19	600	17	96.9
Z_GJ1	0.02	238124	295	0.03	159707	71	0.06058	0.38	0.8186	1.9	0.09789	1.6	0.82	623	16	602	18	607	18	96.6
Z_GJ1	0.01	244018	301	0.04	44905	105	0.06046	0.35	0.8225	2.0	0.09856	1.7	0.97	619	15	606	19	609	19	97.9
Z_GJ1	0.03	210242	274	0.03	8496	314	0.06031	0.39	0.8232	1.9	0.09884	1.6	0.85	614	17	608	18	610	18	99.0
Z_GJ1	0.08	213685	285	0.03	23639	39	0.06029	0.35	0.8058	1.9	0.09679	1.6	0.72	613	15	596	18	600	17	97.2
Z_GJ1	0.10	221460	293	0.02	15086	57	0.06061	0.39	0.8370	2.1	0.10001	1.7	0.95	624	17	614	20	617	19	98.4
Z_GJ1	0.01	209904	275	0.04	25731	86	0.06035	0.41	0.8163	2.0	0.09797	1.6	0.86	615	18	603	18	606	18	97.9
Z_GJ1	0.06	211854	281	0.03	1146	1554	0.06042	0.33	0.8104	1.9	0.09715	1.6	0.85	618	14	598	18	603	17	96.8
Z_GJ1	0.10	221702	295	0.04	25081	124	0.06038	0.31	0.8176	1.9	0.09809	1.6	0.84	616	14	603	18	607	17	97.9

Moque-D2-BU4 - 91500																				
Z_91500	0.09	69039	44	1.06	48	10032	0.07654	0.48	1.9364	1.7	0.18160	1.6	0.59	1108	19	1076	32	1094	23	97.1
Z_91500	0.20	66121	43	1.06	6968	129	0.07522	0.68	1.8916	1.7	0.18059	1.6	0.21	1073	27	1070	32	1078	23	99.7
Z_91500	0.02	68213	46	1.15	15445	118	0.07532	0.64	1.8646	2.0	0.17859	2.0	0.86	1076	25	1059	39	1068	27	98.5
Z_91500	0.00	69916	46	1.16	5246	111	0.07591	0.42	1.9145	1.8	0.18182	1.7	0.88	1092	17	1077	34	1086	24	98.7
Z_91500	0.09	66222	46	1.09	1788	177	0.07522	0.56	1.8692	1.8	0.17918	1.7	0.66	1073	22	1062	32	1070	24	99.0
Z_91500	0.25	73717	51	1.08	68129	97	0.07593	0.48	1.8818	1.8	0.17863	1.6	0.84	1092	19	1059	32	1075	24	97.0
Z_91500	0.23	60141	43	1.08	209	1549	0.07491	0.84	1.8417	2.9	0.17669	2.5	0.96	1065	34	1049	48	1060	38	98.5
Z_91500	0.01	66535	51	1.04	43155	57	0.07507	0.55	1.7853	2.5	0.17123	2.4	0.97	1069	22	1019	46	1040	33	95.3
Z_91500	0.21	61642	47	1.13	1196	429	0.07476	0.64	1.8090	1.9	0.17508	1.8	0.81	1061	26	1040	34	1049	25	98.0
Z_91500	0.15	66766	51	1.16	9176	66	0.07473	0.63	1.8019	1.8	0.17458	1.8	0.75	1060	26	1037	34	1046	24	97.9
Z_91500	0.32	85996	62	0.98	6192	42	0.07494	0.58	1.8181	1.3	0.17577	0.9	0.54	1066	23	1044	18	1052	17	97.9
Z_91500	0.23	88244	64	0.98	7230	37	0.07484	0.30	1.8463	1.4	0.17871	1.1	0.96	1063	12	1060	22	1062	19	99.7
Z_91500	0.33	65594	51	0.93	3125	69	0.07578	0.64	1.8434	1.2	0.17615	0.9	0.14	1088	25	1046	17	1061	16	96.1
Z_91500	0.04	66378	53	0.91		94	0.07546	0.44	1.8268	1.2	0.17530	0.9	0.62	1080	18	1041	17	1055	16	96.4
Z_91500	0.22	77567	59	1.02	5264	489	0.07484	0.38	1.8440	1.1	0.17897	0.9	0.42	1063	15	1061	17	1061	15	99.8
Z_91500	0.13	111230	85	1.05	12892	137	0.07552	0.40	1.8191	1.3	0.17500	0.9	0.86	1081	16	1040	18	1052	17	96.1
Z_91500	0.14	61709	43	0.94	2290	470	0.07501	0.45	1.8189	1.3	0.17676	1.0	0.80	1068	18	1049	20	1052	17	98.3
Z_91500	0.52	62231	44	0.95	199	3833	0.07505	0.46	1.7867	1.1	0.17355	1.0	0.48	1069	18	1032	19	1041	15	96.5
Z_91500	0.26	88116	60	1.03	1498	174	0.07531	0.60	1.8112	1.2	0.17455	0.9	0.21	1075	24	1037	17	1049	16	96.4
Z_91500	0.01	113866	66	1.28	20986	70	0.07566	0.58	2.1013	1.3	0.20150	1.2	0.72	1085	23	1183	25	1149	18	109.1
Z_91500	0.03	145975	97	1.11	7036	182	0.07500	0.39	1.8325	2.0	0.17685	1.6	0.89	1067	16	1050	31	1057	26	98.3
Z_91500	0.10	157878	105	1.16	4124	115	0.07514	0.36	1.8456	1.9	0.17779	1.6	0.85	1071	14	1055	31	1062	25	98.5
Z_91500	0.02	134742	90	1.18	8050	212	0.07489	0.43	1.8726	2.0	0.18116	1.6	0.82	1064	17	1073	32	1071	26	100.8
Z_91500	0.14	150514	101	1.20	8816	141	0.07536	0.49	1.8709	2.0	0.17986	1.6	0.75	1077	20	1066	31	1071	26	99.0
Z_91500	0.19	125112	88	1.15	32048	41	0.07535	0.54	1.8621	2.0	0.17898	1.6	0.82	1077	22	1061	32	1068	27	98.6
Z_91500	0.02	119601	84	1.13	11691	117	0.07501	0.46	1.8903	2.0	0.18250	1.6	0.80	1068	19	1081	32	1078	26	101.2
Z_91500	0.01	140006	99	1.23	1622	637	0.07503	0.44	1.8758	2.1	0.18108	1.7	0.96	1068	18	1073	33	1072	28	100.4
Z_91500	0.04	133533	94	1.20	38721	97	0.07541	0.39	1.8701	1.9	0.17965	1.6	0.59	1079	16	1065	31	1071	25	98.7
Z_91500	0.14	133870	97	1.16	12235	86	0.07532	0.29	1.8312	1.9	0.17613	1.6	0.92	1076	12	1046	31	1057	25	97.2
Z_91500	0.14	103614	75	1.08		94	0.07544	0.31	1.8545	2.0	0.17807	1.7	0.93	1079	12	1056	32	1065	26	97.9

GR4-ICAL4-VAR6 - GJ1																				
Z_GJ1	0.08	261252	302	0.03	17819	168.5	0.06043	0.29	0.8051	2.2	0.09651	2.2	0.88	618	12	594	24	600	20	96.1
Z_GJ1	0.09	247744	282	0.03	35420	47.8	0.06038	0.23	0.8190	2.2	0.09822	2.1	0.77	616	10	604	25	607	20	98.0
Z_GJ1	0.05	238919	280	0.03	8633	129.7	0.06039	0.42	0.8164	2.2	0.09742	2.1	0.65	616	18	599	25	606	20	97.2
Z_GJ1	0.01	235618	277	0.03	85188	73.3	0.06051	0.30	0.8281	2.2	0.09863	2.2	0.78	621	13	606	25	613	21	97.7
Z_GJ1	0.04	246245	295	0.03	28425	109.7	0.06035	0.37	0.7993	2.3	0.09511	2.2	0.78	615	16	586	25	596	20	95.2
Z_GJ1	0.08	244992	291	0.03	6314	343.2	0.06039	0.18	0.8063	2.2	0.09590	2.2	0.87	616	8	590	25	600	20	95.8
Z_GJ1	0.04	235635	278	0.03	4636	387.8	0.06061	0.50	0.8223	2.2	0.09798	2.1	0.44	624	21	603	24	609	20	96.6
Z_GJ1	0.02	237145	284	0.03	119910	77.1	0.06038	0.37	0.8202	2.2	0.09821	2.1	0.65	616	16	604	24	608	20	98.0
Z_GJ1	0.28	256879	281	0.03	10466	28.9	0.06008	0.48	0.8655	2.6	0.10672	1.8	0.79	605	21	654	22	633	24	108.0
Z_GJ1	0.10	258580	309	0.03	39927	32.4	0.06064	0.42	0.7960	2.6	0.09705	1.6	0.50	626	18	597	18	595	23	95.5
Z_GJ1	0.04	224554	285	0.03	2308	1427.4	0.06052	0.62	0.8095	2.6	0.09751	1.6	0.65	621	27	600	19	602	24	96.6
Z_GJ1	0.05	219322	283	0.04	49820	111.0	0.06042	0.43	0.8091	2.6	0.09759	1.6	0.74	618	19	600	19	602	24	97.2
Z_GJ1	0.00	217295	283	0.03	1552	518.1	0.06021	0.42	0.8194	2.6	0.09872	1.6	0.84	610	18	607	19	608	24	99.5
Z_GJ1	0.11	220979	291	0.03	6833	124.1	0.06054	0.42	0.8141	2.6	0.09754	1.6	0.56	622	18	600	19	605	24	96.5
Z_GJ1	0.00	221791	288	0.01	12043	246.2	0.06045	0.38	0.8181	2.6	0.09806	1.6	0.60	618	16	603	19	607	24	97.5
Z_GJ1	0.01	216187	286	0.03	3021	422.5	0.06039	0.42	0.8136	2.6	0.09767	1.6	0.38	616	18	601	19	604	24	97.5
Z_GJ1	0.07	236191	291	0.03	3334	602.6	0.06051	0.46	0.8277	1.2	0.09886	1.1	0.16	621	20	608	12	612	11	97.9
Z_GJ1	0.14	225126	282	0.03	23033	24.4	0.06036	0.41	0.8084	1.2	0.09679	1.1	0.23	615	18	596	12	602	11	96.8
Z_GJ1	0.12	216776	284	0.03	17629	115.3	0.06045	0.50	0.8163	1.2	0.09812	1.1	0.19	619	21	603	13	606	11	97.5
Z_GJ1	0.00	219560	290	0.03	82418	88.9	0.06030	0.43	0.8091	1.2	0.09751	1.1	0.65	613	19	600	12	602	11	97.8
Z_GJ1	0.02	208884	281	0.03	49909	53.2	0.06023	0.40	0.8163	1.2	0.09842	1.1	0.27	611	17	605	13	606	11	99.1
Z_GJ1	0.05	216065	293	0.03	3456	232.3	0.06067	0.39	0.8175	1.2	0.09783	1.1	0.47	626	17	602	12	607	11	96.1
Z_GJ1	0.01	207121	289	0.03	7174	88.3	0.06051	0.44	0.8232	1.2	0.09842	1.1	0.54	621	19	605	12	610	11	97.5
Z_GJ1	0.04	204890	285	0.03	22281	52.9	0.06034	0.35	0.8098	1.2	0.09696	1.1	0.62	615	15	597	12	602	11	97.1

GR4-ICAL4-VAR6 - 91500																				
Z_91500	0.27	70036	44	0.64	1510	573.5	0.07461	0.53	1.8661	2.4	0.18119	2.3	0.84	1057	21	1073	45	1069	31	101.6
Z_91500	0.11	71888	46	0.64	12475	73.8	0.07518	0.46	1.8643	2.2	0.17958	2.2	0.62	1072	19	1065	44	1068	30	99.3
Z_91500	0.04	68782	43	0.67	2816	232.9	0.07505	0.48	1.9522	2.4	0.18755	2.3	0.88	1069	19	1108	47	1099	33	103.7
Z_91500	0.33	70798	47	0.66	4457	47.5	0.07537	0.47	1.8722	2.4	0.17916	2.4	0.90	1077	19	1062	47	1071	32	98.6
Z_91500	0.31	73302	48	0.67	4505	38.9	0.07555	0.34	1.8833	2.4	0.17923	2.3	0.96	1082	13	1063	44	1075	32	98.2
Z_91500	0.03	70065	45	0.67	3286	108.0	0.07523	0.46	1.8649	2.4	0.17820	2.3	0.88	1074	18	1057	45	1069	32	98.5
Z_91500	0.33	70855	47	0.67	11420	75.3	0.07553	0.59	1.8647	2.3	0.17861	2.3	0.68	1081	24	1059	45	1069	31	98.0
Z_91500	0.14	63041	43	0.66	6657	63.7	0.07521	0.67	1.8298	2.4	0.17621	2.3	0.72	1073	27	1046	44	1056	31	97.5
Z_91500	0.50	64635	44	0.65	6626	31.3	0.07412	0.44	1.7702	2.6	0.17652	1.7	0.81	1044	18	1048	33	1035	34	100.4
Z_91500	0.19	63990	44	0.64	3891	108.3	0.07484	0.52	1.7452	2.6	0.17204	1.7	0.63	1063	21	1023	31	1025	34	96.3
Z_91500	0.16	64044	46	0.71	2561	183.1	0.07452	0.75	1.8085	2.6	0.17682	1.7	0.10	1054	30	1050	33	1048	34	99.6
Z_91500	0.14	64971	46	0.70	3961	72.5	0.07450	0.47	1.8343	2.6	0.17931	1.6	0.63	1054	19	1063	32	1058	34	100.9
Z_91500	0.00	64093	46	0.74	960	2181.8	0.07513	0.41	1.8696	2.6	0.18057	1.7	0.80	1071	17	1070	33	1070	35	99.9
Z_91500	0.23	62712	45	0.71	9483	65.7	0.07552	0.49	1.8594	2.8	0.17854	1.8	0.93	1081	20	1059	35	1067	37	97.9
Z_91500	0.32	61014	44	0.66	1215	214.1	0.07719	1.54	1.8925	3.0	0.17774	1.7	0.21	1122	61	1055	33	1078	40	94.0
Z_91500	0.30	61564	44	0.66	2688	173.8	0.07531	0.70	1.8728	2.6	0.18031	1.7	0.22	1075	28	1069	34	1071	35	99.4
Z_91500	0.06	74757	52	0.60	845	227.5	0.07521	0.42	1.8375	1.2	0.17682	1.1	0.49	1073	17	1050	21	1059	16	97.8
Z_91500	0.10	60213	44	0.61	2992	69.9	0.07580	0.58	1.8128	1.3	0.17372	1.1	0.50	1089	23	1033	21	1050	17	94.9
Z_91500	0.21	59383	43	0.63	80769	67.0	0.07527	0.54	1.8282	1.3	0.17644	1.2	0.70	1075	21	1047	23	1056	17	97.5
Z_91500	0.54	58193	44	0.61	1870	125.2	0.07528	0.58	1.8538	1.5	0.17882	1.2	0.85	1075	23	1061	24	1065	19	98.7
Z_91500	0.23	62476	47	0.62	7559	40.3	0.07529	0.57	1.8298	1.5	0.17625	1.3	0.85	1075	23	1046	25	1056	20	97.3
Z_91500	0.11	60251	47	0.63	7752	82.5	0.07533	0.47	1.8588	1.3	0.17854	1.3	0.81	1076	19	1059	25	1066	18	98.4
Z_91500	0.18	66903	53	0.62	5328	98.5	0.07506	0.57	1.8205	1.4	0.17536	1.3	0.78	1069	23	1042	26	1053	19	97.5

Following http://www.plasmage.org/recommendations

[1] concentration uncertainty c.20%

[3] Concordance calculated as (^{206}Pb-^{238}U age/^{207}Pb-^{235}U age)*100

Decay constants of Jaffey et al. (1971) used

bd = below detection; #N/A = not available

Uncertainties quoted without components related to systematic error unless otherwise stated

Total systematic uncertainties (s_{sys}): ^{206}Pb/^{238}U = 1.0%, ^{207}Pb/^{206}Pb = 0.55% (2s)

2.10 Análise de traços de fissão em apatita

As amostras BU4 e VAR5 foram analisadas no laboratório LA.TE. ANDES S.A., Salta, Argentina. O processo de preparação da amostra segue as técnicas padronizadas de Grist e Ravenhurst (1992a, b). As amostras foram purificadas e montadas em resina epóxi com uma quantidade de aproximadamente 100 cristais de apatita por amostra. Em geral, as apatitas montadas são subédricas a euédricas e fraturadas. As amostras montadas em resina são polidas em espelho e posteriormente condicionadas com ácido (Etching 1), a fim de revelar traços espontâneos. As amostras são irradiadas segundo o método de Detector Externo, em conjunto com padrões Durango e vidros dosimétricos IRMM 540 (15 mg/Kg de U), cada um acompanhado de uma lâmina de mica em contato com a superfície polida. O lote foi irradiado nas instalações do Reator RA-3 (Centro Atômico Ezeiza, Buenos Aires). O conjunto de amostras foi irradiado por 76 horas contínuas, integrando uma fluência de 7E15 n/cm^2, necessária para o tipo de análise. Após o período de decaimento no Reator após a irradiação, o lote foi enviado de volta ao laboratório LA.TE. ANDES S.A. para sua medição. Do total de grãos montados, são medidos aproximadamente 35 grãos ou a quantidade máxima possível, que atendem aos requisitos mínimos de área mensurável (600 μm^2) e são dispostos paralelamente ao eixo cristalográfico c (poços de corrosão de traços de fissão paralelos), evitando áreas com deslocamentos cristalográficos.

Todas as medidas foram realizadas com microscópio binocular Zeiss® AXIO Imager Z2m, para observação com luz refletida e transmitida, platina motorizada, câmera digital, computador e software para análise mineral. Todo o sistema é controlado pelo software Tra-ckWorks® Autoscan® com o qual a contagem da densidade do traço e outros parâmetros (comprimentos confinados e DPar) são realizados.

As idades dos traços de fissão foram determinadas usando o método do valor ζ (método do detector externo) descrito por Huford e Green (1982, 1983) e Wagner Van den Haute (1992). O processamento dos dados foi realizado em consultório por meio do programa TrackKey © (Dunkl, 2002) para o cálculo das idades e seu erro associado (1σ). Nas amostras com alta dispersão na

distribuição de idade por grão, a análise populacional é realizada por meio do software BinomFit © (Brandom, 1992, 1996, 2002).

CAPÍTULO 3
ARTIGO 1

Geological Magazine

www.cambridge.org/geo

Emplacement conditions and exhumation of the Varvarco Tonalite and associated plutons from the Cordillera del Viento, Southern Central Andes

Omar Sebastian Assis[1], Claudia Beatriz Zaffarana[2], Darío Orts[2], Carla Puigdomenech[3], Víctor Ruiz González[3], Gloria Gallastegui[4], Natalia Hauser[1], Ekaterina S. Kiseeva[5], José Francisco Molina[6] and Sebastián Pernich[2]

[1]Instituto de Geociências, Universidade de Brasília, Laboratório de Geocronologia e geoquímica isotópica, Brasília, 70910 900, DF, Brasil; [2]Universidad Nacional de Río Negro, Sede Alto Valle-Valle Medio e Instituto de Investigación en Paleobiología y Geología (IIPG-CONICET), General Roca, Río Negro, Argentina; [3]Instituto de Geociências Básicas, Aplicadas y Ambientales de Buenos Aires (IGeBA); CONICET; Universidad de Buenos Aires; [4]Instituto Geológico y Minero de España (IGME, CSIC), España; [5]School of Biological, Earth and Environmental Sciences, University College Cork, Distillery Fields, North Mall, Cork, Ireland and [6]Departamento de Mineralogía y Petrología, Universidad de Granada, España

Original Article

Cite this article: Assis OS, Zaffarana CB, Orts D, Puigdomenech C, Ruiz González V, Gallastegui G, Hauser N, Kiseeva ES, Molina JF, and Pernich S (2022) Emplacement conditions and exhumation of the Varvarco Tonalite and associated plutons from the Cordillera del Viento, Southern Central Andes. *Geological Magazine* **159**: 645–672. https://doi.org/10.1017/S0016756821001163

Received: 24 March 2021
Revised: 6 October 2021
Accepted: 18 October 2021
First published online: 14 March 2022

Keywords:
granitoids; Andean orogeny; AMS; fission-track dating; fast exhumation rate

Author for correspondence:
Omar Sebastian Assis,
Emails: seba_assis@outlook.com; sebaoassis@gmail.com

Abstract

During the Late Cretaceous Andean orogeny, the compressive deformation associated with the shallowing of the subducting slab caused the development of the arc-related igneous rocks known as the Naunauco Belt. This study presents petrographic, mineralogical and anisotropy of magnetic susceptibility data for the Varvarco Intrusives (the Varvarco Tonalite, Butalón Tonalite and Radales Aplite), which crop out in the Cordillera del Viento, Neuquén Province, Argentina. The assembly of plutons was formed by mafic magma episodic injection. Amphibole and biotite compositions suggest that the Varvarco Tonalite is related to calc-alkaline, I-type magmas, typical of subduction environments. Different geothermobarometers based on amphibole and plagioclase compositions for the Varvarco Tonalite suggest shallow emplacement conditions (~2–3 kbar, equivalent to ~12 km depth). Apatite fission-track analyses give exhumation ages of 67.5 ± 8 Ma for the Varvarco Tonalite and 50.3 ± 5.9 Ma for the Butalón Tonalite. A calculated continuous fast exhumation rate of at least 330 °C Ma^{-1} is consistent with the shallow emplacement conditions, textural data and geobarometric estimations. In agreement with the thermal profile, the magmatic system was exhumed by ~12 km within *c.* 2.1 Ma implying a geothermal gradient of ~62.5 °C km^{-1}. The last step of exhumation occurred between ~65.3 and 56.9 Ma. The magmatic fabrics observed in the studied plutons reflect mostly magma chamber processes. The Varvarco Intrusives represent satellite calc-alkaline plutons of the North Patagonian Batholith which were emplaced syn- to post-tectonically with respect to a major deformation stage of the Southern Central Andes.

1. Introduction

Cordilleran batholiths are large magmatic bodies that result from the accumulation of many smaller plutons, spatially and chemically associated, which may or may not be temporally related. Most of these batholiths are composed of granodiorite and tonalite, such as the Sierra Nevada Batholith (Bateman & Eaton, 1967) and the North Patagonian Batholith (Ramos *et al.* 1982). The Patagonian Batholith represents a large granite intrusive complex that extends from 39° to 56° S, and is mainly composed of tonalites (Ramos *et al.* 1982). The main peak of intrusion relates to the development of the North Patagonian Batholith formed in Early Cretaceous time, between 136 and 127 Ma (Pankhurst *et al.* 1999; Hervé *et al.* 2007), slightly before the onset of Late Cretaceous compression coeval with the Neuquén foreland basin development (Ramos, 1999). In addition, in Late Cretaceous–Palaeogene times, the magmatic arc was expanded into the retro-arc region, including the present-day Cordillera del Viento range, by the intrusion of satellite igneous bodies at 130–150 km east of the present arc trend (Hervé *et al.* 2007; Fig. 1).

Here, we study the internal structure of some of these satellite igneous bodies, the Varvarco Intrusives (Varvarco Tonalite, Radales Aplite and Butalón Tonalite) that are exposed in the Varvarco–Butalón region in the Cordillera del Viento (Neuquén Andes; Figs 1, 2a). We applied the anisotropy of magnetic susceptibility (AMS) method, combined with petrographic and mineral chemistry data to define magmatic structures and, thus, to infer magma emplacement

© The Author(s), 2022. Published by Cambridge University Press.

CAMBRIDGE UNIVERSITY PRESS

Downloaded from https://www.cambridge.org/core, on subject to the Cambridge Core terms of use, available at https://www.cambridge.org/core/terms. https://doi.org/10.1017/S0016756821001163

3 ARTIGO 1: "EMPLACEMENT CONDITIONS AND EXHUMATION OF THE VARVARCO TONALITE AND ASSOCIATED PLUTONS FROM THE CORDILLERA DEL VIENTO, SOUTHERN CENTRAL ANDES"

Omar Sebastian ASSIS[1]*, Claudia Beatriz ZAFFARANA[2], Darío ORTS[2], Carla PUIGDOMENECH[3], Víctor RUIZ GONZÁLEZ[3], Gloria GALLASTEGUI[4], Natalia HAUSER[1], Ekaterina S. KISEEVA[5], José Francisco MOLINA[6] and Sebastián PERNICH[2]

[1]Instituto de Geociências, Universidade de Brasília, Laboratório de Geocronologia e geoquímica isotópica, Brasília, 70910 900, DF, Brasil.

[2]Universidad Nacional de Río Negro, Sede Alto Valle-Valle Medio, General Roca e Instituto de Investigación en Paleobiología y Geología (IIPG-CONICET).

[3]Instituto de Geociencias Básicas, Aplicadas y Ambientales de Buenos Aires (IGeBA); CONICET; Universidad de Buenos Aires.

[4]Instituto Geológico y Minero de España (IGME, CSIC), España.

[5] School of Biological, Earth and Environmental Sciences, University College Cork, Distillery Fields, North Mall, Cork, Ireland

[6]Departamento de Mineralogía y Petrología, Universidad de Granada, España.

*Corresponding author; E-mail: seba_assis@outlook.com, sebaoassis@gmail.com

Abstract

During the Late Cretaceous Andean orogeny, the compressive deformation associated with the shallowing of the subducting slab caused the development of the arc-related igneous rocks known as the Naunauco Belt. This study presents petrographic, mineralogical, and anisotropy of magnetic susceptibility (AMS) data of the Varvarco Intrusives (the Varvarco Tonalite, Butalón Tonalite and Radales Aplite), which crop out in the Cordillera del Viento, Neuquén Province, Argentina. The assembly of plutons was formed by mafic magma episodic injection. Amphibole and biotite compositions suggest that the Varvarco Tonalite is related to calc-alkaline, I-type magmas, typical of subduction environments. Different geothermobarometers based on amphibole and plagioclase compositions on the Varvarco Tonalite suggest shallow emplacement conditions (~2-3 kbar, equivalent to ~12 km depth). Apatite fission track analyses give exhumation ages of 67.5 ± 8 Ma for the Varvarco Tonalite and 50.3 ± 5.9 Ma for the Butalón Tonalite. A calculated continuous fast exhumation rate of at least 330 °C/My is consistent with the shallow emplacement conditions, textural data and geobarometric estimations. In agreement with thermal profile, the magmatic system was exhumed by ~12 km within ca. 2.1 Ma implying a geothermal gradient of ~62.5 °C/km. The last step of exhumation occurred between ~65.3 Ma and 56.9 Ma. The magmatic fabrics observed in the studied plutons reflect mostly magma chamber processes. The Varvarco Intrusives represent satellite calc-alkaline plutons of the North Patagonian Batholith which were emplaced syn- to post-tectonically with respect to a major deformation stage of the Southern Central Andes.

Keywords: granitoids, Andean orogeny, AMS, fission track dating, fast exhumation rate.

3.1 Introduction

Cordilleran batholiths are large magmatic bodies that result from the accumulation of many smaller plutons, spatially and chemically associated, which may or may not be temporally related. Most of these batholiths are composed of granodiorite and tonalite, such as the Sierra Nevada Batholith (Bateman & Eaton, 1967) and the North Patagonian Batholith (Ramos *et al*. 1982). The Patagonian Batholith represents a large granite intrusive complex that extends from 39º to 56º S, and is mainly composed of tonalites (Ramos *et al*. 1982). The main peak of intrusion relates to the development of the North Patagonian Batholith formed in Early Cretaceous, between 136 and 127 Ma (Pankhurst *et al*. 1999; Hervé *et al*. 2007), slightly before the onset of Late Cretaceous compression coeval with the Neuquén foreland basin development (Ramos, 1999). In addition, in Late Cretaceous-Paleogene, the magmatic arc was expanded into the retroarc region, including the present-day Cordillera del Viento range, by the intrusion of satellite igneous bodies at 130-150 km east of the present arc trend (Hervé *et al*. 2007; Fig. 1).

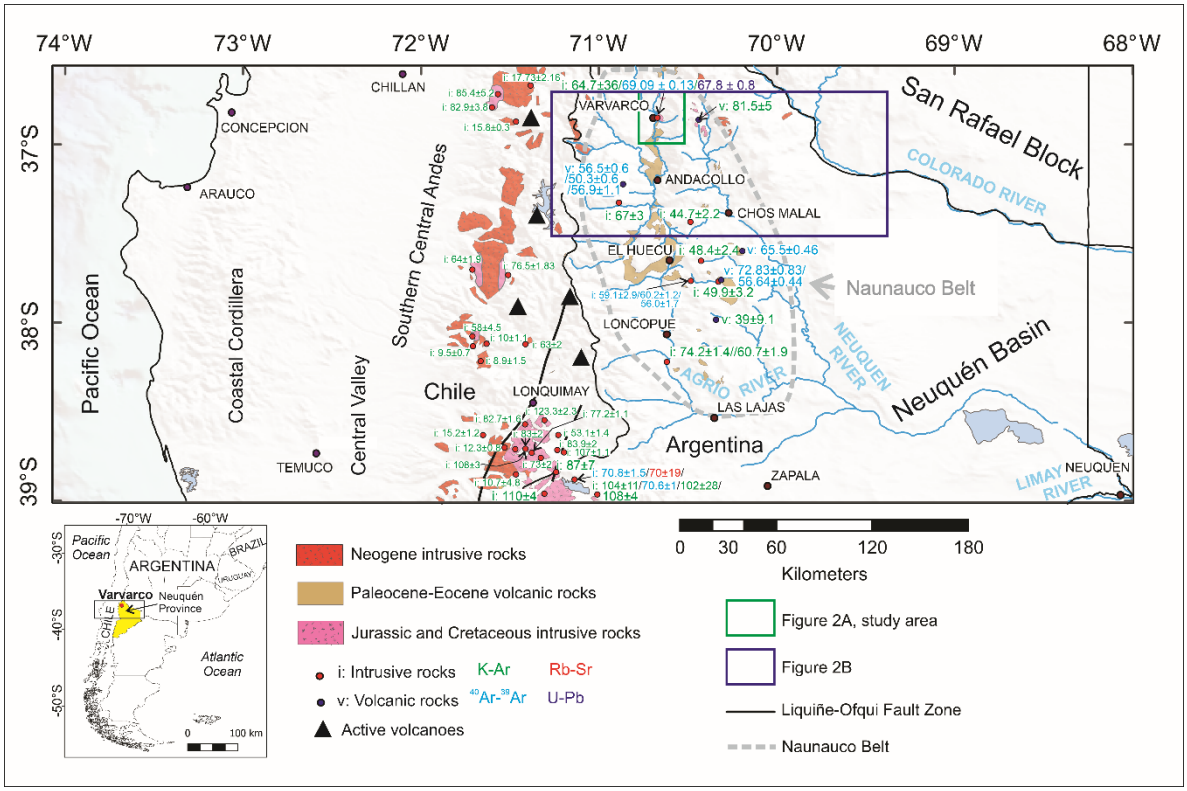


Figure 1: Regional geological map of the Southern Central Andes. Ages for intrusive and volcanic rocks are listed in Supplementary Table S1. Black rectangle indicates study area (Figures 2A and

2B). The Naunauco Belt is marked with a grey dotted line, it comprises both plutonic rocks of Late Cretaceous-Paleogene age and volcanic rocks of Paleocene-Eocene age. Numbers indicate ages obtained by different methods, as shown in legend.

Here, we study the internal structure of some of these satellite igneous bodies, the Varvarco Intrusives (Varvarco Tonalite, Radales Aplite and Butalón Tonalite) that are exposed in the Varvarco-Butalón region in the Cordillera del Viento (Neuquén Andes, Fig. 1 and 2a). We applied the anisotropy of magnetic susceptibility (AMS) method, combined with petrographic and mineral chemistry data to define magmatic structures and, thus, to infer magma emplacement mechanisms. The AMS method has been proven to be a very useful tool to study the internal structure of weakly foliated bodies (e.g., Archanjo *et al*. 1995, 2002; de Saint Blanquat & Tikoff, 1997; Ferré & Améglio, 2000; McNulty *et al*. 2000; Neves *et al*. 2003; Žák *et al*. 2005; D'Eramo *et al*. 2006; Stevenson, 2009; Somoza *et al*. 2015; Nédélec & Bouchez, 2015; Olivier *et al*. 2016; Zaffarana *et al*. 2017). In particular, the AMS method is relevant for the resolution of magmatic lineations, which are generally hard to measure in the field. The interpretation of the internal structure of plutons and their relationship with the country rock may be classified into three main types: reflecting internal magma chamber, regional deformation processes (Paterson *et al*. 1998), or a combination of both.

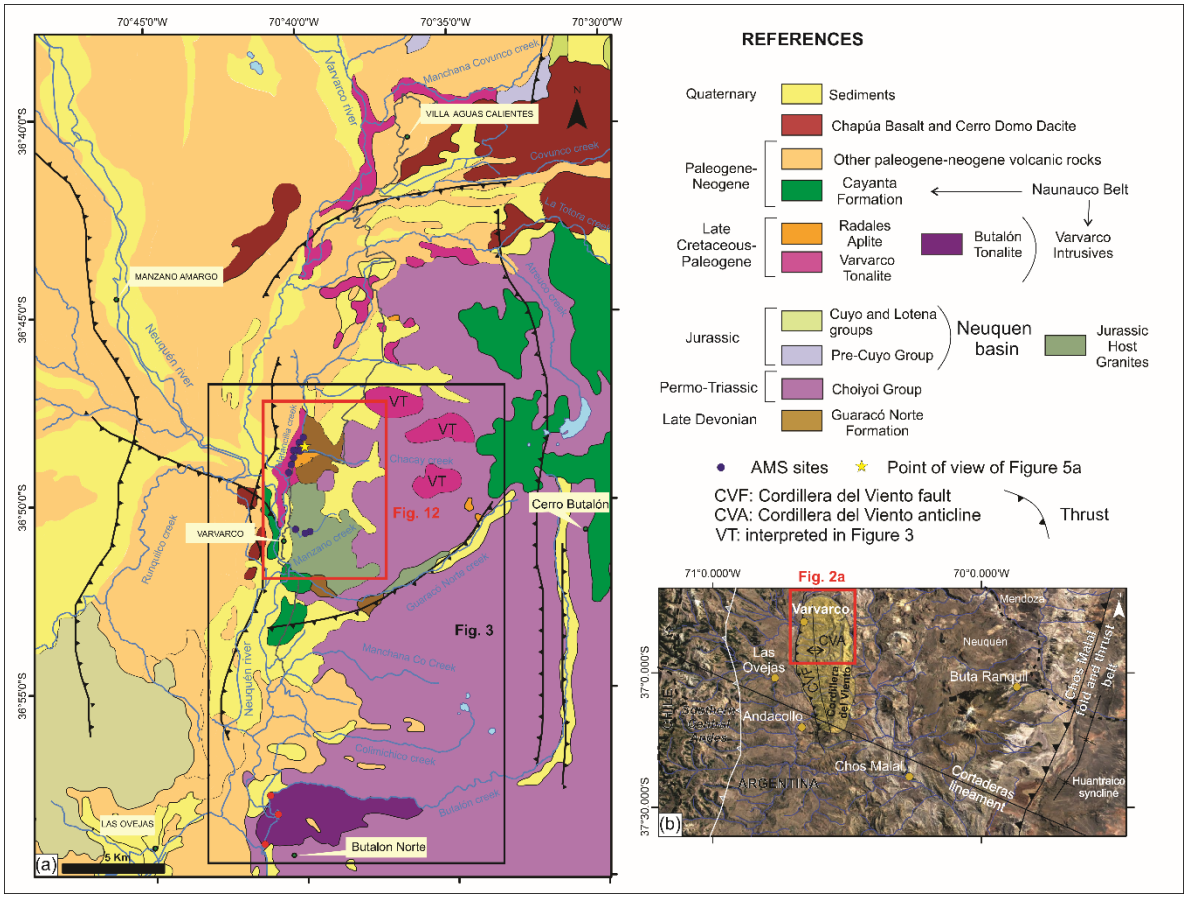


Figure 2: Local (a) and regional (b) maps of the study area. The maps are based on Zanettini et al. (2001), Ramos et al. (2011), Giacosa et al. (2014), and Sagripanti et al. (2014). Black rectangle indicates the area in Figure 3, and red rectangle indicates the area of Figure 12.

The timing of intrusion with respect to the exhumation of the Varvarco Tonalite and the Butalón Tonalite was also investigated by obtaining apatite fission track ages for these intrusives. Crustal thickness estimates at the time of magma generation were aided by geochemical data (mineral chemistry for amphibole, plagioclase, and biotite), with the aim of developing a model for emplacement and exhumation of the Varvarco Tonalite. Mineral compositions were used to constrain magma chamber temperature and depth through geothermobarometric analysis (Hammarstrom & Zen 1986; Hollister *et al*. 1987; Johnson & Rutherford 1989; Schmidt 1992; Holland & Blundy 1994; Anderson & Smith 1995; Ridolfi *et al*. 2010; Ridolfi & Renzulli 2012; Putirka 2016; Molina *et al*. 2015; 2021). The combination of these methods allows us to unravel the history of Varvarco satellite intrusives, from their emplacement to fast exhumation during the Late Cretaceous-Paleogene times of the Andean orogeny.

3.2 Geological and structural framework

The three plutons investigated in this work: the Varvarco Tonalite, the Butalón Tonalite, and the Radales Aplite, are located in the Varvarco and Butalón areas (Fig. 2a) and were originally named by Pesce (1981) as Varvarco Intrusives. They were later attributed to the Colipilli Formation (Franchini *et al*. 2003; Kay *et al*. 2006; Casé *et al*. 2008), the intrusive part of the volcanic and plutonic Late Cretaceous Naunauco Belt (Llambías & Malvicini 1978; Zamora Valcarce *et al*. 2011).

Pesce (1981) had originally described the Varvarco pluton as a granodiorite body, but the average modal composition that we found in all our sites is more compatible with a tonalitic intrusive. Therefore, we renamed this pluton as Varvarco Tonalite. In the same way, the Radales Granite (Zanettini *et al*. 2001) is renamed here as Radales Aplite because its general texture is aplitic, typical of subvolcanic igneous bodies.

The Varvarco Tonalite has a K-Ar cooling age (whole-rock) of 64.7 ± 3.2 Ma (J.I.C.A./M.M.A.J., 2000 in Franchini *et al*. 2003), and an ^{40}Ar-^{39}Ar cooling age for biotite of 69.09 ± 0.13 Ma (Kay *et al*. 2006). A U-Pb SHRIMP zircon age of 67.8 ± 0.8 Ma was thoroughly documented by Assis (2019); thus the crystallisation age of Varvarco Tonalite coincides with the K-Ar cooling age. The geochemistry of the Butalón Tonalite was studied by Casé *et al*. (2008), who indicated these igneous rocks are meta- to peraluminous calc-alkaline with low to medium K_2O content, coincidental with I-type granitoids like other granitoids in the area (e.g., Cerro Nevazón; Franchini *et al*. 2003). The Radales Aplite is a granophyric granite intruding the Varvarco Tonalite (Zanettini *et al*. 2001). The Au-Ag veins which are intruding the Radales Aplite and Permian and Jurassic rocks were dated by the ^{40}Ar-^{39}Ar stepwise method in adularia and yielded the age of 65.68 ± 0.22 Ma (Zappettini *et al*. 2014). These ^{40}Ar-^{39}Ar data indicate that break between the emplacement of Varvarco Tonalite and the intrusion of the Radales Aplite was short.

The Varvarco Intrusives crop out in the Cordillera del Viento range in the Neuquén Andes of southwestern Argentina, which is a structurally complex area, with convergence of structures developed during different periods of time. The

currently observed structural features in this region were mainly formed between the Late Cretaceous and Miocene (Giacosa *et al*. 2014; Turienzo *et al*. 2018; Sánchez *et al*. 2018), when the main compressive structures were developed (Fig. 2a, b).

The Cordillera del Viento Fault is one of the main compressional structures formed by the inversion of N-S normal faults that controlled the Late Triassic to Early Jurassic rift sedimentation in the westernmost part of the Neuquén Basin (Vergani *et al*. 1995). During the Andean orogeny, in pre-Eocene times, the inversion of the extensional system occurred, and the Cordillera del Viento Fault became a reverse fault that uplifted Paleozoic rocks to form the Cordillera del Viento Anticline (Giacosa *et al*. 2014).

The core of the Cordillera del Viento anticline (Giacosa *et al*. 2014) exposes a basement of Middle Paleozoic metamorphic rocks (Fig. 2a), grouped together in the Guaracó Norte Formation (Zappettini *et al*. 1987; Zanettini *et al*. 2001). These rocks include quartz-rich metasandstones and laminated quartzite layers, with slates towards the top of the sequence which are all cut by numerous quartz and granitic veins (Giacosa *et al*. 2014). The sedimentary protolith is characterised by rhythmic alternation of sandstone and pelite layers showing current ripples (Giacosa *et al*. 2014). The age of the Guaracó Norte Formation is Late Devonian, considering a maximum depositional age, based on the youngest peak of 369 ± 5 Ma (younger than 374 and older than 326 Ma, U-Pb SHRIMP dating of detrital zircon, Zappettini *et al*. 2012).

The Carboniferous sedimentary rocks of the Cordillera del Viento crop out south of the study area, near the Andacollo locality (Fig. 2b), and they are grouped into the Andacollo Group (Digregorio, 1972; Digregorio & Uliana, 1980; Llambías *et al*. 2007). Volcanic and plutonic facies from the Permo-Triassic Choiyoi Group (Stipanicic, 1966; Digregorio, 1972) crop out in the Cordillera del Viento. In the Varvarco area, the Choiyoi Group is composed of two sections, where andesites and rhyolites predominate in the lower and upper sections, respectively (Digregorio, 1972; Zanettini *et al*. 2001).

An extensional deformation period, associated with Gondwana break-up is registered for the Cordillera del Viento. This extensional phase initiated N–S-trending and NNE–SSW in the northern part of the Cordillera del Viento to E–W-

trending faults in the southern part, where interbedded shale strata and ignimbrites with wedge geometry are separated by normal faults (Giacosa *et al*. 2014). Magnetic and gravimetric data, combined with field observations, suggest that Late Triassic rifting in the Cordillera del Viento area would have taken place in a regional WNW-ESE to NW trend, with minor local NE structures (Sagripanti *et al*. 2014). Magnetic data revealed that basement rocks are segmented by nearly orthogonal structures (Sagripanti *et al*. 2014).

Between the Late Triassic and Cenozoic, the Neuquén Basin (Fig. 1) developed between 32º and 40º S (e.g., Howell *et al*. 2005). During the Jurassic and Early Cretaceous, the Paleo-Pacific Ocean transgressions produced marine strata which alternated with the deposition of continental sequences in the back-arc setting of this basin, which was affected by thermal subsidence (Legarreta & Uliana, 1991; Vergani *et al*. 1995; Howell *et al*. 2005; Arregui *et al*. 2011).

On the eastern flank of the Cordillera del Viento, the Early to Late Jurassic syn-rift deposits of the early phase of the Neuquén Basin crop out, characterised by variable thickness and normal fault association (Sagripanti *et al*. 2014). The Pre-Cuyo Group (Hettangian-Sinemurian) is represented by the Cordillera del Viento and Milla Michicó formations (Gulisano *et al*. 1984; Riccardi & Stipanicic, 2002). The Jurassic Cuyo and Lotena groups crop out in the northeastern corner of the studied area (Suárez & de la Cruz, 1997; Leanza *et al*. 2005; Llambías *et al*. 2007; Fig. 2).

We discovered that an igneous body, previously assigned to the Radales aplite, has an Early Jurassic age (~ 185 Ma). This aplite is here referred as the Jurassic Host Granite (Fig. 2a, 3a-b). These felsic intrusives are coeval with the Pre-Cuyo Group. The provisional name highlights that they are a part of the host rocks for the Late Cretaceous granites studied in this work.

As mentioned in the Introduction chapter, the Andean orogeny was mainly active in the Cordillera del Viento region between Late Cretaceous and Miocene. Andean orogeny reactivated Late Triassic WNW-ESE to NW and NE normal structures (Giacosa *et al*. 2014; Turienzo *et al*. 2018; Sánchez *et al*. 2018). Sánchez *et al*. (2018) reported zircon (U-Th)/He thermochronological data from 72.2 ± 2.8 to 66.0 ± 6.1 Ma and the apatite fission track ages are 51.7 ± 3.2 and 56.5 ± 10.7 Ma for exhumation in the Chos Malal fold-and-thrust belt. The WNW-

ESE and NW structures acted as transfer zones, whereas the NE ones as frontal contractional structures (Sagripanti *et al*. 2014). The N-S structures have been interpreted as the result of Andean deformation, as these contractional structures are not related to the rifting architecture and cross-cut the depocentres (Sagripanti *et al*. 2014; Giacosa *et al*. 2014). They concluded that Andean crustal shortening caused the formation of the N-S faults and thrusts, and associated folds, as well as W-E to WNW-ESE strike slip structures. The latter are regarded as lateral structures that control the N and S propagation of the Andean thrusts.

During the Andean compressive stage in the Mid Cretaceous and slightly after, volcanic rocks of the Cayanta Formation (Rapela & Llambías, 1985) were extruded, and subvolcanic magmatic bodies were emplaced into a satellite position with respect to the present magmatic arc in Late Cretaceous-Paleogene times (Llambías & Rapela, 1989; Franchini *et al*. 2003; Cobbold & Rossello, 2003; Hervé *et al*. 2007; Zamora Valcarce 2007; Llambías & Aragón, 2011; Spagnuolo *et al.* 2012; Fig. 1, 2a).

3.3 Analytical methods

Field studies were carried out in the area of Varvarco, Radales and Butalón plutons, and their host rocks, resulting in 23 thin sections for petrographic studies. The Anisotropy of Magnetic Susceptibility (AMS) study was performed in 17 sites, where nine sites belong to the Varvarco Tonalite, three sites to the Butalón Tonalite, one site to the Radales Aplite, three sites to the Jurassic Host Granites, and one site to the Guaracó Norte Formation. A portable rock drill for paleomagnetic sampling was used. From each site we collected at least five orientated cylinders, summing up to a of 95 specimens (Table 1). The cylinders were orientated using solar and magnetic compasses. Sites are presented in Table 1; their distribution is placed along roads and creeks (Fig. 2a).

The high elevation of the Cordillera del Viento region makes it difficult to map the exact morphology of the Varvarco, Radales and Butalón igneous bodies. ASTER level 1B data were used to complement the mapping of the plutonic bodies (Fig. 3a, b). The studied geological units at 1:200000 scale are presented in Figures 2a and 3a, b. Their recognition in ASTER satellite images was possible through combining two false-color RGB compositions (RGB: 4 3 1 and RGB: 7 4

14), as shown in Figures 3a and b, respectively. False-color RGB composition 7 4 14 is useful to discriminate rocks with different silica content. In map shown in Figure 3b orange/yellow regions correspond to felsic litho-units that are richer in quartz, as shown by the diagnostic SiO-bond spectral absorption at 10.30-11.70 μm (Clark, 1999; bands 13-14 in ASTER).

Site	Litology	GPS data	N	Kaver	K1d	K1i	C1a	C1b	K2d	K2i	C2a	C2b	K3d	K3i	C3a	C3b	K1	K2	K3	Lmean	Fmean	Pmean	Pjmean	Tmean
V1	Varvarco Tonalite (main facies)	Lat: 36º48´36.1" S; Long: 70º40´14.6" W	5	5.98E-02	143.2	74.5	8.3	3.5	337.7	15.1	9.9	2.9	246.7	3.7	6.6	4.1	1.087	0.982	0.931	1.107	1.055	1.167	1.170	-0.312
V2		Lat: 36º48´36.3" S; Long: 70º40´09.5" W	5	1.86E-02	137.2	47.8	23.9	19.5	5.2	31.2	32.4	20.5	258.6	25.3	32.7	15.9	1.023	0.997	0.980	1.026	1.017	1.044	1.044	-0.189
V3		Lat: 36º48´36.4" S; Long: 70º40´04.3" W	7	1.15E-02	323.2	3.5	20.8	9.9	53.8	8.6	21.0	8.5	211.2	80.7	10.9	7.9	1.019	0.999	0.982	1.019	1.018	1.037	1.037	-0.051
V6		Lat: 36º48´23.8" S; Long: 70º40´03.2" W	6	4.70E-02	68.7	59.2	18.6	6.7	338.0	0.4	33.5	8.4	247.7	30.8	31.9	6.2	1.050	0.986	0.963	1.065	1.024	1.091	1.094	-0.457
V7		Lat: 36º48´15.7" S; Long: 70º39´55.0" W	6	1.23E-02	63.7	61.2	11.0	4.9	306.1	14.3	49.5	10.4	209.4	24.4	49.5	5.1	1.069	0.980	0.951	1.090	1.031	1.124	1.129	-0.478
V8		Lat: 36º48´58.7" S; Long: 70º40´20.2" W	5	4.20E-02	124.9	53.5	21.6	10.3	28.3	4.9	21.6	16.4	294.7	36.1	18.9	3.3	1.049	1.017	0.934	1.031	1.089	1.123	1.128	0.479
V9		Lat: 36º48´47.8" S; Long: 70º40´15.1" W	7	6.49E-02	135.9	53.3	30.0	13.0	353.4	30.6	34.1	14.7	252.1	18.3	25.6	9.4	1.039	1.004	0.957	1.035	1.049	1.086	1.086	0.154
V17		Lat: 36º49´11.1" S; Long: 70º40´26.1" W	6	4.35E-02	119.1	50.6	40.1	4.9	219.8	8.7	39.5	11.9	316.6	38.1	12.9	10.1	1.035	1.014	0.951	1.020	1.067	1.088	1.093	0.524
V4	Qtz-dioritic dike (Varvarco Tonalite)	Lat: 36º48´35.8" S; Long: 70º40´05.4" W	5	4.74E-02	119.7	38.3	12.0	3.8	329.5	47.7	13.5	3.6	222.1	15.2	10.2	5.6	1.048	1.005	0.946	1.043	1.063	1.108	1.108	0.185
V14	Butalón Tonalite	Lat: 36º57´46.0" S; Long: 70º41´12.0" W	5	3.74E-02	305.5	64.7	6.7	2.8	105.6	24.0	9.0	5.0	199.0	7.6	9.2	4.8	1.037	1.006	0.957	1.031	1.051	1.084	1.084	0.250
V15		Lat: 36º58´16.3" S; Long: 70º40´57.7" W	5	4.39E-02	191.5	14.9	46.7	7.2	64.3	66.2	46.7	15.2	286.5	18.1	15.4	7.1	1.013	1.005	0.982	1.008	1.024	1.032	1.034	0.522
V16		Lat: 36º59´03.2" S; Long: 70º41´24.9" W	5	4.94E-02	129.5	65.0	11.5	2.2	269.2	19.6	15.0	9.2	4.6	14.9	13.5	2.3	1.038	1.005	0.957	1.033	1.050	1.084	1.084	0.202
V5	Radales Granite	Lat: 36º48´36.8" S; Long: 70º40´02.3" W	5	2.37E-03	152.7	50.6	20.2	7.1	318.2	38.5	20.7	10.2	53.9	7.2	12.0	8.3	1.025	1.004	0.971	1.021	1.033	1.055	1.055	0.220
V10	Jurassic Host Granites	Lat: 36º50´42.1" S; Long: 70º40´14.0" W	5	9.53E-04	120.0	33.5	30.4	12.1	261.7	49.9	46.0	12.7	16.5	19.4	43.6	8.0	1.016	0.998	0.986	1.018	1.013	1.031	1.031	-0.151
V11		Lat: 36º50´42.1" S; Long: 70º40´14.0" W	5	3.16E-02	19.3	40.2	3.0	1.0	154.7	40.1	16.5	2.7	267.0	24.2	16.5	1.4	1.066	0.983	0.951	1.084	1.034	1.121	1.125	-0.420
V12		Lat: 36º50´46.3" S; Long: 70º39´45.3" W	5	2.80E-02	135.5	30.2	22.1	4.1	4.2	48.7	21.8	6.4	241.5	25.4	11.3	3.2	1.015	1.006	0.979	1.009	1.029	1.037	1.039	0.533
V13	Guaracó Norte Fm.	Lat: 36º50´48.5" S; Long: 70º39´54.5" W	5	4.40E-04	92.4	63.6	55.2	6.2	331.2	14.5	55.4	10.6	235.3	21.6	15.1	6.0	1.008	1.005	0.987	1.003	1.018	1.021	1.023	0.681

Table 1: AMS sites of the Varvarco, Radales and Butalón plutons, Jurassic Host Granites and of the Guaracó Norte Formation. GPS data is given in latitude and longitude. N is the number of samples used in statistics. Km=(K1+K2+K3)/3 is the mean magnetic susceptibility (SI units). L is the magnetic lineation (K1/K3); F is the magnetic foliation (K2/K3); P is the degree of anisotropy (Jelinek, 1981); T=(lnF − lnL)/(lnF + lnL) is the Jelinek's parameter (Jelinek, 1981). K1, K2 and K3 are mean AMS eigenvectors which represent the maximum, intermediate and minimum susceptibility intensities, respectively. Dec, declination in degrees; Inc, inclination in degrees; C1a and C1b are the semiangles of the major and minor axes of the 95% confidence ellipse, respectively, calculated by the bootstrap method.

3.3.1 Anisotropy of magnetic susceptibility (AMS)

An MFK1-B Kappabridge susceptibilimeter, located at the IGEBA, CONICET, Argentina, was used to perform the anisotropy of the magnetic susceptibility measurements. A minimum of five specimen per site were used (Jelínek, 1978, 1981) to obtain the anisotropy of the magnetic susceptibility ellipsoids (with principal axes $K_1 > K_2 > K_3$) with the programs ANISOFT 4.2 (Chadima & Jelinek, 2009).

The rock magnetic fabric is defined by the three principal axes of the anisotropy of the magnetic susceptibility ellipsoid ($K_1 > K_2 > K_3$; Bouchez, 2000). A magnetic lineation is defined parallel to K_1. A magnetic foliation is the plane containing K_1 and K_2, with K_3 being the pole to foliation. The magnetic lineation is parallel to the structural lineation (stretching or flow), and the magnetic foliation is parallel to the structural foliation (flattening or flow; Borradaile & Henry, 1997). However, sometimes this relationship may be obliterated by fabric overprinting or by the presence of single domain magnetite (e.g., Rochette *et al*. 1992, 1999; Borradaile & Henry, 1997).

The domain state of magnetite was studied using the diagram of Day *et al*. (1977), which was constructed with the Hc, Ms and Mr (coercive force, saturation magnetisation and remanent magnetisation, respectively) hysteresis parameters, together with the remanent coercive force Hcr (obtained from the backfield curve, Bouchez, 2000). Anhysteretic remanence measurements (Somoza *et al*. 2015) were also performed in some representative samples to check the coaxial behavior of the ferromagnetic and the paramagnetic fabric of the rocks.

The minerals that control the magnetic fabric were investigated by hysteresis curves, isothermal remanent magnetisation-backfield analyses in 6 representative samples (four from Varvarco Tonalite and two from the Jurassic Host Granites). The anisotropy of anhysteretic remanent magnetisation (AARM; e.g., Somoza *et al*. 2015) was applied in three sites. Measurements were performed in the Ludwing-Maximilians University in München, Department of Earth and Environment Sciences, using an equipment called “sushi bar” (Wack & Gilder, 2012).

3.3.2 Apatite fission track dating (AFT)

Apatite fission tracks (AFT) from samples VAR5 from the Varvarco Tonalite and BU4 from the Butalón Tonalite were analysed in the LA.TE. ANDES laboratory (www.lateandes.com), Salta, Argentina. Both apatite fractions were obtained by mechanical separation, magnetic separation (Frantz isodynamic separator) and heavy liquid treatment (LTS and diiodomethane). Approximately 100 apatite crystals for each sample were then mounted in epoxy. In general, the apatite crystals are subhedral to euhedral, and fractured. The mounted samples were polished and then leached under nitric acid (HNO_3) 5.5 N for 20 seconds at 20 °C, to reveal spontaneous tracks. The samples were then irradiated with the External Detector in the RA-3 Reactor (Centro Atómico Ezeiza, Buenos Aires, Argentina). The irradiation process took place over 76 hours, with a fluency of $7x10^{15}$ n/cm^2. After the decay period in the reactor, the batch was sent back to the LA.TE. ANDES S.A. laboratory for the fission track measurements. Overall, ~35 grains were used for measurements with a surface greater than 600 μm^2. Areas with obvious crystallographic dislocations were avoided.

All measurements were made with a Zeiss AXIO Imager Z2m binocular microscope. The system is equipped with the TrackWorks Autoscan software, which carried out the counting of the tracks and determination of other parameters, such as fission-track etch pit diameter (Dpar). The ages were determined with the method of ζ value from Hurford & Green (1982, 1983) and Wagner *et al*. (1992). Data processing was done using TrackKey software (Dunkl, 2002) that allowed age calculation. The uncertainty on obtained ages is reported at the 1-2 σ level (Fig. 15a, b).

3.3.3 Electron microprobe analysis

Electron microprobe analysis of major element concentrations was performed at the Technical-Scientific Services of Oviedo University (Spain) using a Cameca SX-100 electron microprobe with a voltage of 15 KV, current of 15 nA, and acquisition time of 10 s per element, in WDS mode. Silicates and oxides were used for calibration. The standards of the Bureau de Recherches Geologiques et Minières (BRGM) were used to refine the results. The obtained mineral compositions are presented in Table 2.

3.4 Results

3.4.1 ASTER data, field observations and petrography

As stated earlier in text, Varvarco intrusives are made of Varvarco Tonalite, Radales Aplite and Butalón Tonalite. Varvarco Tonalite and Radales Aplite are a part of a composite intrusion of approximately 10 km diameter. Varvarco Tonalite is located in the outer region, Radales Aplite forms a small stock along the Chacay creek (Fig. 3a, b). These units intrude the rocks of the Guaracó Norte Formation and the Jurassic Host Granites. ASTER data suggest that the shape of the Varvarco pluton is broadly circular, with a typical normal zoning pattern, more felsic towards the centre of the intrusion, if we consider that the Radales Aplite is located towards the centre of the Varvarco Tonalite.

The shape of the Butalón Tonalite is more irregular; the body has a length of 8 km and is elongated in E-W direction (Fig. 3a, b). The similar response of pink colors in composition 431 (Fig. 3a) and yellow (Fig. 3b) in composition 7414 of Butalón Tonalite to Varvarco Tonalite, reflects the same composition. The results of the petrographic analysis are shown in the QAP diagram (Fig. 4) and a detailed description of the outcrops visited in the field is presented below.

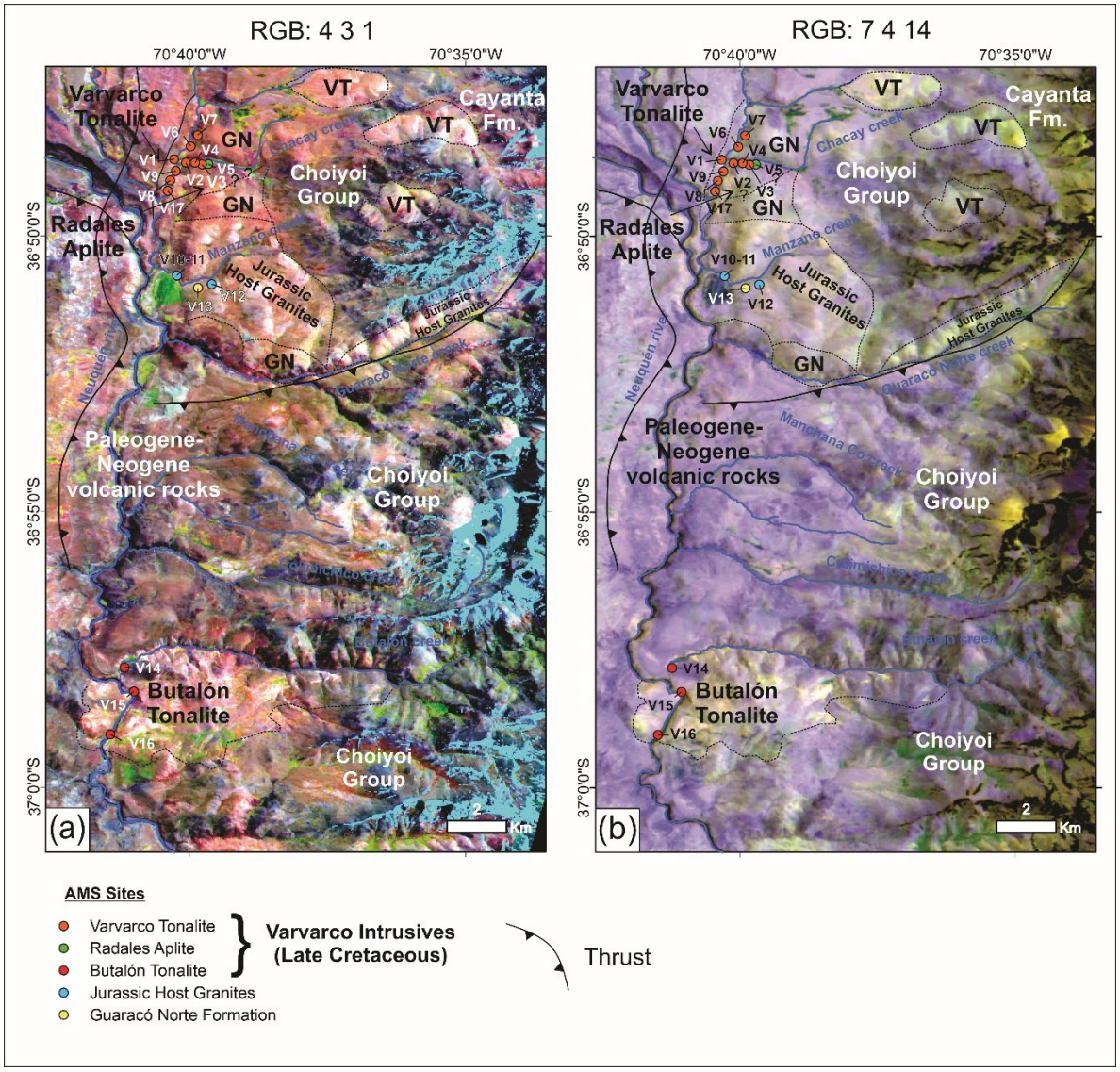


Figure 3: ASTER images of the study area: (a) RGB: 4 6 1 and (b) RGB: 7 4 14. VT: Varvarco Tonalite, GN: Guaracó Norte Formation.

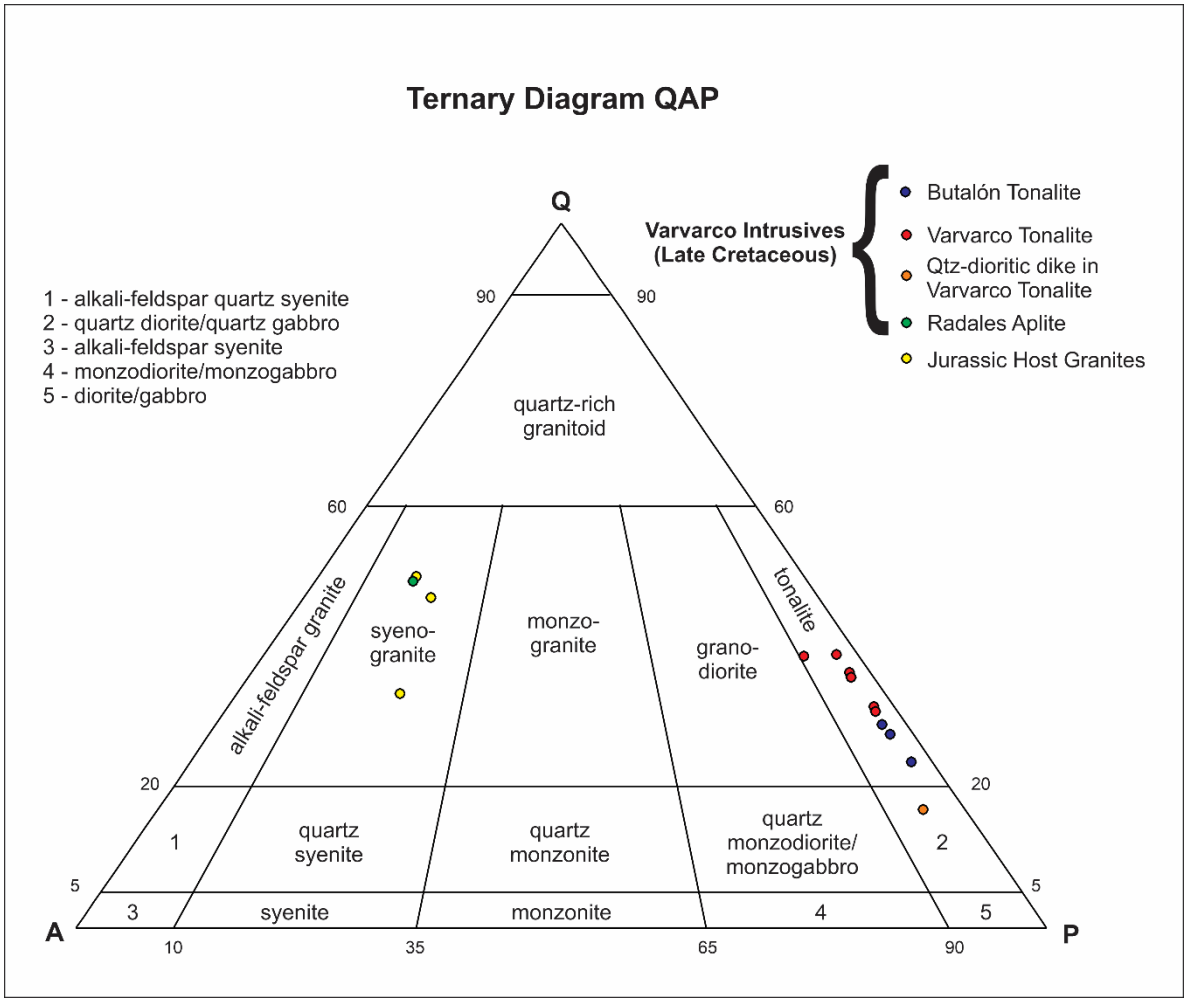


Figure 4: QAP ternary diagram for Varvarco Intrusives and Jurassic Host Granite.

Guaracó Norte Formation

The Guaracó Norte Formation, representing the host rock of the Varvarco Tonalite and Radales Aplite, was investigated along the Chacay, Matancilla, Manzano and Guaracó Norte creeks (Fig. 2a, 3a-b, 5a). This formation comprises quartzites affected by low-grade metamorphism. Generally, the metamorphic foliation has a NE-SW to N-S strike and steep dip (80º); steep inclinations were also measured close to the contact with the Varvarco Tonalite. In the Guaracó Norte creek, shales and phyllites strike N-S and have low dip (22º) towards the east. The pelitic rocks and sandstones of this formation are affected by hornblende-hornfels metamorphism that led to the development of andalusite, biotite, diopside and hornblende. This has been related to the intrusion of the Late Cretaceous Varvarco Tonalite (Giacosa *et al*. 2014).

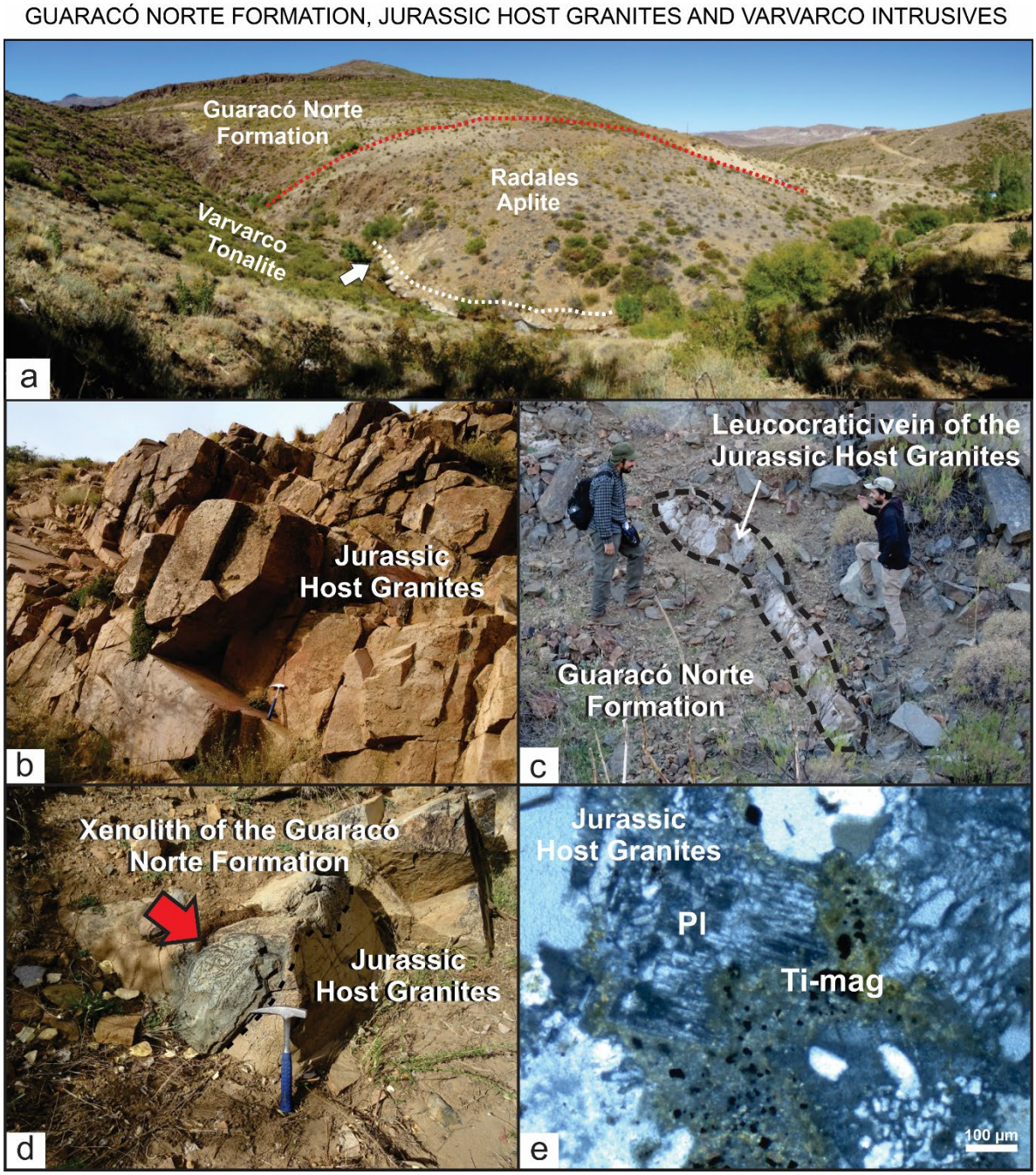


Figure 5: Outcrops of the Guaracó Norte Formation, Jurassic Host Granites and Varvarco Intrusives. (a) View towards the SE from Puesto Hernández, Chacay creek area, with the outcrops of the Varvarco Tonalite, Radales Aplite and the Guaracó Norte Formation. b) Outcrops of the Jurassic Host Granites in the Manzano creek area c) Leucocratic dyke assigned to the Radales Aplite in the Manzano creek area d) Xenolith of Guaracó Norte Formation in the Jurassic Host Granites and e) Plagioclase phenocrysts in granophyric matrix for the Jurassic Host Granites (cross-polarised light).

Jurassic Host Granites

Along the Manzano and Guaracó Norte creeks we discovered a new unit at site V12 (Figs 2a, 3a, b, 5b–e), which we tentatively name the Jurassic Host Granites because it has a 182 ± 3 Ma U–Pb age that was obtained by laser ablation multi-collector inductively coupled plasma mass spectrometry on 12 magmatic zircon crystals (unpub. data). This unit was previously described by Zanettini *et al*. (2001) as part of the Radales Aplite (formerly considered the Radales Granite, see *Radales Aplite Section*). The U–Pb geochronology data of the Jurassic Host Granites are part of a work in progress.

The Jurassic Host Granites enclose xenoliths derived from the Guaracó Norte Formation (Fig. 5d). Dykes of granitic composition that intrude the Guaracó Norte Formation in the Manzano creek (36º50´42.1"S; 70º40´14.0"W; site V10 in Table 1) can be assigned to the Jurassic Host Granites as well (Fig. 5c). The Jurassic Host Granites have the same syenogranitic composition (Fig. 4) and graphic texture (Fig. 5e) as the Radales Aplite, making it difficult to differentiate them in the field.

Varvarco Tonalite

Along the Matancilla and Chacay creeks, the Varvarco Tonalite can be observed in excellent exposures (Fig. 2a, 5a, 6a-d), which includes the contact relationships with the Guaracó Norte Formation host rock and with the intruding Radales Aplite (Fig. 5a). The Varvarco Tonalite is represented by medium- to fine-grained, equigranular to porphyritic tonalites, in which mafic minerals appear concentrated in blocks (Fig. 6a-b). The Varvarco Tonalite also hosts microgranular enclaves of dioritic composition (Fig. 6b-d). They have a fine-grained, equigranular texture and are composed of amphibole, biotite, plagioclase, quartz, and opaque minerals. The mafic magma was mixed and partially hybridised, as the enclaves show transitional contacts with the host rock (Fig. 6c). Enclave swarms that grade into disintegrated mafic dykes with different hybridisation degrees were also observed (Fig. 6d).

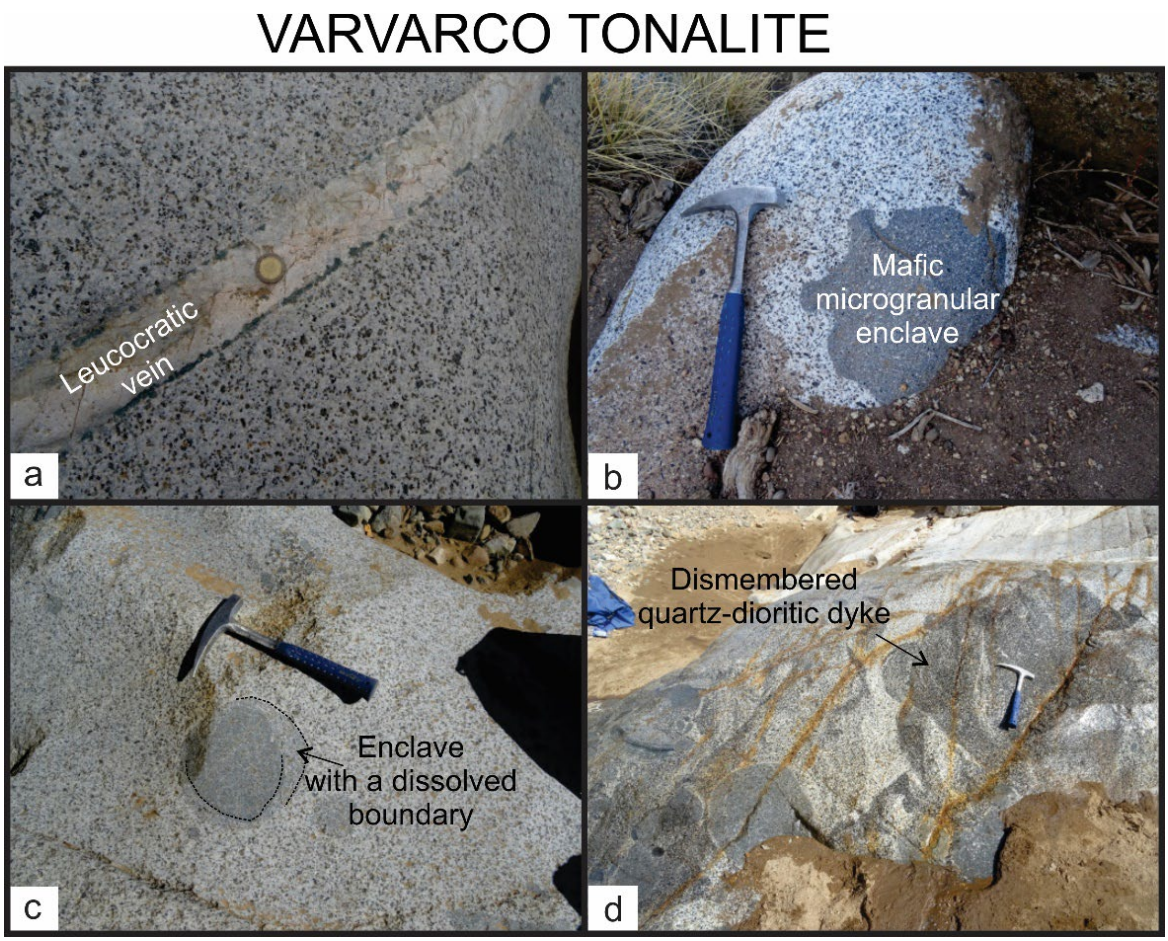


Figure 6: Outcrop images of the Varvarco Tonalite. (a) Thin leucocratic vein intruding the Varvarco Tonalite in the Chacay creek area. (b) Mafic microgranular enclave. (c) Partially dissolved (corroded) enclave in a hybrid magma of the Varvarco Tonalite. (d) Disintegrated quartz-dioritic dykes in the Varvarco Tonalite, where different degrees of hybridisation are observed.

The average modal composition of the Varvarco Tonalite is plagioclase (50%), quartz (30%), orthoclase (4%), amphibole (10%), biotite (5%), and titanomagnetite, titanite, apatite and zircon (1%). Plagioclase crystals are subhedral with complex zoning patterns (Fig. 7a). Incipient sericitic alteration of plagioclase is observed in concentric areas. The observed orthoclase phenocrysts have oikocrystic texture with amphibole and plagioclase inclusions (Fig. 7b). Amphibole is present as subhedral poikilitic megacrysts of nearly 2 cm length that contain plagioclase inclusions. In some areas these large amphibole crystals give the rocks porphyritic appearance. Subhedral biotite is pleochroic from light to dark brown, and mostly fresh (Fig. 7c, d). Quartz is interstitial and contains inclusions of amphibole. Apatite is frequently acicular. All observed

textures are magmatic; grain boundaries are straight, especially between plagioclase and orthoclase (Fig. 7b). Locally polygonal contacts between quartz grains are observed, suggesting that static recrystallisation has occurred.

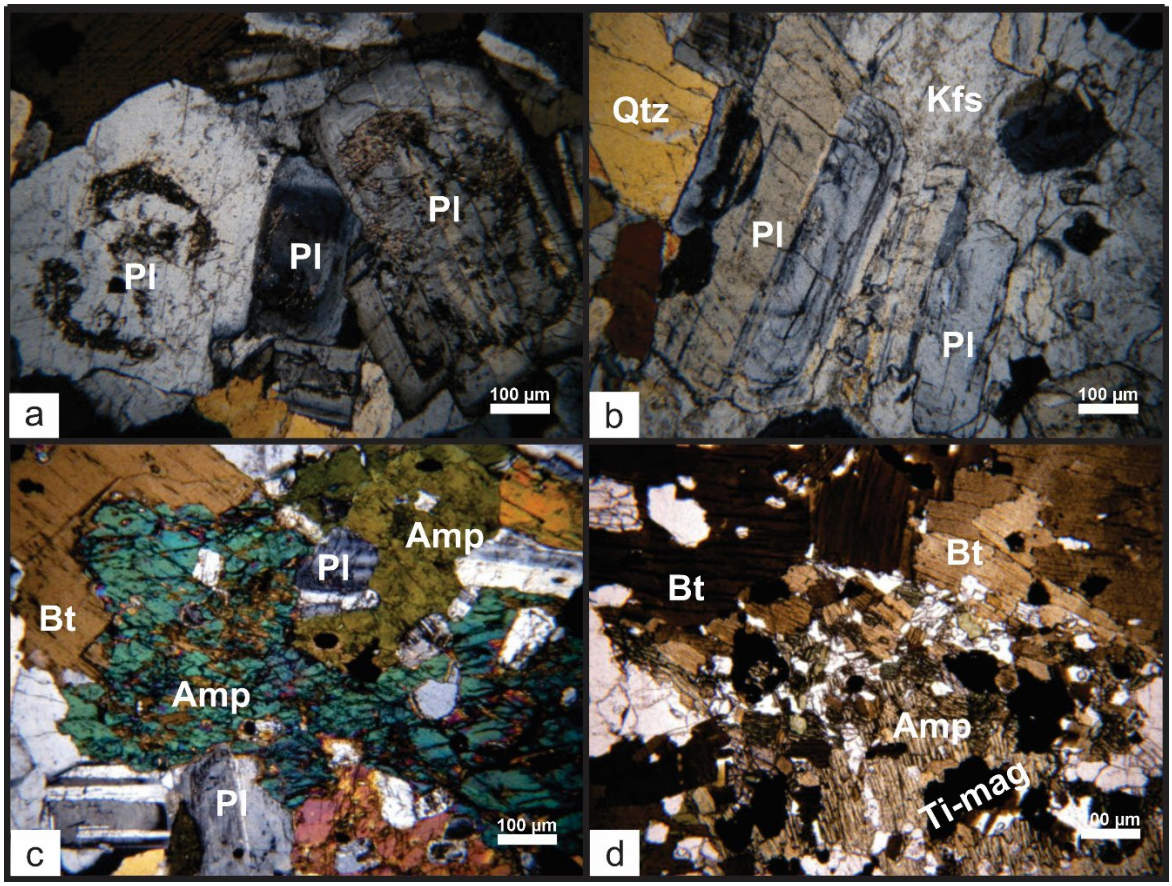


Figure 7: Petrographic image of the Varvarco Tonalite in cross-polarised light. (a) Plagioclase (Pl) with cores of more calcic composition and lighter rims of more sodic composition. (b) Euhedral plagioclase crystals included in anhedral K-feldspar (Kfs; orthoclase) crystals. (c) Euhedral plagioclase and subhedral amphibole (Amp) and biotite (Bt). (d) Biotite, amphibole and titanomagnetite (Ti-mag) concentrated in blocks in the Varvarco Tonalite. Other mineral abbreviations: Qtz: quartz.

Late aplitic veins of granitic composition (Fig. 6a) intrude the Varvarco Tonalite in the Chacay creek area (orientations: 285º/75º ENE, 320º/65º ENE). Disintegrated porphyritic quartz-dioritic dykes also cross cut the Varvarco Tonalite in the Chacay creek area (Fig. 8a). The dykes have poikilitic amphibole and plagioclase phenocrysts in a granular groundmass that is composed of plagioclase, amphibole, biotite, quartz, and opaque minerals (Fig. 8b). Amphibole has inclusions of plagioclase and rounded quartz (Fig. 8c). Quartz “ocelli” with

reaction rims of amphibole and opaque minerals were occasionally observed (Fig. 8d).

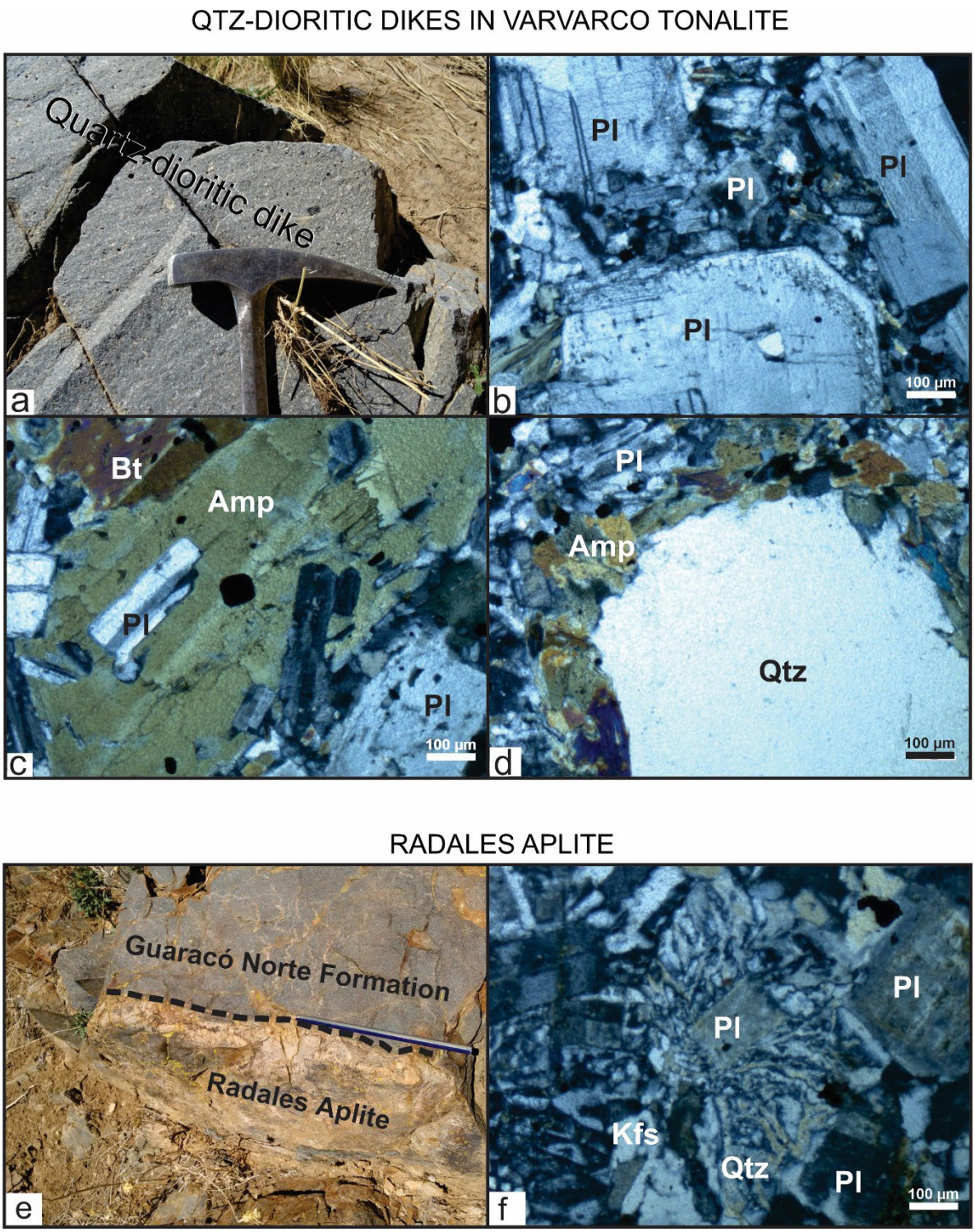


Figure 8: Quartz-dioritic dykes intruding the Varvarco Tonalite and Radales Aplite. (a) Fine-grained texture of a quartz-dioritic dykes. (b) Plagioclase phenocrysts in a fine-grained matrix mainly composed of plagioclase. (c) Amphibole phenocryst with inclusions of plagioclase and opaque minerals. (d) Rounded quartz xenocryst rimmed by amphibole and opaque minerals

(quartz ocelli). (e) Contact between the Radales Aplite and the hosting Guaracó Norte Formation. (f) Xenolith of Guaracó Norte Formation in the Radales Aplite. Mineral abbreviations as in Fig. 7.

Butalón Tonalite

This intrusive body crops out in the Butalón Norte area, approximately 15 km to the south of the Varvarco locality (Fig. 2a, 3a-b). In the RGB compositions of Fig. 3 the Butalón Tonalite is well distinguished from the hosting Permo-Triassic Choiyoi Group. Many granitic dykes and veins of steep to moderate dips and NW to NE strike cross cut the Butalón Tonalite. They have highly variable width between 5 and 50 cm (Fig. 9a). The Butalón Tonalite is classified as fine-grained tonalitic rock with an average composition of plagioclase (63%), quartz (23%), amphibole, biotite (12%), orthoclase (2%), and minor euhedral opaque minerals and acicular apatite (Fig. 4). Mafic microgranular enclaves of dioritic composition are present in this facies as well (Fig. 9b). Amphibole (hornblende determined optically) tends to form poikilitic phenocrysts with plagioclase and biotite inclusions (Fig. 9c). Plagioclase has complex zoning and many plagioclase cores are altered to sericite. Orthoclase is interstitial. Opaque minerals, amphibole and biotite are concentrated in blocks (Fig. 9d).

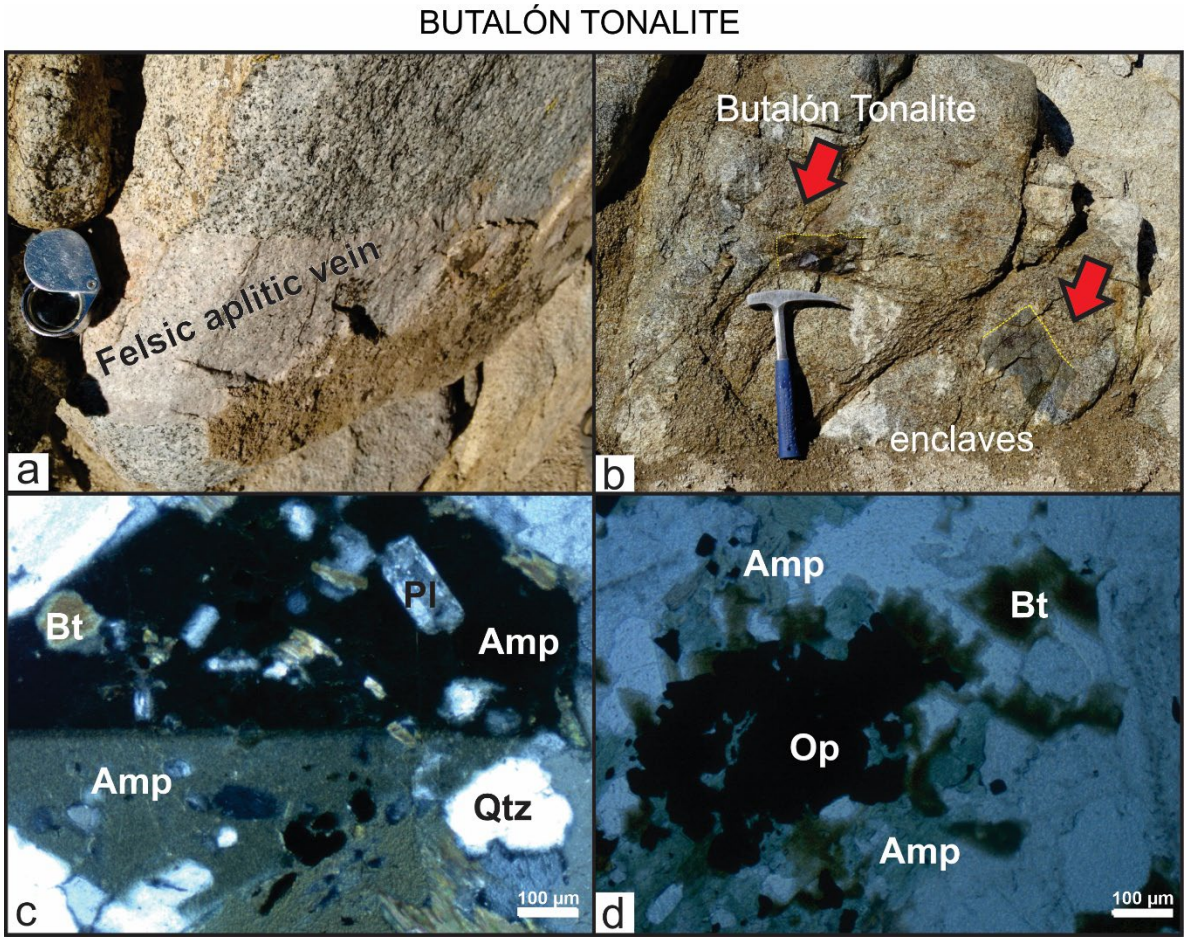


Figure 9: Outcrops and petrographic images of the Butalón Tonalite in cross-polarised light. (a) Felsic aplitic vein intruding the Butalón Tonalite. (b) Mafic microgranular enclaves. (c) Amphibole megacryst with inclusions of plagioclase and biotite. (d) Mafic minerals. Mineral abbreviations as in Fig. 7 and Op: opaque minerals.

Radales Aplite

The Radales Aplite crops out only along the Chacay creek (Fig. 2a, 5a, and 8e). In the satellite image of Fig. 3b, the Radales Aplite is shown in yellow due to its high silica content. The quartz-rich composition of the Guaracó Norte Formation is shown with a very similar colour, making these two units, which were relatively easy to distinguish in the field (red line in Fig. 5a), not clearly separated in terms of compositions (fig. 3b). Therefore, the boundary was highlighted by dotted line with question marks (Fig. 3a-b).

The contact between the Radales Aplite and the Guaracó Norte Formation is distinctive (Fig. 8e). The Radales Aplite has fine-grained to aplitic texture and a syenogranitic composition (Fig. 4). Plagioclase phenocrysts (12%) are

immersed in a granophyric matrix formed of quartz (43%) and orthoclase (40%) (Fig. 8f). The Radales Aplite is considered as late stage of the Varvarco Intrusives because late leucocratic veins intrude the Varvarco Tonalite (Fig. 6a) and the Butalón Tonalite (Fig. 9a), and these veins could correlate with the small stock cropping out along the Chacay creek (Fig. 5a).

3.4.2 Plagioclase, amphibole and biotite compositions for the Varvarco Tonalite

Electron microprobe analyses of plagioclase, amphibole and biotite from the Varvarco Tonalite are presented in Table 2.

Table 2: Mineral compositions analysed by electron microprobe in the Varvarco Tonalite. a) Plagioclases (Pl). b) Amphiboles (Amp). c) Biotites (Bt). In this table the results given by amphibole-only thermometers of Ridolfi *et al*. (2010) (equation 1), Ridolfi & Renzulli (2012) (equation 2) and Putirka (2016) (equation 5) were added, as well as the results from the geothermometers of Ridolfi *et al*. (2010) (equation 4) and Ridolfi & Renzulli (2012) (average between equations 1a and 1b). In table 2c, temperatures are calculated with the geothermometer of Henry *et al*. (2005).

Table 2a

Mineral	Pl	Pl	Pl	Pl	Pl	Pl	Pl	Pl	Pl	Pl	Pl
Texture	rim	centre	rim	centre	centre	centre	rim	rim	rim	centre	centre
Analysis	9	10	21	22	25	26	27	28	31	32	33
SiO_2	59.32	56.99	60.05	54.44	52.57	52.87	52.91	58.91	57.07	55.46	55.95
TiO_2	b.d.l.	0.02	0.02	b.d.l.	0.03	b.d.l.	b.d.l.	b.d.l.	b.d.l.	0.01	0.03
Al_2O_3	24.73	26.62	24.48	28.08	29.31	29.15	29.19	25.68	26.79	28.12	27.38
Cr_2O_3	b.d.l.	b.d.l.	b.d.l.	b.d.l.	b.d.l.	b.d.l.	b.d.l.	b.d.l.	0.05	b.d.l.	0.03
NiO	b.d.l.	0.06	b.d.l.	0.04	0.02	b.d.l.	b.d.l.	b.d.l.	b.d.l.	b.d.l.	b.d.l.
FeO_t	0.21	0.14	0.26	0.39	0.14	0.17	0.19	0.16	0.18	0.18	0.18
MnO	0.01	0.01	b.d.l.	0.05	b.d.l.	0.01	0.01	0.01	0.01	0.01	b.d.l.
MgO	0.02	b.d.l.	b.d.l.	b.d.l.	b.d.l.	b.d.l.	0.01	b.d.l.	0.02	0.01	b.d.l.
CaO	7.11	9.11	6.35	11.03	12.46	12.40	12.24	7.69	8.68	10.42	9.84
Na2O	7.53	6.45	7.90	5.38	4.57	4.74	4.66	7.24	6.58	5.78	5.90
K_2O	0.36	0.26	0.44	0.20	0.15	0.15	0.16	0.32	0.23	0.24	0.33
TOTAL	99.37	99.78	99.50	99.78	99.32	99.62	99.48	100.06	99.66	100.31	99.70
xAN	33.61	43.18	30.01	52.48	59.60	58.62	58.65	36.33	41.61	49.24	47.05

Pl	Pl	Pl	Pl	Pl	Pl	Pl	Pl	Pl	Pl	Pl
centre	centre	centre	centre	centre	rim	centre	centre	centre	centre	centre
34	35	36	37	38	39	40	41	42	43	44

55.99	54.18	53.53	55.05	54.34	59.03	56.32	52.01	55.35	54.76	55.80
0.03	b.d.l.	b.d.l.	b.d.l.	0.01	b.d.l.	b.d.l.	b.d.l.	b.d.l.	0.02	0.01
27.07	28.09	28.75	28.65	28.61	25.19	26.68	30.20	27.75	28.02	27.68
b.d.l.	0.01	0.05	b.d.l.	0.01	b.d.l.	b.d.l.	b.d.l.	0.01	0.01	0.01
b.d.l.	0.01	b.d.l.	b.d.l.	b.d.l.	b.d.l.	0.02	b.d.l.	b.d.l.	b.d.l.	b.d.l.
0.17	0.17	0.14	0.15	0.21	0.16	0.16	0.15	0.11	0.16	0.17
b.d.l.	b.d.l.	0.02	b.d.l.	0.04	b.d.l.	b.d.l.	b.d.l.	0.01	b.d.l.	0.02
b.d.l.	b.d.l.	0.01	0.01	0.02	0.01	b.d.l.	b.d.l.	b.d.l.	0.01	0.01
9.73	10.95	11.35	11.10	11.19	7.63	9.48	13.50	10.55	10.74	10.36
5.99	5.39	5.11	5.39	5.17	7.33	6.12	3.88	5.54	5.57	5.91
0.29	0.26	0.22	0.22	0.19	0.24	0.27	0.13	0.22	0.22	0.24
99.31	99.17	99.23	100.62	99.93	99.68	99.16	99.99	99.62	99.58	100.32
46.52	52.10	54.43	52.56	53.87	36.02	45.40	65.33	50.63	50.94	48.55

Pl	Pl	Pl	Pl	Pl	Pl	Pl	Pl	Pl
centre	centre	centre	rim	centre	rim	rim	rim	centre
45	46	59	60	66	67	71	73	74
55.41	56.54	53.25	56.55	47.90	56.36	56.42	55.68	53.65
b.d.l.	b.d.l.	0.01	0.02	0.02	0.02	b.d.l.	b.d.l.	0.03
27.94	27.01	29.05	26.85	32.50	27.74	27.07	27.07	26.99
0.02	b.d.l.	b.d.l.	0.01	b.d.l.	0.01	b.d.l.	b.d.l.	b.d.l.
b.d.l.	b.d.l.	0.01	b.d.l.	0.04	b.d.l.	0.04	0.07	0.04
0.17	0.21	0.21	0.31	0.17	0.26	0.22	0.19	0.15
b.d.l.	0.02	b.d.l.	b.d.l.	0.02	0.02	b.d.l.	b.d.l.	b.d.l.
b.d.l.	0.01	0.01	0.01	0.01	b.d.l.	0.01	0.01	0.01
10.25	9.50	11.93	9.06	16.01	9.39	9.45	9.31	10.57
5.79	6.14	4.88	6.48	2.41	6.17	6.11	6.10	5.18
0.19	0.25	0.17	0.23	0.08	0.18	0.26	0.19	0.21
99.84	99.77	99.57	99.57	99.26	100.16	99.65	98.71	96.89
48.89	45.45	56.90	43.05	78.23	45.23	45.40	45.26	52.34

Table 2b

Mineral	Amp	Amp	Amp	Amp	Amp	Amp	Amp	Amp	Amp	Amp
Analysis	2	3	4	5	6	13	14	16	47	48
Texture	rim	centre	centre	centre	rim			centre	centre	centre
SiO_2	50.36	48.50	49.33	51.13	49.59	50.77	52.85	53.83	43.37	43.64
TiO_2	0.40	0.65	0.43	0.33	0.36	0.22	0.16	0.12	1.61	1.69
Al_2O_3	3.85	5.30	4.42	3.69	4.12	3.65	1.80	1.26	8.45	8.39
Cr_2O_3	0.02	0.01	0.02	0.03	0.01	b.d.l.	0.04	0.03	b.d.l.	b.d.l.
NiO	b.d.l.	0.04	b.d.l.	0.06	b.d.l.	b.d.l.	b.d.l.	b.d.l.	b.d.l.	0.05
FeO_t	17.38	17.63	17.96	16.01	15.43	16.30	14.41	12.60	17.62	17.66
MnO	1.66	1.57	2.15	1.73	1.34	1.68	1.62	1.37	1.02	0.95
MgO	13.46	12.42	12.72	13.77	13.23	13.51	15.01	15.66	10.33	10.44

CaO	10.21	10.64	9.45	10.98	11.93	11.29	11.17	12.05	11.27	11.36
Na_2O	0.55	0.75	0.58	0.48	0.42	0.40	0.20	0.18	1.19	1.04
K_2O	0.28	0.42	0.29	0.25	0.25	0.24	0.08	0.06	0.76	0.72
TOTAL	98.26	97.97	97.39	98.52	96.79	98.10	97.45	97.21	95.64	96.03
Geothermometers (ºC)										
Ridolfi *et al*. (2010)-Eqn.1	773	800	750	752	717	742	703	672	841	837
Ridolfi & Renzulli (2012)-Eqn.2	343	459	313	470	774	515	449	550	876	851
Amph-only-Putirka (2016)-Eqn.5	666.26	699.34	668.48	668.90	682.23	663.59	639.80	642.81	791.41	785.93
Geobarometers (kbar)										
Ridolfi *et al*. (2010)-Eqn.4	0.5	0.7	0.6	0.5	0.5	0.5	0.3.	0.2	17	17
Ridolfi & Renzulli (2012)-Average between Eqn. 1a and Eqn. 1b	1.1	1.4	2.3	1	0.7	0.9	0.6	0.4	2	1.7

Amp	Amp	Amp	Amp	Amp	Amp	Amp	Amp	Amp	Amp	Amp
49	50	54	55	56	61	62	63	65	68	70
rim	rim	rim	centre	centre	centre	centre	centre	centre	centre	rim
51.08	53.53	45.54	44.51	43.84	48.09	48.40	44.60	48.34	44.61	46.33
0.16	0.09	0.66	1.12	1.65	0.96	1.03	1.64	1.16	1.66	0.65
2.55	1.20	6.61	7.74	8.17	6.15	6.20	8.36	6.23	8.63	6.56
0.04	0.03	b.d.l.	b.d.l.	0.04	0.03	0.03	b.d.l.	0.03	b.d.l.	b.d.l.
0.02	0.06	0.06	b.d.l.	b.d.l.	0.04	0.01	b.d.l.	b.d.l.	b.d.l.	b.d.l.
16.07	11.97	18.34	17.84	17.37	14.50	14.10	15.15	14.04	17.51	18.11
1.67	1.34	1.24	1.04	0.94	0.69	0.73	0.69	0.79	0.89	1.06
14.10	15.99	10.53	10.26	10.60	13.76	14.04	12.33	14.06	10.95	10.97
10.67	11.46	11.29	11.24	11.33	11.42	11.08	10.80	11.10	11.24	11.46
0.33	0.13	0.77	0.95	0.99	0.93	1.06	1.44	0.83	1.22	0.79
0.13	0.06	0.63	0.86	0.73	0.42	0.35	0.48	0.41	0.64	0.54
96.87	95.92	95.79	95.59	95.73	97.08	97.14	95.60	97.08	97.47	96.52
837	734	774	808	831	772	769	836	779	835	771
414	464	821	830	850	782	807	872	808	860	787
645.44	641.23	716.56	753.23	781.33	749.50	755.59	813.07	752.52	791.86	716.61
0.3	invalid	11	14	16	9	9	16	9	17	10
0.7	0.4	1.3	1.6	1.6	0.9	1.1	1.9	1	1.9	1.1

Table 2c

Mineral	Bt	Bt	Bt	Bt	Bt	Bt	Bt	Bt	Bt	Bt	Bt	Bt	Bt	Bt
Analysis	1	8	12	17	20	23	30	52	53	58	64	69	72	75
Texture	centre	centre	centre	centre	centre	centre	centre	centre	centre	*	*	centre	*	*

SiO_2	35.95	36.51	35.98	36.07	36.10	36.28	35.87	36.03	34.11	36.36	35.94	35.93	35.34	36.15
TiO_2	3.62	3.83	3.52	2.67	3.21	3.77	4.00	3.36	4.66	4.06	4.09	3.46	3.84	3.99
Al_2O_3	13.62	14.55	14.01	14.12	14.01	13.82	13.87	13.62	13.21	13.82	13.35	13.84	13.48	13.60
Cr_2O_3	0.04	0.03	0.02	0.04	b.d.l.	0.03	0.01	b.d.l.	0.02	b.d.l.	b.d.l.	b.d.l.	b.d.l.	b.d.l.
NiO	0.02	0.01	b.d.l.	b.d.l.	0.03	0.08	b.d.l.	0.02	b.d.l.	0.03	0.01	0.01	0.09	b.d.l.
FeO_t	19.65	18.70	19.63	19.64	20.27	19.68	20.77	20.56	20.66	18.62	17.84	20.60	20.49	17.88
MnO	0.81	0.81	0.69	0.82	0.70	0.72	0.72	0.60	0.58	0.31	0.38	0.63	0.50	0.29
MgO	11.33	11.40	11.50	12.00	11.44	11.48	10.65	11.23	9.96	12.29	12.35	11.07	10.90	12.76
CaO	0.04	0.06	0.01	0.04	0.02	0.03	0.08	0.02	1.16	0.03	0.04	b.d.l.	0.02	0.04
Na_2O	0.08	0.09	0.08	0.10	0.09	0.08	0.08	0.10	0.09	0.15	0.14	0.11	0.11	0.19
K_2O	9.43	9.64	9.65	9.63	9.52	9.47	9.24	9.43	8.63	9.50	9.20	9.61	9.57	9.05
P_2O_5	b.d.l.	b.d.l.	b.d.l.	0.02	b.d.l.	b.d.l.	0.01	0.01	0.03	b.d.l.	b.d.l.	b.d.l.	b.d.l.	b.d.l.
TOTAL	94.59	95.63	95.09	95.15	95.39	95.43	95.29	94.97	93.11	95.18	93.33	95.25	94.34	93.95
T(°C) (Henry et al. 2005)	728.14	733.13	723.56	689.18	709.61	732.41	733.47	715.09	744.45	746.37	753.34	717.22	731.73	751.74

* Small crystal included in amphibole

Plagioclase compositions were calculated based on a 32 oxygen formula unit (Table 2a). Plagioclases are labradorite-andesine or andesine (Fig. 10a-c Table 2a). They show oscillatory zoning with decreasing anorthite component (An_{60-30}) from core to rim (Fig. 10a). In some profiles, plagioclase shows slight increase in An_{45-51} from core to more external zones and a labradoritic spike of An_{65} separating an external rim of An_{45-30} (Fig. 10b). These compositional spikes correspond to the inner rings observed in many crystals of Varvarco Tonalite (Fig. 7a). In plagioclases included in amphibole, cores with anorthite content of up to An_{78} were found.

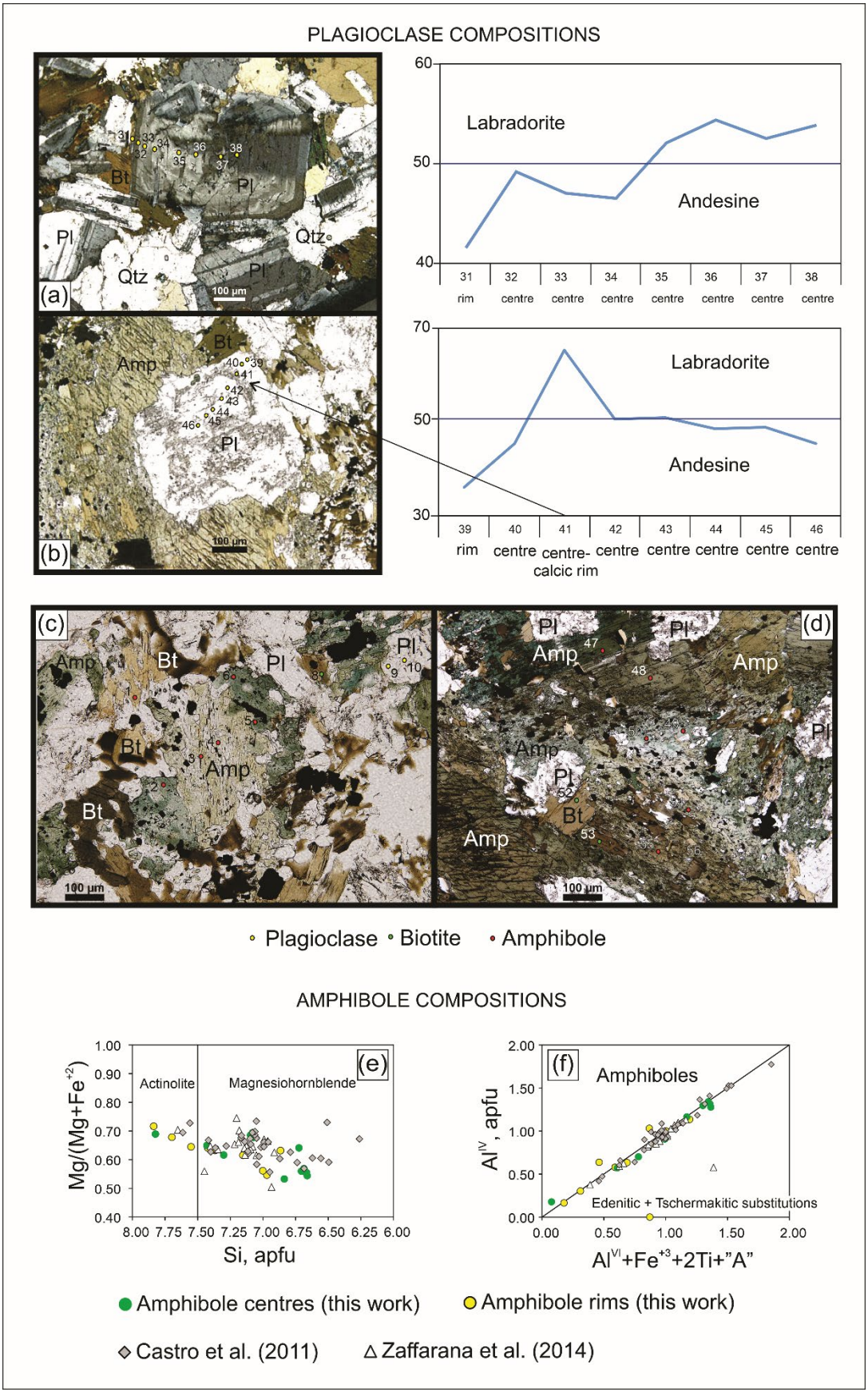

PLAGIOCLASE COMPOSITIONS
(a)
(b)
Bt
Pl
Qtz
Amp
100 µm
Labradorite
Andesine
rim
centre
centre-
calcic rim
(c)
(d)
Plagioclase
Biotite
Amphibole
AMPHIBOLE COMPOSITIONS
(e)
Actinolite
Magnesiohornblende
Mg/(Mg+Fe+2)
Si, apfu
(f)
Amphiboles
AlIV, apfu
Edenitic + Tschermakitic substitutions
AlVI+Fe+3+2Ti+"A"
Amphibole centres (this work)
Amphibole rims (this work)
Castro et al. (2011)
Zaffarana et al. (2014)

Figure 10: Plagioclase and amphibole compositional classification. (a) and (b) Plagioclase zoning profiles for the Varvarco Tonalite. (c) and (d) Photomicrographs with cross-polarised light showing some analysed spots of amphibole (red), biotite (green) and plagioclase (yellow). (e) Amphibole classification diagrams of Leake *et al*. (1997). (f) Al^{IV} vs. $Al^{VI} + Fe^{+3} + 2Ti$ +"A″ graph (Kawakatsu & Yamaguchi, 1987), shows that nearly all amphiboles have a good 1:1 fit between vertical and horizontal axes. This suggests that charge compensation due to the introduction of Al^{IV} was accomplished by both the edenitic and tschermakitic substitutions.

Amphibole structural formulae were calculated based on a 23 oxygen formula unit and with all Ca in the M4 site (Dale *et al*. 2005; Table 2b). Calcic amphibole compositions were obtained, with $Fe_t/(Fe_t+Mg)$ in the 0.30-0.49 range, and low to moderate TiO_2 contents (0.09 to 1.69 wt%, and 0.01 to 0.19 a.p.f.u., respectively). Amphibole cores are mostly magnesiohornblende, whereas amphibole rims are magnesiohornblende to actinolite (Fig. 10c-e). All amphiboles balance the Al tetrahedral site occupancy by both tschermakitic and edenitic substitutions (Fig. 10f).

Compositions of fresh ***biotite*** are shown in Figure 10d). In order to calculate biotite formula, we used the method of Li *et al*. (2020). Most biotites are eastonites boundary to phlogopites with only one biotite (sample 53) falling into siderophyllite field (Fig. 11a). $Fe_t/(Fe_t + Mg)$ ratios vary between 0.44 and 0.58, and aluminium contents vary between 13.21 and 14.55 wt% Al_2O_3 (Table 2c). In the diagram of Foster (1960) and in the trioctahedral Tischendorf *et al*. (1997) diagram, the analysed grains are classified as Mg-biotites (Fig. 11b, c), with biotite from sample 53 falling into the Fe-biotite field (Fig. 11c). In the ternary diagram of Nachit *et al*. (2005), the compositions are compatible with primary and re-equilibrated primary biotites (Fig. 11d). Given that biotite is prone to secondary alteration, Ti was proposed to act as a discriminator, with Ti content <0.55 Ti per 22 oxygen formula unit indicative of fresh magmatic biotite (e.g. Li *et al*. 2017). Varvarco biotites contain 2.6-4.66 wt% TiO_2 which converts to 0.31-0.56 Ti pfu. Only one biotite grain (sample 53) is above 0.55 Ti pfu, supporting their magmatic origin.

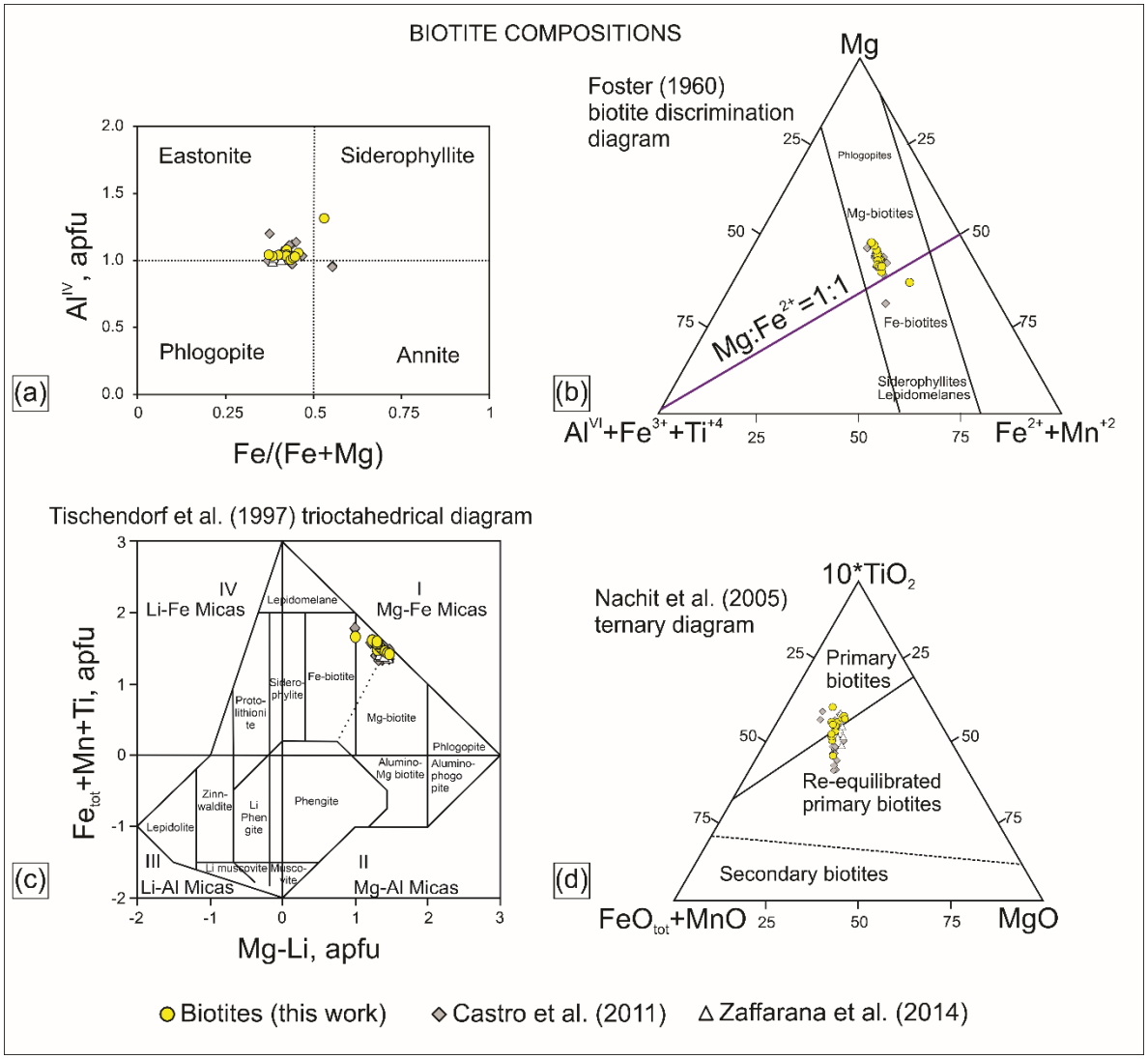


Figure 11: Biotite compositional classification. (a) Biotite classification (Al^{IV} as a function of its Fe/(Fe+Mg) ratio; Deer *et al*. 2013). (b) Biotite discrimination diagram after Foster (1960). (c) Trioctahedrical classification diagram after Tischendorf *et al*. (1997). (d) Ternary diagram for discriminating between primary magmatic biotites and re-equilibrated and secondary biotites after Nachit *et al*. (2005).

3.4.3 Anisotropy of magnetic susceptibility (AMS)

As was stated in the introduction, AMS studies are used here to evaluate timing and possible emplacement mechanisms of the Varvarco Intrusives in relationship to regional deformation affecting the Cordillera del Viento range. At all investigated sites, the petrofabric was magmatic, with most minerals of euhedral shapes, and no evidence of late solid-state deformation. The AMS ellipsoids for the individual sites obtained for each lithology are presented in Supplementary Figure S1a-e. As a usual practice in AMS studies, mineral and

magnetic fabrics are assumed to be parallel. This could only be accomplished for in the site V8, the only site where we could measure the magmatic foliation in the field, whereas sampling in the other sites was carried out in isotropic rocks.

The corrected anisotropy degree Pj value and the shape parameter T (Jelinek 1981) can be used to describe the geometry of the magnetic ellipsoid. The general positive correlation between Km and Pj shows that titanomagnetite controls the anisotropy in the three analysed plutonic rocks, at both sample and site scale (Supplementary Figure S1a-f). Most values of the shape parameter T at the site scale lie between -0.5 and 0.5 (Supplementary Figure S1f, Table 1). Thus, the magnetic ellipsoids are predominantly triaxial, with good determinations of K1 and K3 axes corresponding, respectively, to magnetic lineations and poles of foliation planes.

The structural mapping of the Varvarco Intrusives was constructed with the AMS data for each sampling site (magnetic foliation and lineation maps; Fig. 12a, b). The orientation of the metamorphic foliation of the Guaracó Norte Formation taken from Giacosa *et al*. (2014) was also added to complete the structural map of the host rock in the Varvarco area (Fig. 12a). In this area, the strike of the magnetic foliation planes of the Varvarco Tonalite oscillate between NNW-SSE and NNE-SSW, and they systematically dip steeply to moderately towards the E (Supplementary Figure S1a; Fig. 12a). In turn, the magnetic foliation of the Radales Aplite and Jurassic Host Granites is steeply dipping as in the Varvarco Tonalite, but the strike of the magnetic foliation of the Jurassic Host Granites is more variable especially in the Manzano creek area (Supplementary Figure S1c, d; Fig. 12a). The Guaracó Norte Formation in the area between the Chacay and Matancilla creeks shows steeply dipping metamorphic foliations in N-S strike direction, changing to NW-SE strike (Giacosa *et al*. 2014; Fig. 12a). The foliation obtained for V13 site in the Manzano creek has a steeply dipping NNW-SSE strike (Supplementary Figure S1e; Fig. 12a).

The average lineations of the Varvarco Tonalite plunge moderately to steeply towards the SE (Supplementary Figure S1a; Fig. 12b); with one site (V3) with a shallowly plunging lineation trending towards the NW (Supplementary Figure S1a; Fig. 12b). The lineations of the Radales Aplite and Jurassic Host Granites are more diverse: they plunge moderately towards the SE, but lineations

plunging to the NE were also found (Supplementary Figure S1c, d; 12b). The lineation found in the Guaracó Norte Formation at V13 site is shallow dipping (Supplementary Figure S1e; 12b).

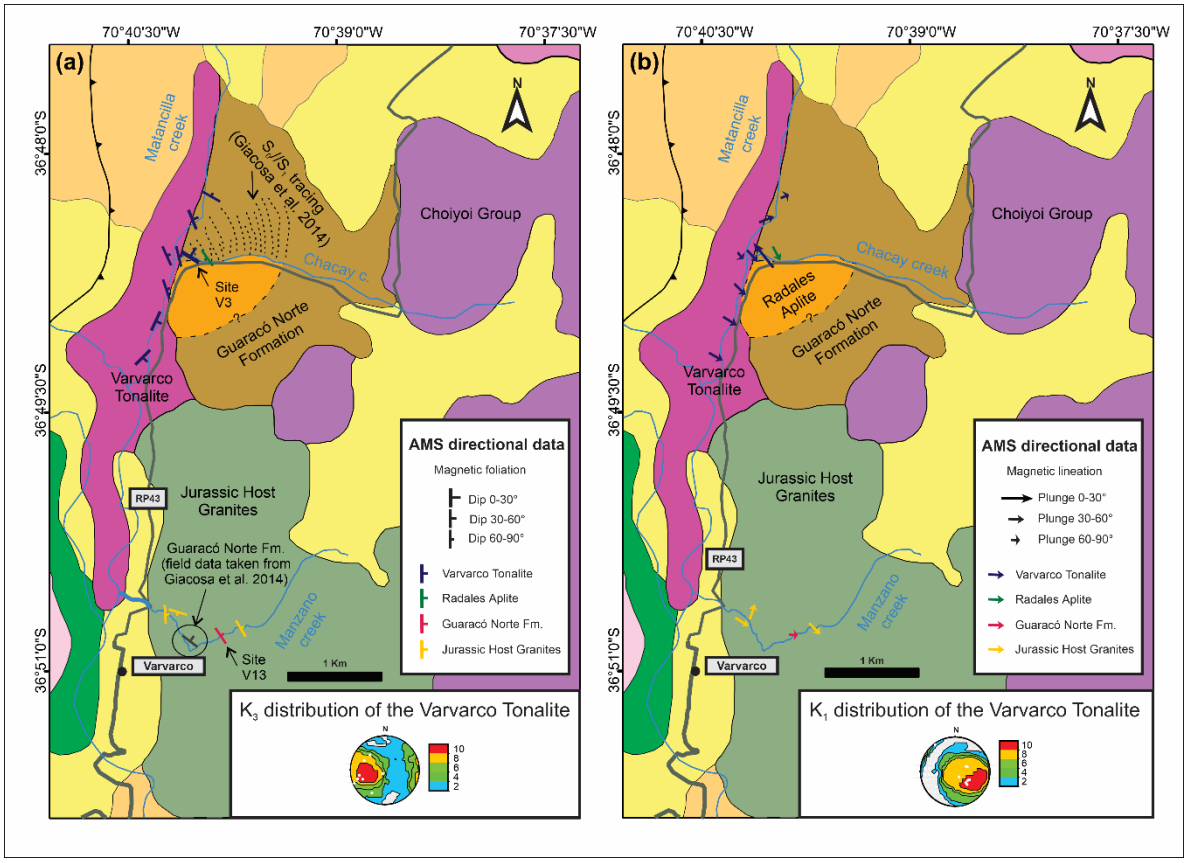


Figure 12: (a) Map showing magnetic foliation planes (K1-K2 planes), defined as the plane perpendicular to K3 in the Varvarco Tonalite. Inset shows K3 distribution of the magmatic foliations. (b) Map showing magnetic lineation (K1 direction) in the Varvarco Tonalite. Inset shows K1 distribution of the magmatic fabrics. The stereonets represent contoured Kamb equal-area lower-hemisphere stereographic projections made with the software Stereonet 9.9.5 (Allmendinger *et al*. 2012; Cardozo & Allmendinger, 2013). The scale represents Kamb contours in standard deviation.

The quartz-dioritic dyke at site V4, belonging to the Varvarco Tonalite, has a steeply dipping NW-SE magnetic foliation plane, parallel to dyke strike (Supplementary Figure S1a). Magnetic lineation plunges moderately to the SE (Supplementary Figure S1a).

In the area of Butalón Norte, the Butalón Tonalite has steeply dipping magmatic foliation planes with different attitudes; two sites have an E-W strike (V14 and V16), whereas the remaining site (V15) has N-S strike (Supplementary

Figure S1b). The magnetic lineation is subhorizontal in the case of V15 site, and sub-vertical in the case of V14 and V16 sites (Supplementary Figure S1b).

3.4.4 Mean susceptibility and minerals responsible for the AMS ellipsoids

The simple exploration of the nominal value of bulk magnetic susceptibility indicates which are the main minerals controlling the magnetic fabric of rocks (Bouchez 2000). The mean magnetic susceptibilities (Km) of the Varvarco Tonalite and the Butalón Tonalite are 38.56 $x10^{-3}$ SI and 43.57 $x10^{-3}$ SI, respectively. These values are significantly higher than that for the Radales Aplite of 2.37 $x10^{-3}$ SI and the Jurassic Host Granites of 20.18 $x10^{-3}$ SI (averages were taken using the data of Table 1). The Guaracó Norte Formation has an even lower Km of 0.44 $x10^{-3}$ SI (Table 1). These high bulk susceptibility values, higher than 4 $x10^{-4}$ SI in most of the samples of the Varvarco and Butalón plutons, suggest that the AMS signal is dominated by magnetite (following the method of Bouchez 2000; Supplementary Figure S2a-b). This is consistent with the mineralogy of the studied granitoids.

Rock magnetic studies can be used to further constrain which minerals dominate the magnetic anisotropy of the rocks. In particular, it is important to determine the domain state of the magnetite, which is essential for the correct interpretation of the magnetic ellipsoids (Grégoire *et al*. 1995; Borradaile & Jackson 2010). Therefore, hysteresis loops, the anisotropy of isothermal remanence (AIRM) and backfield curves were performed in the Varvarco Tonalite (Supplementary Figure S2a) and the Jurassic Host Granites (Supplementary Figure S2b), all in agreement with the presence of magnetite. Magnetite is mostly of pseudo-single domain (PSD) type, as is suggested by the diagram of Day *et al*. (1977) (Fig. 13). However, two samples from the Varvarco Tonalite have a fine-grained, single-domain (SD) magnetite signature (samples from V7 and V8 sites, Fig. 13). Consequently, for these AMS sites, anisotropy of the anhysteretic remanence ellipsoids (AARM) was determined. The coincidence of AARM and AMS ellipsoids (Fig. 14) further supports that magnetite controls the AMS signal and no axis inversion is necessary due to the presence of SD magnetite. It can be concluded that the interpretation of the AMS fabric in all sites is direct, as the magnetic lineation coincides with the K_1 axis and the pole of the magnetic foliation

corresponds to the K_3 axis; with the K_1 and K_3 directions taken from the AMS ellipsoids.

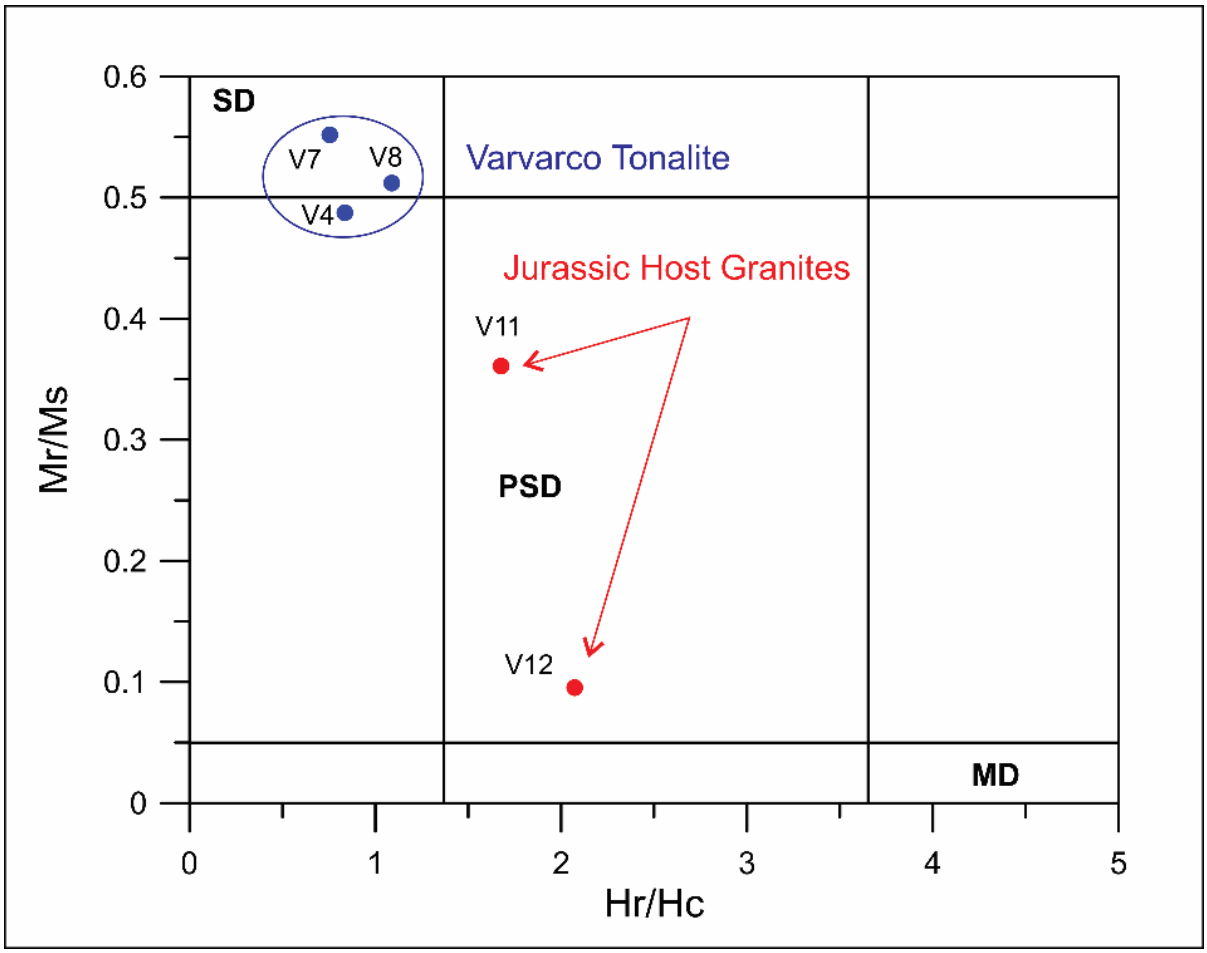


Figure 13: Domain state of the magnetite of the Varvarco Tonalite and Jurassic Host Granites. Diagram of Day *et al*. (1977). Hc = coercive force, Ms = saturation magnetisation and Mr = remanent magnetisation, SD = single-domain, PSD = pseudo-single domain, MD = multidomain.

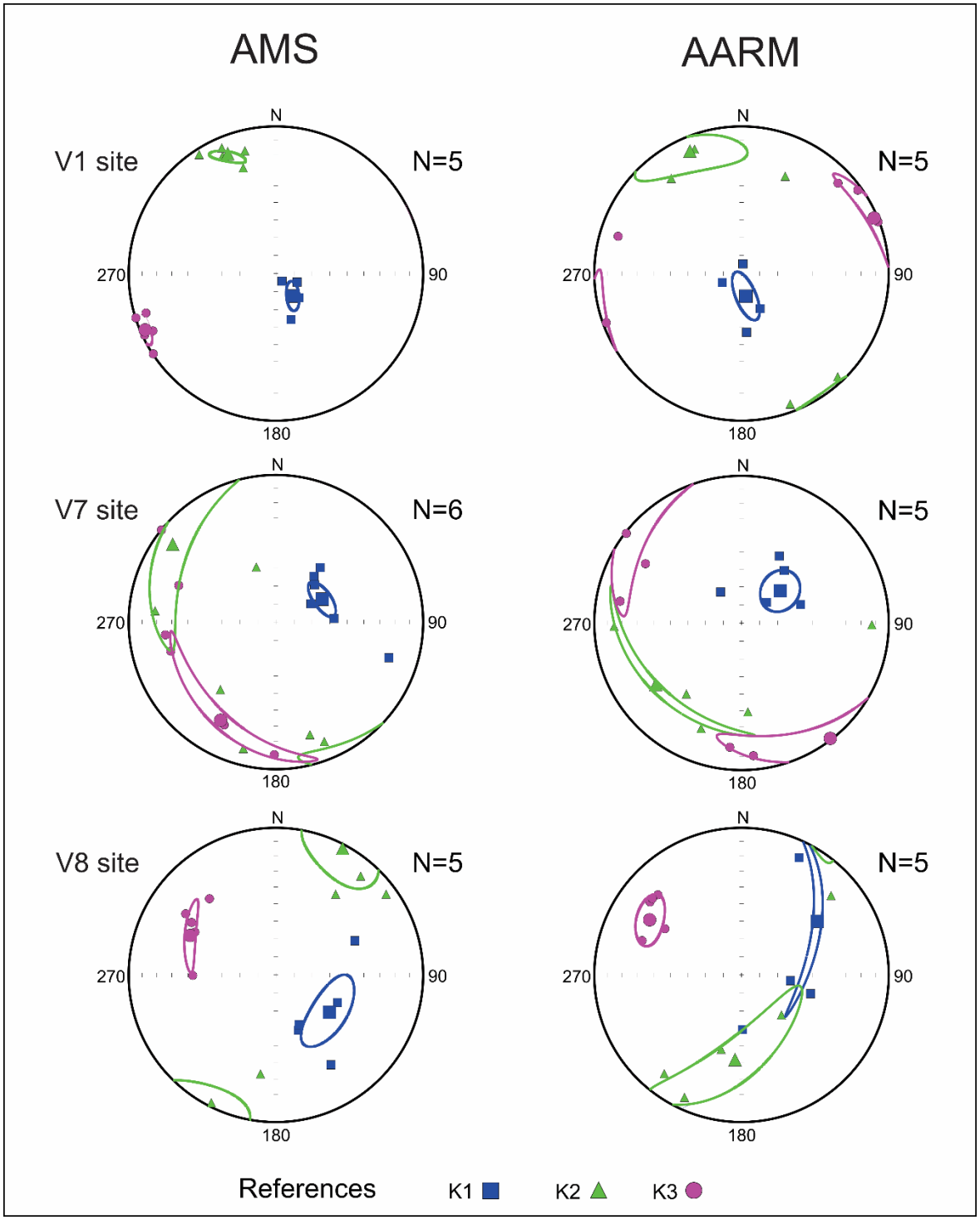


Figure 14: Comparison of AMS and of AARM ellipsoids showing that magnetite and paramagnetic minerals have fabrics with the same orientations. Equal area projection in geographic coordinate system.

3.4.5 Apatite fission tracks (AFT) results

Samples VAR5 (36º48´58.7"S; 70º40´20.2"W) from the Varvarco Tonalite and BU4 (36º59´03.2"S; 70º41´24.9"W) from the Butalón Tonalite were analysed by AFT. For sample VAR5, AFT results were obtained for 21 apatite crystals. In the radial plot, the mean age obtained is 67.5 ± 8.0 Ma (Late Cretaceous, Fig. 15a; Table 3), with low dispersion of ages from individual crystals. This sample passed the chi-square test suggesting that there is a sole age distribution ($P(\chi^2)$ = 90.72 % > 5%; (Galbraith, 1981; Green, 1981). From sample BU4, 13 apatite crystals were measured. The mean age in the radial plot is 50.3 ± 5.9 Ma (Early Eocene), with low age dispersion for individual grains (Fig. 15b; Table 3). The sample also passed the chi-square test (44.37 %), suggesting that the single grain ages have a sole age distribution ($P(\chi^2)$ = 44.37% > 5%).

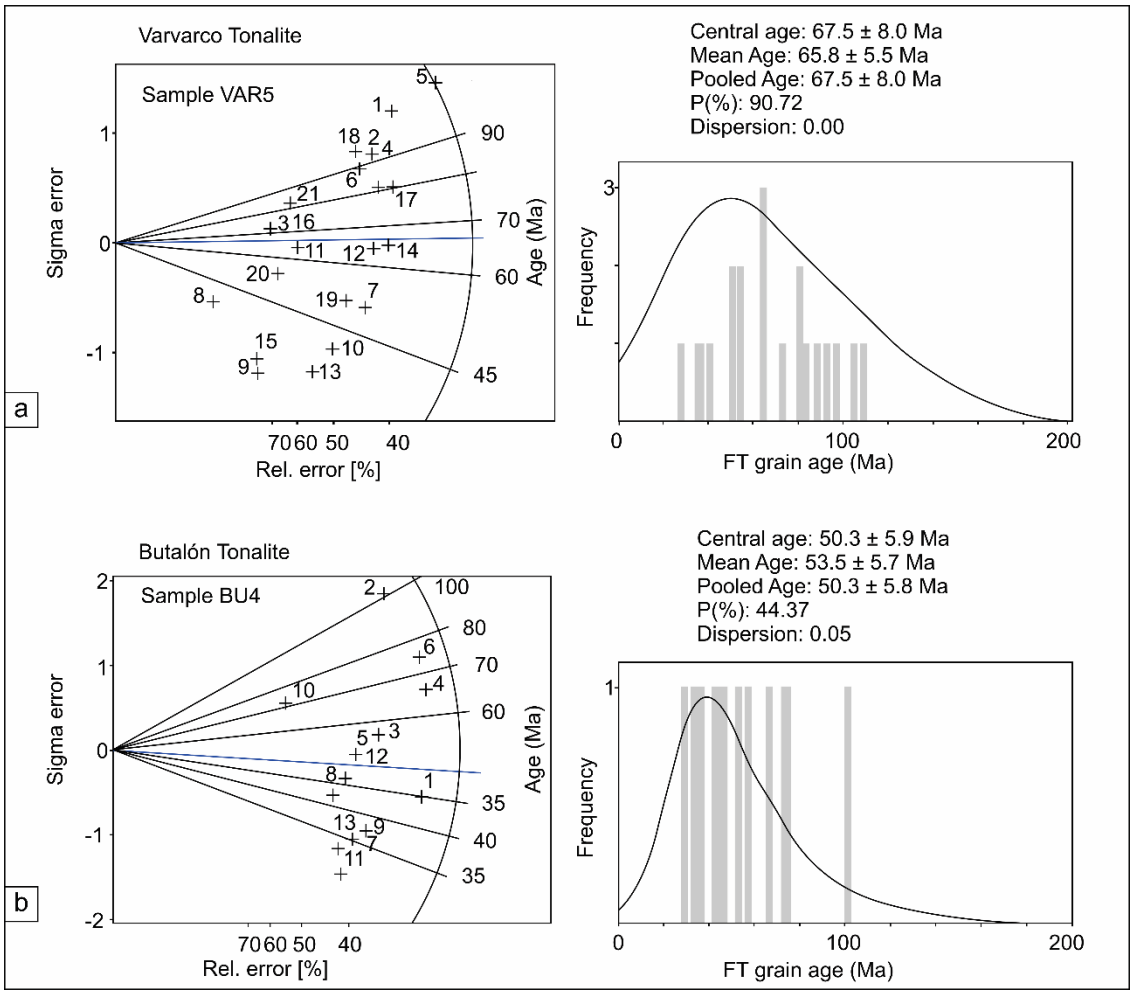


Figure 15: Apatite fission track data of samples (a) VAR 5 and (b) BU4. Diagrams on the left of the figure show the radial distribution of ages of each grain, where the central age is marked in blue. Diagrams on the right, show the frequency histogram for obtained ages.

Table 3: Apatite fission track data. a) Central ages calculated with a calibration of 330.40 ± 20.16 Ma. n: number of measured grains. b) Kinetic parameters.

Sample	Lithology	n	U (ppm)	Dosimeter		Spontaneous		Induced		$P(x)^2$	Age dispersion	Central age (Ma) ± 1s
				ρD	***ND***	**ρ_S**	**N_S**	**ρi**	***N*i**			
VAR5	tonalite	21	9.19	8.43	5000	2.61	131	5.61	281	90.72	0	67.5 ± 8.0
BU4	tonalite	13	14.18	8.42	5000	2.95	131	8.48	377	44.37	0.05	50.3 ± 5.8

3.5 Discussion

3.5.1 Magma hybridisation processes in the I-type Varvarco and Butalón intrusive bodies

According to the field and petrographic observations presented above, we interpreted that Varvarco and Butalón tonalites are hybridised igneous bodies which have experienced magma mingling-mixing at their sources. In the area, the more mafic part is represented by the quartz-dioritic dykes, that are intermediate in composition, whereas the more felsic products are represented by the Radales Aplite. The intermediate composition of the quartz-dioritic dykes indicates that the hybridisation process was strong in the area.

The presence of enclaves with different degrees of hybridisation such as enclaves with distinct contacts with the host tonalite (Fig. 5c) or enclaves partially absorbed (corroded) and rimmed by a new hybrid magma (Fig. 5d), and the varied degree of hybridisation observed in enclave swarms (Fig. 5e), suggest that the mingling process would have started before the emplacement (i.e., at the source). Magmatic flow had possibly favoured the incorporation of heterogeneous enclaves such as those shown in Figure 5c-e (e.g., Bateman, 1995). At higher temperatures, mixing processes are likely to have taken place in the magma chamber. A schematic hybridisation trend is shown in Figure 16, based on Barbarin (2005)'s model.

Increasing crystallisation stages of the intermediate host magma (given mainly by the more voluminous tonalite), would produce the magma hybridisation textures that are observed, which range from early to late mingling features. Scattered mafic magmatic enclaves from the Varvarco and Butalón plutons represent early mingling textures (Fig. 16a, b), whereas the presence of needle-

like apatite in these enclaves points to early mafic magma quenching (Wyllie *et al*. 1962). The lack of chilled margins shown by most of the enclaves suggests that local mixing was caused by partial dissolution of the originally chilled borders (Barbarin, 2005). The presence of outer zones of calcic plagioclase (labradoritic spikes) in more sodic plagioclase of the Varvarco Tonalite (Fig. 10b) has also been interpreted as a result of mixing processes involving coeval acid and mafic magmas (Fig. 7b in Hibbard, 1981), and can be due to quenching related to magma hybridisation (Mollo *et al*. 2011; Molina *et al*. 2012).

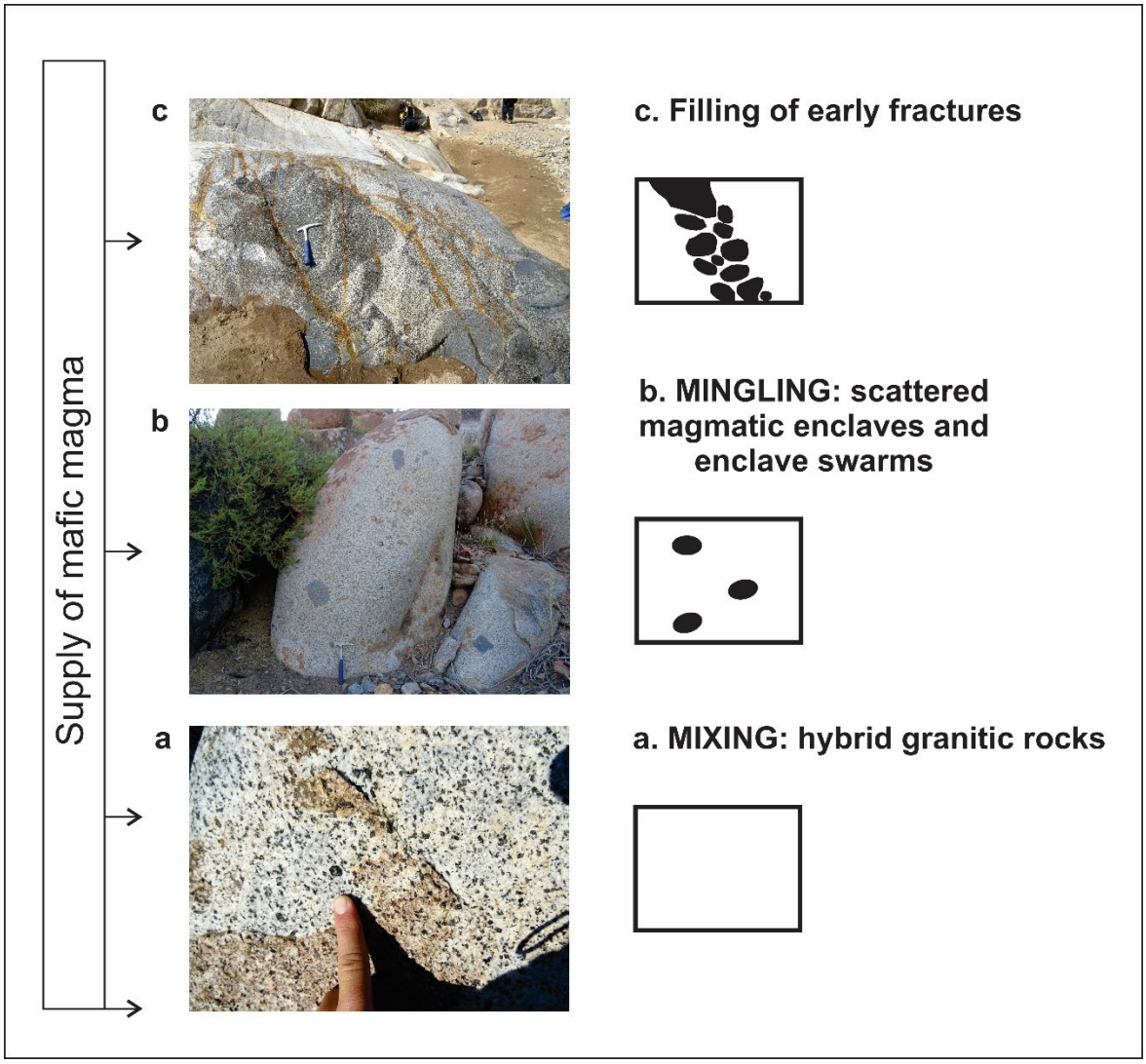


Figure 16: Schematic magma hybridisation processes proposed for the Varvarco Tonalite, based on the model of Barbarin (2005).

The enclave swarms present in the Varvarco Tonalite represent magma channels that were used by new pulses of magma arriving to the chamber (e.g., Bateman, 1995; Tobisch *et al*. 1997). The disrupted quartz-dioritic dykes (Fig.

16c) suggest that mafic magma intruded through early fractures in the increasingly more crystallised Varvarco Tonalite (Barbarin, 2005).

The presence of K-feldspar and amphibole oikocrysts with inclusions of early-formed minerals are an evidence of mafic magma undercooling and thermal adjustment (Castro *et al*. 1991). Separate plagioclase crystals constitute chadocrysts included in relatively larger, late amphibole oikocrysts. Chadocrysts remain representatives of an earlier textural development stage (Higgins & Roberge, 2003).

Rounded quartz phenocrysts rimmed by amphibole ("quartz ocelli", Fig. 8d, Vernon, 1990; Hibbard, 1991) are observed in the dioritic to quartz-dioritic dykes and are assigned to the liquid-dominated hybridisation stage (compare Fig. 16a). For quartz ocelli, the parental magma of the quartz-dioritic dykes would have already mixed-mingled by the time when it intruded the solidified host rock, suggesting that the hybridisation process had been achieved in several stages.

No solid-state recrystallisation textures were observed in the Varvarco Intrusives. The only modification of grain boundaries was locally observed is some polygonisation of quartz grains. This suggests that the rocks underwent some degree of static recrystallisation (textural coarsening – Higgins, 2011). The Radales Aplite sample from the V5 site sampled for this study has a granophyric texture suggesting that it cooled under shallow subvolcanic conditions (Vernon, 2010).

The affinity of the Varvarco Intrusives with calc-alkaline I-type magmas (Franchini *et al*. 2003; Casé *et al*. 2008) and the predominance of intermediate compositions in the suite, with hornblende as the main mafic mineral, is typical of Cordilleran magmas. These water-rich compositions are characteristic of subduction environments (Bachmann & Bergantz, 2008). Amphibole and biotite crystals from the Varvarco Tonalite crystallised from magmas of calc-alkaline composition (Fig. 17a-f). According to the classification of Molina *et al*. (2009), the amphibole cores and rims crystallised in equilibrium with subalkaline magmas (Fig. 17a-d), although some amphibole cores fall into the field of subalkaline trachytoid magmas (Fig. 17b). Given that the Varvarco area is poorly studied, there are no granitoid rocks in vicinity to directly compare the mineralogy of Varvarco intrusive. In figures 10, 11, 17 and 18 we compare compositions of

amphiboles and biotites with amphiboles and biotites of Zaffarana *et al*. (2014) and of Castro *et al*. (2011). Zaffarana *et al*. reports granitoids of Late Triassic age from the Central Patagonian Batholith at Gastre (North Patagonian Massif) which were emplaced during the early stages of Gondwana break-up. In turn, Castro *et al*. (2011) reports Jurassic granites of the North Patagonian Batholith in the area of Bariloche (North Patagonian Andes) which were, like the Varvarco rocks, formed by the Andean subduction system. Varvarco amphiboles largely overlap in compositions with the amphiboles reported for the Late Triassic granites of the Gastre Superunit of the Central Patagonian Batholith studied by Zaffarana *et al*. (2014) and have less variable TiO_2 concentrations than amphiboles reported for the Jurassic granites of the Patagonian Batholith studied by Castro *et al*. (2011).

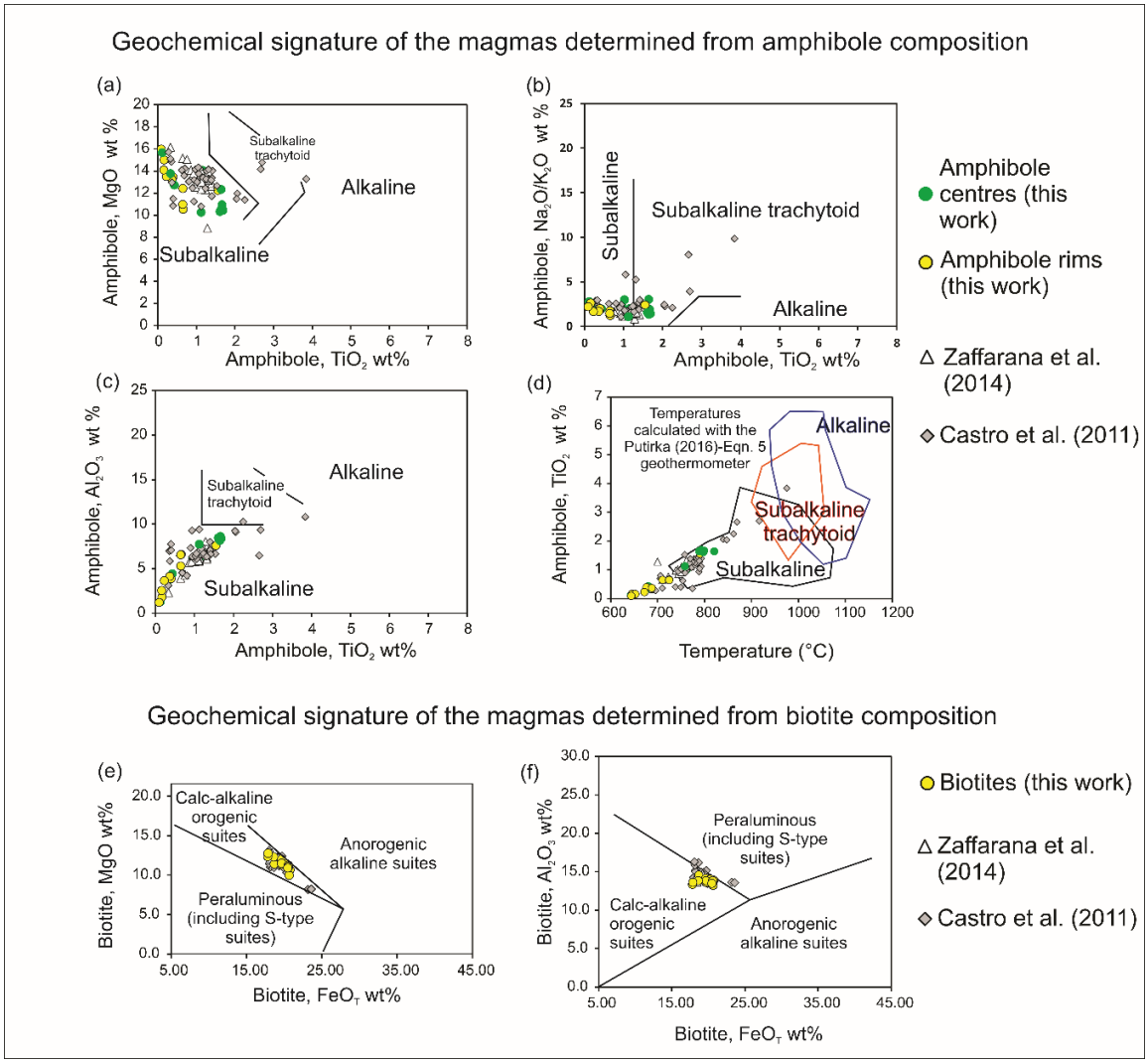


Figure 17: Geochemical signature of the magmas in equilibrium with amphibole and biotite from the Varvarco Tonalite. (a) to (d) Amphibole compositions of the Varvarco Tonalite plotted on the diagrams of Molina *et al*. (2009). (a) MgO vs. TiO_2. (b) Na_2O/K_2O vs. TiO_2. (c) Al_2O_3 vs. TiO_2. (d)

TiO_2 vs. Temperature calculated using geothermometer of Putirka (2016). (e) and (f) Tectonic discrimination diagrams for biotites of the Varvarco Tonalite: (e) Al_2O_3 vs MgO and f) Al_2O_3 vs FeO_T (Abdel-Rahman, 1994).

The composition of the biotite crystals is comparable with those from calc-alkaline orogenic suites (Fig. 17e-f) in the tectonic discrimination diagram of Abdel-Rahman (1994). The presence of titanomagnetite as the main oxide in these rocks (Varvarco Tonalite, Fig. S2a) is also compatible with granites being of the magnetite series of Ishihara (1977), in agreement with the results of Casé *et al*. (2008). Similarly, to amphiboles, Varvarco biotites are largely overlapping in Al_2O_3, MgO and FeO_T concentrations with biotites reported by Zaffarana *et al*. (2014) and Castro *et al*. (2011) (Fig. 17e-f), with the biotites by Castro *et al*. (2011) showing slightly larger variations.

3.5.2 Parental melt conditions of the Varvarco Tonalite

Thermobarometry

To estimate the magma storage temperatures we used geothermometers based on amphibole-plagioclase compositions (Holland & Blundy, 1994, expression B; Molina *et al*. 2021, expressions A1, A2 and B2), amphibole compositions (Ridolfi *et al*. 2010; Ridolfi & Renzulli, 2012; Putirka, 2016), biotite (Henry *et al*. 2005) and melt compositions (Molina *et al*. 2015; Putirka, 2016). Individual results are presented in Table 2, and a summary is presented in Table 4.

Temperatures obtained with the expressions A1, A2, and B2 from Molina *et al*. (2021) agree reasonably and are between 612 and 703 °C (Table 4). In general, temperatures obtained with expression A1 are lower than those obtained with expressions A2 and B2 (Table 4). In the case of the pressure-dependent expressions A1 and A2, results obtained at 1 and at 5 kbar are almost identical (Table 4). For these calculations, we used amphibole compositions 61, 62, 63 and 65, which are from cores of amphibole crystals that satisfy the validation criteria of these geothermometers (Molina *et al*. 2021). These amphibole cores were combined with plagioclases 9, 21, 28 and 39, of andesine composition An_{30-}

36, which also pass the validation criteria proposed by the authors (Table 2a and 2b).

The expression B from the Holland & Blundy (1994) amphibole and plagioclase thermometer was used for the same plagioclase cores as in the Molina *et al*. (2021) geothermometer, and amphibole cores with 0.2 Ti (a.p.f.u.) and 1.5 (a.p.f.u.) Al^{IV} contents. This filter yielded a temperature of 784-716 °C for the amphibole cores, and these temperatures agree with the amphibole core-only temperatures (Ridolfi *et al*. 2010; Ridolfi & Renzulli, 2012; Putirka, 2016; Table 2b). However, the higher temperatures could be due to either their high Al^{VI} or to low Mg occupancies, and therefore we consider that the crystallisation temperatures around 612-703 °C obtained with the expressions from Molina *et al*. (2021) are more likely.

Liquid-only temperatures of Molina *et al*. (2015) and Putirka (2016) for amphibole-saturated magmas are, as expected, higher than the temperatures calculated by using amphibole crystals and by the combination of amphibole and plagioclase crystal cores. They range from 922 to 958 ºC (Table 4), and for these calculations the liquid composition was estimated using the whole-rock composition of sample BPN11 from of the Varvarco Tonalite (sample reported in Kay *et al*. 2006). The obtained liquid-only temperatures are compatible with the amphibole stability field in subalkaline liquids (see Fig. 15 in Molina *et al*. 2009 and Fig. 9 in Kiss *et al*. 2014), consistent with a system that involved amphibole-saturated parental melts.

The combination of Ti and Mg/(Mg+Fe) ratios of biotites were used to determine temperature following the method by Henry *et al*. (2005). Biotite compositions are well within the calibration range of the method (X_{Mg} = 0.275-1,000, Ti = 0.04-0.6 a.p.f.u.) and yielded temperatures between 689 and 753ºC, in an excellent agreement with amphibole temperatures determined by Molina *et al*. (2021) (Table 4).

Crystallisation pressures were estimated using the Ridolfi & Renzulli (2012) amphibole-only geobarometers (average between the results of equations 1a and 1b) and the Molina *et al*. (2015) and Anderson & Smith (1995) amphibole-plagioclase barometers. For these calculations, as in the case of geothermometers, only amphiboles 63 and 68 and plagioclases 9, 21, 28 and 39

(Tables 2a and b) that passed all the validation parameters from Molina *et al*. (2015, 2021) were used. We also estimated pressures using the Al in hornblende geobarometers of Hammarstrom & Zen (1986), Hollister *et al*. (1987), Johnson & Rutherford (1989), and Schmidt (1992) (Table 4).

The highest pressures were calculated using Schmidt (1992) calibration, yielding ~4 kbars for amphibole cores (amphibole rim compositions were not suitable for the Al in hornblende calibrations, because of their high silica content, higher than 50% wt; Table 2b). However, Al in hornblende geobarometers tend to overestimate pressures, as both the pressure-dependent tschermakitic and the temperature-dependent edenitic substitutions govern the total Al content in amphiboles (Erdmann *et al*. 2014).

Pressures range from 1.12 to 1.68 kbar when calculated with the geobarometer of Molina *et al*. (2015) and the temperatures obtained with the pressure-independent thermometer B2 from Molina *et al*. (2021).

Similar pressures were obtained using the Molina *et al*. (2015) geobarometer combined with the temperatures obtained with the Ridolfi & Renzulli (2012) and Putirka (2016) thermometers (Table 4). These pressures broadly agree with the ones obtained with the Anderson & Smith (1995) amphibole barometer (2.26-3.13; Table 4).

Table 4: Summary of the temperatures and pressures calculated for the sample of the Varvarco Tonalite. In the amphibole-plagioclase barometer of Molina *et al*. (2015), T1 is the temperature obtained with Ridolfi & Renzulli (2012) geothermometer (equation 5) and T2 with the Putirka (2016) geothermometer (equation 5). Standard deviation of the data is signaled in the appropriate cases.

Sample name			**VARVARCO TONALITE**	
Analysed material			**Centres**	**Rims**
Calibration		**Calibration uncertainty**		
Geothermometers (°C)	Amp-Pl thermometer (Molina *et al*. 2021-expression A1 at 15 kbar)	± 50ºC	**612**-690	-
	Amp-Pl thermometer (Molina *et al*. 2021-expression A1 at 1 kbar)	± 50ºC	615-692	-
	Amp-Pl thermometer (Molina *et al*. 2021-expression A2 at 15 kbar)	± 50ºC	625-697	-

	Amp-Pl thermometer (Molina *et al*. 2021- expression A2 at 1 kbar)		± 50ºC	628-699	-
	Amp-Pl thermometer (Molina *et al*. 2021- expression B2)		± 50ºC	633-**703**	-
	Amp-Pl thermometer (Holland & Blundy 1994 - expression B)		± 40ºC	784-716	-
	Amphibole data (available in Table 2b)	Amp-only thermometer of Ridolfi *et al*. (2010) - Eqn. 1. Average data	± 22ºC	801	772
		Amp-only thermometer of Ridolfi & Renzulli (2012) - Eqn. 2. Average data	± 23.5ºC	836	803
		Amp-only thermometer of Putirka (2016) - Eqn. 5. Average data.	± 30ºC	767	717
	Whole-rock data (calculated with sample BPN11 of Varvarco Tonalite from Kay *et al*. 2006)	Liquid-only - Molina *et al*. (2015)	± 35 to ± 45ºC	958	
		Liquid-only - Putirka (2016) - Eqn. 3	± 33ºC	922	
	Biotite (available in Table 2c)	Henry *et al.* (2005)	± 12ºC	689-753	
Geobarometers (kbar)	Amphibole data (some of them are available in Table 2b)	Hammarstrom & Zen (1986) (average data)	± 3 kbar	3.47	-
		Hollister *et al*. (1987) (average data)	± 1 kbar	3.53	-
		Johnson & Rutherford (1989) (average data)	± 0.5 kbar	2.76	-
		Schmidt (1992) (average data)	± 0.6 kbar	3.99	-
		Ridolfi *et al.* (2010) - Eqn. 4 (average data)	± 11%	1.29	1.03
		Ridolfi & Renzulli (2012) (average data)	± 11.5%	1.77	1.25
	Amp-Pl barometer (Anderson & Smith 1995)		± 0.6 kbar	3.13-2.26	-
	Amp-Pl barometer (Molina *et al*. 2015) at T1*		± 1.5 to ± 2.3 kbar	3.34-2.15	-
	Amp-Pl barometer (Molina *et al*. 2015) at T2**			2.78-1.80	-
	Amp-Pl barometer (Molina *et al*. 2015) at T3***			1.68-1.12	-

T1* (Ridolfi and Renzulli, 2012, Eqn.2)

T2**(Putirka 2016. Eqn.5)

T3*** (Molina *et al*. 2021-expression B2)

errors are 1 sigma standard deviations

Oxygen fugacity

The oxygen fugacity of the parental melt to the Varvarco Tonalite was calculated using the method by Ridolfi *et al*. (2010) and Wones & Eugster (1965) (Fig. 18a, d). Ridolfi *et al*. (2010) uses amphibole chemistry to derive P-T conditions, H_2O and fO_2. It should be noted that Ridolfi *et al*. (2010) barometer estimates pressures of about 1.29 kbars for amphibole cores and 1.03 kbars for rims, which is significantly lower than pressures derived by other barometers. However, pressure differences within 1-3 kbars have very little effect (~0.2 log unit) on the fO_2 estimates by Ridolfi *et al*. (2010) oxybarometer, which is within the uncertainty of the method (0.4 log unit). According to Ridolfi *et al*. (2010) oxybarometer, amphibole cores and rims from the Varvarco Tonalite have similar fO_2s in the range of -12.2-14.9 logfO_2, which indicates that they crystallised under relatively high fO_2 conditions between the nickel-nickel oxide (NNO) and NNO + 2, typical of calc-alkaline magmas (ΔNNO from -1 to +3; e.g., Gill, 1981; Behrens & Gaillard, 2006).

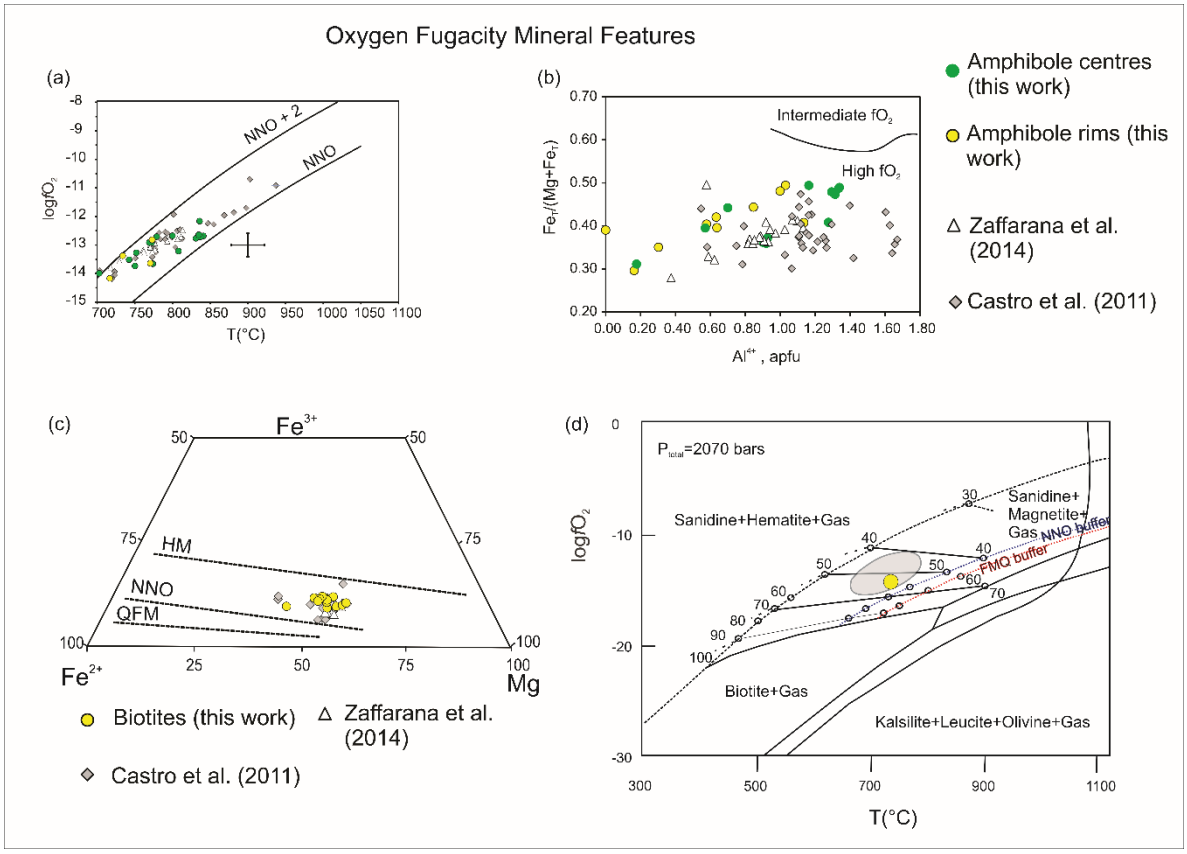


Figure 18: Oxygen fugacity conditions of the magmas in equilibrium with the amphiboles and biotites of the Varvarco Tonalite. Data by Zaffarana *et al*. (2014) and Castro *et al*. (2011) are plotted for comparison. (a) log*f*O2 vs. temperature diagram by Ridolfi *et al*. (2010). Error bars represent maximum log*f*O2 errors of 0.4 log unit and the expected σ (22 °C). (b) Diagram of Anderson & Smith (1995) showing the effect of *f*O2 on amphibole compositions in terms of $Fe_T/(Fe_T + Mg)$ vs. Al^{IV} (a.p.f.u.). (c) Ternary diagram for oxygen fugacity in biotites (Wones and Eugster, 1965). (d) logfO_2 vs T diagram (Wones & Eugster, 1965). Numbers represent 100*Mg/(Mg+Fe) ratios in biotites. Yellow circle shows an average of all biotite compositiosn from this study. Biotites by Zaffarana *et al*. (2014) overlaps with the yellow circle. Biotites by Castro *et al*. (2011) is shown in grey oval. Oxygen fugacity buffers are nickel-nickel oxide (NNO), hematite-magnetite (HM), quartz-fayalite-magnetite (QFM).

Wones & Eugster (1965) use (Mg/(Mg+Fe) ratios in biotite and temperatures in order to estimate oxygen fugacity. We used temperatures derived by Henry *et al*. (2005) and biotite cations by Li *et al*. (2020). All biotites plot in the area outlined by a yellow circle (Figure 18d). For comparison, biotites by Castro *et al*. (2011) plot over the wider ranges of fO_2, but still between the NNO and hematite-magnetite (HM) buffers.

Oxygen fugacities between NNO and HM buffers are also suggested by Fe^{2+}-Fe^{3+}-Mg ternary for biotite compositions by Wones & Eugster (1965) (Figure

18c). Additionally, high fO_2s of the studied rocks are also in inferred by $Fe_t/(Fe_t+Mg)$ ratios in amphibole (Czamanske & Wones, 1973; Anderson & Smith, 1995), and by titanomagnetite as the main oxide phase of these rocks (see below, Fig. 18b; Supplementary Figure S2a).

3.5.3 Cooling history and exhumation of the Late Cretaceous and Paleogene plutons

To date, three ages have been obtained for the Varvarco Tonalite: a recalculated K-Ar biotite age of 64.7 ± 3.2 Ma (J.I.C.A./M.M.A.J 2000 in Franchini *et al*. 2003), an $^{40}Ar/^{39}Ar$ biotite age of 69.09 ± 0.13 Ma (Kay *et al*. 2006), and recently a U-Pb SHRIMP zircon age of 67.8 ± 0.8 Ma (Assis, 2019). Zappettini *et al*. (2014) and Zappettini *et al*. (2021) reported an ^{40}Ar-^{39}Ar age of 65.68 ± 0.22 Ma for adularia from veins associated with the hydrothermal alteration of basic volcanic rocks from the Jurassic Colomichicó Formation (Zappettini *et al*. 2018).

If the closure temperatures of the specific minerals for the various geochronological methods are taken into account, it is possible to construct a thermal profile and to calculate the exhumation rate (England and Moldnar 1990). Thus, the thermal profile/cooling curve for the Varvarco Tonalite was constructed (Fig. 19) considering the more accurate geochronological data, namely those obtained by Assis (2019) and by Zappettini *et al*. (2014). The typical closure temperature for U-Pb on zircon is greater than 800 ºC (Lee *et al*. 1997). Siégel *et al*. (2018) showed that the zircon saturation temperature in igneous rocks is variable, but normally between 780 and 860 °C for intrusive rocks. Since we do not have Ti in zircon data that would allow to calculate temperatures more precisely, we assume a closure temperature for zircon of ca. 850 °C. Considering that the closure temperature of radiogenic argon in K-feldspar can be as low as 120–150°C (Foland 1974, Harrisson and McDougall 1982), we opted for using a closure temperature of 150 °C for adularia.

A ***one-step*** theoretical curve between 67.8 ± 0.8 Ma (U-Pb in zircon) and 65.68 ± 0.22 Ma (^{40}Ar-^{39}Ar in adularia from hydrothermal veins) was constructed for the exhumation of the Varvarco Tonalite (Fig. 19). This curve gives a continuous cooling rate of approximately 330 °C per Ma. Sánchez *et al*. (2018) proposed tectonically driven continuous exhumation for the Cordillera del Viento

during the latest Cretaceous-early Paleogene deformation event. Considering continuous and fast exhumation, the theoretical curve can be extended below 100 °C towards the graphically obtained age of 65.3 Ma (Fig. 19). Fast cooling and exhumation of the Varvarco Tonalite also agrees with the low pressures obtained by geothermobarometry (Tables 2 and 4). The highest pressures calculated for amphibole and plagioclase cores are of the order of 3.34 kbars (Table 4), which correspond to a source at ~12 km depth. Amphibole rims crystallised at lower pressures of ~1-2 kbars, which is compatible with shallower emplacement at ~4-7 km depth. It means that if the exhumation was a continuous process, as suggested by the thermal profile, the magmatic system could have been exhumed by ~12 km in ca. 2.1 Ma.

Considering that the Paleogene Cayanta Volcanics intruded over the already eroded Varvarco Tonalite and Radales Aplite between 50-56.9 Ma (^{40}Ar-^{39}Ar hornblende ages, Jordan *et al*. 2001) and 67.5 ± 8 Ma (apatite FT age), and Varvarco Tonalite has a final stage of exhumation (below 4-5 km) at least at 59.5 Ma, one important question that we are trying to answer is “When was the final exhumation of the Varvarco Tonalite plus Radales Aplite?” The final tectonic exhumation must have occurred after the crystallisation of the adularia veins in the Radales Aplite at 65.68 ± 0.22 Ma and prior to the extrusion of the Cayanta volcanic rocks at 50-56.9 Ma. The Varvarco Tonalite magmatic fabric was not affected by any solid-state deformation that could have been superimposed onto these rocks, and shallow emplacement conditions helped in the fast exhumation process. The Radales Aplite has granophyric texture, which suggests that it would have experienced a greater degree of undercooling than the Varvarco Tonalite (Vernon, 2010) - consistent with emplacement at a shallower crustal level. At this point, we do not have any crystallisation age for the Radales Aplite that may corroborate the relationship between cooling and exhumation. The final exhumation possibly occurred coevally with the generation of the adularia veins in the Radales Aplite at 65.68 Ma or later as part of the continuous process of exhumation at 65.3 Ma (Fig. 19), or between 65.3 and 59.5 Ma, considering the apatite FT age. We do not exclude that the final exhumation could have happened after 59.5 Ma, but certainly before 56.9 Ma.

Note that the K-Ar biotite cooling age of 64.7 ± 3.2 Ma (Franchini *et al*. 2003) falls onto this cooling curve given the uncertainty of the fission track ages. The biotite age of 69.09 ± 0.13 Ma - also from the Varvarco Tonalite (Kay *et al*. 2006) - is much older than the U-Pb zircon age of Assis (2019). These two ages are not within the uncertainty. It is difficult to explain this age difference in the context of the thermal profile, but it could be related with an early (c. 69 Ma) input of mafic hydrated magma into the magmatic system of the Varvarco Tonalite.

Given the age of 50.3 ± 5.9 Ma (AFT, sample BU4), the Butalón Tonalite was exhumed a little later than the Varvarco Tonalite, in Paleogene. However, the exact age of its exhumation is not yet fully constrained. The AFT age of Butalón Tonalite is not as well defined as that for the Varvarco Tonalite, because less fission track data could be obtained from the dated sample BU4 (Table 3). It seems that the Butalón Tonalite was emplaced in an already exhumed orogenic system. This is also in agreement with the different cooling rates of the Varvarco Tonalite and the Radales Aplite, as inferred from their magmatic textures discussed before.

Temperature and pressure estimates derived from mineral chemistry are here integrated with the temperature-time path reconstruction in order to derive a geothermal gradient for the Cordillera del Viento area. In the first place, amphibole core compositions provide temperatures around ~610-700°C and pressures around 2-3.34 kbars, which correspond to nearly ~12 km depth (Fig. 19). At these P-T (pressure-temperature) conditions the Varvarco Tonalite was almost completely crystallised and already cooling. Then, amphibole rim compositions record pressures of 1-2 kbars which correspond to ~4-7 km depth (Fig. 19), and, at this stage, the temperatures were no higher than 120°C, as apatite fission tracks anneal at temperatures higher than this threshold (Ehlers and Farley, 2003; Reiners and Ehlers, 2005). From these two T and P regimes, a geothermal gradient of ~62.5°C/km can be obtained, revealing the cooling and exhumation history of the Varvarco Tonalite. Such high geothermal gradient suggests that the intrusive rocks were cooling down and exhumed at the same time. The lower geothermal gradients of ~51°C/km (Sigismondi 2013; Sigismondi and Ramos 2009a, 2009b, see Galetto *et al*. 2021) can be reflecting the pre-

Andean tectonic scenario in the modern easternmost region of the Neuquén Basin which was not affected by Andean deformation (Galetto *et al*. 2021).

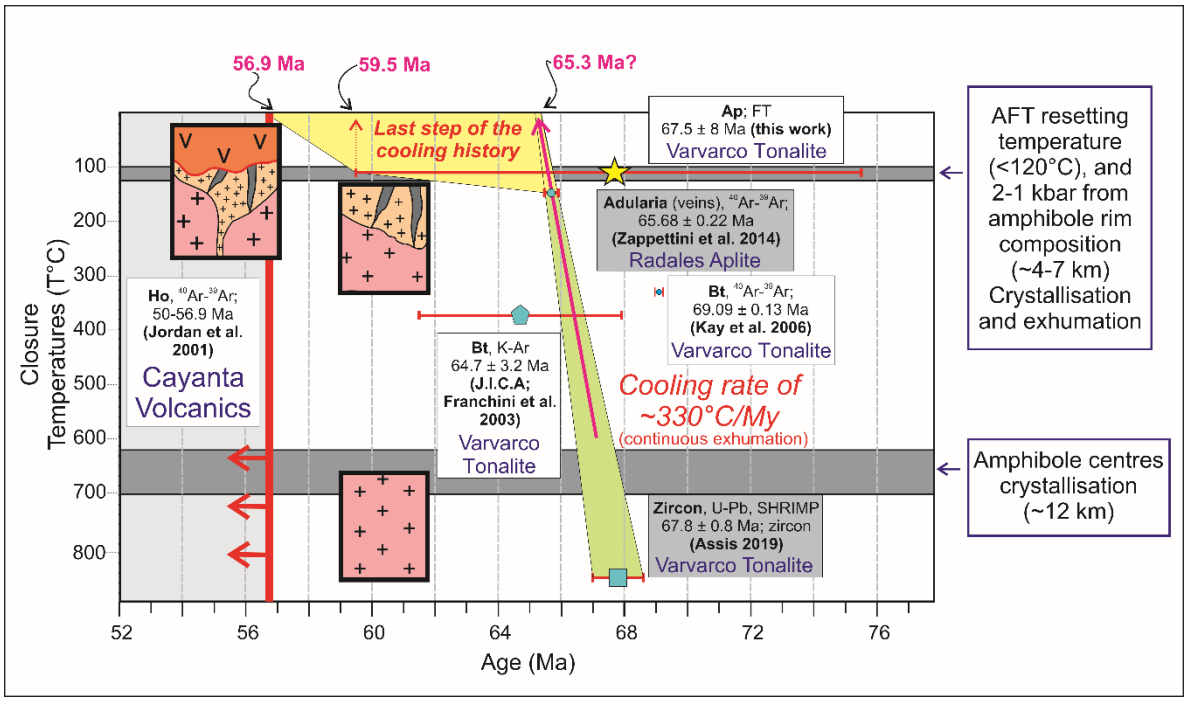


Figure 19: Cooling history of the Varvarco Tonalite. See main text for details.

3.5.4 Magnetic fabrics of magmatic origin in the Late Cretaceous and Paleogene plutons

As previously shown in section 4.d, the magnetic fabrics determined by the ASM method in the Varvarco Tonalite, Butalón Tonalite and the Radales Aplite can be interpreted as of pure magmatic origin representative of magma flow during the Late Cretaceous-Paleogene. In particular, the fast-cooling rate estimated from the U-Pb, ^{40}Ar-^{39}Ar, and AFT ages suggest that the magmatic fabrics of the Varvarco Tonalite were acquired during pluton cooling and exhumation.

The magmatic fabrics from the Varvarco Tonalite and Radales Aplite are steeply dipping, with a predominant N-S strike (Supplementary Figure S1a), which is mostly consistent with the orientation of the regional structures from the Andean orogenic cycles (Giacosa *et al*. 2014; Turienzo *et al*. 2018; Sánchez *et al*. 2018). The oscillating character of the magmatic fabrics strongly suggests that they could have been influenced by intrinsic dynamics inside the magma chamber. However, there is some evidence of regional stress influence, such as

N-S elongation of the pluton along the Matancillas creek (Fig. 2a, 3a-b) and NNE-SSW to NNW-SSE fabrics. Even though coupling with the wall rock may not occur, the Andean stress field might have influenced magma flow to some extent. The N-S Matancillas creek goes along the trace of the N-S directed Cordillera del Viento Fault (Fig. 2a, b). This fault was active during the Andean deformation and could have favoured magma ascent through the crust. The lack of tectonic deformation suggests that pluton emplacement took place either during or soon after the Late Cretaceous deformation event in the Neuquén Andes. Alternatively, similar fabrics may be possible even during a regional deformation event if strain partitioning in low- vs high-strain domains is present. However, post-tectonic emplacement is also in agreement with observations made in the other parts of the Naunauco Belt, where other subvolcanic bodies were post-tectonically emplaced (Llambías & Malvicini, 1978; Zamora Valcarce *et al*. 2011).

Other plutons which were emplaced late with respect to main tectonic deformation events have been described as having flat roofs and steeply dipping foliation planes along the pluton walls (de Saint-Blanquat *et al*. 2006; Payacán *et al*. 2014). Their internal fabric is strongly decoupled from the host rock fabrics, likely reflecting magma chamber processes (Paterson *et al*. 1998).

Unfortunately, the areas of the Varvarco Tonalite (marked as “VT” in Fig. 2 and in Fig. 3a-b) where we expected to see flattened magmatic foliations in the roof of the intrusion, were only inferred by satellite images and inaccessible for sampling. Some sites, such as site V3, within the Varvarco Tonalite show flat foliation planes, suggesting a location near the pluton roof. But in general, steeply dipping magmatic foliations are dominant and probably reflect closeness to the contact with the host rocks. The contact area is the place where the highest degree of coupling between the magmatic and the host rock fabrics usually occurs (Paterson *et al*. 1998). In this sense, the parallel foliations presented by the metamorphic rocks of the Guaracó Norte Formation and the magmatic rocks of the Varvarco and Radales plutons in the area between the Matancilla and Chacay creeks suggest that some degree of mechanical coupling existed between them (Fig. 12a). However, the contact aureole in the margin-parallel fabrics rules out regional deformation as a significant cause of fabric formation, and instead suggests late fabric formation due to internal processes during

emplacement (Paterson *et al*. 1998). In addition, the thermal contrast between the Guaracó Norte Formation and the Varvarco Tonalite is consistent with the results obtained from geothermobarometry, which suggests that the Varvarco pluton was emplaced at a high crustal level at ~2-3 kbars (between ~12 km depth).

Lastly, magma feeder zones, where magma upwelled, can be traced by the existence of vertical magmatic lineations at sites for which AMS ellipsoids of prolate shape (T<0) were measured, such as V1, V2, V6 and V7 from the Varvarco Tonalite (Supplementary Figure S1f).

3.6 Conclusions

Field observations and petrographic analysis indicates that magma hybridisation was the main process in the Varvarco and Butalón plutons. The magnetic fabrics of these plutons are dominated by titanomagnetite. This, together with mineral chemistry data (amphibole and biotite) confirms that these magmatic phases belong to the I-type series of calc-alkaline igneous bodies.

The fabrics are, without exception, magmatic, and the AMS data can be interpreted as the result of emplacement and rapid exhumation of fast-cooled plutons. The AFT ages of the Varvarco Tonalite are close to its crystallisation age, as well as the fast-cooling age calculated for this pluton (330°C/My; Fig. 19). Shallow emplacement conditions were estimated based on geothermobarometry (2-3 kbars, equivalent to 12 km depth). These combined data allow us to infer uplift in the region between 66 and 64.9 Ma. Geothermobarometry and AFT data suggest the geothermal gradient of the area of ~62.5 °C/km. The magmatic system in the Varvarco area could have been exhumed by ~12 km in ca. 2.1 Ma.

The orientation of the magmatic fabrics implies that they formed mostly owing to magma chamber processes. However, they could have been controlled, in part, by the regional Late Cretaceous compressive deformation. As the plutons are located along the trace of the Cordillera del Viento Fault, and because they are devoid of post-emplacement tectonic deformation, reactivations of this fault are not supported.

3.7 Acknowledgements

We want to thank Dr. Sebastián Oriolo and an anonymous reviewer for their valuable suggestions that greatly improved the manuscript. We cordially thank Fuat Yavuz for help with biotite diagrams in the earlier version of this article. The research projects from the Universidad Nacional de Río Negro (UNRN) 40A-466, 40A-547, PI-40A-631 and PI-40A-798; project PIP CONICET 11220150100736; project CGL 2012-38396-C01 of the Spanish Program for Science Technology (I+D+i) and FEDER Funds of the EU, contributed to finance this work. The research of José F. Molina has been supported for the Ministerio de Economía y Competitividad (Gobierno de España), grant numbers: CGL2013-40785-P and CGL2017-84469-P, and Consejería de Economía y Conocimiento (Junta de Andalucía), grant number: RNM2163. The research of Natalia Hauser has been supported in part by CNPq fellowships (grants 309878/2019-5). This study was financed in part by the Coordenação de Aperfeiçoamento de Pessoal de Nivel Superior – Brasil (CAPES) – Finance Code 001.

3.8 Competing Interest

The authors declare that they have no known competing financial interests or personal relationships that could have appeared to influence the work reported in this paper.

3.9 Supplementary Material

Supplementary Figure S.1: (a-e) ASM data for the 17 studied sites, showing the individual magnetic ellipsoids for each site, and the P vs. Km and T vs. P diagrams, as obtained with the software Anisoft 4.2. (f) AMS scalar data at the site scale, showing the Pj vs. Km and T vs. Pj graphs (Jelinek, 1981). Equal area projection in geographic coordinate system.

Supplementary Figure S.2: Hysteresis loops and backfield curves obtained for samples from the Varvarco Tonalite and Jurassic Host Granites.

Supplementary Table S.1: Summary of the compiled ages of intrusive and volcanic rocks shown in Figure 1.

Supplementary material is online at http://journals.cambridge.org/geo'

3.10 References

Abdel-Rahman Abdel-Fattah, M. 1994. Nature of Biotites from Alkaline, Calc-alkaline, and Peraluminous Magmas. *Journal of Petrology* 35, 525–541. https://doi.org/10.1093/petrology/35.2.525

Allmendinger, R. W., Cardozo, N. & Fisher, D. M. 2012. *Structural Geology Algorithms: Vectors and Tensors*. Cambridge University Press, Cambridge, 289 pp. https://doi.org/10.1017/CBO9780511920202

Anderson, J. L. & Smith, D. R. 1995. The effects of temperature and fO2 on the Al-in-hornblende barometer. *American Mineralogist* 80, 549–559. https://doi.org/10.2138/am-1995-5-614

Archanjo, C. J., Launeau, P. & Bouchez, J. L. 1995. Magnetic fabric vs. magnetite and biotite shape fabrics of the magnetite-bearing granite pluton of Gameleiras (Northeast Brazil). *Physics of the Earth and Planetary Interiors* 89, 63-75. https://doi.org/10.1016/0031-9201(94)02997-P

Archanjo, C. J., Trindade, R. I. F., Bouchez, J. L. & Ernesto, M. 2002. Granite fabrics and regional-scale strain partitioning in the Seridó belt (Borborema Province, NE Brazil). *Tectonics* 21, 3-1-3–14. https://doi.org/10.1029/2000TC001269

Arregui, C., Carbone, O. & Leanza, H. A. 2011. Contexto tectosedimentario, in: *Relatorio Del 18° Congreso Geológico Argentino, Neuquén*. Neuquén, pp. 29-36.

Assis, O. S. 2019. Petrografía y fábrica magnética de la Granodiorita Varvarco y plutones asociados, Cretácico Tardío-Paleoceno de los Andes Neuquinos. Universidad Nacional de Río Negro. http://rid.unrn.edu.ar/jspui/handle/20.500.12049/2256

Bachmann, O. & Bergantz, G. W. 2008. Deciphering Magma Chamber Dynamics from Styles of Compositional Zoning in Large Silicic Ash Flow Sheets. *Reviews in Mineralogy and Geochemistry* 69, 651–674. https://doi.org/10.2138/rmg.2008.69.17

Barbarin, B. 2005. Mafic magmatic enclaves and mafic rocks associated with some granitoids of the central Sierra Nevada batholith, California: nature, origin, and relations with the hosts. *Lithos* 80, 155–177. https://doi.org/10.1016/j.lithos.2004.05.010

Bateman, P. C. & Eaton, J. P. 1967. Sierra Nevada Batholith. *Science* 158, 1407-1417.

Bateman, R. 1995. The interplay between crystallization, replenishment and hybridization in large felsic magma chambers. *Earth-Science Reviews* 39, 91-106. https://doi.org/10.1016/0012-8252(95)00003-S

Baxter, S. & Feely, M. 2002. Magma mixing and mingling textures in granitoids: Examples from the Galway Granite, Connemara, Ireland. *Mineralogy and*

Petrology 76, 63-74. https://doi.org/10.1007/s007100200032

Behrens, H. & Gaillard, F. 2006. Geochemical Aspects of Melts: Volatiles and Redox Behavior. *Elements* 2, 275-280. https://doi.org/10.2113/gselements.2.5.275

Borradaile, G. J. & Henry, B. 1997. Tectonic applications of magnetic susceptibility and its anisotropy. *Earth-Science Reviews* 42, 49-93. https://doi.org/10.1016/S0012-8252(96)00044-X

Borradaile, G. J. & Jackson, M. 2010. Structural geology, petrofabrics and magnetic fabrics (AMS, AARM, AIRM). *Journal of Structural Geology* 32(10), 1519-1551. https://doi.org/10.1016/j.jsg.2009.09.006

Bouchez, J.-L., 2000. Anisotropie de susceptibilité magnétique et fabrique des granites. *Comptes Rendus de l'Académie des Sciences - Series IIA - Earth and Planetary Science* 330, 1–14. https://doi.org/10.1016/S1251-8050(00)00120-8

Cardozo, N. & Allmendinger, R. W. 2013. Spherical projections with OSXStereonet. *Computers & Geosciences* 51, 193-205. https://doi.org/10.1016/j.cageo.2012.07.021

Casé, A. M., López-Escobar, L., Danieli, J. C. & Schalamuk, A. 2008. Butalón igneous rocks, Neuquén, Argentina: Age, stratigraphic relationships and geochemical features. *Journal of South American Earth Sciences* 26, 188-203. https://doi.org/10.1016/j.jsames.2007.11.001

Castro, A., Moreno-Ventas, I., Fernández, C., Vujovich, G., Gallastegui, G., Heredia, N., Martino, R. D. D., Becchio, R., Corretgé, L. G. G., Díaz-Alvarado, J., Such, P., García-Arias, M., & Liu, D.-Y. 2011. Petrology and SHRIMP U–Pb zircon geochronology of Cordilleran granitoids of the Bariloche area, Argentina. *Journal of South American Earth Sciences* 32(4), 508-530. https://doi.org/10.1016/j.jsames.2011.03.011

Castro, A., Moreno-Ventas, I. & de la Rosa, J. D. 1991. Multistage crystallization of tonalitic enclaves in granitoid rocks (Hercynian belt, Spain): implications for magma mixing. *Geologische Rundschau* 80, 109-120. https://doi.org/10.1007/BF01828770

Chadima, M. & Jelinek, V. 2009. Anisoft 4.2: Anisotropy data browser for windows.

Clark, R. N. 1999. Spectroscopy of Rocks and Minerals and Principles of Spectroscopy. Manual of Remote Sensing. *Remote Sensing for the Earth Sciences: Manual of Remote Sensing*.

Cobbold, P. R. & Rossello, E. A. 2003. Aptian to recent compressional deformation, foothills of the Neuquén Basin, Argentina. *Marine and Petroleum Geology* 20, 429–443. https://doi.org/10.1016/S0264-8172(03)00077-1

Czamanske, G. K. & Wones, D. R. 1973. Oxidation During Magmatic Differentiation,

Finnmarka Complex, Oslo Area, Norway: Part 2, The Mafic Silicates. *Journal of Petrology* 14, 349-380. https://doi.org/10.1093/petrology/14.3.349

D'Eramo, F., Pinotti, L., Tubía, J. M., Vegas, N., Aranguren, A., Tejero, R. & Gómez, D. 2006. Coalescence of lateral spreading magma ascending through dykes: a mechanism to form a granite canopy (El Hongo pluton, Sierras Pampeanas, Argentina). *Journal of the Geological Society* 163, 881–892. https://doi.org/10.1144/0016-764905-060

Dale, J., Powell, R., White, R. W., Elmer, F. L. & Holland, T. J. B. 2005. A thermodynamic model for Ca-Na clinoamphiboles in Na_2O-CaO-FeO-MgO-Al_2O_3-SiO_2-H_2O-O for petrological calculations. *Journal of Metamorphic Geology* 23, 771-791. https://doi.org/10.1111/j.1525-1314.2005.00609.x

Day, R., Fuller, M. & Schmidt, V. A. 1977. Hysteresis properties of titanomagnetites: grain-size and compositional dependence. *Physics of the Earth and Planetary Interiors* 13, 260-267.

de Saint-Blanquat, M., Habert, G., Horsman, E., Morgan, S. S., Tikoff, B., Launeau, P. & Gleizes, G. 2006. Mechanisms and duration of non-tectonically assisted magma emplacement in the upper crust: The Black Mesa pluton, Henry Mountains, Utah. *Tectonophysics* 428, 1–31. https://doi.org/10.1016/j.tecto.2006.07.014

de Saint Blanquat, M. & Tikoff, B. 1997. Development of Magmatic to Solid-State Fabrics during Syntectonic Emplacement of the Mono Creek Granite, Sierra Nevada Batholith, in: *Granite: From Segregation of Melt to Emplacement Fabrics* (ed J. L., Bouchez), pp. 231-252. Springer, Dordrecht. https://doi.org/10.1007/978-94-017-1717-5_15

Deer, W. A., Howie, R. A. & Zussman, J. 2013. *An Introduction to the Rock-Forming Minerals*. Mineralogical Society of Great Britain and Ireland, London.

Digregorio, J. H. 1972. Neuquén. In *Geología Regional Argentina* (ed A. F. Leanza), pp. 439-505. Academia Nacional de Ciencias, Córdoba.

Digregorio, J. H. & Uliana, M. A. 1980. Cuenca Neuquina. In *Geología Regional Argentina* (ed J. C. M., Turner), pp. 985-1032. Academia Nacional de Ciencias, Córdoba.

Dunkl, I. 2002. Trackkey: a Windows program for calculation and graphical presentation of fission track data. *Computers & Geosciences* 28, 3-12. https://doi.org/10.1016/S0098-3004(01)00024-3

Ehlers, T. A., Farley, K. A., 2003. Apatite (U–Th)/He thermochronometry: methods and applications to problems in tectonics and surface processes. *Earth and Planetary Science Letters* 206, 1-14.

England P. & Molnar, P. 1990. Surface uplift, uplift of rocks, and exhumation of rocks. *Geology* 18, 1173-1177. https://doi.org/10.1130/0091-7613(1990)018<1173:SUUORA>2.3.CO;2

Erdmann, S., Martel, C., Pichavant, M. & Kushnir, A. 2014. Amphibole as an archivist of magmatic crystallization conditions: problems, potential, and implications for inferring magma storage prior to the paroxysmal 2010 eruption of Mount Merapi, Indonesia. *Contributions to Mineralogy and Petrology* 167, 1016. https://doi.org/10.1007/s00410-014-1016-4

Ferré, E. C. & Améglio, L. 2000. Preserved magnetic fabrics vs. annealed microstructures in the syntectonic recrystallised George granite, South Africa. *Journal of Structural Geology* 22, 1199-1219. https://doi.org/10.1016/S0191-8141(00)00026-2

Foland K A, 1974. Ar^{40} diffusion in homogeneous orthoclase and an interpretation of Ar diffusion in K-feldspars. *Geochimica et cosmochimica Acta* 38, 151-166.

Foster, M. D. 1960. Interpretation of the Composition of Trioctahedral Micas. *USGS Professional Paper* 354, 11-48.

Franchini, M., López-Escobar, L., Schalamuk, I. B. A. & Meinert, L. 2003. Magmatic characteristics of the Paleocene Cerro Nevazón region and other Late Cretaceous to Early Tertiary calc-alkaline subvolcanic to plutonic units in the Neuquén Andes, Argentina. *Journal of South American Earth Sciences* 16, 399-421. https://doi.org/10.1016/S0895-9811(03)00103-2

Galbraith, R. F. 1981. On statistical models for fission track counts. *Journal of the International Association for Mathematical Geology* 13, 471-478. https://doi.org/10.1007/BF01034498

Galetto, A., Georgieva, V., García, V. H., Zattin, M., Sobel, E. R., Glodny, J., Bordese, S., Arzadún, G., Bechis, F., Caselli, A. T. & Becchio, R. 2021. Cretaceous and Eocene rapid cooling phases in the Southern Andes (36°-37°S): insights from low-temperature thermochronology, U-Pb geochronology and inverse thermal modeling from Domuyo area, Argentina. *Tectonics* 40, 1-30. https://doi.org/10.1029/2020TC006415

Giacosa, R., Allard, J., Foix, N. & Heredia, N. 2014. Stratigraphy, structure and geodynamic evolution of the Paleozoic rocks in the Cordillera del Viento (37° S latitude, Andes of Neuquén, Argentina). *Journal of Iberian Geology* 40, 331-348. https://doi.org/10.5209/rev_JIGE.2014.v40.n2.45301

Gill, J. B. 1981. *Orogenic Andesites and Plate Tectonics, Minerals and Rocks*. Springer Berlin Heidelberg, Berlin. https://doi.org/10.1007/978-3-642-68012-0

Green, P. F. 1981. A new look at statistics in fission-track dating. *Nuclear Tracks* 5, 77-86. https://doi.org/10.1016/0191-278X(81)90029-9

Grégoire, V., de Saint Blanquat, M., Nédélec, A. & Bouchez, J.-L. 1995. Shape anisotropy versus magnetic interactions of magnetite grains: Experiments and application to AMS in granitic rocks. *Geophysical Research Letters*

22(20), 2765-2768. https://doi.org/10.1029/95GL02797

Gulisano, C. A., Gutiérrez Pleimling, A. R. & Digregorio, R. E. 1984. Esquema estratigráfico de la secuencia jurásica del oeste de la provincia del Neuquén. In *9º Congreso Geológico Argentino*, pp. 236-259.

Hammarstrom, J. M. & Zen, E. 1986. Aluminum in hornblende: an empirical igneous geobarometer. *American Mineralogist* 71, 1297–1313.

Harrison T M, McDougall I, 1982. The thermal significance of potassium feldspar K-Ar ages inferred from $^{40}Ar/^{39}Ar$ age spectrum results. *Geochimica et cosmochimica Acta* 46, 1811-1820.

Henry, D. J., Guidotti, C. V. & Thomson, J. A. 2005. The Ti-saturation surface for low-to-medium pressure metapelitic biotites: Implications for geothermometry and Ti-substitution mechanisms. *American Mineralogist* 90(2-3), 316-28.

Hervé, F., Pankhurst, R. J., Fanning, C. M., Calderón, M. & Yaxley, G. M. 2007. The South Patagonian batholith: 150 my of granite magmatism on a plate margin. *Lithos* 97, 373-394. https://doi.org/10.1016/j.lithos.2007.01.007

Hibbard, M. J. 1981. The magma mixing origin of mantled feldspars. *Contributions to Mineralogy and Petrology* 76, 158–170. https://doi.org/10.1007/BF00371956

Hibbard, M. J. 1991. Textural anatomy of twelve magma-mixed granitoid systems. In *Enclaves and Granite Petrology*, pp. 431-444.

Higgins, M. D. 2011. Textural coarsening in igneous rocks. *International Geology Review* 53(3-4), 354-376. https://doi.org/10.1080/00206814.2010.496177

Higgins, M. D. & Roberge, J. 2003. Crystal Size Distribution of Plagioclase and Amphibole from Soufriere Hills Volcano, Montserrat: Evidence for Dynamic Crystallization-Textural Coarsening Cycles. *Journal of Petrology* 44, 1401-1411. https://doi.org/10.1093/petrology/44.8.1401

Holland, T. & Blundy, J. 1994. Non-ideal interactions in calcic amphiboles and their bearing on amphibole-plagioclase thermometry. *Contributions to Mineralogy and Petrology* 116, 433-447. https://doi.org/10.1007/BF00310910

Hollister, L. S., Grissom, G. C., Peters, E. K., Stowell, H. H. & Sisson, V. B. 1987. Confirmation of the empirical correlation of Al in hornblende with pressure of solidification of calc-alkaline plutons. *American Mineralogist* 72, 231-239.

Howell, J. A., Schwarz, E., Spalletti, L. A., Veiga, G. D. 2005. The Neuquén Basin: an overview. In *The Neuquén Basin, Argentina: A Case Study in Sequence Stratigraphy and Basin Dynamics* (eds G. D. Veiga, L. A. Spalletti, J. A. Howell & E. Schwarz), pp. 1-14. Geological Society, Special Publication, 252, London.

Hrouda, F. 1982. Magnetic anisotropy of rocks and its application in geology and

geophysics. *Geophysical Surveys* 5, 37-82. https://doi.org/10.1007/BF01450244

Hurford, A. J. & Green, P. F. 1983. The zeta age calibration of fission-track dating. *Chemical Geology* 41, 285-317. https://doi.org/10.1016/S0009-2541(83)80026-6

Hurford, A. J. & Green, P. F. 1982. A users' guide to fission track dating calibration. *Earth and Planetary Science Letters* 59, 343-354. https://doi.org/10.1016/0012-821X(82)90136-4

Ishihara, S. 1977. The Magnetite-series and Ilmenite-series Granitic Rocks. *Mining Geology* 27, 293-305.

Jelinek, V. 1981. Characterization of the magnetic fabric of rocks. *Tectonophysics* 79, T63-T67. https://doi.org/10.1016/0040-1951(81)90110-4

Jelínek, V. 1978. Statistical processing of anisotropy of magnetic susceptibility measured on groups of specimens. *Studia Geophysica et Geodaetica* 22, 50-62. https://doi.org/10.1007/BF01613632

Johnson, M. C. & Rutherford, M. J. 1989. Experimental calibration of the aluminum-in-hornblende geobarometer with application to Long Valley caldera (California) volcanic rocks. *Geology* 17, 837-841. https://doi.org/10.1130/0091-7613(1989)017<0837:ECOTAI>2.3.CO;2

Jordan, T. E., Burns, W. M., Veiga, R., Pángaro, F., Copeland, P., Kelley, S. & Mpodozis, C. 2001. Extension and basin formation in the southern Andes caused by increased convergence rate: A mid-Cenozoic trigger for the Andes. *Tectonics* 20, 308-324. https://doi.org/10.1029/1999TC001181

Kawakatsu, K. & Yamaguchi, Y. 1987. Successive zoning of amphiboles during progressive oxidation in the Daito-Yokota granitic complex, San-in belt, southwest Japan. *Geochimica et Cosmochimica Acta* 51, 535-540. https://doi.org/10.1016/0016-7037(87)90067-6

Kay, S. M., Burns, W. M., Copeland, P. & Mancilla, O. 2006. Upper Cretaceous to Holocene magmatism and evidence for transient Miocene shallowing of the Andean subduction zone under the northern Neuquén Basin In *Evolution of an Andean Margin: A Tectonic and Magmatic View from the Andes to the Neuquén Basin (35°-39°S Lat)*, pp. 16-90. Geological Society of America. https://doi.org/10.1130/2006.2407(02)

Kiss, B., Harangi, S., Ntaflos, T., Mason, P. R. D. & Pál-Molnár, E. 2014. Amphibole perspective to unravel pre-eruptive processes and conditions in volcanic plumbing systems beneath intermediate arc volcanoes: a case study from Ciomadul volcano (SE Carpathians). *Contributions to Mineralogy and Petrology* 167, 986. https://doi.org/10.1007/s00410-014-0986-6

Leake, B. E., Woolley, A. R., Arps, C. E. S., Birch, W. D., Gilbert, M. C., Grice, J. D., Hawthorne, F. C., Kato, A., Kisch, H. J., Krivovichev, V. G., Linthout, K.,

Laird, J., Mandarino, J., Maresch, W. V., Nickel, E. H., Rock, N. M. S., Schumacher, J. C., Smith, D. C., Stephenson, N. C. N., Ungaretti, L., Whittaker, E. J. W. & Youzhi, G. 1997. Nomenclature of Amphiboles; Report of the Subcommittee on Amphiboles of the International Mineralogical Association Commission on New Minerals and Mineral Names. *Mineralogical Magazine* 61, 295-321. https://doi.org/10.1180/minmag.1997.061.405.13

Leanza, H. A., Llambías, E. J. & Carbone, O. 2005. Unidades estratigráficas limitadas por discordancias en los depocentros de la Cordillera del Viento y la Sierra de Chacaico durante los inicios de la Cuenca Neuquina. In *6º Congreso de Exploración de Hidrocarburos*, p. 13.

Lee, J. K. W., Williams, I. S. & Ellis, D. J. 1997. Pb, U and Th diffusion in natural zircon. *Nature* 390, 159-162. https://doi.org/10.1038/36554

Legarreta, L. & Uliana, M. A. 1991. Jurassic-Cretaceous marine oscillations and geometry of back-arc basin fill, central Argentine Andes. In *Sedimentation, Tectonics and Eustasy*, pp. 429-450. Blackwell Publishing Ltd., Oxford, UK. https://doi.org/10.1002/9781444303896.ch23

Li, X., Chi, G., Zhou, Y., Deng, T. & Zhang, J. 2017. Oxygen fugacity of Yanshanian granites in South China and implications for metallogeny. *Ore Geology Reviews* 88, 690-701.

Li, X., Zhang, C., Behrens, H. & Holtz, F. 2020. Calculating biotite formula from electron microprobe analysis data using a machine learning method based on principal components regression. *Lithos* 356-357, 105371.

Llambías, E. J. & Aragón, E. 2011. Volcanismo Paleógeno. In *Relatorio Del 18° Congreso Geológico Argentino, Neuquén*, pp. 265-274.

Llambías, E. J., Leanza, H. A. & Carbone, O. 2007. Evolución tectono-magmática durante el Pérmico al Jurásico temprano en la Cordillera del Viento (37°05′S - 37°15′S): Nuevas evidencias geológicas y geoquímicas del inicio de la Cuenca Neuquina. *Revista de la Asociación Geologica Argentina* 62, 217-235.

Llambías, E. J. & Malvicini, L. 1978. Geología, Petrología y Metalogénesis del área de Colipilli, provincia del Neuquén, República Argentina. *Revista de la Asociación Geológica Argentina* 33, 257-276.

Llambías, E. J. & Rapela, C. W. 1989. Las volcanitas de Collipilli, Neuquén (37ºS) y su relación con otras unidades paleógenas de la cordillera. *Revista de la Asociación Geológica Argentina* 44, 224-236.

McNulty, B. A., Tobisch, O. T., Cruden, A. R. & Gilder, S. 2000. Multistage emplacement of the Mount Givens pluton, central Sierra Nevada batholith, California. *Geological Society of America Bulletin* 112, 119-135. https://doi.org/10.1130/0016-7606(2000)112<119:MEOTMG>2.0.CO;2

Molina, J. F., Cambeses, A., Moreno, J. A., Morales, I., Montero, P. & Bea, F. 2021. A reassessment of the amphibole-plagioclase NaSi–CaAl exchange thermometer with applications to igneous and high-grade metamorphic rocks. *American Mineralogist* 106, 782-800.

Molina, J. F., Montero, P., Bea, F., Scarrow & J. H. 2012. Anomalous xenocryst dispersion during tonalite-granodiorite crystal mush hybridization in the mid crust: Mineralogical and geochemical evidence from Variscan appinites (Avila Batholith, Central Iberia). *Lithos* 153, 224-242. https://doi.org/10.1016/j.lithos.2012.03.021

Molina, J. F., Moreno, J. A., Castro, A., Rodríguez, C. & Fershtater, G. B. 2015. Calcic amphibole thermobarometry in metamorphic and igneous rocks: New calibrations based on plagioclase/amphibole Al-Si partitioning and amphibole/liquid Mg partitioning. *Lithos* 232, 286-305. https://doi.org/10.1016/j.lithos.2015.06.027

Molina, J. F., Scarrow, J. H., Montero, P. G. & Bea, F. 2009. High-Ti amphibole as a petrogenetic indicator of magma chemistry: evidence for mildly alkalic-hybrid melts during evolution of Variscan basic–ultrabasic magmatism of Central Iberia. *Contributions to Mineralogy and Petrology* 158, 69-98. https://doi.org/10.1007/s00410-008-0371-4

Mollo, S., Putirka, K., Iezzi, G., Del Gaudio, P. & Scarlato, P. 2011. Plagioclase-melt (dis)equilibrium due to cooling dynamics: Implications for thermometry, barometry and hygrometry. *Lithos* 125, 221-235. https://doi.org/10.1016/j.lithos.2011.02.008

Nachit, H., Ibhi, A., Abia, E. H., Ben Ohoud & M. 2005. Discrimination between primary magmatic biotites, reequilibrated biotites and neoformed biotites. *Comptes Rendus Geoscience* 337, 1415–1420. https://doi.org/10.1016/j.crte.2005.09.002

Nédélec, A. & Bouchez, J.-L. 2015. *Granites: Petrology, Structure, Geological Setting, and Metallogeny*. Oxford University Press, Oxford.

Neves, S. P., Araújo, A. M. B., Correia, P. B. & Mariano, G. 2003. Magnetic fabrics in the Cabanas Granite (NE Brazil): interplay between emplacement and regional fabrics in a dextral transpressive regime. *Journal of Structural Geology* 25, 441-453. https://doi.org/10.1016/S0191-8141(02)00003-2

Olivier, P., Druguet, E., Castaño, L. M. & Gleizes, G. 2016. Granitoid emplacement by multiple sheeting during Variscan dextral transpression: The Saint-Laurent – La Jonquera pluton (Eastern Pyrenees). *Journal of Structural Geology* 82, 80-92. https://doi.org/10.1016/j.jsg.2015.1b.d.l.6

Pankhurst, R. J., Weaver, S. D., Hervé, F. & Larrondo, P. 1999. Mesozoic-Cenozoic evolution of the North Patagonian Batholith in Aysen, southern Chile. *Journal of the Geological Society* 156, 673-694. https://doi.org/10.1144/gsjgs.156.4.0673

Paterson, S. R., Fowler, T. K., Schmidt, K. L., Yoshinobu, A. S., Yuan, E. S. & Miller, R. B. 1998. Interpreting magmatic fabric patterns in plutons. *Lithos* 44(1–2), 53-82.

Payacán, I., Gutiérrez, F., Gelman, S. E., Bachmann, O. & Parada, M. A. 2014. Comparing magnetic and magmatic fabrics to constrain the magma flow record in La Gloria pluton, central Chile. *Journal of Structural Geology* 69, 32-46. https://doi.org/10.1016/j.jsg.2014.09.015

Pesce, A. H. 1981. Estratigrafía de las nacientes del río Neuquén y Nahuever, Provincia del Neuquén. In *Actas 8º Congreso Geológico Argentino*, pp. 439-455.

Putirka, K. 2016. Amphibole thermometers and barometers for igneous systems and some implications for eruption mechanisms of felsic magmas at arc volcanoes. *American Mineralogist* 101, 841-858. https://doi.org/10.2138/am-2016-5506

Ramos, V. 1999. Rasgos estructurales del territorio argentino. In *Geología Argentina*. Buenos Aires, pp. 715-784.

Ramos, V. Mosquera, A., Folguera, A. & García Morabito, E. 2011. Evolución tectónica de los Andes y del Engolfamiento Neuquino adyacente. In *Relatorio Del 18° Congreso Geologico Argentino, Neuquén*, pp. 335-348.

Ramos, V. A., Niemeyer, H., Skarmeta, J. & Muñoz, J. 1982. Magmatic evolution of the Austral Patagonian Andes. *Earth Science Reviews* 18, 411-431. https://doi.org/10.1016/0012-8252(82)90047-2

Rapela, C. W. & Llambías, E. J. 1985. La secuencia andesítica terciaria de Andacollo, Neuquén, Argentina. In *4º Congreso Geológico Chileno*, pp. 458-488.

Reiners, P. W., Ehlers, T. A. (Eds.), 2005. Low-temperature thermochronolog: Techniques, Interpretations, and Applications. Reviews in Mineralogy & Geochemistry, vol. 58

Riccardi, A. C. & Stipanicic, P. N. 2002. Fase diastrófica Río Atuel. In *Léxico Estratigráfico de La Argentina. Triásico* (eds P. N. Stipanicic & C. A. Marsicano), p. 245. Asociación Geológica Argentina, Buenos Aires.

Ridolfi, F., Puerini, M., Renzulli, A., Menna, M. & Toulkeridis, T. 2008. The magmatic feeding system of El Reventador volcano (Sub-Andean zone, Ecuador) constrained by texture, mineralogy and thermobarometry of the 2002 erupted products. *Journal of Volcanology and Geothermal Research* 176, 94-106. https://doi.org/10.1016/j.jvolgeores.2008.03.003

Ridolfi, F. & Renzulli, A. 2012. Calcic amphiboles in calc-alkaline and alkaline magmas: thermobarometric and chemometric empirical equations valid up to 1,130°C and 2.2 GPa. *Contributions to Mineralogy and Petrology* 163, 877-895. https://doi.org/10.1007/s00410-011-0704-6

Ridolfi, F., Renzulli, A. & Puerini, M. 2010. Stability and chemical equilibrium of amphibole in calc-alkaline magmas: an overview, new thermobarometric formulations and application to subduction-related volcanoes. *Contributions to Mineralogy and Petrology* 160, 45-66. https://doi.org/10.1007/s00410-009-0465-7

Rochette, P., Aubourg, C. & Perrin, M. 1999. Is this magnetic fabric normal? A review and case studies in volcanic formations. *Tectonophysics* 307, 219-234. https://doi.org/10.1016/S0040-1951(99)00127-4

Rochette, P., Jackson, M. & Aubourg, C. 1992. Rock magnetism and the interpretation of anisotropy of magnetic susceptibility. *Reviews of Geophysics* 30, 209. https://doi.org/10.1029/92RG00733

Rovere, E. I., Caselli, A., Tourn, S., Leanza, H. A., Hugo, C. A., Folguera, A., Escosteguy, L., Geuna, S., González, R., Colombino, J. & Danieli, J. C. 2004. *Hoja Geológica 3772- IV, Andacollo, provincia del Neuquén*, Boletín 26. ed. Instituto de Geología y Recursos Minerales. Servicio Geológico Minero Argentino, Buenos Aires.

Sagripanti, L., Folguera, A., Giménez, M., Rojas Vera, E. A., Fabiano, J. J., Molnar, N., Fennell, L. & Ramos, V. A. 2014. Geometry of Middle to Late Triassic extensional deformation pattern in the Cordillera del Viento (Southern Central Andes): A combined field and geophysical study. *Journal of Iberian Geology* 40, 349-366. https://doi.org/10.5209/rev_JIGE.2014.v40.n2.45305

Sánchez, N. P., Coutand, I., Turienzo, M., Lebinson, F., Araujo, V. & Dimieri, L. 2018. Tectonic Evolution of the Chos Malal Fold-and-Thrust Belt (Neuquén Basin, Argentina) From (U-Th)/He and Fission Track Thermochronometry. *Tectonics* 37, 1907-1929. https://doi.org/10.1029/2018TC004981

Schmidt, M. W. 1992. Amphibole composition in tonalite as a function of pressure: an experimental calibration of the Al-in-hornblende barometer. *Contributions to Mineralogy and Petrology* 110, 304-310. https://doi.org/10.1007/BF00310745

Siégel, C., Bryan, S. E., Allen, C. M. & Gust, D. A. 2018. Use and abuse of zircon-based thermometers: A critical review and a recommended approach to identify antecrystic zircons. *Earth-Science Reviews* 176, 87-116. https://doi.org/10.1016/j.earscirev.2017.08.011

Sigismondi, M. E. 2013. Estudio de la deformacion litosférica de la cuenca Neuquina: Estructura termal, datos de gravedad y sísmica de reflexion. Facultad de Ciencias Exactas y Naturales. Universidad de Buenos Aires. http://digital.bl.fcen.uba.ar/Download/Tesis/Tesis_5361_Sigismondi.pdf

Sigismondi, M., & Ramos, V. A. 2009a. El flujo de calor de la cuenca neuquina, Argentina, segunda parte. Instituto Argentino del Petróleo y Gas, Petrotecnia, 2(9), 58–76.

Sigismondi, M., & Ramos, V. A. 2009b. El flujo de calor de la cuenca Neuquina, Argentina, primera parte (Vol. 1, pp. 64–81). Instituto Argentino del Petroleo y Gas., p. 662.

Somoza, R., Tomlinson, A. J., Zaffarana, C. B., Singer, S. E., Puigdomenech Negre, C. G., Raposo, M. I. B. & Dilles, J. H. 2015. Tectonic rotations and internal structure of Eocene plutons in Chuquicamata, northern Chile. *Tectonophysics* 654, 113-130. https://doi.org/10.1016/j.tecto.2015.05.005

Spagnuolo, M. G., Folguera, A., Litvak, V., Rojas Vera, E. A. & Ramos, V. A. 2012. Late Cretaceous arc rocks in the Andean retroarc region at 36.5°S: Evidence supporting a Late Cretaceous slab shallowing. *Journal of South American Earth Sciences* 38, 44-56. https://doi.org/10.1016/j.jsames.2012.05.002

Stevenson, C. 2009. The relationship between forceful and passive emplacement: The interplay between tectonic strain and magma supply in the Rosses Granitic Complex, NW Ireland. *Journal of Structural Geology* 31, 270-287. https://doi.org/10.1016/j.jsg.2008.11.009

Stipanicic, P. N. 1966. El Jurásico en Vega de la Veranada (Neuquén), el Oxfordense y el diastrofismo Divesiano (Agassiz-Yaila) en Argentina. *Revista de la Asociación Geológica Argentina* 20, 403-478.

Suárez, M. & de la Cruz, R. 1997. Volcanismo pliniano del Lías durante los inicios de la cuenca de Neuquén, Cordillera del Viento, Neuquén, Argentina. In *Actas 7º Congreso Geológico Chileno. Concepción*, Vol. 1, pp. 266-270.

Tischendorf, G., Gottesmann, B., Förster, H.-J. & Trumbull, R. B. 1997. On Li-bearing micas: estimating Li from electron microprobe analyses and an improved diagram for graphical representation. *Mineralogical Magazine* 61, 809-834. https://doi.org/10.1180/minmag.1997.061.409.05

Tobisch, O. T., McNulty, B. A. & Vernon, R. H. 1997. Microgranitoid enclave swarms in granitic plutons, central Sierra Nevada, California. *Lithos* 40, 321-339. https://doi.org/10.1016/S0024-4937(97)00004-2

Turienzo, M., Sánchez, N., Lebinson, F. & Dimieri, L. 2018. The Structure of the Southern Central Andes (Chos Malal Fold and Thrust Belt). In *The Evolution of the Chilean-Argentinean Andes*, pp. 411-441. Springer. https://doi.org/10.1007/978-3-319-67774-3_17

Vergani, G. D., Tankard, A. J., Belotti, H. J. & Welsink, H. J. 1995. Tectonic Evolution and Paleogeography of the Neuquén Basin, Argentina. In *Petroleum Basins of South America: AAPG Memoir 62*, pp. 383-402. https://doi.org/https://doi.org/10.1306/M62593C19

Vernon, R. H. 2010. Granites Really Are Magmatic: Using Microstructural Evidence to Refute Some Obstinate Hypotheses. *Journal of the Virtual Explorer* 35, 1-36. https://doi.org/10.3809/jvirtex.2011.00264

Vernon, R. H. 1990. Crystallization and hybridism in microgranitoid enclave

magmas: Microstructural evidence. *Journal of Geophysical Research* 95, 17849. https://doi.org/10.1029/JB095iB11p17849

Wack, M. R., Gilder, S. A. 2012. The SushiBar: An automated system for paleomagnetic investigations. *Geochemistry, Geophysics, Geosystems* 13, 1-24. https://doi.org/10.1029/2011GC003985

Wagner, M., Altherr, R., Van den haute, P. 1992. Apatite fission-track analysis of Kenyan basement rocks: constraints on the thermotectonic evolution of the Kenya dome. A reconnaissance study. *Tectonophysics* 204, 93-110. https://doi.org/10.1016/0040-1951(92)90272-8

Wones, D. R. & Eugster, H. P. 1965. Stability of Biotite: Experiment, Theory, and Application. *The American Mineralogist* 50, 1228-1272.

Wyllie, P. J., Cox, K. G. & Biggar, G. M. 1962. The Habit of Apatite in Synthetic Systems and Igneous Rocks. *Journal of Petrology* 3, 238-243. https://doi.org/10.1093/petrology/3.2.238

Yavuz, F. 2003. Evaluating micas in petrologic and metallogenic aspect: I–definitions and structure of the computer program MICA+. *Computers & Geosciences* 29, 1203-1213. https://doi.org/10.1016/S0098-3004(03)00142-0

Zaffarana, C. B., Somoza, R., Orts, D. L., Mercader, R., Boltshauser, B., González, V. R. & Puigdomenech, C. 2017. Internal structure of the Late Triassic Central Patagonian batholith at Gastre, southern Argentina: Implications for pluton emplacement and the “Gastre fault system.” *Geosphere* 13, 1973-1992. https://doi.org/10.1130/GES01493.1

Zaffarana, C. B., Somoza, R. & López de Luchi, M. 2014. The Late Triassic Central Patagonian Batholith: Magma hybridization, $^{40}Ar/^{39}Ar$ ages and thermobarometry. *Journal of South American Earth Sciences* 55, 94-122. https://doi.org/10.1016/j.jsames.2014.06.006

Žák, J., Schulmann, K. & Hrouda, F. 2005. Multiple magmatic fabrics in the Sázava pluton (Bohemian Massif, Czech Republic): a result of superposition of wrench-dominated regional transpression on final emplacement. *Journal of Structural Geology* 27, 805-822. https://doi.org/10.1016/j.jsg.2005.01.012

Zamora Valcarce, G. 2007. Estructura y Cinemática de la Faja Plegada y Corrida del Agrio, Cuenca Neuquina. PhD Thesis. Universidad de Buenos Aires. Published thesis.

Zamora Valcarce, G., Zapata, T. & Ramos, V. A. 2011. La Faja Plegada y Corrida del Agrio. In *Relatorio Del XVIII Congreso Geológico Argentino, Neuquén*, pp. 367-374.

Zanettini, J. C. M., Santamaría, G. R. & Leanza, H. 2001. *Hoja Geológica 3772-II, Las Ovejas. Provincia del Neuquén*. Instituto de Geología y Recursos Minerales. Servicio Geológico Minero Argentino, Buenos Aires.

Zappettini, E., Korzeniewski, L. I. & Segal, S. 2014. Nuevos datos de las mineralizaciones polimetálicas del distrito Varvarco, Neuquén. In *19º Congreso Geológico Argentino, Córdoba*. pp. S6-4.

Zappettini, E., Méndez, V. & Zanettini, J. C. 1987. Metasedimentitas mesopaleozoicas en el noroeste de la Provincia del Neuquén. *Revista de la Asociación Geológica Argentina* 42, 206-207.

Zappettini, E. O., Chernicoff, C. J., Santos, J. O. S., Dalponte, M., Belousova, E. & McNaughton, N. 2012. Retrowedge-related Carboniferous units and coeval magmatism in the northwestern Neuquén province, Argentina. *International Journal of Earth Sciences* 101, 2083-2104. https://doi.org/10.1007/s00531-012-0774-3

Zappettini, E. O., Cozzi, G., Dalponte, M., Godeas, M., Korzeniewski, L. I., Peroni, J., Segal, S. & Castro Godoy, S. 2021. *Análisis Geológico y Metalogenético del Sector Norte de la Cordillera del Viento, provincia del Neuquén*. Instituto de Geología y Recursos Minerales, Servicio Geológico Minero Argentino. Serie Contribuciones Técnicas Recursos Minerales Nº44, 51 pp. Buenos Aires.

Zappettini, E. O., Lagorio, S. L., Dalponte, M., Orestes, J. & Belousova, E. 2018. Evidencias de magmatismo precuyano (Pliensbachiano - Toarciano) en el norte de la Cordillera del Viento, provincia del Neuquén: caracterización geoquímica, isotópica e implicancias tectónicas. *Revista de La Asociación Geológica Argentina* 75(4), 533-558.

CAPÍTULO 4
ARTIGO 2

4 ARTIGO 2: JURASSIC AND PALEOGENE ANDEAN MAGMATIC EVOLUTION OF THE SOUTHERN CENTRAL ANDES (36º-42ºS) THROUGH U-Pb/Hf, Sr-Nd AND GEOCHEMICAL DATA

Omar Sebastian ASSIS[1]*, Natalia HAUSER[1], Claudia Beatriz ZAFFARANA[2], Darío ORTS[2], Sebastián PERNICH[2] Gloria GALLASTEGUI[3], Wolf Uwe REIMOLD[1], Cristiano LANA[4].

[1]Instituto de Geociências, Universidade de Brasília, Laboratório de Geocronologia e geoquímica isotópica, Brasília, 70910 900, DF, Brasil.
[2]Universidad Nacional de Río Negro, Sede Alto Valle-Valle Medio, General Roca e Instituto de Investigación en Paleobiología y Geología (IIPG-CONICET).
[3]Instituto Geológico y Minero de España (IGME, CSIC), España.

*Corresponding author; E-mail: seba_assis@outlook.com, sebaoassis@gmail.com

Abstract

With the aim to understand the evolution of magmatism in the Southern Central Andes, this work presents new U-Pb geochronological data and Hf isotopes in zircon, geochemical analysis and Sr-Nd isotopic data from rocks from three key areas: Pre-Cuyo Group of Neuquen Basin in Varvarco area, North Patagonian Batholith in Villa Pehuenia area and Naunauco Paleogene Andesitic Belt in Varvarco-Butalón area. An age of 67 ± 1 Ma and 65 ± 1 Ma was obtained for the Varvarco Tonalite and associated dyke respectively. The age of 67 Ma also obtained for the Butalón Tonalite, demonstrate that it does not correspond to Eocene as previously was suggested. These rocks have initial negative to positive $(\varepsilon_{Nd})i$ between -0.13 to 1.09, positive $(\varepsilon_{Hf})i$ between 1.00 and 7.81 and Mesoproterozoic to Neoproterozoic Nd and Hf model ages. The Jurassic age of 184 ± 3 Ma obtained for Jurassic Host Granite in the region demonstrates that Jurassic magmatism was also present in the Varvarco area. To the south, in the Villa Pehuenia area, an age of 184 ± 2 Ma and initial positive $(\varepsilon_{Nd})i$ value of +0.88 and positive $(\varepsilon_{Hf})i$ between 1.71 and 4.98 and Mesoproterozoic to Neoproterozoic Nd and Hf model ages was obtained for the Moquehue granite. In the same area an age of 71 ± 1 Ma was obtained for the Icalma Granodiorite, and initial positive $(\varepsilon_{Nd})i$ value of +2.93 and positive $(\varepsilon_{Hf})i$ between +6.99 and +9.13, with Neoproterozoic Nd and Hf model ages. To the northeast, in the Naunauco area, the rocks of the Colipilli Formation have a positive initial $(\varepsilon_{Nd})i$ values between +2.10 and +4.05 and the Cayanta Formation a positive initial $(\varepsilon_{Nd})i$ value of +1.89 and Neoproterozoic Nd model age.

REE elements in zircon allow us to identify characteristics of a possible porphyry-type deposit for the Moquehue granite and the Butalon tonalite, although more data are needed to have a greater probability.

The isotopic and geochemical data indicate that the Early Jurassic magmatism is more crustal derived than the Late Cretaceous-Paleogene, attribute a flare-up event to the Jurassic at 140 Ma and a steady-state event to the Cretaceous-Paleogene at 67 Ma.

During the Jurassic, the dominant geodynamic process was slab roll-back, which produced extension and migration of magmatism from the coast of Chile to the east, developing retro arc deposits in the extensional environment. In the

Cretaceous-Paleogene, the subduction of the Farallon-Aluk ridge further north increased the "buoyancy" of the subducted plate with a consequent decrease in the convergence speed and subduction angle. This change in angle causes the magmatic arc to expand and migrate towards the foreland.

Keywords: Andean magmatism, Cretaceous-Paleogene, Geochronology, Sr-Nd isotopes, Lu-Hf isotopes

4.1 Introduction

Continental magmatic arcs are characterized by cyclic and episodic behavior (Ducea, 2001; DeCelles et al., 2009). where a short-lived (~10–20 Ma) steady low-volume magmatism is followed by high intensity flare-ups, or high-flux events with magma production rates 3–4 times greater than during the steady state. This episodic behavior produces changes in the magma production, geochemical and isotopic signature. For example, during the steady low-volume magmatism, composite volcanoes and minor centers and their tonalitic and dioritic plutonic equivalents occur. In contraposition, during the high intensity flare-ups cordilleran batholiths and their volcanic equivalents, caldera fields and ignimbrite plateaux (Lipman et al., 1972; DeCelles et al., 2009; Best et al., 2013) can be produced.

Several techniques can be used to better understand these changes in the production of magmas, like Sm-Nd radiogenic isotopes. During the steady low-volume magmatism event, there is a pull-up in the radiogenic isotopic composition, means that the initial εNd values become more positive. For the contrary, during a high-flux events or flare ups, the radiogenic isotopic composition of continental arc rocks suffers an isotopic pull-downs (DeCelles et al., 2009), means that the initial εNd values become more negative (Ducea, 2001; Ducea and Barton, 2007). There are several examples of Cordilleran batholiths that exhibits this episodic magmatic activity (for example Chapman et al., 2021 Arc migration (Chapman and Ducea, 2019), underplating related to subduction erosion (e.g., Chapman et al., 2013, 2014; Kay et al., 2005), punctuated melt extraction from the lower crust (Ducea et al., 2020b) or a semi-episodic change in plate convergence rates (Hughes and Mahood, 2008; Zellmer, 2008) are some of the proposed processes that explain this episodic behavior in arc systems.

This conceptual model, called the “Cordilleran cycle” links arc flare ups with a series of upper plate processes in Cordilleran orogens, including contractional to extensional deformation of orogenic interiors, propagation of the retroarc thrust belt, foreland basin development, arc root delamination, crustal thickening, surface uplift, forearc subsidence, and accretionary wedge

exhumation (DeCelles et al., 2009, 2015; DeCelles and Graham, 2015; Ducea et al., 2015a).

The Andean Arc, that started in the Early Jurassic, is an excellent example of a continental arc systems that exhibit episodic magmatic behavior. It was related to changes in the tectonic setting of subduction from an extensional/transtensional tectonic setting (Ruiz et al. 1965; Vicente 1975; Coira et al. 1982; Charrier et al. 2007) during the Early Andean stage (210–100 Ma), to a compressive/transpressive tectonic conditions during the Late Cretaceous-Paleogene stage (Arriagada et al., 2006; Charrier et al., 2014; Pichowiak et al., 1990; Scheuber et al., 1994).

Isotopic compositions of magmatic bodies are widely applied to trace their origin as the source rocks leave their isotopic fingerprint on the magmas (e.g. Beard et al., 2005). Granitoids with isotopic signatures intermediate between those of crustal and mantle sources, indicate that mixing of different magmas may have been involved (e.g. Andersson, 1991; Guillot and Le Fort, 1995; Hawkesworth and Vollmer, 1979). In this sense, the Andean Cycle is dominated by mantle additions to magmatism differentiation, through crystallization or melting, of mantle-derived basaltic material (Lucassen et al., 2006; Oliveros et al., 2007; Rossel et al., 2013). Recently, Oliveros et al. (2020) showed that subduction was the most likely process by with the magmatic record in the Pre- to Early Andean convergent margin. The sub-alkaline geochemical affinities, as well as the isotopic signatures typical of a mixture of depleted mantle and variable contribution from the continental crust are better explained through this continuous subduction process (Oliveros et al. 2020).

Here, we contribute to the understanding of an Arc evolution by reporting and interpreting new geochemistry, geochronologic and isotopic data together with a dataset of pre-existing data for an outstanding example of Mesozoic-Cenozoic granitic magmatism from the Andean Magmatic Arc in the Southern Central Andes (36- 42ºS, Fig. 1). In this sense, this study presents new geochemical data of the magmatic rocks focusing on firstly, the Early Jurassic period of the Early Andean stage of the Andean Cycle, which was developed under mainly extensional/transtensional conditions, and which was coeval with the opening of the Neuquén Basin and, secondly, the Paleogene period of the

Andean Cycle, developed under compressive/transpressive tectonic conditions, and during which the volcanic arc expanded into the retroarc region.

Three key areas were selected (Fig. 1 and 2): first, the host granitic rocks in the Varvarco area that correspond to the Early Jurassic period assigned to the Pre-Cuyo Group of the Nequén Basin (Fig. 1), second, the granitic rocks of Villa Pehuenia area that correspond to the North Patagonian Batholith and third, the Naunauco Belt in the areas of Varvarco and Naunauco. The second and third areas correspond only to the Late Cretaceous-Paleogene Andean Cycle. The new whole-rock geochemical and Sr-Nd isotopic data, as well as U-Pb, Hf and REE data on zircon (Table 1) are integrated with compiled bulk-rock geochemistry, geochronological (Ar-Ar, Rb-Sr, K-Ar, U-Pb) and isotopic (Sr-Nd and Lu-Hf) data from the region of Argentina and Chile between the latitudes 36°-42°S (Table 1A-D-Appendix). Our compilation highlights the very few U-Pb ages and scares Hf data on zircon from these belts, which makes this work a valuable contribution to the knowledge of the magmatism on the region in two important periods of time. This study concludes that the Andean magmatism shows a progression towards more mantle derived magmas through time: the younger the more represented is the mantle component of the magmatism, as was also seen by other studies (Oliveros et al. 2020).

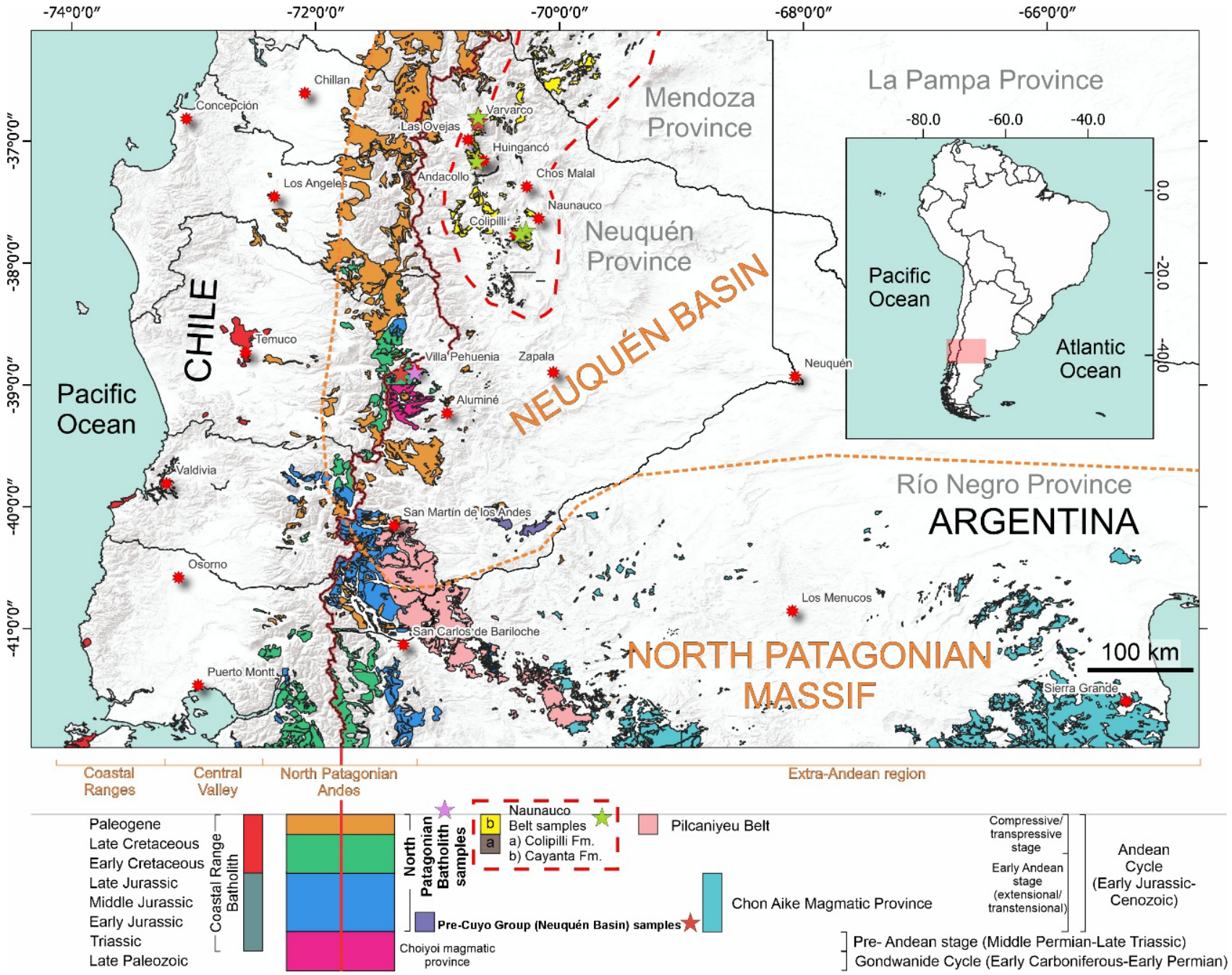

-74°0'0"
-72°0'0"
-70°0'0"
-68°0'0"
-66°0'0"
-37°0'0"
-38°0'0"
-39°0'0"
-40°0'0"
-41°0'0"
Chillan
Concepción
Varvarco
Las Ovejas
Huingancó
Andacollo
Chos Malal
Los Angeles
Naunauco
Colipilli
Mendoza Province
Neuquén Province
NEUQUÉN BASIN
La Pampa Province
-80.0
-60.0
-40.0
0.0
-20.0
-40.0
Pacific Ocean
Atlantic Ocean
CHILE
Temuco
Villa Pehuenia
Zapala
Neuquén
Aluminé
Pacific Ocean
Valdivia
Río Negro Province
ARGENTINA
San Martín de los Andes
Osorno
Los Menucos
San Carlos de Bariloche
NORTH PATAGONIAN MASSIF
100 km
Puerto Montt
Sierra Grande
Coastal Ranges
Central Valley
North Patagonian Andes
Extra-Andean region
Paleogene
Late Cretaceous
Early Cretaceous
Late Jurassic
Middle Jurassic
Early Jurassic
Triassic
Late Paleozoic
Coastal Range Batholith
North Patagonian Batholith samples
b
a
Naunauco Belt samples
a) Colipilli Fm.
b) Cayanta Fm.
Pre-Cuyo Group (Neuquén Basin) samples
Choiyoi magmatic province
Pilcaniyeu Belt
Chon Aike Magmatic Province
Compressive/ transpressive stage
Early Andean stage (extensional/ transtensional)
Andean Cycle (Early Jurassic-Cenozoic)
Pre- Andean stage (Middle Permian-Late Triassic)
Gondwanide Cycle (Early Carboniferous-Early Permian)

Figure 1: Regional map of Argentina and Chile between 36-42° S showing the exposition of Jurassic to Cretaceous-Paleogene magmatic rocks related with the Andean Cycle. The red, green and purple stars represent the Varvarco, Naunauco and Villa Pehuenia areas where samples were collected from this work.

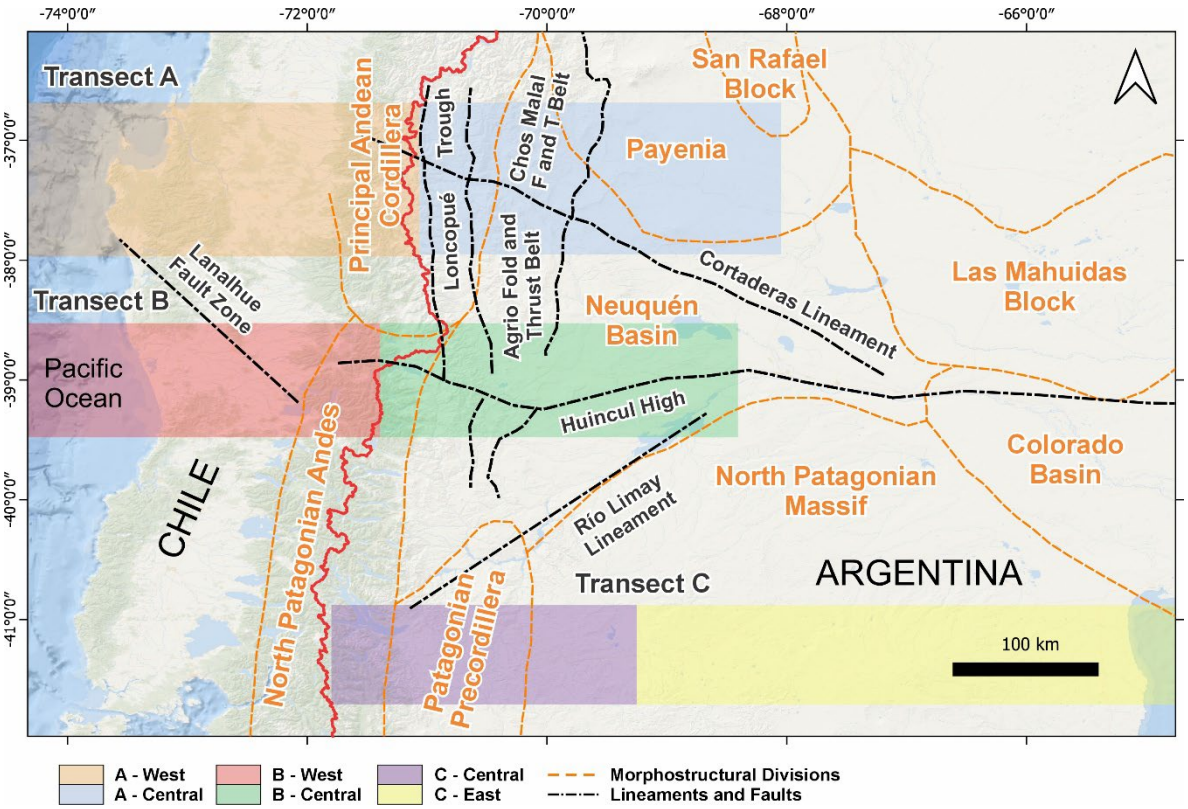


Figure 2: Regional map of Argentina and Chile between 36-42° S showing the principal morfoestructural divisions and lineaments. Transects A, B and C, represents the transects of the Arc for geochemical and isotopic comparison.

4.2 Regional geology of Andes between 36-42ºS

The Andean orogeny, that started in the Early Jurassic, can be divided into several stages with different tectonic styles. In this work, we focalize into two periods: the Early Andean stage, mostly of Jurassic age and developed under extensional/transtensional tectonic conditions, and the Andean stage of Early Cretaceous-Paleogene age, which developed under compressive/transpressive tectonic conditions. Figure 1 is a compilation of the outcrops of western South America showing the main morphostructural units and the main outcrops of igneous rocks related with the Pre-Andean and Andean cycles in the area between 36-42ºS as well as their basement rocks.

4.2.1 Basement of Andean Arc between 36-42°S

The Andean rocks are hosted by a basement related with the evolution of southwestern Gondwana margin. Different stages that differ in their magmatic source and deformational style were recognized. First, the *Early Carboniferous-Early Permian Gondwanide Cycle* was characterized by the production of Cordilleran-type magmas in a compressive tectonic setting (~330–280 Ma, e.g. Bahlburg et al., 2009; Charrier et al., 2007, 2014; Mpodozis and Ramos, 1989; Willner et al., 2008). Relevant amounts of crustal additions to arc magmatism were typical of this magmatic cycle, as well as the mantle source which is also present (e.g. Hervé et al., 2014; Lucassen et al., 1999; Mpodozis and Ramos, 1989). This cycle is also represented in the 36-42º S segment by the Late Paleozoic granitoids (quarz-diorites and tonalite-granodiorites) which crop out in the Pulmarí River area (Fig. 1, Table 1A-Appendix; Urraza et al. 2011 and references therein). The end of the Gondwanide Cycle is marked by the Permo-Triassic Choiyoi Magmatic Province (Sato et al. 2008; Sato et al. 2015; Bastías-Mercado et al. 2020) well exposed in the North Patagonian Andes.

Then, a *Middle Permian to Late Triassic Pre-Andean stage* (~280–210 Ma), was recognized in the Southern Central Andes (Coira et al. 1982; Charrier et al. 2007). It was related to orogenic collapse and possible slab break-off with subsequent continental rifting and extensive crustal melting. West of the Central Valley of Chile, the Coastal Range Batholith shows representative rocks of this stage, like the Late Triassic Constitución and Pichilemu granites (Gana and Hervé, 1983 and Vásquez Illanes, 2008; Table 1A-Appendix). The ca. 100-km wide belt of the North Patagonian Batholith also started during this stage. It is limited to the west by the volcanic and sedimentary modern rocks of the Central Valley of Chile, which separates it from the Paleozoic subduction complex (Hervé et al. 1981a). Eastward from the central axis of the actual Andes, within an intraplate setting and associated with the Gondwana break-up stage, the volcanic and (less represented, but also present) plutonic rocks of the Jurassic Chon Aike Magmatic Province (Kay et al. 1989; Pankhurst and Rapela 1995; Navarrete et al. 2024) are found (Fig. 1).

4.2.2 The Andean cycle

Early Andean stage

The Early Andean stage is represented by the Coastal Range Batholith, the North Patagonian Batholith, the Pre-Cuyo Group of the Neuquén Basin and by the Chon Aike Magmatic Province (Table 1). Compare with the Coastal Range Batholith, the North Patagonian Batholith displays a more varied distribution of ages. For instance, to the north of 38 ºS, the magmatic rocks within this batholith are primarily from the Cretaceous period related with the Andean stage, while between 39 and 42 ºS, Jurassic rocks from the Early Andean stage, are predominantly exposed. The North Patagonian Batholith is formed by several individual plutons that normally receive the geographic name from the areas where they crop out. One of the three key areas correspond to outcrops of the North Patagonian Batholith at Villa Pehuenia area (Fig. 1, Table 1, Supplementary Material II), where the granite Moque was sampled.

Between the Late Triassic and Cenozoic periods, the Neuquén Basin (Fig. 1) developed between 32° and 40° S (e.g. Howell et al. 2005). During Jurassic and Early Cretaceous times, the Palaeo-Pacific Ocean transgressions produced marine strata that alternated with the deposition of continental sequences in the backarc setting of this basin, which was affected by thermal subsidence (Legarreta & Uliana, 1991; Vergani et al. 1995; Howell et al. 2005; Arregui et al. 2011). The opening of the Neuquén Basin took place during the Pre-Andean and the Early Andean stages, and the deposition of the Pre-Cuyo volcanic and sedimentary sequences (Gulisano et al. 1984; Riccardi & Stipanicic, 2002) took place during the Early Andean stage (Fig. 1).

On the eastern flank of the Cordillera del Viento, the Lower to Upper Jurassic syn-rift deposits of the early phase of the Neuquén Basin crop out, characterized by variable thicknesses and normal fault associations (Sagripanti et al. 2014). The Pre-Cuyo Group (Hettangian–Sinemurian) is represented by the Cordillera del Viento and Milla Michicó formations (Gulisano et al. 1984; Riccardi and Stipanicic, 2002). The Jurassic Cuyo and Lotena groups also represent this Early Andean magmatic stage (Suárez and de la Cruz, 1997; Leanza et al. 2005;

Llambías et al. 2007). Assis et al. (2022) discovered that an igneous body, previously assigned to the Radales Aplite of Cretaceous age, has an Early Jurassic age (185 ± 3 Ma). This aplite received an informal designation as Jurassic Host Granite (Assis et al. 2022). In this work we sampled the felsic intrusive rocks which are coeval with the Pre-Cuyo Group in the Varvarco area, microgranite GR4 (Fig. 1, Table 1, Supplementary Material II).

Sample	Lithology	Magmatic Cycles	Unit	Area	Latitude	Longitude	Geochemistry		U-Pb in zircon		Sr-Nd isotopes		Lu-Hf isotopes		REE in zircon	
							Lab	Metod	Age (Lab.)	Metod	Lab	Metod	Lab	Metod	Lab	Metod
D2	Dioritic dike	Andean stage	Naunauco Belt (Dike intruding Varvarco Tonalite)	Varvarco	-36.810	-70.668	AcmeLabs	ICP-MS	65 ± 1 Ma (LEGGA)	LA-ICP-MS	LEGGA	ID-TIMS	UFOP	LA-ICP-MS	LEGGA	LA-ICP-MS
VAR1	Tonalite		Naunauco Belt (Varvarco Tonalite)	Varvarco	-36.810	-70.671	AcmeLabs	ICP-MS								
VAR2	Tonalite			Varvarco	-36.810	-70.669	AcmeLabs	ICP-MS								
VAR3	Tonalite			Varvarco	-36.807	-70.668	SGIker Bilbao	ICP-MS	SGIker Bilbao	SHRIMP	SGIker Bilbao	ID-TIMS				
VAR4A	Tonalite			Varvarco	-36.804	-70.665	AcmeLabs	ICP-MS								
VAR5	Tonalite			Varvarco	-36.816	-70.672	AcmeLabs	ICP-MS								
VAR6	Tonalite			Varvarco	-36.820	-70.674			67 ± 1 Ma (LEGGA)	LA-ICP-MS	LEGGA	ID-TIMS	UFOP	LA-ICP-MS	LEGGA	LA-ICP-MS
GV	Tonalite			Varvarco	-36.807	-70.667	AcmeLabs	ICP-MS								
NAU4	Andesite		Naunauco Belt (Colipilli Formation)	Colipilli	-37.768	-70.324	SGS Geosol	ICP-MS	LEGGA	LA-ICP-MS	LEGGA	ID-TIMS				
NAU3-B	Andesite			Colipilli	-37.741	-70.275	SGS Geosol	ICP-MS	LEGGA	LA-ICP-MS	LEGGA	ID-TIMS				
CY1	Andesite		Naunauco Belt (Cayanta Formation)	Andacollo	-37.173	-70.680	SGS Geosol	ICP-MS	LEGGA	LA-ICP-MS	LEGGA	ID-TIMS				
BU4	Tonalite		Naunauco Belt (Butalon Tonalite)	Varvarco	-36.984	-70.690			67 ± 1 Ma (LEGGA)	LA-ICP-MS	LEGGA	ID-TIMS	UFOP	LA-ICP-MS	LEGGA	LA-ICP-MS
ICAL4	Granodiorite		North Patagonian Batholith (Moquehue Granite)	Villa Pehuenia	-38.904	-71.187	SGS Geosol	ICP-MS	71 ± 1 Ma (LEGGA)	LA-ICP-MS	LEGGA	ID-TIMS	UFOP	LA-ICP-MS	LEGGA	LA-ICP-MS
Moque	Granite	Early Andean stage		Villa Pehuenia	-38.917	-71.302	SGS Geosol	ICP-MS	184 ± 2 Ma (LEGGA)	LA-ICP-MS	LEGGA	ID-TIMS	UFOP	LA-ICP-MS	LEGGA	LA-ICP-MS
GR1	Microgranite		Pre-Cuyo Group (Jurassic Host Granite)	Varvarco	-36.810	-70.668	AcmeLabs	ICP-MS								
GR2	Microgranite			Varvarco	-36.845	-70.671	AcmeLabs	ICP-MS								
GR4	Microgranite			Varvarco	-36.846	-70.663	AcmeLabs	ICP-MS	184 ± 3 Ma (LEGGA)	LA-ICP-MS	LEGGA	ID-TIMS	UFOP	LA-ICP-MS	LEGGA	LA-ICP-MS

Table 1: Summary of the 18 samples collected and studied with different techniques.

The Andean stage

The Andean stage of Early Cretaceous-Paleogene age, developed under compressive/transpressive tectonic conditions. Representants of this stage are the Coastal Range Batholith in Chile, the North Patagonian Batholith and the Naunauco and Pilcaniyeu belts in Argentina. During this stage, the Coastal Range Batholith continues to be developed. Nevertheless, this batholith developed throughout the Mesozoic and the Cenozoic (Fig. 1), it shows a predominance of Cretaceous rocks. In the Villa Pehuenia area and from the North Patagonian Batholith, a granodiorite ICAL4 was sampled as representant of the Andean stage.

In Late Cretaceous-Paleogene period, as consequence of compressive-transpressive tectonic conditions, the magmatism was expanded to the east in the retroarc area with the development of the of the Naunauco Belt magmatism (Llambías & Malvicini, 1978; Zamora Valcarce et al. 2011). The Naunauco Belt comprises two distinct formations: the intrusive rocks known as the Colipilli Formation (Franchini et al. 2003; Kay et al. 2006; Casé et al. 2008) and the volcanic rocks known as the Cayanta Formation (Rapela and Llambías, 1985). Both units were sampled in the areas of Varvarco and Colipilli-Naunauco (Fig. 1, Table 1, Table 1-Appendix). From this belt, we sampled the Butalón Tonalite (BU4) and the Varvarco tonalite plus a dioritic dike (D2) intruded into the Varvarco Tonalite. The source of the Naunauco Belt is also compared with the geochemical data of the Los Ángeles Unit (67 Ma), a suite of basaltic to andesitic lava flows interbedded with volcanic breccias and lithic sandstones (Iannelli et al. 2018; Supplementary Material II-A). They are located slightly north of the area of study in the Mendoza Province (Argentina).

Lastly, the Paleogene rocks of the Pilcaniyeu Belt (57.8 – 42 Ma; Rapela et al., 1988; Aragón et al. 2015) were extruded partially coevally with (and slightly after) the magmatism of the Naunauco Belt (Fig. 1). The Pilcaniyeu Belt bears an intraplate geochemical signature and its origin is linked to the steepening of the formerly flat-slab which took place during the Cretaceous (Echaurren et al., 2016), or as the result of the formation of an asthenospheric window due to the collision of the Farallon-Aluk ridge against the South American margin (Aragón

et al., 2011; 2013; Iannelli et al., 2020; Fernández Paz et al., 2018). The Pilcaniyeu Belt consists of a NW-SE belt of volcanic rocks that are apparently controlled by pre-Cretaceous crustal lineaments (Cingolani et al. 1991). Non samples were obtained from this Belt, but we compared our data with previously published data.

4.3 Analytical methods

Three campaigns were carried out within the studied area in Varvarco, Naunauco, and Villa Pehuenia (36°-42°S, Fig. 1). Whole-rock geochemical and Sr-Nd characterization, U-Pb, Lu-Hf and REE in zircon were performed. Table 1 summarizes the collected samples, and the studies performed in each of them.

4.3.1 Geochemical analyses

Whole-rock geochemical analyzes were done using ICP-ES/MS at the Geochronology and Geochemistry-SGIker facility of the Universidad del País Vasco/EHU, Laboratorio Bureau Veritas (Acmelabs) in Mendoza, Argentina and at the SGS Geosol laboratory, in Goiás, Brazil. Following procedures adapted from those described in detail in García de Madinabeitia et al. (2008). Reagents were concentrated HF and HNO_3 Merck Pro-Analysi further distilled in the laboratory by surface distillation using Savillex PFA and Acidest quartz distillers. Deionized water was obtained using a Millipore Elix device and polished to obtain a resistivity ≥ 18 M Ohm cm with a Barnstead EasyPure system. In and Bi solutions, used as internal standard, and multielemental solutions for the initial tuning and calibration of the spectrometer were prepared from 1000 ppm Merck multi-element standard solutions for ICP, stabilized in HNO_3 2 to 6 %.

Internal standard was added by means of an automatic online addition kit in order to prevent random errors. Weighing to 0.1 mg precision was done with an electronic balance GRAM SV 205-A. Calcination was performed in two steps, one our each at ~500 and 1050 °C in muffle furnace to remove H_2O and compounds of C and S. The alkaline fusion of the samples is carried out using an automatic Claisse Fluxy 30 system over butane gas in Pt-Au (95-5) crucibles with lithium metaborate ($LiBO_2$) as fluxer and LiBr as non-wetting agent. The melt is automatically poured onto a polystyrene beaker containing 100 ml of HNO_3 and

~ 0.05 ml of HF placed in a magnetic agitator. The solution is gravimetrically diluted to a factor adequate for the analysis. Trace element concentrations were determined using a Thermo XSeries 2 ICP-MS equipped with collision cell, an interphase specific for elevated total dissolved solids (Xt cones), shielded torch and a gas dilution system. A concentric nebulizer and quartz expansion chamber were employed. Uncertainty of the results corresponds to a 95 % confidence level.

4.3.2 Bulk rock Sr-Nd isotopes

Sr and Sm-Nd isotope dilution thermal ionization mass spectrometry (ID-TIMS) analyses were performed in part of the Geochronology and Geochemistry-SGIker facility of the Universidad del País Vasco/EHU using a Finnigan MAT262 mass spectrometer and at Laboratório de Estudos Geodinâmicos, Geocronológicos e Ambientais (LEGGA), Instituto de Geociências, Universidade de Brasília (UnB), Brazil.

SGIker facility procedure: Chemical procedures for Sr extraction are described by Pin and Bassin (1992), and for Sm and Nd by Pin and Santos Zalduegui (1997). A $^{150}Nd/^{149}Sm$ mixed isotope tracer was used. Blanks for Sm and Nd are negligible. Sr, Nd and Sm were loaded over Ta filaments and measured by Faraday in multicollection with corrections for mass fractionation by normalization to $^{86}Sr/^{88}Sr$ = 0.1194 and $^{146}Nd/^{144}Nd$ = 0.7219. Analytical uncertainty was estimated to be ± 0.2% on the $^{147}Sm/^{144}Nd$ ratio, the incertitude for individual measurements under the same conditions of $^{143}Nd/^{144}Nd$ and the $^{143}Nd/^{144}Nd$ and $^{87}Sr/^{86}Sr$ ratios for Jndi-1 and NBS-987 standards over different periods of analyses are given in the Tables.

LEGGA procedure: The separation procedures and analytical method applied at UnB were reported by Gioia and Pimentel (2000). The samples were washed and weathered parts were removed, then were crushed and pulverized to a very fine size powder. Approximately 50 mg of rock powder were mixed with $^{149}Sm/^{150}Nd$ rapid solution and dissolved in Savillex capsules. All whole rock samples used for Sm-Nd extraction were subjected to conventional cation exchange techniques based on Teflon® columns containing LN-Spec resin (HDEHP - Di-(2-ethylhexyl) phosphoric acid supported by polytetrafluoroethylene

powder). Samples were analyzed using a Thermo Scientific TRITON™ Plus Thermal Ionization Mass Spectrometer (TIMS) operating in the static multi-collector mode. Mass fractionation was corrected by normalizing the $^{143}Nd/^{144}Nd$ ratio to $^{146}Nd/^{144}Nd=0.7219$. The radioactive decay constant used for Sm-Nd was $6.54x10^{-12}$ a^{-1} (Lugmair and Marti, 1978). The average $^{143}Nd/^{144}Nd$ obtained for the USGS BHVO-2 standard was 0.512970 ± 0.00002 (2s) during the course of this study, which is consistent with the most recently published values (e.g., 0.512986 ± 0.000009, Weis et al., 2005 or 0.51295 ± 0.000005, Raczek et al., 2003 by ID-TIMS). Laboratory blanks were ~0.25 ng for Nd and ~0.04 ng for Sm. The precision in Sm/Nd and $^{143}Nd/^{144}Nd$ ratios were better than ± 0.1% (2s) and ± 0.001% (2s), respectively, based on repeated analysis of the international BHVO-2 and BCR-1 rock standards.

4.3.3 Zircon U-Pb dating

The samples were analysed at the Laboratório de Estudos Geodinâmicos, Geocronológicos e Ambientais (LEGGA), Instituto de Geociências, Universidade de Brasília (UnB), Brazil, using a LA-ICP-MS equipment. Approximately 5 kg of sample were crushed, followed by grinding in a vibratory cup mill, and sieving to different grain sizes (120 to 63 μm). Then, lighter and heavier minerals were separated by their densities with water. The concentrate of heavy minerals was subjected to magnetic separation with a Frantz isodynamic separator. No chemical treatment was applied. Over 50 zircon grains were separated from the samples. After separation, the grains were cast into an epoxy mount, polished to approximately half thickness, and the polished surfaces were characterized by back-scattered electron (BSE) imaging using a FEI QUANTA 450 scanning electron microscope (SEM) at the same Laboratory. BSE imaging was performed using a SEM Quanta 450, 10 nA, 20 kV, 13.8 mm working distance. The laser ablation was performed by an ESI/New Wave Research, UP-213, Nd: YAG under the following conditions: 25 μm spot size, 10 Hz, 3.0 - 3.5 J cm^{-2}, ablation time of 40 s and pit depth of ~10 μm. The ICP-MS instrument is a Thermo-Fischer, Neptune, MC-ICP-MS with a detection system of mixed Faraday cups and multiple ion counting (MIC) array. The ^{238}U mass is measured in the Faraday cup and ^{202}Hg, ^{204}Pb, ^{206}Pb and ^{207}Pb masses in the MICs collectors. The calibration

consists in GJ1 (Jackson et al. 2004, Horstwood et al. 2016) used as primary reference material and 91500 (Wiedenbeck et al. 1995) used as secondary/validation. The procedure for mass discrimination is standard-sample bracketing with $^{207}Pb/^{206}Pb$ and $^{206}Pb/^{238}U$ ratios normalized to reference material GJ1. Data processing package used is Iolite v.4.0 (Paton et al., 2011) and VizualAge (Petrus and Kamber, 2012) using exponential plus linear modelling for LIEF correction. Ages are quoted at 2s absolute, and propagation is by quadratic addition. Excess variance and age uncertainty of reference material are propagated where appropriate. Systematic uncertainty for propagation is ca. 1% (2s) of the final age. No common lead correction was applied. The software Isoplot v4.15 (Ludwig 2012) was utilized for the presentation of the results, using the Tera-Wasserburg Concordia diagrams (Tera and Wasserburg, 1972) and the TuffZirc algorithm function (Ludwig and Mundil, 2002) to distinguish complex populations of zircon ages.

4.3.4 Lu-Hf isotopes on zircon

The analyzes were performed in the Applied Isotope Research Group (AIR-G) laboratory of the Federal University of Ouro Preto (UFOP), Brazil, using a Neptune MC-ICP-MS coupled to a 193 Photonmachines laser ablation system. The procedure used is detailed in Matteini et al. (2010). The laser conditions were a 40 μm spot size, 8 hz, 0.3 He gas, and the ICP-MS conditions were 1.01 Ar gas and 0.02 N gas. Five reference materials were used for the bracketing correction: BB (560 Ma): $^{176}Hf/^{177}Hf = 0.281674 \pm 0.0000028$ (Santos et al. 2017), Mudtank (732 Ma): $^{176}Hf/^{177}Hf = 0.282507 \pm 0.000006$ (Woodhead and Hergt 2005), GJ1 (602 Ma): $^{176}Hf/^{177}Hf = 0.2820000 \pm 0.0000005$ (Morel et al. 2008), Plešovice (337 Ma): $^{176}Hf/^{177}Hf = 0.282482 \pm 0.000013$ (Slama et al. 2008) and Temora (417 Ma): $^{176}Hf/^{177}Hf = 0.282686 \pm 0.000007$ (Woodhead et al. 2004). The $\varepsilon Hf_{(t)}$ values were calculated using the constant of $^{176}Lu = 1.867x10^{-11}$ (Söderlund et al. 2004) and values for the CHUR of $^{176}Hf/^{177}Hf = 0.282785$ and $^{176}Lu/^{177}Hf = 0.0336$ (Bouvier at al. 2008). The recalculation of the initial $^{176}Hf/^{177}Hf_{(t)}$ ratio was done from the measured initial $^{176}Hf/^{177}Hf$ ratio and the $^{206}Pb/^{238}U$ age of each zircon. The two-stage T_{DM} model age was calculated using the values of the ratios $^{176}Hf/^{177}Hf = 0.283250$ and $^{176}Lu/^{177}Hf = 0.0384$ for the DM (Chauvel and Blichert-

Toft 2001) and the value of $^{176}Lu/^{177}Hf$ = 0.015 for an average crust (Griffin et al. 2002).

4.3.5 REE in zircon

Trace element compositions of zircon were obtained at the Laboratório de Estudos Geodinâmicos, Geocronológicos e Ambientais (LEGGA), Instituto de Geociências, Universidade de Brasília (UnB), Brazil, using a Thermo Finningan Element XR high-resolution single-collector sector field ICP-MS coupled to a 193 nm Iridia laser ablation system. The following masses were analyzed: ^{29}Si, ^{43}Ca, ^{45}Sc, ^{49}Ti, ^{51}V, ^{88}Sr, ^{89}Y, ^{93}Nb, ^{139}La, ^{140}Ce, ^{141}Pr, ^{143}Nd, ^{147}Sm, ^{151}Eu, ^{157}Gd, ^{159}Tb, ^{163}Dy, ^{165}Ho, ^{166}Er, ^{169}Tm, ^{172}Yb, ^{175}Lu, ^{177}Hf, ^{208}Pb, ^{232}Th, ^{238}U. The laser parameters included an ablation spot size of 40 μm, a laser fluence of 4.0 J/cm² and a laser repetition rate of 20 Hz. Each spot analysis consisted of 10s of background measurement and 30 s of sample ablation. The primary reference material was the NIST-612 glass (Jochum et al. 2016) and the references materials used for quality control were the NIST-610 glass (Jochum et al. 2016), Diamantina monazite (Gonçalves et al. 2018) and Durango apatite (Chew et al., 2011). Raw data were processed off-line on Iolite 4.0 (Paton et al. 2011) as time-resolved signals. The internal reference value used for calibration was the stoichiometric Si value for zircon (14.76 wt%), Ca for apatite (40 wt.%) and EPMA Ce data for monazite (28 wt.%). The precision of multiple analyses of quality control reference material is better than 5% for most elements and agrees within uncertainty with published data from Gonçalves et al. (2018), Chew et al. (2011) and Jochum et al. (2016).

The REE data in zircon were filtered by removing the values that are below the limit of detection (LOD) and using only those that have an error less than 100%SE. To recalculate REE values that do not meet the 100%SE error, the *imputREEapp* application (Carrasco-Godoy and Campbell 2023) was used with the Chondrite-Onuma method. To evaluate mantle-equilibrated zircon, the Ni et al. (2020) filter based on P, Ti, Y, Nb, REE, Hf, Th and U (in this case the calculations with P were not considered, as it was not analyzed) was applied, with a maximum score of 14 points. The best zircons with scores greater than or equal to 10 points were chosen (Supplementary Material IV). To calculate the

temperature, Ti-in-zircon thermometry were used based on the concentration of Ti in zircon, activity of quartz (aSiO$_2$) = 0.9 and rutile (aTiO$_2$) = 0.7 and the pressure: T1 (Watson et al. 2006), T2 (Ferry and Watson 2007), T3 (Loucks et al. 2020) and T4 (Crisp et al. 2023). fO$_2$ and ∆FMQ were calculated from the oxybarometer of Loucks et al. (2020) using the concentrations of Ce, U and Ti in zircon. The depths to the Moho Z4 were calculated with the equation of Tang et al. (2020), using the Eu/Eu* = ($Eu/\sqrt{Sm_n x Gd_n}$) anomaly in zircon. All data were normalized to the McDonough and Sun (1995) chondrite.

4.4 Field and petrographic descriptions

4.4.1 Early Andean Cycle: extensional/transtensional stage

The Jurassic Host Granite - Varvarco area

The plutonic rocks equivalent to the Pre-Cuyo Group of the Neuquén Basin are represented by the Jurassic Host Granite, well described in Assis et al. (2022). This unit hosts the Late Cretaceous Varvarco Tonalite described in Assis et al. (2022). In this work, these felsic intrusive rocks sampled for analyses are the GR1, GR2 and GR4 microgranites (Table 1, Supplementary Material II). The petrographic description is detailed in this work.

Moquehue Granodiorite (NPB) - Villa Pehuenia area

The Early Jurassic granites of the North Patagonian Batholith are represented by the Moquehue Granodiorite (Fig. 3a, b) in the area near Villa Pehuenia (Fig. 1). These rocks, previously described by Cingolani et al. (1991), have a Rb/Sr isochron age of 209 ± 13 Ma for a biotitic granite from the area around Lago Moquehue. However, an Early Jurassic age obtained from MOQUE sample collected in this study provides a more precise dating for the unit. The Moquehue Granite is an equigranular to inequigranular-porphyritic medium grained biotite-amphibole granodiorite. Mafic microgranular enclaves (MME) composed of amphibole are common. (Fig. 3a). In thin section, the texture of the Moquehue Granodiorite is characterized by subhedral to euhedral plagioclase

penocrysts immersed in a groundmass of plagioclase, quartz and minor orthoclase. Amphibole and biotite are partially chloritized and are concentrated in clots, together with titanomagnetite (Fig. 3b).

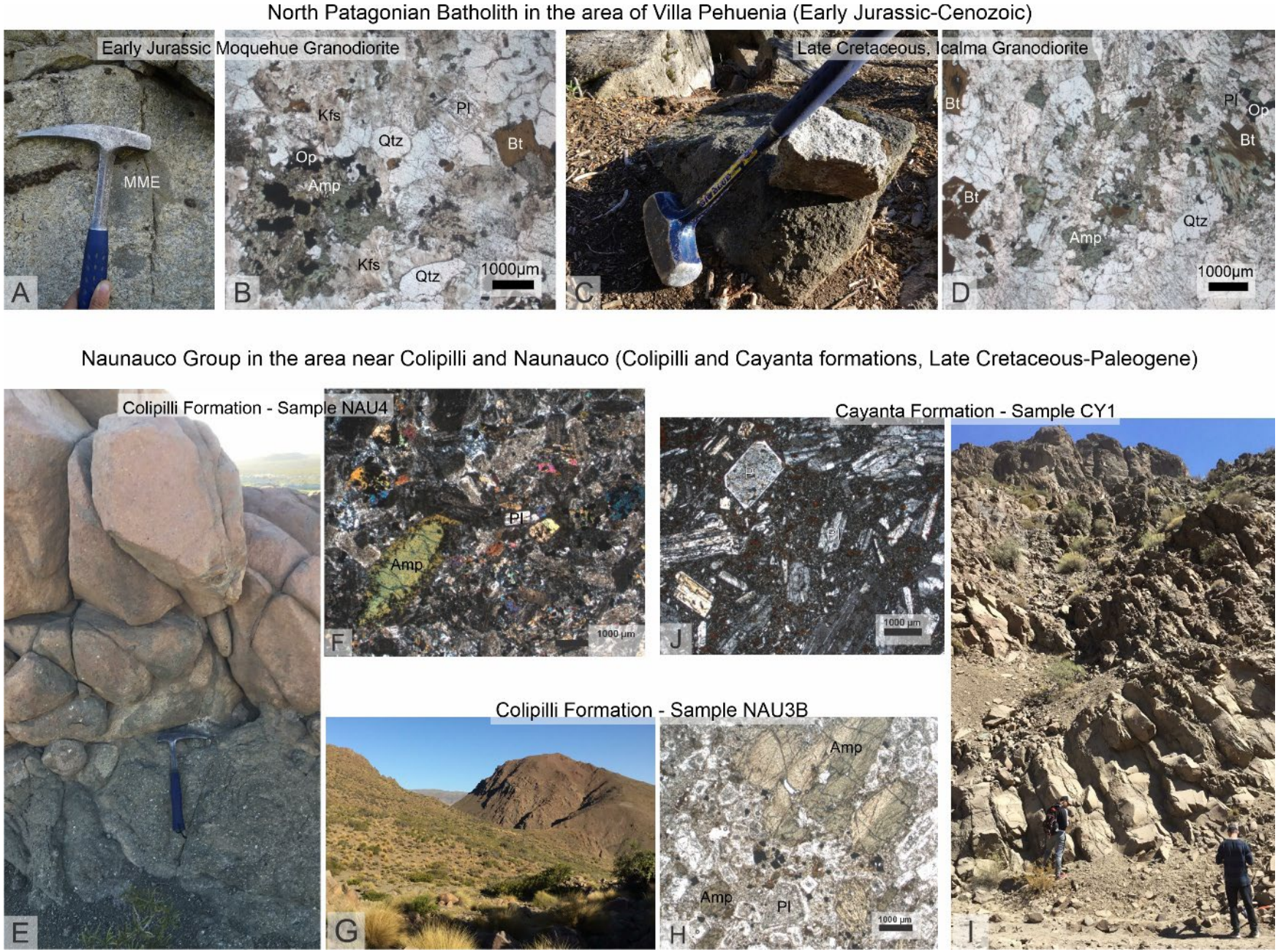

North Patagonian Batholith in the area of Villa Pehuenia (Early Jurassic-Cenozoic)
Early Jurassic Moquehue Granodiorite
MME
A
Kfs
Pl
Qtz
Bt
Op
Amp
Kfs
Qtz
1000µm
B
Late Cretaceous, Icalma Granodiorite
C
Bt
Pl
Op
Bt
Bt
Qtz
Amp
1000µm
D
Naunauco Group in the area near Colipilli and Naunauco (Colipilli and Cayanta formations, Late Cretaceous-Paleogene)
Colipilli Formation - Sample NAU4
E
Pl
Amp
1000 µm
F
Cayanta Formation - Sample CY1
P
P
1000 µm
J
Colipilli Formation - Sample NAU3B
G
Amp
Amp
Pl
1000 µm
H
I

Figure 3: Outcrops and petrography of some of the samples studied and which complement and expand the study of Assis et al. (2022) from Varvarco area. The North Patagonian Batholith was studied in the locality of Villa Pehuenia and represented by the Early Jurassic sample MOQUE of the Moquehue Granodiorite and by sample ICAL4 from the Late Cretaceous Icalma Granodiorite. The Late Cretaceous-Paleocene Naunauco Belt was sampled in the area near Colipilli and it is represented by samples NAU4 and NAU3B from the Colipilli Formation and by sample CY1 from the Cayanta Formation. A) Medium-grained equigranular Moquehue Granodiorite (sample MOQUE) with rounded mafic microgranular enclaves (MME); B) Microphotograph under plane polarized light of sample MOQUE showing the equigranular to inequigranular-seriate hypidiomorphic texture with euhedral plagioclase, subhedral biotite, green amphibole, anhedral quartz and altered orthoclase. Opaque minerals and amphibole are concentrated in clots; C) Sample ICAL4 showing the gray-coloured rocks with medium grained texture; D) Microphotograph under plane polarized light of sample ICAL4 showing the hypidiomorphic texture with amphibole and biotite partially chloritized and subhedral/euhedral plagioclase and anhedral quartz and K-feldspar; E) Andesitic stock represented by sample NAU4; F) Cross polar microphotograph of sample NAU4 showing the inequigranular seriate texture with plagioclase and resorbed amphibole phenocrysts; G) Outcrop of the stock of porphyritic andesites represented by sample NAU3B; H) Porphyritic andesite with amphibole and plagioclase phenocrysts. The phenocryst of plagioclase exhibits sieve textures and zonation; I) Andesitic lavas represented by sample CY1 and J) Crossed-polars view of sample CY1 with plagioclase phenocrysts immersed in a hyalopilitic groundmass with plagioclase and pyroxene microliths. Mineral abbreviations: Amp: amphibole, Pl: plagioclase, Op: opaque minerals, Qtz: quartz, Kfs: K-feldspar (orthoclase).

4.4.2 Andean Cycle: Late Cretaceous-Paleogene compressive/transpressive stage

Icalma Granodiorite (NPB) - Villa Pehuenia area

The Icalma Granodiorite (Zanettini et al. 2010) is part of the Late Cretaceous outcrops of the North Patagonian Batholith around the locality of Villa Pehuenia (Fig. 1). It is composed of tonalites and granodiorites with some subordinate monzogranites (Zanettini et al. 2010). Whole rock K/Ar ages of 110 ± 4 and 87 ± 7 Ma were obtained by Latorre et al. (2001) and a whole rock K/Ar age of 70 ± 10 Ma was reported by Cucchi and Leanza (2006) for this unit. Additionally, Gregori et al. (2011) describe ^{40}Ar-^{39}Ar amphibole cooling ages of 70.8 ± 1.5, 72.2, and 70.6 ± 1 for the Icalma Granodiorite. From this granodiorite, the sample ICAL4, a medium-grained hypidiomorphic granodiorite, was collected

(Fig. 3c, d). It is composed of euhedral to subhedral zoned plagioclase (70%), partially altered to sericite (Fig. 3d), anhedral quartz (20%) and a 10% of biotite plus amphibole (both altered to chlorite) and opaque minerals (Fig. 3d).

Varvarco and Butalón tonalites - Naunauco Belt

The Varvarco and Butalón tonalites and their associated dikes represent the Late Cretaceous-Paleogene rocks of the Naunauco Belt. Assis et al. (2022) characterized the Varvarco Tonalite as medium- to fine-grained tonalites, ranging from equigranular to inequigranular-porphyritic, with clots of amphibole. Additionally, the tonalite hosts microgranular enclaves of dioritic composition, exhibiting a fine-grained, equigranular texture and composed of plagioclase (50%), quartz (30%), amphibole (10%), biotite (5%), orthoclase (4%) and minor amounts of titanomagnetite, titanite, apatite, and zircon (less than 1%) (Assis et al. 2022). This unit is represented here by samples VAR1, VAR2, VAR3, VAR4A, VAR 5, VAR 6 and GV (Table 1, Supplementary Material II).

The dikes that intrude the Varvarco Tonalite have plagioclase phenocrysts and amphibole within a fine-grained groundmass of plagioclase, amphibole, biotite, quartz, and opaque minerals. Some amphiboles are poikilitic and contains inclusions of plagioclase and rounded quartz (Quartz "ocelli") with occasional reaction rims of amphibole and opaque minerals (Assis et al. 2022). These dikes are represented by sample D2 (Table 1, Supplementary Material II).

The Butalón Tonalite, situated approximately 15 km south of the Varvarco locality, is a fine-grained tonalitic stock composed of plagioclase (63%), quartz (23%), amphibole plus biotite (12%), orthoclase (2%), and minor euhedral opaque minerals and acicular apatite (Assis et al. 2022). This unit is represented by sample BU4 (Table 1, Supplementary Material II).

The Colipilli Formation

The outcrops of the Colipilli Formation are dikes, domes and sills located near Colipilli (Fig. 1, Table 1). The andesitic stock represented by sample NAU4 is composed of hornblende and plagioclase phenocrysts immersed in a

hyalopilitic groundmass composed by plagioclase microliths (Fig. 3 e-f). The andesitic stock represented by sample NAU3-B has porphyritic texture with resorbed amphibole and plagioclase phenocrysts immersed in a groundmass of seriated texture of plagioclase microliths, carbonate patches and brown glass (Fig. 3g-h).

The Cayanta Formation

The studied outcrops of the Cayanta Formation are situated northwest of Andacollo (Sample CY1, Table 1). These outcrops predominantly comprise andesitic and basaltic lava flows and tuffs characterized by a porphyritic texture, where subhedral, tabular, normally zoned plagioclase phenocrysts are immersed in a groundmass of hyalopilitic texture composed of plagioclase and pyroxene microliths (Fig. 3 i-j).

4.5 Whole rock major- and trace-element geochemistry

4.5.1 Early Andean Cycle during the extensional/transtensional stage

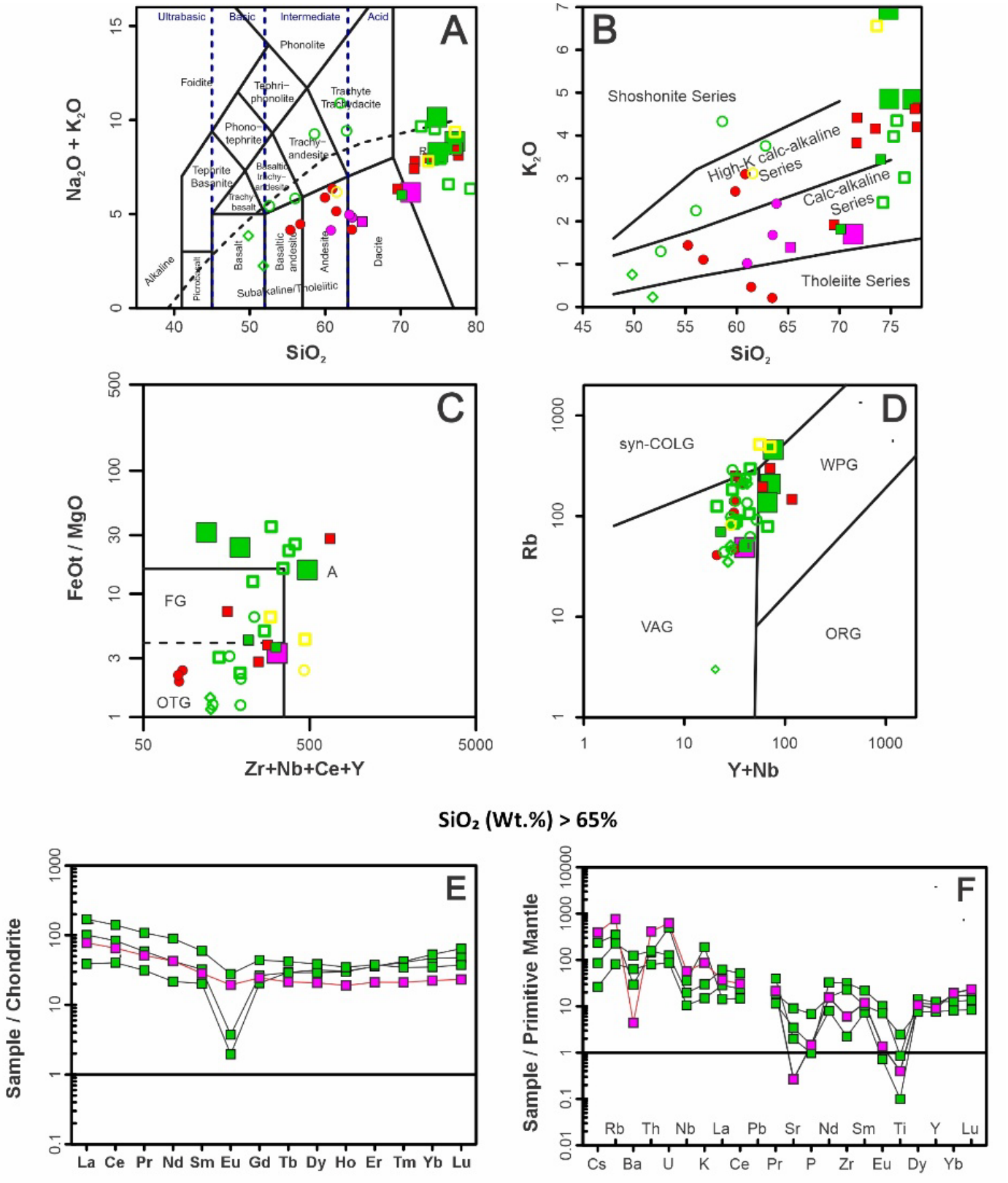
The Jurassic Host Granite, GR1, GR2 and GR4 samples, as part of the plutonic rocks related with the development of the Neuquén Basin (Table 2). They are alkaline to subalkaline granites (Fig. 4a) belonging to the high-K calc-alkaline to shoshonitic series (Fig. 4b). They are plotted in the A-type granite field (Whalen et al., 1987) and in the transition between within plate and syn-collisional fields (Pearce et al., 1984, Fig. 4c, d). They show moderate to strong negative Eu anomalies indicating a plagioclase-rich reduced source. They show moderate enrichment in light REE and flat heavy REE patterns (Fig. 4e). In the spider diagram, the negative anomalies in Nb and Ta and the Pb spike are typical of subduction settings, as well as of crustal derived magmas. The Ba and Sr negative anomalies indicate plagioclase and K-feldspar fractionation, whereas the negative anomalies in Ti and P indicate titanomagnetite and apatite fractionation (Fig. 4f).

The Moquehue Granite, MOQUE sample, is geochemically classified as a granite (Fig. 4a) of the calc-alkaline magma series (Fig. 4b), and it is plotted in

the orogenic granitoid field according to the diagram of Whalen et al. (1987) and into the volcanic arc field in the diagram of Pearce et al. (1984) (Fig. 4c, d). It shows a gentle negative Eu anomaly, a moderate enrichment in light REE and a gentle depletion in middle REE, indicative of amphibole fractionation in the source (Fig. 4e). A flat heavy REE pattern was also observed. The pattern in the primitive mantle-normalized diagram is very similar to the Jurassic Host Granite samples, and suggests fractionation of plagioclase, K-feldspar, titanomagnetite and amphiboles/clinopyroxenes in the source (Fig. 4f).

Sample	GR1	GR2	GR4	Moque	ICAL4	VAR1	VAR2	VAR3	VAR4A	VAR5	GV	D2	NAU4	NAU3-B	CY1
Latitude (°S)	-36.810	-36.845	-36.846	-38.917	-38.904	-36.810	-36.810	-36.807	-36.804	-36.816	-36.807	-36.810	-37.768	-37.741	-37.173
Longitude (°W)	-70.668	-70.671	-70.663	-71.302	-71.187	-70.671	-70.669	-70.668	-70.665	-70.672	-70.667	-70.668	-70.324	-70.275	-70.680
SiO_2	74.55	77.07	74.30	70.61	66.60	58.01	62.81	65.32	61.85	62.35	61.81	57.72	53.09	61.60	52.07
TiO_2	0.02	0.08	0.17	0.49	0.52	0.67	0.48	0.60	0.51	0.49	0.51	0.63	0.73	0.47	1.05
Al_2O_3	13.81	12.48	12.36	13.92	15.22	17.67	17.26	13.72	17.30	17.50	17.72	18.16	16.99	17.99	19.78
Fe_2O_3t	0.70	1.06	3.31	3.66	4.21	7.09	5.46	8.42	5.88	5.53	5.86	6.89	8.12	6.38	8.88
MnO		0.03	0.05	0.09	0.07	0.16	0.14	0.21	0.13	0.12	0.18	0.16	0.18	0.17	0.16
MgO	0.02	0.04	0.19	1.00	1.70	3.73	2.07	2.69	2.25	2.05	2.18	3.51	5.82	2.16	3.08
CaO	0.41	0.25	0.60	3.02	3.73	6.50	6.33	5.38	6.36	6.00	6.34	7.35	5.61	5.86	8.81
Na_2O	3.16	4.01	3.39	4.41	3.62	2.93	3.40	2.49	3.24	3.27	3.29	3.00	5.38	3.84	3.07
K_2O	6.96	4.84	4.82	1.68	3.21	1.71	1.16	2.10	1.47	1.71	1.41	1.12	1.33	1.88	1.01
P_2O_5	0.03	0.03	0.02	0.14	0.11	0.18	0.13	0.20	0.14	0.13	0.11	0.13	0.29	0.22	0.27
LOI	0.20	0.00	0.60	1.48	0.81	1.10	0.60	-	0.70	0.70	0.40	1.10	3.54	2.03	0.85
Total	99.90	99.90	99.87	100.50	99.80	99.86	99.87	-	99.86	99.85	99.87	99.84	101.08	102.60	99.03
Cs	4.90	8.20	1.80	0.55	3.52	2.50	1.50	2.94	2.80	4.40	2.70	2.50	10.58	2.43	0.78
Rb	208.40	456.30	136.30	48.70	133.10	58.30	35.00	77.32	46.70	49.20	49.40	29.20	39.60	55.10	26.70
Ba	194.00	29.00	819.00	419.00	465.00	475.00	381.00	549.00	365.00	413.00	354.00	291.00	423.00	600.00	370.00
Sr	68.50	5.30	39.60	180.00	298.00	348.10	443.00	441.80	409.70	415.40	384.90	447.60	513.00	570.00	507.00
Th	11.50	32.90	12.50	6.40	13.50	4.10	2.50	8.95	4.50	4.00	4.10	3.60	5.60	7.60	5.40
U	10.00	12.40	2.50	1.73	2.85	1.20	0.80	2.00	1.70	1.30	0.80	1.10	1.50	2.10	1.22
Zr	23.40	63.00	331.60	239.00	192.00	90.20	91.80	159.00	109.60	112.90	103.70	81.30	119.00	134.00	140.00
Hf	2.20	4.10	9.10	6.08	5.16	2.80	2.50	5.15	3.00	3.00	2.80	2.50	2.65	3.08	3.26
Ta	7.00	3.20	1.10	0.55	0.40	0.50	0.30		0.70	0.40	0.40	0.40	0.34	0.46	0.39
Y	48.10	38.80	53.70	32.68	23.02	26.70	15.20	22.69	17.00	15.40	14.40	17.40	17.03	18.45	24.97
Nb	23.40	37.40	12.90	6.93	4.79	6.50	4.40	8.54	4.70	4.80	4.30	3.70	4.36	5.38	5.63
Sc	6.00	15.00	11.00			23.00	12.00		13.00	12.00	11.00	22.00			
Cr	-	-	-	-	-	-	-	25.07							
Ni	-	-	-	7.00	16.00	24.00		43.74	-	-	-	-	40.00	9.00	16.00
Co	0.20	0.40	-	33.40	51.90	14.50	8.30	10.47	10.70	10.00	9.00	14.40	41.40	48.00	53.70
V			-	46.00	78.00	135.00	79.00	200.30	107.00	104.00	98.00	160.00	186.00	86.00	207.00
W	9.00	9.90	2.00	306.10	399.70	0.60	0.60	-	0.80	1.70	4.00		97.40	218.30	162.50
Ga	13.60	21.00	15.30	18.30	17.90	16.90	15.20	-	14.20	13.90	15.60	14.80	21.10	21.80	21.40
Zn	-	-	-	36.00	38.00	-	-	124.80	-	-	-	-	85.00	81.00	64.00
Cu	-	-	-	34.00	30.00	-	-	4.81	-	-	-	-	78.00	15.00	59.00
La	9.20	23.90	40.20	18.40	16.10	15.40	13.20	21.09	13.60	13.00	12.00	11.20	16.40	18.50	14.90
Ce	24.70	51.10	86.00	40.00	36.00	34.30	27.10	45.15	29.70	26.20	24.40	24.40	34.20	36.00	33.30
Pr	2.91	5.45	10.04	4.76	4.40	4.43	3.25	5.36	3.36	3.02	3.09	3.00	4.15	4.20	4.33
Nd	9.90	19.30	40.90	19.50	17.70	19.70	13.00	20.99	13.50	12.10	12.00	12.80	18.10	17.50	18.60
Sm	2.99	4.79	8.84	4.20	3.80	4.39	2.76	3.87	2.89	2.49	2.52	2.78	3.70	3.60	4.30
Eu	0.11	0.21	1.56	1.09	0.79	1.11	0.84	0.82	0.83	0.80	0.78	0.84	1.06	1.01	1.19
Gd	4.08	5.25	8.76	4.86	3.44	4.48	2.68	3.74	2.77	2.46	2.43	2.80	3.29	3.13	4.30
Tb	1.06	1.05	1.51	0.77	0.58	0.77	0.44	0.60	0.45	0.42	0.39	0.49	0.49	0.43	0.65
Dy	7.76	7.15	9.49	5.10	3.50	4.56	2.75	3.77	2.77	2.59	2.45	3.09	3.16	2.98	4.21
Ho	1.67	1.63	1.90	1.04	0.70	1.00	0.56	0.75	0.63	0.55	0.53	0.67	0.58	0.61	0.79
Er	5.71	5.74	6.03	3.38	2.11	3.19	1.69	2.39	1.97	1.57	1.59	2.03	1.75	1.82	2.53
Tm	1.01	1.04	0.85	0.52	0.33	0.43	0.25	0.40	0.29	0.23	0.24	0.29	0.27	0.28	0.37
Yb	7.50	8.51	5.62	3.60	2.20	2.99	1.69	2.67	2.03	1.83	1.59	1.91	1.70	1.90	2.40
Lu	1.17	1.58	0.92	0.57	0.33	0.48	0.28	0.47	0.33	0.28	0.27	0.34	0.28	0.30	0.38
Be	2.00	8.00	-	-	-	2.00	2.00	-	-	-	2.00	-	-	-	-
Sn	-	4.00	3.00	1.80	1.40	4.00	-	0.83	-	-	2.00	-	1.40	1.60	1.30
Mo	-	-	-	-	4.00	-	-	-	-	-	-	-	-	2.00	-

Table 2: Whole-rock major and trace element data for Jurassic and Cretaceous-Paleogene rocks analyzed in this work. Empty values were not measured and items with the symbol "-" are below the detection limit.



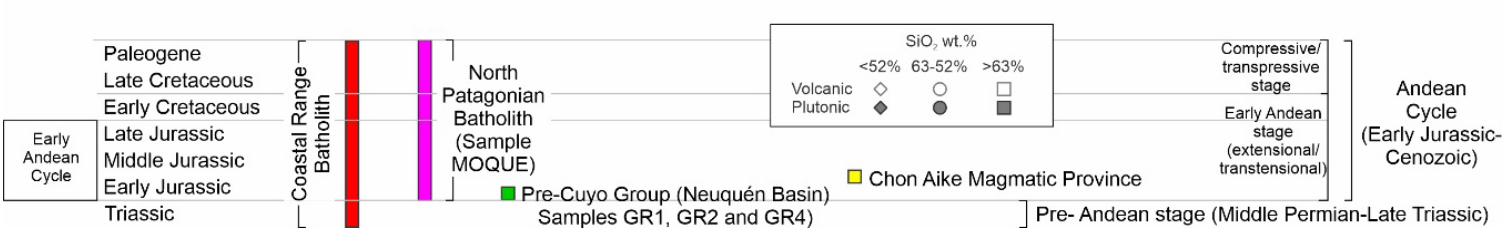
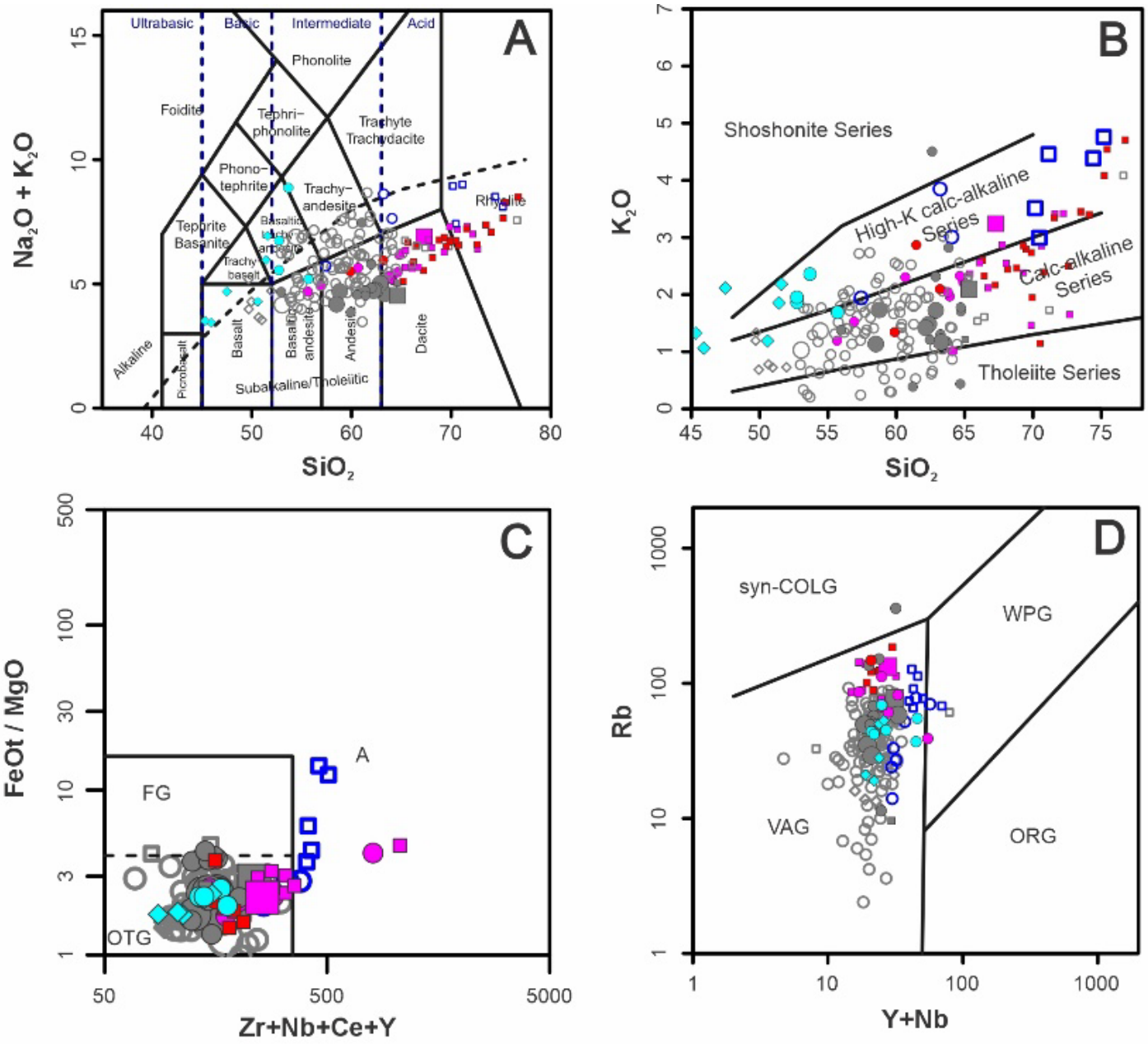


Figure 4: Bulk-rock geochemistry of the Early Andean Cycle (202-150 Ma) studied rocks (big symbols), as well as coeval samples from the Coastal Range Batholith (Chile) and Pre-Cuyo Group from Neuquen Basin, Argentina (small symbols). For comparison, the composition of Chon Aike Magmatic Province also is shown. The studied rocks from the Early Andean Cycle are: Constitución Granite, Pichilemu Granite, La Estrella Granite, Cerros del Hualve Granites, Montecillos intrusive (Vázquez Illanez 2008), Jurassic Host Granite (GR1, GR2 and GR4 of this work), Moquehue granite (ICAL4 sample and compiled of Urraza et al. 2011), Milla Michicó Fm., La Primavera Fm., Colomichicó Fm. (Zappettini et al. 2018), Marifil Complex (Pankhurst and Rapela 1995), Panguipulli Batholith (Parada and Munizaga 1978). A) TAS diagram for volcanic rocks, subalkaline/alkaline fields according to Le Bas et al. (1986); B) Magmatic series diagram of Piccerillo and Taylor (1976); C) Zr+Nb+Ce+Y versus FeOt/MgO plot of Whalen et al. (1987) to distinguish A-type granites from other granite types. FG: fractionated felsic granites, and unfractionated M-, I- and S-type granites (OGT: other granite types); D) Rb versus Nb-Y diagram (after Pearce, 1996). Fields for volcanic arc (VAG), syn-collision (syn-COLG), within-plate (WPG) and ocean ridge (ORG) granites are indicated; E) Chondrite-normalized plot of the high silica samples of this work (SiO2 >65 wt.%, samples GR1, GR2, GR4 and MOQUE); F) Primitive mantle normalized plot of the high silica samples of this work (SiO2 >65 wt.%, samples GR1, GR2, GR4 and MOQUE). Primitive mantle and chondrite compositions are from McDonough and Sun (1995).

4.5.2 Andean Cycle during the compressive/transpressive stage

From the North Patagonian Batholith and belonging to the Late Cretaceous-Paleogene period (Table 2), the sample ICAL4, is classified as a subalkaline granodiorite (dacite in the TAS diagram for volcanic rocks, Fig. 5a), belonging to the high-potassium calc-alkaline series (Fig. 5b), which plots in the I- and S-field in the diagram of Whalen et al. (1987) (Fig. 5c) and in the volcanic arc granite in the diagram of Pearce et al. (1984) (Fig. 5d). This rock also shows a moderate Eu anomaly, a moderate enrichment in light REE and a flat heavy REE pattern (Fig. 6c), as well as the typical geochemical signature of subduction settings, negative anomalies of Nb and Ta (Fig. 6d).

In turn, the plutonic and volcanic samples from the Naunauco Belt are subalkaline andesites and dacites (Fig. 5a) and belong to the calc-alkaline magma serie (Fig. 5b). They plot in the I- and S-type orogenic granite field (Fig. 5c) and in the volcanic arc granite field (Fig. 5d). Both low- and high-silica rocks of this belt show flat heavy REE patterns and almost no Eu anomalies, or gentle (Fig. 6a, c). The high- and low- silica rocks of this belt show negative Nb and Ta throughs and positive Pb peaks typical of subduction settings (Fig. 6b, d).



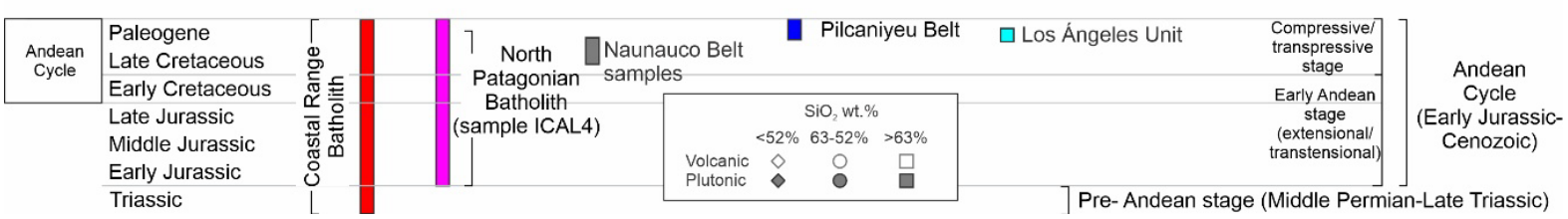


Figure 5: Bulk-rock geochemistry of the Andean Cycle (202-150 Ma) studied rocks (big symbols), as well as coeval samples from the Coastal Range Batholith (Chile), North Patagonian Batholith, Pilcaniyeu Belt, Naunauco Belt and Los Angeles Unit, Argentina (small symbols). The studied rocks from the Andean Cycle are: Oncol Porphyry, Laurel Dacitic Porphyry, Los Boldos Granitoid, Loncoche Dacitic Porphyry (De la Fuente et al. 2021), Chaihuín Pluton (Mella et al. 2012, De la Fuente et al. 2021), Dacita Laurel (Mella et al. 2012), Paso de Icalma Granodiorite (Gallegos et al. 2010, Urraza et al. 2011), Gualletué Plutonic Group (De la Fuente et al. 2021), Varvarco tonalite (Casé et al. 2008, samples VAR1, VAR2, VAR4A, VAR5 and D2 of this work), Butalon tonalite (Casé et al. 2008, sample BU4 of this work), Colipilli Fm. (Llambías and Malvicini 1978, Llambias and Rapela 1989, Franchini et al. 2000, Franchini et al. 2003, Zamora Valcarce et al. 2006, Mateo Fernández Caso et al. 2011, D'Annunzio et al. 2023, samples NAU3-B and NAU4 of this work), Cayanta Fm. (Llambias and Rapela 1989, Spagnuolo et al. 2012, Mateo Fernández Caso et al. 2011, sample CY1 of this work), Huitrera Fm. (Iannelli et al. 2017) and Los Angeles Unit (Iannelli et al. 2017). A) TAS diagram for volcanic rocks, subalkaline/alkaline fields according to Le Bas et al. (1986); B) Magmatic series diagram of Piccerillo and Taylor (1976); C) Zr+Nb+Ce+Y versus FeOt/MgO plot of Whalen et al. (1987) to distinguish A-type granites from other granite types. FG: fractionated felsic granites, and unfractionated M-, I- and S-type granites (OGT: other granite types); D) Rb versus Nb-Y diagram (after Pearce, 1996). Fields for volcanic arc (VAG), syn-collision (syn-COLG), within-plate (WPG) and ocean ridge (ORG) granites are indicated.

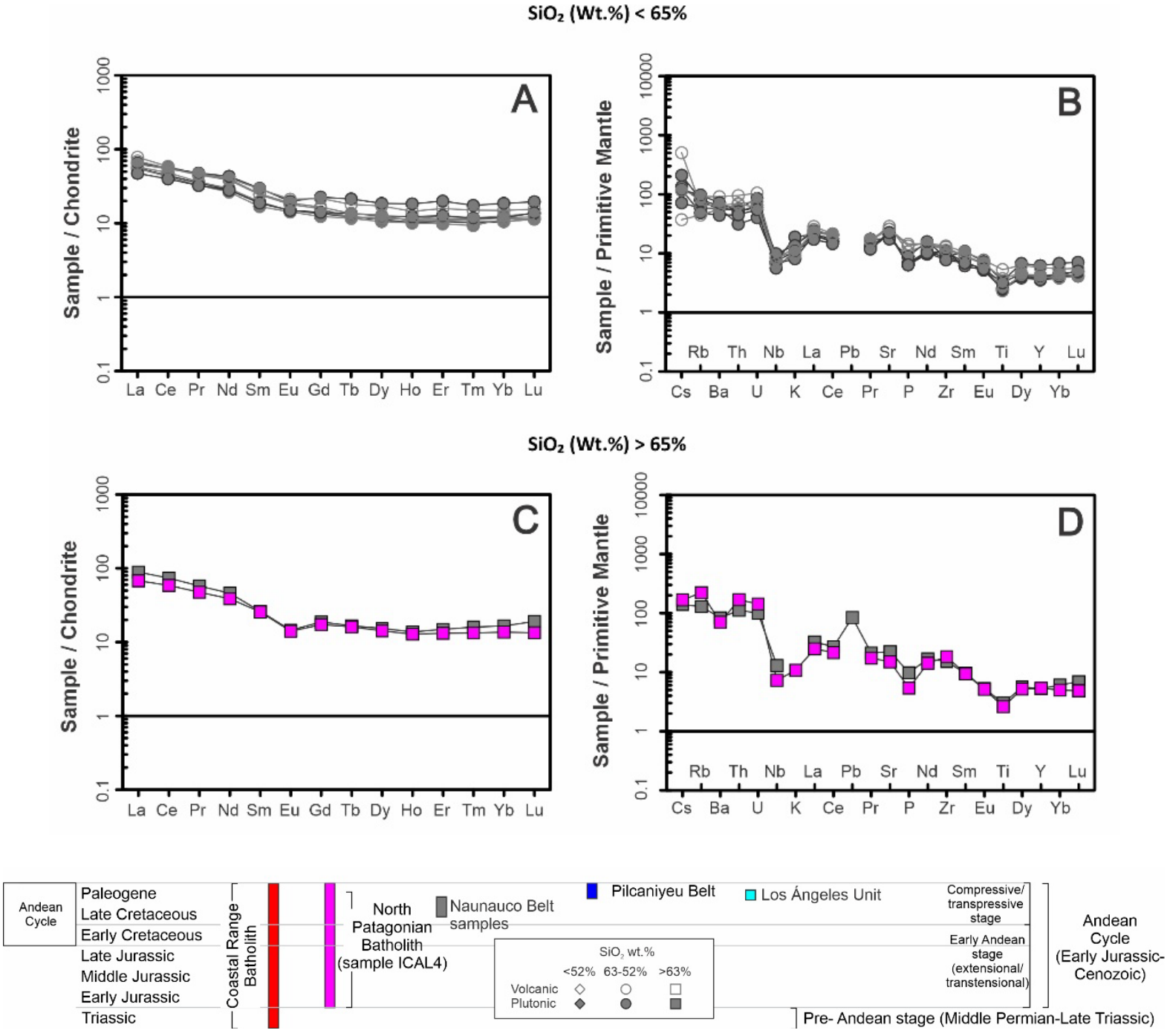


Figure 6: Continuation of figure 5: A) Chondrite-normalized plot of the low silica samples of this work (SiO2 <65 wt.%, samples VAR1, VAR2, VAR4A, VAR5, D2, NAU3-B, NAU4 and CY1); B) Primitive mantle normalized plot of the low silica samples of this work (SiO2 <65 wt.%, samples VAR1, VAR2, VAR4A, VAR5, D2, NAU3-B, NAU4 and CY1); C) Chondrite-normalized plot of the high silica samples of this work (SiO2 >65 wt.%, samples ICAL4 and VAR3); D) Primitive mantle normalized plot of the high silica samples of this work (SiO2 >65 wt.%, samples ICAL4 and VAR3). Primitive mantle and chondrite compositions are from McDonough and Sun (1995).

4.6 U–Pb ages and Hf isotopes on zircon

4.6.1 The Host Granite: GR4 microgranite

Zircon crystals have sizes between 50 and 150 μm, are transparent and occur mostly as subhedral and broken crystals. In the CL images (Supplementary Material I-GR4) most of the zircons appear fractured, and in a few crystals magmatic zonation can be seen. Twenty-four zircons were analyzed, eighteen in rims and ten in cores. From a total of twenty-eight U-Pb data, nineteen were concordant (between 95 and 105% of concordance). The TuffZirc algorithm (Ludwig and Mundil, 2002) allow us to obtain an age of 183.45 +1.92 -1.22 Ma with six outliers. Using the concordant data and one outlier, a lower intercept of 184 ± 3 Ma (MSWD = 1.3) was calculated (Fig. 7a). The Th/U values for these zircon grains are between 0.90 and 1.70 (Table 3).

Eighteen Hf data on zircon crystals (n = 14) with ages between 182-195 Ma were obtained. The values of ($^{176}Hf/^{177}Hf$)i ratios area between 0.282677 and 0.282819. The ε_{Hfi} values are positive between 0.31 and 5.26, that correspond to Meso to Neoproterozoic T_{DM} (average/mafic crust) values of 1.18/1.60 and 0.87/1.15 Ga respectively (Fig. 8, Table 4).

Spot #	Position	f206c	^{206}Pb (cps)	U[1] (ppm)	Th/U	^{206}Pb/^{204}Pb	1s (%)	Ratios[2] ^{238}U/^{206}Pb	2s (%)	^{207}Pb/^{206}Pb	2s (%)	Ages ^{207}Pb/^{206}Pb	2s (Ma)	^{206}Pb/^{238}U	2s (Ma)	^{207}Pb/^{235}U	2s (Ma)	% Conc[3]
JURASSIC ROCKS																		
The Host Granite: GR4 microgranite																		
#21	rim	0.92	30667	125	1.11	3479	46	33.66	4.65	0.04951	2.7	171	63	189	9	189	9	100.1
#08	rim	0.16	16077	68	1.02	23391	99	34.28	4.31	0.04985	4.0	184	94	185	8	186	10	99.9
#10	rim	0.45	32660	140	1.34	9111	52	34.70	4.56	0.05010	1.6	198	37	183	8	185	9	99.3
#13	rim	0.83	22549	94	1.01	4500	46	35.63	4.40	0.04987	2.5	186	58	178	8	180	8	99.2
#27	rim	1.63	11592	44	0.96	677	85	34.71	4.37	0.04969	4.5	175	104	183	8	185	11	99.1
#38	rim	3.13	17964	71	1.35	655	13	36.44	4.73	0.04962	2.7	175	62	175	8	176	9	99.1
#36	rim	0.44	26107	102	1.39	1902	160	34.88	4.32	0.04988	1.8	188	41	182	8	184	8	98.9
#26	rim	0.02	22909	84	1.04	4416	55	33.03	4.47	0.05008	2.3	196	54	192	9	195	9	98.8
#42	core	1.05	18880	76	1.25	1955	74	34.04	4.42	0.05032	2.6	206	62	187	8	189	9	98.7
#23	core	0.67	29593	119	1.43	46346	92	34.55	4.39	0.05008	2.0	197	46	184	8	186	8	98.7
#06	rim	0.42	18752	72	1.14	2068	63	35.23	4.40	0.05033	2.3	208	53	180	8	183	8	98.5
#28	core	0.77	38653	153	1.70	4298	20	34.29	4.34	0.05040	2.2	211	50	185	8	189	8	98.0
#37	core	0.25	22532	86	1.34	1402	88	33.44	4.59	0.05058	2.7	219	62	190	9	194	10	98.0
#33	**rim**	**0.16**	**21547**	**96**	**0.94**	**1958**	**52**	**39.74**	**5.41**	**0.05007**	**3.8**	**195**	**88**	**160**	**9**	**164**	**9**	**97.7**
#41	rim	0.30	34619	141	1.65	10600	77	34.29	4.39	0.05087	1.3	233	30	185	8	190	8	97.6
#14	core	0.21	37734	154	1.58	1611	326	34.15	4.33	0.05094	1.3	237	31	186	8	191	8	97.6
#20	**core**	**1.57**	**16311**	**68**	**1.30**	**28613**	**94**	**38.16**	**4.68**	**0.05047**	**2.2**	**215**	**52**	**167**	**8**	**172**	**8**	**97.2**
#19	rim	0.62	19115	77	1.20	2975	82	35.26	4.55	0.05124	3.3	247	78	180	8	187	10	96.5
#22	rim	0.87	21298	80	0.90	4393	97	32.52	4.37	0.05208	6.3	278	134	195	8	204	15	95.6
#34	**rim**	**5.43**	**14063**	**75**	**0.98**	**403**	**19**	**49.78**	**4.45**	**0.05152**	**2.1**	**262**	**48**	**128**	**6**	**137**	**7**	**93.7**
#25	**core**	**3.23**	**21869**	**90**	**1.31**	**680**	**20**	**36.01**	**4.58**	**0.05291**	**3.5**	**322**	**80**	**177**	**8**	**189**	**11**	**93.4**
#12	**rim**	**0.60**	**17734**	**72**	**1.11**	**943**	**53**	**35.45**	**4.65**	**0.05332**	**5.8**	**330**	**129**	**179**	**8**	**192**	**14**	**93.3**
#40	**core**	**1.61**	**26958**	**115**	**1.47**	**1348**	**19**	**34.63**	**4.88**	**0.05408**	**2.3**	**373**	**51**	**184**	**9**	**199**	**11**	**92.4**
#24	**core**	**0.53**	**41727**	**216**	**1.53**	**2660**	**248**	**43.65**	**4.48**	**0.05582**	**3.4**	**441**	**77**	**146**	**7**	**166**	**10**	**87.8**
#05	**rim**	**2.68**	**25678**	**106**	**1.31**	**1034**	**39**	**34.87**	**4.67**	**0.05866**	**4.5**	**551**	**99**	**182**	**8**	**212**	**12**	**86.0**
#35	**rim**	**4.85**	**13290**	**52**	**1.31**	**394**	**12**	**34.68**	**4.90**	**0.06323**	**8.2**	**708**	**181**	**183**	**9**	**230**	**20**	**79.9**
#11	**core**	**2.69**	**42758**	**203**	**1.18**	**677**	**11**	**38.40**	**4.30**	**0.07056**	**3.6**	**943**	**74**	**166**	**7**	**230**	**12**	**72.2**
#09	**rim**	**3.59**	**26035**	**92**	**1.14**	**552**	**14**	**30.92**	**4.37**	**0.07266**	**7.0**	**992**	**146**	**205**	**9**	**286**	**22**	**71.8**

Moquehue granodiorite: MOQUE

#21	rim	1.31	9922	42	2.10	497	130	34.84	3.69	0.04878	2.8	170	58	183	7	180	7	101.4
#05	core	1.28	13139	55	2.70	917	269	33.81	3.21	0.04916	1.7	154	40	188	6	187	6	100.7
#34	core	1.13	15591	65	2.06	5416	48	32.66	3.35	0.04945	3.4	186	76	195	6	193	8	100.5
#49	**rim**	**1.85**	**8834**	**44**	**2.01**	**7705**	**87**	**37.09**	**3.29**	**0.04910**	**4.2**	**147**	**97**	**172**	**6**	**171**	**8**	**100.3**
#07	rim	0.71	6704	27	2.08	504	150	34.22	3.33	0.04955	6.8	227	100	186	6	186	14	99.7
#54	rim	0.32	26625	123	2.32	1220	103	34.30	3.37	0.04976	2.1	181	50	185	6	186	7	99.7
#37	rim	0.31	19287	87	2.88	1463	145	35.55	3.25	0.04953	3.0	200	40	179	6	180	7	99.5
#09	rim	1.39	7501	30	1.95	2478	70	33.19	3.29	0.04989	4.5	222	82	191	6	192	10	99.5
#08	core	1.85	11706	49	2.90	1268	147	34.55	3.25	0.04987	3.4	185	77	184	6	186	8	99.2
#10	core	1.80	10358	44	2.34	1356	102	34.17	3.29	0.05006	4.2	193	96	186	6	188	9	99.1
#26	rim	0.82	9720	41	1.96	4	26765	34.17	3.21	0.05012	2.1	198	49	186	6	188	6	99.0
#19	rim	0.73	17459	74	2.72	1268	133	35.07	3.41	0.05018	3.5	199	80	181	6	184	8	98.7
#33	rim	0.31	58348	250	3.71	7503	107	34.89	3.31	0.05012	2.5	198	58	182	6	185	7	98.7
#55	core	2.79	8802	41	1.84	573	64	34.71	3.59	0.05026	4.3	241	74	183	6	186	11	98.7
#40	rim	6.67	6246	27	1.89	4670	86	33.73	3.76	0.05022	3.7	201	87	188	7	191	9	98.6
#36	core	0.28	23970	109	2.08	627	159	34.91	3.40	0.05023	2.3	203	54	182	6	185	7	98.6
#42	core	0.41	9114	41	2.04	1193	51	35.47	3.37	0.05008	4.2	244	86	179	6	182	9	98.5
#57	core	3.66	6881	32	1.79	338	251	34.71	3.55	0.05055	3.2	216	72	183	6	186	8	98.3
#56	core	0.92	38276	180	3.51	3648	28	35.64	4.07	0.05044	2.1	213	50	179	7	182	9	98.2
#12	rim	0.50	14748	62	2.81	6376	102	34.92	3.31	0.05048	2.1	215	49	182	6	186	7	98.0
#28	core	0.06	44118	188	3.09	2446	179	34.55	3.27	0.05064	1.6	223	38	184	6	188	7	98.0
#48	core	1.32	14520	69	2.90	1050	185	35.19	3.35	0.05059	2.4	221	55	181	6	185	8	97.9
#06	**core**	**0.15**	**223354**	**349**	**1.65**	**25695**	**107**	**12.66**	**3.30**	**0.05822**	**1.2**	**537**	**26**	**490**	**15**	**501**	**14**	**97.8**
#41	rim	0.52	10476	47	2.30	10896	65	35.60	3.63	0.05059	4.3	252	78	179	6	183	10	97.6
#20	rim	1.40	10866	48	2.02	3346	39	34.30	3.32	0.05119	3.6	247	82	185	6	190	9	97.3
#11	core	0.17	18470	76	3.29	283	258	33.26	3.46	0.05131	1.8	252	42	191	7	197	7	97.0
#47	core	1.03	17185	81	2.32	677	140	34.53	3.33	0.05120	3.4	247	79	184	6	190	9	97.0
#27	rim	0.42	11913	51	2.78	225	526	34.30	3.65	0.05136	3.5	252	78	185	7	191	9	96.9
#14	core	4.60	10286	43	2.66	163	337	34.18	4.36	0.05142	2.6	257	60	186	8	192	7	96.8
#13	core	1.99	16247	69	2.57	2443	35	34.68	3.31	0.05143	3.1	257	73	183	6	190	9	96.5
#51	rim	0.34	89642	434	4.79	6485	23	34.32	4.15	0.05191	2.2	280	50	185	8	193	9	96.1
#38	rim	0.51	21403	90	1.60	532	263	34.51	3.44	0.05178	3.7	272	84	184	6	193	9	95.7
#22	rim	3.97	7309	31	2.34	192	163	33.78	3.44	0.05251	4.6	301	106	188	7	198	11	95.0
#39	**core**	**1.12**	**9727**	**40**	**2.09**	**382**	**235**	**33.45**	**3.41**	**0.05282**	**3.7**	**317**	**82**	**190**	**6**	**202**	**10**	**94.2**
#35	**rim**	**0.67**	**6966**	**30**	**1.50**	**251**	**180**	**34.98**	**3.29**	**0.05315**	**4.0**	**330**	**92**	**182**	**6**	**194**	**9**	**93.6**
#53	**rim**	**0.57**	**24248**	**105**	**3.13**	**980**	**162**	**35.52**	**4.64**	**0.05303**	**3.8**	**328**	**87**	**179**	**8**	**192**	**12**	**93.4**
#52	**core**	**1.05**	**22920**	**107**	**2.21**	**1253**	**296**	**34.82**	**3.74**	**0.05416**	**4.3**	**374**	**96**	**183**	**7**	**198**	**10**	**92.2**
#24	**rim**	**8.27**	**10297**	**44**	**2.17**	**325**	**19**	**34.92**	**4.90**	**0.05535**	**2.4**	**424**	**54**	**183**	**9**	**202**	**10**	**90.4**
#23	**core**	**2.39**	**6157**	**25**	**2.23**	**38**	**652**	**34.58**	**4.72**	**0.05537**	**4.2**	**423**	**91**	**184**	**8**	**204**	**8**	**90.3**
#25	**core**	**0.79**	**12338**	**52**	**2.69**	**514**	**128**	**34.12**	**3.98**	**0.05585**	**6.8**	**428**	**149**	**186**	**7**	**208**	**16**	**89.8**
#50	**core**	**2.51**	**17763**	**81**	**2.08**	**331**	**253**	**35.04**	**4.30**	**0.05997**	**10.1**	**570**	**209**	**182**	**8**	**216**	**22**	**84.0**

CRETACEOUS-PALEOGENE ROCKS																		
Icalma granodiorite (NPB): ICAL4																		
#21	rim	2.14	3897	45	1.24	10	3057	90.68	3.62	0.04521	8.8	203	170	71	3	67	6	105.1
#28	core	3.58	6298	74	1.58	243	297	88.41	3.45	0.04546	6.7	154	116	73	3	69	5	104.5
#24	core	0.36	5435	63	1.35	65307640	94	89.44	3.50	0.04553	5.7	118	71	72	3	69	5	104.3
#05	core	0.32	7324	80	1.37	668	141	94.32	3.31	0.04617	3.9	96	74	68	2	65	4	104.0
#12	core	2.02	7923	91	2.18	1163	16	88.23	3.46	0.04610	7.9	94	26	73	2	70	6	103.9
#25	core	0.60	5475	63	1.34	175	142	89.35	3.42	0.04616	3.1	105	73	72	2	70	4	102.8
#40	rim	4.85	6632	78	1.68	378	3	91.67	3.81	0.04607	4.6	54	0	70	3	68	5	102.7
#19	core	3.00	7964	89	1.68	494	39	86.79	3.27	0.04679	3.7	113	54	74	2	73	4	101.9
#22	rim	0.13	6568	78	1.84	564	70	89.60	3.57	0.04675	5.8	195	130	72	3	70	5	101.8
#34	core	3.25	7305	84	2.09	16038	63	88.35	3.33	0.04675	4.3	192	50	73	2	71	5	101.5
#35	core	0.26	9514	111	2.21	307	248	90.97	3.36	0.04668	3.3	122	44	70	2	69	4	101.5
#08	core	3.72	7323	82	1.32	4516	55	91.72	3.40	0.04747	6.8	190	137	70	2	69	6	101.1
#26	core	1.83	6593	74	2.07	811	58	86.99	3.34	0.04708	5.5	184	106	74	2	73	5	101.0
#06	core	10.76	5540	56	1.34	247	21	89.15	3.55	0.04761	9.4	186	0	72	3	71	8	100.9
#27	rim	3.37	5078	56	1.34	38	522	87.81	3.33	0.04721	4.7	160	116	73	2	73	5	100.6
#37	core	1.29	5666	65	1.44	1453	67	89.64	3.38	0.04746	5.0	150	57	72	2	72	5	99.9
#09	rim	0.03	32455	336	1.71	1585	524	88.02	3.34	0.04801	2.6	125	34	73	2	73	4	99.9
#38	rim	1.36	4610	54	1.52	245	583	89.90	3.50	0.04767	7.2	220	98	71	2	72	6	99.7
#23	core	3.15	7257	84	1.24	684	101	90.12	3.60	0.04799	3.6	154	54	71	3	72	5	99.0
#33	rim	1.28	7578	89	2.02	465	103	91.36	3.29	0.04789	4.8	135	81	70	2	71	5	99.0
#41	core	2.47	4870	57	1.33	1073	63	91.10	3.86	0.04806	6.0	203	137	70	3	71	6	98.6
#07	core	1.61	6336	68	1.33	445	369	90.37	3.32	0.04892	2.8	141	63	71	2	72	4	98.3
#42	rim	0.30	25842	297	2.90	706	470	93.03	3.48	0.04836	3.1	115	72	69	2	70	4	97.9
#36	core	1.05	13998	162	1.62	546	192	92.60	3.32	0.04890	4.2	172	90	69	2	71	4	96.9
#20	core	0.36	10869	122	1.99	75	624	88.96	3.34	0.04924	3.8	211	67	72	2	74	5	96.7
#13	rim	1.68	12066	139	2.13	849	183	88.71	3.30	0.05021	2.3	203	55	72	2	76	4	95.5
#39	core	0.54	5648	65	1.49	3501	67	89.12	3.25	0.05188	2.4	278	53	72	2	78	4	91.7
#14	**core**	**4.22**	**6005**	**63**	**1.66**	**912**	**41**	**89.09**	**3.44**	**0.05427**	**4.5**	**379**	**99**	**72**	**2**	**82**	**5**	**88.3**
#11	**core**	**8.00**	**4572**	**54**	**2.56**	**434**	**37**	**91.56**	**3.22**	**0.06517**	**14.1**	**765**	**294**	**70**	**2**	**94**	**14**	**74.5**
#10	**core**	**4.13**	**6756**	**70**	**2.34**	**425**	**3**	**84.60**	**3.26**	**0.07898**	**10.8**	**1160**	**215**	**76**	**2**	**122**	**14**	**62.2**

Varvarco tonalite: VAR6

#12	**core**	**0.79**	**3196**	**39**	**0.96**	**1443**	**93**	**93.87**	**2.62**	**0.04301**	**6.9**	**33**	**37**	**68**	**2**	**62**	**5**	**110.1**
#11	**rim**	**1.39**	**4404**	**56**	**0.58**	**2261**	**97**	**97.56**	**2.82**	**0.04404**	**5.7**	**43**	**19**	**66**	**2**	**61**	**3**	**107.6**
#10	**rim**	**1.19**	**4940**	**59**	**0.99**	**173**	**219**	**95.87**	**2.42**	**0.04466**	**8.1**	**102**	**111**	**67**	**2**	**63**	**5**	**105.9**
#33	**core**	**9.94**	**2458**	**33**	**0.95**	**81**	**154**	**98.44**	**2.57**	**0.04474**	**10.8**	**215**	**120**	**65**	**2**	**62**	**7**	**105.7**
#24	core	0.28	4048	51	0.92	217	70	93.89	2.61	0.04530	6.9	105	38	68	2	65	4	104.9
#06	core	2.75	3602	43	1.31	438	160	96.66	2.42	0.04580	9.8	235	85	66	2	64	6	103.2
#20	core	0.01	3896	49	1.15	99	363	94.40	3.31	0.04638	7.4	217	38	68	2	66	4	102.6
#37	rim	5.64	3810	51	1.25	148	115	95.09	2.79	0.04641	9.6	193	53	67	2	66	6	102.3
#38	core	0.92	9147	122	1.30	534	147	96.36	2.41	0.04645	3.9	129	76	67	2	65	3	101.9
#22	core	0.12	5400	65	1.23	92	540	92.78	2.87	0.04755	6.4	211	162	69	2	69	4	100.1
#21	rim	0.99	3556	43	0.92	12204461	94	93.15	3.92	0.04771	8.3	237	214	69	3	69	5	100.0
#08	core	1.15	3330	41	1.33	269	188	95.50	3.06	0.04799	5.7	180	100	67	2	68	4	98.9
#05	**core**	**0.02**	**36445**	**142**	**2.07**	**7050**	**102**	**33.19**	**2.22**	**0.05034**	**0.5**	**210**	**12**	**191**	**4**	**194**	**4**	**98.9**
#41	rim	2.78	6703	90	1.20	658	75	98.16	2.50	0.04784	3.9	148	63	65	2	66	3	98.8
#26	rim	2.04	7162	99	1.10	896	48	96.29	2.39	0.04834	9.7	225	18	67	2	67	7	98.7
#42	core	2.71	1807	23	0.91	265	94	96.46	2.36	0.04786	10.4	169	289	66	2	67	7	98.7
#13	core	4.27	4516	55	1.30	78	288	94.84	2.66	0.04834	7.6	236	158	68	2	69	5	98.3
#34	core	0.81	5292	70	1.22	6224	78	96.54	2.26	0.04847	2.1	120	50	66	1	68	2	97.9
#07	rim	2.65	4997	61	0.78	827	58	97.28	2.75	0.04870	4.6	167	89	66	2	68	3	97.4
#09	rim	0.11	3770	48	0.81	234	207	97.33	2.51	0.04880	4.2	174	79	66	2	68	3	97.3
#14	core	4.40	4415	58	1.09	48	393	96.08	3.23	0.04934	15.5	269	329	67	2	69	10	96.8
#28	core	2.63	5989	79	1.03	2665	84	94.47	2.82	0.04924	4.1	156	96	68	2	70	3	96.8
#35	core	5.38	4694	61	1.27	1196	103	97.28	2.35	0.04956	6.2	218	124	66	2	69	4	95.6
#36	rim	0.99	6054	79	0.90	2500	72	94.88	2.86	0.05013	6.8	240	143	68	2	71	5	94.8
#23	**rim**	**0.13**	**4769**	**58**	**0.92**	**961**	**128**	**93.43**	**2.40**	**0.05111**	**6.4**	**319**	**117**	**69**	**2**	**74**	**5**	**93.3**
#39	**core**	**16.71**	**1934**	**24**	**0.94**	**40**	**168**	**90.81**	**3.08**	**0.05638**	**14.2**	**496**	**316**	**71**	**2**	**83**	**10**	**85.0**
#19	**rim**	**5.09**	**4249**	**54**	**0.99**	**482**	23	**92.45**	**2.75**	**0.06235**	**7.2**	**678**	**145**	**69**	**2**	**90**	**7**	**77.2**
#25	**core**	**18.72**	**3968**	**43**	**1.06**	**85**	**16**	**84.57**	**2.30**	**0.15270**	**3.1**	**2375**	**54**	**76**	**2**	**225**	**8**	**33.6**

Varvarco dioritic dique: D2

#48	**rim**	**18.50**	**2173**	**26**	**1.6**	**398**	**112**	**97.79**	**2.25**	**0.04444**	**12.2**	**204**	**184**	**66**	**1**	**61**	**7**	**106.9**
#21	**rim**	**4.59**	**8836**	**119**	**1.1**	**491**	**22**	**95.98**	**1.97**	**0.04462**	**4.7**	**108**	**9**	**67**	**1**	**63**	**3**	**105.8**
#36	rim	2.30	5819	75	1.3	610	33	97.76	1.93	0.04498	7.8	153	114	66	1	62	5	105.4
#07	core	1.76	4617	60	1.7	407	54	99.63	1.91	0.04485	6.6	134	92	64	1	61	4	105.2
#57	**rim**	**4.09**	**3462**	**42**	**1.3**	**76**	**268**	**101.86**	**2.03**	**0.04529**	**6.6**	**172**	**84**	**63**	**1**	**60**	**4**	**104.5**
#42	rim	4.28	4625	57	1.6	575	49	98.83	1.95	0.04633	6.0	166	77	65	1	63	4	102.7
#55	rim	4.16	5215	62	1.4	300	39	99.09	2.19	0.04619	7.8	155	70	65	1	63	5	102.6
#12	core	21.60	2171	30	1.0	90	9	98.75	3.50	0.04611	7.8	175	137	65	2	63	5	102.5
#24	rim	2.22	5401	75	1.9	156	100	96.62	2.24	0.04627	6.2	159	201	66	1	65	4	102.2
#37	core	13.58	3197	41	1.9	72	84	97.72	1.91	0.04647	5.3	149	169	66	1	64	4	102.1
#27	rim	10.71	3076	43	1.6	4327	83	99.52	2.59	0.04655	11.3	289	164	65	2	63	7	101.8
#34	core	7.83	4350	57	2.3	142	104	97.19	2.03	0.04659	7.1	208	113	66	1	65	5	101.8
#19	**core**	**4.94**	**7740**	**104**	**2.04**	**1143**	**62**	**101.19**	**2.24**	**0.04676**	**5.8**	**177**	**82**	**63**	**1**	**63**	**4**	**100.9**
#50	**rim**	**10.57**	**3779**	**46**	**1.61**	**162**	**13**	**100.26**	**2.10**	**0.04718**	**7.4**	**185**	**131**	**64**	**1**	**64**	**5**	**100.6**
#47	rim	2.84	5187	64	2.05	339	37	99.23	2.24	0.04728	5.0	190	77	65	1	64	3	100.6
#49	core	8.28	2697	33	1.31	3172	90	99.81	2.38	0.04734	9.4	332	209	64	2	64	6	100.5
#38	**rim**	**5.42**	**9009**	**112**	**1.40**	**305**	**37**	**95.39**	**2.13**	**0.04736**	**16.9**	**393**	**381**	**67**	**1**	**67**	**11**	**100.5**
#53	rim	8.96	3976	48	1.54	286	26	99.87	2.25	0.04735	6.5	192	86	64	1	64	4	100.2
#13	**rim**	**9.00**	**3433**	**45**	**0.85**	**519**	**59**	**95.61**	**2.05**	**0.04750**	**4.0**	**130**	**78**	**67**	**1**	**67**	**3**	**99.5**
#22	rim	8.10	4329	59	1.54	197	49	98.38	2.18	0.04763	5.0	170	97	65	1	66	3	99.3
#54	core	1.05	31032	384	1.72	5432	67	95.65	2.96	0.04793	1.9	94	45	67	2	68	3	99.1
#09	**rim**	**6.91**	**3524**	**48**	**1.46**	**128**	**178**	**100.28**	**2.14**	**0.04787**	**9.3**	**226**	**146**	**64**	**1**	**65**	**6**	**98.7**
#10	rim	4.07	11430	149	2.21	503	16	100.11	2.17	0.04798	3.4	131	44	64	1	65	2	98.5
#56	core	1.86	6662	81	1.77	549	136	99.70	2.20	0.04834	4.8	169	92	64	1	66	3	98.1
#11	core	12.93	3705	50	1.91	305	38	95.89	2.56	0.04831	7.3	267	107	67	2	68	4	98.0
#41	rim	2.78	15535	196	1.71	817	10	95.91	2.01	0.04859	4.0	181	73	67	1	68	3	98.0
#20	rim	4.12	4758	69	1.83	404	20	97.31	3.04	0.04843	8.1	185	174	66	2	68	6	97.7
#25	core	6.69	3609	51	1.41	41	284	99.23	2.13	0.04860	4.8	180	108	65	1	66	4	97.4
#26	rim	8.05	3603	50	1.45	251	18	98.64	2.51	0.04867	7.5	251	201	65	2	67	6	97.3
#06	core	4.38	3708	47	2.09	696	115	98.37	2.01	0.04866	2.1	130	49	65	1	67	2	97.2
#05	**core**	**12.94**	**4659**	**60**	**2.06**	**180**	**15**	**103.28**	**2.36**	**0.04895**	**3.6**	**181**	**47**	**62**	**1**	**64**	**3**	**96.5**
#14	**core**	**0.40**	**139048**	**840**	**4.05**	**6111**	**23**	**46.66**	**2.56**	**0.05058**	**1.6**	**220**	**36**	**137**	**3**	**142**	**4**	**96.5**
#39	rim	1.02	10932	140	1.26	1824	167	97.74	1.99	0.04938	4.8	208	80	66	1	68	4	96.4
#08	rim	3.15	4609	62	1.34	343	125	100.11	1.95	0.04911	5.7	207	78	64	1	67	4	96.3
#23	core	10.32	5639	80	2.24	245	20	97.54	2.08	0.04918	6.1	235	138	66	1	68	4	96.3
#51	rim	6.06	4084	48	1.65	3972	106	99.11	2.83	0.05023	5.5	233	114	65	2	68	4	94.8
#35	**rim**	**6.54**	**3696**	**49**	**1.43**	**46**	**648**	**100.42**	**2.10**	**0.05026**	**6.2**	**236**	**132**	**64**	**1**	**68**	**4**	**94.6**
#40	**core**	**3.90**	**5726**	**71**	**2.01**	**2331**	**53**	**97.56**	**2.11**	**0.05046**	**5.6**	**250**	**112**	**66**	**1**	**70**	**4**	**94.4**
#33	**core**	**8.08**	**6137**	**83**	**1.62**	**1491**	**111**	**100.21**	**2.00**	**0.05047**	**13.6**	**398**	**357**	**64**	**1**	**68**	**9**	**94.2**
#52	**core**	**7.08**	**5900**	**71**	**2.53**	**953**	**54**	**96.30**	**2.49**	**0.05143**	**8.5**	**319**	**184**	**67**	**2**	**72**	**6**	**92.6**
#28	**rim**	**8.66**	**8140**	**111**	**1.84**	**259**	**18**	**96.26**	**2.44**	**0.06326**	**7.9**	**707**	**175**	**67**	**2**	**88**	**8**	**75.7**

Butalón tonalite: BU4

#49	**rim**	**14.16**	**2934.48**	**37.59**	**1.69**	**355**	**40**	**98.52**	**4.09**	**0.04225**	**14.1**	**249**	**16**	**65**	**3**	**58**	**8**	**111.7**
#34	**core**	**0.36**	**2625.76**	**32.71**	**1.61**	**668**	**93**	**93.27**	**3.44**	**0.04266**	**15.8**	**254**	**21**	**69**	**2**	**62**	**9**	**110.8**
#35	**rim**	**4.57**	**3506.23**	**43.01**	**1.85**	**317**	**59**	**99.51**	**3.77**	**0.04291**	**19.2**	**317**	**0**	**64**	**2**	**59**	**12**	**109.7**
#33	**core**	**9.57**	**3651.44**	**46.36**	**1.91**	**165**	**123**	**98.03**	**3.99**	**0.04315**	**4.7**	**68**	**0**	**65**	**3**	**60**	**4**	**109.3**
#57	**rim**	**5.51**	**4683.10**	**57.35**	**1.18**	**150**	**215**	**96.08**	**3.58**	**0.04328**	**10.3**	**229**	**337**	**67**	**2**	**61**	**7**	**109.0**
#14	**rim**	**8.99**	**2798.94**	**32.63**	**1.42**	**198**	**69**	**93.00**	**4.34**	**0.04331**	**5.7**	**46**	**0**	**69**	**3**	**63**	**5**	**109.0**
#48	**rim**	**0.47**	**3435.18**	**42.53**	**1.57**	**300**	**121**	**96.58**	**3.35**	**0.04489**	**6.8**	**197**	**108**	**66**	**2**	**63**	**5**	**105.1**
#27	core	3.88	1793.77	23.16	1.20	202	41	95.01	4.21	0.04509	6.2	140	0	68	3	65	5	104.7
#08	core	9.29	3632.79	42.29	1.98	6	2530	96.32	3.70	0.04562	7.3	114	69	67	2	64	5	103.6
#19	core	0.18	4668.53	55.40	2.14	120	173	97.67	3.43	0.04570	8.6	258	64	66	2	63	5	103.5
#07	core	9.46	3095.80	36.22	1.78	282	23	94.66	3.51	0.04640	6.5	127	44	68	2	67	5	101.9
#51	rim	1.81	2443.77	31.00	1.76	200	110	95.91	3.27	0.04643	7.7	264	176	67	2	66	6	101.8
#26	core	9.68	2780.33	34.01	0.99	2444	93	92.36	4.53	0.04696	11.0	226	130	70	3	69	9	100.7
#39	core	3.77	3709.16	45.84	2.39	361	127	93.63	3.24	0.04700	10.9	226	140	68	2	68	8	100.7
#55	**rim**	**1.18**	**32476.41**	**146.97**	**1.74**	**1330**	**66**	**34.70**	**3.50**	**0.04937**	**2.1**	**163**	**48**	**183**	**6**	**182**	**7**	**100.6**
#22	core	0.88	2449.50	28.13	1.48	2453	54	91.75	3.57	0.04722	7.0	204	199	70	3	70	5	100.4
#05	**core**	**2.62**	**3562.30**	**43.07**	**1.90**	**139**	**80**	**101.32**	**3.73**	**0.04701**	**8.7**	**173**	**139**	**63**	**2**	**63**	**6**	**100.3**
#25	rim	1.76	6506.88	78.22	2.17	770	118	95.46	3.42	0.04719	3.7	133	74	67	2	67	3	100.3
#10	core	0.54	6322.08	74.22	1.88	398	161	97.14	3.45	0.04720	3.7	96	43	66	2	66	3	100.2
#06	rim	4.61	6354.60	70.84	1.14	78	530	95.30	3.27	0.04728	3.2	138	75	67	2	67	3	100.0
#20	rim	0.86	3537.87	41.21	1.74	343	204	92.51	3.29	0.04764	9.0	280	229	69	2	70	6	99.5
#53	**core**	**0.06**	**40535.91**	**96.66**	**1.99**	**230**	**1367**	**19.68**	**3.15**	**0.05320**	**2.4**	**336**	**54**	**320**	**10**	**322**	**12**	**99.3**
#50	core	11.77	2220.55	27.77	1.81	215	29	94.61	3.81	0.04774	21.0	352	588	68	3	68	14	99.2
#24	rim	1.78	5927.79	72.12	1.53	741	22	95.21	4.32	0.04776	6.4	209	64	67	3	68	6	99.0
#40	rim	2.77	3058.97	37.85	2.54	169	190	93.87	3.53	0.04784	3.1	165	19	68	2	69	4	98.9
#42	rim	0.50	7104.89	90.87	2.17	1602	83	94.58	3.26	0.04786	4.6	163	74	68	2	69	4	98.9
#54	**rim**	**0.12**	**94497.94**	**226.39**	**1.03**	**9628**	**226**	**20.02**	**4.00**	**0.05346**	**2.2**	**347**	**49**	**314**	**12**	**319**	**10**	**98.7**
#52	rim	0.88	3306.04	41.28	1.80	560	100	96.99	3.53	0.04809	6.6	216	119	66	2	67	5	98.5
#12	core	2.62	4917.32	59.01	2.32	1839	123	96.01	3.50	0.04841	11.5	286	341	67	2	68	8	97.7
#56	core	3.52	7684.89	101.22	1.65	2948	98	99.59	3.53	0.04848	2.7	120	63	64	2	66	3	97.5
#11	rim	0.00	7436.20	85.18	1.86	6503	107	95.03	3.31	0.04871	6.4	187	152	68	2	69	5	97.3
#28	rim	5.44	3074.23	37.14	1.26	268	111	95.53	3.65	0.04866	5.8	266	19	67	2	69	6	97.2
#37	rim	3.63	5524.57	67.86	1.23	641	72	97.41	3.51	0.04879	4.7	192	97	66	2	68	4	97.0
#21	core	2.63	3260.39	38.42	2.13	19	1221	96.02	3.43	0.04956	4.4	194	96	67	2	70	4	95.6
#09	rim	0.60	3696.78	43.23	1.33	284	48	95.23	3.51	0.04956	5.0	211	103	67	2	70	5	95.5
#47	core	0.15	4132.29	53.82	2.23	151	109	97.97	3.28	0.04969	4.5	230	33	65	2	69	4	95.2
#13	rim	0.87	8751.81	101.10	1.47	3296	40	94.26	3.17	0.04988	3.5	224	43	68	2	72	4	95.0
#41	rim	3.32	4393.08	51.90	1.45	1579	57	93.94	3.15	0.05043	2.3	213	53	68	2	73	3	94.0
#23	core	1.14	4467.20	53.17	2.28	164	116	93.34	3.49	0.05166	7.8	256	168	69	2	75	6	92.0
#36	core	4.35	4769.83	57.98	1.85	349	69	91.27	3.61	0.07074	22.4	879	472	70	2	103	24	68.0
#38	**rim**	**1.34**	**2797.39**	**32.82**	**1.53**	**83**	**192**	**89.59**	**3.38**	**0.07633**	**10.5**	**1081**	**213**	**72**	**2**	**113**	**12**	**63.4**

[1] concentration uncertainty c.20%

[2] data not corrected for common-Pb

[3] Concordance calculated as (206Pb-238U age/207Pb-235U age)*100

Decay constants of Jaffey et al. (1971) used

Uncertainties quoted without components related to systematic error unless otherwise stated

Total systematic uncertainties (ssys): 206Pb/238U = 1.0%, 207Pb/206Pb = 0.55% (2s)

Table 3: Results of U-Pb analysis by LA-ICP-MS on zircon from samples BU4, VAR6, D2, GR4, ICAL4 and Moque. Results in bold were not used for age determination.

4.6.2 Moquehue Granite (NPB): MOQUE granite

Zircon crystals have sizes between 50 and 200 μm, are transparent and occur mostly as subhedral and broken crystals. In the CL images (Supplementary Material I-MOQUE) most of the zircons appear fractured, and in a few crystals magmatic zonation can be seen. Thirty-three zircons were analyzed, twenty in rims and twenty-one in cores. From a total of forty-one U-Pb analyzes in this sample, thirty-three of those were concordant (between 95 and 105% of concordance). The TuffZirc algorithm (Ludwig and Mundil, 2002) allows us to obtain an age of 183.99 +1.32 -1.42 Ma with one outlier. Using the concordant data, a weighted average age of 184 ± 2 Ma (MSWD = 1.09) was calculated (Fig. 7b). The Th/U values for these zircon grains are between 1.60 and 4.79 (Table 3). One inherited core zircon (analyses #06, Supplementary Material I -MOQUE) brings a $^{206}Pb/^{238}U$ age of 490 ± 15 Ma and the Th/U value of 1.65.

Fifteen zircons with ages between 179 and 195 Ma were analyzed by Lu-Hf isotopes. Values of $(^{176}Hf/^{177}Hf)i$ ratios between 0.282716 and 0.282807, positive ε_{Hfi} values between 1.71 and 4.98, which determines Meso to Neoproterozoic T_{DM} (average/mafic crust) values of 1.09/1.48 and 0.89/1.19 Ga respectively, were obtained (Fig. 8, Table 4).

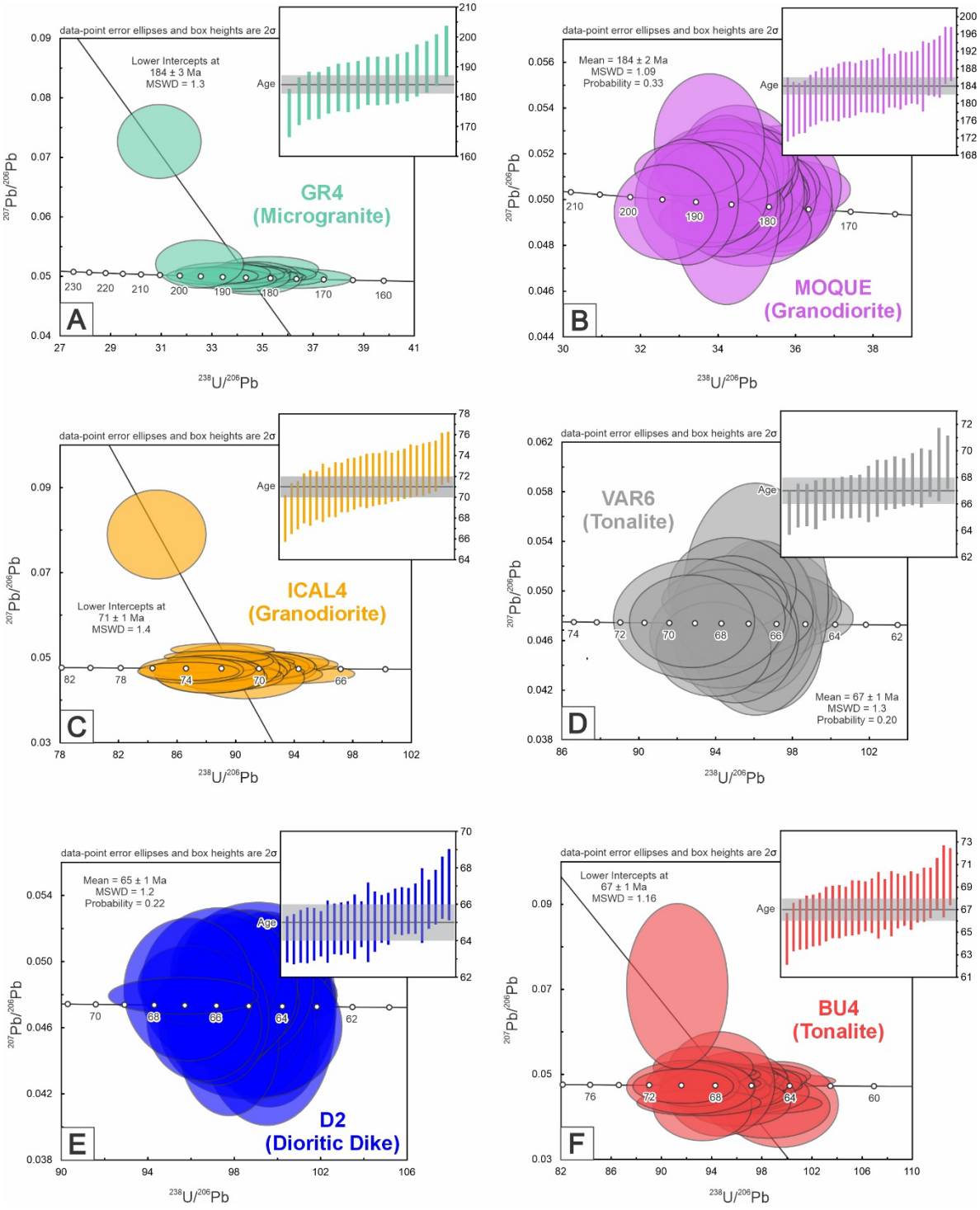


Figure 7: Thera-Wasseburg diagram of the Early Andean rocks: A) sample GR4 and B) sample Moque and of the Andean rocks: C) sample ICAL4, D) sample BU4, E) sample VAR6 and F) sample D2. The location of the samples is in Table 1.

Spot ID	J-Pb Spot ID	$T_{(U-Pb)}$ (Ma)	$^{176}Hf/^{177}Hf$	2SE	$^{176}Lu/^{177}Hf$	2SE	$^{176}Yb/^{177}Hf$	2SE	$(^{176}Hf/^{177}Hf)i$	2SE	$\varepsilon_{Hf}(0)$	$\varepsilon_{Hf}(T)$	error	T_{DM} (Ga) $_{Average}$	T_{DM} (Ga) $_{Mafic}$	T_{DM} (Ga) $_{Felsic}$
JURASSIC ROCKS																
The Host Granite: GR4 microgranite																
52	36	182	0.282782	47	0.001611	11	0.042966	37	0.282776		-0.11	3.75	2.34	0.96	1.29	0.81
54	42	187	0.282774	59	0.001459	10	0.038916	34	0.282769		-0.37	3.60	2.95	0.97	1.31	0.82
57	37	185	0.282684	54	0.001798	13	0.048494	48	0.282677		-3.58	0.31	2.69	1.18	1.60	0.99
58	27	183	0.282803	56	0.001280		0.033718		0.282799		0.65	4.57	2.82	0.91	1.22	0.77
60	22	195	0.282778	43	0.001231	9	0.032487	30	0.282774		-0.24	3.94	2.15	0.96	1.28	0.81
61	10	183	0.282826	33	0.002091		0.055292		0.282819		1.44	5.26	1.65	0.87	1.15	0.73
63	41	185	0.282716	53	0.001795	15	0.048634	49	0.282710		-2.44	1.46	2.65	1.11	1.50	0.93
66	26	192	0.282794	49	0.001517	10	0.040704	36	0.282789		0.32	4.40	2.43	0.93	1.24	0.78
Moquehue granodiorite: MOQUE																
82	21	183	0.282752	29	0.001184	19	0.029535	56	0.282748		-1.15	2.76	1.44	1.02	1.38	0.86
83	5	188	0.282812	37	0.001561	12	0.040120	38	0.282807		0.96	4.94	1.84	0.89	1.19	0.75
84	34	195	0.282768	35	0.001352	8	0.033608	28	0.282763		-0.61	3.54	1.73	0.99	1.32	0.83
85	7	186	0.282772	30	0.001088	8	0.026961	24	0.282769		-0.44	3.55	1.51	0.98	1.31	0.82
86	54	185	0.282775	27	0.001608		0.040706		0.282770		-0.34	3.58	1.37	0.97	1.31	0.82
87	37	179	0.282788	29	0.001479	9	0.037169	31	0.282783		0.11	3.91	1.44	0.95	1.27	0.80
88	9	191	0.282810	33	0.001193	8	0.029950	26	0.282806		0.88	4.98	1.67	0.89	1.19	0.75
89	8	184	0.282789	31	0.001493	9	0.037516	30	0.282784		0.13	4.04	1.53	0.94	1.27	0.80
90	10	186	0.282781	30	0.001801	14	0.046302	45	0.282774		-0.15	3.76	1.48	0.96	1.29	0.81
91	26	186	0.282722	37	0.001502	13	0.038511	40	0.282716		-2.24	1.71	1.84	1.09	1.48	0.92
92	19	181	0.282771	37	0.001026	7	0.025402	21	0.282767		-0.51	3.39	1.84	0.98	1.32	0.83
93	33	182	0.282777	23	0.001916	15	0.047977	46	0.282771		-0.28	3.54	1.17	0.98	1.31	0.82
94	55	183	0.282753	28	0.001165	12	0.028548	35	0.282749		-1.12	2.81	1.41	1.02	1.38	0.86
95	40	188	0.282748	36	0.000921	6	0.022319	18	0.282745		-1.30	2.78	1.78	1.03	1.38	0.87
96	36	182	0.282782	34	0.001300	10	0.032350	30	0.282778		-0.11	3.78	1.69	0.96	1.29	0.81
CRETACEOUS-PALEOGENE ROCKS																
Icalma granodiorite (NPB): ICAL4																
67	21	71	0.282958	30	0.000841	5	0.020836	17	0.282956		6.10	7.63	1.48	0.62	0.86	0.52
68	28	73	0.282945	29	0.000645	4	0.016244	14	0.282944		5.66	7.24	1.46	0.65	0.90	0.54
69	24	72	0.282949	25	0.000695		0.017198		0.282948		5.81	7.37	1.26	0.64	0.88	0.53
70	5	68	0.282968	29	0.001016	7	0.025318	22	0.282966		6.46	7.93	1.44	0.60	0.83	0.50
71	12	73	0.282976	28	0.001067	12	0.027631	35	0.282975		6.76	8.32	1.41	0.58	0.80	0.48
72	25	72	0.282976	32	0.000937	13	0.024041	39	0.282975		6.76	8.31	1.59	0.58	0.80	0.48
73	40	70	0.282948	27	0.000792	5	0.019979	17	0.282947		5.78	7.30	1.33	0.64	0.89	0.53
74	19	74	0.282950	29	0.000628	4	0.015665	13	0.282949		5.84	7.45	1.45	0.64	0.88	0.53
75	22	72	0.282944	29	0.001177	7	0.030892	25	0.282942		5.61	7.15	1.47	0.66	0.90	0.54
76	34	73	0.282999	30	0.001168	16	0.029786	49	0.282997		7.57	9.13	1.49	0.53	0.72	0.44
77	35	70	0.282962	33	0.001418	13	0.037311	41	0.282960		6.26	7.76	1.64	0.62	0.85	0.51
78	8	70	0.282968	35	0.000626	7	0.015546	20	0.282967		6.46	7.99	1.74	0.60	0.83	0.50
79	26	74	0.282955	30	0.000852	11	0.022113	31	0.282954		6.01	7.61	1.52	0.63	0.86	0.52
80	6	72	0.282938	34	0.000701	5	0.017304	14	0.282937		5.42	6.99	1.72	0.67	0.92	0.55
81	27	73	0.282944	25	0.000550	4	0.013596	12	0.282944		5.63	7.23	1.27	0.65	0.90	0.54

Varvarco tonalite: VAR6														
97	24	68	0.282903	29	0.001342	9	0.030130	25	0.282901	4.17	5.63	1.45	0.75	1.04	0.62
98	6	66	0.282867	34	0.000845	8	0.019743	23	0.282866	2.91	4.35	1.72	0.83	1.15	0.68
99	20	68	0.282895	31	0.000884	5	0.018971	15	0.282894	3.89	5.36	1.56	0.77	1.06	0.63
100	37	67	0.282960	36	0.000843	6	0.019150	18	0.282959	6.20	7.66	1.79	0.62	0.85	0.51
101	38	67	0.282912	25	0.000951		0.020337		0.282911	4.51	5.94	1.27	0.73	1.01	0.60
102	22	69	0.282868	27	0.000991		0.020999		0.282867	2.94	4.44	1.37	0.83	1.15	0.68
103	21	69	0.282883	38	0.000526		0.010825		0.282882	3.46	4.96	1.89	0.79	1.10	0.65
104	8	67	0.282908	41	0.000612	5	0.013312	14	0.282907	4.33	5.80	2.07	0.74	1.02	0.61
105	41	65	0.282773	32	0.000688	4	0.015442	13	0.282772	-0.42	1.00	1.61	1.04	1.45	0.85
106	26	67	0.282921	27	0.001142		0.024536		0.282919	4.80	6.22	1.36	0.71	0.98	0.59
107	42	66	0.282873	28	0.000826		0.019697		0.282872	3.11	4.55	1.42	0.82	1.14	0.67
108	13	68	0.282928	30	0.001329		0.031878		0.282926	5.05	6.49	1.49	0.69	0.96	0.57
109	34	66	0.282867	33	0.001073	6	0.023315	19	0.282866	2.91	4.34	1.63	0.83	1.15	0.68
110	9	66	0.282903	29	0.000586	4	0.012170	10	0.282902	4.16	5.60	1.47	0.75	1.04	0.62
111	7	66	0.282885	34	0.000827	5	0.017223	14	0.282884	3.52	4.95	1.72	0.79	1.10	0.65
Varvarco dioritic dique: D2															
37	36	66	0.282904	29	0.000405	3	0.008053	7	0.282903	4.19	5.63	1.44	0.75	1.04	0.61
38	7	64	0.282928	45	0.000905	5	0.020174	16	0.282927	5.06	6.45	2.27	0.69	0.96	0.57
39	42	65	0.282879	29	0.000620	4	0.013338	12	0.282878	3.32	4.74	1.44	0.80	1.12	0.66
40	55	65	0.282883	31	0.000494	3	0.009869	8	0.282882	3.47	4.88	1.54	0.80	1.10	0.65
41	12	65	0.282860	46	0.000607		0.013424		0.282860	2.67	4.09	2.28	0.85	1.18	0.69
42	24	66	0.282920	41	0.000739		0.016476		0.282920	4.79	6.23	2.07	0.71	0.98	0.58
43	37	66	0.282890	34	0.000767		0.017755		0.282889	3.71	5.14	1.71	0.78	1.08	0.64
44	27	65	0.282863	36	0.000588	4	0.012300	12	0.282863	2.77	4.18	1.80	0.84	1.17	0.69
45	34	66	0.282873	47	0.000836	5	0.018534	15	0.282872	3.11	4.54	2.33	0.82	1.14	0.67
46	47	65	0.282896	39	0.000634	5	0.013292	13	0.282896	3.94	5.35	1.96	0.77	1.06	0.63
47	49	64	0.282902	31	0.000739	5	0.016737	14	0.282901	4.15	5.55	1.57	0.75	1.04	0.62
48	53	64	0.282884	34	0.000463	5	0.009610	12	0.282883	3.48	4.89	1.69	0.79	1.10	0.65
49	22	65	0.282858	40	0.000737		0.015684		0.282857	2.59	4.01	1.99	0.85	1.18	0.70
50	54	67	0.282918	32	0.000580		0.011886		0.282917	4.70	6.16	1.61	0.72	0.99	0.59
51	10	64	0.282852	34	0.002034	13	0.044547	36	0.282849	2.36	3.70	1.70	0.87	1.21	0.71
Butalón tonalite: BU4															
21	27	68	0.282902	33	0.000854	5	0.019687	16	0.282901	4.15	5.61	1.64	0.75	1.04	0.62
22	8	67	0.282899	34	0.000783	5	0.017179	14	0.282898	4.04	5.49	1.70	0.76	1.05	0.62
23	19	66	0.282892	28	0.000780	5	0.016742	14	0.282891	3.80	5.22	1.41	0.77	1.07	0.64
24	7	68	0.282929	25	0.000704	4	0.016006	13	0.282928	5.10	6.58	1.26	0.69	0.95	0.57
25	51	67	0.282965	27	0.000813	6	0.018515	16	0.282964	6.36	7.81	1.34	0.61	0.84	0.50
26	26	70	0.282865	32	0.000583	4	0.012179	10	0.282864	2.83	4.34	1.59	0.83	1.16	0.68
27	39	68	0.282925	25	0.000770	5	0.017551	15	0.282924	4.94	6.43	1.25	0.70	0.97	0.58
28	22	70	0.282881	23	0.000720	6	0.015153	15	0.282880	3.40	4.92	1.16	0.80	1.10	0.66
29	25	67	0.282915	31	0.000783	5	0.017070	14	0.282914	4.60	6.05	1.54	0.72	1.00	0.59
30	10	66	0.282895	26	0.000705	4	0.015821	13	0.282894	3.90	5.34	1.29	0.77	1.06	0.63
31	6	67	0.282926	32	0.000475	3	0.009438	8	0.282925	4.97	6.44	1.59	0.70	0.96	0.57
32	20	69	0.282931	35	0.000618	4	0.014531	12	0.282930	5.15	6.66	1.74	0.69	0.95	0.57
33	50	68	0.282925	32	0.000878	5	0.020303	16	0.282924	4.94	6.41	1.60	0.70	0.97	0.58
34	24	67	0.282924	30	0.000680	4	0.014739	12	0.282923	4.90	6.36	1.50	0.70	0.97	0.58
35	40	68	0.282880	29	0.000916	6	0.022200	18	0.282879	3.37	4.84	1.43	0.80	1.11	0.66
36	42	68	0.282910	37	0.000607	4	0.012492	10	0.282909	4.43	5.91	1.84	0.73	1.01	0.60

Parameters

$^{176}Lu = 1.867x10^{-11}$

$^{176}Hf/^{177}Hf$ CHUR = 0.282785 (Bouvier et al. 2008)

$^{176}Lu/^{177}Hf$ CHUR 0.0336 (Bouvier et al. 2008)

$^{176}Hf/^{177}Hf$ DM = 0.283250 (Chauvel and Blichert-Toft 2001)

$^{176}Lu/^{177}Hf$ DM = 0.0384 (Chauvel and Blichert-Toft 2001)

Average Crust = 0.015 (Griffin et al. 2002)

Mafic Crust = 0.022 (Vervoort and Patchett 1996)

Felsic Crust = 0.0093 (Amelin et al. 1999)

Table 4: Results of Lu-Hf isotopes on zircon from samples BU4, VAR6, D2, GR4, ICAL4 and Moque.

4.6.3 Icalma Granodiorite (NPB): ICAL4 granodiorite

Zircon crystals from ICAL4 granodiorite have sizes between 50 and 350 µm, are transparent and occur mostly as subhedral and broken crystals. In the CL images (Supplementary Material I-ICAL4) most of the zircons appear fractured, and in a few crystals magmatic zonation can be seen. Twenty-nine zircons were analyzed, obtaining a total of Thirty U-Pb analyzes in this sample, nine in rims and twenty-one in cores. Twenty-six of those analyzes were concordant (between 95-105% of concordance). Twenty-nine zircons were analyzed, nine in rims and twenty-one in cores. From a total of thirty U-Pb analyzes in this sample, twenty-six analyzes were concordant (between 95-105% of concordance). The TuffZirc algorithm (Ludwig and Mundil, 2002) obtained an age of 71.58 +0.39 -0.84 Ma with one outlier. Using the concordant data and one outlier, a lower intercept of 71 ± 1 Ma (MSWD = 1.4) was calculated (Fig. 7c). The Th/U values for these zircon grains are between 1.24 and 2.90 (Table 3).

Fifteen zircon crystals with ages between 67 and 81 Ma yielded ($^{176}Hf/^{177}Hf$)i values between 0.282937 and 0.282997, positive ε_{Hfi} values between 6.99 and 9.13 and Neoproterozoic-Cambrian T_{DM} (average/mafic crust) values of 0.67/0.92 and 0.53/0.72 Ga respectively (Fig. 8, Table 4).

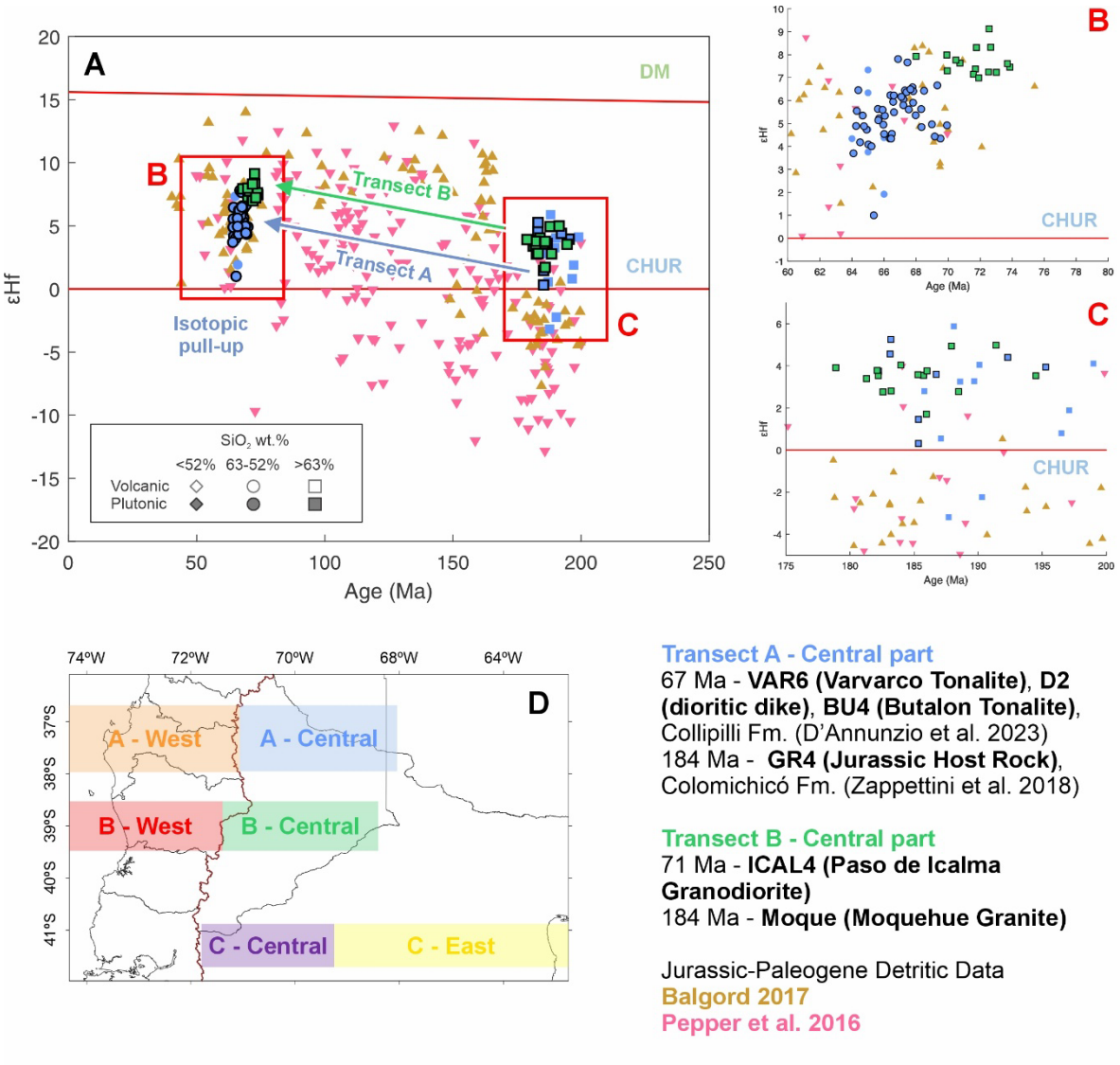


Figure 8: ε_{Hf} diagram of the different transects analyzed. The samples with the thicker black border belong to this work. A) ε_{Hf} diagram of the Jurassic and Cretaceous-Paleogene rocks in the transects A-Central and B-Central. B) Detailed view of Cretaceous-Paleogene part of the graph. C) Detailed view of Jurassic part of the graph. D) Schematic map of the study area showing the location of the transects studied in this work. The construction parameters of the diagrams are in Table 5.

4.6.4 Varvarco tonalite: VAR6

Zircon crystals from VAR6 tonalite have sizes between 100 and 400 μm, are transparent and occur mostly as subhedral and prismatic crystals. In the CL images (Supplementary Material I-VAR6) most of the zircons appear homogeneous, and in a few crystals magmatic zonation can be seen. Twenty-four zircons were analyzed, eleven in rims and seventeen in cores. From a total

of twenty-eight U-Pb analyzes, twenty of those were concordant (between 95-105% of concordance). The TuffZirc algorithm (Ludwig and Mundil, 2002) obtained an age of 66.84 +1.06 -0.48 Ma with three outliers. Using the concordant data, a weighted average age of 67 ± 1 Ma (MSWD = 1.3) was calculated (Fig. 7d). The Th/U values for these zircon grains are between 0.78 and 1.33 (Table 3). One inherited subhedral prismatic zircon shows a marked distinction in the CL images between core and rim (analyzes #40 and #41 respectively, Supplementary Material I-VAR6). The core has a $^{206}Pb/^{238}U$ age of 555 ± 15 Ma and the rim of 65 ± 2 Ma with Th/U values of 0.86 and 1.20 respectively (Table 3). A subhedral prismatic zircon shows a core with a $^{206}Pb/^{238}U$ age of 191 ± 4 Ma and the Th/U value of 2.07 (analysis #5, Supplementary Material I and Table 3). slight zonation in the core.

Fifteen zircon crystals with ages between 65 and 69 Ma yielded ($^{176}Hf/^{177}Hf$)i values between 0.282772 and 0.282959, positive ε_{Hfi} values between 1.00 and 7.66 and Meso to Neoproterozoic T_{DM} (average/mafic crust) values of 1.04/1.45 and 0.62/0.85 Ga (Fig. 8, Table 4).

4.6.5 Varvarco dioritic dike: D2

Zircon crystals from D2 dioritic dike, have sizes between 100 and 350 μm, are transparent and occur mostly as subhedral and prismatic crystals, with few ovoid crystals. In the CL images (Supplementary Material I-D2) most of the zircons appear homogeneous, and in a few crystals magmatic zonation can be seen. Thirty zircons were analyzed, twenty-four in rims and seventeen in cores. From a total of forty-one U-Pb analyzes thirty-four of those were concordant (between 95-105% of concordance). The TuffZirc algorithm (Ludwig and Mundil, 2002) obtained an age of 64.84 +0.77 -0.45 Ma with eight outliers. Using the concordant data, a weighted average age of 65 ± 1 Ma (MSWD = 1.2) was calculated (Fig. 7e). The Th/U values for these zircon grains are between 0.95 and 2.28 (Table 3). The sample presents one inherited zircon, corresponding to analyses #14 (Supplementary Material I-D2). The zircon is subhedral prismatic with a no visible zonation in CL. The core has a $^{206}Pb/^{238}U$ age of 137 ± 3 Ma and the Th/U value of 4.05 (Supplementary Material I-D2 and Table 3).

Fifteen zircon crystals with ages between 64 and 67 Ma yielded ($^{176}Hf/^{177}Hf$)i values between 0.282849 and 0.282927, positive ε_{Hfi} values between 3.70 and 6.45 and Meso to Neoproterozoic T_{DM} (average/mafic crust) values of 0.87/1.21 and 0.69 /0.96 Ga (Fig. 8, Table 4).

4.6.6 Butalón tonalite: BU4

Zircon crystals from sample BU4 tonalite have sizes between 100 and 300 µm, are transparent and occur mostly as subhedral and prismatic crystals, with few ovoid crystals. In the CL images (Supplementary Material I-BU4) most of the zircons appear homogeneous, and in a few crystals show magmatic zonation. Thirty-two zircons were analyzed, twenty-two in rims and nineteen in cores. From a total of forty-one U-Pb analyzes, twenty-nine of those were concordant (between 95-105% of concordance). The TuffZirc algorithm (Ludwig and Mundil, 2002) obtained an age of 67.33 +0.48 -0.52 Ma with two outliers. Using the concordant data, a lower intercept of 67 ± 1 Ma (MSWD = 1.16) was calculated (Fig. 7f). The Th/U values for these zircon grains are between 0.99 and 2.54 (Table 3). The sample presents two inherited zircons, corresponding to three analyses: #53, #54 and #55 (Supplementary Material I-BU4). The zircon corresponding to analyzes #53 and #54 (core and rim, respectively) is subhedral prismatic and shows magmatic zonation in the CL images. The core has a $^{206}Pb/^{238}U$ age of 320 ± 10 Ma and the rim of 314 ± 12 Ma. The Th/U values for this analysis are 1.99 and 1.03 respectively (Table 3). The zircon corresponding to analysis #55 is subhedral and prismatic, presenting a complex zonation in the center. The edge has a $^{206}Pb/^{238}U$ age of 183 ± 6 Ma and a Th/U value of 1.74 (Supplementary Material I-BU4 and Table 3).

Sixteen zircon crystals with ages between 66 and 70 Ma yielded ($^{176}Hf/^{177}Hf$)i values between 0.282864 and 0.282964, positive ε_{Hfi} values between 4.34 and 7.81 and Meso to Neoproterozoic T_{DM} (average/mafic crust) values of 0.83/1.16 and 0.61 /0.84 Ga (Fig. 8, Table 4).

4.7 Sr-Nd isotopes

The Jurassic and Cretaceous-Paleogene plutonic rocks samples analyzed by Sr-Nd are shown in Table 5. In figures are also shown the compiled data from

the Coastal Batholith in Chile, the North Patagonian Batholith, the Naunauco Paleogene Andesitic Belt, Pilcaniyeu Belt, Neuquen Basin, Chon Aike, Los Ángeles Unit (Ianelli et al. 2018). This compilation is found in Supplementary Material II and the correlation with the studied samples is discussed later.

Sample	Lithology	U-Pb Age (Ma)	Rb (ppm)	Sr (ppm)	$(^{87}Sr/^{86}Sr)_m$	2 sigma	$(^{87}Sr/^{86}Sr)i$	$(^{87}Sr/^{86}Sr)_{40\ Ma}$	Sm (ppm)	Nd (ppm)	$^{143}Sm/^{144}Nd$	$(^{143}Nd/^{144}Nd)_m$	2 sigma	$(^{143}Nd/^{144}Nd)i$	eNdi	$(^{143}Nd/^{144}Nd)_{40\ Ma}$	$(\varepsilon Nd)_{40\ Ma}$	T_{DM} (Ga)[1]
JURASSIC ROCKS																		
GR4	Microgranite/Varvarco	184	136.3	39.6	0.72470	0.00002	0.69860	0.71903	9.5	41.6	0.1379	0.512526	0.000018	0.512360	-0.80	0.512490	-1.89	1.04
Moque	Granite/Villa Pehuenia	184	48.7	180	0.70729	0.00003	0.70524	0.70685	4.3	19.6	0.1318	0.512605	0.000014	0.512446	0.88	0.512571	-0.31	0.83
CRETACEOUS-PALEOGENE ROCKS																		
ICAL4	Granodiorite/Villa Pehuenia	71	133.1	298	0.70559	0.00003	0.70429	0.70486	4.7	23.2	0.1234	0.512754	0.000018	0.512697	2.93	0.512722	2.64	0.51
VAR3	Tonalite/Varvarco		77.32	441.8	0.70504	0.00001	0.70455	0.70475	4.0	20.2	0.1210	0.512598	0.000006	0.512545	-0.13	0.512566	-0.39	0.74
VAR6		67	49.2	415.4	0.70728	0.00003	0.70695	0.70709	3.6	16.8	0.1310	0.512665	0.000006	0.512608	1.09	0.512631	0.86	0.71
D2	Dioritic dike/Varvarco	65	29.2	447.6	0.70460	0.00002	0.70443	0.70449	2.5	10.6	0.1423	0.513190	0.000016	0.513130	11.22	0.513153	11.05	-
BU4	Tonalite/Varvarco	67	49.4	425	0.70502	0.00003	0.70470	0.70483	3.3	15.7	0.1264	0.512637	0.000004	0.512582	0.58	0.512604	0.34	0.72
NAU4	Andesite/Colipilli								5.0	24.4	0.1230	0.512814	0.000006	0.512761	4.05	0.512782	3.81	0.41
NAU3-B									3.7	19.5	0.1158	0.512711	0.000023	0.512661	2.10	0.512681	1.84	0.54
CY1	Andesite/Andacollo								5.5	24.9	0.1341	0.512735	0.000010	0.512735	1.89	0.512700	2.21	0.61

[1] Calculate using the DM model of DePaolo (1981b)

$\lambda^{147}Sm = 6.54x10^{-11}$ (Lugmair and Marti 1978)

CHUR values: $^{143}Nd/^{144}Nd = 0.512638$ (Hamilton et al. 1983), $^{147}Sm/^{144}Nd = 0.1967$ (Jacobsen and Wasserburg 1980, Lugmair et al. 1985)

DM values: $^{143}Nd/^{144}Nd = 0.513150$ (Peucat et al. 1988), $^{147}Sm/^{144}Nd = 0.2137$ (Peucat et al. 1988)

$\lambda^{87}Rb = 1.42x10^{-10}$ (Steiger and Jäger 1977)

$^{87}Sr/^{86}Sr = 0.7045$

$^{87}Rb/^{86}Sr = 0.827$

Table 5: Results of Bulk rock Sr-Nd isotopes from samples BU4, VAR3, VAR6, D2, GR4, ICAL4, Moque, NAU3-B, NAU4 and CY1.

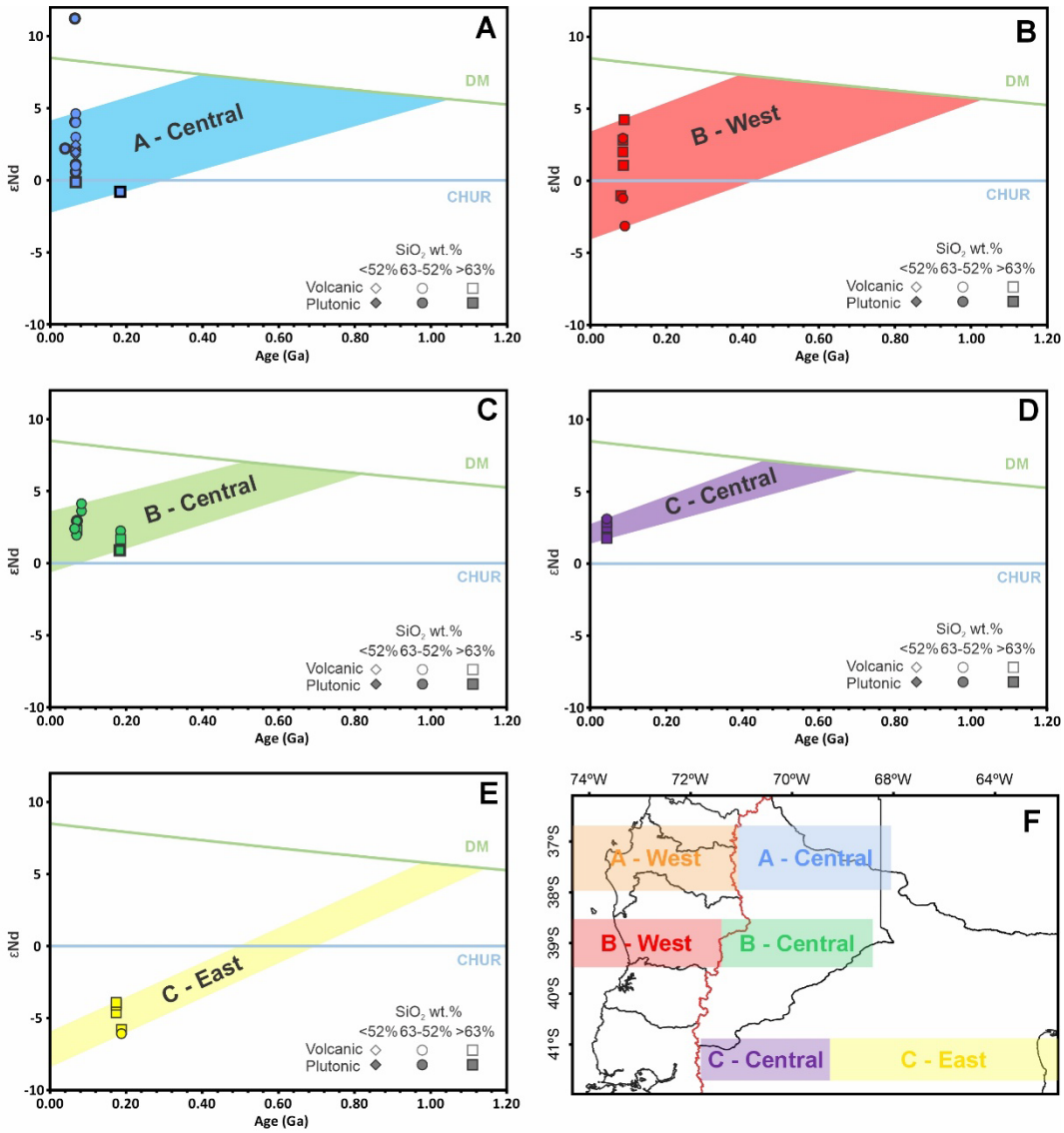
4.7.1 Early Andean Cycle during the extensional/transtensional stage

The Jurassic Host microgranite (GR4) shows a low ($^{87}Sr/^{86}Sr$)i value of 0.69860, (ε_{Nd})i value of -0.80 and the T_{DM} value is 1.04 Ga (Fig. 9A). The Moquehue granodiorite (Moque) shows a ($^{87}Sr/^{86}Sr$)i value of 0.70524, , (ε_{Nd})i value of 0.88 and Neoproterozoic T_{DM} value of 0.82 Ga (Fig. 9C).

4.7.2 Andean Cycle during the compressive/transpressive stage

The Icalma Granodiorite shows a ($^{87}Sr/^{86}Sr$)i value of 0.70429, (ε_{Nd})i value of 2.93 and Lower Paleozoic T_{DM} value of 0.51 Ga (Fig. 9C). The Varvarco Tonalite shows a ($^{87}Sr/^{86}Sr$)i values between 0.70455 and 0.70695 (ε_{Nd})i between -0.13 and 1.09, and Neoproterozoic T_{DM} values between 0.74 and 0.71 Ga (Fig. 9A). The dioritic dique intruded in the Varvarco Tonalite shows a ($^{87}Sr/^{86}Sr$)i value of 0.70443 and ($^{143}Nd/^{144}Nd$)i ratio of 0.513130. The anomalous positive (ε_{Nd})i value of 11.22, above the depleted mantle line, do not allow to calculate the T_{DM} (Fig. 9A). The Butalon Tonalite shows a ($^{87}Sr/^{86}Sr$)i value of 0.70470, (ε_{Nd})i value of 0.58 and Neoproterozoic T_{DM} value of 0.72 Ga (Fig. 9A).

The Colipilli Formation (NAU3-B and NAU4) shows a ($^{143}Nd/^{144}Nd$)i ratios of 0.512661 and 0.512761, which correspond to an (ε_{Nd})i between 2.10 and 4.05, and T_{DM} values between 0.54 and 0.41 Ga. The Cayanta Formation (CY1) shows ($^{143}Nd/^{144}Nd$)i ratio of 0.512735, (ε_{Nd})i value of 1.89 and T_{DM} value of 0.61 Ga (Fig. 9A).



Transect A - Central part
39 Ma - **CY1 (Cayanta Fm.)**
65 Ma - **NAU3B-NAU4 (Collipilli Fm.)**
67 Ma - **VAR3-VAR6 (Varvarco Tonalite)**, **D2 (dioritic dike)**, **BU4 (Butalon Tonalite)**, Los Ángeles Unit (Ianelli et al. 2020)
184 Ma - **GR4 (Jurassic Host Rock)**, Colomichicó Fm. (Zappettini et al. 2018)

Transect B - West part
83-92 Ma - Coastal Batholith: Chaihuín Pluton, Oncol Porphyry, Los Boldos Granitoid, Loncoche Dacitic Porphyry, Laurel Dacitic Porphyry (De la Fuente et al. 2021)

Transect B - Central part
71 Ma - Paso de Icalma Granodiorite (Lucassen et al. 2004), **ICAL4**
184 Ma - **Moque (Moquehue Granite)**
83-86 Ma - Gualletué Plutonic Group (De la Fuente et al. 2021)

Transect C - Central part
Pilcaniyeu Belt (Ianelli et al. 2017)

Transect C - East part
Chon Aike (Pankhurst and Rapela 1985)

Figure 9: ε_{Nd} diagram of the different transects analyzed. The samples with the thicker black border belong to this work. A) ε_{Nd} diagram of the Transect A-Central Part; B) ε_{Nd} diagram of the Transect B-West Part; C) ε_{Nd} diagram of the Transect B-Central Part; D) ε_{Nd} diagram of the Transect C-Central Part; E) ε_{Nd} diagram of the Transect C-East Part; F) Schematic map of the study area showing the location of the transects studied in this work. The construction parameters of the diagrams are in Table 5.

4.8 Trace elements in zircon geochemical data

4.8.1 The Host Granite: GR4 microgranite

All zircons present a depleted LREE (Sm_N/La_N between 0.96 and 90043.81) and enrichment HREE (Lu_N/Gd_N between 15.22 and 24.02) pattern. Have a positive Ce/Ce* anomaly between 11.72 and 19.24, and the negative Eu/Eu* anomaly between 0.13 and 0.85. The Hf values are 6635 and 8224 ppm. The U/Nb and Th/Nb ratios range from 12.62 to 70.78 and 7.65 to 49.24, respectively (Supplementary Material III).

The zircons present scores between 5 and 12 (Ni et al. 2020), with the best zircons being 1, 6 and 9. The calculated temperatures were T1: 704-735°C and T2: 729-763°C. T3 and T4 were not calculated because the sample does not have pressure data. For the calculation of fO_2 and ΔFMQ, the temperature T2 was used and zircons 1 and 9 that did not pass the criterion Ce/Ce* ≤ 100 were discarded. The value of log fO_2 is -13.50 and corresponds to a value of ΔFMQ = 2.07. For the calculation of depth to Moho Z4, zircon 1 that did not pass the criterion Eu/Eu* = 0.1-0.6 was discarded, obtaining values in the range of 39-52 km (Supplementary Material IV).

4.8.2 Moquehue Granodiorite (NPB): MOQUE granodiorite

All zircons present a depleted LREE (Sm_N/La_N between 0.83 and 587.77) and enrichment HREE (Lu_N/Gd_N between 9.61 and 37.23) pattern. Have a positive Ce/Ce* anomaly between 1.42 and 128.14, and the negative Eu/Eu* anomaly between 0.05 and 1.12. The Hf values are 6696 and 9024 ppm. The U/Nb and Th/Nb ratios range from 17.71 to 90.73 and 9.81 to 91.50, respectively (Supplementary Material III).

The zircons present scores between 3 and 11 (Ni et al. 2020), with the best zircons being 3, 9, 10, 11, 13 and 15. The calculated temperatures were T1: 726-776°C and T2: 753-810° C, discarding zircons 3 and 11 that do not meet the criterion Ti = 2-24 ppm. T3 and T4 were not calculated because the sample does not have pressure data. For the calculation of fO_2 and ΔFMQ, the temperature T2 was used and zircons 10, 11, 12 and 13 that do not pass the criterion Ce/Ce* ≤ 100 were discarded. The values of log fO_2 are -6.73 to -12.82 and corresponds to values of ΔFMQ = 0.21-1.72. For the calculation of depth to Moho Z4, zircons 9, 12 and 13 that did not pass the criterion Eu/Eu* = 0.1-0.6 were discarded, obtaining values in the range of 41-58 km (Supplementary Material III).

4.8.3 Icalma Granodiorite (NPB): ICAL4 granodiorite

All zircons present a depleted LREE (Sm_N/La_N between 0.06 and 51104.93) and enrichment HREE (Lu_N/Gd_N between 16.67 and 63.00) pattern. Have a positive Ce/Ce* anomaly between 1.96 and 1503.52, and the negative Eu/Eu* anomaly between 0.17 and 1.30. The Hf values are 7038 and 9460 ppm. The U/Nb and Th/Nb ratios range from 98.22 to 221.66 and 69.25 to 366.75, respectively (Supplementary Material III).

The zircons present scores between 3 and 10 (Ni et al. 2020), with the best zircons being 1, 13 and 15. The calculated temperatures were T1: 754-808°C and T2: 784-845°C, discarding zircon 13 that does not meet the criterion Ti = 2-24 ppm. T3 and T4 were not calculated because the sample does not have pressure data. For the calculation of fO_2 and ΔFMQ, the temperature T2 was used and zircon 1 that did not pass the criterion Ce/Ce* ≤ 100 was discarded. The value of log fO_2 is -12.26 and corresponds to a value of ΔFMQ = 2.83. For the calculation of depth to Moho Z4, zircons 1 and 15 that did not pass the criterion Eu/Eu* = 0.1-0.6 were discarded, obtaining values in the range of 39-50 km (Supplementary Material III).

4.8.4 Varvarco tonalite: VAR6

All zircons present a depleted LREE (Sm_N/La_N between 0.23 and 1522.55) and enrichment HREE (Lu_N/Gd_N between 9.94 and 189.17) pattern. Have a positive Ce/Ce* anomaly between 1.09 and 16.35, and the negative Eu/Eu*

between of 0.34 and 1.42. The Hf values are 7362 and 10297 ppm. The U/Nb and Th/Nb ratios range from 48.34 to 143.39 and 23.14 to 101.66, respectively (Supplementary Material III).

The zircons present scores between 3 and 11 (Ni et al. 2020), with the best zircons being 2, 5, 6, 8 and 14. The calculated temperatures were T1: 710-730°C and T2: 735-758°C. The temperatures T3: 780-888°C and T4: 716-737°C were calculated with the pressure data in amphiboles of Assis et al. (2022). For the calculation of fO_2 and ∆FMQ, the temperature T3 was used, and it was necessary to choose zircon 1 with a score of 6, since the others do not pass the criterion Ce/Ce* ≤ 100. The value of log fO_2 is -12.37 and corresponds to a value of ∆FMQ = 2.52. For the calculation of depth to Moho Z4, zircons 5, 6 and 8 that did not pass the criterion Eu/Eu* = 0.1-0.6 were discarded, obtaining values in the range of 56-71 Km (Supplementary Material III).

4.8.5 Varvarco dioritic dike: D2

All zircons present a depleted LREE (Sm_N/La_N between 0.25 and 644.70) and enrichment HREE (Lu_N/Gd_N between 6.96 and 113.27) pattern. Have a positive Ce/Ce* anomaly between 1.07 and 321.66, and the negative Eu/Eu* between of 0.29 and 0.95. The Hf values are 7569 and 10084 ppm. The U/Nb and Th/Nb ratios range from 53.97 to 114.33 and 26.57 to 121.56, respectively (Supplementary Material III).

The zircons of this sample present scores from 2 to 11 (Ni et al. 2020), with the best zircons being 3, 4, 5, 7 and 13. The calculated temperatures were T1: 696-729°C and T2: 720-756°C. T3 and T4 were not calculated because the sample does not have pressure data. For the calculation of fO_2 and ∆FMQ, the temperature T2 was used and zircon 7 that did not pass the criterion Ce/Ce* ≤ 100 was discarded. The values of log fO_2 are -13.93 to -12.88 and corresponds to values of ∆FMQ = 2.07-2.86. For the calculation of depth to Moho Z4, zircons 5 and 13 that do not pass the criterion Eu/Eu* = 0.1-0.6 were discarded, obtaining values in the range of 43-74 km (Supplementary Material III).

4.8.6 Butalón tonalite: BU4

All zircons present a depleted LREE (Sm_N/La_N between 1.16 and 1657) and enrichment HREE (Lu_N/Gd_N between 30.13 and 73.90) pattern. Have a positive Ce/Ce* anomaly between 17.17 and 402.37, and the negative Eu/Eu* anomaly between 0.20 and 0.97. The Hf values are between 7469 and 9701 ppm. The U/Nb and Th/Nb ratios range from 48.20 to 128.14 and 23.67 to 69.81, respectively (Supplementary Material III).

The zircons present scores between 4 and 12 (Ni et al. 2020), with the best zircons being 2, 11, 13, and 14. The calculated temperatures were T1: 711-748°C and T2: 736-777°C. T3 and T4 were not calculated because the sample does not have pressure data. For the calculation of fO_2 and ΔFMQ, the temperature T2 was used and zircons 2 and 13 that did not pass the criterion Ce/Ce* ≤ 100 were discarded. The values of log fO_2 are -14.12 to -13.29 and corresponds to values of ΔFMQ = 1.20-1.96. The depth to Moho Z4 exhibits values in the range of 37-80 km (Supplementary Material III).

4.9 Discussion

The Andes represent an exceptional example of continental margin magmatism related to subduction. Different subduction segments in two main periods of time show different magma sources, either more crustal or more mantle derived as it was indicated by chemical composition and Nd-Sr-Hf isotopes. Different tectonic regimes, such as compressive or extensional, and different emplacement mechanisms developed under these major tectonic regimes, were invoked in the past as the main causes for these major changes in the magmatic record.

Our data and data from the bibliography, were put together and they analyzed by sector. We divided the areas from north to south into three transects (Fig. 2, Supplementary Material II): North (~37°S, Transect A, denoted with TA), Central (~39°S, Transect B, denoted with TB) and South (~42°S, Transect C, denoted with TC) transects. Every Transect were divided from west to east into West, Central and East parts. The dataset is distributed for Jurassic time into TA-West and Central, TB-West and Central, and TC-East transects. The Cretaceous-

Paleogene time comprise dataset distributed into TA-Central, TB-West and Central, and TC-Central transect. Our data are specifically from TA-Central part (Early Jurassic to Paleocene) and TB-Central part also (Early Jurassic to Late Cretaceous).

So, in this section, we compare the geochemistry, geochronology, Sr-Nd-Hf isotopic data and REE elements in zircon of the studied units with those intrusive/extrusive units that crop out in this sector of the Andes. The objective is to contribute with the understand of evolution of the Andes in the Early Andean Cycle and during the Andean cycle through the evolution in composition and isotopes of the analyzed available dataset for the Andes in this sector.

4.9.1 Isotopic magmatic characterization of the Early Andean and Andean Cycles

The Pre and Jurassic Early Andean Cycle: extensional/transtensional stage

Northern Transect (TA)

West part (TA-West) is represented by the collected data from the north part of Coastal Batholith (Cordani et al. 1976; Dávila et al. 1979; Gana and Hervé 1983; Hervé et al. 1988; Vásquez Illanes 2008), with ages between 308 Ma and 155 Ma. Composed by quartz-diorite to granite, with tholeiite to high-k calc-alkaline signatures (Fig. 4A-B). Two groups of rocks can be differentiated: intermediate rocks classified as arc volcanic, and more acidic ones related with intraplate magmatism (Fig. 4B-C). The Carboniferous rocks have more radiogenic ($^{87}Sr/^{86}Sr$)i values of 0.74688 than Jurassic rocks with ($^{87}Sr/^{86}Sr$)i of 0.70058 (Fig. 10 and 11).

Central part (TA-Central) is represented by the collected data from the Jurassic Host Granite (GR4) at Varvarco locality and rocks of Colomichicó Fm. (Zappettini et al. 2018). The micrographic texture exhibits by the Jurassic Host Granite is a very common texture in A-type granitoids (Whalen et al. 1987). This granite plots in the alkaline magma field, showing high K_2O content, with negative Eu anomalies, typical of hot-dry-reduced magmas (Fig. 4; Christiansen 2005;

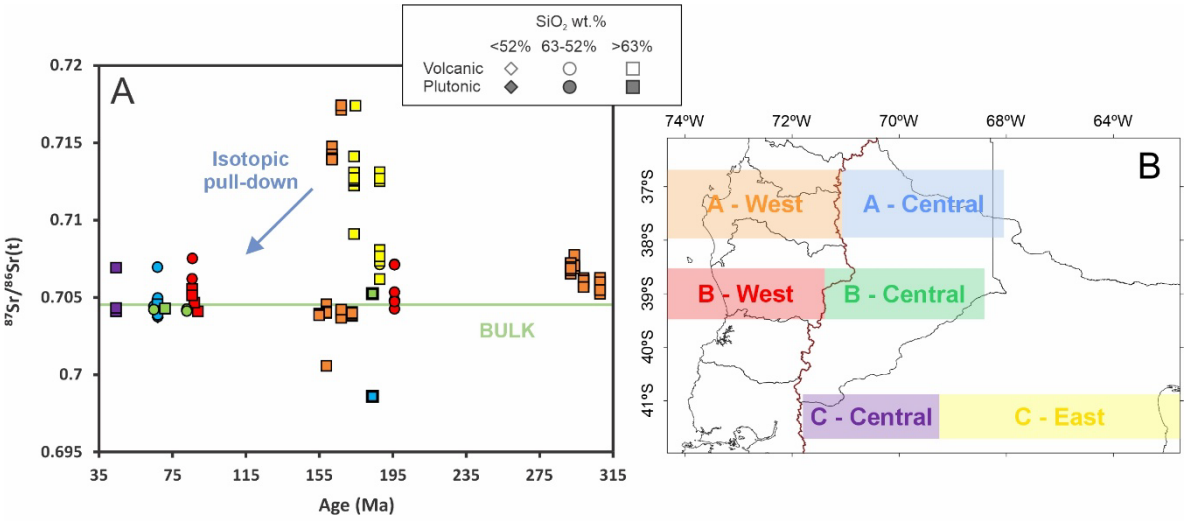
Christiansen and McCurry 2008; Bachmann and Bergantz 2008). In rift-related tectonic environments high melting temperatures (>830ºC) (Clemens et al. 1986) are required to generate A-type granite magmas, probably related with the emplacement of mantle derived basic magmas in the crust.

The GR4 sample shows a anormal low ($^{87}Sr/^{86}Sr$)i value of 0.69860 (Fig. 9 and 10) and ($^{143}Nd/^{144}Nd$)i ratio of 0.512360, that represents a nearly negative (ε_{Nd})i value of -0.80 and a Mesoproterozoic T_{DM} value of 1.04 Ga (Fig. 9). It is possible to see an increase in the (ε_{Nd})i to the eats, when our data are compared with the volcanic rocks of the Neuquén Basin. These rocks show a positive (ε_{Nd})i between 1.66 and 2.24, and Tonian T_{DM} values between 0.98 and 0.83 Ga (Fig. 9).

The values of ε_{Nd} and ε_{Hf} are mantellic (considering the error associated with the slightly negative ε_{Nd} value) and the corresponding values of T_{DM} for the average crust are close (1.04 Ga for Nd and a maximum of 1.00 Ga for Hf, Fig. 8 and 9)

The Colomichicó Fm. is composed by basaltic andesites to rhyolites, with a tholeiitic to High-K calc-alkaline trend, classified in volcanic arc ambient with a component of within-plate for the more acidic rocks.

In terms of Hf isotopes, the Jurassic Host Granite plus volcanic rocks from the Colomichicó Fm., show similar less positive ε_{Hf} data (Fig. 8), with some negative ε_{Hf} data for the volcanics of the Colomichicó Fm.



Transect A - West part
308-155 Ma - Santo Domingo, Reñaca, Nahuelbuta, Albarrobo, Cuesta de Zapata, Quintay, Las Cruces, Laguna Verde (Cordani et al. 1976, Hervé et al. 1988)

Transect A - Central part
67 Ma - **VAR3-VAR6 (Varvarco Tonalite)**, **D2 (dioritic dike)**, **BU4 (Butalon Tonalite)**, Los Ángeles Unit (Ianelli et al. 2020)
184 Ma - **GR4 (Jurassic Host Rock)**, Colomichicó Fm. (Zappettini et al. 2018)

Transect B - West part
83-92 Ma - Coastal Batholith: Chaihuín Pluton, Oncol Porphyry, Los Boldos Granitoid, Loncoche Dacitic Porphyry, Laurel Dacitic Porphyry (De la Fuente et al. 2021)
196 Ma - Panguipulli Batholith (Parada and Munizaga 1978)

Transect B - Central part
71 Ma - Paso de Icalma Granodiorite (Lucassen et al. 2004), **ICAL4**
83-86 Ma - Gualletué Plutonic Group (De la Fuente et al. 2021)
184 Ma - **Moque (Moquehue Granite)**

Transect C - Central part
44 Ma - Pilcaniyeu Belt (Ianelli et al. 2017)

Transect C - East part
174-188 Ma - Chon Aike (Pankhurst and Rapela 1985)

Figure 10: A) ($^{87}Sr/^{86}Sr$)i vs. Age diagram. B) Schematic map of the study area showing the location of the transects studied in this work. The construction parameters of the diagrams are in Table 5.

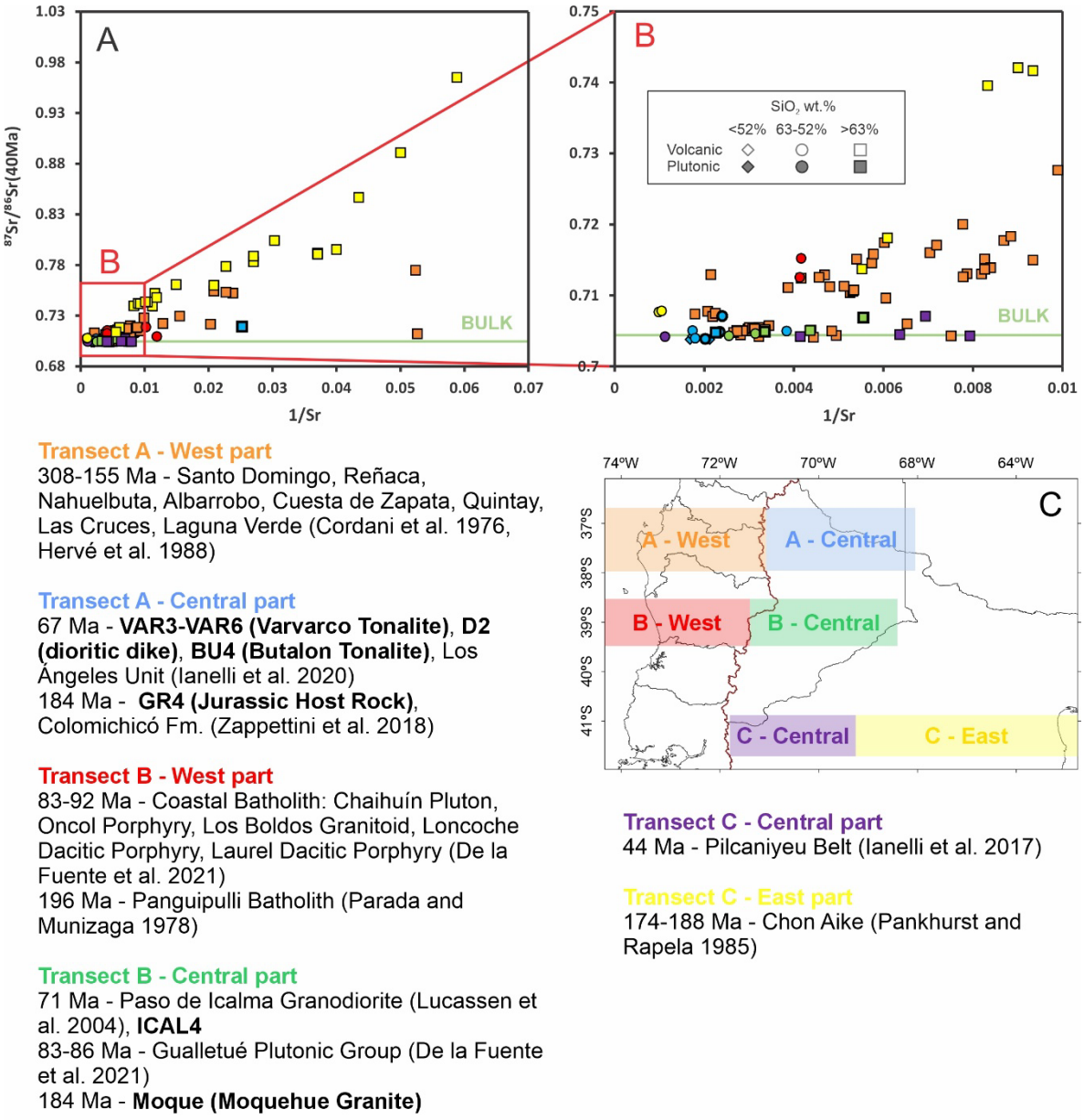


Figure 11: A) ($^{87}Sr/^{86}Sr$)i vs. 1/Sr diagram. B) Detailed view of the 1/Sr values between 0 and 0.01. C) Schematic map of the study area showing the location of the transects studied in this work. The construction parameters of the diagrams are in Table 5.

Central Transect (TB)

West part (TB-West) is represented by the Jurassic part of Panguipulli Batholith of 196 Ma (Parada and Munizaga 1978; Munizaga et al. 1988), composed for calc-alkaline tonalites with ($^{87}Sr/^{86}Sr$)i between 0.70426 to 0.70714 (Fig. 10 and 11). These rocks of intermediate character do not have Nd, Hf or geochemistry data of minor elements that allow a better classification and

suggests a subcortical origin with an enrichment in Sr radiogenic (Parada and Munizaga 1978).

Central part (TB-Central), represented by the Moquehue Granite (Moque), shows a ($^{87}Sr/^{86}Sr$)i value of 0.70524, ($^{143}Nd/^{144}Nd$)i ratio of 0.512446, a nearly positive (ε_{Nd})i value of 0.88 and Neoproterozoic T_{DM} value of 0.82 Ga. A geochemical signature is typical of arc magmas, as it shows moderate K_2O content, and plots in the volcanic arc granite fields (Fig. 4b, c, d). Its Eu anomaly is not highly negative, suggesting a less important plagioclase fractionation, as it probably is related with a cold-wet-oxydized magmatism (Fig. 4e, Christiansen 2005; Christiansen and McCurry 2008; Bachmann and Bergantz 2008), because in water-rich andesitic melts liquidus of plagioclase is suppressed by > 100 °C (Sisson and Grove, 1993; Molina et al., 2009). In terms of Hf, ε_{Hf} values for these rocks are between 1.71 and 4.98, with T_{DM} between 0.91 and 0.70 Ga, coinciding with the positive trend and T_{DM} of Nd.

Southern Transect (TC)

Eastern part (TC-East), represented for volcanic rocks from Chon Aike (Pankhurst and Rapela 1995). These rocks are composed for andesites to rhyolites with High-K calc-alcaline to shoshonite signatures, classified into within plate ambient (Fig. 4).

The Sr-Nd isotopic data indicate crustal sources or mantle magmas contaminated with crust (Fig. 8). It shows a ($^{87}Sr/^{86}Sr$)i values between 0.70381 and 0.71653, negative (ε_{Nd})i between -6.09 and -3.92, and Meso to Neoproterozoic T_{DM} values between 1.14 and 0.98 Ga (Fig. 9 and 12).

The andesitic part of these rocks would have an origin derived from the partial melting of Greenvillian mafic crust, while the magmas of rhyolitic composition would derive from the fractional crystallization of these andesites, becoming contaminated with crust during their ascension (Pankhurst and Rapela 1995).

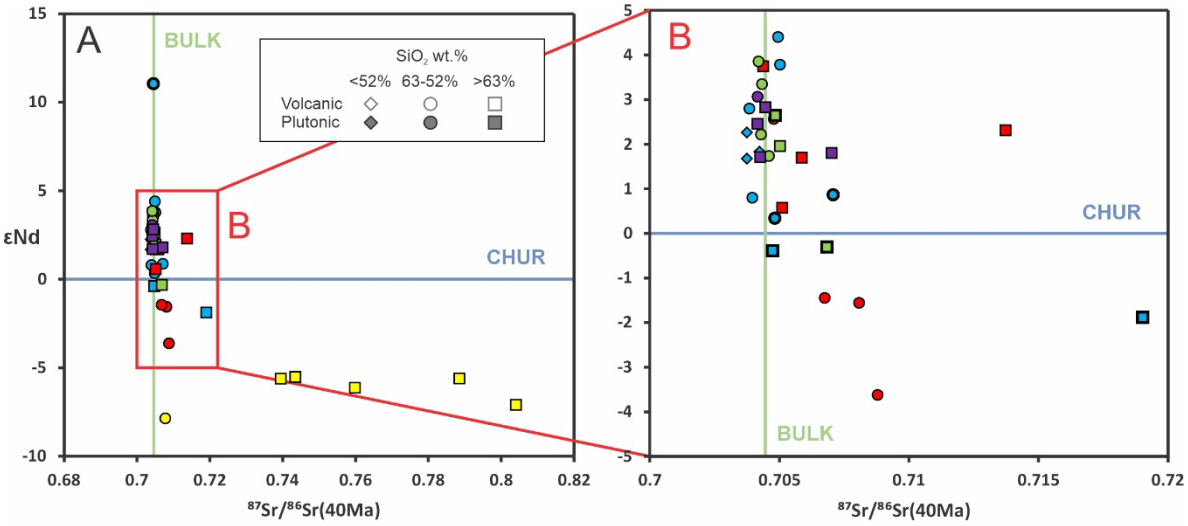
In conclusion, Jurassic magmatism extends through transects A and B and through the eastern part of transect C, in a NW-SE orientation. The TA present

in the west, plutonic rocks, composed by diorites to granites with tholeiitic to High-k calc-alkaline trend, classified in volcanic arc and within-plate ambient. In the Central part, have mostly acidic rocks, granites with a high-K calc-alkaline trend, and rhyolites with a tholeiitic to high-K calc-alkaline trend, both classified in the within-plate ambient.

The TB present in the west, intermediate rocks with a subcortical origin, while for the central part, the rock are more acidic, with calc-alkaline granites typical of volcanic arc environments.

The Jurassic rocks in the TC are found only in the eastern part, consisting mostly of acidic volcanic rocks. These rocks exhibit a high-K calc-alkaline to shoshonitic trend and share the same within-plate tectonic setting.

The Sr, Nd and Hf isotopic data of Andes between 36º to 42º S show that the plutonic rocks related with the Pre-Cuyo Group (Jurassic Host Granite) and the Moquehue granite representative of the North Patagonian Batholith in the Early Andean stage show Sr and Nd data more compatible with a formerly mantle-derived magma related with subduction environments with crustal contamination. The $^{87}(Sr/^{86}Sr)i$ looks like nearly constant for the studied rocks with values ~0.705, except for the Coastal Batholith (western part) and Chon Aike volcanic rocks (Southern Transect-Eastern part), that shows more heterogeneous sources.



Transect A - Central part
67 Ma - **VAR3-VAR6 (Varvarco Tonalite)**, **D2 (dioritic dike)**, **BU4 (Butalon Tonalite)**, Los Ángeles Unit (Ianelli et al. 2020)
184 Ma - **GR4 (Jurassic Host Rock)**, Colomichicó Fm. (Zappettini et al. 2018)

Transect B - West part
83-92 Ma - Coastal Batholith: Chaihuín Pluton, Oncol Porphyry, Los Boldos Granitoid, Loncoche Dacitic Porphyry, Laurel Dacitic Porphyry (De la Fuente et al. 2021)

Transect B - Central part
71 Ma - Paso de Icalma Granodiorite (Lucassen et al. 2004), **ICAL4**
184 Ma - **Moque (Moquehue Granite)**
83-86 Ma - Gualletué Plutonic Group (De la Fuente et al. 2021)

Transect C - Central part
44 Ma - Pilcaniyeu Belt (Ianelli et al. 2017)

Transect C - East part
174-188 Ma - Chon Aike (Pankhurst and Rapela 1985)

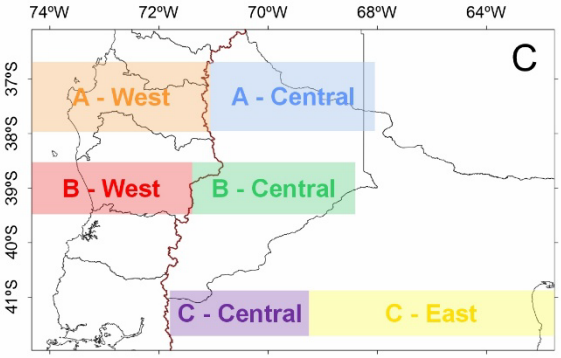


Figure 12: A) ε_{Nd} vs. ($^{87}Sr/^{86}Sr$) recalculated to 40 Ma. B) Detailed view of the red rectangle of figure A. C) Schematic map of the study area showing the location of the transects studied in this work.

The Andean Cycle during the Late Cretaceous-Paleogene time: compressive/transpressive stage

Northern Transect (TA)

Central part (TA-Central) is represented in this work by the Butalon Tonalite (BU4), Varvarco tonalite (VAR6) and dioritic dike (D2) intruded into the Varvarco tonalite (this work). Varvarco and Butalon tonalites are similar characteristics, composed for tonalites with cal-alkaline signature typical of volcanic arc ambient (Fig. 5). The ($^{87}Sr/^{86}Sr$)i values of this rocks are between 0.70455 and 0.70695 (Fig. 10 and 11). The (ε_{Nd})i values of this rocks are slightly positive, between -0.13 to 1.09, and T_{DM} of 0.71-0.74 Ga (Fig. 9 and 12). These values are coincident with the positive (ε_{Hf})i values, and average T_{DM} of 0.54-0.76 Ga (Fig. 8).

The dioritic dike intruded in Varvarco tonalite are calc-alkaline and have a volcanic arc signature in agree with the host rock (Fig. 5), however, the (ε_{Nd})i value is above the depleted mantle, so the T_{DM} cannot be calculated (Fig. 9 and 12). Have a minor value of ($^{87}Sr/^{86}Sr$)i of 0.70443 (Fig. 9 and 10). In terms of Hf isotopes, the (ε_{Hf})i present positive and similar values and coincident T_{DM} of 0.63-0.80 Ga (Fig. 8).

The Colipilli Formation (NAU3-B and NAU4) are composed by andesites with calc-alkaline and volcanic arc signature (Fig. 5) with shows a positive (ε_{Nd})i between 2.10 and 4.05, and Cambrian-Ordovician T_{DM} values between 0.54 and 0.41 Ga (Fig. 9). The Cayanta Formation (CY1), composed by andesites with the same chemical characteristics shows less positive (ε_{Nd})i value of 1.89 and Ediacaran T_{DM} of 0.61 Ga (Fig. 9).

The Ángeles Unit is composed for basaltic to andesitic rocks, characterized by a subalkaline tholeiitic to alkaline trend, and classified in the volcanic arc ambient (Fig. 5). Shows a ($^{87}Sr/^{86}Sr$)i values between 0.70371 and 0.70496 (Fig. 10 and 11) and a (ε_{Nd})i between 1.00 and 4.62, and T_{DM} values between 0.76 and 0.40 Ga (Fig. 9). Los Angeles Unit could potentially be interpreted as the beginning of an incipient slab window associated with the subduction of the Farallon-Aluk spreading center (Ianelli et al. 2018).

So, the TA-Central part is characterized by low ($^{87}Sr/^{86}Sr)_I$ between 0.70371 for Los Angeles Unit and 0.70695 for Varvarco Tonalite. The (ε_{Nd})i is nearly negative to positive with values between -0.13 for Varvarco Tonalite and 4.62 for Los Angeles Unit. The T_{DM} vary from Neoproteroic to Paleozoic.

Central Transect (TB)

Western part (TB-West) is represented for compilated rocks of the Coastal Batholith (De la Fuente et al. 2021) composed for microtonalites to microgranites with a calc-alkaline to high-K calc-alcaline trend (Fig. 5). In tectonic environment diagrams, they are classified as volcanic arc rocks and show the evolution from tonalite to granite by successive fractional crystallization. The ($^{87}Sr/^{86}Sr$)i ratio (0.70411-0.70745) and (ε_{Nd})i (+4.24 to -3.09) values of these rocks (Figs. 9, 10, 11 and 12) indicate that depleted mantle derived-magmas were contaminated by assimilation of crustal material at the base of the paleo accretionary prism or by subduction erosion (De la Fuente et al. 2021).

Central part (TB-Central) is represented by plutonic rocks compiled of the North Patagonian Batholith, composed by tonalites and granodiorites with calc-alkaline to High-K cal-alkaline trend, classified in volcanic arc environment (Fig. 5). shows a ($^{87}Sr/^{86}Sr$)i values between 0.70420 and 0.70428 (Fig. 9 and 10). The ($^{143}Nd/^{144}Nd$)i ratios are 0.512648 and 0.512677, which correspond to an (ε_{Nd})i between 1.95 and 2.39, and T_{DM} values between 0.70 and 0.66 Ga (Fig. 9). Compared to these rocks, the ICAL4 sample of this work, presents similar ($^{87}Sr/^{86}Sr$)i value and slightly more positive (ε_{Nd})i values (Fig. 10 and 11), with a T_{DM} lower than 0.51 Ga. The (ε_{Hf})i in this sample have values equally positive and the average T_{DM} coincides with that calculated with Nd isotopes (Between 0.46 to 0.59 Ga, Fig. 8, Table 4).

Southern Transect (TC)

Central part (TC-Central) is represented in this work by the Pilcaniyeu Belt (Ianelli et al. 2017) composed by dacites and rhyolites with a High-K calc-alkaline trend, with a whitin-plate signature (Fig. 4) that shows a ($^{87}Sr/^{86}Sr$)i values between 0.70411 and 0.70692 (Fig. 10 and 11). The ($^{143}Nd/^{144}Nd$)i ratios are 0.512670 and 0.512740, which correspond to an (ε_{Nd})i between 1.75 and 3.10, and Cambrian-Ordovician T_{DM} values between 0.55 and 0.46 Ga (Fig. 9).

In conclusion, Cretaceous-Paleogene magmatism extends from the central part of transect A, into transect B and into the central part of transect C, with an N-S orientation following the volcanic arc.

The Central part of TA is composed by volcanic and plutonic rocks of intermediate composition and calc-alkaline signature. Only some rocks in the Los Angeles Unit, in the northern part of this area tend to high-K calc-alkaline rocks and all the rocks in the transect have a volcanic arc signature.

The western part of TB is composed by plutonic rocks, tonalites to granites with a trend calc-alkaline to high-K and a volcanic arc signature. In the central part, tonalites and granodiorites predominate, with a typical arc signature and calc-alkaline trend.

The central part of TC is composed by volcanic rocks, dacites and rhyolites with a high-K calc-alkaline trend and a within-plate affinity.

The Late Cretaceous-Paleogene rocks of the Naunauco Belt, as well as the Late Cretaceous Granodiorite, represented in this work by sample ICAL4, from the North Patagonian Batholith are typical of arc environments (Fig. 5). They show gentle Eu anomalies, typical of cold-wet-oxydized magmas, and, on the other hand, fractionation of amphibole and clinopyroxene (without garnet fractionation) in the residual source. In general, the Late Cretaceous-Paleogene rocks bear more mantle-like sources than the Early Jurassic rocks.

4.9.2 Magmatic fertility and crustal thickness

The REE values in zircon show a dispersed and depleted LREE pattern in the most of samples (Supplementary Material III), because LREEs elements tend to be incompatible in zircon and more susceptible to alteration, unlike HREEs elements with a normal enriched pattern (Lu_N/Gd_N between 10 and 74).

The U/Nb > 20, U/Th > 10 and Hf values between 5000 and 14000 ppm belong to magmatic arc granitic rocks without interaction with fluids or surface materials. The Ti values between 2 and 24 ppm and temperatures between 600 and 850ºC represent that the magmatic system remained closed, without alteration in the zircon chemistry.

The high Ce/Ce* and low Eu/Eu* anomalies in all the samples patterns correspond to oxidized magmas, in agree with positive ΔFMQ values between

+1.20 and +3.36. For subduction systems, the ΔFMQ values are between +0.5 to +2 (Richards 2015) and for porphyry-type ore deposits, requires a moderate oxidation state (ΔFMQ ≈ +1) in combination with high water and sulfide content to mobilize metals such as Cu and Mo from the asthenospheric mantle wedge above subduction zones into the upper crust (Richards 2015).

In terms of fO_2 and temperature, for rocks between 700 and 800ºC such as those in this work, the transition between I-type magmas and porphyry Cu-Au deposits depends on fO_2. Values between 700-750ºC with log fO_2 between -12 to -14 approx. could be a fertile rock and be a possible deposit (Burnhamand Ohmoto 1980, Hedenquist and Richards 1998, Richards 2015).

For this work, all samples approximately meet the temperature and fO_2 requirements, however, Butalon tonalite (BU4) and Moquehue granite (MOQUE) have the lowest ΔFMQ values close to +1 (1.20 and 1.72 respectively) and could mean a possible deposit. Remarking that near of the Varvarco area, locality where the BU4 sample was collected, exist porphyritic deposits associated with Colipilli Fm. in the Caycayén and Andacollo districts.

Respect of crustal thickness or depth to Moho, the values often with geochemical data (Sr/Y_N, La/Yb_N and Ce/Y ratios) are lower than REE values in zircon (Eu/Eu* anomalies). For the TA-Central, geochemical values of BU4, D2, VAR6 and GR4 are between 27 and 37 km deep and the REE values between 37 and 80 km. For the TB-Central, geochemical values of ICAL4 and MOQUE are between 25 and 30 km deep and the REE values between 39 and 58 km. The differences between the two systems are large, if we consider that the average crust in these areas should be ≈ 30 km. For this reason, the depths obtained with geochemical data are more realistic and this difference may be due to the selection of the zircons used for the calculation.

4.9.3 Crustal evolution of the Andes between 38-43°S

For the Jurassic, the oldest plutonic rocks representing the magmatic arc are found in the Coastal Batholith (for example Panguipulli Batholith, 198 Ma, Parada and Munizaga, 1978). The eastward extension of this arc is represented by basaltic lavas from the lower member of the Nacientes del Bío Bío Formation (Icalma Member, De La Cruz and Suárez, 1997). Rossel et al. (2020) analyzed

evidence of the oldest volcanic rocks in the region related to this arc and obtained detrital zircon ages for the Rincón de Nuñez Formation (maximum depositional age of 167 Ma), the Icalma Member of the Nacientes del Bío Bío Formation (maximum depositional age of 161 Ma), and a crystallization age of 169.0 ± 1.8 Ma for the Altos del Hualmapu Formation. There is no evidence of Jurassic magmatism after 155 Ma in the region. These rocks possess characteristics of a subduction environment and represent a non-thickened crust for this period. They distinguish an eastward displacement of the magmatic arc during the Late Jurassic, which resumed in the Coastal Batholith during the Early Cretaceous as result of slab roll back and posterior back arc extension.

Acevedo et al. (2022) analyzed rocks from the Tordillo Formation in the Neuquén Basin, identifying syn-extensional structures with NNW to NW orientations that also affected the lower levels of the Vaca Muerta Formation at Cerro Domuyo. Provenance studies of this unit determined maximum depositional ages between 151.88 ± 0.32 Ma and 148.69 ± 0.27 Ma, with western magmatic zones as the primary sediment sources. This extension developed in the Late Jurassic would represent a stage of extensional back-arc in the Neuquén Basin due to retreat of the subducted slab during the initial opening phases of the Atlantic Ocean.

North of the study area (approx. 32°S), Singleton et al. (2024) determined three main deformation events (D1, D2, and D3) for the Jurassic in the Papudo-Quintero Complex (173–164 Ma): 166–164 Ma, NW–SE to WNW–ESE transpressive shortening; 164–150 Ma, N–S extension under a transtensional regime; 153–100 Ma, NNW–SSE shortening and ENE–WSW extension in a strike-slip regime. In contrast to the study area, this Complex is incompatible with E–W extension linked to slab retreat.

Within the generally more mantle-like magmatism of the Late Cretaceous-Paleogene Andean Cycle, there are some differences between arc and retroarc regions. The Late Cretaceous North Patagonian Batholith describes a more subalkaline (lower) Na_2O+K_2O trend with respect to silica than the Naunauco Belt (Fig. 5a). These differences can be explained because the Naunauco Belt represents the expansion of the magmatic arc in the retroarc, and it would have been formed under thicker crust, where crustal contamination was more possible,

whereas the North Patagonian Batholith was formed in normal arc thickness (≈30 km), so it would have had less possibility of crustal contamination.

The isotopic data point to the same direction, as the North Patagonian Batholith (Icalma Granodiorite) shows lower $^{87}Sr/^{86}Sr$ initial values of 0.70429 than the Naunauco Belt (Varvarco Tonalite) with $^{87}Sr/^{86}Sr$ initial values between 0.70455 and 0.70695. Magma sources can become more crustal, for example, in the Central Volcanic Zone (16º to 26ºS latitude), where the crustal Sr, O and Nd isotopic signature of the Neogene to Recent magmas was explained due to crustal contamination of mantle-derived magmas (Davidson et al. 1991). In the case of the Central Volcanic Zone, the exceptionally thick (c. 70 km) continental crust favors crustal contamination, as parent magmas are likely to have ponded and differentiated extensively at one or more levels in the crust during ascent.

In the North Patagonian Batholith, the Early Jurassic rocks (the Jurassic Host Granite and the Moquehue Granodiorite) exhibit a more pronounced crustal signature compared to the Late Cretaceous rocks (Icalma Granodiorite) evidencing an assimilation and subsequent thinning of the crust in the region.

In the Southern Patagonian Batholith, extensional tectonics were proposed as the likely condition, given that most plutons in this region are undeformed (Bruce et al. 1991). Similarly, the Moquehue (~184 Ma) and Icalma plutons (~71 Ma) in the North Patagonian Batholith also display no deformation, suggesting the possibility of extensional conditions prevailing in this area as well.

We compared our Hf data against Hf results from the literature to visualize better the mantle contribution and crustal contamination. As it is possible to appreciate in Figure 7, there are not many Hf data for this part of the Andes. All collected data belong to transects A and B, central part and compare with detrital zircons, Jurassic and Cretaceous-Paleogene of Pepper et al. (2016) and Balgord (2017). These data were plotted in our diagram of Figure 7, but the meaning of them in the geological context of our objective is limited because there is not a lithological and special control of them.

The Jurassic detrital zircons analyzed from Pepper et al. (2016) have ages between 146 and 200 Ma and values of $(^{176}Hf/^{177}Hf)i$ ratios between 0.282305 and 0.283013. The $(\varepsilon_{Hf})i$ values between -12.84 and 11.57, determines average T_{DM} values of 2.01 and 0.44 Ga (Fig. 7). The Jurassic detrital zircons of Balgord

(2017) have ages between 199.7 and 145.8 Ma and values of ($^{176}Hf/^{177}Hf$)i ratios between 0.282452 and 0.283037. The (ε_{Hf})i values between -7.68 and 12.15, determines average T_{DM} values of 1.50 and 0.25 Ga (Fig. 8).

The Cretaceous-Paleogene zircons analyzed from Pepper et al. (2016) have ages between 50 and 145 Ma and values of ($^{176}Hf/^{177}Hf$)i ratios between 0.282430 and 0.283087. The (ε_{Hf})i values between -11.28 and 12.92, determines average T_{DM} values of 1.81 and 0.32 Ga (Fig. 8). The data compiled for Balgord (2017) have ages between 144 and 40.3 Ma and values of ($^{176}Hf/^{177}Hf$)i ratios between 0.282770 and 0.283138. The (ε_{Hf})i values between 0.46 and 14, determines average T_{DM} values of 1.02 and 0.14 Ga (Fig. 8).

The Cretaceous rocks of these two transects show more positive (ε_{Hf})i data than the previous considered Jurassic rocks. Between the Cretaceous rocks, the Paso de Icalma Granodiorite shows the more positive data whereas the Varvarco tonalite show the more disperse (ε_{Hf})i values. The compiled detrital data, show a same tend as the igneous rocks of this work, with a marked isotopic pull-up from the Jurassic to the Cretaceous time.

Nevertheless, these compiled data are not so many, they show preliminary that the Evolution of the Andes between Jurassic and Cretaceous time for this sector was nearly similar, with Jurassic rocks showing more crust component and Cretaceous ones showing more mantellic ones.

The explanation for this isotopic pull-up, is a combination of different thicknesses of crust crossed by rocks between the Jurassic and the Cretaceous, helped in the Cretaceous by the influence of the subduction of a ridge that increased the mantle input, this part will be approached in the next chapter.

4.9.4 Paleotectonic configuration

At 180 Ma was postulated a subduction with a retreating margin due to Pangea break-up (Oliveros et al. 2020). In this moment, rift magmatism of the Pre-Cuyo Group and subduction magmatism of the North Patagonian Batholith occurred under extensional characteristics.

At 70-63 Ma the Farallon-Aluk ridge impacts the Southern Gondwana margin at the segment centered at 35ºS (Fig. 13). The subduction is highly oblique, and it is a system of subduction and extension (Fig. 13; Somoza and

Ghidella 2005; Müller et al. 2016; Wright et al. 2016). In this moment the magmatism of the Los Angeles Unit is formed (Iannelli et al. 2018), slightly north of the area of study, and it describes a higher Na_2O+K_2O trend (Fig. 5a), and it shows a less slab-fluid influence than its coeval southern units (Iannelli et al. 2018). In turn, the Los Angeles Unit is more mantle-derived, as it shows $^{87}Sr/^{86}Sr$ initial values between 0.70371 and 0.70496 (Iannelli et al. 2018). It could represent an incipient slab window magmatism. Adakitic magmas of Late Cretaceous age were produced by the melting of the subducting slab were detected in the forearc region at 39ºS by De la Fuente et al. (2012; 2021) in the area near Valdivia in Chile (~39º-40º S). In turn, Hf positive values in the Late Cretaceous-Eeocene Charraruca porphyry (Andacollo area, Fig. 1) would suggest a mantle derived magmatism (D'Anunzio et al. 2023).

From 65 Ma, trench normal absolute velocities of the South American plate lowers from 2 cm/year to 1 cm/yr, triggering extension in many areas (Maloney et al. 2013). The magmatism of the Naunauco Belt forms in this period, and its source is more mantle-derived than the source of the Early Andean magmatism, as the Nd-Hf data also indicated. The Naunauco Belt was formed slightly after a Late Cretaceous slab shallowing event, where the magmatism expanded to the retroarc region (Spagnuolo et al. 2012). Slab-shallowing events are correlated with higher crustal contamination due to the enhancement of subduction erosion, a process which is typical of flat-slab events (Kay et al. 1991). The development of a flat slab leads to crustal thickening, and as the region undergoes compression, ductile deformation in the lower crust is probably responsible for the rapid increase in crustal thickness (Kay et al. 1991).

In contrast, extensional tectonic regimes may be a context that causes the fast ascent of magmas to the surface, with little opportunity of contamination with the crust during ascent. For example, this process was involved in the generation of Cretaceous granitoids in the North Patagonian Andes (segment between 39º and 42º S), where the steepening of the subduction angle in Cretaceous times would have caused the lesser crustal input of the magmas (Cingolani et al. 1991).

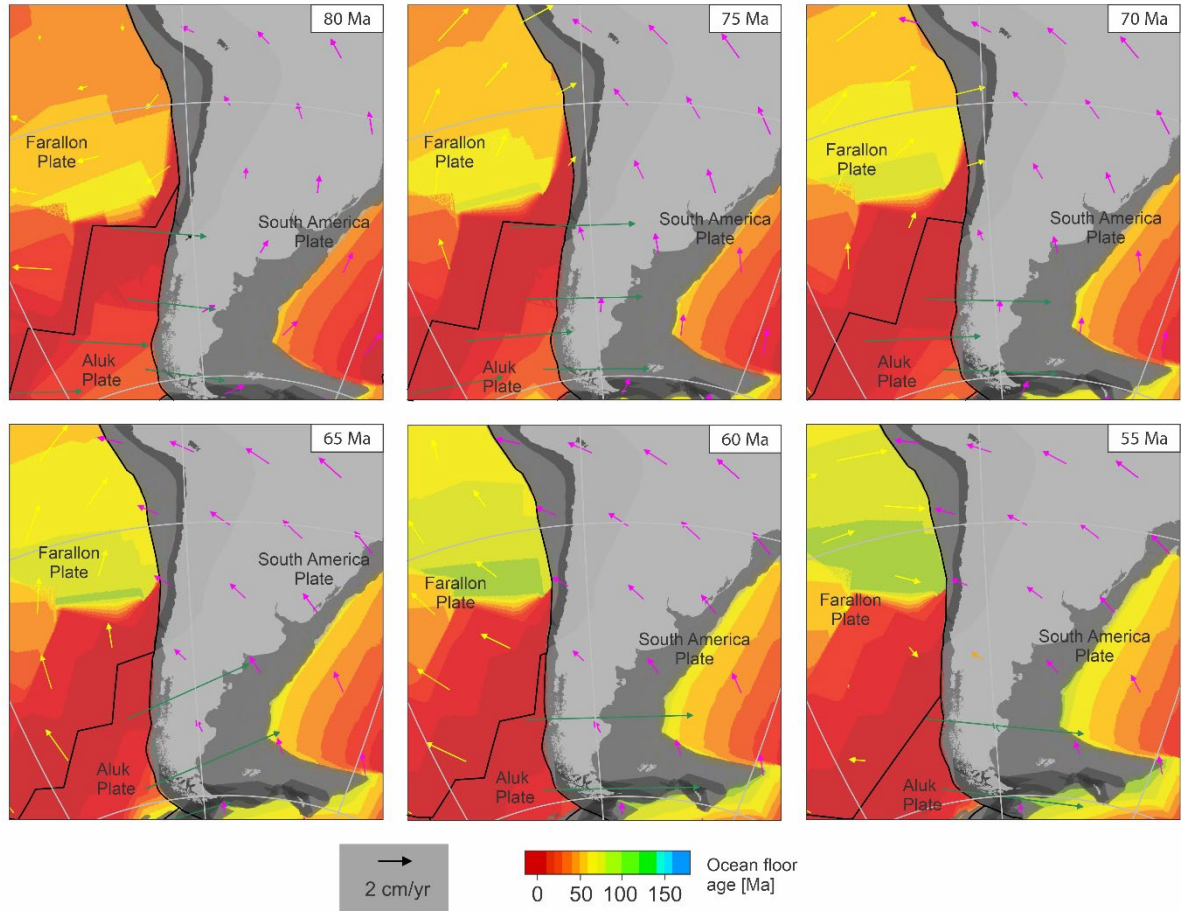


Figure 13: Paleotectonic configuration on the southwestern margin of Gondwana between 80 and 55 Ma, showing the subduction of the active Farallon-Aluk ridge.

In figure 14, evolution of (ε_{Nd})i for Andes between 36 and 53°S is indicated. Chapman et al. (2021) postulated that at ~100 Ma a flare up event occurred in the NPB. Our data plotted into the same (ε_{Nd})i curve show that at 71-64 Ma, was a clear Nd isotopic pull-up. As it was indicated before, isotopic pull-up is related with a steady low-volume magmatism event that can be related with different like: 1) arc migration (Chapman and Ducea, 2019), 2) underplating related to subduction erosion (e.g., Chapman et al., 2013, 2014; Kay et al., 2005), 3) punctuated melt extraction from the lower crust (Ducea et al., 2020b) or 4) a semi-episodic change in plate convergence rates (Hughes and Mahood, 2008; Zellmer, 2008).

In the context of our study, and taking into consideration that at 70-63 Ma the Farallon-Aluk ridge impacts the Southern Gondwana margin at the segment centered at 35ºS and that from 65 Ma, trench normal absolute velocities of the South American plate lowers from 2 cm/year to 1 cm/yr, triggering extension in

many areas (Maloney et al. 2013) this steady low-volume magmatism could be related with arc migration due to a semi-episodic change in plate convergence rates. As the results of this work, in the North Patagonian Andes, pre-Andean and Andean magmas were seen to show a decrease in magma source over time, as pre-Andean magmas have higher initial $^{87}Sr/^{86}Sr$ ratios (typically 0.706 to 0.710) than Andean granitoids, suggesting greater crustal involvement in their petrogenesis (Cingolani et al. 1991). A similar pattern of more crustal pre-Andean than the Andean magmas was seen by Oliveros et al. (2020), in a thorough geochemical and isotopic study of the pre-Andean and Andean magmatism in northern Chile between 25º and 30º S. The decline in the contribution of crustal/lithospheric sources to the magmatism was interpreted to have occurred due the shift from dominant compressional (Carboniferous-Early Permian) to transtentional (Middle Permian-Jurassic) stresses in the upper crust, suggesting that the margin went from advancing to retreating due to Pangea reorganization and break-up (Oliveros et al. 2020).

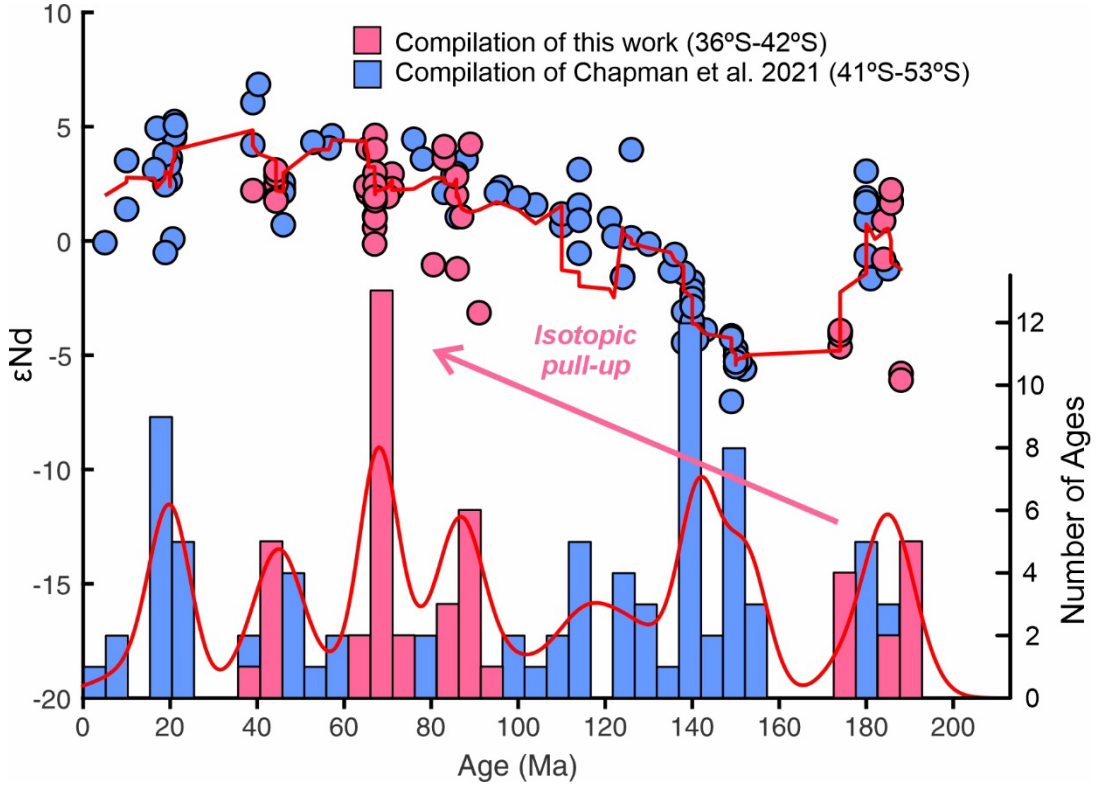


Figure 14: Compilation of U-Pb ages and ε_{Nd} data from the study area, compared to the southern part of the north-Patagonian batholith by Chapman et al. (2021). Red lines are running medians of bivariate kernel density estimates.

The igneous rocks of the Naunauco Belt are undeformed (Assis et al. 2021), and they are clearly post-tectonic with respect to the deformation in the Agrio Fold and Thrust Belt (Llambías and Malvicini 1978; Zamora Valcarce 2007), as the Naunauco Belt is clearly discordantly emplaced on previously deformed sedimentary rocks of the Neuquén Basin.

4.10 Conclusions

New U-Pb ages were obtained for the igneous rocks of the Late Cretaceous-Paleogene Naunauco belt and the North Patagonian Batholith in this region. The age of 184 ± 3 Ma obtains for the Jurassic Host Rocks unit allows be separated from the Cretaceous belt, demonstrating that Jurassic magmatism also extended to Varvarco area.

The age of 67 ± 3 Ma for the Butalon Tonalite allows this unit to be reassigned to the Cretaceous-Paleogene, contrary to the previous Miocene age assignment.

REE data on zircon characterize all rocks studied as oxidized, from a subduction environment. The depths calculated with Eu anomalies in zircon are much greater than those calculated with geochemical reasons, considering the latter as the most representative (30-35 km). The calculated temperatures are like those calculated with geothermobarometry in amphibole and plagioclase of previous works. For the Butalon Tonalite and the Moquehue Granite, REE elements in zircon analyses assign characteristics of possible Cu porphyry deposits, however, the data is not sufficient to have a high probability of deposit.

In general, the Jurassic in the region was characterized by acidic igneous and volcanic rocks, with a high-K alc-alkaline trend and mostly characteristics of within-plate rocks. The $(\varepsilon_{Nd})i$ and $(\varepsilon_{Hf})i$ values presents an isotopic pull-up towards the Cretaceous-Paleogene times, with a marked flare-up in 140 Ma and steady-state in the 67 Ma. This Cretaceous-Paleogene rocks are mainly intermediate plutonic and volcanic rocks, calc-alkaline and with typical volcanic arc signature, and present more positive values of $(\varepsilon_{Nd})i$ and $(\varepsilon_{Hf})i$ isotopes.

The Jurassic Host Rock and the Moquehue Granite, in this context, would represent plutons intruded in a back-arc extensional environment, related to slab

roll back, consistent with their lack of deformation, also observed in the Varvarco Tonalite (Assis et al. 2022).

The retroarc magmas of the Late Cretaceous-Paleogene Naunauco Belt are mantle-derived and underwent some degree of crustal contamination and were probably produced by extensional processes after the trench normal velocity of the South American Plate decrease after the Late Cretaceous shallowing event.

4.11 Acknowledgments

This study was financed in part by the Coordenação de Aperfeiçoamento de Pessoal de Nivel Superior – Brasil (CAPES) – Finance Code 001.

4.12 References

Acevedo, E., Fernández Paz, L., Encinas, A., Horton, B.K., Hernando, A., Valencia, V., Folguera, A., 2022. Late Jurassic back-arc extension in the Neuquén Basin (37°S): Insights from structural, sedimentological and provenance analyses. Basin Res. 35, 1012–1036. https://doi.org/10.1111/bre.12744

Andersson, U.B., 1991. Granitoid episodes and mafic-felsic magma interaction in the Svecofennian of the Fennoscandian Shield, with main emphasis on the ~1.8 Ga plutonics. Precambrian Res. 51, 127–149. https://doi.org/10.1016/0301-9268(91)90097-T

Aragón, E., D'Eramo, F., Castro, A., Pinotti, L., Brunelli, D., Rabbia, O., Rivalenti, G., Varela, R., Spakman, W., Demartis, M., Cavarozzi, C.E., Aguilera, Y.E., Mazzucchelli, M., Ribot, A., 2011. Tectono-magmatic response to major convergence changes in the North Patagonian suprasubduction system; the Paleogene subduction–transcurrent plate margin transition. Tectonophysics 509, 218–237. https://doi.org/10.1016/j.tecto.2011.06.012

Aragón, E., D'Eramo, F., Pinotti, L., Aguilera, Y., Cavarozzi, C., Demartis, M., Gómez Dacal, L., Castro, A., Rabbia, O., Hernando, I., Fuentes, T., 2015. El rift invertido Paleógeno de los Patagonides, Patagonia septentrional: Evolución y cambios de estilo extensional, in: XIV Congreso Geológico Chileno. pp. 162–165.

Aragón, E., Pinotti, L., D'Eramo, F., Castro, A., Rabbia, O., Coniglio, J., Demartis, M., Hernando, I., Cavarozzi, C.E., Aguilera, Y.E., 2013. The Farallon-Aluk ridge collision with South America: Implications for the geochemical changes of slab window magmas from fore- to back-arc. Geosci. Front. 4, 377–388. https://doi.org/10.1016/j.gsf.2012.12.004

Arregui, C., Carbone, O., Leanza, H.A., 2011. Contexto tectosedimentario, in: Relatorio Del XVIII Congreso Geológico Argentino. pp. 29–36.

Arriagada, C., Roperch, P., Mpodozis, C., Fernandez, R., 2006. Paleomagnetism and tectonics of the southern Atacama Desert (25–28°S), northern Chile. Tectonics 25, TC4001. https://doi.org/10.1029/2005TC001923

Assis, O.S., Zaffarana, C.B., Orts, D., Puigdomenech, C., Ruiz González, V., Gallastegui, G., Hauser, N., Kiseeva, E.S., Molina, J.F., Pernich, S., 2022. Emplacement conditions and exhumation of the Varvarco Tonalite and associated plutons from the Cordillera del Viento, Southern Central Andes. Geol. Mag. 159, 645–672. https://doi.org/10.1017/S0016756821001163

Bachmann, O., Bergantz, G.W., 2008. Deciphering Magma Chamber Dynamics from Styles of Compositional Zoning in Large Silicic Ash Flow Sheets. Rev. Mineral. Geochemistry 69, 651–674. https://doi.org/10.2138/rmg.2008.69.17

Bahlburg, H., Vervoort, J.D., Du Frane, S.A., Bock, B., Augustsson, C., Reimann, C., 2009. Timing of crust formation and recycling in accretionary orogens: Insights learned from the western margin of South America. Earth-Science Rev. 97, 215–241. https://doi.org/10.1016/j.earscirev.2009.10.006

Balgord, E.A., 2017. Triassic to Neogene evolution of the south-central Andean arc determined by detrital zircon U-Pb and Hf analysis of Neuquén Basin strata, central Argentina (34°S–40°S). Lithosphere 9, 453–462. https://doi.org/10.1130/L546.1

Bastías-Mercado, F., González, J., Oliveros, V., 2020. Volumetric and compositional estimation of the Choiyoi Magmatic Province and its comparison with other Silicic Large Igneous Provinces. J. South Am. Earth Sci. 103, 102749. https://doi.org/10.1016/j.jsames.2020.102749

Beard, J.S., Ragland, P.C., Crawford, M.L., 2005. Reactive bulk assimilation: A model for crust-mantle mixing in silicic magmas. Geology 33, 681–684. https://doi.org/10.1130/G21470.1

Best, M.G., 2013. Igneous and Metamorphic Petrology, 2nd Edition. Blackwell Science.

Bouvier, A., Vervoort, J.D., Patchett, P.J., 2008. The Lu–Hf and Sm–Nd isotopic composition of CHUR: Constraints from unequilibrated chondrites and implications for the bulk composition of terrestrial planets. Earth Planet. Sci. Lett. 273, 48–57. https://doi.org/10.1016/j.epsl.2008.06.010

Bruce, R.M., Nelson, E.P., Weaver, S.G., Lux, D.R., 1991. Temporal and spatial variations in the southern Patagonian batholith; Constraints on magmatic arc development, in: Harmon, R.S., Rapela, C.W. (Eds.), Andean Magmatism and Its Tectonic Setting. Geological Society of America Special Paper 265, Boulder, Colorado, pp. 1–12. https://doi.org/10.1130/SPE265-p1

Burnham, C.W., Ohmoto, H., 1980. Late-stage processes of felsic magmatism.

Min. Geol. Spec. Issue 8, 1–11.

Carrasco-Godoy, C., Campbell, I.H., 2023. Application of Onuma and lattice strain derived methods to calculate missing REE and Ce and Eu anomalies in magmatic zircons. Contrib. to Mineral. Petrol. 178, 42. https://doi.org/10.1007/s00410-023-02025-9

Casé, A.M., López-Escobar, L., Danieli, J.C., Schalamuk, A., 2008. Butalón igneous rocks, Neuquén, Argentina: Age, stratigraphic relationships and geochemical features. J. South Am. Earth Sci. 26, 188–203. https://doi.org/10.1016/j.jsames.2007.11.001

Chapman, A.D., Ducea, M.N., Kidder, S., Petrescu, L., 2014. Geochemical constraints on the petrogenesis of the Salinian arc, central California: Implications for the origin of intermediate magmas. Lithos 200–201, 126–141. https://doi.org/10.1016/j.lithos.2014.04.011

Chapman, A.D., Saleeby, J.B., Eiler, J., 2013. Slab flattening trigger for isotopic disturbance and magmatic flareup in the southernmost Sierra Nevada batholith, California. Geology 41, 1007–1010. https://doi.org/10.1130/G34445.1

Chapman, J.B., Ducea, M.N., 2019. The role of arc migration in Cordilleran orogenic cyclicity. Geology 47, 627–631. https://doi.org/10.1130/G46117.1

Chapman, J.B., Shields, J.E., Ducea, M.N., Paterson, S.R., Attia, S., Ardill, K.E., 2021. The causes of continental arc flare ups and drivers of episodic magmatic activity in Cordilleran orogenic systems. Lithos 398–399, 106307. https://doi.org/10.1016/j.lithos.2021.106307

Charrier, R., Pinto, L., Rodríguez, M.P., 2007. Tectonostratigraphic evolution of the Andean Orogen in Chile, in: Moreno, T., Gibbons, W. (Eds.), The Geology of Chile. The Geological Society of London, pp. 21–114. https://doi.org/10.1144/GOCH.3

Charrier, R., Ramos, V.A., Tapia, F., Sagripanti, L., 2014. Tectono-stratigraphic evolution of the Andean Orogen between 31 and 37°S (Chile and Western Argentina). Geol. Soc. London, Spec. Publ. 399, 13–61. https://doi.org/10.1144/SP399.20

Chauvel, C., Blichert-Toft, J., 2001. A hafnium isotope and trace element perspective on melting of the depleted mantle. Earth Planet. Sci. Lett. 190, 137–151. https://doi.org/10.1016/S0012-821X(01)00379-X

Chew, D.M., Sylvester, P.J., Tubrett, M.N., 2011. U–Pb and Th–Pb dating of apatite by LA-ICPMS. Chem. Geol. 280, 200–216. https://doi.org/10.1016/j.chemgeo.2010.11.010

Christiansen, E.H., 2005. Contrasting processes in silicic magma chambers: evidence from very large volume ignimbrites. Geol. Mag. 142, 669–681. https://doi.org/10.1017/S0016756805001445

Christiansen, E.H., McCurry, M., 2008. Contrasting origins of Cenozoic silicic volcanic rocks from the western Cordillera of the United States. Bull. Volcanol. 70, 251–267. https://doi.org/10.1007/s00445-007-0138-1

Cingolani, C., Dalla Salda, L., Hervé, F., Munizaga, F., Pankhurst, R.J., Parada, M.A., Rapela, C.W., 1991. The magmatic evolution of northern Patagonia; New impressions of pre-Andean and Andean tectonics, in: Harmon, R.S., Rapela, C.W. (Eds.), Andean Magmatism and Its Tectonic Setting. Geological Society of America Special Paper 265, Boulder, Colorado, pp. 29–44. https://doi.org/10.1130/SPE265-p29

Clemens, J.D., Holloway, J.R., White, A.J.R., 1986. Origin of an A-type granite: experimental constraints. Am. Mineral. 71, 317–324.

Coira, B., Davidson, J., Mpodozis, C., Ramos, V., 1982. Tectonic and magmatic evolution of the Andes of northern Argentina and Chile. Earth-Science Rev. 18, 303–332. https://doi.org/10.1016/0012-8252(82)90042-3

Cordani, U., Munizaga, F., Hervé, F., Hervé, M., 1976. Edades radiométricas provenientes del basamento cristalino de la Cordillera de la Costa de las provincias de Valparaíso y Santiago, Chile, in: I Congreso Geológico Chileno. pp. 213–221.

Crisp, L.J., Berry, A.J., Burnham, A.D., Miller, L.A., Newville, M., 2023. The Ti-in-zircon thermometer revised: The effect of pressure on the Ti site in zircon. Geochim. Cosmochim. Acta 360, 241–258. https://doi.org/10.1016/j.gca.2023.04.031

Cucchi, R., Leanza, H.A., Repol, D., Escosteguy, L., González, R., Danieli, J.C., 2005. Hoja Geológica 3972-IV, Junín de los Andes. Provincia del Neuquén. Buenos Aires.

D'Annunzio, M.C., Strazzere, L., Rubinstein, N., Cócola, M.A., Pavón Pivetta, C., Geraldes, M.C., 2023. The Charrarruca porphyry-type alteration zone: New evidence of mineralizing Late Cretaceous-Eocene magmatism in the Southern Central Andes of Argentina. J. South Am. Earth Sci. 125, 104298. https://doi.org/10.1016/j.jsames.2023.104298

Davidson, J.P., Harmon, Russell S., Wörner, G., 1991. The source of central Andean magmas; Some considerations, in: Harmon, R. S., Rapela, C.W. (Eds.), Andean Magmatism and Its Tectonic Setting. Geological Society of America Special Paper 265, Boulder, Colorado, pp. 233–244. https://doi.org/10.1130/SPE265-p233

Dávila, A.D., Hervé, F.A., Munizaga, F. V., 1979. Edades K/Ar en granitoides de la Cordillera de la Costa de la Provincia de Colchagua, VI Región, Chile Central, in: II Congreso Geológico Chileno. pp. F107–F121.

de La Cruz, R., Suárez, M., 1997. El Jurásico de la Cuenca de Neuquén en Lonquimay, Chile: Formación Nacientes del Biobío (38-39°S). Rev.

Geológica Chile 24, 3–24.

de la Fuente, D., Figueroa, Ó., Demaiffe, D., Mella, M., Duhart, P., Quiroz, D., Muñoz, J., Oliveros, V., 2021. Upper Cretaceous intrusives in the Coastal Cordillera near Valdivia: forearc magmatism related to the passage of a triple junction? Andean Geol. 48, 24–53. https://doi.org/10.5027/andgeoV48n1-3062

de la Fuente, D., Figueroa, Ó., Duhart, P., Quiroz, D., Demaiffe, D., Oliveros, V., 2012. Los Intrusivos de Antearco del Cretácico Superior de Chile Centro Sur (39ºS - 40ºS): Petrografía y geoquímica., in: XIII Congreso Geológico Chileno. pp. 342–344.

DeCelles, P.G., Ducea, M.N., Kapp, P., Zandt, G., 2009. Cyclicity in Cordilleran orogenic systems. Nat. Geosci. 2, 251–257. https://doi.org/10.1038/ngeo469

DeCelles, P.G., Graham, S.A., 2015. Cyclical processes in the North American Cordilleran orogenic system. Geology 43, 499–502. https://doi.org/10.1130/G36482.1

DeCelles, P.G., Zandt, G., Beck, S.L., Currie, C.A., Ducea, M.N., Kapp, P., Gehrels, G.E., Carrapa, B., Quade, J., Schoenbohm, L.M., 2015. Cyclical orogenic processes in the Cenozoic central Andes, in: DeCelles, P.G., Ducea, M.N., Carrapa, B., Kapp, P.A. (Eds.), Geodynamics of a Cordilleran Orogenic System: The Central Andes of Argentina and Northern Chile. Geological Society of America, pp. 459–490. https://doi.org/10.1130/2015.1212(22)

Ducea, M., 2001. The California Arc: Thick Granitic Batholiths, Eclogitic Residues, Lithospheric-Scale Thrusting, and Magmatic Flare-Ups. GSA Today 11, 4. https://doi.org/10.1130/1052-5173(2001)011<0004:TCATGB>2.0.CO;2

Ducea, M.N., Barton, M.D., 2007. Igniting flare-up events in Cordilleran arcs. Geology 35, 1047–1050. https://doi.org/10.1130/G23898A.1

Ducea, M.N., Saleeby, J.B., Bergantz, G., 2015. The Architecture, Chemistry, and Evolution of Continental Magmatic Arcs. Annu. Rev. Earth Planet. Sci. 43, 299–331. https://doi.org/10.1146/annurev-earth-060614-105049

Ducea, M.N., Triantafyllou, A., Krcmaric, J., 2020. New Timing and Depth Constraints for the Catalina Metamorphic Core Complex , Southeast Arizona. Tectonics 39, 1–15. https://doi.org/https://doi.org/10.1029/2020TC006383

Echaurren, A., Folguera, A., Gianni, G., Orts, D., Tassara, A., Encinas, A., Giménez, M., Valencia, V., 2016. Tectonic evolution of the North Patagonian Andes (41°–44° S) through recognition of syntectonic strata. Tectonophysics 677–678, 99–114. https://doi.org/10.1016/j.tecto.2016.04.009

Fernández Paz, L., Litvak, V.D., Echaurren, A., Iannelli, S.B., Encinas, A.,

Folguera, A., Valencia, V., 2018. Late Eocene volcanism in North Patagonia (42°30′–43°S): Arc resumption after a stage of within-plate magmatism. J. Geodyn. 113, 13–31. https://doi.org/10.1016/j.jog.2017.11.005

Ferry, J.M., Watson, E.B., 2007. New thermodynamic models and revised calibrations for the Ti-in-zircon and Zr-in-rutile thermometers. Contrib. to Mineral. Petrol. 154, 429–437. https://doi.org/10.1007/s00410-007-0201-0

Franchini, M., López-Escobar, L., Schalamuk, I.B.A., Meinert, L., 2003. Magmatic characteristics of the Paleocene Cerro Nevazón region and other Late Cretaceous to Early Tertiary calc-alkaline subvolcanic to plutonic units in the Neuquén Andes, Argentina. J. South Am. Earth Sci. 16, 399–421. https://doi.org/10.1016/S0895-9811(03)00103-2

Franchini, M.B., Meinert, L.D., Montenegro, T.F., 2000. Skarns Related to Porphyry-Style Mineralization at CaicayenHill, Neuquen, Argentina: Composition and Evolution of Hydrothermal Fluids. Econ. Geol. 95, 1197–1213. https://doi.org/10.2113/gsecongeo.95.6.1197

Fuller Ruiz, C., Aguirre, L., Corvalán, J., Klohn, C., Klohn, E., Levi, B., 1965. Geología y Yacimientos Metalíferos de Chile. IIG, Santiago.

Gallegos, E., Vattuone, M.E., Ostera, H.A., 2010. Petrología preliminar de la Granodiorita Paso de Icalma en el Valle del Río Pulmarí, Neuquén, in: X Congreso de Mineralogía y Metalogenia. pp. 277–282.

Gana, P.F., Hervé, F.A., 1983. Geología del basamento cristalino en la cordillera de la costa entre los ríos Mataquito y Maule, VII Región. Rev. Geológica Chile 19–20, 37–56.

García de Madinabeitia, S., Lorda, M.E.S., Ibarguchi, J.I.G., 2008. Simultaneous determination of major to ultratrace elements in geological samples by fusion-dissolution and inductively coupled plasma mass spectrometry techniques. Anal. Chim. Acta 625, 117–130. https://doi.org/10.1016/j.aca.2008.07.024

Gioia, S.M.C.L., Pimentel, M.M., 2000. The Sm-Nd isotopic method in the geochronology laboratory of the University of Brasília. An. Acad. Bras. Cienc. 72, 219–245. https://doi.org/10.1590/S0001-37652000000200009

Gonçalves, G.O., Lana, C., Scholz, R., Buick, I.S., Gerdes, A., Kamo, S.L., Corfu, F., Rubatto, D., Wiedenbeck, M., Nalini, H.A., Oliveira, L.C.A., 2018. The Diamantina Monazite: A New Low-Th Reference Material for Microanalysis. Geostand. Geoanalytical Res. 42, 25–47. https://doi.org/10.1111/ggr.12192

Gregori, D.A., Rossi, A.C., Benedini, L., 2011. Geocronología de la Faja Batolítica Aluminé, Provincia De Neuquén, Argentina, in: XVIII Congreso Geológico Argentino. p. S1.

Griffin, W.L., Wang, X., Jackson, S.E., Pearson, N.J., O'Reilly, S.Y., Xu, X., Zhou, X., 2002. Zircon chemistry and magma mixing, SE China: In-situ analysis of

Hf isotopes, Tonglu and Pingtan igneous complexes. Lithos 61, 237–269. https://doi.org/10.1016/S0024-4937(02)00082-8

Guillot, S., Le Fort, P., 1995. Geochemical constraints on the bimodal origin of High Himalayan leucogranites. Lithos 35, 221–234. https://doi.org/10.1016/0024-4937(94)00052-4

Gulisano, C.A., Gutiérrez Pleimling, A.R., Digregorio, R.E., 1984. Esquema estratigráfico de la secuencia Jurásica del oeste de la Provincia del Neuquén, in: IX Congreso Geológico Argentino, Actas I. pp. 236–259.

Hawkesworth, C.J., Vollmer, R., 1979. Crustal contamination versus enriched mantle: 143Nd/144Nd and 87Sr/86Sr evidence from the Italian volcanics. Contrib. to Mineral. Petrol. 69, 151–165. https://doi.org/10.1007/BF00371858

Hedenquist, J.W., Richards, Jeremy P., 1998. The Influence of Geochemical Techniques on the Development of Genetic Models for Porphyry Copper Deposits, in: Richards, J. P., Larson, P.B. (Eds.), Techniques in Hydrothermal Ore Deposits Geology: Reviews in Economic Geology. Society of Economic Geologists, pp. 235–256. https://doi.org/10.5382/Rev.10.10

Hervé, F., Davidson, J., Godoy, E., Mpodozis, C., Covacevich, V., 1981. The Late Paleozoic in Chile: Stratigraphy, structure and possible tectonic framework. An. Acad. Bras. Cienc. 53, 361–373.

Hervé, F., Fanning, C.M., Calderón, M., Mpodozis, C., 2014. Early Permian to Late Triassic batholiths of the Chilean Frontal Cordillera (28°–31°S): SHRIMP U–Pb zircon ages and Lu–Hf and O isotope systematics. Lithos 184–187, 436–446. https://doi.org/10.1016/j.lithos.2013.10.018

Hervé, F., Munizaga, F., Parada, M.A., Brook, M., Pankhurst, R.J., Snelling, N.J., Drake, R., 1988. Granitoids of the Coast Range of central Chile: Geochronology and geologic setting. J. South Am. Earth Sci. 1, 185–194. https://doi.org/10.1016/0895-9811(88)90036-3

Horstwood, M.S.A., Košler, J., Gehrels, G., Jackson, S.E., McLean, N.M., Paton, C., Pearson, N.J., Sircombe, K., Sylvester, P., Vermeesch, P., Bowring, J.F., Condon, D.J., Schoene, B., 2016. Community-Derived Standards for LA-ICP-MS U-(Th-)Pb Geochronology – Uncertainty Propagation, Age Interpretation and Data Reporting. Geostand. Geoanalytical Res. 40, 311–332. https://doi.org/10.1111/j.1751-908X.2016.00379.x

Howell, J.A., Schwarz, E., Spalletti, L.A., Veiga, G.D., 2005. The Neuquén Basin: an overview. Geol. Soc. London, Spec. Publ. 252, 1–14. https://doi.org/10.1144/GSL.SP.2005.252.01.01

Hughes, G.R., Mahood, G.A., 2008. Tectonic controls on the nature of large silicic calderas in volcanic arcs. Geology 36, 627–630.

https://doi.org/10.1130/G24796A.1

Iannelli, S.B., Fennell, L.M., Litvak, V.D., Fernández Paz, L., Encinas, A., Folguera, A., 2018. Geochemical and tectonic evolution of Late Cretaceous to early Paleocene magmatism along the Southern Central Andes (35-36°S). J. South Am. Earth Sci. 87, 139–156. https://doi.org/10.1016/j.jsames.2017.12.008

Iannelli, S.B., Fernández Paz, L., Litvak, V.D., Gianni, G., Fennell, L.M., González, J., Lucassen, F., Kasemann, S., Oliveros, V., Folguera, A., 2020. Southward-Directed Subduction of the Farallon–Aluk Spreading Ridge and Its Impact on Subduction Mechanics and Andean Arc Magmatism: Insights From Geochemical and Seismic Tomographic Data. Front. Earth Sci. 8, 121. https://doi.org/10.3389/feart.2020.00121

Iannelli, S.B., Litvak, V.D., Fernández Paz, L., Folguera, A., Ramos, M.E., Ramos, V.A., 2017. Evolution of Eocene to Oligocene arc-related volcanism in the North Patagonian Andes (39–41°S), prior to the break-up of the Farallon plate. Tectonophysics 696–697, 70–87. https://doi.org/10.1016/j.tecto.2016.12.024

Jackson, S.E., Pearson, N.J., Griffin, W.L., Belousova, E.A., 2004. The application of laser ablation-inductively coupled plasma-mass spectrometry to in situ U–Pb zircon geochronology. Chem. Geol. 211, 47–69. https://doi.org/10.1016/j.chemgeo.2004.06.017

Jochum, K.P., Weis, U., Schwager, B., Stoll, B., Wilson, S.A., Haug, G.H., Andreae, M.O., Enzweiler, J., 2016. Reference Values Following ISO Guidelines for Frequently Requested Rock Reference Materials. Geostand. Geoanalytical Res. 40, 333–350. https://doi.org/10.1111/j.1751-908X.2015.00392.x

Kay, S.M., Godoy, E., Kurtz, A., 2005. Episodic arc migration, crustal thickening, subduction erosion, and magmatism in the south-central Andes. Geol. Soc. Am. Bull. 117, 67. https://doi.org/10.1130/B25431.1

Kay, S.M., Mpodozis, C., Ramos, V.A., Munizaga, F., 1991. Magma source variations for mid–late Tertiary magmatic rocks associated with a shallowing subduction zone and a thickening crust in the central Andes (28 to 33°S), in: Harmon, R.S., Rapela, C.W. (Eds.), Andean Magmatism and Its Tectonic Setting. Geological Society of America Special Paper 265, Boulder, Colorado, pp. 113–138. https://doi.org/10.1130/SPE265-p113

Kay, S.M., Ramos, V.A., Mpodozis, C., Sruoga, P., 1989. Late Paleozoic to Jurassic silicic magmatism at the Gondwana margin: Analogy to the Middle Proterozoic in North America? Geology 17, 324–328. https://doi.org/10.1130/0091-7613(1989)017<0324:LPTJSM>2.3.CO;2

Kay, Suzanne Mahlburg, Burns, W.M., Copeland, P., Mancilla, O., 2006. Upper Cretaceous to Holocene magmatism and evidence for transient Miocene

shallowing of the Andean subduction zone under the northern Neuquén Basin, in: Kay, S. M., Ramos, V.A. (Eds.), Evolution of an Andean Margin: A Tectonic and Magmatic View from the Andes to the Neuquén Basin (35°-39°S Lat). Geological Society of America, pp. 19–60. https://doi.org/10.1130/2006.2407(02)

Latorre, C.O., Vattuone, M.E., Linares, E., Leal, P.R., 2001. K-Ar Ages of Rocks From Lago Alumine , Rucachoroi and Quillen, North Patagonian Andes, neuquén, República Argentina, in: III South American Symposium on Isotope Geology. pp. 577–580.

Le Bas, M.J., Le Maitre, R.W., Streckeisen, A., Zanettin, B., 1986. A Chemical Classification of Volcanic Rocks Based on the Total Alkali-Silica Diagram. J. Petrol. 27, 745–750. https://doi.org/10.1093/petrology/27.3.745

Leanza, H.A., Llambías, E.J., Carbone, O., 2005. Unidades estratigráficas limitadas por discordancias en los depocentros de la Cordillera del Viento y la Sierra de Chacaico durante los inicios de la Cuenca Neuquina, in: 6° Congreso de Exploración y Desarrollo de Hidrocarburos. p. 13.

Legarreta, L., Uliana, M.A., 1991. Jurassic—Marine Oscillations and Geometry of Back-Arc Basin Fill, Central Argentine Andes, in: Macdonald, D.I.M. (Ed.), Sedimentation, Tectonics and Eustasy: Sea-Level Changes at Active Margins. Wiley, pp. 429–450. https://doi.org/10.1002/9781444303896.ch23

Lipman, P.W., Prostka, H.J., Christiansen, R.L., 1972. A Discussion on volcanism and the structure of the Earth - Cenozoic volcanism and plate-tectonic evolution of the Western United States. I. Early and middle cenozoic. Philos. Trans. R. Soc. London. Ser. A, Math. Phys. Sci. 271, 217–248. https://doi.org/10.1098/rsta.1972.0008

Llambías, E.J., Leanza, H.A., Carbone, O., 2007. Evolución tectono-magmática durante el Pérmico al Jurásico temprano en la Cordillera del Viento (37°05´S - 37°15´S): Nuevas evidencias geológicas y geoquímicas del inicio de la Cuenca Neuquina. Rev. la Asoc. Geológica Argentina 62, 217–235.

Llambías, E.J., Malvicini, L., 1978. Geología, petrología y metalogénesis del área de Colipilli, provincia del Neuquén, República Argentina. Rev. la Asoc. Geológica Argentina 33, 257–276.

Llambías, E.J., Rapela, C.W., 1989. Las volcanitas de Collipilli, Neuquén (37°S) y su relación con otras unidades Paleógenas de la cordillera. Rev. la Asoc. Geológica Argentina 44, 224–236.

Loucks, R.R., Fiorentini, M.L., Henríquez, G.J., 2020. New Magmatic Oxybarometer Using Trace Elements in Zircon. J. Petrol. 61, 1–29. https://doi.org/10.1093/petrology/egaa034

Lucassen, F., Franz, G., Thirlwall, M.F., Mezger, K., 1999. Crustal Recycling of Metamorphic Basement: Late Palaeozoic Granitoids of Northern Chile

(~22°S). Implications for the Composition of the Andean Crust. J. Petrol. 40, 1527–1551. https://doi.org/10.1093/petroj/40.10.1527

Lucassen, F., Kramer, W., Bartsch, V., Wilke, H.-G., Franz, G., Romer, R.L., Dulski, P., 2006. Nd, Pb, and Sr isotope composition of juvenile magmatism in the Mesozoic large magmatic province of northern Chile (18–27°S): indications for a uniform subarc mantle. Contrib. to Mineral. Petrol. 152, 571–589. https://doi.org/10.1007/s00410-006-0119-y

Ludwig, K.R., 2012. User's manual for Isoplot version 3.75–4.15: a geochronological toolkit for Microsoft Excel.

Ludwig, K.R., Mundil, R., 2002. Extracting reliable U-Pb ages and errors from complex populations of zircons from Phanerozoic tuffs, in: 12th Goldschmidt Conference Abstracts. p. A463.

Maloney, K.T., Clarke, G.L., Klepeis, K.A., Quevedo, L., 2013. The Late Jurassic to present evolution of the Andean margin: Drivers and the geological record. Tectonics 32, 1049–1065. https://doi.org/10.1002/tect.20067

Mateo Fernández Caso, P.M., Montero, D.G., Leal, P.R., Ramos, V.A., 2011. Petrografía y geoquímica del magmatismo Cretácico Superior-Eoceno en el área de Pichaihue, Provincia de Neuquén. Rev. la Asoc. Geol. Argentina 68, 173–184.

Matteini, M., Junges, S.L., Dantas, E.L., Pimentel, M.M., Bühn, B., 2010. In situ zircon U–Pb and Lu–Hf isotope systematic on magmatic rocks: Insights on the crustal evolution of the Neoproterozoic Goiás Magmatic Arc, Brasília belt, Central Brazil. Gondwana Res. 17, 1–12. https://doi.org/10.1016/j.gr.2009.05.008

McDonough, W.F., Sun, S. -s., 1995. The composition of the Earth. Chem. Geol. 120, 223–253. https://doi.org/10.1016/0009-2541(94)00140-4

Mella, M., Duhart, P., McDonough, M., Antinao, J., Elgueta, S., Crignola, P., 2012. Geología del Área Valdivia-Corral, Región de Los Ríos. Santiago.

Molina, J.F., Scarrow, J.H., Montero, P.G., Bea, F., 2009. High-Ti amphibole as a petrogenetic indicator of magma chemistry: evidence for mildly alkalic-hybrid melts during evolution of Variscan basic–ultrabasic magmatism of Central Iberia. Contrib. to Mineral. Petrol. 158, 69–98. https://doi.org/10.1007/s00410-008-0371-4

Morel, M.L.A., Nebel, O., Nebel-Jacobsen, Y.J., Miller, J.S., Vroon, P.Z., 2008. Hafnium isotope characterization of the GJ-1 zircon reference material by solution and laser-ablation MC-ICPMS. Chem. Geol. 255, 231–235. https://doi.org/10.1016/j.chemgeo.2008.06.040

Mpodozis, C., Ramos, V., 1989. The Andes of Chile and Argentina, in: Ericksen, G.E., Cañas Pinochet, M.T., Reinemund, J.A. (Eds.), Geology of the Andes and Its Relation to Hydrocarbon and Mineral Resources. Circum-Pacific

Council for Energy and Mineral Resources Earth Science Series, v. 11, Houston, Texas, pp. 59–90.

Müller, R.D., Seton, M., Zahirovic, S., Williams, S.E., Matthews, K.J., Wright, N.M., Shephard, G.E., Maloney, K.T., Barnett-Moore, N., Hosseinpour, M., Bower, D.J., Cannon, J., 2016. Ocean Basin Evolution and Global-Scale Plate Reorganization Events Since Pangea Breakup. Annu. Rev. Earth Planet. Sci. 44, 107–138. https://doi.org/10.1146/annurev-earth-060115-012211

Munizaga, F., Herve, F., Drake, R., Pankhurst, R.J., Brook, M., Snelling, N., 1988. Geochronology of the Lake Region of south-central Chile (39°–42°S): Preliminary results. J. South Am. Earth Sci. 1, 309–316. https://doi.org/10.1016/0895-9811(88)90009-0

Navarrete, C., Gianni, G., Tassara, S., Zaffarana, C., Likerman, J., Márquez, M., Wostbrock, J., Planavsky, N., Tardani, D., Perez Frasette, M., 2024. Massive Jurassic slab break-off revealed by a multidisciplinary reappraisal of the Chon Aike silicic large igneous province. Earth-Science Rev. 249, 104651. https://doi.org/10.1016/j.earscirev.2023.104651

Ni, Z., Arevalo, R., Piccoli, P., Reno, B.L., 2020. A Novel Approach to Identifying Mantle-Equilibrated Zircon by Using Trace Element Chemistry. Geochemistry, Geophys. Geosystems 21, 1–22. https://doi.org/10.1029/2020GC009230

Oliveros, V., Morata, D., Aguirre, L., Féraud, G., Fornari, M., 2007. Jurassic to Early Cretaceous subduction-related magmatism in the Coastal Cordillera of northern Chile (18°30'-24°S): geochemistry and petrogenesis. Rev. Geol. Chile 34, 209–232.

Oliveros, V., Vásquez, P., Creixell, C., Lucassen, F., Ducea, M.N., Ciocca, I., González, J., Espinoza, M., Salazar, E., Coloma, F., Kasemann, S.A., 2020. Lithospheric evolution of the Pre- and Early Andean convergent margin, Chile. Gondwana Res. 80, 202–227. https://doi.org/10.1016/j.gr.2019.11.002

Pankhurst, R.J., Rapela, C.R., 1995. Production of Jurassic rhyolite by anatexis of the lower crust of Patagonia. Earth Planet. Sci. Lett. 134, 23–36. https://doi.org/10.1016/0012-821X(95)00103-J

Parada, M.Á.R., Munizaga, F. V., 1978. El Batolito de Panguipulli: Caracterización del plutonismo Jurásico en la Cordillera de Los Andes de la Provincia de Valdivia, X Región (39°30'-40°15'S). Comunicaciones 23, 12–25.

Paton, C., Hellstrom, J., Paul, B., Woodhead, J., Hergt, J., 2011. Iolite: Freeware for the visualisation and processing of mass spectrometric data. J. Anal. At. Spectrom. 26, 2508. https://doi.org/10.1039/c1ja10172b

Pearce, J.A., 1996. A user's guide to basalt discrimination diagrams, in: Wyman, D.A. (Ed.), Trace Element Geochemistry of Volcanic Rocks: Applications for Massive Sulphide Exploration. Geological Association of Canada, Short Course Notes, pp. 79–113.

Pearce, J.A., Harris, N.B.W., Tindle, A.G., 1984. Trace Element Discrimination Diagrams for the Tectonic Interpretation of Granitic Rocks. J. Petrol. 25, 956–983. https://doi.org/10.1093/petrology/25.4.956

Peccerillo, A., Taylor, S.R., 1976. Geochemistry of eocene calc-alkaline volcanic rocks from the Kastamonu area, Northern Turkey. Contrib. to Mineral. Petrol. 58, 63–81. https://doi.org/10.1007/BF00384745

Pepper, M., Gehrels, G., Pullen, A., Ibanez-Mejia, M., Ward, K.M., Kapp, P., 2016. Magmatic history and crustal genesis of western South America: Constraints from U-Pb ages and Hf isotopes of detrital zircons in modern rivers. Geosphere 12, 1532–1555. https://doi.org/10.1130/GES01315.1

Petrus, J.A., Kamber, B.S., 2012. VizualAge: A Novel Approach to Laser Ablation ICP-MS U-Pb Geochronology Data Reduction. Geostand. Geoanalytical Res. 36, 247–270. https://doi.org/10.1111/j.1751-908X.2012.00158.x

Pichowiak, S., Buchelt, M., Damm, K.-W., 1990. Magmatic activity and tectonic setting of the early stages of the Andean cycle in northern Chile, in: Special Paper of the Geological Society of America. pp. 127–144. https://doi.org/10.1130/SPE241-p127

Pin, C., Bassin, C., 1992. Evaluation of a strontium-specific extraction chromatographic method for isotopic analysis in geological materials. Anal. Chim. Acta 269, 249–255. https://doi.org/10.1016/0003-2670(92)85409-Y

Pin, C., Santos Zalduegui, J.F., 1997. Sequential separation of light rare-earth elements, thorium and uranium by miniaturized extraction chromatography: Application to isotopic analyses of silicate rocks. Anal. Chim. Acta 339, 79–89. https://doi.org/10.1016/S0003-2670(96)00499-0

Rapela, C.W., Llambías, E.J., 1985. La secuencia andesítica terciaria de Andacollo, Neuquén, Argentina, in: IV Congreso Geológico Chileno. pp. 458–486.

Rapela, C.W., Spalletti, L.A., Merodio, J.C., Aragón, E., 1988. Temporal evolution and spatial variation of early tertiary volcanism in the Patagonian Andes (40°S–42°30′S). J. South Am. Earth Sci. 1, 75–88. https://doi.org/10.1016/0895-9811(88)90017-X

Riccardi, A.C., Stipanicic, P.N., 2002. Fase diastrófica Río Atuel, in: Léxico Estratigráfico de La Argentina. Volumen VIII. Triásico. Asociación Geológica Argentina, Buenos Aires, p. 245.

Richards, J.P., 2015. The oxidation state, and sulfur and Cu contents of arc magmas: implications for metallogeny. Lithos 233, 27–45.

https://doi.org/10.1016/j.lithos.2014.12.011

Rossel, P., Echaurren, A., Ducea, M.N., Maldonado, P., Llanos, K., 2020. Jurassic segmentation of the early Andean magmatic Province in southern central Chile (35–39°S): Petrological constrains and tectonic drivers. Lithos 364–365, 105510. https://doi.org/10.1016/j.lithos.2020.105510

Rossel, P., Oliveros, V., Ducea, M.N., Charrier, R., Scaillet, S., Retamal, L., Figueroa, O., 2013. The Early Andean subduction system as an analog to island arcs: Evidence from across-arc geochemical variations in northern Chile. Lithos 179, 211–230. https://doi.org/10.1016/j.lithos.2013.08.014

Sagripanti, L., Folguera, A., Giménez, M., Rojas Vera, E.A., Fabiano, J.J., Molnar, N., Fennell, L., Ramos, V.A., 2014. Geometry of Middle to Late Triassic extensional deformation pattern in the Cordillera del Viento (Southern Central Andes): A combined field and geophysical study. J. Iber. Geol. 40, 349–366. https://doi.org/10.5209/rev_JIGE.2014.v40.n2.45305

Santos, M.M., Lana, C., Scholz, R., Buick, I., Schmitz, M.D., Kamo, S.L., Gerdes, A., Corfu, F., Tapster, S., Lancaster, P., Storey, C.D., Basei, M.A.S., Tohver, E., Alkmim, A., Nalini, H., Krambrock, K., Fantini, C., Wiedenbeck, M., 2017. A New Appraisal of Sri Lankan BB Zircon as a Reference Material for LA-ICP-MS U-Pb Geochronology and Lu-Hf Isotope Tracing. Geostand. Geoanalytical Res. 41, 335–358. https://doi.org/10.1111/ggr.12167

Sato, A.M., Llambías, E.J., Basei, M.A.S., Castro, C.E., 2015. Three stages in the Late Paleozoic to Triassic magmatism of southwestern Gondwana, and the relationships with the volcanogenic events in coeval basins. J. South Am. Earth Sci. 63, 48–69. https://doi.org/10.1016/j.jsames.2015.07.005

Sato, A.M., Llambías, E.J., Basei, M.A.S., Leanza, H.A., 2008. The Permian Choiyoi cycle in Cordillera del Viento (Principal Cordillera, Argentina): Over 25 Ma of magmatic activity, in: VI South American Symposium on Isotope Geology.

Scheuber, E., Bogdanic, T., Jensen, A., Reutter, K.-J., 1994. Tectonic Development of the North Chilean Andes in Relation to Plate Convergence and Magmatism Since the Jurassic, in: Reutter, K.-J. (Ed.), Tectonics of the Southern Central Andes. Springer Berlin Heidelberg, Berlin, Heidelberg, pp. 121–139. https://doi.org/10.1007/978-3-642-77353-2_9

Singleton, J.S., Arancibia, G., Morata, D., Pérez De La Maza, I., 2024. Magmatism and Polyphase Deformation in the Middle Jurassic Arc of Central Chile: Implications for the Tectonic Development of the Early Andean Margin. Tectonics 43, 1–28. https://doi.org/10.1029/2023TC008241

Sisson, T.W., Grove, T.L., 1993. Experimental investigations of the role of H2O in calc-alkaline differentiation and subduction zone magmatism. Contrib. to Mineral. Petrol. 113, 143–166. https://doi.org/10.1007/BF00283225

Sláma, J., Košler, J., Condon, D.J., Crowley, J.L., Gerdes, A., Hanchar, J.M., Horstwood, M.S.A., Morris, G.A., Nasdala, L., Norberg, N., Schaltegger, U., Schoene, B., Tubrett, M.N., Whitehouse, M.J., 2008. Plešovice zircon — A new natural reference material for U–Pb and Hf isotopic microanalysis. Chem. Geol. 249, 1–35. https://doi.org/10.1016/j.chemgeo.2007.11.005

Söderlund, U., Patchett, P.J., Vervoort, J.D., Isachsen, C.E., 2004. The 176Lu decay constant determined by Lu–Hf and U–Pb isotope systematics of Precambrian mafic intrusions. Earth Planet. Sci. Lett. 219, 311–324. https://doi.org/10.1016/S0012-821X(04)00012-3

Somoza, R., Ghidella, M.E., 2005. Convergencia en el margen occidental de América del sur durante el Cenozoico: Subducción de las placas de Nazca, Farallón y Aluk. Rev. la Asoc. Geológica Argentina 60, 797–809.

Spagnuolo, M.G., Folguera, A., Litvak, V., Rojas Vera, E.A., Ramos, V.A., 2012. Late Cretaceous arc rocks in the Andean retroarc region at 36.5°S: Evidence supporting a Late Cretaceous slab shallowing. J. South Am. Earth Sci. 38, 44–56. https://doi.org/10.1016/j.jsames.2012.05.002

Suárez, M., De La Cruz, R., 1997. Volcanismo pliniano del Lías durante los inicios de la cuenca de Neuquén, Cordillera del Viento, Neuquén, Argentina, in: Actas VII Congreso Geológico Chileno, Vol. 1. pp. 266–270.

Tang, M., Ji, W.-Q., Chu, X., Wu, A., Chen, C., 2020. Reconstructing crustal thickness evolution from europium anomalies in detrital zircons. Geology 49, 76–80. https://doi.org/10.1130/G47745.1

Tera, F., Wasserburg, G.J., 1972. U-Th-Pb systematics in three Apollo 14 basalts and the problem of initial Pb in lunar rocks. Earth Planet. Sci. Lett. 14, 281–304. https://doi.org/10.1016/0012-821X(72)90128-8

Urraza, I.A., Grecco, L.E., Delpino, S.H., Arrese, M.L., Rapela, C.W., 2011. Petrología y Estructura del Complejo Ígneo-Metamórfico Aluminé, Provincia de Neuquén, Argentina. Andean Geol. 38, 98–118.

Vázquez Illanes, P.S., 2008. Late Triassic to Early Jurassic Plutonism in south Chile (34°-37°S): Its significance for the geodynamic evolution in the transition from Gondwana to Andean orogeny. Technischen Universität Berlin.

Vergani, G.D., Tankard, A.J., Belotti, H.J., Welsink, H.J., 1995. Tectonic Evolution and Paleogeography of the Neuquén Basin, Argentina, in: Tankard, A.J., Soruco, R.S., Welsink, H.J. (Eds.), Petroleum Basins of South America. American Association of Petroleum Geologists, pp. 383–402. https://doi.org/10.1306/M62593C19

Vicente, P.J.-C., 1975. Essai d'organisation paléogéographique et structurale du PaléozoÏque des Andes Méridionales. Geol. Rundschau 64, 343–394.

Watson, E.B., Wark, D.A., Thomas, J.B., 2006. Crystallization thermometers for

zircon and rutile. Contrib. to Mineral. Petrol. 151, 413–433. https://doi.org/10.1007/s00410-006-0068-5

Whalen, J.B., Currie, K.L., Chappell, B.W., 1987. A-type granites: geochemical characteristics, discrimination and petrogenesis. Contrib. to Mineral. Petrol. 95, 407–419. https://doi.org/10.1007/BF00402202

Wiedenbeck, M., Allé, P., Corfu, F., Griffin, W.L., Meier, M., Oberli, F., Von Quadt, A., Roddick, J.C., Spiegel, W., 1995. Three natural zircon standards for U-Th-Pb, Lu-Hf, trace element and REE analyses. Geostand. Newsl. 19, 1–23. https://doi.org/10.1111/j.1751-908X.1995.tb00147.x

Willner, A.P., Gerdes, A., Massonne, H.-J., 2008. History of crustal growth and recycling at the Pacific convergent margin of South America at latitudes 29°–36° S revealed by a U–Pb and Lu–Hf isotope study of detrital zircon from late Paleozoic accretionary systems. Chem. Geol. 253, 114–129. https://doi.org/10.1016/j.chemgeo.2008.04.016

Woodhead, J., Hergt, J., Shelley, M., Eggins, S., Kemp, R., 2004. Zircon Hf-isotope analysis with an excimer laser, depth profiling, ablation of complex geometries, and concomitant age estimation. Chem. Geol. 209, 121–135. https://doi.org/10.1016/j.chemgeo.2004.04.026

Woodhead, J.D., Hergt, J.M., 2005. A Preliminary Appraisal of Seven Natural Zircon Reference Materials for In Situ Hf Isotope Determination. Geostand. Geoanalytical Res. 29, 183–195. https://doi.org/10.1111/j.1751-908X.2005.tb00891.x

Wright, N.M., Seton, M., Williams, S.E., Müller, R.D., 2016. The Late Cretaceous to recent tectonic history of the Pacific Ocean basin. Earth-Science Rev. 154, 138–173. https://doi.org/10.1016/j.earscirev.2015.11.015

Zamora Valcarce, G., 2007. Estructura y cinemática de la Faja Plegada y Corrida del Agrio, Cuenca Neuquina. Universidad de Buenos Aires.

Zamora Valcarce, G., Zapata, T., del Pino, D., Ansa, A., 2006. Structural evolution and magmatic characteristics of the Agrio fold-and-thrust belt, in: Kay, S.M., Ramos, V.A. (Eds.), Evolution of an Andean Margin: A Tectonic and Magmatic View from the Andes to the Neuquén Basin (35°-39°S Lat). Geological Society of America, pp. 125–145. https://doi.org/10.1130/2006.2407(06)

Zamora Valcarce, G., Zapata, T., Ramos, V.A., 2011. La Faja Plegada y Corrida del Agrio, in: Relatorio Del XVIII Congreso Geológico Argentino. pp. 367–374.

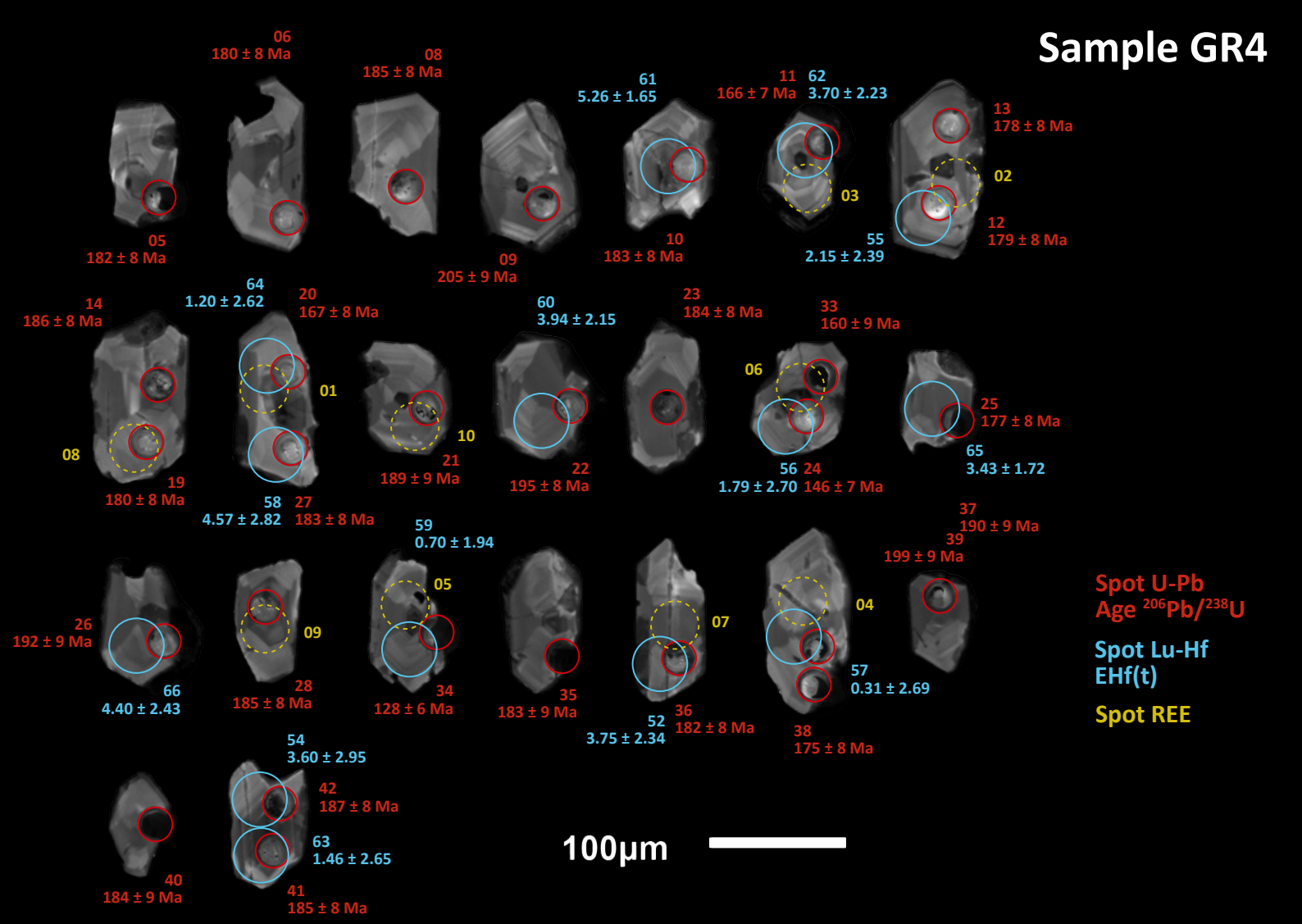
Zanettini, J.C., Leanza, H.A., Giusiano, A., Santamaría, G., 2010. Hoja Geológica 3972-II, Loncopué, Provincia del Neuquén. Buenos Aires.

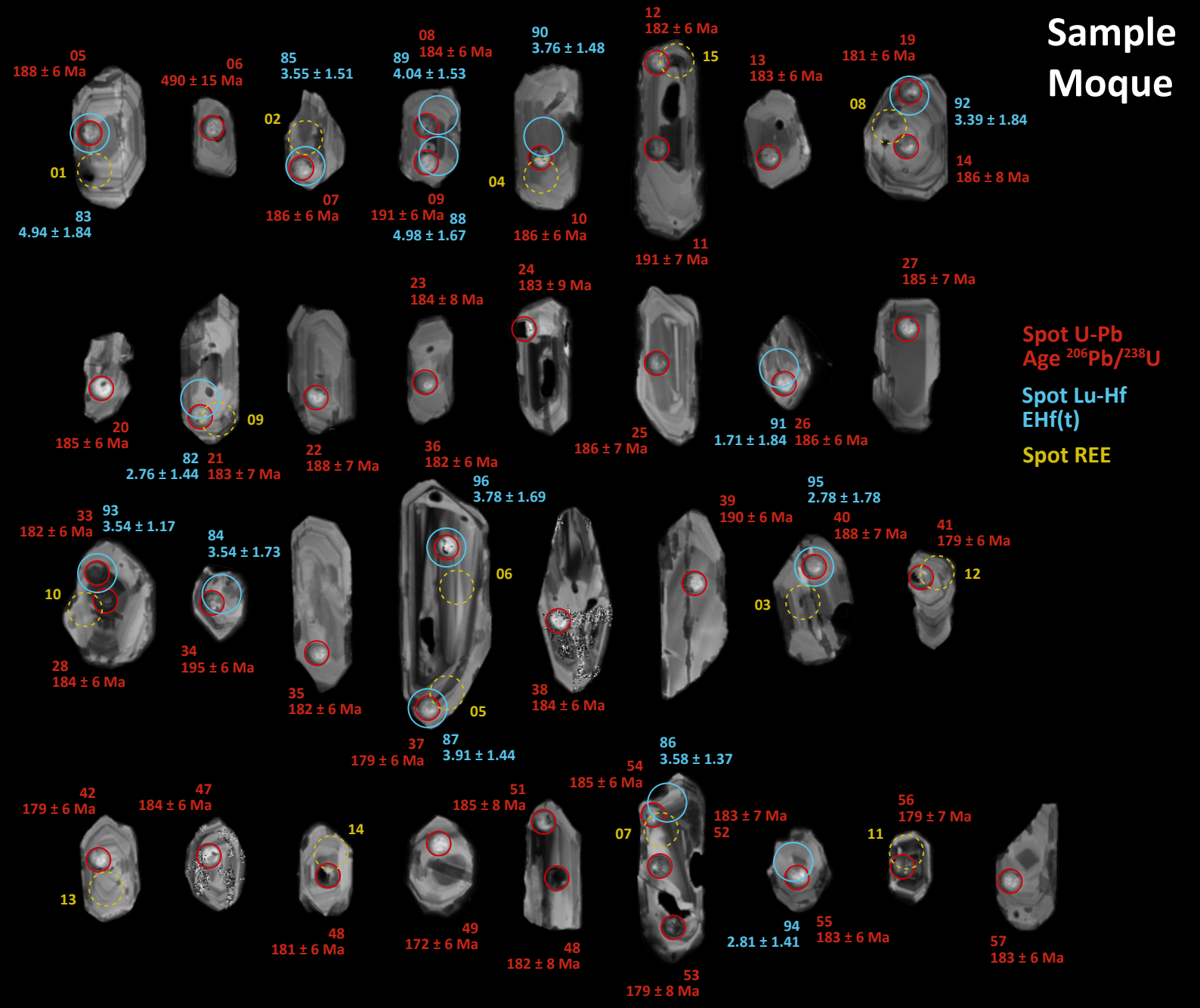
Zappettini, E.O., Lagorio, S.L., Dalponte, M., Santos, J.O., Belousova, E., 2018. Evidencias de magmatismo precuyano (Pliensbachiano – Toarciano) en el

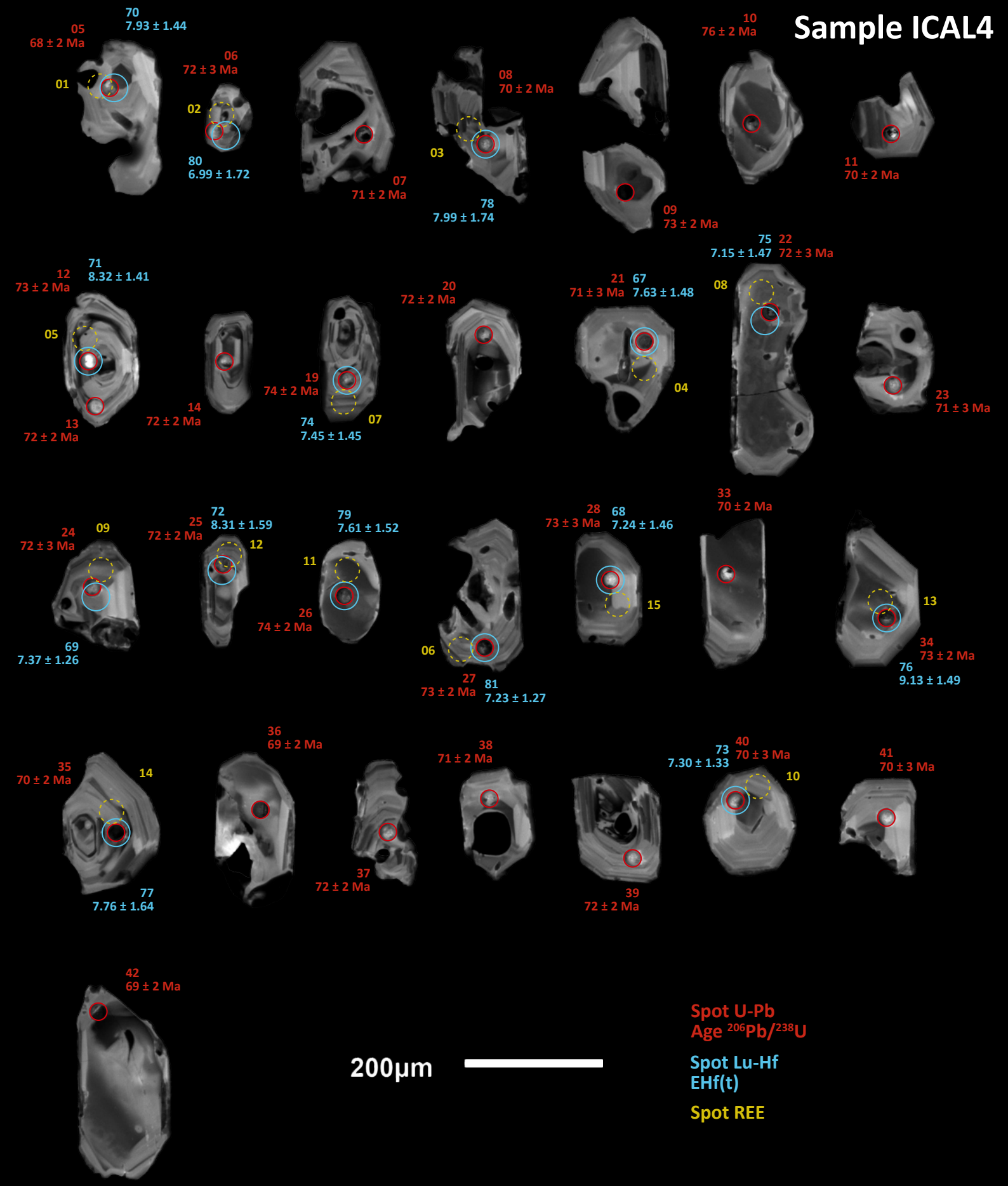
norte de la Cordillera del Viento, provincia del Neuquén: caracterización geoquímica, isotópica e implicancias tectónicas. Rev. la Asoc. Geológica Argentina 75, 533–558.

Zellmer, Georg F., 2008. Some first-order observations on magma transfer from mantle wedge to upper crust at volcanic arcs, in: Annen, C., Zellmer, G. F. (Eds.), Dynamics of Crustal Magma Transfer, Storage and Differentiation. Geological Society, London, Special Publications, 304, pp. 15–31. https://doi.org/https://doi.org/10.1144/SP304.2

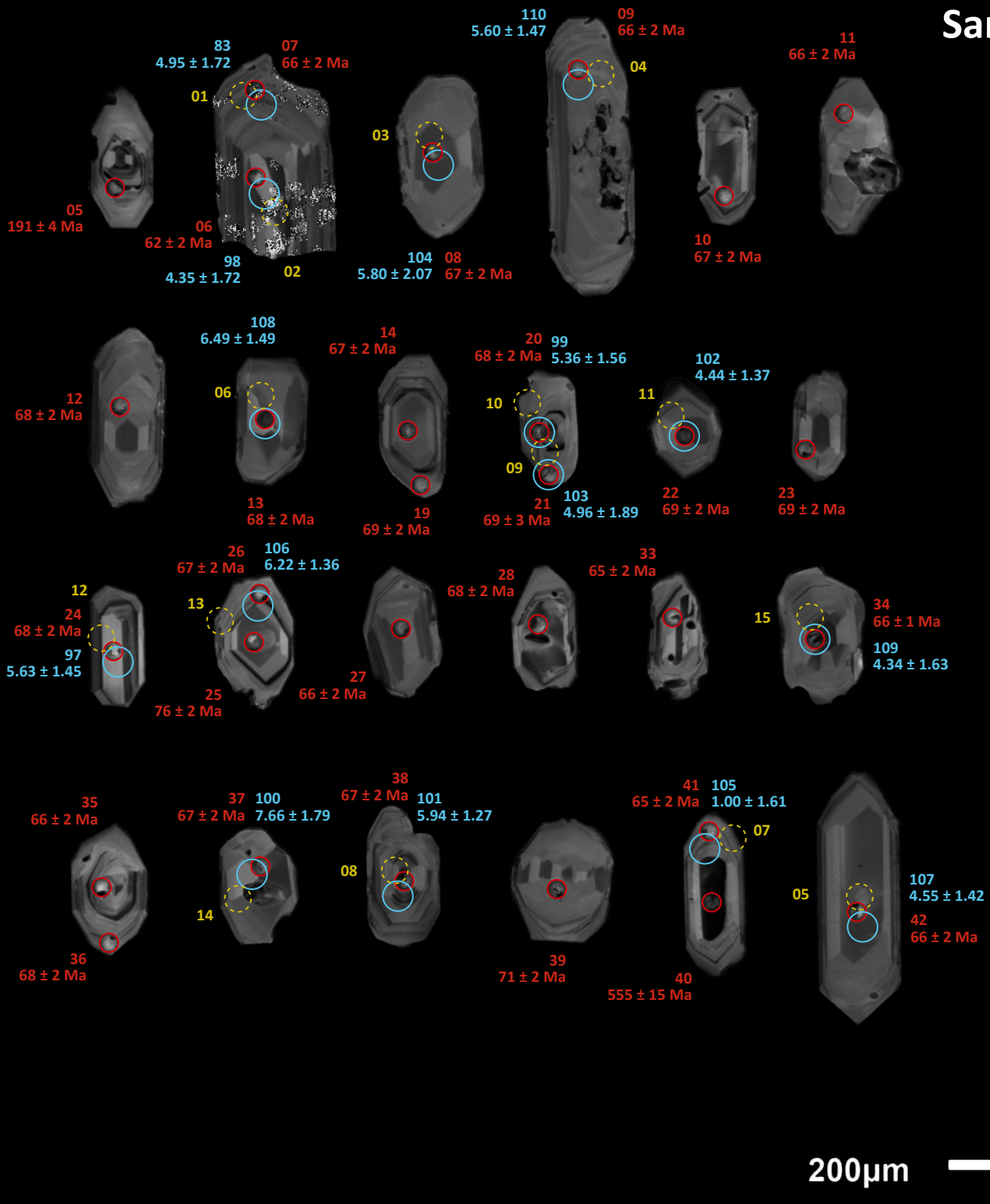
MATERIAL COMPLEMENTAR PARA O ARTIGO 2


Sample GR4
06
180 ± 8 Ma
08
185 ± 8 Ma
61
5.26 ± 1.65
11
166 ± 7 Ma
62
3.70 ± 2.23
13
178 ± 8 Ma
02
03
12
179 ± 8 Ma
05
182 ± 8 Ma
09
205 ± 9 Ma
10
183 ± 8 Ma
55
2.15 ± 2.39
64
1.20 ± 2.62
20
167 ± 8 Ma
14
186 ± 8 Ma
60
3.94 ± 2.15
23
184 ± 8 Ma
33
160 ± 9 Ma
06
25
177 ± 8 Ma
01
08
10
21
189 ± 9 Ma
22
195 ± 8 Ma
65
3.43 ± 1.72
19
180 ± 8 Ma
56
1.79 ± 2.70
24
146 ± 7 Ma
58
4.57 ± 2.82
27
183 ± 8 Ma
59
0.70 ± 1.94
37
190 ± 9 Ma
39
199 ± 9 Ma
26
192 ± 9 Ma
05
09
04
07
66
4.40 ± 2.43
28
185 ± 8 Ma
34
128 ± 6 Ma
35
183 ± 9 Ma
52
3.75 ± 2.34
36
182 ± 8 Ma
57
0.31 ± 2.69
38
175 ± 8 Ma
54
3.60 ± 2.95
42
187 ± 8 Ma
63
1.46 ± 2.65
40
184 ± 9 Ma
41
185 ± 8 Ma
100µm
Spot U-Pb Age 206Pb/238U
Spot Lu-Hf EHf(t)
Spot REE


Sample
Moque
Spot U-Pb
Age $^{206}Pb/^{238}U$
Spot Lu-Hf
EHf(t)
Spot REE
05
188 ± 6 Ma
06
490 ± 15 Ma
85
3.55 ± 1.51
08
184 ± 6 Ma
89
4.04 ± 1.53
90
3.76 ± 1.48
12
182 ± 6 Ma
15
13
183 ± 6 Ma
19
181 ± 6 Ma
08
92
3.39 ± 1.84
14
186 ± 8 Ma
01
02
07
186 ± 6 Ma
09
191 ± 6 Ma
88
4.98 ± 1.67
04
10
186 ± 6 Ma
11
191 ± 7 Ma
83
4.94 ± 1.84
23
184 ± 8 Ma
24
183 ± 9 Ma
27
185 ± 7 Ma
20
185 ± 6 Ma
09
82
2.76 ± 1.44
21
183 ± 7 Ma
22
188 ± 7 Ma
36
182 ± 6 Ma
25
186 ± 7 Ma
91
1.71 ± 1.84
26
186 ± 6 Ma
33
182 ± 6 Ma
93
3.54 ± 1.17
84
3.54 ± 1.73
96
3.78 ± 1.69
39
190 ± 6 Ma
95
2.78 ± 1.78
40
188 ± 7 Ma
41
179 ± 6 Ma
10
06
12
03
28
184 ± 6 Ma
34
195 ± 6 Ma
35
182 ± 6 Ma
38
184 ± 6 Ma
05
37
179 ± 6 Ma
87
3.91 ± 1.44
86
3.58 ± 1.37
42
179 ± 6 Ma
47
184 ± 6 Ma
51
185 ± 8 Ma
54
185 ± 6 Ma
56
179 ± 7 Ma
183 ± 7 Ma
52
07
11
13
14
48
181 ± 6 Ma
49
172 ± 6 Ma
48
182 ± 8 Ma
53
179 ± 8 Ma
94
2.81 ± 1.41
55
183 ± 6 Ma
57
183 ± 6 Ma
100µm


Sample ICAL4
05
68 ± 2 Ma
70
7.93 ± 1.44
01
06
72 ± 3 Ma
02
80
6.99 ± 1.72
07
71 ± 2 Ma
08
70 ± 2 Ma
03
78
7.99 ± 1.74
09
73 ± 2 Ma
10
76 ± 2 Ma
11
70 ± 2 Ma
12
73 ± 2 Ma
71
8.32 ± 1.41
05
13
72 ± 2 Ma
14
72 ± 2 Ma
19
74 ± 2 Ma
74
7.45 ± 1.45
07
20
72 ± 2 Ma
21
71 ± 3 Ma
67
7.63 ± 1.48
04
08
75
7.15 ± 1.47
22
72 ± 3 Ma
23
71 ± 3 Ma
24
72 ± 3 Ma
09
69
7.37 ± 1.26
25
72 ± 2 Ma
72
8.31 ± 1.59
12
11
26
74 ± 2 Ma
79
7.61 ± 1.52
06
27
73 ± 2 Ma
81
7.23 ± 1.27
28
73 ± 3 Ma
68
7.24 ± 1.46
15
33
70 ± 2 Ma
13
34
73 ± 2 Ma
76
9.13 ± 1.49
35
70 ± 2 Ma
14
77
7.76 ± 1.64
36
69 ± 2 Ma
37
72 ± 2 Ma
38
71 ± 2 Ma
39
72 ± 2 Ma
73
7.30 ± 1.33
40
70 ± 3 Ma
10
41
70 ± 3 Ma
42
69 ± 2 Ma
200µm
Spot U-Pb
Age $^{206}Pb/^{238}U$
Spot Lu-Hf
EHf(t)
Spot REE

Sample VAR6



Spot U-Pb Age $^{206}Pb/^{238}U$

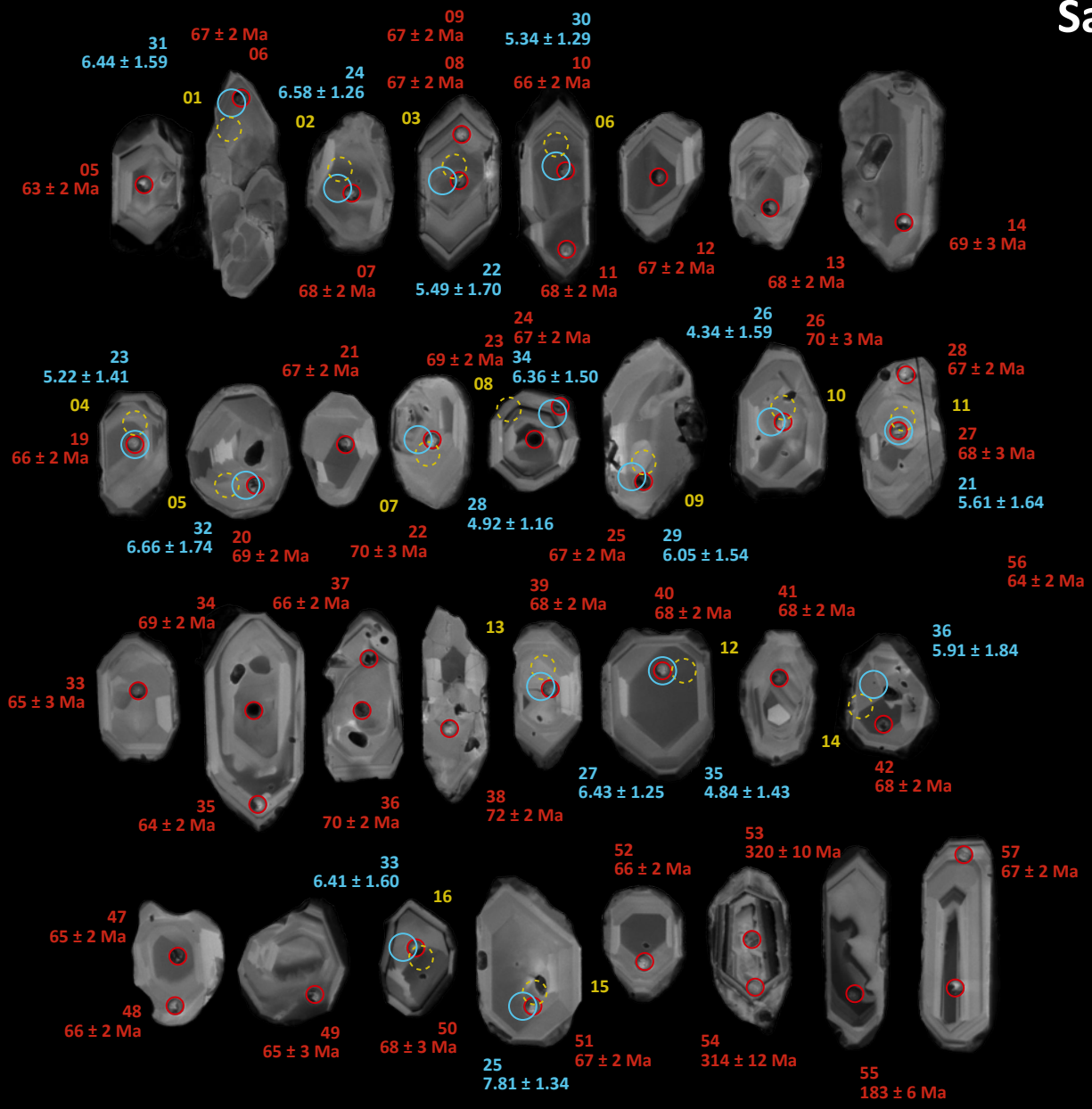
Spot Lu-Hf EHf(t)

Spot REE

200µm


Sample D2
Spot U-Pb
Age $^{206}Pb/^{238}U$
Spot Lu-Hf
EHf(t)
Spot REE
200μm
05
62 ± 1 Ma
06
65 ± 1 Ma
08
64 ± 1 Ma
06
07
64 ± 1 Ma
38
6.45 ± 2.27
09
64 ± 1 Ma
51
3.70 ± 1.70
11
67 ± 1 Ma
08
10
64 ± 1 Ma
07
41
4.09 ± 2.28
12
65 ± 1 Ma
13
67 ± 1 Ma
20
66 ± 2 Ma
21
67 ± 1 Ma
23
66 ± 1 Ma
24
66 ± 1 Ma
42
6.23 ± 2.07
10
25
65 ± 1 Ma
14
137 ± 3 Ma
19
63 ± 1 Ma
11
22
65 ± 1 Ma
49
4.01 ± 1.99
26
65 ± 2 Ma
04
27
65 ± 2 Ma
44
4.18 ± 1.80
28
67 ± 2 Ma
33
64 ± 1 Ma
45
4.54 ± 2.33
34
66 ± 1 Ma
12
35
64 ± 1 Ma
36
66 ± 1 Ma
01
37
5.63 ± 1.44
38
67 ± 1 Ma
37
66 ± 1 Ma
02
43
5.14 ± 1.71
39
66 ± 1 Ma
40
66 ± 1 Ma
41
67 ± 1 Ma
42
65 ± 1 Ma
03
39
4.74 ± 1.44
47
65 ± 1 Ma
46
5.35 ± 1.96
09
48
66 ± 1 Ma
49
64 ± 2 Ma
05
47
5.55 ± 1.57
50
64 ± 1 Ma
51
65 ± 2 Ma
13
53
64 ± 1 Ma
48
4.89 ± 1.69
50
6.16 ± 1.61
54
67 ± 2 Ma
15
40
4.88 ± 1.54
55
65 ± 1 Ma
14
56
64 ± 1 Ma
57
63 ± 1 Ma

Sample BU4

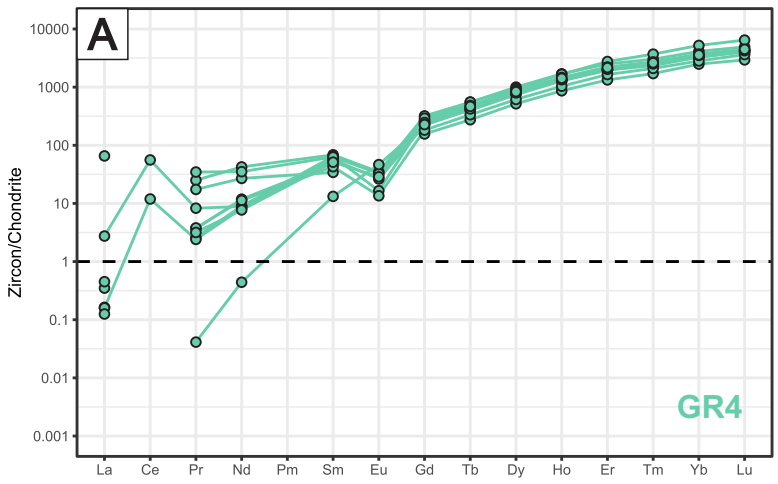


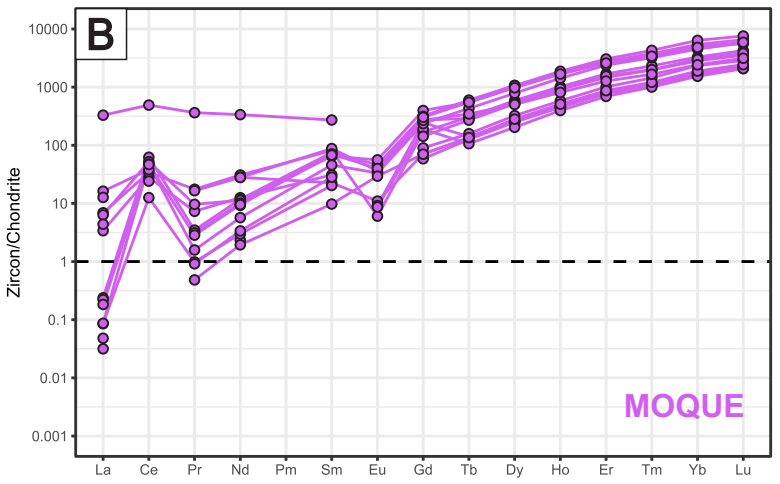
Spot U-Pb Age $^{206}Pb/^{238}U$

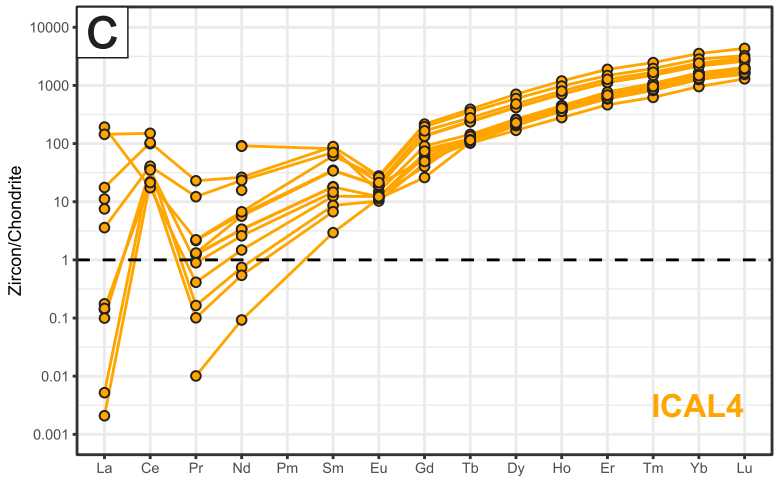
Spot Lu-Hf EHf(t)

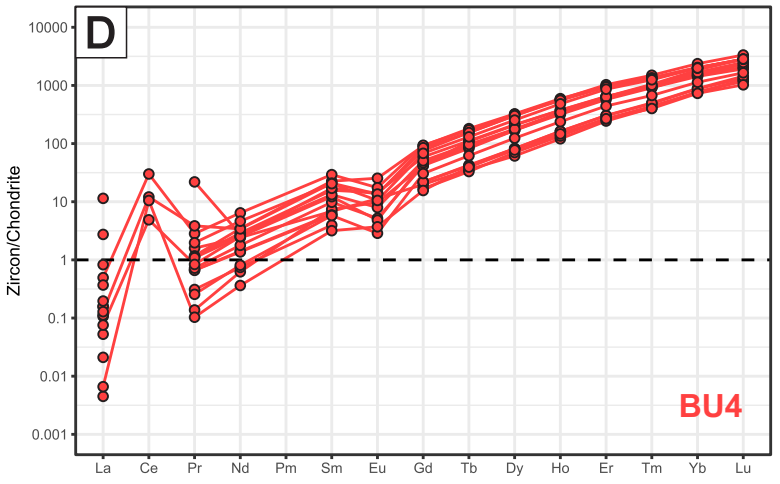
Spot REE

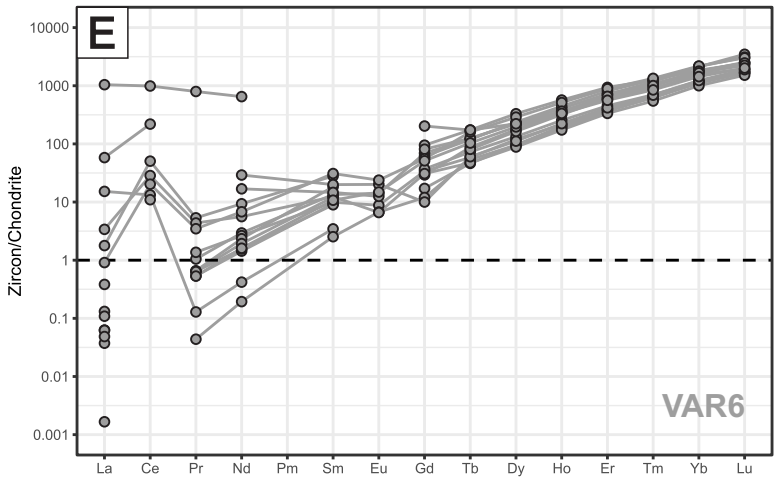
200µm

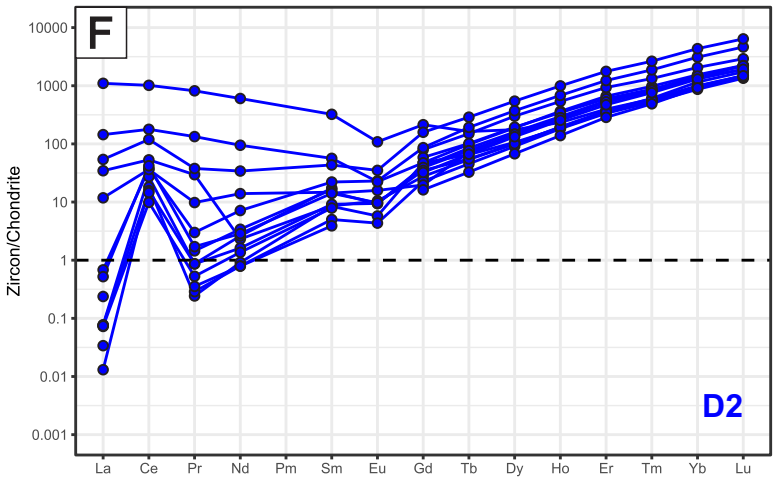

A
GR4
Zircon/Chondrite
10000
1000
100
10
1
0.1
0.01
0.001
La Ce Pr Nd Pm Sm Eu Gd Tb Dy Ho Er Tm Yb Lu


B
MOQUE
Zircon/Chondrite
10000
1000
100
10
1
0.1
0.01
0.001
La Ce Pr Nd Pm Sm Eu Gd Tb Dy Ho Er Tm Yb Lu


C
ICAL4
Zircon/Chondrite
10000
1000
100
10
1
0.1
0.01
0.001
La Ce Pr Nd Pm Sm Eu Gd Tb Dy Ho Er Tm Yb Lu


D
BU4
Zircon/Chondrite
10000
1000
100
10
1
0.1
0.01
0.001
La Ce Pr Nd Pm Sm Eu Gd Tb Dy Ho Er Tm Yb Lu


E
VAR6
Zircon/Chondrite
10000
1000
100
10
1
0.1
0.01
0.001
La Ce Pr Nd Pm Sm Eu Gd Tb Dy Ho Er Tm Yb Lu


F
D2
Zircon/Chondrite
10000
1000
100
10
1
0.1
0.01
0.001
La Ce Pr Nd Pm Sm Eu Gd Tb Dy Ho Er Tm Yb Lu

CAPÍTULO 5
CONCLUSÕES PARCIAIS

5 CONCLUSÕES PARCIAIS

5.1 Artigo 1

1- Observações de campo e análises petrográficas indicam que a hibridização de magma foi o processo principal nos plútons de Varvarco e Butalón. As fábricas magnéticas desses plútons são dominados por titanomagnetita. Isso, juntamente com dados de química mineral (anfibólio e biotita), confirma que essas fases magmáticas pertencem à série tipo I de corpos ígneos cálcio-alcalinos.

2- As fábricas são, sem exceção, magmáticas, e os dados AMS podem ser interpretados como o resultado da colocação e exumação rápida de plútons resfriados rapidamente.

3- As idades AFT do Tonalito Varvarco estão próximas de sua idade de cristalização, assim como a idade de resfriamento rápida calculada para este plúton (330°C/My).

4- As condições de colocação rasas foram estimadas com base na geotermobarometria (2-3 kbars, equivalente a 12 km de profundidade). Esses dados combinados nos permitem inferir soerguimento na região entre 64.9 e 66 Ma. Dados de geotermobarometria e AFT sugerem o gradiente geotérmico da área de ~ 62,5°C/km. O sistema magmático na área de Varvarco poderia ter sido exumado em aproximadamente 12 km em ca. 2.1 Ma.

5- A orientação das fábricas magmáticas implica que eles se formaram principalmente devido aos processos da câmara magmática. No entanto, eles poderiam ter sido controlados, em parte, pela deformação compressiva regional do Cretáceo Superior. Como os plútons estão localizados ao longo do traço da falha da Cordillera del Viento, e pelo fato de serem desprovidos de deformação tectônica pós-colocação, as reativações desta falha não são suportadas.

5.2 Artigo 2

1- Novas idades U-Pb foram obtidas para as rochas ígneas do Cretáceo Superior-Paleogeno do Naunauco Belt e do Batólito Nordpatagônico nesta região. A idade de 184 ± 3 Ma obtida para a unidade Jurassic Host Rocks permite

que seja separada do cinturão Cretáceo, demonstrando que o magmatismo jurássico também se estendeu para a área de Varvarco.

2- A idade de 67 ± 3 Ma para o Tonalito Butalon permite reassinar esta unidade ao Cretácico-Paleogeno, ao contrário da atribuição anterior de idade Miocena.

3- Os dados de REE em zircão caracterizam todas as rochas estudadas como oxidadas, de ambiente de subducção. As profundidades calculadas com anomalias de Eu no zircão, são muito maiores do que as calculadas com razões geoquímicas, considerando estas últimas como as mais representativas (30-35 km). As temperaturas calculadas são similares as calculadas com geotermobarometria em anfibólio e plagioclásio

4- Em geral, o Jurássico na região foi caracterizado por rochas ígneas e vulcânicas ácidas, com uma tendência alc-alcalina de alto-K e principalmente características de rochas de intraplaca. Os valores de (ƐNd)i e (ƐHf)i apresentam um aumento isotópico em direção ao Cretácico-Paleogeno, com um aumento acentuado em 67 Ma. Essas rochas Cretácico-Paleogenas são principalmente rochas plutônicas e vulcânicas intermediárias, cálcio-alcalinas e com assinatura típica de arco vulcânico, e apresentam valores mais positivos de isótopos ($Ɛ_{Nd}$)i e ($Ɛ_{Hf}$)i.

CAPÍTULO 6

CONCLUSÕES FINAIS E RECOMENDAÇÕES

6 CONCLUSÕES FINAIS E RECOMENDAÇÕES

1- Durante o Jurássico, o processo geodinâmico dominante foi o *slab rollback*, que produziu extensão e migração do magmatismo da costa do Chile para o leste, desenvolvendo depósitos de retroarco no ambiente extensional. No Cretáceo-Paleógeno, a subducção da dorsal ativa de Farallon-Aluk mais ao norte aumentou a "flutuabilidade" da placa subdutada com a consequente diminuição da velocidade de convergência e do ângulo de subducção. Esta mudança de ângulo faz com que o arco magmático se expanda e migre em direção ao antepaís.

2- Devido às características geoquímicas e isotópicas, podemos atribuir um evento de *flare-up* para o Jurássico em 140 Ma e um evento de *steady-state* para o Cretáceo-Paleógeno aos 67 Ma.

3- Os estudos de fertilidade magmática apontam a dois posíveis depósitos de tipo pórfiro de Cu, o Granito Moquehue de idade Jurássica e o Tonalito Butalón de idade Cretácea-Paleógena.

Como os dados de fugacidade de oxigênio em zircão não são suficientes para afirmar que existe um depósito mineral, recomenda-se analisar outras *proxies* para determinar se realmente existem depósitos associados a essas unidades (Granito Moquehue e Tonalito Butalón), como a presença de sulfetos, que possam complementar essas afirmações.

A idade U-Pb obtida de 184 ± 3 Ma para *Jurassic Host Rocks* permitiu que elas fossem separadas do Aplito Radales do Cretáceo-Paleógeno, seria necessário datar mais rochas desta última unidade para determinar se realmente pertencem ao granito e até que ponto o magmatismo Jurássico se estendia naquela região.

Seria interessante aumentar a quantidade de dados geocronológicos e isotópicos na região, principalmente Lu-Hf e Sm-Nd, para avaliar a evolução crustal do Jurássico ao Paleógeno de uma forma mais robusta.

Os dados de REE em zircão permitem-nos obter diversas informações importantes, mas a dispersão comum das LREE torna necessária uma melhor forma de selecionar análises válidas, que preservem as anomalias de Ce e Eu.

Neste caso, recomenda-se a utilização do aplicativo *imputREEapp* (Carrasco-Godoy e Campbell 2023) e dos parâmetros de Ni et al. 2020 para esse fim.

REFERENCIAS

Azcuy, C. L. e Caminos, R. 1987. El Sistema Carbonifero en la Republica Argentina. Diastrofismo. In El sistema carbonífero en la República Argentina (pp. 239-251).

Burns, D.H., de Silva, S.L., Tepley III, F., Schmitt, A.K. e Loewen, M.W. 2015. Recording the transition from flare-up to steady-state arc magmatism at the Purico–Chascon volcanic complex, northern Chile. Earth Planet. Sci. Lett. 422, 75–86. https://doi.org/10.1016/j.epsl.2015.04.002

Casé, A. M. M., López-Escobar, L., Danieli, J. C. C. e Schalamuk, A. 2008. Butalón igneous rocks, Neuquén, Argentina: Age, stratigraphic relationships and geochemical features. Journal of South American Earth Sciences, 26(2), 188–203. https://doi.org/10.1016/j.jsames.2007.11.001

Cingolani, C., Dalla Salda, L., Hervé, F., Munizaga, F., Pankhurst, R. J., Parada, M. A. e Rapela, C. W. 1991. The magmatic evolution of northern Patagonia; New impressions of pre-Andean and Andean tectonics. In R. S. Harmon & C. W. Rapela (Eds.), Andean Magmatism and Its Tectonic Setting (Vol. 265, pp. 29–44). https://doi.org/10.1130/SPE265-p29

Cristallini, E.O. y R.W. Allmendinger. 2000. Estructura de la Faja Plegada del Agrio, Provincia del Neuquén. Informe Inédito, 115 p., Buenos Aires.

Chapman, J. B. e Ducea, M. N. 2019. The role of arc migration in Cordilleran orogenic cyclicity. Geology, 47(7), 627-631.

Cucchi, R. e Leanza, H.A. 2006. Hoja Geológica 3972-IV Junín de los Andes. Provincia del Neuquén. Programa Nacional de Cartas Geológicas de la República Argentina 1:250.000. Servicio Geológico Minero Argentino, Boletín 357, 103 p., Buenos Aires.

Dalla Salda, L. H., Cingolani, C. e Varela, R. 1991. El basamento cristalino de la región nordpatagónica de los lagos Gutiérrez, Mascardi y Guillelmo, Provincia de Río Negro. Revista de la Asociación Geológica Argentina, 46(3-4), 263-276.

de Madinabeitia, S. G., Lorda, M. S. e Ibarguchi, J. G. 2008. Simultaneous determination of major to ultratrace elements in geological samples by fusion-dissolution and inductively coupled plasma mass spectrometry techniques. Analytica Chimica Acta, 625(2), 117-130.

de Silva, S. 2008. Arc magmatism, calderas, and supervolcanoes. Geology, 36(8), 671–672. https://doi.org/10.1130/focus082008.1

de Silva, S., Zandt, G. e Trumbull, R. 2006. Large-Scale Silicic Volcanism - The Result of Thermal Maturation of The Crust, in: Advances in Geosciences. World Scientific Publishing Co, pp. 215–230.

de Silva, S.L. e Gosnold, W.D. 2007. Episodic construction of batholiths: Insights

from the spatiotemporal development of an ignimbrite flare-up. J. Volcanol. Geotherm. Res. 167, 320–335. https://doi.org/10.1016/j.jvolgeores.2007.07.015

de Silva, S.L., Riggs, N.R. e Barth, A.P. 2015. Quickening the Pulse: Fractal Tempos in Continental Arc Magmatism. Elements 11, 113–118. https://doi.org/10.2113/gselements.11.2.113

DeCelles, P. G., Ducea, M. N., Kapp, P. e Zandt, G. 2009. Cyclicity in Cordilleran orogenic systems. Nature Geoscience, 2(4), 251–257. https://doi.org/10.1038/ngeo469

Digregorio, J. H. 1972. Neuquén. In A. F. Leanza (Ed.), Geología Regional Argentina (pp. 439–505). Academia Nacional de Ciencias.

Ducea, M. 2001. The California Arc: Thick Granitic Batholiths, Eclogitic Residues, Lithospheric-Scale Thrusting, and Magmatic Flare-Ups. GSA Today 11, 4–10. https://doi.org/10.1130/1052-5173(2001)011<0004:TCATGB>2.0.CO;2

Ducea, M. N., Saleeby, J. B. e Bergantz, G. 2015. The Architecture, Chemistry, and Evolution of Continental Magmatic Arcs. Annual Review of Earth and Planetary Sciences, 43(1), 299–331. https://doi.org/10.1146/annurev-earth-060614-105049

Emparan, C. e Suárez, M. 1992. Hoja Curacautín, escala 1:250.000. Carta Geológica de Chile. Servicio Nacional de Geología y Minería, borrador de texto, 1-249, inédito, Santiago.

Ferrari, L., López-Martínez, M. e Rosas-Elguera, J. 2002. Ignimbrite flare-up and deformation in the southern Sierra Madre Occidental, western Mexico: Implications for the late subduction history of the Farallon plate. Tectonics 21, 17-1-17–24. https://doi.org/10.1029/2001TC001302

Franchini, M., López-Escobar, L., Schalamuk, I. B. A. A. e Meinert, L. 2003. Magmatic characteristics of the Paleocene cerro Nevazón region and other late Cretaceous to Early Tertiary calc-alkaline subvolcanic to plutonic units in the Neuquén Andes, Argentina. Journal of South American Earth Sciences, 16(5), 399–421. https://doi.org/10.1016/S0895-9811(03)00103-2

Franzese, J. R. e Spalletti, L. A. 2001. Late Triassic–early Jurassic continental extension in southwestern Gondwana: tectonic segmentation and pre-break-up rifting. Journal of South American Earth Sciences, 14(3), 257-270.

García de Madinabeitia, S., Sánchez Lorda, M. E. e Gil Ibarguchi, J.I. 2008. Simultaneous determination of major to ultratrace elements in geological samples by fusion-dissolution and inductively coupled plasma mass spectrometry techniques. Analytica Chimica Acta, 625, 2, 117-130

García-Sansegundo, J., Farias, P., Gallastegui, G., Giacosa, R. E. e Heredia, N. 2009. Structure and metamorphism of the Gondwanan basement in the Bariloche region (North Patagonian Argentine Andes). International Journal

of Earth Sciences, 98(7), 1599–1608. https://doi.org/10.1007/s00531-008-0330-3

Giacosa, R., Allard, J., Foix, N. e Heredia, N. 2014. Stratigraphy, structure and geodynamic evolution of the Paleozoic rocks in the Cordillera del Viento (37º S latitude, Andes of Neuquén, Argentina). J. Iber. Geol. 40, 331–348. https://doi.org/10.5209/rev_JIGE.2014.v40.n2.45301

Gregori, D., Kostadinoff, J. e Alvarez G. 2013 Preandean geological configuration of the eastern North Patagonian Massif, Argentina. Geos Front 4(6):693-708

Gregori D, Kostadinoff, J. e Strazzere, L. 2008 Tectonic significance and consequences of the Gondwanide orogeny in northern Patagonia, Argentina. Gond Res 14:429-450

Gregori, D. A., Rossi, A. C. e Benedini, L. 2011. Geocronología de la Faja Batolítica Aluminé, Provincia de Neuquén, Argentina. XVIII Congreso Geológico Argentino, Mayo 2011.

Groeber, P. 1929. Líneas fundamentales de la geología del Neuquén, sur de Mendoza y regiones adyacentes. Ministerio de Agricultura. Dirección General de Minas, Geología e Hidrología..

Hervé, F., Calderón, M., Fanning, C.M., Pankhurst, R.J. e Godoy, E. 2013. Provenance variations in the Late Paleozoic accretionary complex of central Chile as indicated by detrital zircons. Gondwana Res. 23, 1122–1135. https://doi.org/10.1016/j.gr.2012.06.016

Hervé, F., Calderón, M., Fanning, M. C., Pankhurst, R. J., Rapela, C. W. e Quezada, P. 2018. The country rocks of Devonian magmatism in the North Patagonian Massif and Chaitenia.

Hofmann, A. 1971. Fractionation corrections for mixed isotope spikes of Sr. K and Pb. Earth and Planetary Science Letters 10, 397-402

Kay, S. M., Burns, W. M., Copeland, P. e Mancilla, O. 2006. Upper Cretaceous to Holocene magmatism and evidence for transient Miocene shallowing of the Andean subduction zone under the northern Neuquén Basin. In Evolution of an Andean Margin: A Tectonic and Magmatic View from the Andes to the Neuque´n Basin (35°-39°S lat) (Vol. 2407, Issue 02, pp. 19–60). Geological Society of America. https://doi.org/10.1130/2006.2407(02)

Kay, S. M., Ramos, V. A., Mpodozis, C. e Sruoga, P. 1989. Late Paleozoic to Jurassic silicic magmatism at the Gondwana margin: Analogy to the Middle Proterozoic in North America?. Geology, 17(4), 324-328.

Latorre, C. O., Vattuone, M. E., Linares, E. e Leal, P. R. 2001. K-Ar ages of rocks from Lago Aluminé, Rucachoroi and Quillen, North Patagonian Andes, Neuquén, República Argentina. 3o South American Symposium on Isotope Geology, Pucon, 577–580.

Lee, C.-T.A., Cheng, X. e Horodyskyj, U. 2006. The development and refinement of continental arcs by primary basaltic magmatism, garnet pyroxenite accumulation, basaltic recharge and delamination: insights from the Sierra Nevada, California. Contrib. to Mineral. Petrol. 151, 222–242. https://doi.org/10.1007/s00410-005-0056-1

Legarreta, L. 1985. Análisis estratigráfico de la Formación Huitrín (Cretácico inferior), provincia de Mendoza.

Llambías, E. J. e Aragón, E. 2011. Volcanismo Paleógeno. Relatorio Del XVIII Congreso Geológico Argentino, Neuquén, 265–274.

Llambías, E. J. e Rapela, C. W. 1989. Las volcanitas de Collipilli, Neuquén (37oS) y su relación con otras unidades paleógenas de la cordillera. Revista de La Asociación Geológica Argentina, 44(1–4), 224–236.

Llambías, E. J. e Sato, A. M. 2011. Ciclo Gondwánico: la provincia magmática Choiyoi en Neuquén. 18o Congreso Geológico Argentino, Neuquén, 53–63.

Llambías, E.J., Leanza, H.A. e Carbone, O. 2007. Evolución Tectono-magmática durante el Pérmico al Jurásico temprano en la Cordillera del Viento (37°05′S - 37°15′S): Nuevas evidencias geológicas y geoquímicas del inicio de la Cuenca Neuquina. Rev. la Asoc. Geol. Argentina 62, 217–235.

Martínez Ardila, A. M., Clausen, B. L., Memeti, V. e Paterson, S. R. 2019. Source contamination, crustal assimilation, and magmatic recycling during three flare-up events in the Cretaceous Peruvian Coastal Batholith: An example from the Ica-Pisco plutons. Journal of South American Earth Sciences, 95(August), 102300. https://doi.org/10.1016/j.jsames.2019.102300

Milan, L.A., Daczko, N.R. e Clarke, G.L. 2017. Cordillera Zealandia: A Mesozoic arc flare-up on the palaeo-Pacific Gondwana Margin. Sci. Rep. 7, 1–9. https://doi.org/10.1038/s41598-017-00347-w

Miller James, N. e Miller Jane, C. 2004. Statistics and Chemometrics for Anaytical Chemistry. 6th, Pearson Education Canada, 296 pp.

Mosquera, A., Ramos, V. A. e Kay, S. M. 2006. Intraplate deformation in the Neuquén Embayment. Special Papers-Geological Society of America, 407, 97.

Newhall, C.G., Self, S., 1982. The Volcanic Explosivity Index (VEI): An Estimate of Explosive Magnitude for Historical Volcanism. J. Geophys. Res. 87, 1231–1238. https://doi.org/10.1029/JC087iC02p01231

Pankhurst, R. J., Rapela, C. W., Fanning, C. M. e Márquez, M. 2006. Gondwanide continental collision and the origin of Patagonia. Earth-Science Reviews, 76, 235–257. https://doi.org/10.1016/j.earscirev.2006.02.001

Pankhurst, R. J., Weaver, S. D., Hervé, F. e Larrondo, P. 1999. Mesozoic-Cenozoic evolution of the North Patagonian Batholith in Aysen, southern

Chile. Journal of the Geological Society, 156(4), 673–694. https://doi.org/10.1144/gsjgs.156.4.0673

Parada, M. A., Lahsen, A. e Palacios, C. 2001. Ages and geochemistry of Mesozoic-Eocene back-arc volcanic rocks in the Aysén region of the Patagonian Andes, Chile. Revista Geológica de Chile, 28(1). https://doi.org/10.4067/S0716-02082001000100002

Paterson, S. R. e Ducea, M. N. 2015. Arc magmatic tempos: Gathering the evidence. Elements, 11(2), 91–98. https://doi.org/10.2113/gselements.11.2.91

Paton, C., Hellstrom, J., Paul, B.,Woodhead, J. e Hergt, J. 2011. Iolite: Freeware for the visualisation and processing of mass spectrometric data. Journal of Analytical Atomic Spectrometry. doi:10.1039/c1ja10172b.

Petrus, J.A. e Kamber, B.S. 2012. VizualAge: A novel approach to laser ablation ICP-MS U-Pb geochronology data reduction. Geostandards and Geoanalytical Research 36(3), p. 247-270.

Pin, C. Briot, D., Bassin, C. e Poitrasson, F. 1994. Concomitant separation of strontium and samarium-neodymium for isotopic analysis in silicate samples, based on specific extraction chromatography. Analytica Chimica Acta 298, 209-217.

Pin, C. e Gannoun, A. 2017. Integrated extraction chromatographic separation of the lithophile elements involved in long-lived radiogenic isotope systems (Rb-Sr. U-Th-Pb, Sm-Nd, La-Ce, and Lu-Hf) useful in geochemical and environmental sciences. Analytical Chemistry 89, 2411-2417.

Pin, C. e Santos Zalduegui, J.F. 1997. Sequential separation of light rare-earth elements, thorium and uranium by miniaturized extraction chromatography: Application to isotopic analyses of silicate rocks. Analytica Chimica Acta 339, 79-89.

Ramos, V. A. 2008. The basement of the Central Andes: the Arequipa and related terranes. Annu. Rev. Earth Planet. Sci., 36, 289-324.

Ramos, V. A. 2009. Anatomy and global context of the Andes: Main geologic features and the Andean orogenic cycle. Backbone of the Americas: Shallow subduction, plateau uplift, and ridge and terrane collision, 204, 31-65.

Ramos, V.A. e Kay, S.M. 2006. Overview of the tectonic evolution of the southern central Andes of Mendoza and Neuquén (35°-39°S latitude). In: Kay, S.M., Ramos, V.A. (Eds.), 2006. Evolution of an Andean Margin: a Tectonic and Magmatic View from the Andes to the Neuquén Basin (35°-39°S Latitude), vol. 407. Geological Society of America, pp. 1-18. Special Paper.

Ramos, V., Mosquera, A., Folguera, A. e García Morabito, E. 2011. Evolución tectónica de los Andes y del Engolfamiento Neuquino adyacente. Relatorio Del 18° Congreso Geologico Argentino, Neuquén, 335–348.

Rapela, C. W. e Llambías, E. J. 1985. La secuencia andesítica terciaria de Andacollo, Neuquén, Argentina. 4o Congreso Geológico Chileno, 458–488.

Sagripanti, L., Folguera, A., Giménez, M., Rojas Vera, E. A., Fabiano, J. J., Molnar, N., Fennell, L. e Ramos, V. A. 2014. Geometry of Middle to Late Triassic extensional deformation pattern in the Cordillera del Viento (Southern Central Andes): A combined field and geophysical study. Journal of Iberian Geology, 40(2), 349–366. https://doi.org/10.5209/rev_JIGE.2014.v40.n2.45305

Sato, A. M., Llambías, E. J., Basei, M. e Leanza, H. A. 2008. The Permian Choiyoi Cycle in Cordillera del Viento (Principal Cordillera, Argentina): Over 25 Ma of magmatic activity. VI South American Symposium on Isotope Geology, April 2016.

Spagnuolo, M. G., Folguera, A., Litvak, V., Rojas Vera, E. A., Ramos, V. A., Vera, E. A. R., e Ramos, V. A. 2012. Late Cretaceous arc rocks in the Andean retroarc region at 36.5°S: Evidence supporting a Late Cretaceous slab shallowing. Journal of South American Earth Sciences, 38, 44–56. https://doi.org/10.1016/j.jsames.2012.05.002

Stipanicic, P. N. e Bonetti, M. I. 1965. Las especies del genero" Saportaea" del triasico de Barreal:(San Juan). Museo Argentino de Ciencias Naturales" Bernardino Rivadavia" e Inst. Nac. de Investigacion de las Ciencias Naturales.

Stipanicic, P. N., Rodrigo, F. E. L. I. X., Baulies, O. L. e Martínez, C. G. 1968. Las formaciones presenonianas en el denominado Macizo Nordpatagónico y regiones adyacentes. Revista de la Asociación Geológica Argentina, 23(2), 67-98.

Suárez, M.; Emparan, C. 1997. Hoja Curacautín. Regiones de la Araucanía y del Bío Bío. Servicio Nacional de Geología y Minería de Chile, Carta Geológica de Chile , No. 71, p. 105.

Suárez, M., de la Cruz, R., Fanning, M. e Etchart, H. 2008. Carboniferous, Permian and Toarcian magmatism in Cordillera del Viento, Neuquén, Argentina: first U-Pb SHRIMP dates and tectonic implications. 17o Congreso Geológico Argentino, S.S. de Jujuy, Argentina. Actas II, 906–907.

Turic, M., Flores, F. A., Omil, R. G., Pombo, R., Sciutto, J., Robles, D. e Cáseres, A. 1987. Geología de las Cuencas petroleras de la Argentina. Evaluación de las Formaciones en la Argentina, 1(1), 1-44.

Urraza, I, Grecco, L., Delpino, S., Arrese, M. e Rapela, C.W. 2011. Petrología y estructura del Complejo Ígneo-Metamórfico Aluminé, Provincia de Neuquen, Argentina. Andean Geology 38 (1): 98-118.

Urraza, I., Grecco, L., Delpino, S., Arrese, M. e Zentilli., M. 2011. Geocronología y geotermobarometría de los cuerpos granodioríticos-tonalíticos del sector

del lago Pulmarí, Neuquen, argentina. XVIII Congreso Geológico Argentino, Mayo 2011, Neuquen.

Zamora Valcarce, G., Rapalini, A. E. e Spagnuolo, C. M. 2007. Reactivación de estructuras Cretácicas durante la deformación Miocena, Faja Plegada del Agrio, Neuquén. Revista de La Asociacion Geologica Argentina, 62(1), 299–307.

Zamora Valcarce, G., Zapata, T. T., Del Pino, D., Ansa, A. A., Valcarce, G. Z., Zapata, T. T., Del Pino, D. e Ansa, A. A. 2006. Structural evolution and magmatic characteristics of the Agrio fold-and-thrust belt. Special Paper of the Geological Society of America, 407(January), 125–145. https://doi.org/10.1130/2006.2407(06)

Zanettini, J. C. M., Leanza, H. A., Giusiano, A., Santamaría, G. R. e Franchi, M. 2010. Hoja Geológica 3972-II Loncopué.

Zapata, T. e Folguera, A. 2005. Tectonic evolution of the Andean fold and thrust belt of the southern Neuquén Basin, Argentina. Geological Society, London, Special Publications, 252(1), 37-56.

Zappettini, E. O., Chernicoff, C. J., Santos, J. O. S. S., Dalponte, M., Belousova, E. e McNaughton, N. 2012. Retrowedge-related Carboniferous units and coeval magmatism in the northwestern Neuquén province, Argentina. International Journal of Earth Sciences, 101(8), 2083–2104. https://doi.org/10.1007/s00531-012-0774-3

Zappettini, E., Méndez, V. e Zanettini, J. C. 1987. Metasedimentitas mesopaleozoicas en el noroeste de la Provincia del Neuquén. Revista de La Asociación Geológica Argentina, 42(1–2), 206–207.

ARTIGOS PUBLICADOS EM COLABORAÇÃO

Orts, D.L., Aguilar Cáceres, C.D., Pernich, S., Zaffarana, C., Gallastegui, G., Assis, S. 2024. Structural evolution and exhumation events recorded in the Huingancó Granodiorite, Cordillera del Viento, Southern Central Andes, Argentina. Journal of South American Earth Sciences 148, 105166. https://doi.org/10.1016/j.jsames.2024.105166

Pernich, S., Zaffarana, C.B., González, V.R., Assis, O.S., Gallastegui, G., Orts, D. 2025. Petrography, magnetic fabrics and timing of emplacement in relation to the San Rafael Orogenic Phase of the Huingancó Granitoids, Permo-Triassic of the Cordillera del Viento, Argentina. Journal of South American Earth Sciences 154, 105390. https://doi.org/10.1016/j.jsames.2025.105390

Journal of South American Earth Sciences 148 (2024) 105166



Contents lists available at ScienceDirect

Journal of South American Earth Sciences

journal homepage: www.elsevier.com/locate/jsames



Structural evolution and exhumation events recorded in the Huingancó Granodiorite, Cordillera del Viento, Southern Central Andes, Argentina

Darío Leandro Orts [a,b,*], Camila Delfina Aguilar Cáceres [a], Sebastián Pernich [a,b], Claudia Zaffarana [a,b], Gloria Gallastegui [c], Sebastián Assis [d]

[a] Universidad Nacional de Río Negro, Instituto de Investigación en Paleobiología y Geología, Río Negro, Argentina
[b] IIPG. UNRN. Consejo Nacional de Investigaciones científicas y Tecnológicas (CONICET), Av. Roca 1242, (R8332EXZ), General Roca, Río Negro, Argentina
[c] Instituto Geológico y Minero de España (IGME-CSIC), Unidad de Oviedo, Oviedo, Spain
[d] Instituto de Geociências, Universidade de Brasília, Laboratório de Geocronología e geoquímica isotópica, 70910-900, Brasília, DF, Brazil

ARTICLE INFO

Keywords:
Andean orogeny
Upper plate deformation
Neuquén basin
Exhumation history
Pluton emplacement
Permian granites

ABSTRACT

This study seeks to unravel the exhumation history of Permian granodiorites corresponding to the Huingancó volcano-plutonic Complex in the southern sector of the Cordillera del Viento (~37°S), located within the Chos Malal fold-thrust belt. In this context, mineral chemistry analyses were conducted on the granodiorites using electron microprobe data to infer the P-T conditions of emplacement, resulting in 700–900 °C and pressures ranging between 1 and 2.4 kbar. Employing a geostatic gradient of 3.7 km/kbar, these values give an estimate of emplacement depths between 4 and 9 km. In order to understand their exhumation path, five samples from the Huingancó Granodiorite were taken along the Huaraco creek on the western flank of the Cordillera del Viento anticline to perform apatite fission track (AFT) analysis. This analysis yielded new cooling ages for the study area ranging between 50 and 80 Ma. Furthermore, inverse thermal modeling using the fission track data revealed two significant exhumation events during the Andean cycle: one during the Late Cretaceous-Paleocene and the other in Miocene times, separated by a period of gradual cooling or stability during Eocene-Oligocene times. These important cooling events are associated with the main construction phases of the Cordillera del Viento. Finally, to characterize its deformation evolution, a structural kinematic model is proposed based on a balanced structural section and its reconstruction to its non-deformed pre-Cretaceous state. The resulting model allows us to identify the structures and mechanisms of uplift rising the Cordillera del Viento, and their association with the main exhumation events depicted in the inverse thermal modeling. The main structure of the Cordillera del Viento corresponds to a fault bending fold that involves the basement in the deformation. Subsequently, its insertion as an intracutaneous wedge is related with the development of the thin-skinned structures at the internal sector of the Chos Malal fold and thrust belt.

1. Introduction

The Andean orogeny shaped the South American landscape, giving rise to various morphostructures, including the Cordillera del Viento (e.g., Giacosa et al., 2014; Sagripanti et al., 2014; Turienzo et al., 2018) (Fig. 1). This structure situated in the southern part of the Principal Cordillera (Ramos, 1999a), reaches elevations between 2800 and 2950 m above sea level. It is bounded to the west by the Loncopué Trough and extends northward to include Cerro Domuyo (4707 m), the highest peak in Neuquén and Patagonia. Within the study area, the oldest rocks belong to the Carboniferous Andacollo Group, deformed during the Permian San Rafael orogenic phase. These rocks are intruded by granodiorite and monzogranite plutons, dikes and rhyolitic domes (Llambías et al., 2007), forming the Huingancó Complex (Sato et al., 2008).

In the southern sector of the Central Andes (Ramos, 1999b), including the Cordillera del Viento, show significant contractional deformation events occurred during the Andean cycle. An initial phase of uplift and exhumation occurred between the Late Cretaceous and Paleogene, evidenced by cooling ages ranging from ~70 to 55 Ma (Jordan et al., 2001; Rojas Vera et al., 2015; Sánchez et al., 2018). Additionally, an Eocene (~55–35 Ma) cooling event was observed by

* Corresponding authorUniversidad Nacional de Río Negro, Instituto de Investigación en Paleobiología y Geología, Río Negro, Argentina.
E-mail address: dorts@unrn.edu.ar (D.L. Orts).

https://doi.org/10.1016/j.jsames.2024.105166
Received 18 May 2024; Received in revised form 9 September 2024; Accepted 16 September 2024
Available online 17 September 2024
0895-9811/© 2024 Elsevier Ltd. All rights are reserved, including those for text and data mining, AI training, and similar technologies.

Galetto et al. (2021) in the Cerro Domuyo area. Finally, a Neogene exhumation phase between ~15 and 7 Ma is documented in the area also linked to contractional deformation (e.g. Zamora-Valcarce et al., 2006; Spagnuolo et al., 2012; Gürer et al., 2016) and reflected in cooling ages (Rojas Vera et al., 2015; Sánchez et al., 2018, 2020, 2024).

The objective of this work is to characterize the cooling history of the Huingancó volcano-plutonic Complex, particularly the Huingancó Granodiorite (Llambías et al., 2007; Sato et al., 2008; Llambías and Sato, 2011), within the context of the deformation in the Chos Malal Fold and Thrust Belt (FTB). Although multi-thermochronological data have been recently published for Permian granitoids in the northern Cordillera del Viento (Galetto et al., 2021), no detailed thermochronological and thermobarometric data have been specifically focused on the Huingancó Granodiorite in the southern Cordillera del Viento. This work aims to provide new insights into the thermal and exhumation history of the Huingancó volcano-plutonic Complex. Specifically, focusing on the Huingancó Granodiorite, the study integrates surface geological mapping, estimates of emplacement depth (via mineral chemistry), and kinematic modeling of structures to develop a comprehensive structural evolution model of the area. This approach allows for the characterization of the Huingancó Granodiorite from its emplacement to its surface exposure, shedding light on the morphostructural evolution of the Cordillera del Viento from pre-deformation stages to the present configuration of this deformation belt.

2. Geological setting

The study area is located is in the southern sector of the Cordillera del Viento, a mountain range that is part of the Southern Central Andes in the northwest of Neuquén province, Argentina (Fig. 1). This is a first-order anticlinal structure, developed during the Andean orogeny, associated with thick-skinned deformation (Kozlowski et al., 1996). The Cordillera del Viento, with a length of approximately 85 km and a width of about 25 km at its widest point, forms the western boundary of the

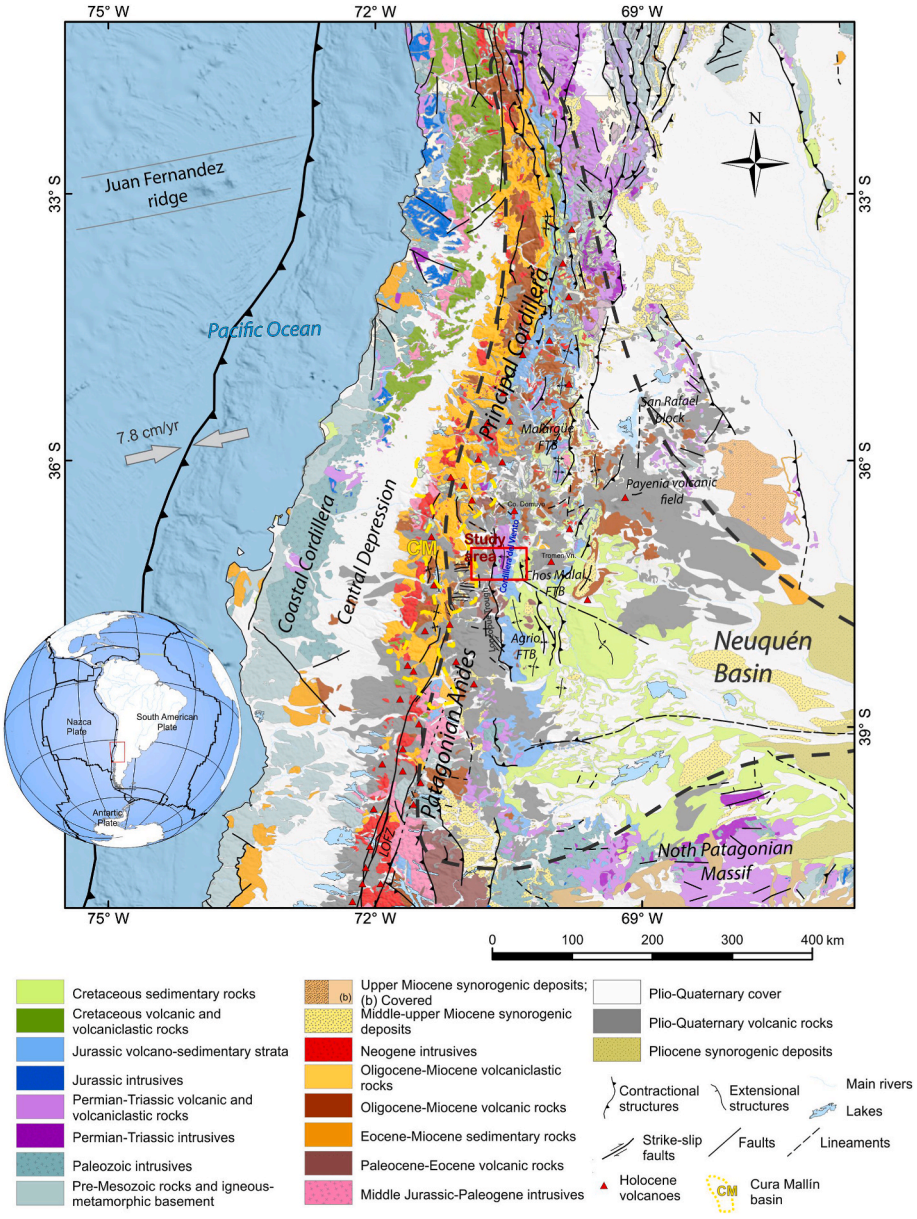


Fig. 1. Present tectonic setting, main geological units and structural features of the southern Central Andes. Geological map (modified from Gómez et al., 2019; Orts et al., 2021), showing the main geological units, morphostructural domains, basins, structural features and location of the study area. LOFZ: Liquiñe-Ofqui fault zone; CM: Cura Mallín basin; FTB: Fold and Thrust Belt.

Chos Malal Fold and Thrust Belt (FTB), which is the northern continuation of the Agrio Fold and Thrust Belt (Giacosa, 2011; Giacosa et al., 2014).

The Cordillera del Viento tectonic and magmatic history that spans from the Paleozoic to the Cenozoic, involving multiple episodes of deformation, sedimentation, and volcanism. The deformation is recognized for Paleozoic rocks, mainly located in its western sector, and Mesozoic rocks, which constitute both the basement and the fill of the Neuquén Basin on its eastern flank (Giacosa, 2011; Giacosa et al., 2014; Sagripanti et al., 2014; Turienzo et al., 2018).

The oldest rocks in the southern region of the Cordillera del Viento belong to the Carboniferous (Zöllner and Amos, 1973). Deformed during the San Rafael orogeny in the early Permian (Giacosa et al., 2014), these rocks form the core of the Cordillera del Viento anticline and belong to the Andacollo Group (Fig. 2)(Llambías et al., 2007). The Arroyo del Torreón Formation, with a thickness of 1500–1800 m, is composed of tuffs, ignimbrites, lava flows, and rhyolite-dacite domes, intercalated with conglomerates, sandstones, and black shales (Giacosa et al., 2014). Arroyo del Torreón is dated to the early Carboniferous (Suárez et al., 2008, 2012; Zappettini et al., 2012), and overlain in angular unconformity by the Huaraco Formation, which consists mainly of dark green to black shales with intercalations of sandstone beds containing marine fossils and plant remains, indicating a late Carboniferous age (Llambías et al., 2007).

The Huingancó volcano-plutonic Complex (Sato et al., 2008) (Fig. 2) consists of at least three facies: 1) granodiorite facies with reported ages between 283.4 ± 1 Ma (U-Pb ID-TIMS in zircons, Sato et al., 2008) and 282.5 ± 2.0 Ma (U-Pb SHRIMP, Hervé et al., 2014), intruding the Andacollo Group; 2) a monzogranite facies intruding the sediments of the Andacollo Group, with an age of 259 ± 9 Ma (U-Pb ID-TIMS in zircons, Sato et al., 2008); 3) small subvolcanic rhyolitic domes intruding the rocks of the Andacollo Group, without evidence of a relationship with the monzogranite and/or granodiorite facies and a K-Ar ages of 260 ± 10 Ma (Llambías, 1986). Finally, a succession of greenish-gray to violet ignimbrites and tuffs, previously assigned to the La Premia Formation (Llambías et al., 2007), discordantly overlies the sediments of the Andacollo Group. Recent geochronological studies on volcaniclastic rocks in this unit yielded ages of 196.29 ± 1.15 Ma and 190.60 ± 0.27 Ma (U-Pb LA-ICP-MS in zircons, Pons et al., 2022), which indicates their equivalence to the Cordillera del Viento Formation and excludes them from the Huingancó volcano-plutonic Complex in the area (Pons et al., 2022).

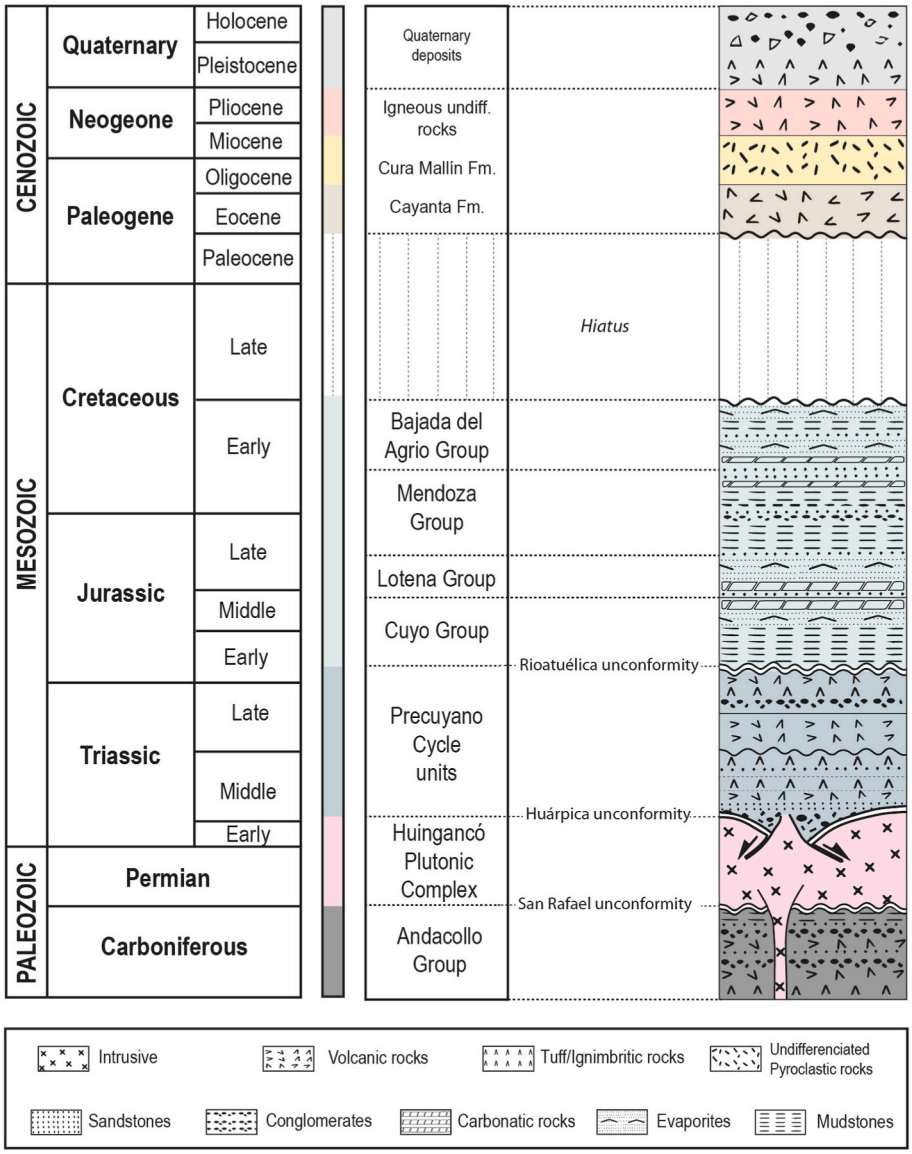


Fig. 2. Stratigraphic chart with the main units comprising the study area. Modified from Orts et al. (2012), Folguera et al. (2015), and Galetto et al. (2021).

The granodiorite facies has the largest areal expression, and in this study, it is referred to as the Huingancó Granodiorite (sensu Llambías and Sato, 2011) (Figs. 3 and 4). The ages attribute the Huingancó volcano-plutonic Complex to the Permian and based on regional correlations with the Choiyoi Group in nearby areas, the age of the complex may extend to the Early Triassic (Giacosa et al., 2014). This entire unit is overlain by the Cordillera del Viento Formation, separated by an extensive erosional surface known as the Huárpica unconformity (Llambías et al., 2007) (Figs. 2 and 4).

During the Early Jurassic, extensional tectonics led to the development of hemigrabens controlling the accumulation of syn-rift sequences, composed of andesitic to rhyolitic volcanic rocks, corresponding to the Precuyano Cycle (Gulisano, 1981; Leanza et al., 2005). The Cordillera del Viento Formation (Figs. 2 and 4), the basal unit of this cycle, consists of up to 2000 m of mainly andesitic to rhyolitic volcanic rocks, reflecting a bimodal character with alternating basaltic-andesitic layers and rhyolitic ignimbrites (Leanza et al., 2005; Llambías et al., 2007; Suárez et al., 2012; Pons et al., 2022). Overlying it, in angular unconformity and contouring the eastern flank of the Cordillera del Viento, is the Milla Michicó Formation (Figs. 2 and 3), characterized by basaltic to basalt-andesitic lavas. Zappettini et al. (2018) dated an equivalent unit in the northern Cordillera del Viento at 187.9 ± 1.8 Ma (U-Pb SHRIMP). Discordantly overlying the Milla Michicó Formation is the La Primavera Formation, representing the first marine transgression that occurred in the study area in Early Jurassic times (Llambías et al., 2007; Suárez et al., 2008, 2012; Zappettini et al., 2018). This unit consists of volcaniclastic deposits with marine fossils, conglomerates, tuffs, and breccias, with reported ages ranging between 184 and 182 Ma (Suárez et al., 2008; Zappettini et al., 2018), and is capped by the Rioatuélica unconformity (Fig. 2).

Overlying the Precuyano Cycle, the Cuyo Group constitutes the first widespread marine sedimentary cycle in the Neuquén Basin (Arregui et al., 2011a) (Fig. 2). The Los Molles Formation, with over 800 m of black shales intercalated with subordinate conglomerate levels, limestones, and calcareous nodules, marks the basal unit (Leanza et al., 2005). The Cuyo Group culminates with the Tábanos Formation, characterized by massive white gypsum and limestone beds, overlying the Los Molles Formation and separated from the Lotena Formation by the Intracallovian unconformity (Fig. 2).

The Lotena Group (Fig. 2), comprising the Lotena, La Manga, and Auquilco formations, consists of siliciclastic to carbonate and evaporitic rocks with an approximate thickness of 180 m (Gulisano and Gutiérrez Pleimling, 1995, Arregui et al., 2011a). Particularly, the gypsum level corresponding to the Auquilco Formation stands out as a major detachment level for the fold-and-thrust belt in this region.

The Mendoza Group comprises the Tordillo, Vaca Muerta, Mulichinco and Agrio formations, which were deposited between the Late Jurassic and Early Cretaceous (Arregui et al., 2011b). This group begins with the fine-grained reddish nonmarine clastic deposits of the Tordillo Formation, which are overlain by the marine black shales of the Vaca Muerta Formation. The Lower Cretaceous Mulichinco Formation is characterized by conglomerates, sandstones, mudstones, and intercalated limestones, indicative of a sudden sea level drop. Subsequently, during the Early Cretaceous, a marine incursion led to the deposition of the Agrio Formation, which is marked by thick sequences of black shales interbedded with limestones and sandstones (Turienzo et al., 2018) (Fig. 2). Overall, the Mendoza Group in the study area has an estimated thickness of 2200 m (Turienzo et al., 2020).

The Bajada del Agrio Group (Fig. 2), from the Early Cretaceous, includes the Huitrín and Rayoso formations, representing a notable regressive event. The Huitrín Formation consists of shallow marine and hypersaline deposits (Leanza, 2003), while the evaporites and red beds

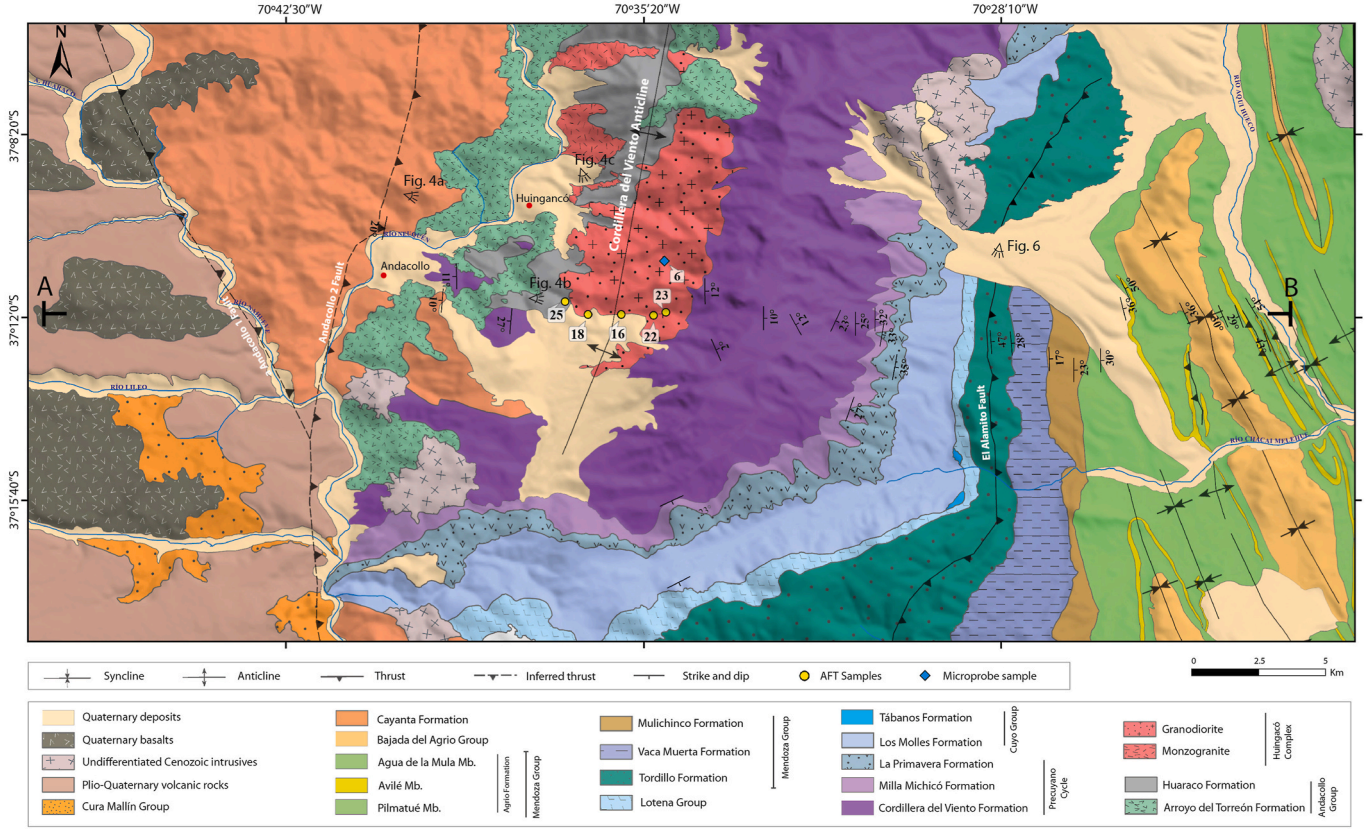


Fig. 3. Geological map of the study area (based on Llambías et al., 2007; Giacosa, 2011; Zappettini et al., 2018; Turienzo et al., 2018, showing the location of the structural section A-B and the samples of apatite fission tracks analyses (CPH16, CPH18, CPH22, CPH23, CPH25 CPH6) and for petrographic description and microprobe analysis (CPH6).

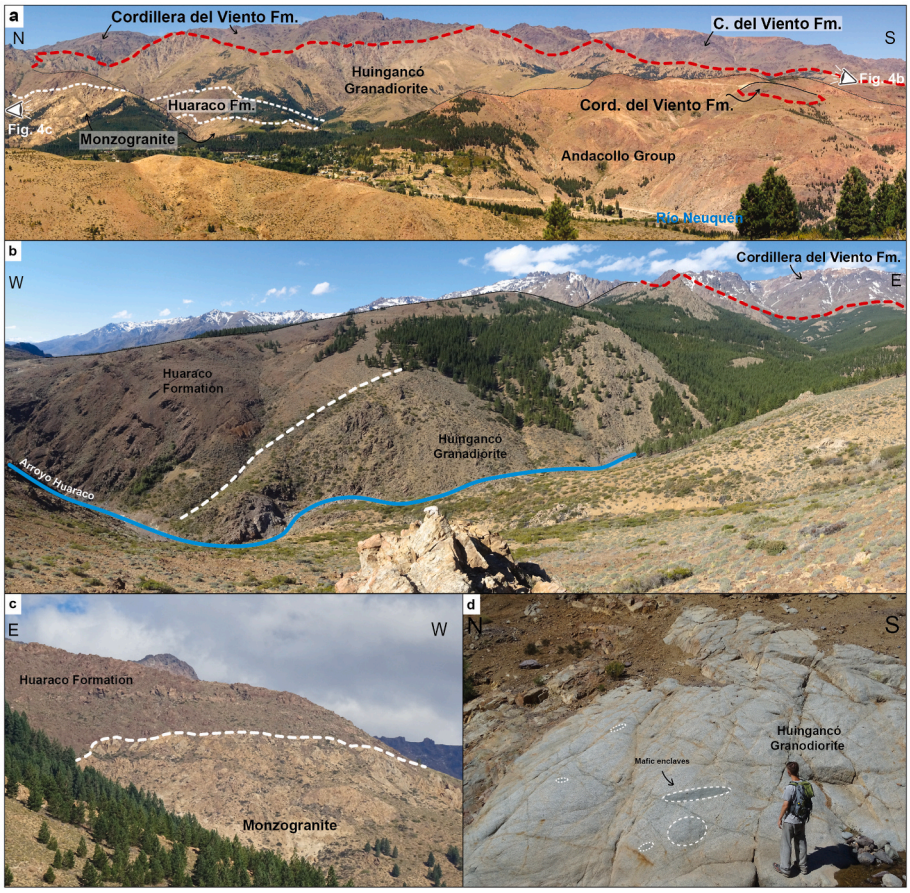


Fig. 4. Outcrops of the study area (see Fig. 3 for locations). a) Panoramic view from the Andacollo viewpoint of the western flank of the Cordillera del Viento, showing main units and contact relations with the Huingancó Granodiorite. Red dashed line: Huárpica unconformity; White dashed line: intrusive contacts. b) Panoramic view of Arroyo Huaraco, where the intrusive contact between the granodiorite facies and the Huaraco Formation is observed. Upstream, the Cordillera del Viento Formation is observed above the Huárpica unconformity. c) Intrusive contact of the monzogranite facies with the Huaraco Formation seen from the Cañada Molina trail. d) Outcrop of the Huingancó Granodiorite with mafic microgranular enclaves in Arroyo Huaraco.

of Rayoso Formation indicate a continental environment, marking the disconnection of the Neuquén Basin from the proto-Pacific Ocean (Zavala and Ponce, 2011). This group reaches an estimated thickness of 300 m (Turienzo et al., 2020).

The Neuquén Basin experienced a renewed phase of tectonic activity between the Late Cretaceous and the Holocene, with both extensional and compressional deformations affecting the strata, coupled with periodic magmatic events (see Fennell et al., 2019 and references within). The Cayanta Formation (Rapela and Llambías, 1985) is part of these magmatic events, primarily composed of andesitic volcanic rocks, with ages ranging from 56 to 50 Ma (Jordan et al., 2001; Kay et al., 2006) (Figs. 2 and 3).

Oligocene to Miocene arc and retroarc magmatism in the Neuquén Basin commenced after a regional magmatic hiatus (Kay et al., 2006). The Cura Mallín Formation (Niemeyer and Muñoz, 1983), also referred to as the Cura Mallín Group (Pedroza et al., 2017) consist of predominantly andesitic lavas, volcanic breccias and reworked silicic pyroclastic deposits, followed by conglomerates, sandstones and tuffs deposited in fluvial, lacustrine and deltaic sedimentary deposits (Niemeyer and Muñoz, 1983), with thicknesses reaching ~3 km in the Cura Mallín basin (Kay et al., 2006) (Fig. 1). On the Argentinian side, the Cura Mallín Formation is dated between 25 and 9 Ma, with its sedimentary section constrained between ~20 and 9 Ma (see Encinas et al., 2024a). The geochronological and structural data presented by Encinas et al. (2024a) also suggest the transition from extensional to contractional deformation around 19 Ma in this basin. The Cura Mallín Formation is overlain by lavas and volcanic breccias of the Trapa Trapa Formation (Niemeyer and Muñoz, 1983), of late Miocene age (see Encinas et al., 2024a for a recent synthesis).

Pliocene rocks are found in the western sector of the Cordillera del Viento as part of the Centinela Formation (Fig. 3), which primarily consist consists of basalts and dacites with K-Ar ages ranging between 3.2 ± 0.2 and 2.6 ± 0.1 Ma (Rovere, 1998; Kay et al., 2006).

In the study area, basalts and andesitic tuffs belonging to the Maipo Basalt unit and equivalents are predominantly present, as described by Groeber (1929). Additionally, Rovere et al. (2004) identified Pleistocene glaciofluvial deposits composed of conglomerates and blocks (Figs. 2 and 3).

3. Methods

Analytical studies were supported by a detailed geological database utilizing geological maps from specific studies by several authors (e.g., Llambías et al., 2007; Giacosa, 2011; Zappettini et al., 2018; Turienzo et al., 2018), as well as geological maps of Neuquén Province at scales of 1:500,000 (Leanza et al., 2011) and 1:250,000 (Rovere et al., 2004) produced by the Argentine Geological and Mining Survey (SEGEMAR). Additionally, SRTM satellite images (digital elevation models) and ASTER images were obtained from the USGS website and processed using ENVI 4.7 software. Field surveys, satellite image processing, and compiled data were combined to create a geological map (Fig. 3) of the southern Cordillera del Viento region using ArcGIS 10 desktop software.

From a sample of the Huingancó Granodiorite (CPH6, see Fig. 3 for location), depth and emplacement temperatures were estimated using

mineral chemistry studies obtained via electron microprobe analysis. Crystallization pressures, correlated with emplacement depth, and temperatures were estimated based on amphibole and plagioclase equilibrium compositions and aluminum content in amphibole.

For structural kinematic modeling, Andino3D software (Cristallini et al., 2021) was employed, utilizing its array of structural tools. A balanced structural section of the southern Cordillera del Viento was constructed and subsequently restored to its undeformed state. Then, integrating data on cooling ages derived from apatite fission track analysis of the Huingancó Granodiorite was spatially analyzed with respect to the section's pre-deformation geometry. These analyses were conducted at LA.TE. ANDES S.A. laboratory, involving five sample analyses processed using Hefty® software (V.1.9.3; Ketcham et al., 2007), resulting in the exhumation history of the Huingancó Granodiorite and identification of key deformational pulses in the study area.

3.1. Petrography and electron microprobe analysis

Petrographic description and electron microprobe analysis were conducted on sample CPH6 (37°10′53.3"S/70°34′56.4"W, see location in Fig. 3), representing the granodiorite of the Huingancó volcano-plutonic Complex. This mineral chemical analysis was carried out through Technical-Scientific Services of the University of Oviedo (Spain). The equipment and analytical conditions used were as follows: Cameca SX-100 electron microprobe with a voltage intensity of 15 kV, current of 15 nA, and acquisition time of 10 s per element. Calibration employed a combination of silicates and oxides. The standards of the Bureau de Recherches Geologiques et Minières (BRGM) were used to refine the results. Analyses of an unknown secondary standard under the same conditions as the sample measurement suggested an accuracy of 1%. Results are given in Supplementary data: Tables S1 and S2. These studies aimed to determine the mineral composition and establish the crystallization/emplacement conditions (pressure and temperature) of plutonic bodies. Data on pressure and temperature for sample CPH6 were calculated based on the geothermometers and geobarometers of Hammerstrom and Zen (1986), Hollister et al. (1987), Johnson and Rutherford (1989), Schmidt (1992), Hollister et al. (1987), Anderson and Schmidt (1995), Ridolfi et al. (2010), and Putirka (2016).

3.2. Balanced structural section

A balanced cross-section enables a two-dimensional study of the structure of an area in its deformed state, providing a representation at depth of the structures observable directly in the field and/or subsurface, which makes it an admissible section. However, the section must also be viable, meaning it can be restored to its undeformed state while respecting certain geometric conditions: conservation of strata length and preservation of area in both states. If these criteria are met, the section is considered balanced. Thus, a balanced structural section is both viable and admissible (Woodward et al., 1989).

Therefore, utilizing the structural modeling software, Andino3D, developed by LA.TE. ANDES S.A., a suitable model was generated to explain the andean structure of the Cordillera del Viento. Additionally, strike and dip data were collected on the field, compiled from previous studies and using the V-rule method tool of the software. A stratigraphic list of geological units with their thicknesses, based on Turienzo et al. (2020), was generated and corroborated using thickness measurement tools in Andino3D to create a structural section. Kinematic modeling of structures was conducted to achieve an admissible model. Subsequently, the section was restored to its undeformed state using the flexural slip unfold mechanism. Andino3D allows for progressive restoration of strata deformation until reaching the initial structure geometry. Through this process, all blocks bounded by faults were restored, integrated into a balanced palinspastic reconstruction.

3.3. Apatite fission-track dating (AFT)

Apatite fission tracks (AFT) from 5 samples from the Huingacó granodiorite were analyzed in the LA.TE. ANDES laboratory (https://www.lateandes.com), Salta, Argentina. Apatite fractions were obtained by mechanical separation, magnetic separation (Frantz isodynamic separator) and heavy liquid treatment (LST = litium heteropolytungstate and DIM = diiodomethane). Approximately 100 apatite crystals for each sample were then mounted in epoxy. In general, the apatite crystals are subhedral to euhedral, and fractured. The mounted samples were polished and then leached under nitric acid (HNO3) 5.5 N for 20 s at 20 °C to reveal spontaneous tracks. The samples were then irradiated with the External Detector in the RA-3 Reactor (Centro Atómico Ezeiza, Buenos Aires, Argentina). The irradiation process took place over 76 h, with a fluency of 7×10^{15} n cm^{-2}. After the decay period in the reactor, the batch was sent back to the LA.TE. ANDES S.A. laboratory for the fission-track measurements. Overall, apatite grains with a surface area greater than 600 μm^2 were used for measurements. Areas with obvious crystallographic dislocations were avoided. All measurements were made with a Zeiss AXIO Imager Z2m binocular microscope. The system is equipped with the TrackWorks Autoscan software, which carried out the counting of the tracks and determination of other parameters, such as fission-track etch pit diameter (Dpar). The ages were determined with the ζ value method from Hurford and Green (1983) and Wagner and Van den haute (1992). Data processing was done using Trackkey software (Dunkl, 2002) that allowed age calculation. The uncertainty on obtained ages is reported at the 1–2 σ level.

4. Results

4.1. Petrography, mineral chemistry, and pressure-temperature conditions of the Huingancó granodiorite

Sample CPH6 was chosen as representative of the granodiorites from the Huingancó volcano-plutonic Complex for mineralogical, textural, and compositional analysis. Petrographically, it exhibits a medium to fine-grained texture, composed of mafic minerals (amphibole and biotite, 41%), quartz (33%), plagioclase (20%), microcline (5%), and epidote (1%) (Fig. 5). Chlorite is also present as alteration of amphiboles and biotites, appearing as aggregates or clots. In the case of amphiboles, two types can be distinguished: hornblende (pleochroic from dark to light green, Fig. 5A) and tremolite-actinolite (light green). Additionally, plagioclases with oscillatory zoning pattern are observed (Fig. 5B), showing alteration to sericite and with sieving, along with quartz exhibiting chessboard extinction. Based on these characteristics, sample CPH6 was classified as a granodiorite.

From the electron microprobe analyses, the composition of amphiboles and plagioclases that constitute the granodiorite of sample CPH6 was obtained (See Supplementary data: Tables S1 and S2). This allowed for the classification of these minerals for subsequent pressure and temperature calculations. The light green amphiboles have very low content of Fe, Ti, Al, and Na, but higher Mg content compared to the dark green ones. Both types of amphiboles are classified as calcic amphiboles based on the number of $(Ca + Na)_B$ and Na_B atoms, meeting the following condition: $(Ca + Na)_B \geq 1.34$ and $Na_B < 0.67$ (Leake et al., 1997). These amphiboles are further subclassified according to the number of Si atoms and the $Mg/(Mg + Fe^{+2})$ ratio (Leake et al., 1997), ranging from actinolite (Si = 7.89 a.p.f.u. (atoms per formula unit) and $Mg/(Mg + Fe^{+2}) = 0.67$) to magnesium-hornblende (Si = 6.89 a.p.f.u. and $Mg/(Mg + Fe^{+2}) = 0.6$) (See Supplementary data: Fig. S1). The latter is the group used for pressure and temperature calculations. On the other hand, plagioclase compositions range from oligoclase to labradorite (An_{17} to An_{55}). They are mostly crystals of andesine, sometime with labradorite cores. In addition, crystals with concentric oscillatory zoning patterns of andesine and labradorite (An_{32}-An_{55}) are

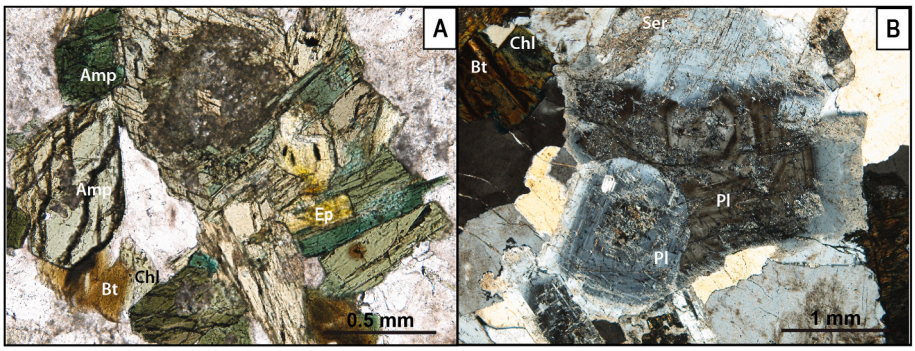


Fig. 5. Petrography of the Huingancó Granodiorite, sample CPH6. A) Amphibole (Amp) crystals epidote (Ep) and biotite (Bt) altered to chlorite (Chl). Plane-polarized light. B) Plagioclase (Pl) crystals showing oscillatory zoning pattern with alteration to sericite (Ser), and biotite (Bt) crystals altered to chlorite (Chl). Crossed polars.

common. In both cases, plagioclase can show rims of oligoclase (An_{17}-An_{25}). Only oligoclase and andesine are used for the calculations (See Supplementary data: Fig. S2).

In Table 1, the thermobarometric results are summarized, involving various methodologies. These include thermometers such as those proposed by Ridolfi et al. (2010) and Putirka (2016), as well as barometers developed by Ridolfi et al. (2010), Hammerstrom and Zen (1986), Hollister et al. (1987), Johnson and Rutherford (1989), and Schmidt (1992). Additionally, methods based on amphibole-plagioclase equilibrium, like the thermometer introduced by Hollister et al. (1987) and the barometer by Anderson and Smith (1995), are featured. The approach by Putirka (2016), which derives temperature data from the melt composition, is also incorporated. Detailed results for individual amphiboles and plagioclases are provided in Supplementary data Table S1 and Table S2, respectively.

4.2. Structure kinematics and balanced cross-section A-B

Several geological constraints were considered to establish the permissible structural section of the Cordillera del Viento: i) layer attitudes; ii) the presence of the passive roof fault "El Alamito" (Sánchez et al., 2018) (Fig. 6), which exhibits a ramp-flat relationship in the repeated strata of the Tordillo Formation; iii) sedimentary cover thickness (for the pre-contractional Cretaceous state); and iv) core structure exhumation and exposure of basement rocks and the Huingancó Granodiorite at the final stage (t4, Fig. 7). The proposed kinematic model for the main structure of the Cordillera del Viento (Fig. 7) was achieved by varying fault geometry and detachment depth until all the aforementioned constraints were satisfied. This included a fault bend folding structure as the primary structure of the section and its insertion into the Chos Malal FTB.

Subsequently, based on surface structural data and kinematically modeled permissible structures, a structural section A-B was constructed (Fig. 8), restoring and balancing each block bounded by faults. The balanced section A-B (Fig. 8a) spans 37 km from west to east. In the western part, it is characterized by the presence of the Andacollo Faults 1 and 2 (AF1 and AF2; Fig. 8). These are inferred high-angle faults associated with the inversion of previous extensional structures as interpreted by previous authors (e.g. Zapata et al., 1999, Cobbold and Rossello, 2003). Turienzo et al. (2018) have also suggested that these inferred faults may function as backthrusts developed in the hanging wall of the Cordillera del Viento Thrust, contemporaneus with the development of the fault-bend fold. These structures lie on the western flank of the main structure, the Cordillera del Viento anticline, and border Cenozoic deposits to the west. The Cordillera del Viento anticline has a wavelength of approximately 25 km, eastward vergence, and is interpreted as a fold generated by the fault bending mechanism (Suppe, 1983), associated with the Cordillera del Viento Thrust (CCV; Fig. 8), which exposes Paleozoic basement rocks and Lower Jurassic rocks forming the anticline core. To the East, it exhibits the passive roof fault named "El Alamito" (Sánchez et al., 2018) (EA; Fig. 8), with a 47° eastward dip, cutting through the repeated strata of the Tordillo Formation and exposing the detachment level located in the Lotena Group evaporites. The easternmost features in the section are the thin-skinned structures of the Chos Malal Fold and Thrust Belt (FTB). These second-order structures, with short wavelengths of approximately 1–2 km, are partly due to the eastward propagation of deformation as the wedge advanced (Fig. 7), as interpreted by previous authors (e.g., Kozlowski et al., 1996; Sánchez et al., 2015, 2018; Turienzo et al., 2014, 2018). In our model, we also interpret that these structures are partially controlled by the Lower Cordillera del Viento Thrust (LCCV; Fig. 8).

The palinspastic reconstruction of the section represents the pre-

Table 1
Summary of the temperatures and pressures obtained for the Huingancó Granodiorite, sample CPH6.

Sample	CPH6	Huingancó Granodiorite		
Calibration				error
Geothermometers (°C)	Hollister et al. (1987)	Amp - PI (Expression B)	724.4	±40 °C
	Ridolfi et al. (2010)	Amphibole - (Ec. 1)	755	±22 °C
	Putirka et al. (2016)	Amphibole - (Ec. 5)	720	±30 °C
		Liquid - (Ec. 3)	968.5	±33 °C
Geobarometers (Kbar)	Hammerstrom and Zen (1986)	Amphibole	1.8	±3 kbar
	Hollister et al. (1987)	Amphibole	1.7	±1 kbar
	Johnson and Rutherford (1989)	Amphibole	1.3	±0.5 kbar
	Schmidt (1992)	Amphibole	2.4	±0.6 kbar
	Anderson and Smith (1995)	Amp — PI	1.8	±0.6 kbar
	Ridolfi et al. (2010)	Amphibole - (Ec. 4)	1	
Abbreviations				
Amp: Amphibole, Pl: Plagioclase.				

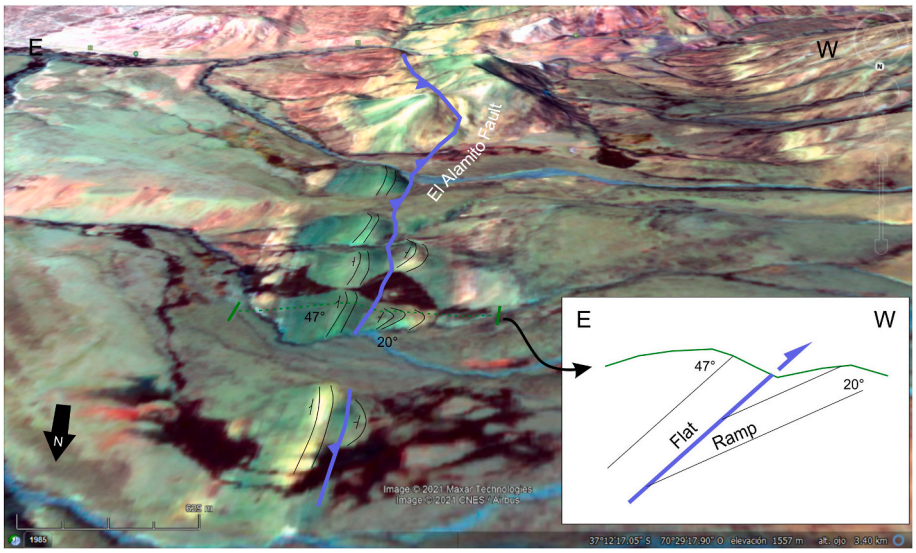


Fig. 6. El Alamito Fault (Sánchez et al., 2018), viewed from Google Earth software, with a diagram indicating the ramp-flat relationship of the strata corresponding to the Tordillo Formation. See Fig. 3 for view location.

Cretaceous undeformed state (Fig. 8b) with an initial length (lo) of 51 km. Considering the final length (lf) of section A-B, a tectonic shortening of 14 km (27%) was determined.

4.3. Low-temperature thermochronology

4.3.1. Apatite fission tracks (AFT)

Age and fission track length data of the five Permian granodiorite samples is summarized in Tables 2 and 3. It can be observed that all samples pass the chi-square test P(χ^2), with values greater than 5%, which is consistent with what is observed in the radial plots showing low data dispersion (Fig. 9), indicating a single population of cooling ages for each sample. See Supplementary Data S3 for raw apatite fission track data, including track counting, grain ages, and confined track lengths for all samples.

The samples CPH16, CPH18, and CPH23 present cooling ages belonging to the Late Cretaceous. From sample CPH16, 34 grains were measured, which yielded a cooling age of 74.8 ± 6.2 Ma, with a P(χ^2) value of 8.1% (Fig. 9A). For sample CPH18, a cooling age of 71.0 ± 4.2 was obtained from the measurement of 34 apatite grains, and the chi-square test P(χ^2) gives a value of 9.94% (Fig. 9B). In the case of sample CPH23, the results were obtained from the measurement of 35 grains, resulting in a central age of 71.9 ± 6.1 Ma, whose P(χ^2) test gives a value of 16.51% > 5% (Fig. 9D).

On the other hand, sample CPH22, from the measurement of 16 apatite grains, yielded a central cooling age of 64.5 ± 6.5 Ma, which locates it close to the Late Cretaceous-Paleogene boundary (Fig. 9C), and gave a chi-square test P(χ^2) value of 81.35%. Finally, sample CPH25 yielded the youngest age in the series, 53.9 ± 4.0 Ma, corresponding to the Ypresian (Early Eocene), from the measurement of 35 grains, with a P(χ^2) value of 30.84% (Fig. 9E).

4.3.2. Thermal history modelling

In this study, an inverse thermal modeling approach was employed to derive optimal time-temperature paths for individual samples by integrating analytical data, including cooling ages, distribution of fission track lengths, and Dpar values. Thermal history simulations were conducted using the HeFTy® software (V.1.9.3; Ketcham et al., 1999), utilizing the AFT data provided by LA.TE ANDES S.A. HeFTy generates random time and temperature paths that adhere to the input data for each sample (Genge, 2021). To ensure accuracy, relevant geological constraints were considered during modeling, defining zones through which the calculated time-temperature paths must traverse. Each model underwent testing with 10,000 random paths using the Monte Carlo inverse model, and goodness-of-fit statistics incorporated in HeFTy were utilized for evaluation, with merit values of 0.5 and 0.05 indicating good and acceptable fits, respectively (Ketcham, 2005). In addition to the best-fit model paths, the weighted mean paths were employed to calculate cooling rates for the samples (Fig. 10). The weighted mean path represents an average thermal trajectory that accounts for the statistical distribution of acceptable solutions, which can be helpful when comparing multiple model results (Flowers et al., 2015).

For the inverse thermal modeling of the five samples, the following geological constraints (black boxes in Fig. 10) were introduced to ensure that the paths conform to known geological data: i) Crystallization ages of the Huingancó Granodiorite at 289 ± 1 Ma (U-Pb ID-TIMS in zircons, Sato et al., 2008) and 282.5 ± 2.0 Ma (U-Pb SHRIMP, Hervé et al., 2014) with subsequent passage through temperatures between 240 and 300 °C; ii) Denudation associated with the Huárpica unconformity generated during the Early to Middle Triassic (Llambías et al., 2007), reaching temperatures between 20 and 40 °C; iii) The heating related to the burial of the samples to depths of ~5.4 km, derived from the palinspastic reconstruction (see "Initial depth" in Fig. 8). This burial heating occurred after the accumulation of the volcano-sedimentary successions of the Neuquén Basin until the late Early Cretaceous. To estimate the maximum temperatures reached by the samples after burial, we considered reported vitrinite reflectance values (% Ro) from sedimentary successions in the inner zone of the Chos Malal FTB (Folguera et al., 2015; Karg and Littke, 2020; Sánchez et al., 2024). Karg and Littke (2020) reported a maximum value of 3.1 % Ro obtained from the kinetic thermal modelling of the Los Molles Formation, while Folguera et al. (2015) and Sánchez et al. (2024) reported maximum values of 1.51 and 2.9 % Ro for Vaca Muerta Formation respectively. Following the empirical algorithm of Barker and Pawlewicz (1994) the value of 3.1 % Ro is equivalent to a maximum temperature of 226.7 ± 3.2 °C. This maximum temperature align with estimations of paleogeothermal gradients between 30 °C/km (Folguera et al., 2015) and 51 °C/km (Galetto et al., 2021), which are characteristic of this retroarc region. However, it is important to note that in deformed regions with complex tectono-magmatic histories, such as this one, the crustal thermal field can be significantly deformed, with isotherms potentially compressed or relaxed over time, and magmatic events further distorting the thermal field (e.g., Malusà and Fitzgerald, 2019). Therefore, while paleogeothermal gradient values provide a useful reference, they should be

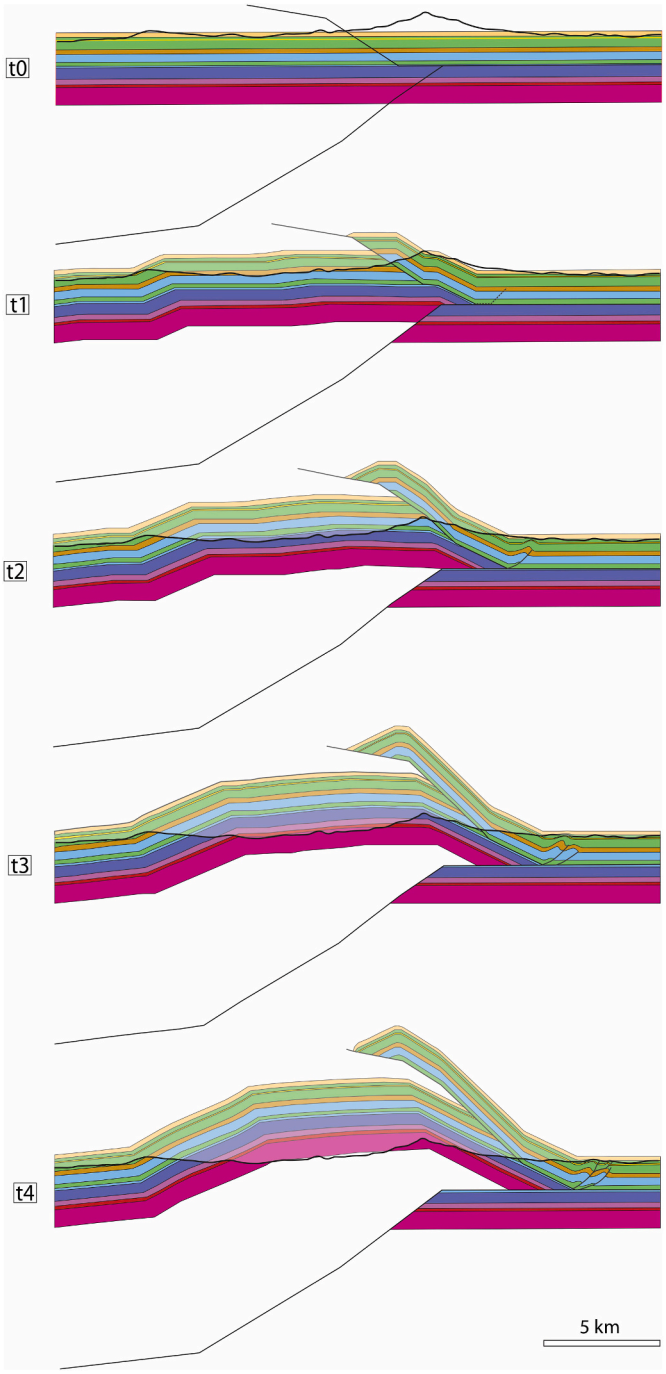


Fig. 7. Structural kinematic model of the Cordillera del Viento anticline, using the fault bending mechanism and its insertion as an intracutaneous wedge, along with the development of the passive roof fault "El Alamito". Note that second-order structures are partly developed due to the eastward propagation of deformation as the wedge advanced.

interpreted with caution, considering the dynamic nature of the thermal field in such settings; iv) AFT ages obtained in this study were used as t-T bounding boxes, with temperatures between 60 and 120 °C, reflecting the AFT partial annealing zone (PAZ). It is worth noting that in the modeling of sample CPH25 (Fig. 10), the temperature range of the graph was expanded to consider the geological constraint obtained through electron microprobe analysis (see Table 1) with maximum temperatures ranging between 700 and 900 °C, representing magma crystallization temperatures. Fission tracks in apatites are not preserved at such high temperatures, so the upper limit of 260 °C was considered for all the samples. Moreover, the t-T boxes representing the geological constraints (see Fig. 10) exceed the limits of the ages and temperatures mentioned to provide greater freedom to the possible good and acceptable cooling paths (pink and green envelopes in Fig. 10).

After the crystallization stage of the granodiorite, the region was affected by denudation, as evidenced by the Huárpica unconformity, responsible for carving the erosive surface and exhuming the domes of the plutons (Llambías et al., 2007), until a temperature of 15–20 °C (see Fig. 10). Subsequently, a burial stage began, accompanied by a progressive increase in temperature, contemporaneous with the increasing lithostatic load due to the accumulation of the sedimentary column of the Neuquén Basin from the Early Jurassic to the Late Early Cretaceous (Fig. 10). For instance, in sample CPH16, the thermal history modeling indicates an exhumation/cooling event from 100 Ma to approximately 70 Ma, with temperatures ranging from 210 to 75 °C, and the possible cooling paths narrowing between 90 and 75 Ma (within the envelope of good t-T paths). This Cretaceous-Paleocene event reflects a cooling rate of ~2.82 °C/Ma, derived from the weighted mean path. This event is followed by gradual cooling (~0.44 °C/Ma) until a second, smaller exhumation event around 20 Ma, with temperatures below 60 °C and a cooling rate of ~1.75 °C/Ma (see Fig. 10). In sample CPH18, two exhumation stages are also highlighted: the first occurs at temperatures ranging from 200 to 120 °C (as shown in the envelope of good t-T paths) and reaches temperatures of ~60 °C during the 90 to 70 Ma period, with a cooling rate of ~3.39 °C/Ma. This is followed by a period of stability between 65 and 20 Ma, characterized by slow cooling (~0.36 °C/Ma) at temperatures between 60 and 40 °C. A second cooling event begins around 20 Ma, with a cooling rate of ~1.63 °C/Ma (see Fig. 10). In sample CPH22, the first cooling event occurs between 100 and 70 Ma with temperatures ranging from 220 to 70 °C, indicating a cooling rate of ~2.39 °C/Ma. This is followed by a slowdown to ~0.80 °C/Ma, with a subsequent increase to ~1.20 °C/Ma in the final stage. Sample CPH23, like CPH18, exhibits a narrower first cooling event (as shown in the good paths envelope) around 90 Ma, with temperatures ranging from 220 °C to 70 °C (cooling rate of ~2.53 °C/Ma), whereas the second exhumation event occurs after 20 Ma, with temperatures below 50 °C and cooling rate of ~1.86 °C/Ma. Finally, in sample CPH25, the first cooling stage occurs between 100 and 60 Ma, with temperatures ranging from 200 to 60 °C (cooling rate of ~2.83 °C/Ma), followed by the next stage at around 10 Ma with temperatures below 50 °C (cooling rate of ~2.66 °C/Ma). Between these two stages, a period of stability is observed, with temperatures remaining near 60 °C between 60 and 10 Ma (Fig. 10).

Across all samples, two significant exhumation events during the Andean cycle stand out: the first during the Late Cretaceous-Paleocene and the second during the Miocene. The cooling rates derived from the weighted mean paths range from ~2.40 to ~3.39 °C/Ma during the Cretaceous event, and from ~1.20 to ~2.66 °C/Ma during the Neogene event, with a period of stability or slower cooling (rates from ~0.36 to ~0.80 °C/Ma) between these events during the Paleocene-Oligocene. It is important to note that while the best-fit model and weighted mean paths offer insights into these events, the full spectrum of acceptable paths should be considered, as all good and acceptable paths represent possible solutions.

5. Discussion

5.1. Emplacement depths, crystallization conditions, and early exhumation stage of the Huingancó granodiorite

The Huingancó Granodiorite has a magmatic crystallization age ranging from 280 to 290 Ma (Suárez and De La Cruz, 1997; Sato et al., 2008; Hervé et al., 2014). Its emplacement would have occurred after the San Rafael deformation phase of the Gondwanan cycle, as evidenced by its intrusion relationship with the deformed rocks of the Andacollo Group (Fig. 11a). According to the thermobarometric results obtained in

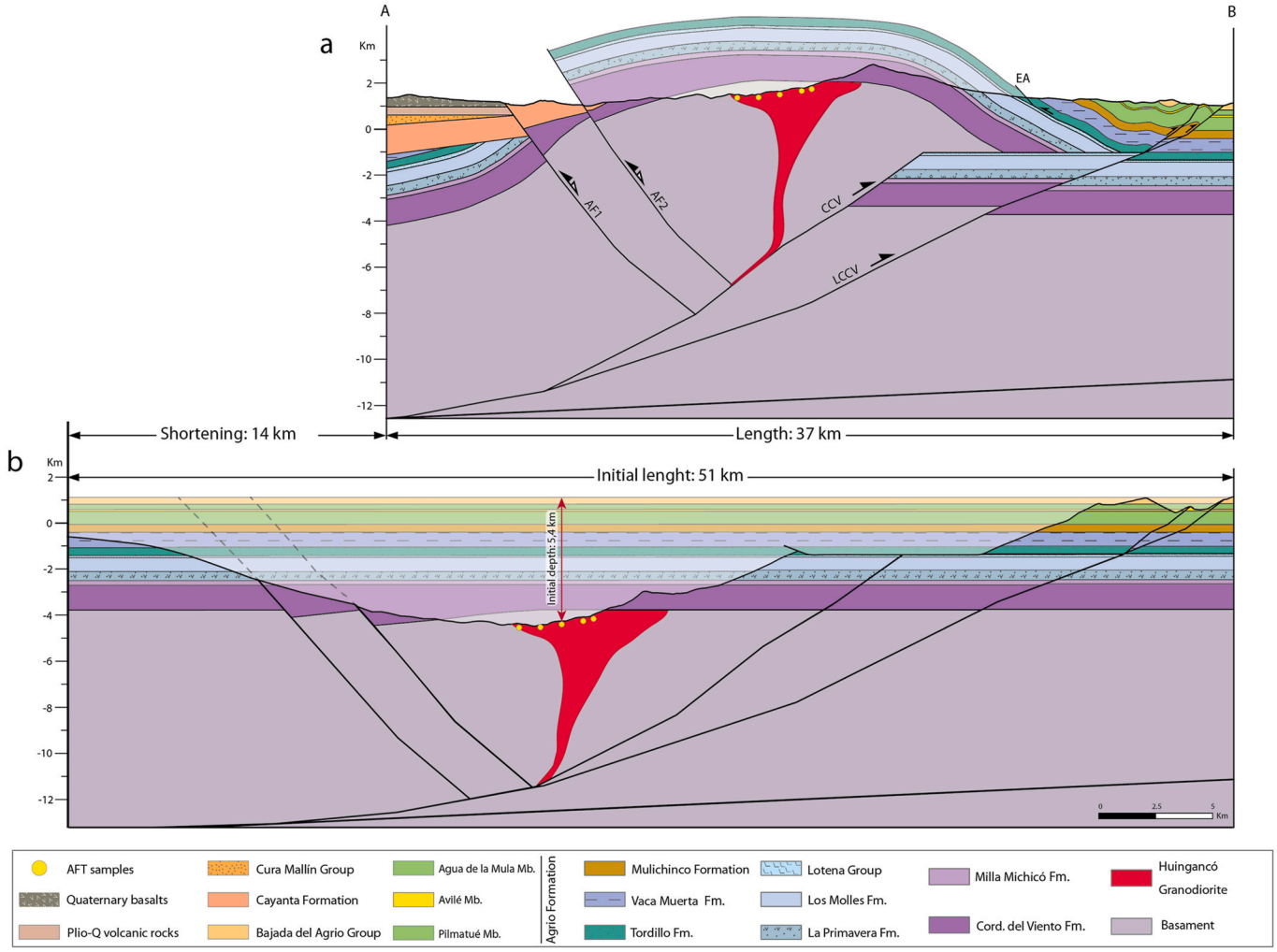


Fig. 8. a) Structural section of the Cordillera del Viento (see Fig. 3 for its location). b) Palinspastic reconstruction of section A-B, AF1 and AF2: Andacollo Fault 1 and 2; CCV: Cordillera del Viento Thrust; LCCV: Lower Cordillera del Viento Thrust; EA: El Alamito.

this study, these are relatively shallow plutons, with emplacement depths ranging between 4 and 9 km. This depth is calculated using a geostatic gradient of 3.7 km/kbar and establishing a direct correlation between pressure (P°) and depth, assuming P° represents lithostatic load only. This coincides with the proposal of Llambías et al. (2007) who suggested that the igneous rocks of the Huingancó volcano-plutonic Complex originated from magmatic chambers situated at shallow levels within the upper crust. Regarding the temperature conditions in the magma chamber, through thermobarometric calculations, it is estimated that the granodiorites formed at between 700 and 900 °C (see Table 1).

The temperatures and pressures calculated in this work correspond to the magmatic stage, that is, to the crystallization conditions of amphibole and plagioclase in the magma chamber. For the thermobarometric calculations, secondary amphiboles such as tremolite-actinolite are not valid compositions and, hence, only primary amphiboles within the compositional range of hornblendes are used. Therefore, thermobarometric calculations were made with this type of amphibole (magnesio-hornblendes) in this work. Perhaps, between the moment of amphibole crystallization and final emplacement, the magma was still in the process of ascent. However, given the high degree of crystallinity exhibited by the magmatic mush (mixture of magma and crystals) at the time of formation of subhedral amphibole crystals, the final emplacement level was likely not far away. Therefore, these temperatures and pressures are not indicative of solid-state recrystallization or linked to the pluton's exhumation stage. Nevertheless, they are included in this work because they complete the overall picture of pressure and temperature conditions to which the granodiorites of the Cordillera del Viento were exposed at the beginning of their thermal history. These are shallow plutons that crystallized during the late to post-orogenic stage of the Gondwanan Orogeny (Llambías et al., 2007). Considering the emplacement depths (4–9 km) derived from these thermobarometric calculations and the crystallization age of the Huingancó Granodiorite (~283 Ma; Sato et al., 2008; Hervé et al., 2014), alongside the age of the oldest unit above the Huárpica unconformity in the area (~198–196 Ma; Suárez et al., 2012; Pons et al., 2022), allows us to estimate a minimum exhumation rate of approximately 0.05–0.1 mm/yr. This rate is considered low to moderate for an extensional tectonic context within a retroarc basin (e.g., Stalder et al., 2020; Lanari et al., 2023). However, these values represent minimum estimates, and it is possible that the granodiorites reached near-surface levels earlier than the Early Jurassic, suggesting potentially higher exhumation rates, particularly in an active tectonic setting.

5.2. *Exhumation events of the Huingancó granodiorite*

Through the integration of geological and thermochronological data presented in this study, along with those published by previous authors (e.g. Sánchez et al., 2015, 2018; Galetto et al., 2021), it is interpreted that the Huingancó Granodiorite, in the Cordillera del Viento,

Table 2
Apatite fission track data. Central ages calculated using ζ - zeta calibration value of 314.94 ± 16.74 for samples CHP16, CHP18 and ζ of 333.26 ± 20.67 for samples CPH22, CPH23, CPH25. ρs: density of spontaneous fission tracks (× 10^5 tracks/cm^2); Ns: total number of spontaneous fission tracks; ρi and ρd: density of induced fission tracks in the samples and in the dosimetric glasses respectively (× 10^5 tracks/cm^2) in the external detector (g = 0.5); Ni: total number of induced fission tracks in the sample. P(χ^2): χ^2 probability test. IRMM 540 dosimetric glasses and total number of dosimetric fission tracks (Nd) > 5000 where used.

Sample	Lithology	Stratigraphic age	Latitude (S)	Longitude (W)	Elevation (m.a.s.l)	No. of grains	U (ppm)	Dosimeter	Spontaneous		Induced		P(χ^2)	Age dispersion	Central Age (Ma ± 1σ)
								ρd	ρs	Ns	ρi	Ni			
CPH16	Granodiorite	Permian (283 Ma)	37°11'57.2"	70°35'46.6"	1585	34	27.44	6.0275	8.178	618	10.59	800	8.1	0.17	74.8 ± 6.2
CPH18	Granodiorite	Permian (283 Ma)	37°11'57.2"	70°36'26.7"	1460	34	77.63	6.094	24.32	3517	32.71	4731	9.94	0.07	71.0 ± 4.2
CPH22	Granodiorite	Permian (283 Ma)	37°11'58.3"	70°35'7.9"	1713	16	22.86	4.062	6.372	313	6.657	327	81.35	0.00	64.5 ± 6.5
CPH23	Granodiorite	Permian (283 Ma)	37°11'54.7"	70°34'53.1"	1785	35	17.65	4.053	4.871	895	4.572	840	16.51	0.16	71.9 ± 6.1
CPH25	Granodiorite	Permian (283 Ma)	37°11'41.9"	70°36'53.9"	1386	35	48.05	4.043	9.958	1238	12.42	1544	30.84	0.08	53.9 ± 4.0

underwent at least three significant exhumation events. Following the emplacement of the Huingancó Granodiorite in a post-orogenic context, the region experienced significant denudation associated with the collapse of the Gondwanan orogeny and the transition to a rifting stage that gave way to the deposition of the Neuquén Basin fill (Llambías et al., 2007) (Fig. 11b and c). This denudation is represented by the Huárpica unconformity, which evidences the erosion of the pluton domes (Fig. 11b). After this exhumation process of the Huingancó Granodiorite, the accumulation of syn-rift and post-rift deposits of the Neuquén Basin occurred from the Late Triassic to the Late Early Cretaceous, reaching a burial depth of around 5.4 km (Fig. 11c).

5.2.1. *Late Cretaceous-Paleocene cooling event*

In all curves of the inverse thermal modeling (Fig. 10), it can be observed that from the Late Cretaceous onwards, a new exhumation pulse begins after burial due to sedimentary accumulation (Fig. 11d). Tunik et al. (2010) propose, based on tectonostratigraphic and geochronological studies conducted in Late Cretaceous deposits in the Neuquén Basin, that the contractional deformation stage begins around 100 Ma, related to the onset of the Andean uplift and the development of a foreland basin. Sánchez et al. (2018) obtained (U-Th)/He cooling ages in zircon ranging from 72 to 66 Ma approximately, and apatite fission track (AFT) ages between 51.7 ± 3.2 and 56.5 ± 10.7 Ma in samples from Upper Triassic-Lower Jurassic successions south of the Cordillera del Viento; these data evidence an early stage of exhumation (Sánchez et al., 2020). This coincides with the data obtained from apatite fission tracks, presented in section 4.3.1 (Table 2 and Fig. 9), which indicates cooling ages ranging between 74.8 ± 6.2 and 53.9 ± 4 Ma. Sample CPH25 presents the youngest age in the set (~54 Ma) (see location in Fig. 3), but, since it is the lowest (1386 m) and the farthest from the axis of the Cordillera del Viento anticline, so it is expected to have crossed the closure isotherm later than those samples located upstream of Arroyo Huaraco. However, its location is closer to the structures (backthrusts) of the western flank, so its exhumation may have been conditioned by a higher erosion rate than those of the samples to the east.

Thermal modeling outputs from the Huingacó Granodiorite samples constrained the onset of the Cretaceous-Paleocene cooling episode to approximately 100 Ma, partially coinciding with findings from previous studies (e.g., ~110-75 Ma; Galetto et al., 2021), but slightly older than other reported cooling onsets in nearby areas, which range from 75 to 90 Ma (e.g., Rojas Vera et al., 2015; Folguera et al., 2015; Sánchez et al., 2014). The cooling rates obtained from the thermal modeling for this time interval (Late Cretaceous-Paleocene) range from approximately 2.40 to 3.39 °C/Ma (see Fig. 10). These values are lower than the rates of 12–23 °C/Ma reported by Galetto et al. (2021) for the Cerro Domuyo area, and by Sánchez et al. (2020) for the Cordillera del Viento, which range from 5.4 to 3.8 °C/Ma. Sánchez et al. (2024) obtained a cooling rate of 1.1–2 °C/Ma in the inner zone of the Agrio Fold and Thrust Belt (FTB), but this was in an eastern, less exhumed structure compared to the Cordillera del Viento anticline. The lower cooling rates in the eastern zone of the Agrio FTB (Sánchez et al., 2024) may reflect the reduced degree of exhumation and deformation in that area compared to the more tectonically active and rapidly exhumed Cordillera del Viento anticline during this cooling episode.

The Cretaceous-Paleocene exhumation coincides with the emplacement and rapid exhumation of intrusive bodies in the central and northern sectors of the Cordillera del Viento such as the Varvarco and Butalón tonalites (Assis et al., 2022). The Varvarco Tonalite reports U-Pb SHRIMP ages in zircons of 67.8 ± 0.8 Ma (Assis et al., 2022) and Ar-Ar age of 69.09 ± 0.13 Ma (Kay et al., 2006). Subsequently, magmatic activity continued during the Paleocene-Eocene, resulting in the extrusion of the Cayanta Formation volcanics dated between 56 and 50 Ma (Jordan et al., 2001), which are deposited in angular unconformity over pre-Cretaceous units on the western flank of the Cordillera del Viento. The analysis of AFT data (Tables 2 and 3, and Fig. 9) indicates that the

Table 3
Kinetic parameters of apatite fission track data. Mean of confined track lengths are corrected using its horizontal angle with respect to the c-axis of the crystal. Dpar: diameter of the measured etch pits.

Sample	No. of measured confined track lengths	Mean of confined track lengths (μm)	Confined track length Std. (μm)	Confined track length skew	No. of measured Dpar	Mean Dpar (μm)	Dpar Std. (μm)	Dpar skew
CPH16	21	14.3	0.99	−0.57	142	2.19	0.25	0.64
CPH18	126	14.6	0.8	−0.7	2261	1.97	0.35	2.89
CPH22	42	14.05	1.41	−0.08	98	1.62	0.27	0.42
CPH23	66	14.21	1.49	6	199	1.75	0.28	0.48
CPH25	118	14.18	1.1	1.28	199	1.9	0.26	0.01

thermal history recorded by the samples does not show significant reheating or overprinting that would suggest a major impact from the intrusive events. The central cooling ages of samples CPH16, CPH18, and CPH23, ranging from 71.0 ± 4.2 to 74.8 ± 6.2 Ma, suggest a coherent cooling signal before the igneous activity, reflecting tectonically driven exhumation rather than localized thermal perturbations. Only the central ages of samples CPH22 and CPH25, ranging from 53.9 ± 4.0 to 64.5 ± 6.5 Ma, partially overlap with the contemporaneous igneous activity. Therefore, the accumulation of the Cayanta Formation volcanic rocks likely postdates the initial exhumation event. These rocks were emplaced during the waning stages of this deformation event or slightly after, indicating that while magmatic activity persisted, the major uplift of the Cordillera del Viento was largely completed by the time of their deposition (Fig. 11e).

5.2.2. Paleogene slow cooling phase

Thermal modeling results (Fig. 10) reveal that cooling began to decelerate after ~70–60 Ma, reaching steady/slow cooling rates of 0.38–0.80 °C/Ma between ~55 and 20 Ma. This suggests that the Eocene cooling event reported by Galetto et al. (2021) in the Domuyo area and by Folguera et al. (2015) in the eastern deformation front of the Malargüe FTB (Sierra de Reyes block) is not strongly evident in our AFT data modeling for the Huingancó Granodiorite region. Only samples CPH16 and CPH22 exhibit a broader range of solutions that could record an Eocene cooling episode (Fig. 10). For the Agrio FTB, Sánchez et al. (2024) reported a slow and steady cooling of 0.1–0.9 °C/Ma between 77 and 14 Ma, similar to our results. In contrast, for the Cordillera del Viento, Sánchez et al. (2020) noted higher cooling rates of 1.3–2.0 °C/Ma between 55 and 20 Ma, following an earlier, more rapid cooling phase of 3.8–5.4 °C/Ma during the Cretaceous exhumation event. The reported Eocene cooling events (Galetto et al., 2021; Folguera et al., 2015) have been linked to orogenic processes related to contractional or transpressive phases of deformation (e.g., Cobbold and Rossello, 2003; see Fennell et al., 2019 and references therein), which are more widely documented further north in the Central Andes (e.g., Charrier et al., 2007; Hongn et al., 2007). For the Neuquén basin region, reduced sedimentation and the development of unconformities in the foreland during the Paleogene have led to the proposal that minor compression or tectonic quiescence occurred during this interval (Horton and Fuentes, 2016; Encinas et al., 2024b). Therefore, these discrepancies may reflect localized deformation, where certain structural blocks, preferentially oriented within the regional stress field, were uplifted.

5.2.3. Neogene cooling event

The inverse thermal modeling represented in Fig. 10, in addition to highlighting the exhumation event during the Cretaceous-Paleogene, also allows observing a last cooling event (Fig. 11f) beginning around 20 Ma. This is evidenced by a more rapid temperature decrease, with cooling rates ranging from ~1.20 to 2.66 °C/Ma. Several authors (e.g., Folguera et al., 2007; Zamora Valcarce et al., 2009; Spagnuolo et al., 2012; Gürer et al., 2016; Sánchez et al., 2018, 2020; Turienzo et al., 2018, 2020) have documented this contractional deformation pulse during the Neogene in the Chos Malal FTB. Sánchez et al. (2018) obtained cooling ages through AFT ranging from 14 to 10 Ma, indicating significant contraction and uplift during this period. At the deformation front of the Chos Malal FTB in the Pampa Tril and Las Yeseras anticlines, they also obtained AFT ages between 9 and 7 Ma from samples of the Tordillo and Mulichinco formations (Upper Jurassic-Cretaceous). The recent study by Sánchez et al. (2024) in the Agrio FTB provides updated cooling rates for the Neogene, ranging from ~4.6 °C/Ma in the inner zone to 8.80 °C/Ma in the outer zone of the Agrio FTB. These rates are higher than our cooling rates for the Huingancó Granodiorite but align with the trend of decreasing rates towards the inner western domains. The comprehensive analysis of all low-temperature thermochronological data suggest that ages are younger towards the east and, therefore, the advance of the orogenic front was in this direction during the Late Miocene.

5.3. Shortening and uplift mechanisms

These exhumation events discussed are closely associated with the uplift of the Cordillera del Viento anticline. Previous studies have proposed that most Andean contractional deformation in this region occurred through the tectonic inversion of pre-existing normal faults from the Late Triassic-Early Jurassic rifting stage, acting as the primary mechanism for uplift (e.g., Zapata et al., 1999; Rojas Vera et al., 2015). On the other hand, Kozlowski et al. (1996) proposed that the first-order structures of the Chos Malal Fold and Thrust Belt were mainly generated by the fault-bend folding mechanism associated with a ramp-flat geometry and with a detachment level located 12 km deep in the Paleozoic basement. Turienzo et al. (2014, 2018) and Sánchez et al. (2014, 2015, 2020) agree that both processes participate, but the mechanism responsible for generating most of the shortening is that proposed by Kozlowski et al. (1996). In this study, the shortening calculated from the structural section (Fig. 8) accounts for a total of 14 km (27%), which is consistent with expected values considering basement-involved thrusts with an east-vergent ramp-flat geometry as the dominant structural configuration in the Cordillera del Viento anticline. For comparison, Sánchez et al. (2015) estimated a similar shortening of 16.9 km (29.7%) for part of the Chos Malal FTB, while Turienzo et al. (2018) reported a shortening estimate of 24.7 km (18%) for the entire belt. In contrast, lower shortening values (e.g. 9.5 km - 7.5%, Rojas Vera et al., 2015) have been estimated by those favoring tectonic inversion as the primary uplift mechanism (see Lebinson et al., 2018 for a review of the variability in shortening values based on different structural interpretations). Finally, in this work, based on the kinematic modeling of structures, the fault-bend folding mechanism is the one that best fits the stratigraphic and structural relationships observed on the surface.

6. Conclusions

Based on the analysis of mineral chemistry data obtained through electron microprobe analysis in the Permian granodiorites of the Huingancó volcano-plutonic Complex, it is inferred that their emplacement level was shallow, between 4 and 9 km depth, at temperatures ranging from 700 to 900 °C.

The study of stratigraphic and structural relationships complemented with analytical data of apatite fission tracks and inverse thermal modeling applied to five samples of the granodiorite, reveals a

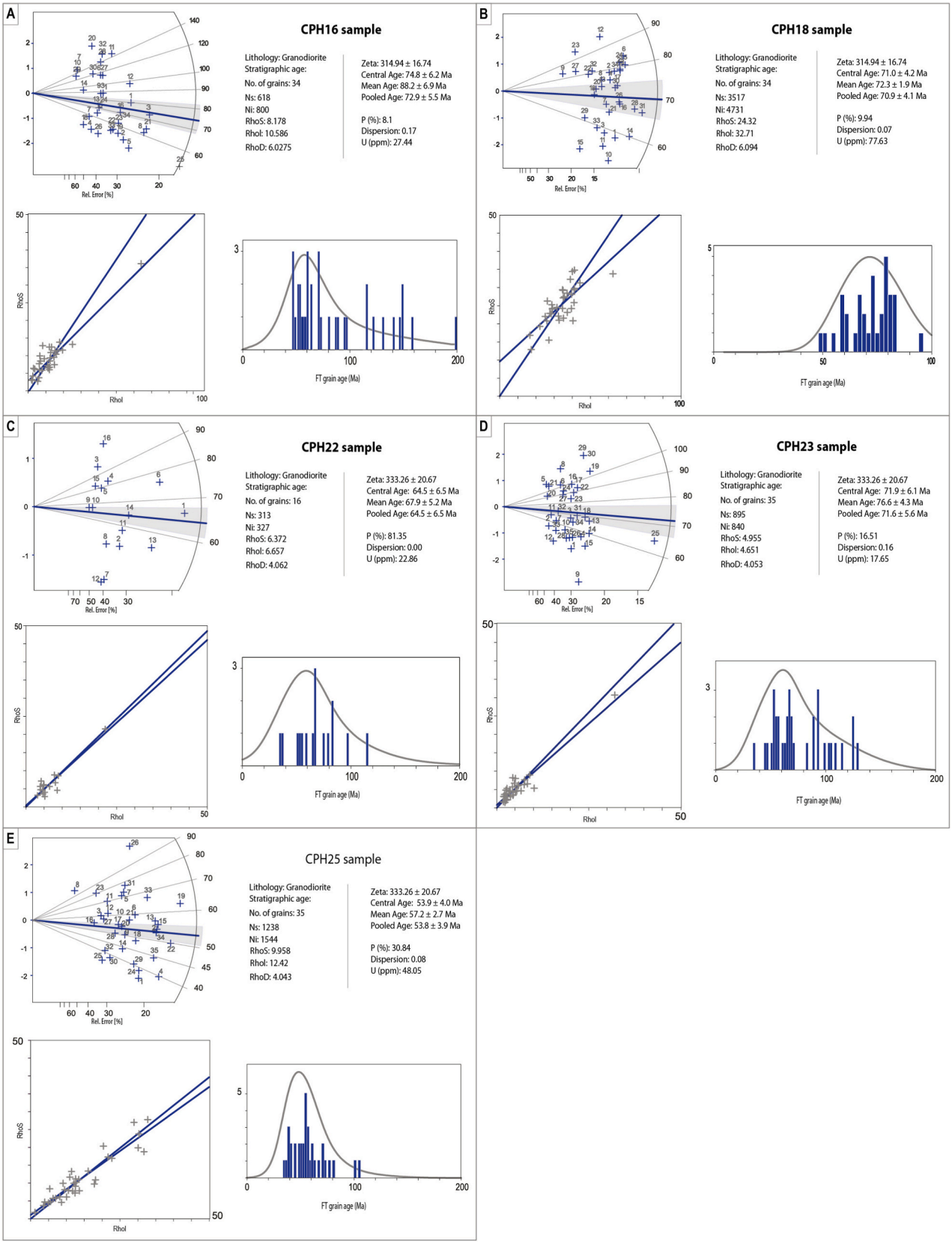


Fig. 9. Apatite fission track data from samples A) CPH16, B) CPH18, C) CPH22, D) CPH23, and E) CPH25. In the top left corner of each panel, the radial distribution of ages per grain is shown, highlighting the central age of each sample; below, a graph indicates the relationship between spontaneous track density (RhoS) and induced track density (RhoI); and to the right, age frequency histograms are displayed.

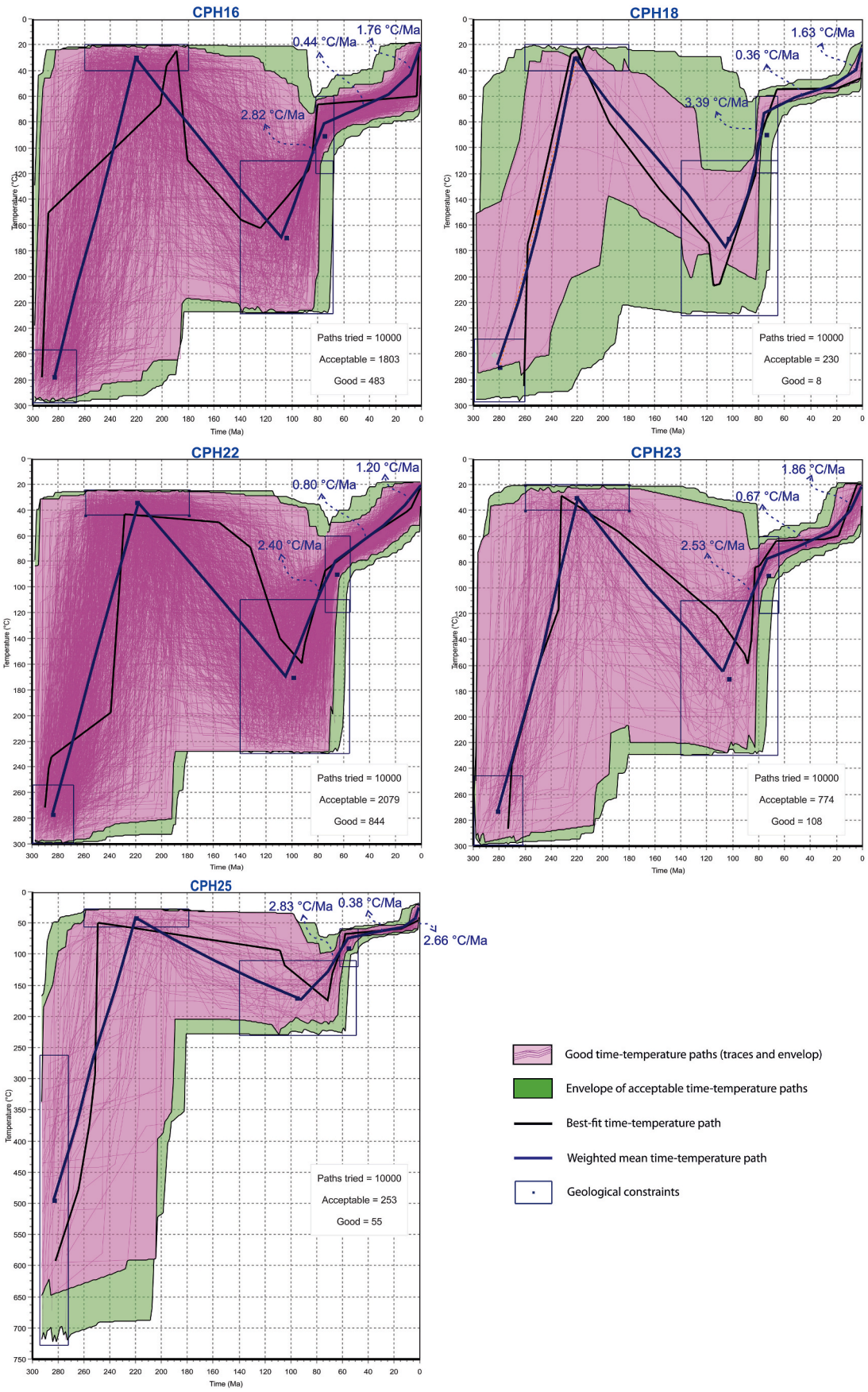


Fig. 10. Thermal history models obtained from the HeFTy Software, illustrating the thermal evolution of samples from the Huingancó Granodiorite.

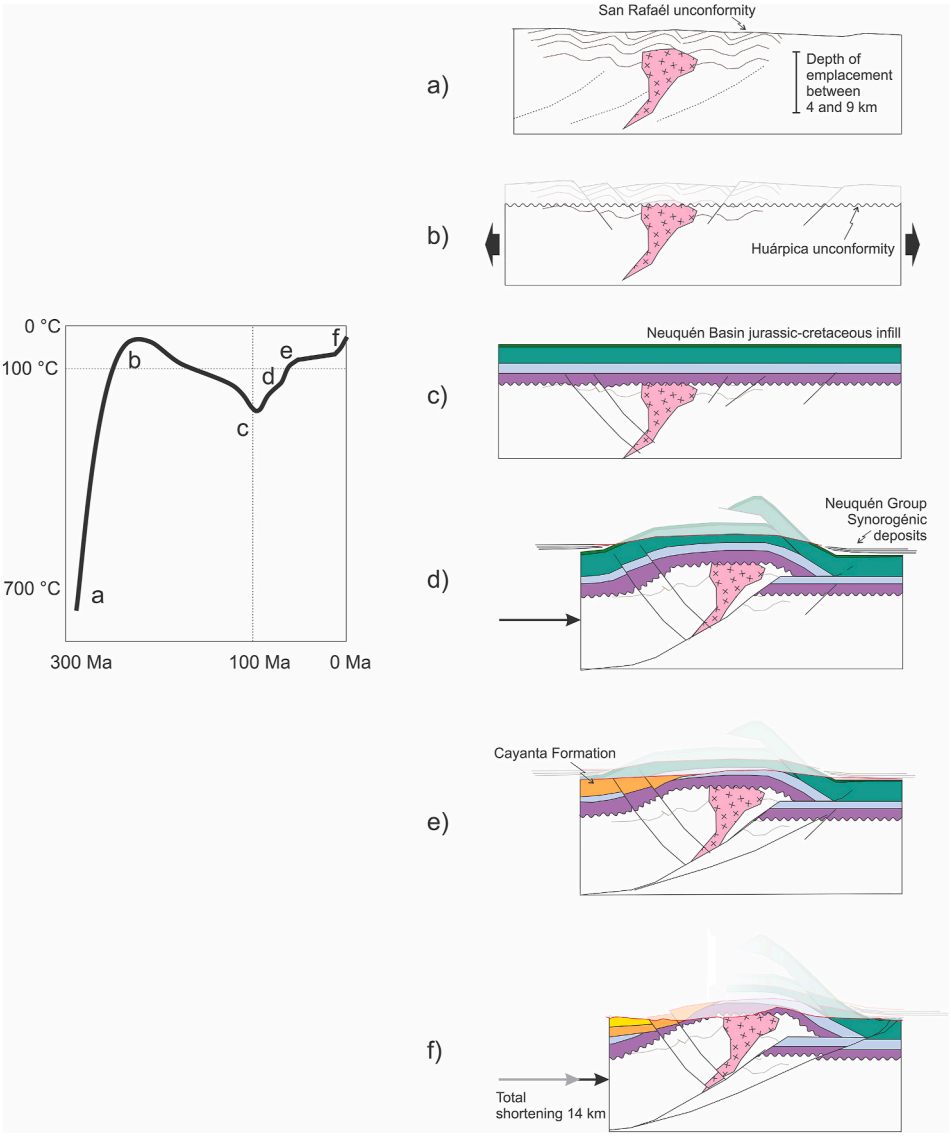


Fig. 11. Left: Thermal evolution diagram of the set of samples from the Huingancó Granodiorite. Right: a) Emplacement of the Huingancó Granodiorite in a post-orogenic stage; b) Rapid denudation and carving represented by the Huárpica unconformity; c) Burial and accumulation of the Neuquén Basin fill until the late Early Cretaceous; d) Cretaceous-Paleocene contractional deformation phase; e) Paleocene-Eocene andesitic volcanic extrusion prior to the tectonic quiescence phase of the Chos Malal Fold and Thrust Belt; f) Neogene contractional deformation phase.

thermal history involving at least three stages of exhumation. The first stage of exhumation corresponds to the collapse of the Gondwanan orogeny and the transition to the syn-rift stage of the Neuquén Basin, which is represented by the characteristic Huárpica unconformity in this area representing the erosion of the domes of the granodiorites. From these relationships, a cooling event from temperatures of 900–700 °C and emplacement depths between 4 and 9 km to their exposure at the surface is inferred. The second exhumation stage occurred during the Late Cretaceous-Paleocene (100–54 Ma), supported by AFT cooling ages data and the unconformity at the base of the Cayanta Formation volcanic rocks. Thermal modeling indicates that during this period, the granodiorites cooled from maximum temperatures of 230 °C–60 °C, followed by a cooling event with rates of ~2.40–3.39 °C/Ma. The third exhumation stage depicted by the inverse thermal modeling, occurred during the Miocene (>20 Ma), indicated by temperatures lower than ~55 °C and cooling rates ranging from ~1.20 to 2.66 °C/Ma. Between the last two stages, an episode of stability or gradual cooling is detected during the Paleocene-Miocene, with temperatures remaining around 60 °C.

The cooling stages during the Cretaceous-Paleogene and Neogene reflect episodes of exhumation driven by contractional deformation. In this context, the first Andean exhumation event (Late Cretaceous-Paleocene) is associated with the main phase of growth of the first-order structure of the Cordillera del Viento. This structure is characterized by a fault-bend fold involving the basement in the deformation. Its uplift occurred through the Cordillera del Viento Thrust (CCV), which originated in the basement, starting at about 12 km depth and then inserting into the Lotena Group evaporites as a wedge accommodated by the El Alamito passive roof fault, on the eastern flank. The eastward displacement of this wedge contributed to the formation of second-order folds within the Chos Malal FTB. The deformation also involved the inversion of pre-existing normal faults on the western flank of the Cordillera del Viento anticline (Andacollo Faults 1 and 2). Finally, the last exhumation event is associated with the Lower Cordillera del Viento Thrust (LCCV), which propagated eastward, increasing the deformation in the sedimentary cover and contributing to the development of folds and thrusts characteristic of the thin-skinned structures of the Chos Malal FTB.

CRediT authorship contribution statement

Darío Leandro Orts: Writing – original draft, Validation, Project administration, Methodology, Investigation, Funding acquisition, Conceptualization. **Camila Delfina Aguilar Cáceres:** Writing – original draft, Visualization, Methodology, Investigation, Data curation, Conceptualization. **Sebastián Pernich:** Validation, Methodology, Investigation, Data curation. **Claudia Zaffarana:** Validation, Supervision, Project administration, Methodology, Investigation, Funding acquisition, Data curation, Conceptualization. **Gloria Gallastegui:** Validation, Resources, Methodology, Formal analysis. **Sebastián Assis:** Methodology, Investigation.

Declaration of competing interest

The authors declare that they have no known competing financial interests or personal relationships that could have appeared to influence the work reported in this paper.

Data availability

Data will be made available on request.

Acknowledgements

This work was funded by PI UNRN 40-A-798, 40-A-916, PIP CONICET 11220200100099CO, PICT 2019-01809 and CGL2012-38396-C03 (I+D+i Spanish Plan with UE-FEDER funds). We thank the Consejo Interuniversitario Nacional (CIN) for providing financial support to C.D. Aguilar Cáceres through the research fellowship Beca-EVC-CIN. We thank Miguel Ángel Fernández for their help in the electron microprobe analysis at the Technical-Scientific services of Oviedo University (Spain). We also thank LA.TE. ANDES S.A. for providing the apatite fission track data and the academic license for the Andino3D software. We appreciate the comments and suggestions from Lucas Fennell and an anonymous reviewer, which greatly helped us to improve the manuscript.

Lastly, we want to express our gratitude to Prof. Dr. Raúl Giacosa for inspiring multiple generations of students, geologists, and colleagues, and for his enduring legacy of knowledge in the geology of southern South America.

Appendix A. Supplementary data

Supplementary data to this article can be found online at https://doi.org/10.1016/j.jsames.2024.105166.

References

Arregui, C., Carbone, O., Sattler, F., Leanza, H., Danieli, J., Vallés, J., 2011a. El Grupo Lotena (Jurásico Medio-Tardío) en la Cuenca Neuquina. In: Leanza, H.A., Arregui, C., Carbone, O., Danieli, J.C., Vallés, J.M. (Eds.), Geología y Recursos Naturales de la Provincia del Neuquén. Relatorio del XVIII Congreso Geológico Argentino, pp. 91–98.

Arregui, C., Carbone, O., Leanza, H., 2011b. Contexto tectosedimentario. In: Leanza, H. A., Arregui, C., Carbone, O., Danieli, J.C., Vallés, J.M. (Eds.), Geología y Recursos Naturales de la Provincia del Neuquén. Relatorio del XVIII Congreso Geológico Argentino, pp. 29–36.

Assis, O.S., Zaffarana, C.B., Orts, D., Puigdomenech, C., Ruiz González, V., Gallastegui, G., Hauser, N., Kiseeva, E.S., Molina, J.F., Pernich, S., 2022. Emplacement conditions and exhumation of the Varvarco Tonalite and associated plutons from the Cordillera del Viento, Southern Central Andes. Geol. Mag. 159, 645–672. https://doi.org/10.1017/S0016756821001163.

Anderson, J.L., Smith, D.R., 1995. The effects of temperature and f O2 on the Al-in-hornblende barometer. Am. Mineral. 80, 549–559.

Barker, C.E., Pawlewicz, M.J., 1994. Calculation of vitrinite reflectance from thermal histories and peak temperatures: a comparison of methods. In: Mukhopadhyay, P.K., Dow, W.G. (Eds.), Vitrinite Reflectance as a Maturity Parameter: Applications and Limitations, ACS Symposium Series. American Chemical Society, Washington, DC, pp. 216–229. https://doi.org/10.1021/bk-1994-0570.ch014.

Charrier, R., Pinto, L., Rodriguez, M.P., 2007. Tectonostratigraphic evolution of the andean orogen in Chile. In: Moreno, T., Gibbons, W. (Eds.), The Geology of Chile. Geological Society, London, pp. 21–114. https://doi.org/10.1144/GOCH.3.

Cobbold, P.R., Rossello, E.A., 2003. Aptian to recent compressional deformation, foothills of the Neuquen Basin, Argentina. Mar. Petrol. Geol. 20, 429–443. https://doi.org/10.1016/S0264-8172(03)00077-1.

Cristallini, E., Sánchez, F., Balciunas, D., Mora, A., Ketcham, R., Nigro, J., Hernández, J., Hernández, R., 2021. Seamless low-temperature thermochronological modeling in Andino 3D, towards integrated structural and thermal simulations. J. S. Am. Earth Sci. 105, 102851.

Dunkl, I., 2002. TRACKKEY: a Windows program for calculation and graphical presentation of fission track data. Comput. Geosci. 28, 3–12.

Encinas, A., Rosselot, E., Sagripanti, L., Folguera, A., Horton, B.K., Orts, D., Valencia, V. A., Arriagada, G., Butikofer, P., Solórzano, A., 2024a. Cenozoic Basin evolution during alternating extension and shortening in the southern central Andes along the Chile-Argentina border, 37–38°S. Am. J. Sci. 324. https://doi.org/10.2475/001c.115328.

Encinas, A., Henríquez, N., Castro, D., Orts, D., Kietzmann, D., Iovino, F., Vásquez, P., Folguera, A., Valencia, V., Fuentes, F., 2024b. The transition from backarc extension to Andean growth: insights from geochronologic, sedimentologic, and structural studies of Mesozoic and Cenozoic sedimentary and volcanic rocks in south-central Chile (36°S). Geosci. Front. 15, 101824. https://doi.org/10.1016/j.gsf.2024.101824.

Fennell, L.M., Iannelli, S.B., Encinas, A., Naipauer, M., Valencia, V., Folguera, A., 2019. Alternating contraction and extension in the southern central Andes (35°–37°S). Am. J. Sci. 319, 381–429. https://doi.org/10.2475/05.2019.02.

Flowers, R.M., Farley, K.A., Ketcham, R.A., 2015. A reporting protocol for thermochronologic modeling illustrated with data from the Grand Canyon. Earth Planet Sci. Lett. 432, 425–435. https://doi.org/10.1016/j.epsl.2015.09.053.

Folguera, A., Bottesi, G., Duddy, I., Martín-González, F., Orts, D., Sagripanti, L., Vera, E. R., Ramos, V., 2015. Exhumation of the Neuquén Basin in the southern Central Andes (Malargüe fold and thrust belt) from field data and low-temperature thermochronology. J. S. Am. Earth Sci. 64, 381–398.

Folguera, A., Ramos, V.A., Zapata, T., Spagnuolo, M.G., 2007. Andean evolution at the Guañacos and Chos Malal fold and thrust belts (36 30′–37 S). J. Geodyn. 44 (3–5), 129–148.

Galetto, A., Georgieva, V., García, V.H., Zattin, M., Sobel, E.R., Glodny, J., Bordese, S., Arzadún, G., Bechis, F., Caselli, A.T., others, 2021. Cretaceous and Eocene rapid cooling phases in the southern Andes (36°–37° S): insights from low-temperature Thermochronology, U-Pb geochronology, and inverse thermal modeling from Domuyo area, Argentina. Tectonics 40, e2020TC006415.

Genge, M., 2021. Tectonic Evolution of the North-Central Patagonia: a Thermochronological Approach (PhD Thesis). Université de Lille; Università degli studi, Padoue, Italie.

Giacosa, R., 2011. Geología estructural de los sistemas vetiformes del cerro Las Minas. Distrito Minero Andacollo, Cordillera del Viento, Provincia del Neuquén. Instituto de Geología y Recursos Minerales, Servicio Geológico y Minero Argentino. Contribuciones Técnicas 33, 23.

Giacosa, R.E., Allard, J.O., Foix, N., Heredia, N., 2014. Stratigraphy, structure and geodynamic evolution of the Paleozoic rocks in the Cordillera del Viento (37° S latitude, Andes of Neuquén, Argentina). J. Iber. Geol. 40 (2), 331–348.

Gómez, J., Schobbenhaus, C., Montes, N.E., 2019. Geological Map of South America, Scale 1:5000000. Commission for the Geological Map of the World (CGMW). Colombian Geological Survey and Geological Survey of Brazil, Paris.

Groeber, P., 1929. Líneas fundamentales de la geología del Neuquén, sur de Mendoza y regiones adyacentes, vol. 158. Dirección Nacional de Geología y Minería. Publicación, Buenos Aires, pp. 1–110.

Gulisano, C., 1981. El Ciclo Cuyano en el norte de Neuquén y sur de Mendoza. In: 8° Congreso Geológico Argentino, pp. 579–592. San Luis.

Gulisano, C.A., Gutiérrez Pleimling, A., 1995. Field guide: the Jurassic of the Neuquén Basin. A) Neuquén province. Asociación Geológica Argentina, Serie E 2, 1–111. Buenos Aires.

Gürer, D., Galland, O., Corfu, F., Leanza, H.A., Sassier, C., 2016. Structure and evolution of volcanic plumbing systems in fold-and-thrust belts: A case study of the Cerro Negro de Tricao Malal, Neuquén Province, Argentina. GSA Bulletin 128, 315–331.

Hammerstrom, J.M., Zen, E., 1986. Aluminum in hornblende: an empirical igneous geobarometer. Am. Mineral. 71 (11–12), 1297–1313.

Hervé, F., Fanning, C.M., Calderón, M., Mpodozis, C., 2014. Early permian to late Triassic batholiths of the Chilean frontal cordillera (28°–31° S): SHRIMP U–Pb zircon ages and Lu–Hf and O isotope systematics. Lithos 184, 436–446.

Hollister, L.S., Grissom, G., Peters, E., Stowell, H., Sisson, V., 1987. Confirmation of the empirical correlation of Al in hornblende with pressure of solidification of calc-alkaline plutons. Am. Mineral. 72 (3–4), 231–239.

Hongn, F., Papa, C.D., Powell, J., Petrinovic, I., Mon, R., Deraco, V., 2007. Middle Eocene deformation and sedimentation in the Puna- Eastern Cordillera transition (23°-26°S): control by preexisting heterogeneities on the pattern of initial Andean shortening. Geology 35 (3), 271–274. https://doi.org/10.1130/g23189a.1.

Horton, B.K., Fuentes, F., 2016. Sedimentary record of plate coupling and decoupling during growth of the Andes. Geology 44, 647–650. https://doi.org/10.1130/g37918.1.

Hurford, A.J., Green, P.F., 1983. The zeta age calibration of fission-track dating. Chem. Geol. 41, 285–317.

Johnson, M.C., Rutherford, M.J., 1989. Experimental calibration of the aluminum-in-hornblende geobarometer with application to Long Valley caldera (California) volcanic rocks. Geology 17 (9), 837–841.

Jordan, T.E., Burns, W.M., Veiga, R., Pángaro, F., Copeland, P., Kelley, S., Mpodozis, C., 2001. Extension and basin formation in the southern Andes caused by increased convergence rate: a mid-Cenozoic trigger for the Andes. Tectonics 20 (3), 308–324.
Kay, S.M., Burns, M., Copeland, P., 2006. Upper Cretaceous to Holocene magmatism and evidence for transient Miocene shallowing of the Andean subduction zone under the northern Neuquén Basin. In: Kay, S.M., Ramos, V.A. (Eds.), Evolution of an Andean Margin: A Tectonic and Magmatic View from the Andes to the Neuquen Basin. Geological Society of America, GSA, Boulder, pp. 35–398S. Special Paper 407: 19–60.
Karg, H., Littke, R., 2020. Tectonic control on hydrocarbon generation in the northwestern Neuquén Basin, Argentina. AAPG (Am. Assoc. Pet. Geol.) Bull. 104, 2173–2208. https://doi.org/10.1306/05082018171.
Ketcham, R.A., Donelick, R. A. y, Carlson, W.D., 1999. Variability of apatite fission-track annealing kinetics: III. Extrapolation to geological time scales. Am. Mineral. 84 (9), 1235–1255.
Ketcham, R.A., 2005. Forward and inverse modeling of low-temperature thermochronometry data. Rev. Mineral. Geochem. 58, 275–314.
Ketcham, R.A., Carter, A., Donelick, R.A., Barbarand, J., Hurford, A.J., 2007. Improved measurement of fission-track annealing in apatite using c-axis projection. Am. Mineral. 92, 789–798.
Kozlowski, E.E., Cruz, C., y Sylwan, C.A., 1996. Geología estructural de la zona de Chos Malal. Cuenca Neuquina. Argentina. 13° Congreso Geológico Argentino y 3° Congreso de Exploración de Hidrocarburos, Actas 1, 15–26. Buenos Aires.
Lanari, R., Boutoux, A., Faccenna, C., Herman, F., Willett, S.D., Ballato, P., 2023. Cenozoic exhumation in the Mediterranean and the Middle East. Earth Sci. Rev. 237, 104328. https://doi.org/10.1016/j.earscirev.2023.104328.
Leanza, H.A., 2003. Las sedimentitas huitrinianas y rayosianas (Cretácico Inferior) en el ámbito central y meridional de la cuenca Neuquina, Argentina. Servicio Geológico Minero Argentino. Instituto de Geología y Recursos Minerales. Serie Contribuciones Técnicas. Geologia 2, 1–31.
Leanza, H.A., Llambías, E.J., Carbone, O., 2005. Unidades estratigráficas limitadas por discordancias en los depocentros de la cordillera del Viento y la sierra de Chacaico durante los inicios de la cuenca Neuquina. In: Congreso de exploración de hidrocarburos, N° 6. Trabajos técnicos. Reservorios y desarrollo de reservas. Resúmenes de trabajos: 53. Edición en CD-ROM. Mar del Plata.
Leanza, H.A., Zanettini, J.C.M., Rodríguez, M.F., 2011. Mapa geológico de la Provincia del Neuquén. Servicio Geológico Minero Argentino. Instituto de Geología y Recursos Minerales.
Leake, B.E., Wooley, A.R., Arps, C.E.S., Birch, W.D., Gilbert, M.C., Grice, J.D., Hawthorne, F.C., 1997. Nomenclature of amphiboles: report of the subcommittee on amphiboles of the International Mineralogical Association Commission on new minerals and mineral names. Can. Mineral. 35, 1571–1606.
Lebinson, F., Turienzo, M., Sánchez, N., Araujo, V., D'Annunzio, M.C., Dimieri, L., 2018. The structure of the northern Agrio fold and thrust belt (37°30′ S), Neuquén Basin, Argentina. andgeo 45, 249. https://doi.org/10.5027/andgeoV45n2-3049.
Llambías, E., 1986. Intrusivos pérmicos del sur de la Cordillera del Viento, provincia del Neuquén. Rev. Asoc. Geol. Argent. 41 (1–2), 22–32.
Llambías, E.J., Leanza, H.A., Carbone, O., 2007. Evolución Tectono-magmática durante el pérmico al Jurásico temprano en la Cordillera del Viento (37°05′S - 37°15′S): Nuevas evidencias geológicas y geoquímicas Del Inicio de la Cuenca Neuquina. Rev. Asoc. Geol. Argent. 62 (2), 217–235.
Llambías, E.J., Sato, A.M., 2011. Ciclo Gondwánico: la provincia magmática Choiyoi en Neuquén. In: Relatorio XVIII Congreso Geológico Argentino, pp. 53–62.
Malusà, M.G., Fitzgerald, P.G., 2019. Fission-track Thermochronology and its Application to Geology. Springer International Publishing, p. 393.
Niemeyer, H., Muñoz, J., 1983. Hoja Laguna de La Laja, Región del Bío Bío, vol. 57. Servicio Nacional de Geología y Minería, Santiago, p. 52. Carta Geológica de Chile, N°.
Orts, D.L., Folguera, A., Giménez, M., Ramos, V.A., 2012. Variable structural controls through time in the southern central Andes (~ 36° S). Andean Geol. 39, 220–241.
Orts, D.L., Álvarez, O., Zaffarana, C., Gimenez, M., Ruiz, F., Folguera, A., 2021. Tectonic segmentation across Patagonia controlled by the subduction of oceanic fracture zones. J. Geodyn. 143, 101806. https://doi.org/10.1016/j.jog.2020.101806.
Pedroza, V., Le Roux, J.P., Gutiérrez, N.M., Vicencio, V.E., 2017. Stratigraphy, sedimentology, and geothermal reservoir potential of the volcaniclastic Cura-Mallín succession at Lonquimay, Chile. J. S. Am. Earth Sci. 77, 1–20.
Pons, J., Zattin, M., Giacosa, R., Greco, G., González, S.N., Dicaro, S., Conedera, M., Nimis, P., Bordese, S., 2022. Silver, gold, and base metals vein systems at southern part of Cordillera del Viento, Neuquén Argentina. Simposio XVI, Exploración y desarrollo minero de la Patagonia. XXI Congreso Geológico Argentino. Actas 1, 1599–1600. Puerto Madryn, Chubut.
Putirka, K., 2016. Amphibole thermometers and barometers for igneous systems and some implications for eruption mechanisms of felsic magmas at arc volcanoes. Am. Min. 101, 841–858. https://doi.org/10.2138/am-2016-5506.
Ramos, V.A., 1999a. Las Provincias Geológicas del territorio Argentino. In: Caminos, R. (Ed.), Geología Argentina. Instituto de Geología y Recursos Minerales, Buenos Aires, pp. 41–96.
Ramos, V.A., 1999b. Plate tectonic setting of the andean cordillera. Episodes Journal of International Geoscience 22, 183–190.
Rapela, C., Llambías, E., 1985. La secuencia andesítica terciaria de Andacollo, Neuquén, Argentina. Relatorio IV Congreso Geológico Chileno 4, 458–488. Antofagasta.
Ridolfi, F., Renzulli, A., Puerini, M., 2010. Stability and chemical equilibrium of amphibole in calc-alkaline magmas: an overview, new thermobarometric formulations and application to subduction-related volcanoes. Contrib. Mineral Petrol 160, 45–66. https://doi.org/10.1007/s00410-009-0465-7.
Rojas Vera, E.R., Mescua, J., Folguera, A., Becker, T., Sagripanti, L., Fennell, L., Orts, D., Ramos, V.A., 2015. Evolution of the Chos Malal and Agrio fold and thrust belts, Andes of Neuquén: insights from structural analysis and apatite fission track dating. J. S. Am. Earth Sci. 64, 418–433.
Rovere, E.I., 1998. Volcanismo Jurásico, Paleógeno y Neógeno en el noroeste del Neuquén, Argentina. In: X Congreso Latinoamericano de Geología, vol. 1, pp. 144–149. Actas.
Rovere, E., Caselli, A.T., Hugo, C., Leanza, H., Folguera, A., Escosteguy, L., Geuna, S., González, R., Colombino, J.E., Danieli, J., 2004. Hoja Geológica Andacollo (3772-IV), Provincia de Neuquén. Instituto de Geología y Recursos Minerales, vol. 298. Servicio Geológico Minero Argentino, Boletín, p. 104. Buenos Aires.
Sagripanti, L., Folguera, A., Giménez, M., Rojas Vera, E.A., Fabiano, J.J., Molnar, N., Fennell, L., Ramos, V.A., 2014. Geometry of Middle to Late Triassic extensional deformation pattern in the Cordillera del Viento (Southern Central Andes): A combined field and geophysical study. J. Iber. Geol. 40 (2), 349–366.
Sánchez, N.P., Turienzo, M.M., Dimieri, L.V., Araujo, V.S., Lebinson, F., 2014. Evolución de las estructuras andinas en la faja corrida y plegada de Chos Malal: interacción entre el basamento y la cubierta sedimentaria de la Cuenca Neuquina. Rev. Asoc. Geol. Argent. 71 (2), 233–246.
Sánchez, N., Turienzo, M., Lebinson, F., Araujo, V., Coutand, I., Dimieri, L., 2015. Structural style of the Chos Malal fold and thrust belt, Neuquén basin, Argentina: relationship between thick- and thin-skinned tectonics. J. S. Am. Earth Sci. 64, 399–417. https://doi.org/10.1016/j.jsames.2015.07.001.
Sánchez, N.P., Coutand, I., Turienzo, M.M., Lebinson, F.O., Araujo, V.S., Bordese, S., Arzadún, G., Dimieri, L.V., 2024. Structural evolution of the Northern Agrio fold and trust belt (~37°30′S), Neuquén Basin, Argentina, derived from low-temperature multi-thermochronometry. Tectonics 43. https://doi.org/10.1029/2023tc007868.
Sánchez, N.P., Coutand, I., Turienzo, M., Lebinson, F., Araujo, V., Dimieri, L., 2018. Tectonic evolution of the Chos Malal Fold-and-Thrust belt (Neuquén Basin, Argentina) from (U-Th)/He and fission track thermochronometry. Tectonics 37 (7), 1907–1929.
Sánchez, N., Turienzo, M., Coutand, I., Lebinson, F., Araujo, V., Dimieri, L., 2020. Structural and thermochronological constraints on the exhumation of the Chos Malal fold and thrust belt (~ 37 S). In: Kietzmann, D., Folguera, A. (Eds.), Opening and Closure of the Neuquén Basin in the Southern Andes. Springer Earth System Sciences. Springer, pp. 323–340.
Sato, A.M., Llambías, E.J., Basei, M.A.S., Leanza, H.A., 2008. The Permian Choiyoi Cycle in cordillera del Viento (Principal Cordillera, Argentina): over 25 Ma of magmatic activity. VI South American Symposium on Isotope Geology, pp. 3–6. April 2016.
Schmidt, M.W., 1992. Amphibole composition in tonalite as a function of pressure: an experimental calibration of the Al-in-hornblende barometer. Contrib. Mineral. Petrol. 110 (2–3), 304–310.
Spagnuolo, M.G., Litvak, V.D., Folguera, A., Bottesi, G., Ramos, V.A., 2012. Neogene magmatic expansion and mountain building processes in the southern Central Andes, 36–37 S, Argentina. J. Geodyn. 53, 81–94.
Stalder, N.F., Herman, F., Fellin, M.G., Coutand, I., Aguilar, G., Reiners, P.W., Fox, M., 2020. The relationships between tectonics, climate and exhumation in the Central Andes (18–36°S): evidence from low-temperature thermochronology. Earth Sci. Rev. 210, 103276. https://doi.org/10.1016/j.earscirev.2020.103276.
Suárez, M., De La Cruz, R., 1997. Volcanismo pliniano del Lias durante los inicios de la cuenca de Neuquen, Cordillera del Viento, Neuquén, Argentina. 7° Congreso Geológico Chileno, Actas I, 266–270.
Suárez, M., De la Cruz, R., Fanning, M., Etchart, H., 2008. Carboniferous, Permian and Toarcian magmatism in Cordillera del Viento, Neuquén, Argentina: first U-Pb SHRIMP dates and tectonic implications. In: 17 Congreso Geológico Argentino Actas 2. San Salvador de Jujuy, pp. 906–907.
Suárez, M., Fanning, C.M., Etchart, H., De La Cruz, R., 2012. New Carboniferous to Toarcian U-Pb SHRIMP ages from Cordillera del Viento, Neuquén, Argentina. Actas XIII° Congreso Geológico Chileno 664–665.
Suppe, J., 1983. Geometry and kinematics of fault-bend folding. Am. J. Sci. 283, 684–721.
Tunik, M., Folguera, A., Naipauer, M., Pimentel, M., Ramos, V.A., 2010. Early uplift and orogenic deformation in the Neuquén Basin: constraints on the Andean uplift from U–Pb and Hf isotopic data of detrital zircons. Tectonophysics 489 (1–4), 258–273.
Turienzo, M., Sánchez, N., Dimieri, L., Lebinson, F., Araujo, V., 2014. Tectonic repetitions of the Early Cretaceous Agrio Formation in the Chos Malal fold-and-thrust belt, Neuquén basin, Argentina: geometry, kinematics and structural implications for Andean building. J. S. Am. Earth Sci. 53, 1–19.
Turienzo, M., Sánchez, N., Lebinson, F., Dimieri, L., 2018. The structure of the southern central Andes (Chos Malal fold and thrust belt). In: Folguera, A., Contreras Reyes, E., Heredia, N., Encinas, A., Iannelli, S., Oliveros, V., Dávila, F., Collo, G., Giambiagi, L., Maksymowicz, A., Iglesia Llanos, M.P., Turienzo, M., Naipauer, M., Orts, D., Litvak, V., Álvarez, O., Arriagada, C. (Eds.), The Evolution of the Chilean Argentinean Andes. Springer Earth System Sciences, Cham, pp. 411–441.
Turienzo, M., Sánchez, N., Lebinson, F., Peralta, F., Araujo, V., Irastorza, A., Dimieri, L., 2020. Basement-cover interaction in the mountain front of the Northern Neuquén fold and thrust belt (37 10'–37 40'S), Argentina. J. S. Am. Earth Sci. 100, 102560.
Wagner, G.A., Van den haute, P., 1992. Fission Track-Dating. Kluwer Academic Publishers, Dordrecht, p. 285.
Woodward, N.B., Boyer, S.E., Suppe, J., 1989. Balanced Geological Cross-Sections, vol. 6. American Geophysical Union, Short Courses in Geology, p. 132.
Zamora Valcarce, G., Zapata, T., Ramos, V.A., Rodríguez, F., Bernardo, L.M., 2009. Evolución tectónica del frente andino en Neuquén. Rev. Asoc. Geol. Argent. 65 (1), 192–203.
Zamora-Valcarce, G., Zapata, T., del Pino, D., Ansa, A., 2006. Structural evolution and magmatic characteristics of the Agrio fold-and-thrust belt. In: Kay, S.M., Ramos, V.A.

(Eds.), Evolution of an Andean Margin: A Tectonic and Magmatic View from the Andes to the Neuquén Basin (35°–39°S Lat), vol. 407. Geological Society of America Special Paper, pp. 125–145.

Zappettini, E.O., Chernicoff, C.J., Santos, J.O.S., Dalponte, M., Belousova, E., McNaughton, N., 2012. Retrowedge-related Carboniferous units and coeval magmatism in the northwestern Neuquén province, Argentina. Int. J. Earth Sci. 101, 2083–2104. https://doi.org/10.1007/s00531-012-0774-3.

Zappettini, E.O., Lagorio, S.L., Dalponte, M., Orestes, J., Belousova, E., 2018. Evidencias de magmatismo precuyano (Pliensbachiano - Toarciano) en el norte de la Cordillera del Viento, provincia del Neuquén: caracterización geoquímica, isotópica e implicancias tectónicas. Rev. Asoc. Geol. Argent. 75 (4), 533–558.

Zapata, T., Brissón, I., Dzelalija, F., 1999. La estructura de la faja plegada y corrida andina en relación con el control del basamento de la Cuenca Neuquina. Boletín de informaciones Petroleras 60, 113–121.

Zavala, C., Ponce, J.J., 2011. La Formación Rayoso (Cretácico Temprano) en la Cuenca Neuquina. In: Leanza, H.A., Arregui, C., Carbone, O., Danieli, J.C., Vallés, J.M. (Eds.), Geología y Recursos Naturales de la Provincia del Neuquén. Relatorio del XVIII Congreso Geológico Argentino, pp. 205–222.

Zöllner, W., Amos, A.J., 1973. Descripción Geológica de la Hoja 32b, Chos Malal Provincia del Neuquén Carta Económica de la República Argentina Escala 1: 200.000. Boletín N°143. Ministerio de Economía Secretaría de Estado de Recursos Naturales y Ambiente Humano. Subsecretaria de Minería Servicio Nacional Minero Geológico, República Argentina.

Journal of South American Earth Sciences 154 (2025) 105390



Contents lists available at ScienceDirect

Journal of South American Earth Sciences

journal homepage: www.elsevier.com/locate/jsames



Petrography, magnetic fabrics and timing of emplacement in relation to the San Rafael Orogenic Phase of the Huingancó Granitoids, Permo-Triassic of the Cordillera del Viento, Argentina

Sebastián Pernich [a,*], Claudia Beatriz Zaffarana [a], Víctor Ruiz González [b], Omar Sebastián Assis [c], Gloria Gallastegui [d], Darío Orts [a]

[a] Universidad Nacional de Río Negro, Instituto de Investigación en Paleobiología y Geología, CONICET, Consejo Nacional de Investigaciones Científicas y Técnicas, General Roca, Río Negro, Argentina
[b] Departamento de Física de la Tierra y Astrofísica, Facultad de Ciencias Físicas, Universidad Complutense de Madrid, Spain
[c] Instituto de Geociências, Universidade de Brasília, Laboratorio de Geocronologia e Geoquímica Isotópica, Brasilia, 70910-900, DF, Brazil
[d] Instituto Geológico y Minero de España (IGME-CSIC), Unidad de Oviedo, Oviedo, Spain

ARTICLE INFO

Keywords:
Syn-tectonic emplacement
Anisotropy of magnetic susceptibility
Choiyoi magmatic province
Neuquén andes

ABSTRACT

This work presents a petrographic and anisotropy of magnetic susceptibility (AMS) study of the Huingancó Volcanic-Plutonic Complex, a suite of granitoids (granodiorites and monzogranites) and minor volcanic rocks that crop out in the Cordillera del Viento, which is located in the Southern Central Andes, Neuquén Province, Argentina. The granodiorites have an Early Permian crystallization age (U-Pb ages of 283 ± 1 Ma and 282 ± 2 Ma), whereas the monzogranites are of Late Permian age (U-Pb age of 258 ± 9 Ma) and belong to the Choiyoi Magmatic Province, which developed before the Andean subduction. Plutons and dikes, metasedimentary host rocks, and the younger volcanic units were studied with the AMS technique to characterize their internal structure, which was integrated with the regional structural framework. The petrographic study revealed that the original magmatic fabrics of the granodiorites and monzogranites of the Huingancó Complex were overprinted by solid-state deformation of varying intensity. However, the magnetic ellipsoids are clearly defined, so we interpret that the magnetic fabrics of the Huingancó Granitoids developed contemporaneously with the emplacement of the granitoids. The magnetic fabrics of the granodiorites are sub-parallel to the NW-SE-oriented and SW-vergent subvertical structures generated by the San Rafael Orogenic Phase in the Cordillera del Viento area. In turn, the magnetic fabrics of the monzogranites are parallel to the contact with the host rocks and farther from the contacts, they become more dispersed, suggesting that they represent magmatic flow fabrics during pluton emplacement. The emplacement of the granodiorites is interpreted as syn-tectonic with respect to the San Rafael Orogenic Phase, whereas the monzogranites are interpreted to have emplaced post-tectonically, ~25 Myr after, in shallower tectonic conditions. The structural study of the Huingancó Granitoids provided insight into the Late Paleozoic deformation in this area, both during and after the San Rafael Orogenic Phase, marking a transition of the magmatism within the Choiyoi Province. Our results exemplify granitoids affected by contrasting tectonic settings, likely reflecting the transition from a compressional regime associated with the final stages of the amalgamation of the Gondwana supercontinent to an extensional regime related to its subsequent break-up.

1. Introduction

Understanding the internal structure of plutons and their host rocks can provide valuable insights into the emplacement conditions of plutons. The time at which this fabric is acquired can be determined by examining the microstructures within the pluton, which can be classified based on whether they were acquired during the magmatic stage, or during solid-state deformation at high or low temperature conditions

This article is part of a special issue entitled: Patagonia published in Journal of South American Earth Sciences.

* Corresponding author. Universidad Nacional de Río Negro, Sede Alto Valle-Valle Medio e Instituto de Investigación en Paleobiología y Geología, General Roca, Río Negro, Argentina.
E-mail addresses: sebapernich@gmail.com, spernich@unrn.edu.ar (S. Pernich).

https://doi.org/10.1016/j.jsames.2025.105390
Received 17 May 2024; Received in revised form 22 January 2025; Accepted 30 January 2025
Available online 31 January 2025
0895-9811/© 2025 Elsevier Ltd. All rights are reserved, including those for text and data mining, AI training, and similar technologies.

(Paterson et al., 1998). While determining the foliations and lineations of plutons can be challenging due to their isotropic appearance, the anisotropy of magnetic susceptibility (AMS) method can be particularly useful, because it helps to determine magnetic foliation and lineation of undeformed to weakly deformed rocks (e.g.: Archanjo et al., 1995, 2002; Assis et al., 2021; Bouchez, 1997; D'Eramo et al., 2006; de Saint Blanquat and Tikoff, 1997; Ferré and Améglio, 2000; McNulty et al., 2000; Neves et al., 2003; Stevenson, 2009; Olivier et al., 2016; Zaffarana et al., 2017; Žák et al., 2005).

In this study, we present the internal structure of the Huingancó Volcanic-Plutonic Complex using the AMS method in conjunction with rock magnetic properties, as well as traditional structural geology techniques at both meso- and microscale. The Huingancó Volcanic-Plutonic Complex (HPVC; in this work we also call it Huingancó Complex and the granitoids are referred to as Huingancó Granitoids) comprises a particular case of study because its plutonic rocks were emplaced during the final stages of the Gondwanide Orogeny (early Carboniferous - early Permian; Giacosa et al., 2014) and were later uplifted during the Jurassic (Pons et al., 2022b) and Cretaceous (Andean Orogeny). The Huingancó Granitoids consist mainly of granodiorites and monzogranites (Digregorio, 1972; Llambías, 1986; Llambías et al., 2007), which are hosted by Carboniferous sedimentary and volcanic rocks (Rovere et al., 2004; Llambías et al., 2007; Giacosa et al., 2014). These granitoids are located in the Cordillera del Viento in the Neuquén Andes (Fig. 1a–c and 2; Llambías et al., 2007; Sato et al., 2008; Ramos et al., 2011a, 2011b; Hervé et al., 2013) and are considered part of the Choiyoi Magmatic Province (Sato et al., 2008, 2015; Bastías-Mercado et al., 2020). Our results contribute to unraveling the structural evolution of this complex area and can serve as an example of granitoids affected by contrasting tectonic contexts, probably reflecting the transition from a compressional to an extensional tectonic regime, where the latter reflected the final stages of amalgamation and posterior breakup of the Gondwana supercontinent.

2. Geological framework

In the Cordillera del Viento, Andean tectonics controls the distribution of Paleozoic rock outcrops (Fig. 1a–c). In this sense, the Cordillera del Viento Fault (CVF; Fig. 1b and c; Giacosa et al., 2014) may have constrained the uplift of the Cordillera del Viento Anticline (CVA; Fig. 1b and c; Giacosa et al., 2014), which was thought to have occurred during the Late Cretaceous and Paleogene (Cobbold and Rossello, 2003; Kay et al., 2006; Giacosa et al., 2014; Sánchez et al., 2020). However, Pons et al. (2022b) report thermochronological data suggesting that the uplift and exhumation of the Paleozoic basement may have begun much earlier, in Late Jurassic times (Kimmeridgian-Tithonian), as proposed by Bracaccini (1970).

In the Cordillera del Viento, at least three distinct orogenic events have been recorded: the Chanic Cycle (late Devonian to early Carboniferous), the Gondwanide Cycle (early Carboniferous to early Permian), and the Andean Cycle (early Permian to Recent) (Giacosa et al., 2014). Outside the study area, the metamorphic rocks of the Guaraco Norte Formation represent the Chanic Orogenic Cycle (Giacosa et al., 2014). Later, the rocks of the Andacollo Group, comprising the Arroyo del Torreón Formation of lower Carboniferous age (U-Pb age of 326 ± 3 Ma, Hervé et al., 2013; U-Pb zircon age of 322 ± 5 Ma, Strazzere et al., 2024), and the Huaraco Formation of upper Carboniferous age, were deposited at the beginning of the Gondwanide Orogenic Cycle in Carboniferous times (Rovere et al., 2004; Llambías et al., 2007). The Arroyo del Torreón Formation consists of gray-green, reddish, and brownish dacitic, rhyolitic, and andesitic tuffs, separated in angular unconformity by the dark green to black sandy clays, shales, and siltstones of the Huaraco Formation (Rovere et al., 2004). These units are intruded by a rhyodacitic dome with a U-Pb age of 328 ± 2 Ma, which is associated with the Arroyo del Torreón Formation (Suárez et al., 2008).

Giacosa et al. (2014) defined two sets of structures affecting the Andacollo Group that are related to the final stages of the Gondwanide cycle: syn-sedimentary N-S and NNE-SSW trending normal faults associated with extensional deformation that occurred simultaneously with the deposition of these units and volcanism (Fig. 2), as well as thrusts and related folds associated with the early Permian San Rafael Orogenic Phase. After this early stage of contractional deformation, a period of almost 39 Myr of magmatic activity occurred, with present-day outcrops consisting mainly of plutonic rocks from the early stages of magmatism and volcanic rocks of younger ages (286-247 Ma; Sato et al., 2015; Bastías-Mercado et al., 2020). This extensive record of intermediate to felsic igneous rocks is known as the Choiyoi Magmatic Province, and outcrops can be found from northern Chile (22°S) to the North Patagonian Massif in Argentina (43°S) and from the Principal and Frontal Cordillera to the Pampean and Ventania Ranges (70-62° W) to the east (Kay et al., 1989; Sato et al., 2015; Bastías-Mercado et al., 2020). This magmatism is constrained between the early Permian San Rafael Orogenic Phase and the Triassic extensional Huárpica phase (Figs. 2 and 3a-b; Sato et al., 2015). The San Rafael Orogenic Phase is associated with the San Rafael Unconformity, while the extensional Huárpica Phase gave rise to the Huárpica Unconformity, which later separates the Huingacó Complex from the Cordillera del Viento Formation. Several authors describe, based on stratigraphic, structural, and magmatic studies, that the Choiyoi Magmatic Province transitioned from Early Permian arc-related syntectonic, transpressive sequences to late Permian-early Triassic (transitional to) intraplate, postorogenic transtensional magma suites (Uliana and Biddle, 1988; Mpodozis and Kay, 1992; Llambías et al., 1993; Kleiman, 1993; Kleiman and Japas, 2002, 2005, 2009).

This study is focused on the plutonic and volcanic rocks Huingancó Volcanic-Plutonic Complex, which are representatives of the Choiyoi Magmatic Province in the Cordillera del Viento region (Llambías et al., 2007). The Huingancó Granitoids are the plutonic rocks of the complex, comprising an older granodioritic facies with U-Pb zircon ages of 283 ± 1 Ma (Sato et al., 2008) and 282 ± 2 Ma (Hervé et al., 2013), and a younger monzogranitic facies with a U-Pb age of 258 ± 9 Ma (Sato et al., 2008) (Fig. 1c). The Huingancó Granitoids are hosted by the Carboniferous rocks of the Andacollo Group (Fig. 3a and b), developing metamorphic aureoles with hornfels (Stoll, 1957; Zöllner and Amos, 1973; Rovere et al., 2004; Llambías et al., 2007).

The volcanic facies of the Huingancó Complex consist of andesitic dikes (Llambías et al., 2007), subvolcanic rhyolitic domes with K-Ar biotite ages between 260 Ma (Llambías, 1986) and 259 ± 18 Ma (JICA, 2001), and greenish gray to black andesitic tuffs and silicic welded ignimbrites of the La Premia Formation (Méndez et al., 1995; Llambías et al., 2007) (Fig. 1b–Table 1). The San Rafael Unconformity (Fig. 1c and 2), related to the San Rafael Orogenic Phase, separates the Andacollo Group from the La Premia Formation (Llambías et al., 2007). The Huárpica Unconformity, on the other hand, separates the Huingancó Volcanic-Plutonic Complex from the Triassic units (Fig. 1c and 2).

The Huemules Andesite (Zöllner and Amos, 1955, 1973) is intruded by pegmatitic dikes associated with the Huingancó Granitoids (Rovere et al., 2004). Based on the stratigraphic relationships of the Huemules Andesite, it is located between the Upper Carboniferous and the Lower Permian (Fig. 1c and 2; Zöllner and Amos, 1955; Stoll, 1957; Rovere et al., 2004).

Above these units lie the sedimentary and volcanic rocks of the Neuquén Basin, which are defined by the Pre-Cuyo Group (Cordillera del Viento, Milla Michicó, and La Primavera Formations), Cuyo Group (Los Molles and Tábanos Formations), Lotena Group (Lotena and Auquilco y La Manga Formations), and Mendoza Group (Tordillo and Vaca Muerta Formations; Rovere et al., 2004; Llambías et al., 2007; Zappettini et al., 2018, Fig. 1c). Intercalations of volcanic rocks are present in the Neuquén Basin sequence due to the activity of the Andean arc, represented in the study area by the Nahueve andesite (Fig. 1b and c; Rovere et al., 2004).

Lapilli tuffs cropping out near the Andacollo and Huingancó

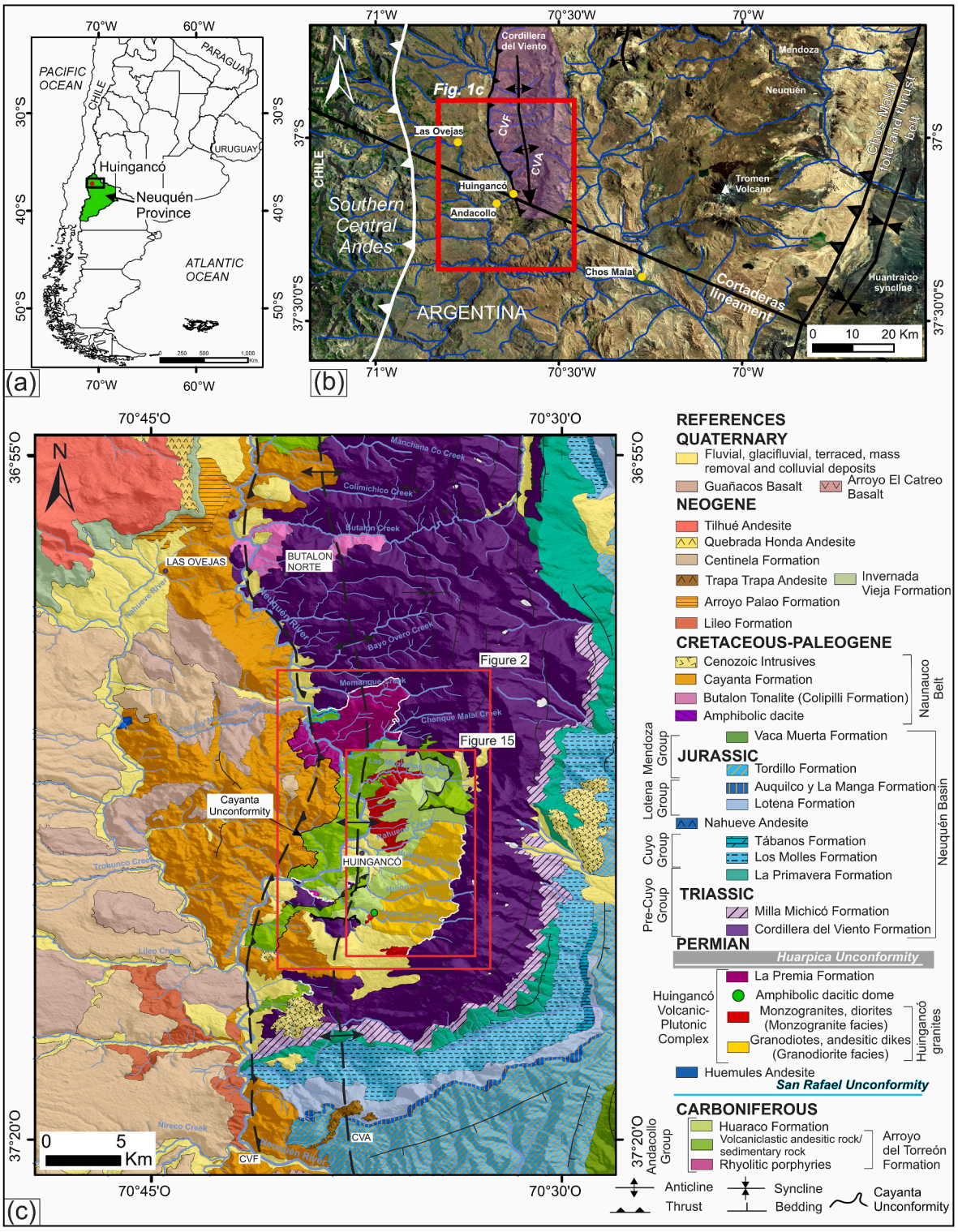


Fig. 1. General location of the study area based on Zannettini et al. (2001), Rovere et al. (2004), Giacosa et al. (2014), Sagripanti et al. (2014), Rojas Vera et al. (2015), Turienzo et al. (2018), Sánchez et al. (2018), Assis et al. (2021) and Pernich (2021). a) Location of the Huingancó area in the Neuquén Province; the black rectangle signals the location of (b). b) Interpreted satellite image showing the main structural features of the Cordillera del Viento area, located in the inner part of the Chos Malal Fold and Thrust Belt, where the Cordillera del Viento fault and the Cordillera del Viento anticline are located. The study area is located to the north of the Cortaderas lineament. The red rectangle shows the location of the study area (c). c) Local geology of the Huingancó area. The red rectangles mark the locations of Fig. 2 (larger) and Fig. 15 (smaller). The Huárpica and San Rafael unconformities are marked, respectively, with yellow and white lines and the angular unconformity between the Cayanta Formation and the Carboniferous and Permian units is marked with a black line. CVF: Cordillera del Viento Fault. CVA: Cordillera del Viento Anticline.

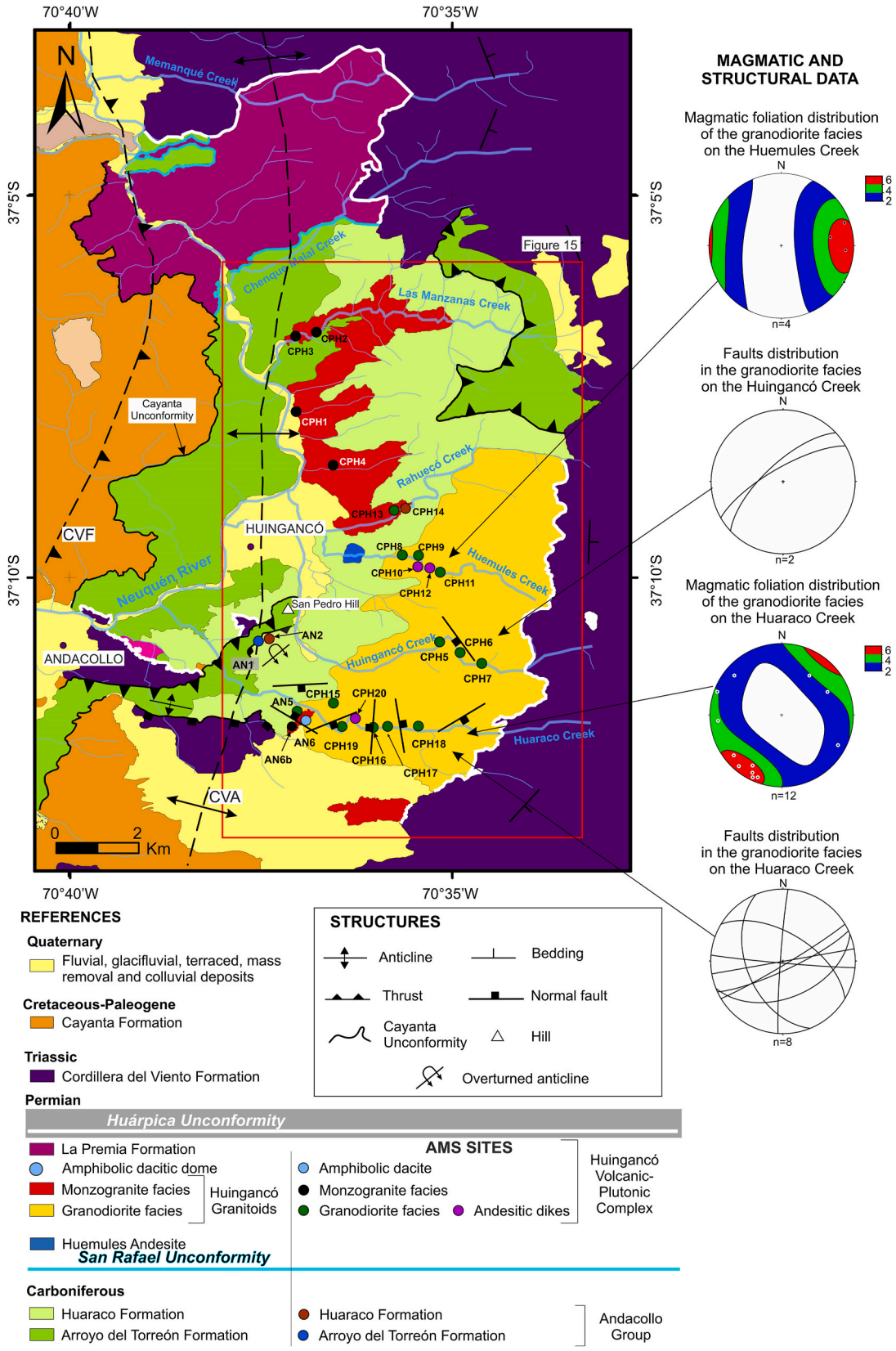


Fig. 2. Geological map of the Huingancó area showing the main structural features (Cordillera del Viento Fault and Cordillera del Viento Anticline, as well as other structures, see the text for further information), unconformities and magmatic and structural data of the Huingancó Granitoids. The location of the AMS sampling sites is also included. The red rectangle indicates the location of Fig. 15. The Huárpica and San Rafael unconformities are marked by yellow and white lines, respectively, and the angular unconformity between the Cayanta Formation and the Carboniferous and Permian units is shown with a black line. The stereonets are contoured Kamb equal-area lower-hemisphere projections of the magmatic foliations and faults, that were made on the Stereonet 11 software (Allmendinger et al., 2012; Cardozo and Allmendinger, 2013). The scale represents Kamb contours in standard deviation.

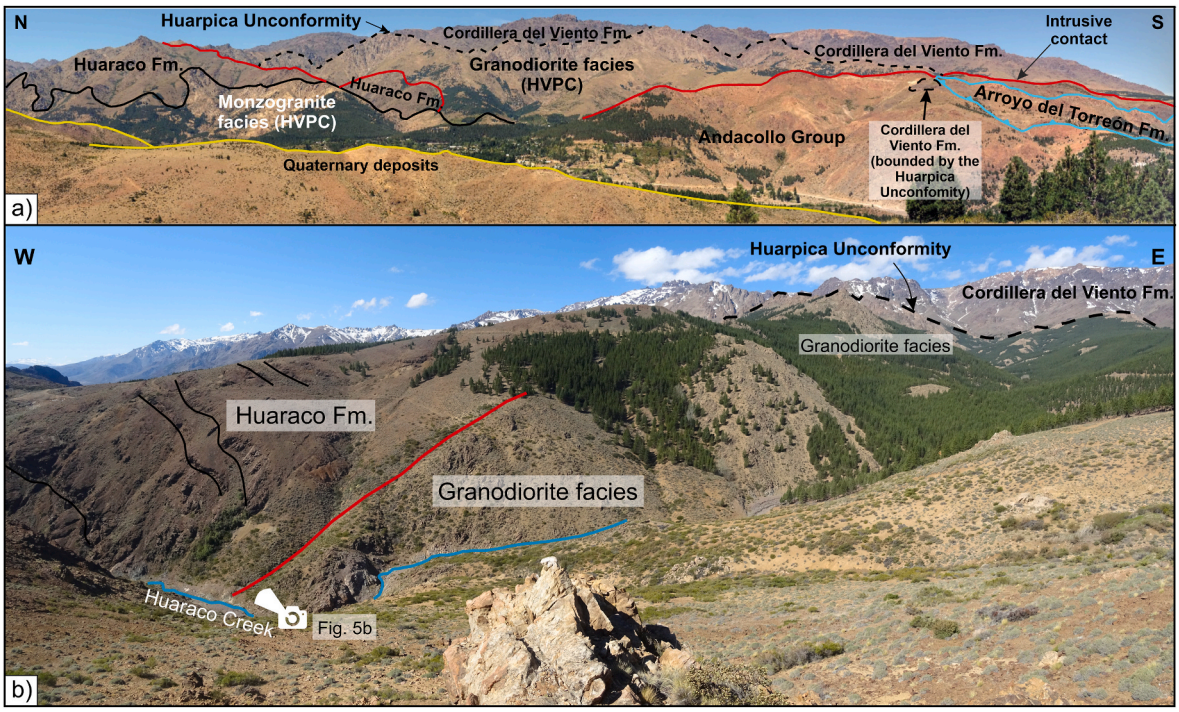


Fig. 3. Field relationships between the Huingancó Granitoids and the other units of the Cordillera del Viento area. a) East oriented general panoramic view of the Cordillera del Viento, where the red line marks the intrusive contact between the Huingancó Granitoids and the Andacollo Group. The black dotted line above is the Huárpica Unconformity, where the granodiorite facies of the Huingancó Volcanic-Plutonic Complex are unconformably covered by the Early Jurassic volcanic rocks of the Cordillera del Viento Formation. b) View of the west-dipping intrusive contact between the granodiorite facies of the Huingancó Volcanic-Plutonic Complex and the Huaraco Formation (photo taken from Huaraco creek, with a view toward the north). Note that the location of the photo corresponding to Fig. 5b is also indicated. The black dashed line along the highest peaks of the Cordillera del Viento marks the Huárpica Unconformity between the Huingancó Granitoids (below) and the Cordillera del Viento Formation (above).

localities yielded U-Pb zircon ages ranging from 191 Ma to 196 ± 1 Ma (Pons et al., 2022a). These new ages support the reclassification of these units, which were previously considered part of the La Premia Formation, to the Cordillera del Viento Formation (Pons et al., 2022a). These deposits are intruded by and overlain by the Late Cretaceous-Paleogene volcanic and plutonic units of the Naunauco Belt (Llambías and Aragón, 2011). The Naunauco Belt comprises a) andesitic volcanic rocks that are represented by the Cayanta Formation, including an amphibolic dacite in the Huingancó area which bears a Late Cretaceous U-Pb age of 68 Ma (Pons et al., 2022a), and b) granodioritic, tonalitic and dioritic plutonic rocks represented by the Varvarco Tonalite (Assis et al., 2019; 2021), the Butalón Tonalite (Casé et al., 2008), and other plutonic rocks belonging to this belt, all grouped in the Colipilli Formation (Franchini et al., 2003; Kay et al., 2006). In the area of study, the Colipilli Formation is represented by the Butalon Tonalite (Assis et al., 2021) and, probably, by some Paleogene intrusive rocks that intrude the Pre-Cuyo and Cuyo Groups, and that are referred to as "Cenozoic Intrusives of the Naunauco Belt" in Fig. 1c (Llambías et al., 2007). Associated with the magmatism of the Naunauco Belt are the mineralizing hydrothermal fluids represented by the Sofía-Julia-Valencia vein systems which accompanied an intense hydrothermal alteration of the surrounding rocks in the Andacollo area (Pons et al., 2023). The Neogene sedimentary and volcanic rocks of the Lileo Formation, Arroyo Palao Formation, Invernada Vieja Formation, Trapa Trapa Andesite, Centinela Formation, Quebrada Honda Andesite and Tilhué Andesite (Fig. 1c), along with the Quaternary sedimentary and volcanic rocks of the Guañacos Basalt, Arroyo El Catreo Basalt and fluvial and glacifluvial deposits, complete the stratigraphy of the area (Rovere et al., 2004; Llambías et al., 2007; Giacosa et al., 2014: Fig. 1c).

3. Methodology

First, this section presents the criteria for field sampling, structural data collection, and petrographic analysis. Next, the theoretical principles of the anisotropy of magnetic susceptibility (AMS) technique are briefly outlined, followed by its application to the studied rocks. Finally, the fundamentals of rock magnetic studies are discussed.

3.1. Field sampling and petrographic analysis

For the petrographic analysis, a collection of 19 thin sections were prepared from the Huingancó Granitoids and the andesitic dikes of the Huingancó Complex, with one thin section corresponding to each AMS sampling site (Table 1). The location of the sampling sites are shown in Fig. 2. Sampling was conducted on fresh granites, away from fragile structures. The orientations of ductile foliations and brittle structures were measured, and their attitudes were transferred to maps and AMS stereograms for comparison with the AMS data. Thin sections were analyzed using a petrographic microscope.

3.2. AMS technique: theoretical principles

The AMS ellipsoid is defined by the principal magnetic susceptibility axes $K_1 > K_2 > K_3$, with which some quantitative parameters of the magnetic petrofabrics can be calculated. The mean (average) susceptibility is $K_m = (K_1 + K_2 + K_3)/3$ (Tarling and Hrouda, 1993). One of these parameters is the anisotropy degree P ($P = K_1/K_3$; Tarling and Hrouda, 1993), and the more generally used corrected anisotropy degree Pj ($Pj = \exp[2\{\ln K_1 - \ln K_m\}^2 + 2\{\ln K_2 - \ln K_m\}^2 + 2\{\ln K_3 - \ln K_m\}^2)^{1/2}$; Jelinek (1981). The Pj parameter is based on the ratio of the maximum and minimum susceptibility axes, but it also considers the intermediate susceptibility axis and the mean susceptibility K_m. The shape of the AMS

Table 1
Table of the AMS sites of the Huingancó Volcanic-Plutonic Complex and the Andacollo Group. Sites are organized following a lithological order. SSD: Solid-state deformation. HT: high-temperature deformation, MLT: moderate low-temperature deformation, ILT: intense low-temperature deformation. N it's the number of samples taken per AMS sites. $K_m = (K_1 + K_2 + K_3)/3$ is the mean magnetic susceptibility (SI units). K_1, K_2 and K_3 are the mean AMS eigenvectors that represent the maximum, intermediate and minimum susceptibility intensities, respectively. L (K_1/K_3) is the magnetic lineation; F is the magnetic foliation (K_2/K_3); P is the anisotropy degree (Jelinek, 1981); Pj is the corrected anisotropy degree of Jelinek (1981); T = (lnF-lnL)/(lnf + lnL) is the Jelinek parameter of shape (Jelinek, 1981). Dec. is the declination in degrees and Inc the inclination in degrees. C_{1a} and C_{1b} correspond to the semi angles of the major and minor axes of the 95% confidence ellipse calculated by the bootstrap method.

Site	Lithology	SSD	GPS coordenates	N	K_m (10^{-3} SI)	K1d	K1i	C1a	C1b	K2d	K2i	C2a	C2b	K3d	K3i	C3a
CPH1	Monzogranite, Huingancó	MLT	37°7′49,7″ S/ 70°37′2,9″ W	6	0.0631	188.2	171.2	62.1	61	288.9	13.8	61.3	12.3	25.1	23.7	25.3
CPH2	Granitoids	MLT	37°6′47,3″ S/ 70°36′49″ W	8	0.0545	215.7	38.1	44.4	10.1	321.1	18.6	46.5	14.6	71.4	46	29.6
CPH3		ILT	37°6′50,4″ S/ 70°37′3,2″ W	9	0.0406	197.7	23	50.5	21.2	317.5	49.5	52.1	27.1	92.8	31.3	34.7
CPH4		ILT	37°8′31,9″ S/ 70°36′33,8″ W	6	0.397	248.1	57.1	32.8	9.6	92.3	30.5	34.2	20.6	355.6	11	24.9
CPH13		MLT	37°9′5,9″ S/ 70°35′40,4″ W	9	0.0291	163.1	60.2	17.2	5.5	46.3	14.5	35	14.7	309.2	25.4	35.2
AN6b		–	37°11′50,7″ S/ 70°36′55,6″ W	6	0.102	329	76.4	55.4	37.1	66.7	1.9	56.9	40.4	157.1	13.4	46
CPH5	Granodiorite, Huingancó	HT	37°10′46″ S/ 70°35′1,5″ W	11	0.516	188.2	27.7	22.9	18.6	64.3	46.8	52.9	18.6	296	30.2	21.5
CPH6	Granitoids	–	37°10′53,3″ S/ 70°34′56,4″ W	10	1.15	359.9	36.4	70.6	34	174.6	53.5	70.5	25.6	268	2.5	36.9
CPH7		MLT	37°11′7,6″ S/ 70°34′37″ W	10	1.47	206.3	12	50.9	16.1	296.4	0.2	50.4	38.5	27.2	78	39.7
CPH8		MLT	37°9′43,8″ S/ 70°35′31,7″ W	10	0.613	217.7	63.1	21	8.2	310.4	1.3	21	6.7	41.1	26.9	19.2
CPH9		MLT	37°9′46″ S/ 70°35′26,6″ W	9	4.9	215.8	76.5	13.5	11.8	347.1	9	14	10.9	78.6	9.9	16.4
CPH11		HT	37°9′51,7″ S/ 70°35′24,9″ W	11	4.3	320.2	73.7	14.6	5.8	185.4	11.7	18.6	12.4	93.1	11.3	19.3
CPH15		MLT	37°11′38,7″ S/ 70°36′33,5″ W	11	0.438	315	54.4	22.4	10.9	108.7	32.7	34.3	21.9	206.9	12.6	34.4
CPH16		MLT	37°11′57,9″ S/ 70°36′2,3″ W	15	6.39	305.6	74.7	36.4	15.3	144.8	14.5	37.2	21.2	53.6	4.8	23.8
CPH17		ILT	37°11′57,2″ S/ 70°35′46,6″ W	11	7.42	136.1	66.3	25.5	19.4	321.2	23.6	43.6	25.4	230.3	1.9	44.6
CPH18		MLT	37°11′57,1″ S/ 70°35′39″ W	10	12.9	355.4	2.9	64.7	16.5	198.7	86.8	64.7	16	85.5	1.3	19.6
CPH19		–	37°11′57,2″ S/ 70°36′26,7″ W	10	0.463	21.9	49.3	19.3	7.9	130.7	15.4	19.9	10.3	232.5	36.5	11.6
AN5		–	37°11′50,5″ S/ 70°36′57,6″ W	6	0.0424	79.4	9.7	45.7	42.1	329.8	63	59.1	45.3	174	24.9	61.3
CPH10	Andesitic dike, Huingancó Complex	–	37°9′46″ S/ 70°35′25,6″ W	8	0.5976	341.1	85.8	18.9	2.1	233	1.3	18.9	6.7	142.9	4	6.9
CPH12		–	37°9′51.7″ S/ 70°35′24,9″ W	10	5.29	177.3	1.9	5.8	2.7	273.1	71.8	8.9	2.7	86.6	18.1	8.6
CPH20		–	37°11′50,8″ S/ 70°36′16,3″ W	12	41.46	252.8	69.9	13.3	7	346.2	1.3	55.5	11.3	76.7	20	55.6
AN6	Amphibole dacite, Huingancó Complex	–	37°11′50,7″ S/ 70°36′55,6″ W	6	21.1	215.2	23.3	13.7	4.7	328.3	42.3	22.2	6.2	105	38.6	19.5
CPH14	Sandstones, Huaraco Fm.	–	37°9′5,8″ S/ 70°35′36,8″ W	8	5.01	182	81.3	15.8	10.6	39.6	6.9	17.3	6.8	309	5.3	12.3
AN1		–	37°10′48,2 S/ 70°37′23,9″ W	6	0.0981	237.1	4.4	50.1	22.9	331	42	52.8	20	142.2	47.7	37
AN2	Ignimbrites, Arroyo del Torreón Fm.	–	37°10′50,1″ S/ 70°37′32,4″ W	6	0.0756	266	20	49.2	12.3	161.3	34.8	50.9	34.5	20.1	48.3	39.3

C3b	K1	K2	K3	Lmean	Fmean	Pmean	Pjmean	Tmean
14.5	1.011	1.006	0.983	1.004	1.023	1.028	1.03	0.68
8.1	1.009	1.003	0.988	1.006	1.016	1.022	1.022	0.457
22	1.004	1.001	0.996	1.003	1.005	1.008	1.008	0.205
13.3	1.012	1.002	0.986	1.01	1.015	1.026	1.026	0.187
9.8	1.005	0.999	0.996	1.006	1.003	1.009	1.01	−0.362
37.2	1.006	1.002	0.992	1.004	1.01	1.013	1.014	0.446
21.5	1.008	0.998	0.994	1.01	1.003	1.013	1.014	−0.498
25.6	1.005	1.003	0.992	1.002	1.012	1.014	1.015	0.698
19.7	1.007	1.033	0.99	1.005	1.013	1.017	1.018	0.46
9.5	1.007	1	0.983	1.017	1.017	1.034	1.034	0.012
6.8	1.014	1	0.986	1.014	1.014	1.028	1.028	.0.018
6.6	1.018	1	0.983	1.018	1.017	1.035	1.035	−0.029
9.6	1.01	0.998	0.992	1.012	1.005	1.018	1.018	−0.384
14.6	1.024	1.006	0.97	1.018	1.038	1.056	1.058	0.344
13.8	1.012	1.001	0.987	1.011	1.014	1.025	1.025	0.122

(*continued on next page*)

Table 1 (*continued*)

C3b	K1	K2	K3	Lmean	Fmean	Pmean	Pjmean	Tmean
13.2	1.012	1.006	0.983	1.006	1.023	1.029	1.031	0.585
7.9	1.017	1.006	0.977	1.011	1.03	1.041	1.043	0.471
26.2	1.003	0.999	0.997	1.004	1.002	1.006	1.006	−0.463
1.7	1.006	1.002	0.993	1.004	1.009	1.013	1.013	0.412
3.5	1.042	0.994	0.964	1.048	1.031	1.081	1.081	−0.208
6.3	1.012	0.995	0.993	1.017	1.003	1.02	1.021	−0.716
5.3	1.012	0.998	0.99	1.015	1.008	1.023	1.023	−0.288
7.7	1.016	1.002	0.982	1.014	1.02	1.034	1.034	0.174
18.9	1.002	1.001	0.997	1.001	1.004	1.005	1.005	0.566
11.6	1.002	1	0.998	1.002	1.002	1.004	1.004	0.147

ellipsoid is reflected by the shape parameter T (T = (ln F- ln L)/(ln F + ln L); where F = K_2/K_3 and L = K_1/K_2 quantify the degree of magnetic foliation and lineation, respectiviley (Tarling and Hrouda, 1993). When T < −0.5, the AMS ellipsoid has a strongly prolate shape; when T > 0.5, it has a strongly oblate shape, and when −0.5<T < 0.5, the ellipsoid has a triaxial shape (Zaffarana et al., 2017). The magnetic lineations are structurally more important when the sites are prolate, having T < 0.5 and high values of anisotropy degree Pj, but less significant when sites are oblate and T→1 (Cruden et al., 1999). The magnetic foliation is represented by the plane that contains K_2 and K_1 axes (the minimum magnetic susceptibility axis K_3 represents the pole of the magnetic foliation), while the orientation of the maximum magnetic susceptibility axis K_1 represents the magnetic lineation. The AMS method is useful because it correlates magnetic susceptibility with fabric ellipsoids (K_1, K_2, and K_3 with λ_1, λ_2, and λ_3, respectively, e.g.: Borradaile and Jackson, 2010). Magnetic foliation is typically parallel to structural foliation, and magnetic lineation is parallel to structural lineation, which reflects flow or stretching direction (Borradaile and Henry, 1997).

The AMS of a rock is closely related to its mineral composition, particularly to the abundance of minerals containing iron. The mean total magnetic susceptibility (K_m) of a rock is largely determined by the predominant magnetic mineral present. As a result, rocks with a K_m value greater than 5×10^{-3} SI its magnetic fabric is dominated by ferromagnetic minerals, if the K_m value is less than 5×10^{-4} SI, then the paramagnetic minerals control the magnetic susceptibility and anisotropy of the rocks (Tarling and Hrouda, 1993). This implies that the AMS ellipsoid of a rock is directly influenced by its mineralogy, and the relative abundance of different minerals will impact the resulting K_m value and the magnetic fabric of the rock.

3.3. Implementation of the AMS technique

All the AMS samples were collected with a portable drilling machine and oriented by sun and magnetic compasses. In each of the 25 ASM sampling sites, a minimum of five oriented cylinders were taken, giving a total of 224 cylinders. Out of the 25 AMS sampling sites, 22 are part of the Huingancó Complex, with 13 representing the granodiorite facies, five belonging to the monzogranite facies, three corresponding to the andesitic dikes, and the last one belonging to an amphibolic dacitic stock (Table 1). The remaining three sites include the sandstones of the Huaraco Formation (2 sites) and the ignimbrites of the Arroyo del Torreón Formation (Table 1).

The AMS measurements were carried out at the IGEBA (Instituto de Geociencias Básicas, Aplicadas y Ambientales de Buenos Aires) using a Kappabridge MFK-1B susceptibility meter. The AMS data were processed using the Anisoft 4.2 software from the Agico company (Chadima and Jelinek, 2008).

3.4. Rock magnetic studies

Finally, rock magnetic studies are essential to determine the domain state of magnetite (whether multi-, pseudo-single-, or single-domain), which is important for accurately interpreting the AMS susceptibility ellipsoids (Rochette et al., 1992). Three representative samples of the Huingancó Complex were selected to perform rock magnetic studies: sample CPH1 of the monzogranitic facies, CPH6 of the granodioritic facies, and CPH10 of the andesitic dikes. These samples were milled, sent and processed for rock magnetic studies at the Laboratory of Paleomagnetism at the Universidad Complutense de Madrid, Spain, for rock magnetic studies. Isothermal Remanent Magnetizations (IRM) and backfield curves, and hysteresis loops were performed with a Kazan University (Russian Federation) J-Meter coercivity spectrometer (Jasonov et al., 1998), and the high-temperature thermomagnetic curves of susceptibility vs. temperature were performed with a CS-3 attachment for the AGICO KLY-4S Kappabridge.

4. Results

First, we show field and petrographic analysis, followed by the rock magnetic studies and the AMS results. Petrographic descriptions belong to the area of each AMS sampling site.

4.1. Field occurrence and petrography

Below, field and petrographic descriptions are presented in stratigraphic order: first, the Andacollo Group; secondly, the Huingancó Granitoids; and lastly, the volcanic facies of the Huingancó Volcanic-Plutonic Complex.

4.1.1. Host rocks of the Huingancó granitoids

The plutonic rocks of the Huingancó Complex are hosted by the Andacollo Group, which comprises the Lower Carboniferous Arroyo del Torreón Formation and the Upper Carboniferous Huaraco Formation. The outcrops of the Arroyo del Torreón Formation are mostly found on the western side of the Neuquén River (Fig. 2). This Formation hosts the monzogranite facies of the Huingancó Granitoids along the Las Manzanas creek, to the north of the study area (Fig. 2).

The Arroyo del Torreón Formation consists of white to brown felsic tuffs and ignimbrites (Fig. 4a–c). The ignimbrites contain elongated fiammes, which define an eutaxitic texture; the fiammes have been partially devitrified into felsitic and axiolitic textures and altered into clay minerals. Banded and massive quartz veins intrude the tuffs and ignimbrites; these veins are likely associated with the intrusion of the monzogranites of the Huingancó Complex (as shown in Fig. 4 and b). In the Cerro San Pedro area (Fig. 2), the tuffs and ignimbrites of the Arroyo del Torreón Formation are intensely silicified, and plagioclase show alteration to green clay minerals (Fig. 4b). This alteration is possibly related to the intrusion of dacitic stocks from the Naunauco Group (not shown on the map as they are out of scale).

The Huaraco Formation crops out in the center of the area of study and constitutes the main host rock of the Huingancó Granitoids (Fig. 2). It unconformably lies above the volcanic and sedimentary sequences of the Arroyo del Torreón Formation (Fig. 4d). The Huaraco Formation constitutes the roof of the monzogranite facies in the area near site CPH1 (Fig. 2), where the contact is subhorizontal (Fig. 5a). In turn, the contact between the granodiorites and the Huaraco Formation is generally not

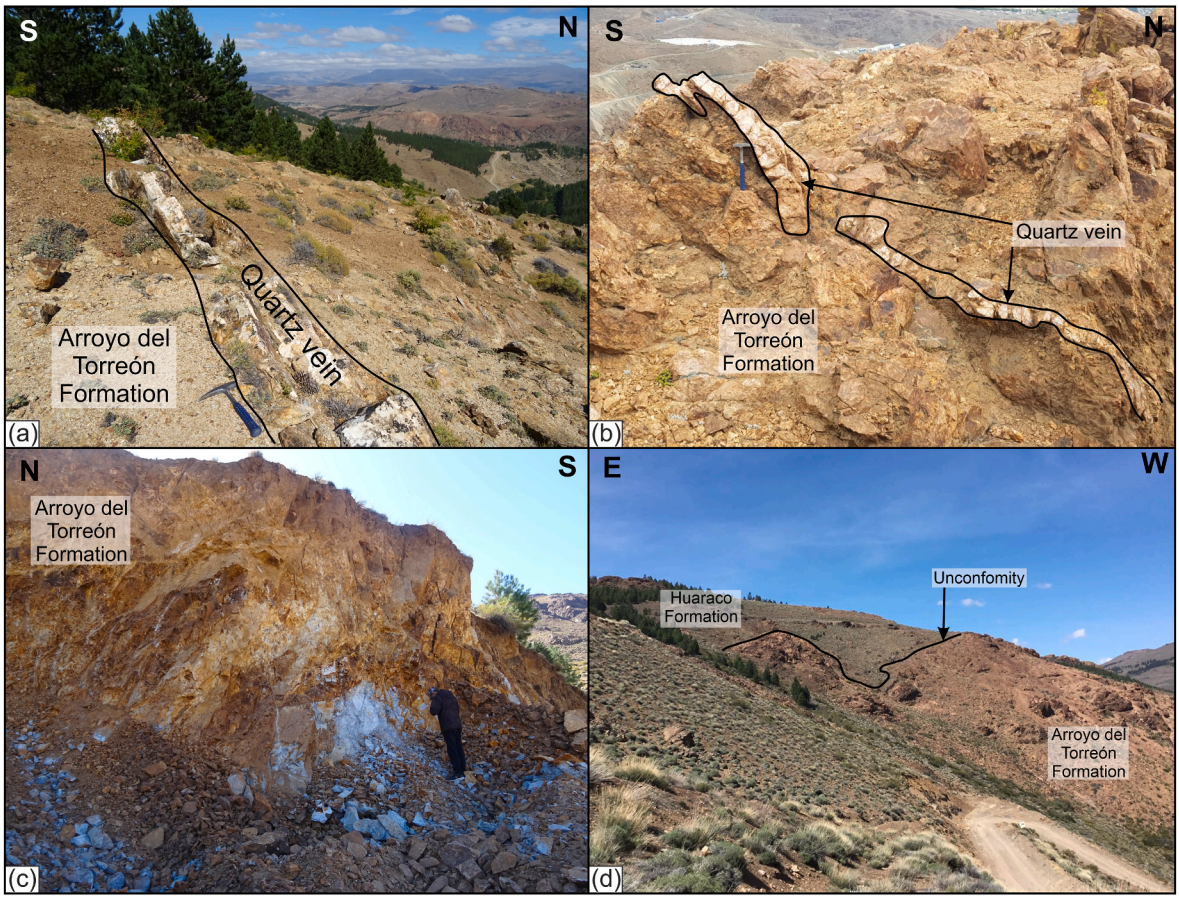


Fig. 4. Field outcrops of the Arroyo del Torreón Formation of the Andacollo Group, host rocks of the Huingancó Granitoids. a) View toward the west, near the Las Manzanas creek, of a quartz vein intruding the Arroyo del Torreón Formation. b) Massive quartz vein intruding the white ignimbrites of the Arroyo del Torreón Formation near the San Pedro Hill, viewed toward the west. c) Tuffs and ignimbrites of the Arroyo del Torreón Formation. d) Huaraco Formation sedimentary rocks unconformably deposited above the Arroyo del Torreón Formation.

horizontal, as in the Huaraco Creek area, to the south of the study area, where it dips moderately to the west (Fig. 5b and c).

The Huaraco Formation is composed of dark brown, silicified quartz-muscovitic sandstones alternated with pelitic layers; asymmetric ripples were recognized (Fig. 5d). Near the Huaraco creek and close to the contact with the monzogranite facies, the sandstones of the Huaraco Formation display evidence of contact metamorphism, shown as muscovite porphyroblasts and intense silicification This alteration is present up to a few meters from the contact with the monzogranite facies of the Huingancó Complex. This contact metamorphism was also mentioned by Llambías et al. (2007) and Capomassi et al. (2023). On sampled site CPH14 the Huaraco Formation has a moderately dipping NNE-SSW stratification.

4.1.2. Granodiorite facies of the Huingancó Volcanic-Plutonic Complex

The granodiorite facies of the Huingancó Complex is exposed in the central part of the study area between the Rahuecó and Huaraco creeks, east of the towns of Huingancó and Andacollo (Fig. 2). The granodioritic rocks span an extensive area of approximately 24 km^2, with an elongated north-south shape (Fig. 2). To the east they are covered by the Huárpica unconformity, above which the Cordillera del Viento Formation lies over (Figs. 2 and 3).

The granodiorite facies intrudes the Huaraco Formation with either clear (Fig. 3b and 5b) or irregular contacts (Fig. 5c). In the contact with the granodiorites, small muscovite porphyroblasts are found in the sedimentary rocks, evidencing contact metamorphism. Additionally, small xenoliths from the sedimentary rocks of the Huaraco Formation were observed within the granodiorite facies (Fig. 5e).

The granodiorites are gray (Fig. 6a–e), with a coarse to medium-grained equigranular texture and mafic microgranular enclaves that have elongated and flattened shapes. Along the Huemules Creek, in the central part of the study area, the granodiorites exhibit a subvertical NW-SE to N-S magmatic foliation, defined by flattened mafic microgranular enclaves (Fig. 6a and 2) and a magmatic lineation marked by elongated mafic microgranular enclaves that plunge steeply toward the SE (Fig. 6b and 2). Further south, along the Huaraco Creek, the magmatic foliations, defined by flattened mafic microgranular enclaves, display NW-SE steeply east-dipping orientations (Fig. 2) and the magmatic lineation, also defined by elongated mafic microgranular enclaves, plunges steeply toward the SE.

Aplitic dikes and veins intrude the granodiorites (Fig. 6b–d). The aplitic dikes have a fine-grained xenomorphic equigranular texture and are composed of quartz, plagioclase, alkali feldspar and muscovite. Occasionally, they have a pegmatitic core with the same mineralogy plus tourmaline. At the margins of some aplitic dikes, plagioclase, quartz and hornblende crystals from the host granodiorites are found; these crystals are interpreted as the product of mechanical mixing between the granodiorites and the aplitic dikes in an assimilation zone (Fig. 6d).

Petrographically, the granodiorites have medium-to coarse-grained equigranular hypidiomorphic texture (Fig. 7a–e). The granodiorites are composed of plagioclase (30 %), quartz (25 %), hornblende (20 %), alkali feldspar (10 %), biotite (10 %), and magnetite, titanite, zircon and apatite (~ 5%; Fig. 7a–h).

Plagioclase is euhedral with oscillatory or normal zonation patterns (Fig. 7a), and plagioclase centers are frequently moderately altered to sericite (Fig. 7a and b). Quartz appears as anhedral crystals with

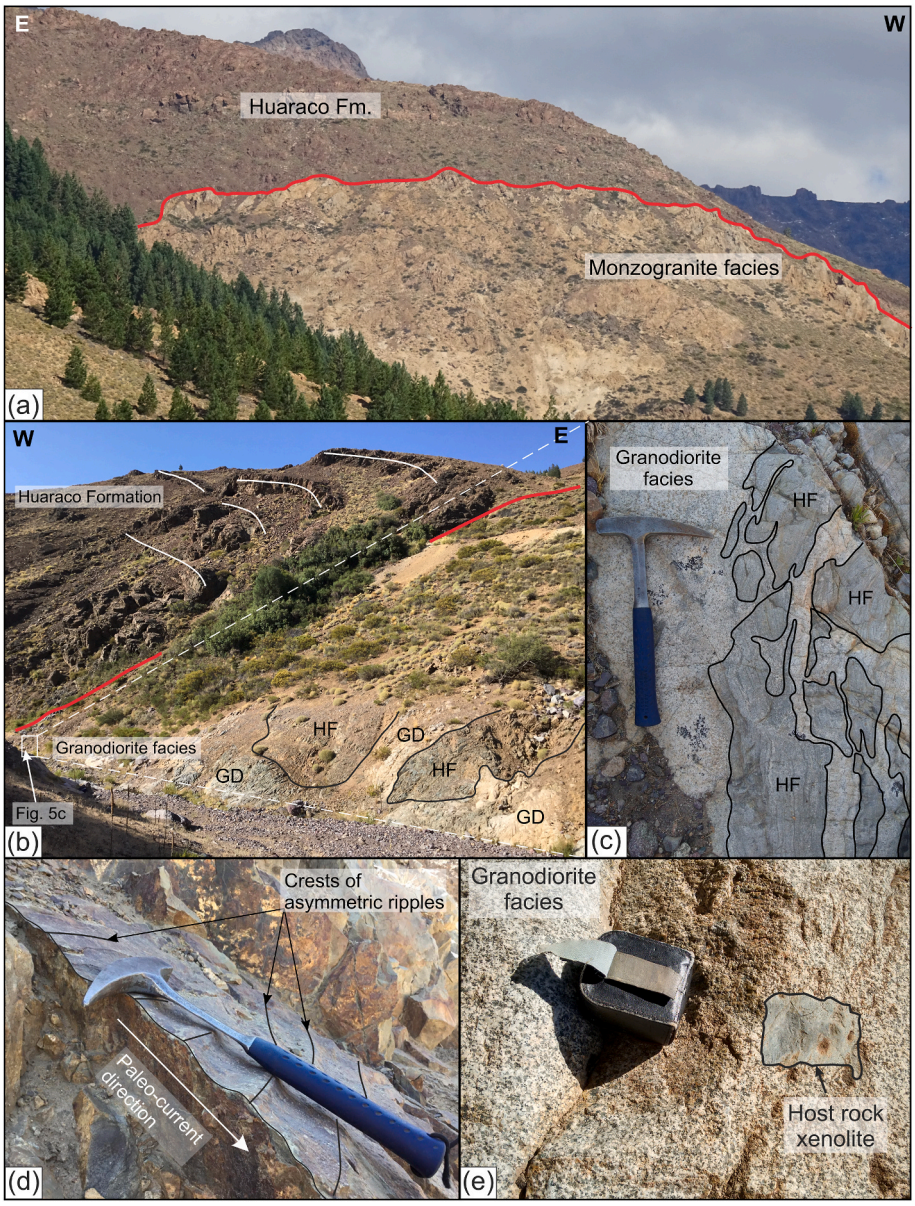


Fig. 5. Field occurrence of the Huaraco Formation of the Andacollo Group, the main host rock of the Huingancó Granitoids. a) Subhorizontal intrusive contact between the monzogranite facies of the Huingancó Volcanic-Plutonic Complex and the sandstones and pelites of the Huaraco Formation, showing that the monzogranites are roofed by the sedimentary rocks. The photo was taken from the sampling site CPH1 (Fig. 2) located along the Neuquén River (view toward the south). b) SW dipping irregular intrusive contact (marked with a red line) between the granodiorite facies of the Huingancó Volcanic-Plutonic Complex and the Huaraco Formation. The granodiorites incorporate irregular fragments (xenoliths or roof pendants) of the sedimentary host rocks of the Huaraco Formation. The white rectangle shows the location of the photograph of Fig. 5c c) The xenoliths of the Huaraco Formation have a very irregular shape, showing that they are partially digested or assimilated by the granodioritic rocks. d) Sandstones of the Huaraco Formation showing asymmetric ripples on their top, the stratification has an E-W strike and a moderate dip to the S and the crests of the asymmetric ripples indicate a paleocurrent direction toward the south. e) Xenolith of the sedimentary rocks of the Huaraco Formation partially digested by the granodioritic rocks. HF: Huaraco Formation. GD: Granodiorite facies.

undulose and chessboard extinctions (Fig. 7a–h). Hornblende is generally euhedral, with a dark to light green color, and bears simple twins; it is moderately altered to chlorite (Fig. 7b, c, and e). Hornblende crystals are usually found in clots together with magnetite and biotite (Fig. 7c). Alkali-feldspar is subhedral and can be either orthoclase or microcline; it is perthitic and moderately altered to clays (Fig. 7a–f).

Biotite is subhedral and pleochroic from light to dark brown (Fig. 7a–c). It is frequently intensely altered to chlorite (and sometimes completely replaced by chlorite; Fig. 7c and d). Additionally, secondary opaque minerals and titanite aggregates align along cleavage planes (Fig. 7a–d). Apatite and magnetite crystals are euhedral, and euhedral zircon crystals are found as inclusions in biotite, producing the characteristic pleochroic halo.

The granodiorites have high- and low-temperature solid-state deformation microstructures. High-temperature solid-state deformation microtextures are quartz with chessboard extinction (Fig. 7e) and inversion of orthoclase to microcline (Fig. 7b) bearing mechanical twins (sites CPH5 and CPH11). Low-temperature solid-state deformation is evidenced by plagioclase with quartz exsolutions with mirmekitic texture adjacent to alkali-feldspar crystals (Fig. 7f) and bulging subgrains in quartz and plagioclase crystal borders (sites CPH7, CPH8, CPH9, CPH15, CPH16 and CPH18; Fig. 7g). When the quartz subgrains are organized around larger quartz crystals, the low-temperature deformation is considered moderate, but when subgrains are

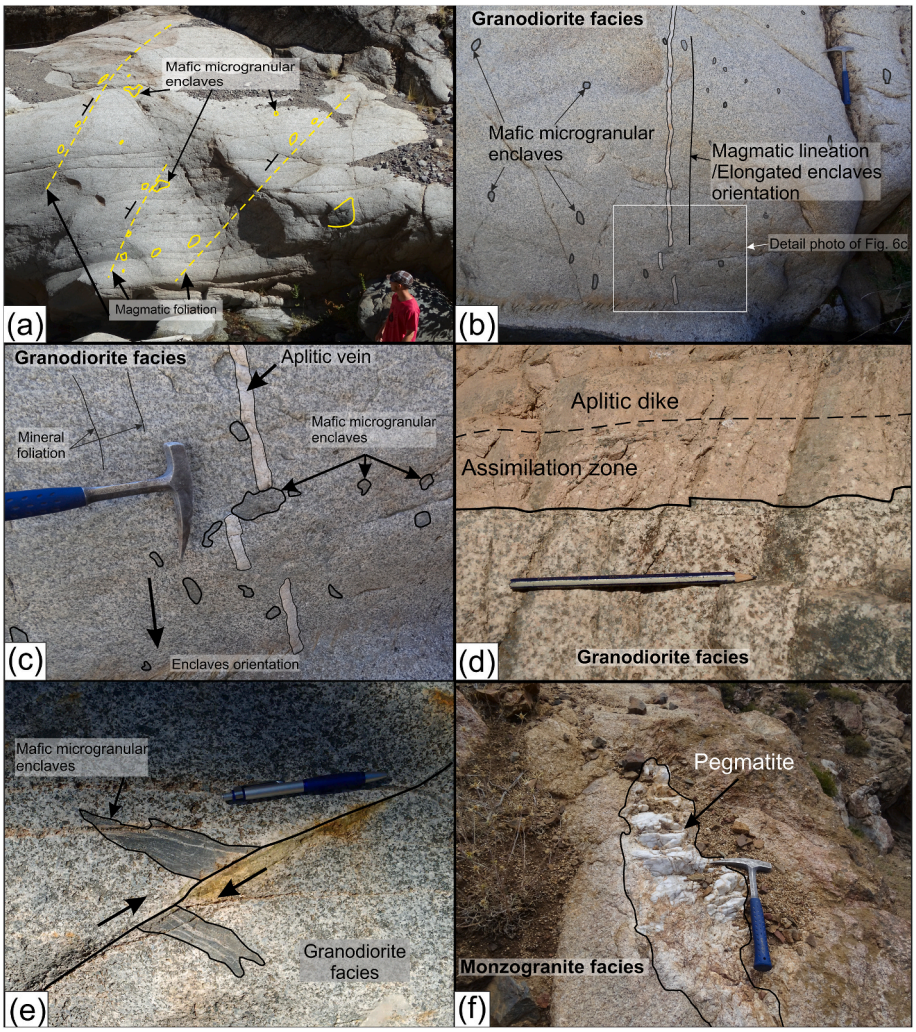


Fig. 6. Detailed view of the outcrops of the Huingancó Granitoids. a) Magmatic foliation defined by the orientation of flattened mafic microgranular enclaves near the site CPH8. b) Granodiorite facies with mafic microgranular enclaves that define a steeply plunging magmatic lineation on the CPH8 site (N184°/78°). White rectangle shows the location of detailed photo of c). c) Detail of the magmatic lineation defined by the orientation of elongated mafic microgranular enclaves, on the site CPH8 of the granodiorite facies. d) Aplitic dike intruding the granodiorite facies of site CPH6, with an assimilation zone, were quartz and plagioclase phenocrystals of the granodiorite are incorporated into the dike. e) Dextral fault affecting a mafic microgranular enclave in the granodiorite facies. f) Quartz pegmatite on the monzogranite facies near sampling CPH3, near Las Manzanas Creek.

organized in bands (Fig. 7h), the solid-state deformation is more intense (site CPH17).

Small (centimeter scale) brittle faults affect the granodiorites along the Huingancó and Huaraco creeks; they are usually subvertical and have NW-SE, N-S, and E-W strike. They can be either normal or dextral (Figs. 2 and 6e).

Pyrite is usually found in the sampled sites along the Huaraco Creek (Fig. 2), where epidote, calcite and quartz veins crosscut the granodiorite. This propylitic hydrothermal alteration mineral assemblage (Py + Cal + Chl + Ep) could be related to the Andacollo Mining District (Pons et al., 2019, 2022a, 2023; Dicaro et al., 2024).

4.1.3. Monzogranite facies of the Huingancó Volcanic-Plutonic Complex

The monzogranite facies crops out in two main areas: to the north between the Rahuecó and Las Manzanas creeks, and to the south along the Huaraco Creek (Fig. 2). Along the Huaraco Creek the monzogranites intrude the granodiorites, although the contacts between both facies could not be observed (the monzogranites were sampled at site AN6b in Fig. 2).

The monzogranite facies are light pink, medium-to coarse-grained equigranular rocks (Fig. 6f). Quartz-feldspathic aplitic dikes of different orientations and small widths (centimeter scale) intrude the monzogranites. Pegmatites up to 1 m in length, composed of quartz, plagioclase, and muscovite are hosted by the monzogranites (Fig. 6f). Miarolitic cavities formed by the same minerals are also frequently found in the monzogranites, with diameters reaching up to 10 cm. Unlike the granodiorite facies, the monzogranites do not have mafic microgranular enclaves.

Petrographically, the monzogranites exhibit a medium-to coarse-grained equigranular hypidiomorphic texture (Fig. 8a). They are composed of quartz (40 %), plagioclase (30 %), alkali feldspar (20 %), biotite and muscovite (5 %), with a small percentage shared by magnetite and garnet (Fig. 8a–h).

Quartz is anhedral, shows undulose extinction, and is frequently recrystallized into smaller subgrains (Fig. 8a). Euhedral to subhedral plagioclase shows an oscillatory to normal zonation pattern and is often moderately to intensely altered to sericite (Fig. 8b).

Subhedral alkali feldspar is primarily orthoclase, but it is frequently inverted to microcline (Fig. 8a and e). Perthitic texture is common, with some perthites exhibiting a flame-shaped pattern (Fig. 8e). Orthoclase and microcline are moderately altered to clays (Fig. 8a and b).

Biotite is scarce and subhedral, showing light to dark brown

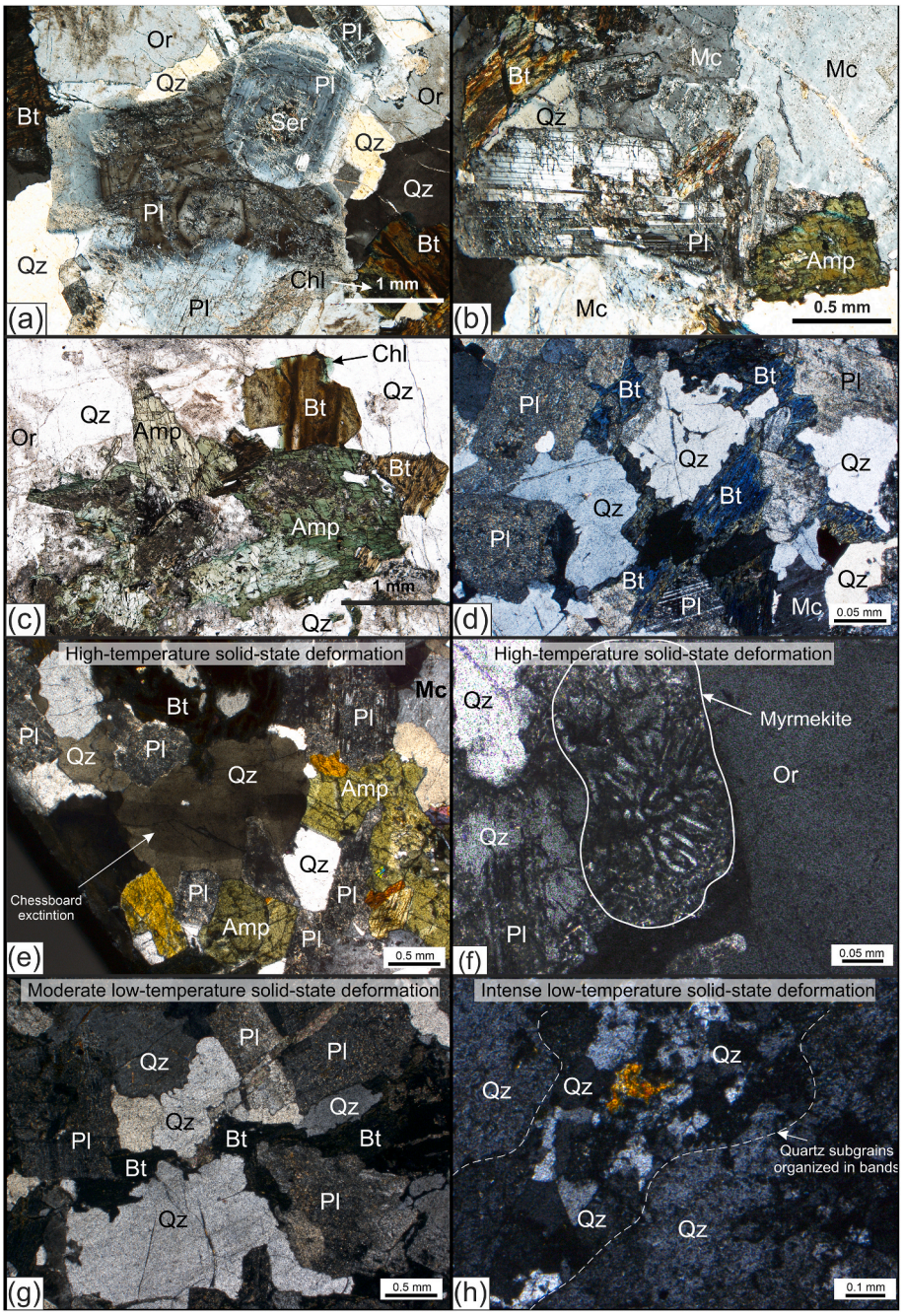


Fig. 7. Petrography of the granodiorite facies of the Huingancó Granitoids. a) Zoned plagioclase phenocrystals showing sericite altered cores. b) Plagioclase phenocrystal with polysynthetic twins and orthoclase with inversion to microcline and biotite with alteration to chlorite. c) Amphibole phenocristals with twins showing different birefringence colours. d) Quartz crystals with serrated borders, surrounded by plagioclases altered to sericite; and biotites entirely altered to chlorite. e) Quartz with chessboard-like extinction on the CPH11 sampling site. f) Plagioclase with quartz exsolution with mirmekitic texture. g) Quartz phenocrystals that have serrated borders on the CPH9 sampling site. h) Quartz sub-grains disposed on an elongated zone. Qz: quartz. Pl: plagioclase. Amp: amphibole. Bt: biotite. Ser: sericite. Mc: microcline. Or: orthoclase.

pleochroism. Biotites are intensely altered to (and sometimes completely replaced by) chlorite, opaque minerals, and secondary muscovite (Fig. 8c). Primary muscovite crystals are subhedral to euhedral (Fig. 8d). Garnet crystals are scarce and subhedral (Fig. 8a); they are usually surrounded by euhedral plagioclase and a chloritic alteration rim (Fig. 8a).

The monzogranite facies predominantly exhibits low-temperature solid-state deformation microstructures, although the inversion of orthoclase to microcline represents a relic high-temperature microstructure (Fig. 8a and e). Low-temperature solid-state deformation is indicated by deformed twins in plagioclase, quartz subgrains and indented quartz and plagioclase borders. When low-temperature deformation was moderate, quartz subgrains were mostly concentrated at the rims of larger quartz crystals (sites CPH1, CPH2 and CPH13; Fig. 8e). However, when the deformation was more intense, the quartz subgrains elongated to form quartz bands (sites CPH3 and CPH4; Fig. 8f).

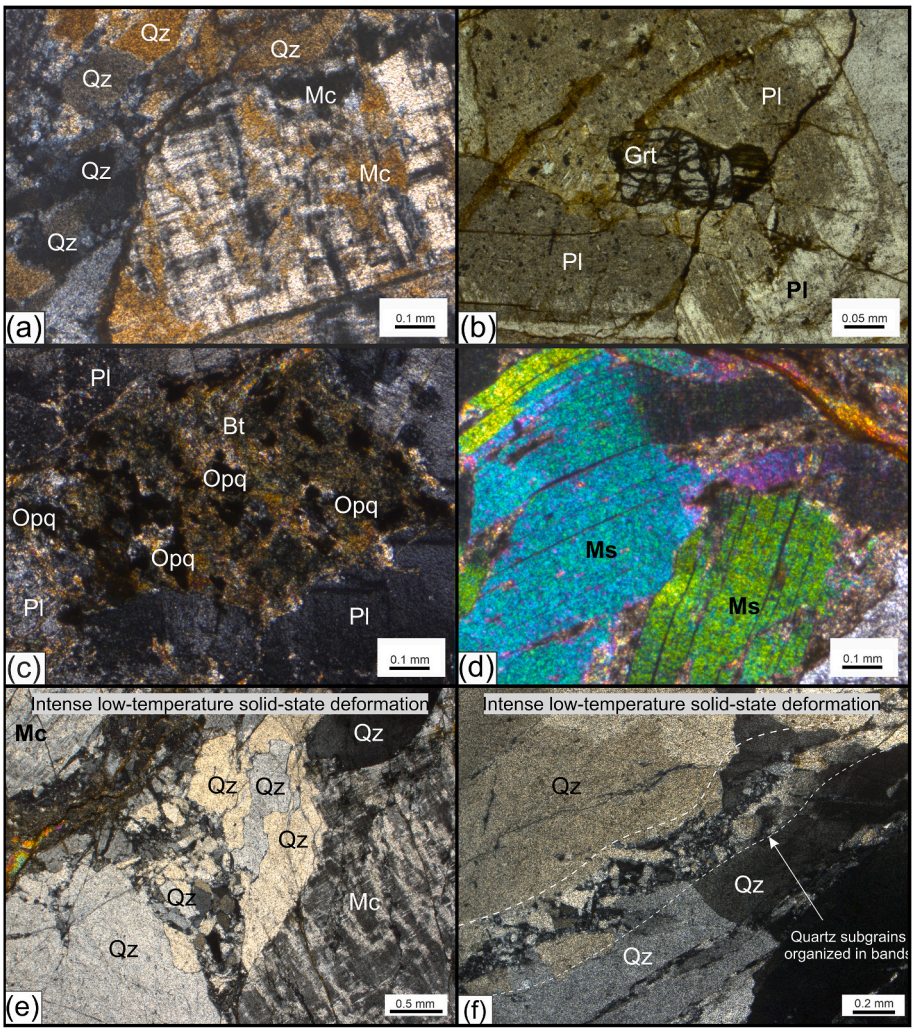


Fig. 8. Petrography of the monzogranite facies of the Huingancó Granitoids. a) Microcline phenocrystal and quartz subgrains. b) Garnet crystal surrounded by euhedral plagioclases altered to sericite. c) Chlorite formed by alteration of biotite where opaque minerals are left. d). Muscovite phenocrystals. e) Quartz sub-grains of minor size in comparison with the quartz phenocrystals; sampling site CPH3. f) Quartz sub-grains disposed on an elongated zone; sampling site CPH3. Grt: garnet. Qz: quartz. Pl: plagioclase. Bt: biotite Mc: microcline. Ms: muscovite. Opq: opaque mineral.

4.1.4. Andesitic dikes and amphibolic dacites: the volcanic facies of the Huingancó Volcanic-Plutonic Complex

The andesitic dikes of the Huingancó Volcanic-Plutonic Complex intrude both the monzogranite and granodiorite facies, with either irregular (Fig. 9a and b) or straight contacts. These dikes may incorporate granodiorite xenoliths, which have irregular, partially digested borders (Fig. 9a). The intrusion of the andesitic dikes is also associated with faults that displace mafic microgranular enclaves or aplitic veins. The dikes are dark gray (Fig. 9b), with a porphyritic texture and typically have steeply plunging NE-SW to E-W orientations. Their widths vary, ranging from 10 cm to 10 m.

Petrographically, the andesitic dikes exhibit holocrystalline intergranular and subophitic textures (Fig. 9c). The primary mineral composition includes plagioclase (50%), amphibole (30%), magnetite (15%), and alkali feldspar (5%). Plagioclase occurs as euhedral phenocrysts and as euhedral laths that form the matrix. The plagioclase phenocrysts are completely replaced by calcite and, locally, by quartz. Plagioclase laths are oriented around the phenocrysts, defining a magmatic flow (Fig. 9d). Amphiboles are generally subhedral to euhedral, ranging from light to dark green, and often exhibit simple twinning. These amphiboles are interstitially located between the plagioclase microlites (Fig. 9c). Amphibole also occurs as euhedral phenocrysts completely replaced by calcite. Magnetite is euhedral and is uniformly distributed throughout the samples (Fig. 9c). Alkali feldspar is subhedral to anhedral and occurs only in small amounts. Chlorite occasionally appears as an alteration product of amphiboles and in the matrix. Hydrothermal alteration affects approximately 50% of the andesitic dikes.

When the andesitic dikes bear a subophitic texture (Fig. 9), they are composed of plagioclase (50%), orthopyroxene (30%), magnetite and titanite (20%). The plagioclase crystals are euhedral and appear as microlites (Fig. 9e), typically exhibiting normal zoning and moderate alteration to sericite. Orthopyroxene crystals are subhedral and partially incorporate plagioclase microlites (Fig. 9e and f). Magnetite is euhedral and often associated with orthopyroxene crystals. Titanite is subhedral to anhedral and occurs primarily as an accessory mineral. These dikes also show intense propylitic alteration, with calcite as an alteration product of plagioclase, as well as in phenocrysts and forming veins. Epidote, which is euhedral to subhedral and strongly pleochroic, is predominantly found in clots along with chlorite and calcite (Fig. 9f).

Along the Huaraco Creek, south of the study area, calcite and epidote veins crosscut the andesitic dikes, with some veins bordered by pyrite. Regardless of the specific texture observed under petrographic analysis, all the andesitic dikes exhibit a propylitic hydrothermal alteration mineral assemblage (Py + Cal + Chl + Ep).

The amphibolic dacite stock intrudes the granodiorite facies of the Huingancó Granitoids near the Huaraco Creek (site AN6; Fig. 2) with a

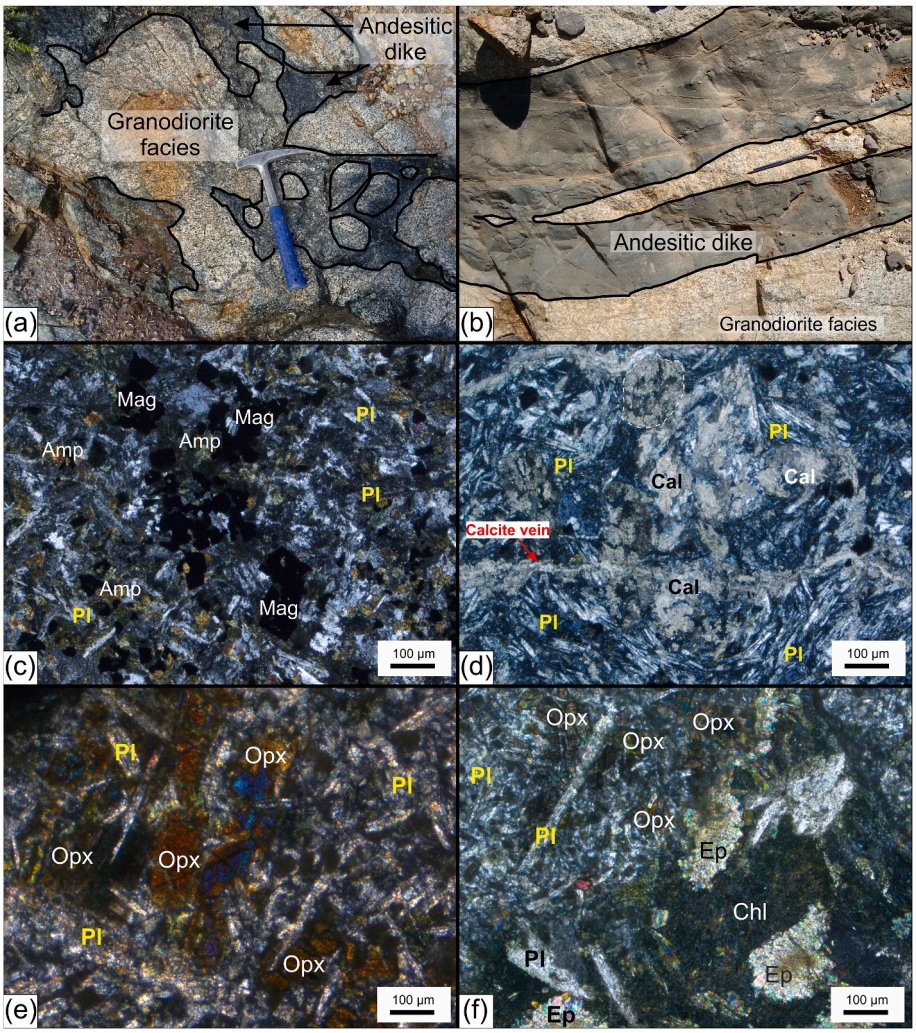


Fig. 9. a) Andesitic dike of site CPH20 with granodiorite facies xenoliths that have irregular, partially digested borders. b) Andesitic dike intruding the granodiorite facies on the site CPH16, with an irregular contact. c) Plagioclase microlites with amphibole crystals in between, and ehuedral magnetite crystals, displaying an intergranular texture. d) Calcite crystals as replacement of former feldspar phenocrystals, surrounded by oriented plagioclase microlites, all cut by a calcite vein (site CPH12). e) Orthopyroxene crystal partially surrounding euhedral microlites of plagioclases, showing a subophitic texture. f) Orthopyroxene crystals partially surrounding ehuedral microlites of plagioclases, showing a subophitic texture. Epidote and chlorite arranged in clots. Pl: plagioclase. Chl: chlorite. Opx: ortho-pyroxene. Ep: epidote. Cal: calcite. Mag: Magnetite.

regular contact. The amphibolic dacitic stock is light gray in color and displays a medium to coarse porphyritic texture, where amphibole and plagioclase phenocrysts, ranging from 2 mm to 1 cm in length, are set within a finer-grained matrix composed of plagioclase, amphibole, quartz, and mafic minerals. The amphibole phenocrysts are aligned, forming a NE-SW steeply dipping magmatic foliation that parallels the contact orientation with the granodiorite facies.

4.2. *Anisotropy of magnetic susceptibility and rock magnetic studies*

The AMS sampling of the Huingancó Volcanic-Plutonic Complex was performed as uniformly as possible following roads and creeks that traverse the steep topography of the Cordillera del Viento (from north to south, the creeks are named: Las Manzanas, Rahuecó, Huemules, Huingancó, and Huaraco; Fig. 2). Table 1 contains a summary of the sampling sites, as well as their number of specimens, their solid-state deformation type, and the main AMS site parameters (scalar parameters K_m, F, L, P, Pj and T, as well as directional AMS parameters).

Hysteresis loops from three representative samples of the granitic rocks constrain the minerals that contribute to their magnetic fabric (Fig. 10). After this magnetic characterization, the description of the scalar parameters of the AMS is presented, followed by the directional parameters of the magnetic fabrics (magnetic foliation and lineation). The AMS data will be shown following the same order than the field and petrographic data section: first, the hosting Andacollo Group; secondly, the Huingancó Granitoids; and lastly, the volcanic facies of the Huingancó Volcanic-Plutonic Complex (Figs. 11 and 12; Table 1).

4.2.1. *Rock magnetic studies performed in all the lithologies*

The hysteresis loop of the granodiorite CPH6 shows a significant contribution of paramagnetic minerals (Fig. 10b). This sample contains original (titano)magnetite, but the high-temperature curve exhibits an increase in magnetic susceptibility during the cooling curve at 300 °C, indicating the presence of pyrrhotite. This is confirmed by the increase in susceptibility in the cooling curve (Martín-Hernández et al., 2008). The Day plot diagram indicates that the (titano)magnetite is in the Pseudo-Single Domain (PSD) range (see Fig. 10d). Additionally, the presence of hematite can be observed in the high-temperature curve.

For sample CPH1 of the monzogranites, the IRM reaches saturation below 500 mT, and the hysteresis loop suggests saturation below 500 mT (Fig. 10a). The high-temperature curve shows an increase in magnetic susceptibility between 400 °C and 500 °C due to the breakdown of

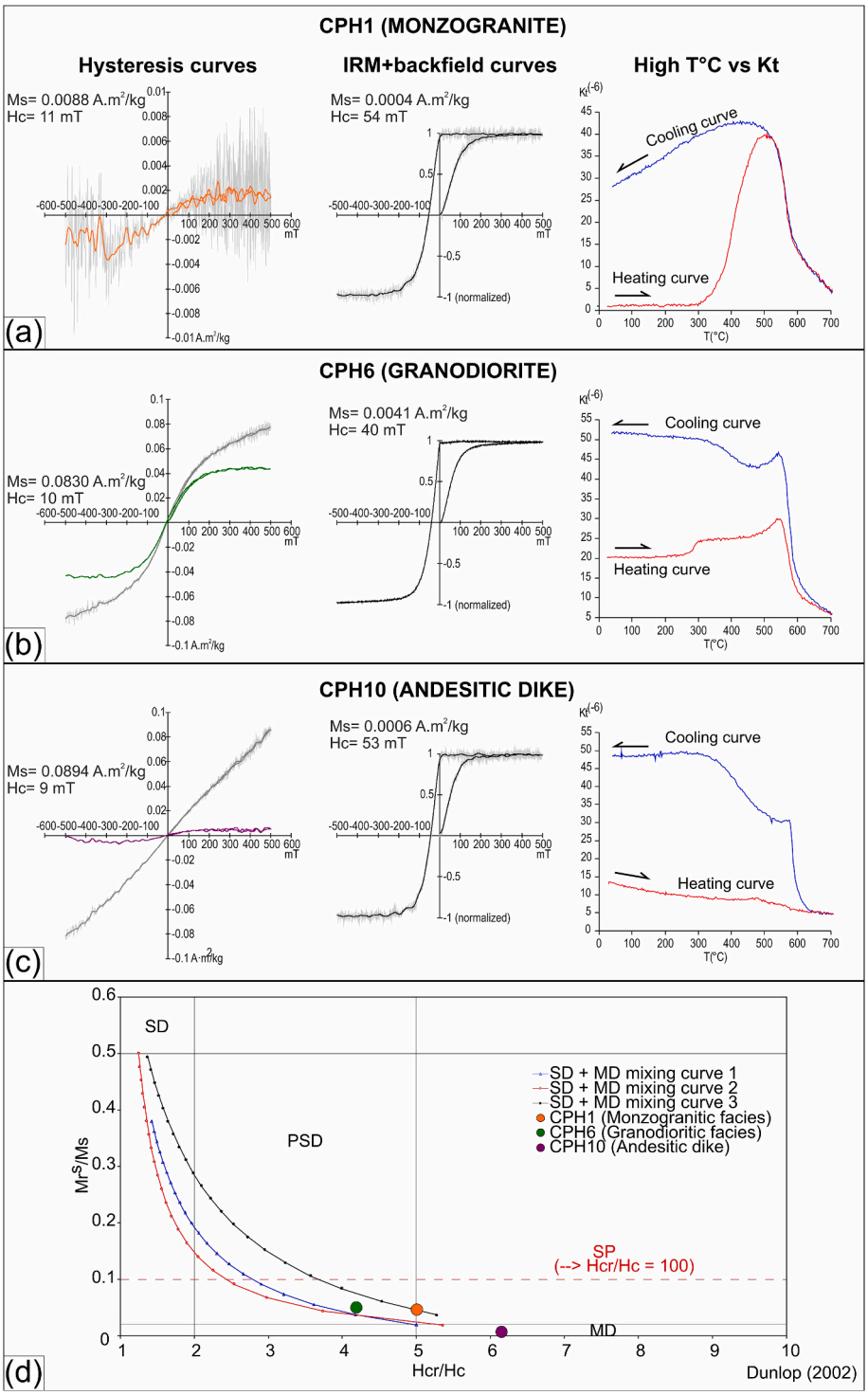


Fig. 10. Isothermal Remanent Magnetizations (IRM) and backfield curves, hysteresis loops and high-temperature thermomagnetic curves of susceptibility vs. temperature of a) Sample CPH1 of the monzogranite facies; b) Sample CPH6 of the granodiorite facies; c) Sample CPH10 of the andesitic dikes and d) Day-Plot of Dunlop (2002).

pyrite into magnetite, as confirmed by the increase in susceptibility during the cooling curve (Jagadeesh and Seehra, 1981). However, as indicated by the IRM and hysteresis loop, some original (titano) magnetite remains in the sample, displaying halfway behavior between PSD and Multi-Domain (MD) (Fig. 10d). Additionally, the presence of hematite can be recognized in the high-temperature curve (Fig. 10a).

On the other hand, the andesitic dike represented by CPH10 presents a dominant contribution of paramagnetic phases in the hysteresis loop (Fig. 10c). However, the presence of ferromagnetic minerals can be determined as it reaches saturation in the IRM and hysteresis loop. The formation of secondary magnetite can be observed in the increase of susceptibility during the cooling curve (see Fig. 10c). The Day plot (Dunlop, 2002) indicates that the original ferromagnetic phase is MD magnetite (Fig. 10d).

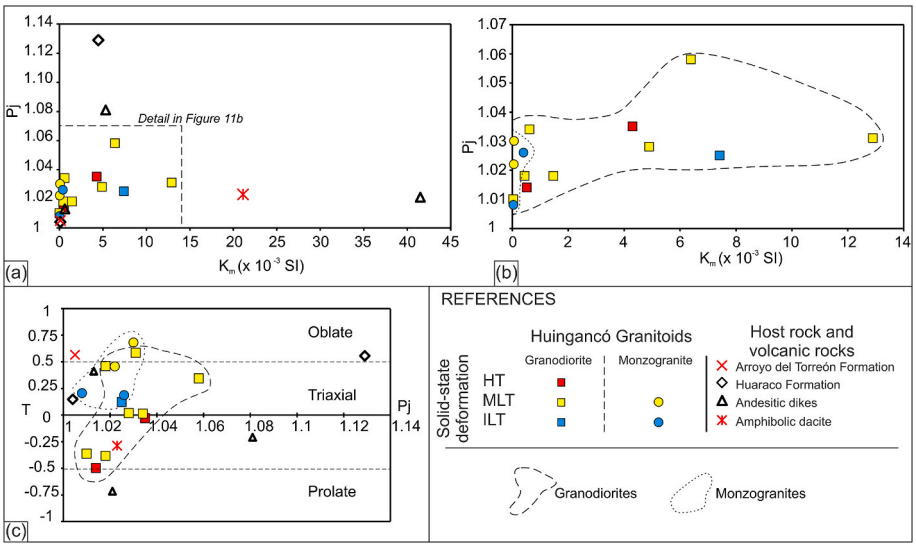


Fig. 11. AMS scalar parameters diagrams of the Andacollo Group and the Huingancó Volcanic-Plutonic Complex. The Huingancó Granitoids are differentiated by the solid-state deformation that they exhibit. a) Pj vs K_m diagram and b) T vs Pj diagram. HT: High-temperature solid-state deformation. MLT: Moderate low-temperature solid-state deformation. ILT: Intense low-temperature solid-state deformation.

4.2.2. *Scalar parameters of the AMS in all the sampled lithologies*

The mean susceptibility K_m of the sandstones of the Huaraco Formation is low to moderate, between 0.09×10^{-3} SI and 5.01×10^{-3} SI. The anisotropy degree (Pj) ranges between 1.005 and 1.03 (Table 1; Fig. 11a). The shape of the ellipsoids is triaxial to oblate, with shape parameter T ranging from 0.174 to 0.566 (Fig. 11c; Table 1). The ignimbrites of the Arroyo del Torreón Formation have a low K_m value of 0.07×10^{-3} SI, a Pj parameter of 1.004 and a triaxial ellipsoid with a shape parameter T = 0.147 and a (Fig. 11a and b; Table 1).

The granodiorites of the Huingancó Granitoids show higher K_m values ranging from 0.04×10^{-3} SI to 12.92×10^{-3} SI (Table 1; Fig. 11a and b), whereas the K_m of the monzogranites is an order of magnitude lower, ranging between 0.04×10^{-3} SI and 0.39×10^{-3} SI (Fig. 11b). Rock magnetic studies showed that multi-domain magnetite was present in the granodiorites and the monzogranites, and therefore, the interpretation of the AMS fabric is direct and simple and results from the analysis of the bulk magnetic fabric of magnetite (Jackson, 1991).

The monzogranites and granodiorites were classified into three categories based on the intensity of solid-state deformation they underwent. Rocks with a higher degree of low-temperature solid-state deformation did not exhibit a higher degree of anisotropy (Pj values) compared to rocks that are only affected by high-temperature solid-state deformation. The Pj parameter of granodiorites and monzogranites is roughly similar (Fig. 11a and b).

Rocks affected only by high-temperature solid-state deformation (only granodiorites belong to this category) displayed a direct relationship between K_m and Pj (Fig. 11a and 13a). These rocks have triaxial ellipsoids, where both lineation and foliation are well defined (Pj values of 1.014 and 1.035; T values of −0.498 and −0.029; Fig. 11c–Table 1). In granodiorites and monzogranites exhibiting moderate low-temperature solid-state deformation, there was no clear correlation between K_m and Pj (Fig. 11a and b, 13b and c). These rocks have triaxial to oblate ellipsoids (Pj values between 1.006 and 1.058; and T values between −0.384 and 0.68; Fig. 11b; Table 1). In addition, granodiorites and monzogranites bearing intense low-temperature solid-state deformation show no trends between K_m and Pj (Fig. 14a and b). The ellipsoids are triaxial to oblate, with Pj ranging values between 1.008 and 1.026, and T that ranges from 0.122 to 0.205 (Fig. 11a and b; Table 1). In oblate ellipsoids, the magnetic foliation is always better defined than magnetic lineation, and this is taken into account in the analysis of magnetic lineations (section 4.2.3).

K_m values of the andesitic dikes of the Huingancó Complex ranges between 0.59×10^{-3} SI and 41.46×10^{-3} SI (Table 1, Fig. 11a and b), and the amphibolic dacitic stock has a similar K_m of 21.12×10^{-3} SI (Table 1; Fig. 11a and b). These K_m values are typical of ferromagnetic rocks (> than 0.5×10^{-3} SI, Tarling and Hrouda, 1993), with the exception of the site CPH10 whose lower K_m of 0.59×10^{-3} SI, shows the contribution of both paramagnetic and ferromagnetic minerals (Tarling and Hrouda, 1993). Rock magnetic data of the andesitic dikes also showed that multidomain titanomagnetite controlled the magnetic susceptibility of these rocks. The anisotropy degree Pj of the andesitic dikes varies from 1.013 to 1.081, while for the amphibolic dacite it is 1.023 (Table 1; Fig. 11c).

Magnetic ellipsoids are triaxial in the andesitic dikes represented by sites CPH10 and CPH12 (T = 0.412 and T = −0.208, respectively; Table 1). In site CPH20, K_3 axes display a girdle pattern around the K_1 mean axis, indicating that the shape of the magnetic ellipsoid of this site is strongly prolate (T < −0.5; Fig. 12c).

4.2.3. *Magnetic foliations and lineations in the host rocks*

The Arroyo del Torreón Formation was sampled near the San Pedro Hill, a structurally complex area where this formation shows two SE dipping thrusts. The magnetic results of site AN2 show a triaxial ellipsoid with a well-defined foliation and lineation. The magnetic foliation is NE-SW, perpendicular to the strike of the thrusts, and dips moderately towards the SW (Fig. 15a). The magnetic lineation dips gently towards the W and can be coherent with the direction of tectonic transport of the thrusts (Giacosa et al., 2014, Fig. 15b).

In turn, the Huaraco Formation, the main host rock of the Huingancó Granitoids, was sampled in the host rock septum which separates the monzogranite facies to the north and the granodiorite facies to the south (Figs. 2 and 15a and b). Along that septum, the magnetic ellipsoids of sites CPH14 and AN1 of the Huaraco Formation are triaxial to oblate, with a well-defined foliation and lineation in site CPH14 (this is the only site with a triaxial ellipsoid, so it bears both reliable magnetic foliation and lineation). On site AN1 the AMS ellipsoid is oblate, so its magnetic foliation is better defined than the magnetic lineation. The magnetic foliation of site AN1 bears a NE-SW strike and a moderate dip towards the NW (Fig. 15a). On site CPH14 the magnetic foliation has a NE-SW strike and a subvertical dip (Fig. 15a), and the magnetic lineation plunges shallowly towards the NE (Fig. 15b).

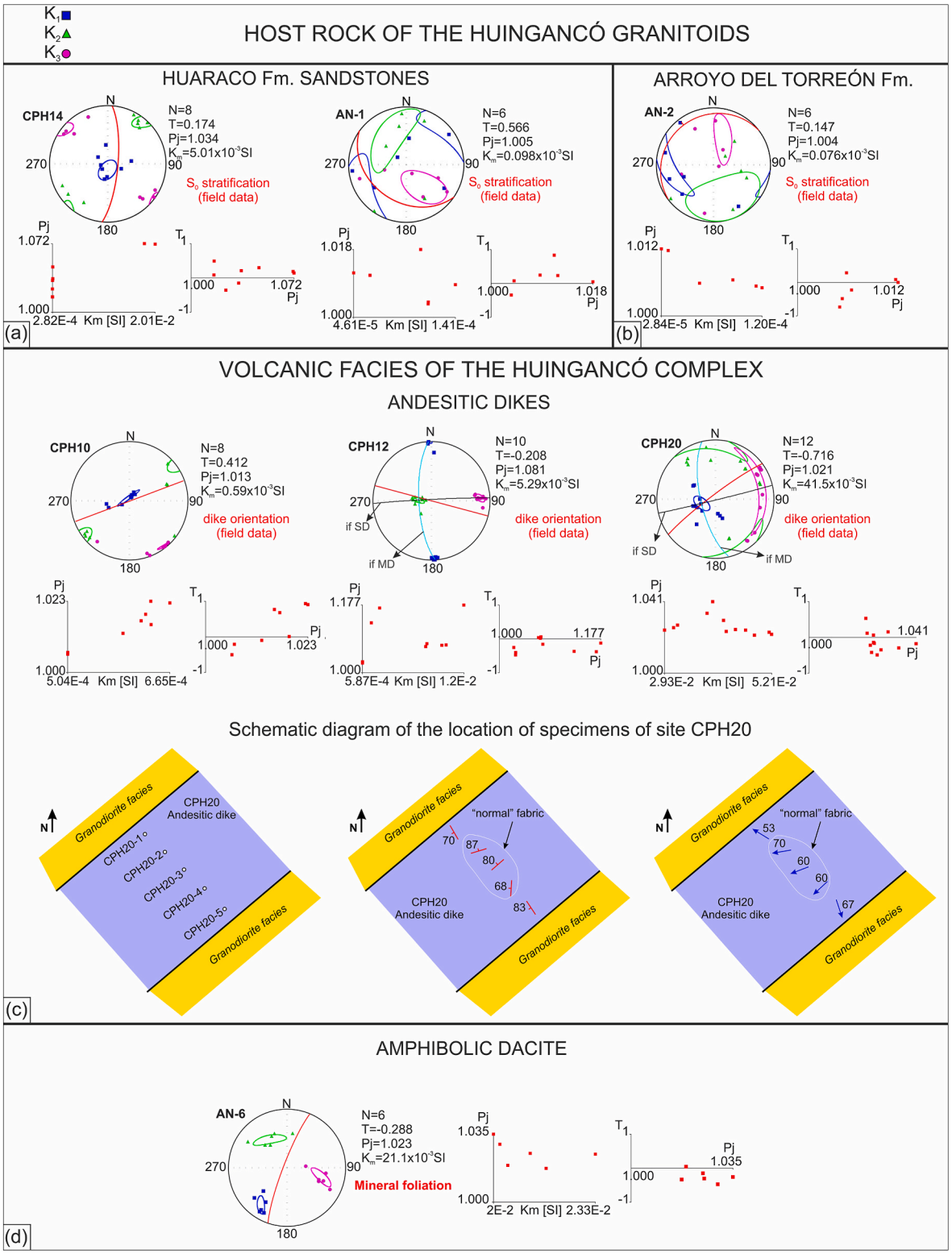


Fig. 12. AMS data of the Andacollo Group and the volcanic facies of the Huinganco Volcanic-Plutonic Complex, showing the magnetic ellipsoids for each site, and the Pj vs K_m and T vs Pj diagrams. a-b) AMS data of the Andacollo Group (host rock of the Huingancó Granitoids). c) AMS data of the volcanic facies of the Huingancó Complex combined with a schematic diagram of each specimen location of the andesitic dike at site CPH20, showing the variable orientations of both foliation and lineation, where the sites located in the center have a "normal" fabric. d) AMS data of the amphibolic dacite that intrudes the granodiorite facies. Equal area projection in geographic coordinate system.

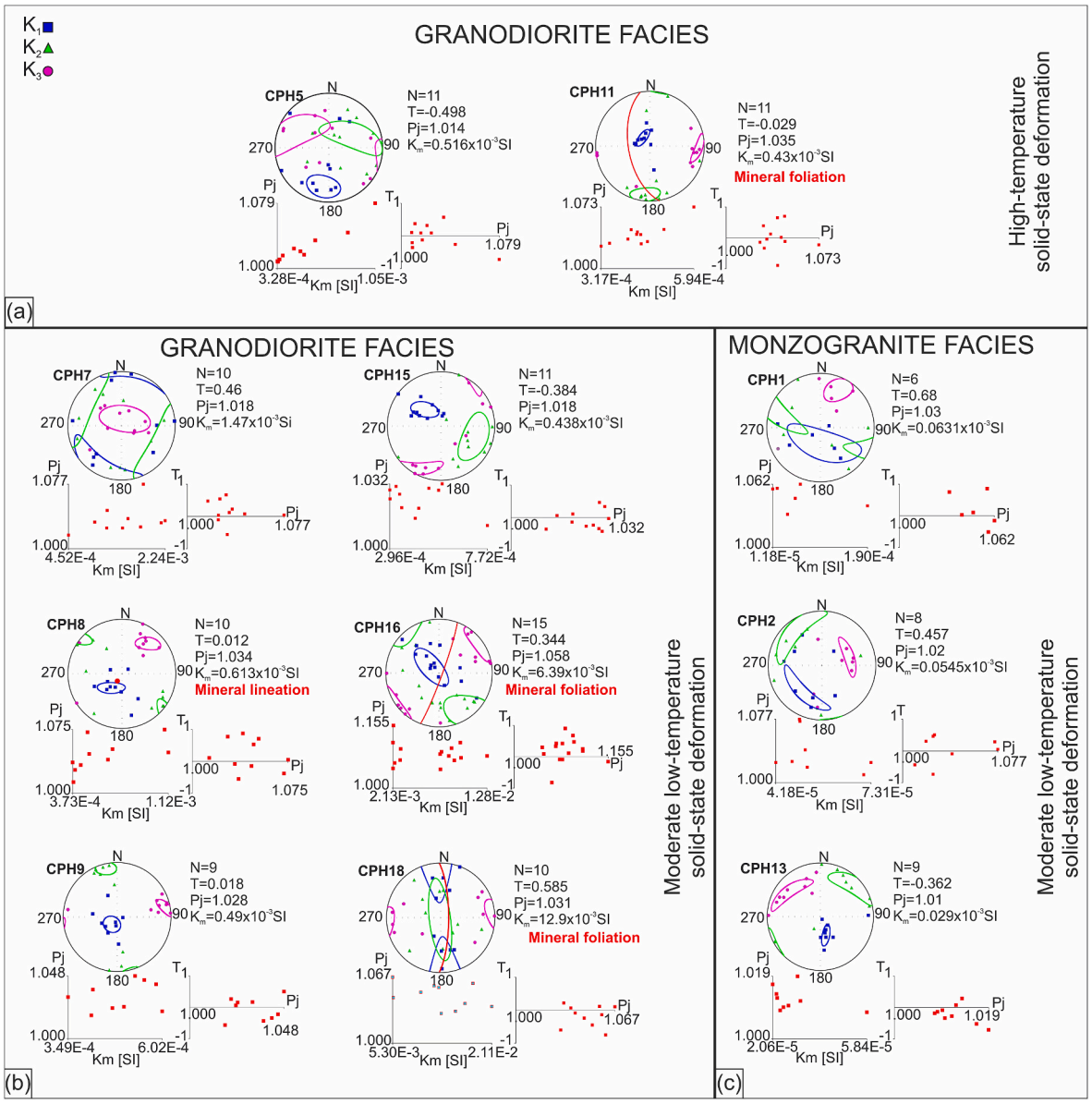


Fig. 13. AMS data of the Huingancó Granitoids with high-temperature and moderate low-temperature solid-state deformation, showing the magnetic ellipsoids for each site, and the Pj vs K_m and T vs Pj diagrams, obtained with the software Anisoft 4.2. a) High-temperature solid-state deformation of the granodiorite facies. b) Moderate low-temperature solid-state deformation of the granodiorite facies. d) Moderate low-temperature solid-state deformation of the monzogranite facies. Magmatic foliations measured in the field are superposed to the stereograms of the sites that have these data, in red color line. Equal area projection in geographic coordinate system.

4.2.4. Magnetic foliations in the Huingancó granitoids

Throughout the granodioritic and monzogranitic plutons, magnetic data show good agreement with the mineral foliation data (compare Figs. 2 and 15a and b). In both intrusive types, magnetic ellipsoids are mostly triaxial, with oblate ellipsoids found only in granitoids bearing moderate low-temperature solid-state deformation (Fig. 11c). In triaxial sites, magnetic foliations and lineations are significative, but in oblate sites, only the magnetic foliation is meaningful (Fig. 15a and b).

The granodiorite facies displays magnetic foliations that are mostly subvertical with varying strikes. Along the Huaraco Creek all sites exhibit moderate to intense low-temperature solid-state deformation and the subvertical magnetic foliations have a NW-SE strike (Fig. 15a).

Between the Huingancó and Huemules creeks, the granodiorite sites exhibit high-temperature to moderate low-temperature solid-state deformation and magnetic foliations are generally subvertical with N-S to NW-SE strikes (Fig. 15a). At site CPH7, located upstream on the Huingancó Creek, near the roof of the granodiorite pluton, the granodiorite displays a nearly subhorizontal magnetic foliation (Fig. 15a). Apart from the photo shown in Fig. 5a, where the monzogranites also crop out with a flat roof, no other sites of the Huingancó Granitoids showed subhorizontal magnetic foliations.

Further north, along the Huemules Creek, the granodiorites exhibit high-temperature to moderate low-temperature solid-state deformation and subvertical magnetic foliations with strikes ranging from N-S to NW-SE (Fig. 15a). The central part of the granodioritic pluton is the only area showing high-temperature solid-state deformation and N-S to NE-SW steeply dipping magnetic foliations (Fig. 15a).

In the monzogranites, the magnetic foliations tend to display an arcuate pattern, with variable strikes and dips (Fig. 15a). The magnetic foliations progressively turn from being subvertical to the south, with W-E, NE-SW and NW-SE strike, to moderately west to southwest dipping in the north, along the Las Manzanas Creek, where miarolitic cavities and

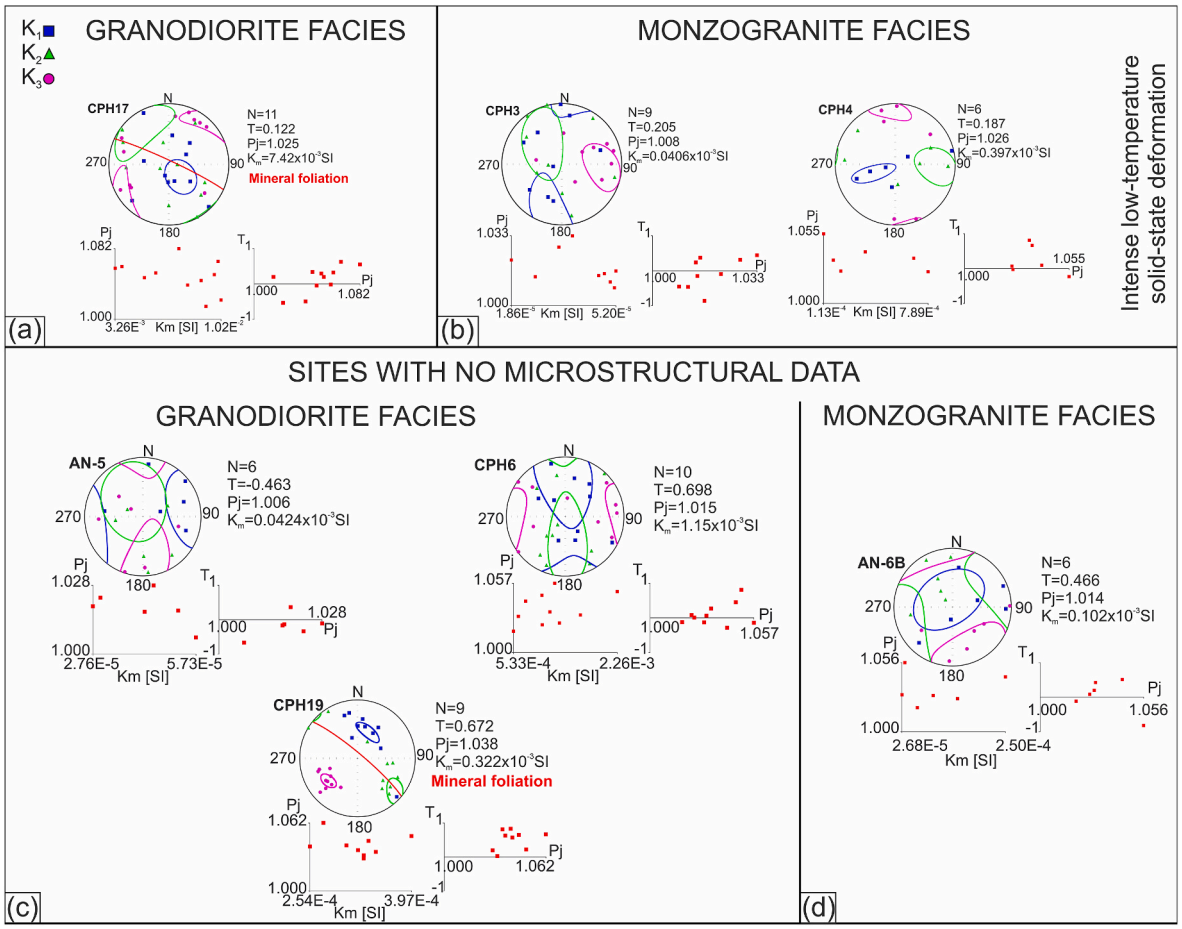


Fig. 14. AMS data of the Huingancó Granitoids with intense low-temperature solid-state deformation and with no microstructural data, showing the magnetic ellipsoids for each site, and the Pj vs K_m and T vs Pj diagrams, obtained with the software Anisoft 4.2. a) Granodiorite facies. b) Monzogranite facies. c) Sites of the Huingancó Granitoids with no microstructural data. Equal area projection in geographic coordinate system.

pegmatites evidence shallow emplacement conditions (Fig. 15a). In site CPH13 to the south, the subvertical NE-SW strike magnetic foliation of the monzogranite is subparallel to the subvertical magnetic foliation of the hosting Huaraco Formation (site CPH14; Fig. 15a).

4.2.5. *Magnetic lineations in the Huingancó granitoids*

Magnetic lineations reasonably agree with the available field data (such as the elongated enclave orientations in site CPH8, Fig. 6b and c). In site CPH1 of the monzogranites and CPH18 of the granodiorites (both with low-temperature solid-state deformation), the AMS ellipsoids are oblate (Fig. 13b and c), and their magnetic lineation given by the K_1 distribution displays a girdle pattern around the K_3 axis (Fig. 13b and c), meaning that their magnetic lineations are not significative. The remaining sites have triaxial magnetic ellipsoids, so their magnetic lineations are trustworthy (Fig. 11c).

Along the Huaraco Creek, the granodiorite facies has steeply to moderately dipping magnetic lineations, whereas along the Huingancó Creek, they are shallower (Fig. 15b). Along the Huemules Creek, the magnetic lineations become subvertical (Fig. 15b). The monzogranite facies show steeply to moderately dipping magnetic lineations in the south, but shallow to moderately dipping magnetic lineations in the north, along the Las Manzanas Creek at sites CPH2 and CPH3 (Fig. 15b).

4.2.6. *Magnetic foliation and lineations in the andesitic dikes*

The sampled andesitic dikes of the Huingancó Complex are subvertical and bear NE-SW or NW-SE strikes (Fig. 12c). In these dikes, the AMS sampling was conducted in two different ways: either focusing solely on the dike center, which was generally fresher than the borders, as in sites CHP10 and CHP12, or collecting AMS cores from the wall to the center, as in the case of the andesitic dike of site CPH20 (see the scheme representing the distribution of specimens of this site in Fig. 12c).

In site CPH10, the magnetic foliation plane is subparallel to the NW-SE subvertical dike walls, and the magnetic lineation is subvertical. The magnetic ellipsoid in this site has a triaxial shape so both foliation and lineation are significant.

In site CPH12, the strike of the dike is NE-SW and the magnetic fabric, though also subvertical, has a different strike (N-S; Fig. 12c). This fabric can be considered slightly anomalous because it is not parallel to the dike walls (see section 5). Here, the magnetic lineation is subhorizontal. As in site CPH10, the triaxial shape of the magnetic ellipsoid of this site suggests that both magnetic foliation and lineation are meaningful at this site.

In site CPH20 only the site steeply dipping magnetic lineation is meaningful (see section 4.2.2). However, as the sampling in this dike was conducted from wall to the center, the analysis of its magnetic fabric can be done at specimen level. Here, the magnetic foliation of each specimen progressively rotates, from the dike walls to the center, changing from being perpendicular to dike walls to being parallel to them (Fig. 12c). Therefore, the fabric is only normal in the center of the dike, registering the magma flow direction.

Lastly, the amphibolic dacitic stock of the Huingancó Complex sampled on site AN6 has a triaxial magnetic ellipsoid, with a NE-SW magnetic foliation that dips moderately towards the NW and that is coherent with the mineral foliation plane (Fig. 12d). The magnetic lineation plunges shallowly towards the SW.

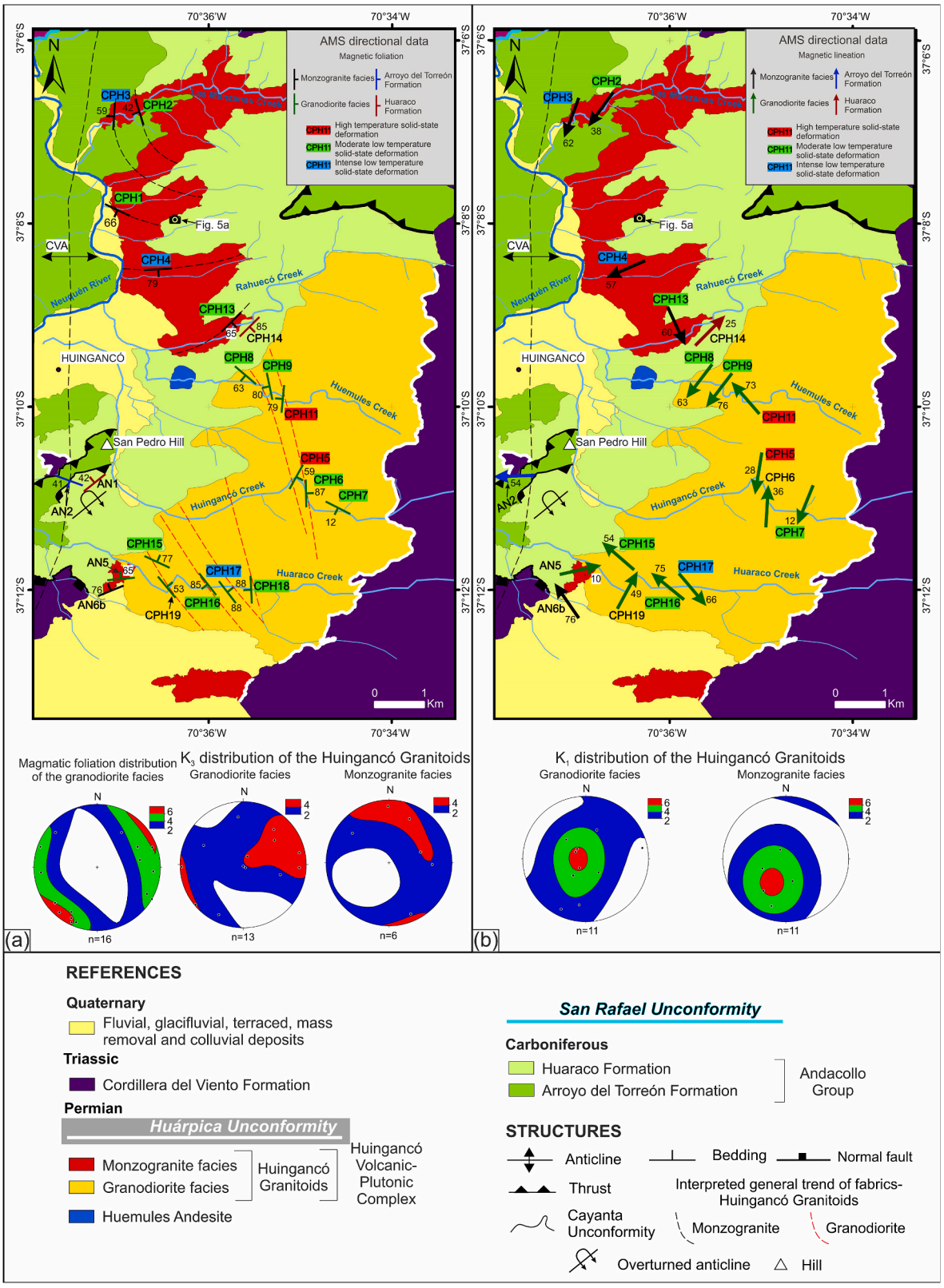


Fig. 15. a) Map showing magnetic foliation planes defined by the perpendicular plane to the K_3 axis of the AMS ellipsoid (K_1-K_2 planes) of the Huingancó Granitoids and their host rocks. The dashed black and red lines on the map represent the interpreted general trend of the monzogranite and granodiorite facies fabrics, respectively. The location of Fig. 5a is shown on this map. b) Map of magnetic lineations (K_1 direction) of the Huingancó Granitoids and their host rocks. The inset corresponds to the distribution of the K_1 axis of the Huingancó Granitoids. The stereonets are contoured with Kamb equal-area lower-hemisphere projections of the K_3 and K_1 axes and the magmatic foliations, which were made using Stereonet 11 software (Allmendinger et al., 2012; Cardozo and Allmendinger, 2013). The scale represents Kamb contours in standard deviation. The sites of the Huingancó Granitoids are represented based on the solid-state deformation they exhibit. The location of the interpreted photograph shown in Fig. 5a, is indicated near site CPH4. CVA: Cordillera del Viento Anticline.

5. Discussion

First, the origin of the magnetic fabrics of the sampled sites of the Huingancó Volcanic-Plutonic Complex is discussed. High-temperature deformation is attributed to the emplacement of the Huingancó Granitoids, while low-temperature deformation can also be attributed to the late stages of emplacement of the granitoids and, probably, to the overprinting of the Paleozoic fabrics by the Andean deformation. However, as the dispersion in the AMS ellipsoids is low, we understand that the Andean overprinting did not affect the orientation of the ellipsoids, and we interpret that the fabrics we are analyzing are mostly paleozoic. All of this is explained in detail below, along with the implications that solid-state deformations have on the interpretation of the AMS data. Then, we present a model of emplacement for the Huingancó Granitoids.

5.1. Origin of the magnetic fabrics of the Huingancó Volcanic-Plutonic Complex

The original magmatic fabric of the Huingancó Granitoids was overprinted by solid state deformation of varying intensity degrees, and the temperature and intensity of the solid-state deformation was classified with the microstructures present in the rocks.

With respect to the time of acquisition of the AMS fabrics, the sites with high-temperature solid-state deformation acquired their fabrics during the cooling of the granites (Bouchez and Nicolas, 2021), and therefore these fabrics were acquired in Permian times.

It is probable that part of the low-temperature deformation of the monzogranites and granodiorites occurred during the Andean Orogeny which reactivated previous extensional Paleozoic structures (Giacosa et al., 2014; Sagripanti et al., 2014). However, the magnetic ellipsoids of the Huinganco Granitoids are well defined, so the low dispersion of the AMS main axes suggests that their magnetic fabrics are mostly coeval with the emplacement of the granitoids. Even though some tectonic overprinting could have been present in the rocks and cannot be ruled out, it would not have been as intense as to completely modify the original fabrics of the plutons. As was mentioned in the methodology, the sampling was always conducted in rocks that were far from brittle structures, and the sampled granitoids were never completely mylonitized, although low-temperature deformation was intense in sites CPH3 and CPH4 of the monzogranites and in CPH17 site of the granodiorites (Fig. 14a and b). It is well known that the AMS technique can help us understand the internal fabric of apparently homogenous rocks, such as granitoids (Bouchez, 1997). But assessing the original fabric that records the emplacement conditions of granitoids can be challenging, mainly because posterior deformation or alterations can modify the original mineral assembly (Bouchez, 1997; Bouchez and Nicolas, 2021). Low-temperature solid-state deformation that occurs after the emplacement of the pluton and under a different stress field that the one that controlled pluton emplacement, can alter the primary fabric of the pluton. This can be observed as a clear dispersion or scattering of the AMS ellipsoids, such as in the case of the La Hoya Pluton (North Patagonian Batholith near the locality of Esquel in Argentina), which was emplaced in extensional conditions in the Late Jurassic times but was much later affected by low-temperature solid-state deformation which dispersed the original emplacement fabrics. This low-temperature deformation has been interpreted as occurring during the Late Cretaceous compressive deformational phase of the Andean Orogeny. However, the Huingancó Granitoids do not exhibit the dispersion in the AMS axes that would suggest that low-temperature solid-state deformation occurred significantly after pluton emplacement.

Regarding the andesitic dikes, when the magnetic fabric is parallel or sub-parallel to the dike walls it is referred to as “normal” (see, for example, Rochette, 1988; Rochette et al., 1992; Lanza and Meloni, 2006; Chadima et al., 2009). If this is not the case, and the fabric is not parallel to the dike walls, the fabric is referred to as “anomalous” (Lanza and Meloni, 2006).

In site CPH10, the magnetic fabric is normal and parallel to the dike walls (see section 4.2.6). In contrast, in site CPH12, its magnetic foliation is not parallel to the dike walls (see section 4.2.6). However, if its magnetite were of SD type instead of MD type (and it is known that the presence of SD magnetite causes reverse fabrics), its magnetic fabric should be inverted, resulting in the inversion of the K_1 and K_3 axes (Lanza and Meloni, 2006). If that were the case, inverting the axes K_1 and K_3 in dike CPH12 would leave a magnetic fabric which would be parallel to the dike walls. However, no rock magnetic studies are available for this dike, so the domain state of its magnetite remains a speculative issue. It is important to remember that in dike CPH10, which was the only one with rock magnetic studies, the magnetite was of MD type (see section 4.2.1).

At site CPH20, where the AMS sampling was performed from the dike walls to the center (Fig. 12c), the magnetic fabric becomes normal in the AMS specimens located in the center of the dike (AMS specimens CPH20-2, CPH20-3, and CPH20-4; Fig. 12c), reflecting the magma flow direction (Lanza and Meloni, 2006; Chadima et al., 2009). In contrast, close to the dike walls, both the magnetic foliation and lineation become almost perpendicular to the plane represented by the dike walls (Fig. 12c). This mixture of orientations in the magnetic fabric could explain the general anomalous fabric of this dike when analyzed at site level.

In conclusion, in the three sampled andesitic dikes the fabrics could be normal, if we accept the hypothesis of the presence of SD magnetite in dike CPH10. Considering that all three dikes are propylitized, the AMS data suggest that the propylitic alteration did not modify their original igneous fabric. This suggests that the alteration occurred during or shortly after the emplacement of the dikes, under the same stress regime that controlled their intrusion.

5.1.1. Syn-tectonic emplacement of the granodiorite facies

The granitoids of the Huingancó Volcanic-Plutonic Complex belong to the intrusive part of the Choiyoi Magmatic Province (Llambías et al., 2007). The intermediate to silicic magmatism of this province was developed after the compressive San Rafael Orogenic Phase (286-247 Ma; Sato et al., 2015), which affected the transitional to marine Carboniferous to Early Permian sequences on the west of Argentina (Azcuy and Caminos, 1987; Ramos, 1988; Rocher et al., 2015). In the Cordillera del Viento region, the San Rafael Orogenic Phase affected the Andacollo Group, generating NW-trending folds and associated thrust with SW vergences, which are retro-vergent structures in the context of the Gondwanide orogen (Giacosa et al., 2014). During the Early Permian a major N-NNW dextral transpressive deformation took place in the foreland basin of the San Rafael Massif, which would be related to an oblique subduction regime (Kleiman and Japas, 2009). Kleiman and Japas (2009) further mentioned that the compressive deformation of the San Rafael Orogenic Phase affected only the syn-orogenic lower sections of the Choiyoi Magmatic Province.

Along the Huaraco, Huingancó and Huemules creeks, the granodiorites predominantly show steeply dipping NW-SE magnetic foliations and steeply plunging magnetic lineations (Fig. 15a and b). The only exception is represented by site CHP7, which is the only one showing shallow magnetic foliation and lineation, and probably this site represents the roof of the granodioritic pluton (Fig. 15a and b).

The predominance of subvertical NW-SE foliations developed under high- and low-temperature solid-state conditions, and steeply plunging lineations, would suggest that the granodiorites were emplaced in a transpressive system (Fossen et al., 1994; Tikoff and Greene, 1997; Fossen and Tikoff, 1998; Saint Blanquat et al., 1998). An example of rocks emplaced in a transpressive tectonic context are the granodioritic to quartz-dioritic rocks of the Late Triassic Central Patagonian Batholith, which exhibit subvertical magmatic and solid-state fabrics of NW-SE strike (Zaffarana et al., 2017).

In this sense, the emplacement of the granodiorites of the Huingancó

Complex could be syn-tectonic with respect to the San Rafael Orogenic Phase, which is the final stage of the Gondwanide Orogenic cycle. The orientation of the magmatic and tectonic foliation of the granodiorites could be parallel to pre-existing NW-SE subvertical wall-rock structures, as general trend of the magnetic foliations of the granodiorites is subparallel to the structures that the San Rafael Orogenic Phase generated in the Cordillera del Viento area (NW-SE trending thrust and folds; Giacosa et al., 2014). The maximum stress was oriented in the NE-SW direction leading to a transpressive deformation of the granodioritic rocks, which is a common tectonic regime in magmatic arcs in conditions of slightly oblique convergence (Saint Blanquat et al., 1998). Approximately ~25 Myr later, the monzogranites were emplaced in a post-orogenic, shallower tectonic context, as will be explained in the next Section.

As a final comment, it is important to mention that Ramos et al. (2011a) considered that the end of the San Rafael Orogenic Phase was dated with the intrusion of the granodiorite facies of the Huingancó Volcanic-Plutonic Complex, around 287-282 Ma. However, when inspecting the magnetic fabrics of the granodiorites of the Huingancó Volcanic-Plutonic Complex, we are proposing here a different scenario, where the granodiorite facies was emplaced syn-tectonically with respect to the San Rafael Orogenic Phase, and the monzogranites were emplaced post-tectonically.

5.1.2. *Post-orogenic emplacement of the monzogranite facies*

The granitoids of the Huingancó Volcanic Plutonic Complex are interpreted by many authors to have been emplaced in the upper crust after the post-orogenic collapse of the Gondwanide orogen (Llambías et al., 2007; Giacosa et al., 2014). As mentioned by Llambías et al. (2007) and inferred from the presence of miarolitic cavities and pegmatites (Fig. 6c), the outcrops of the monzogranites correspond to a volatile-rich dome of a (probably) larger pluton. The presence of miarolitic cavities suggests that the monzogranites underwent volatile phase exsolution, simultaneously with crystallization driven by increasing undercooling (Candela, 1997). Shallow, post-orogenic plutons typically show subhorizontal magnetic fabrics, especially when the roof is exposed (e.g.: Horsman et al., 2009; Martínez Dopico et al., 2017). The flat roof of the monzogranitic pluton was exposed near site CPH4 (Fig. 5a cited in section 4.1.3 and Fig. 15a).

The monzogranites show local (in the borders) coupled fabrics (parallel to their contacts) with the hosting Huaraco Formation (sites CPH13 and CPH14; Fig. 15a) and with the hosting granodiorites in the Huaraco Creek area, in the southwestern part of the study area (the monzogranites of site AN6 have a steeply dipping E-W magnetic foliation, which is subparallel to the hosting granodiorites of site AN5; Fig. 15a and b). This coupling of pluton and host rock fabrics is typical of post-tectonic granitoids emplaced in an extensional context (Paterson et al., 1989). In addition, when there is only local coupling with the host rocks, the more dispersed or discontinuous internal fabrics of the plutons are interpreted in terms of the internal dynamics of the magma chamber (Paterson et al., 1998), which is the situation seen in the center of the monzogranitic pluton, in the northern part of the study area, where the foliation planes are interpreted as arcuate at sites CPH2, CHP3, CHP1 and CPH4 (Fig. 15a).

6. Conclusions

The internal fabric of the Huingancó Granitoids and of its host rocks and intruding andesitic dikes was characterized using field, microstructural, and AMS data, as well as rock magnetic studies. The main findings of our work are summarized below:

** We suggest that the granodiorites of the Huingancó Volcanic-Plutonic Complex may have been emplaced during the San Rafael Orogenic Phase, reflecting solid-state deformation fabrics formed under both high- and low-temperature conditions. High- and low-temperature solid-state deformation are associated with the cooling of the pluton under syntectonic, transpressive conditions. Some of the low-temperature solid-state deformation could be related to the overprinting of the magnetic fabrics by the Andean Orogeny, of previous paleozoic structures. Although this deformation does not seem to have modified the original fabric of the granodiorite facies. The magnetic fabric agrees well with the field data, and they exhibit a predominantly NW-SE subvertical orientation, closely aligned with the NW-SE-oriented, SW-vergent subvertical structures produced by the San Rafael Orogenic Phase in the Cordillera del Viento region.

** In contrast, the monzogranites were most likely emplaced in a shallower, post-orogenic, extensional tectonic context after the San Rafael Orogenic Phase. The magnetic fabrics of the monzogranites are parallel to the contact with the host rocks, however, farther from the contacts the magnetic fabrics become more dispersed and generally display an arcuate pattern. The local coupling between the monzogranite facies and their host rock is interpreted as due to the internal dynamics of the magma chamber.

** The magnetic fabrics of the Huingancó Granitoids document the change of stresses from compressive (during the emplacement of the granodiorites) to extensional (during the emplacement of the monzogranites) which is typically seen in the Choiyoi Magmatic Province and had not been reported before.

CRediT authorship contribution statement

Sebastián Pernich: Writing – review & editing, Writing – original draft, Visualization, Validation, Supervision, Software, Resources, Project administration, Methodology, Investigation, Formal analysis, Data curation, Conceptualization. **Claudia Beatriz Zaffarana:** Validation, Supervision, Methodology, Funding acquisition, Formal analysis. **Víctor Ruiz González:** Writing – review & editing, Supervision, Methodology. **Omar Sebastián Assis:** Software, Methodology. **Gloria Gallastegui:** Supervision, Software, Methodology. **Darío Orts:** Writing – review & editing, Supervision, Methodology, Funding acquisition, Formal analysis.

Declaration of competing interest

The authors declare that they have no known competing financial interests or personal relationships that could have appeared to influence the work reported in this paper.

Acknowledgements

We sincerely thank Dr. Eber Cristofolini and Dr. Fernando Hongn and two other anonymous reviewers for their valuable feedback, which significantly improved this manuscript. We also extend our gratitude to managing guest editor Dr. Pablo Diego González for his careful handling throughout the review process.

This work was financed by grants PIP CONICET 112-200901-00766, PIT 2014-1394, PI-40A-631, PI-40A-916, PI-40A-1072 (Universidad Nacional de Río Negro), PICT 019–01809 and CGL2012-38396-C03 (I + D + I Spanish Plan with UE-FEDER funds).

Data availability

The data used is presented in the article itself.

References

Allmendinger, R.W., Cardozo, N., Fisher, D., 2012. Structural Geology Algorithms: Vectors and Tensors in Structural Geology. Cambridge University Press (book to be published in early 2012).

Archanjo, C.J., Launeau, P., Bouchez, J.L., 1995. Magnetic fabric vs. magnetite and biotite shape fabrics of the magnetite-bearing granite pluton of Gameleiras (Northeast Brazil). Physics of the Earth and Planetary Interiors 89 (1–2), 63–75.
Archanjo, C.J., Trindade, R.I.F., Bouchez, J.L., Ernesto, M., 2002. Granite fabrics and regional-scale partitioning in the Seridó belt (Borborema Province, NE Brazil). Tectonics 21 (1), 3–14. https://doi.org/10.1029/2000TC001269, 3-1.
Assis, O.S., 2019. Petrografía y fábrica magnética de la granodiorita varvarco y plutones asociados, cretácico tardío-paleoceno de los Andes neuquinos. Final Degree Project in Geology. Universidad de Río Negro. Published thesis. http://rid.unrn.edu.ar/jspui/handle/20.500.12049/2256.
Assis, O.S., Zaffarana, C.B., Orts, D., Puigdomenech, C., Ruiz González, V., Gallastegui, G., Hauser, N., Kiseeva, E.S., Molina, J.F., Pernich, S., 2021. Emplacement conditions and exhumation of the Varvarco Tonalite and associated plutons from the Cordillera del Viento, Southern Central Andes. Geological Magazine. https://doi.org/10.1017/S0016756821001163.
Azcuy, C.L., Caminos, R., 1987. In: Diastrofismo, En Archangelsky, S. (Eds.), El sistema Carbonífero en la República Argentina. Academia Nacional de Ciencias, Córdoba, pp. 239–251.
Bastías-Mercado, F., González, J., Oliveros, V., 2020. Volumetric and compositional estimation of the Choiyoi magmatic province and its comparison with other silicic large igneous provinces. Journal of South American Earth Sciences 103, 102749.
Borradaile, G.J., Henry, B., 1997. Tectonic applications of magnetic suscep- tibility and its anisotropy. Earth-Science Reviews 42, 49–93. https://doi.org/10.1016/S0012-8252(96)00044-X.
Borradaile, G.J., Jackson, M., 2010. Structural geology, petrofabrics and magnetic fabrics (AMS, AARM, AIRM). Journal of Structural Geology 32 (10), 1519–1551. https://doi.org/10.1016/j.jsg.2009.09.006.
Bouchez, J.L., 1997. Granite Is Never Isotropic: an Introduction to AMS Studies of Granitic Rocks, pp. 95–112. https://doi.org/10.1007/978-94-017-1717-5_6.
Bouchez, J.L., Nicolas, A., 2021. Principles of Rock Deformation and Tectonics. Oxford University Press.
Bracaccini, O., 1970. Rasgos tectónicos de las acumulaciones mesozoicas en las provincias de Mendoza y Neuquén, República Argentina. Revista de la Asociación Geológica Argentina 25 (2), 275–282.
Candela, P.A., 1997. A review of shallow, ore-related granites: textures, volatiles, and ore metals. Journal of Petrology 38 (12), 1619e1633.
Capomassi, J.I., D'Annunzio, M.C., Strazzere, L., 2023. Petrografía, geoquímica y relaciones estratigráficas de las unidades paleozoicas y mesozoicas del cerro Las Minas, Distrito Minero Andacollo, Neuquén, Argentina. Revista de la Asociación Geológica Argentina 80 (3), 418–435.
Cardozo, N., Allmendinger, R.W., 2013. Spherical projections with OSXStereonet. Computers & Geosciences 51, 193–205. https://doi.org/10.1016/j.cageo.2012.07.021.
Casé, A.M., López-Escobar, L., Danieli, J.C., Schalamuk, A., 2008. Butalón igneous rocks, Neuquén, Argentina: age, stratigraphic relationships and geo- chemical features. Journal of South American Earth Sciences 26, 188–203. https://doi.org/10.1016/j.jsames.2007.11.001.
Chadima, M., Cajz, V., Týcová, P., 2009. On the interpretation of normal and inverse magnetic fabric in dikes: examples from the Eger Graben, NW Bohemian Massif. Tectonophysics 466 (1–2), 47–63.
Cruden, A.R., Tobisch, O.T., Launeau, P., 1999. Magnetic fabric evidence for conduitfed emplacement of a tabular intrusion: dinkey Creek Pluton, central Sierra Nevada batholith, California. Journal of Geophysical Research 104, 10–511. https://doi.org/10.1029/1998JB900093, 10,530.
Chadima, M., Jelinek, V., 2008. Anisoft 4.2 - Anisotropy Data Browser. Contributions to Geodesy 38 (Special Issue), 38–41.
Cobbold, P.R., Rossello, E.A., 2003. Aptian to recent compressional deformation, foothills of the Neuquén Basin, Argentina. Marine and Petroleum Geology 20 (5), 429–443.
de Saint Blanquat, M., Tikoff, B., 1997. Development of magmatic to solid-state fabrics during syntectonic emplacement of the mono creek granite, sierra Nevada batholith. In: Granite: from Segregation of Melt to Emplacement Fabrics. Springer, Dordrecht, pp. 231–252. Netherlands.
de Saint Blanquat, M., Tikoff, B., Teyssier, C., Vigneresse, J.L., 1998. Transpressional kinematics and magmatic arcs. In: Holdsworth, R.E., Strachan, R.A., Dewey, J.F. (Eds.), Continental Transpressional and Transtensional Tectonics, vol. 135. Geological Society of London Special Publication, pp. 327–340. https://doi.org/10.1144/GSL.SP.1998.135.01.21.
D'Eramo, F., Pinotti, L., Tubía, J.M., Vegas, N., Aranguren, A., Tejero, R., Gómez, D., 2006. Coalescence of lateral spreading magma ascending through dykes: a mechanism to form a granite canopy (El Hongo pluton, Sierras Pampeanas, Argentina). Journal of the Geological Society 163 (5), 881–892.
Dicaro, S., Pons, M.J., González, S.N., Greco, G.A., 2024. Pre-choiyoi volcanism at the southwestern margin of Gondwana (~ 37° S): characterisation of the Arroyo Del Torreón Formation and Sofía Dacite and Their Regional Implications. J. S. Am. Earth Sci. 148, 105158.
Digregorio, J.H., 1972. Neuquén. In: Leanza, A.F. (Ed.), Geología Regional Argentina. Academia Nacional de Ciencias, Córdoba, pp. 439–505.
Dunlop, D.J., 2002. Theory and application of the Day plot (Mrs/Ms versus Hcr/Hc) 1. Theoretical curves and tests using titanomagnetite data. Journal of Geophysical Research: Solid Earth 107 (B3), EPM–4.
Ferré, E.C., Améglio, L., 2000. Preserved magnetic fabrics vs. annealed microstructures in the syntectonic recrystallised George granite, South Africa. Journal of structural geology 22 (8), 1199–1219.
Franchini, M., López-Escobar, L., Schalamuk, I.B.A., Meinert, L., 2003. Magmatic characteristics of the paleocene cerro nevazón region and other late cretaceous to early tertiary calc-alkaline subvolcanic to plutonic units in the Neuquén Andes, Argentina. Journal of South American Earth Sciences 16, 399–421. https://doi.org/10.1016/S0895-9811(03)00103-2.
Fossen, H., Tikoff, B., Teyssier, C., 1994. Strain modeling of transpressional and transtensional deformation. Norsk Geologisk Tidsskrift 74, 134–145.
Fossen, H., Tikoff, B., 1998. Extended models of transpression and transtension, and application to tectonic settings. In: Holdsworth, R.E., Strachan, R.A., Dewey, J.F. (Eds.), Continental Transpressional and Transtensional Tectonics, vol. 135. Geological Society of London Special Publication, pp. 15–33. https://doi.org/10.1144/GSL.SP.1998.135.01.02.
Giacosa, R., Allard, J., Foix, N., Heredia, N., 2014. Stratigraphy, structure and geodynamic evolution of the Paleozoic rocks in the Cordillera del Viento (37° S latitude, Andes of Neuquén, Argentina). Journal of Iberian Geology 40 (2), 331–348. https://doi.org/10.5209/rev_JIGE.2014.v40.n2.45301.
Hervé, F., Calderón, M., Fanning, C.M., Pankhurst, R.J., Godoy, E., 2013. Provenance variations in the Late Paleozoic accretionary complex of central Chile as indicated by detrital zircons. Gondwana Research 23 (3), 1122–1135. https://doi.org/10.1016/j.gr.2012.06.016.
Horsman, E., Morgan, S., de Saint-Blanquat, M., Habert, G., Nugent, A., Hunter, R.A., Tikoff, B., 2009. Emplacement and assembly of shallow intrusions from multiple magma pulses, Henry Mountains, Utah. Earth and Environmental Science Transactions of the Royal Society of Edinburgh 100 (1–2), 117–132.
Jackson, M., 1991. Anisotropy of magnetic remanence - a brief review of mineralogical sources, physical origins and geological applications, and comparison with susceptibility anisotropy. Pure and Applied Geophysics 136, 1–28.
Jasonov, P.G., Nourgaliev, D.K., Burov, B.V., Heller, F., 1998. A modernized coercivity spectrometer. Geologica Carpathica 49 (3), 224–226.
Jagadeesh, M.S., Seehra, M.S., 1981. Principal magnetic susceptibilities of MnO and their temperature dependence. Physical Review B 23 (3), 1185.
Jelinek, V., 1981. Characterization of the magnetic fabric of rocks. Tectonophysics 79 (3–4), 63–67. https://doi.org/10.1016/0040-1951(81)90110-4.
JICA, Japan International Cooperation Agency, 2001. Report on Re- Gional Survey for Mineral Resources in the Southern Andes Area. Argentine Republic. Final Report, p. 378. March 2001. Informe MPN- JR-01-077, Tokio - Buenos Aires, (unpublished).
Kay, S.M., Ramos, V.A., Mpodozis, C., Sruoga, P., 1989. Late paleozoic to jurassic silicic magmatism at the Gondwana margin: analogy to the middle proterozoic in north America? Geology 17 (4), 324–328.
Kay, S.M., Burns, W.M., Copeland, P., Mancilla, O., 2006. Upper Cretaceous to Holocene magmatism and evidence for transient Miocene shallowing of the Andean subduction zone under the northern Neuquén Basin. In: Evolution of an Andean Margin: A Tectonic and Magmatic View from the Andes to the Neuquén Basin (35°–39°S Lat), vol. 407. Geological Society of America, Special Papers, pp. 16–90. https://doi.org/10.1130/2006.2407(02. SM Kay and VA Ramos.
Kleiman, L.E., 1993. El volcanismo permo-triásico y triásico del Bloque de San Rafael (Provincia de Mendoza): Su potential uranífero. XII Congreso Geológico Argentino y II Congreso de Exploración de Hidrocarburos Actas 5, 284–293.
Kleiman, L.E., Japas, M.S., 2002. The lower Choiyoi volcanic sequence at 34-35 30'S, san Rafael, Mendoza, Argentina: evidence of active plate convergence. In: IGCP 436 Symposium: Pacifie Margin of Gondwana, Gondwana XI. Christchurch, New Zealand.
Kleiman, L.E., Japas, M.S., 2005. The upper Choyoi volcanism, San Rafael, Mendoza, Argentina: a transitional sequence emplaced under changing geodynamic conditions, paper presented at Gondwana XII. Academia Nacional de Ciencias, Mendoza, Argentina 211.
Kleiman, L.E., Japas, M.S., 2009. The Choiyoi volcanic province at 34 S–36 S (san Rafael, Mendoza, Argentina): implications for the late palaeozoic evolution of the southwestern margin of Gondwana. Tectonophysics 473 (3–4), 283–299. Sato.
Lanza, R., Meloni, A., 2006. The earth's magnetism: an introduction for geologists. https://doi.org/10.1007/978-3-540-27980-8.
Llambías, E., 1986. Intrusivos Permicos del Sur de la Cordillera del Viento, Provincia del Neuquen. Asociación Geológica Argentina, Revista XLI 11, 11.
Llambías, E.J., Kleiman, L.E., Salvarredi, J.A., 1993. El magmatismo gondwánico. In: Ramos, V. (Ed.), Geología y Recursos Naturales de Mendoza, Congreso Geológico Argentino, vol. 12, pp. 53–64.
Llambías, E.J., Leanza, H.A., Carbone, O., 2007. Evolución Tectono-magmática durante el pérmico al Jurásico temprano en la Cordillera del Viento (37°05′S - 37°15′S): Nuevas evidencias geológicas y geoquímicas Del Inicio de la Cuencas Neuquina. Revista de La Asociacion Geologica Argentina 62 (2), 217–235.
Llambías, E.J., Aragón, E., 2011. Volcanismo paleógeno. In: Relatorio Del 18° Congreso Geológico Argentino, pp. 265–274. Neuquén.
Martínez Dopico, C.I., López de Luchi, M.G., Rapalini, A.E., Wemmer, K., Fanning, C.M., Basei, M.A.S., 2017. Emplacement and temporal constraints of the Gondwanan intrusive complexes of northern Patagonia: La Esperanza plutono-volcanic case. Tectonophysics 712–713, 249–269. https://doi.org/10.1016/j.tecto.2017.05.015.
Martín-Hernández, F., Dekkers, M.J., Bominaar-Silkens, I.M.A., Maan, J.C., 2008. Magnetic anisotropy behaviour of pyrrhotite as determined by low-and high-field experiments. Geophysical Journal International 174 (1), 42–54.
McNulty, B.A., Tobisch, O.T., Cruden, A.R., Gilder, S., 2000. Multistage emplacement of the Mount Givens pluton, central Sierra Nevada batholith, California. Geological Society of America Bulletin 112 (1), 119–135.
Méndez, V., Zanettini, J.C., Zappettini, E.O., 1995. Geología y metalogénesis del Orógeno Andino Central, República Argentina. Dirección Nacional de Servicio Geológico, Anales 23, Buenos Aires, p. 190.
Mpodozis, C., Kay, S.M., 1992. Late paleozoic to triassic evolution of the Gondwana margin: evidence from Chilean frontal cordilleran batholiths (28 S to 31 S). Geological Society of America Bulletin 104 (8), 999–1014.

Neves, S.P., Araújo, A.M., Correia, P.B., Mariano, G., 2003. Magnetic fabrics in the Cabanas Granite (NE Brazil): interplay between emplacement and regional fabrics in a dextral transpressive regime. Journal of Structural Geology 25 (3), 441–453.
Olivier, P., Druguet, E., Castaño, L.M., Gleizes, G., 2016. Granitoid emplacement by multiple sheeting during Variscan dextral transpression: the Saint-Laurent–La Jonquera pluton (eastern Pyrenees). Journal of Structural Geology 82, 80–92.
Paterson, S.R., Vernon, R.H., Tobisch, O.T., 1989. A review of criteria for the identification of magmatic and tectonic foliations in granitoids. Journal of structural geology 11 (3), 349–363.
Paterson, S.R., Fowler Jr, T.K., Schmidt, K.L., Yoshinobu, A.S., Yuan, E.S., Miller, R.B., 1998. Interpreting magmatic fabric patterns in plutons. Lithos 44 (1–2), 53–82. https://doi.org/10.1002/anie.198505761.
Pernich, S., 2021. Fábrica magnética y petrología del complejo volcánico-plutónico Huingancó, pérmico de la Cordillera del Viento, Andes neuquinos. Final Degree Project in Geology. Universidad Nacional de Río Negro. Published thesis. http://rid.unrn.edu.ar/handle/20.500.12049/7907.
Pons, A., D'Annunzio, M.C., Strazzere, L., Cócola, M.A., 2019. Características metalogenéticas de la veta Buena Vista, distrito minero Andacollo, Neuquén, Argentina. Revista de La Asociación Geológica Argentina 76 (3), 254–262.
Pons, M.J., Giacosa, R.E., Greco, G.A., González, S.N., Conedera, M., Nimis, P., Bordese, S., 2022a. Silver, gold, and base metals vein systems at Southern part of Cordillera del Viento, Neuquén Argentina. XXI Congreso Geológico Argentino. Puerto Madryn, Chubut.
Pons, M.J., Zattin, M., Giacosa, R.E., González, S.N., Greco, G.A., 2022b. Zircon and apatite fission track analyses: new insight about the exhumation of Cordillera del Viento. Neuquén Basin, Argentina.
Pons, M.J., Mendiberri, J., Arce, M., Greco, G.A., Musso, T.B., Fernández, M.L., Hauser, N., González, P.A., 2023. Geología, alteración hidrotermal y mineralogía del sistema de vetas Sofía-Julia-Valencia, distrito minero Andacollo, Neuquén, Argentina. Andean geology 50 (1), 93–126.
Ramos, V.A., 1988. The Tectonics of the Central Andes; 30 to 33 S Latitude.
Ramos, V.A., Mosquera, A., Folguera, A., García Morabito, E., 2011a. Evolución tectónica de los Andes y del Engolfamiento Neuquino adyacente. In: Geología y Recursos Naturales de la Provincia de Neuquén. Relatorio del VXIII Congreso Geológico Argentino, Buenos Aires, pp. 335–348.
Ramos, V.A., Folguera, A., García Morabito, E., 2011b. Las provincias geológicas del Neuquén. In: Geología y Recursos Naturales de la Provincia del Neuquén. Relatorio 18° Congreso Geológico Argentino, Neuquén, pp. 317–326.
Rocher, S., Vallecillo, G., De Machuca, B.C., Alasino, P., 2015. El Grupo Choiyoi (Pérmico temprano-medio) en la Cordillera Frontal de Calingasta, San Juan, Argentina: Volcanismo de arco asociado a extensión. Revista Mexicana de Ciencias Geologicas 32 (3), 415–432.
Rochette, P., 1988. Inverse magnetic fabric in carbonate-bearing rocks. Earth and Planetary Science Letters 90, 229–237.
Rochette, P., Jackson, M., Aubourg, C., 1992. Rock magnetism and the interpretation of magnetic susceptibility. Reviews of Geophysics 30 (92), 209–226.
Rojas Vera, E.A., Mescua, J., Folguera, A., Becker, T.P., Sagripanti, L., Fennell, L., Orts, D., Ramos, V.A., 2015. Evolution of the Chos Malal and Agrio fold and thrust belts, Andes of Neuquén: insights from structural analysis and apatite fission track dating. Journal of South American Earth Sciences 64 (April 2016), 418–433. https://doi.org/10.1016/j.jsames.2015.10.001.
Rovere, E., Caselli, A.T., Hugo, C., Leanza, H., Folguera, A., Escosteguy, L., Geuna, S., González, R., Colombino, J.E., Danieli, J., 2004. Hoja Geológica Andacollo (3772-IV), Provincia de Neuquén. Programa Nacional de Cartas Geológicas de La República Argentina, Escala 1, 250000–250104.
Sagripanti, L., Folguera, A., Giménez, M., Rojas Vera, E.A., Fabiano, J.J., Molnar, N., Fennell, L., Ramos, V.A., 2014. Geometry of Middle to Late Triassic extensional deformation pattern in the Cordillera del Viento (Southern Central Andes): A combined field and geophysical study. Journal of Iberian Geology 40 (2), 349–366. https://doi.org/10.5209/rev_jige.2014.v40.n2.45305.
Sánchez, N.P., Coutand, I., Turienzo, M., Lebinson, F., Araujo, V., Dimieri, L., 2018. Tectonic evolution of the Chos Malal Fold-and-Thrust belt (Neuquén Basin, Argentina) from (U-Th)/He and fission track thermochronometry. Tectonics 37 (7), 1907–1929. https://doi.org/10.1029/2018TC004981.
Sánchez, N., Turienzo, M., Coutand, I., Lebinson, F., Araujo, V., Dimieri, L., 2020. Structural and thermochronological constraints on the exhumation of the Chos Malal fold and thrust belt (~ 37 S). Opening and closure of the Neuquén Basin in the southern Andes 323–340.
Sato, A.M., Llambías, E.J., Basei, M.A.S., Leanza, H.A., 2008. The Permian Choiyoi cycle in Cordillera del Viento (Principal Cordillera, Argentina): Over 25 Ma of magmatic activity. In: VI° South American Symposium on Isotope Geology.
Sato, A.M., Llambías, E.J., Basei, M.A.S., Castro, C.E., 2015. Three stages in the Late Paleozoic to Triassic magmatism of southwestern Gondwana, and the relationships with the volcanogenic events in coeval basins. Journal of South American Earth Sciences 63, 48–69. https://doi.org/10.1016/j.jsames.2015.07.005.
Stoll, W.C., 1957. Geología y depósitos minerales de Andacollo, Pro- vincia de Neuquén. Dirección Nacional de Minería, Buenos Aires, Anales 11, 36.
Stevenson, C., 2009. The relationship between forceful and passive emplacement: the interplay between tectonic strain and magma supply in the Rosses Granitic Complex, NW Ireland. Journal of Structural Geology 31 (3), 270–287.
Strazzere, L., Geraldes, M.C., Gregori, D., 2024. Geochronological data from the Arroyo del Torreón Formation, Andacollo minning District. Neuquén, Argentina. In: Paper presented at the Proceedings of the XIII South American Symposium on Isotope Geology.
Suárez, M., De la Cruz, R., Fanning, M., Etchart, H., 2008. Carboniferous, Permian and Toarcian magmatism in Cordillera del Viento, Neuquén, Argentina: first U-Pb shrimp dates and tectonic implications. Actas 17, 906–907.
Tarling, D.H., Hrouda, F., 1993. Magnetic Anisotropy of Rocks. Springer Science & Business Media.
Tikoff, B., Greene, D., 1997. Stretching lineations in transpressional shear zones: an example from the Sierra Nevada Batholith, California. Journal of Structural Geology 19, 29–39. https://doi.org/10.1016/S0191-8141(96)00056-9.
Turienzo, M., Sánchez, N., Lebinson, F., Dimieri, L., 2018. The structure of the southern central Andes (Chos Malal Fold and thrust belt). The Evolution of the Chilean-Argentinean Andes 411–441.
Uliana, M.A., Biddle, K.T., 1988. Mesozoic-Cenozoic paleogeographic and geodynamic evolution of southern South America. Revista Brasileira de geociencias 18 (2), 172–190.
Zaffarana, C.B., Somoza, R., Orts, D.L., Mercader, R., Boltshauser, B., González, V.R., Puigdomenech, C., 2017. Internal structure of the late triassic central patagonian batholith at gastre, southern Argentina: implications for pluton emplacement and the gastre fault system. Geosphere 13 (6), 1973–1992.
Žák, J., Schulmann, K., Hrouda, F., 2005. Multiple magmatic fabrics in the Sázava pluton (Bohemian Massif, Czech Republic): a result of superposition of wrench-dominated regional transpression on final emplacement. J. Struct. Geol. 27 (5), 805–822.
Zannettini, J.C.M., Santamaria, G.R., Leanza, H., 2001. Hoja geologica las ovejas - 3772-II. Programa Nacional de Cartas Geológicas de La República Argentina, Escala 1, 250000–250066.
Zappettini, E.O., Lagorio, S.L., Dalponte, M., Orestes, J., Belousova, E., 2018. Evidencias de magmatismo precuyano (Pliensbachiano - Toarciano) en el norte de la Cordillera del Viento, provincia del Neuquén: caracterización geoquímica, isotópica e implicancias tectónicas. Revista de La Asociación Geológica Argentina 75 (4), 533–558.
Zöllner, W., Amos, A.J., 1955. Acerca del Paleozoico superior y Triásico del cerro La Premia, Neuquén. Revista de la Asociación Geológica Argentina 10 (2), 127–135. Buenos Aires.
Zöllner, W., Amos, A.J., 1973. Descripción geológica de la Hoja 32b, Chos Malal, provincia del Neuquén, vol. 143. Servicio Geológico Minero Argentino, Boletín, p. 91. Buenos Aires.